Ligand binding, activation, and stabilization of the orphan G protein-coupled receptor GPR17

Dissertation

zur

Erlangung des Doktorgrades (Dr. rer. nat.)

der

Mathematisch-Naturwissenschaftlichen Fakultät

der

Rheinischen Friedrich-Wilhelms-Universität Bonn

vorgelegt von

Michael Lewash

aus

Berlin

Bonn 2025

Angefertigt mit Genehmigung der Mathematisch-Naturwissenschaftlichen Fakultät der Rheinischen Friedrich-Wilhelm-Universität Bonn

Gutachterin/Betreuerin: Prof. Dr. Christa E. Müller
Gutachterin: PD Dr. Anke C. Schiedel

Tag der Promotion: 12.12.2025
Erscheinungsjahr: 2026

Die vorliegende Arbeit wurde in der Zeit von August 2021 bis Juli 2025 am Pharmazeutischen Institut der Rheinischen Friedrich-Wilhelms-Universität Bonn unter der Leitung von Frau Prof. Dr. Christa E. Müller angefertigt.

Table of contents

1 Abstract

G protein-coupled receptors (GPCRs) are one of the largest protein families in the human genome with more than 800 different sequences. They are transmembrane proteins that mediate the transduction of signals from extracellular to intracellular compartments. GPCRs are one of the most important classes of drug targets. More than 30 % of all approved therapeutics activate or inhibit GPCRs. However, drugs that are used to treat human diseases target only about 10 % of human GPCRs. Orphan GPCRs, for which the physiological agonist is still unknown or unconfirmed, represent an untapped group of potential drug targets.

The orphan GPCR GPR17 belongs to the δ-branch of class A (rhodopsin-like) receptors and is primarily expressed in the central nervous system, particularly in oligodendrocyte progenitor cells and pre-oligodendrocytes. It has emerged as a promising therapeutic target for a range of diseases including multiple sclerosis, neurodegenerative disorders, diabetes, glioblastoma, and ischemic stroke.

However, GPR17 is still underresearched. This dissertation presents research results from several subprojects related to the receptor. The first major part (Chapters 4–6) focuses on the modulation of GPR17 by agonists and antagonists, which were tested in calcium mobilization and radioligand binding assays. Since the endogenous agonist of GPR17 has not been identified yet, efforts to deorphanize GPR17 have been pursued, including the evaluation of previously proposed endogenous ligand 24(*S*)-hydroxycholesterol and further candidates. A virtual screening approach was employed to identify potential endogenous ligands based on molecular docking utilizing a homology model of the receptor. In parallel, novel synthetic ligands were investigated. A previous collaboration led to the discovery and optimization of anthranilic acid-based GPR17 antagonists. Through systematic structure–activity relationship studies, potent and selective compounds were identified, including PSB-22269 and PSB-24040, which showed nanomolar inhibitory activity and high binding affinity. Further GPR17 antagonists were also investigated, including 3-(3-carboxypropyl)indole-based, indolylsulfonamide-based, and peptide-mimetic scaffolds. These tool compounds will facilitate future studies and may serve as lead structures for therapeutic development.

The second major part (Chapter 7) addresses the stabilization of GPR17 for structural studies to identify and characterize the ligand binding site as a basis for further drug development. Multiple strategies were employed, including point mutations, truncations, junction site optimization of the fusion protein BRIL, varying expression conditions in *Sf9* and *Tni* insect cells, and varying purification conditions. These efforts significantly improved receptor yield and thermostability, laying the foundation for its future structural elucidation by X-ray crystallography or cryo-electron microscopy.

2 Introduction

2.1 Receptors and ligands

Receptors are specialized proteins that translate chemical signals into biological responses, allowing cells and organisms to respond to their environment. These signals are typically carried by ligands – endogenous molecules such as neurotransmitters and hormones, or exogenous compounds such as drugs and toxins – that bind to receptors and induce changes in their conformational state. This triggers a signaling cascade that ultimately leads to physiological responses dictated by the receptor type and the nature of the ligand. This interaction is highly selective, akin to a lock and key, ensuring that only the appropriate signal elicits a response.[1]

The interaction between ligands and receptors can be characterized by various key parameters: Affinity describes the strength of ligand-receptor interactions and is expressed as the dissociation constant (K_d) or the inhibition constant (K_i), representing the concentration required to occupy half of the available receptor sites. Efficacy, quantified as E_{max}, represents the maximum effect a ligand can achieve. Potency, expressed as EC_{50} (half-maximal effective concentration), reflects the ligand concentration required to elicit 50 % of the maximal response (see **Figure 1**).[2] These parameters are assessed in pharmacological assays. Binding assays measure direct ligand-protein interactions, often employing radiolabeled or fluorescent ligands.[3; 4] Functional assays evaluate receptor activity in biological systems, including cellular assays measuring second messengers like calcium ions (Ca^{2+}) or cyclic adenosine monophosphate (cAMP).[5; 6]

Even in the absence of a ligand, a receptor is thought to exist in a dynamic balance between its active and inactive states.[1] Ligands can shift this equilibrium: Agonists are ligands that, upon binding, stabilize the receptor in its active state and increase receptor signaling, while inverse agonists stabilize the inactive state and reduce the basal activity.[7] Naturally occurring agonists within the body that bind to and activate specific receptors are called endogenous, physiological, or cognate agonists. Agonists can be full (eliciting maximal response) or partial (producing submaximal activation).[2] Agonists and inverse agonists can be thought of as drugs with affinity and efficacy (or negative efficacy in the case of inverse agonists). In contrast, neutral antagonists show affinity but no efficacy: they bind to the receptor without shifting the equilibrium, effectively stabilizing the receptor and preventing binding of (inverse) agonists. The potency of inverse agonists and neutral antagonists (commonly subsumed as antagonists) is expressed

as IC_{50} (half-maximal inhibitory concentration), the ligand concentration required to reduce the agonist response, typically determined at its EC_{50} or EC_{80} concentration, to 50 % (see **Figure 1**).[2]

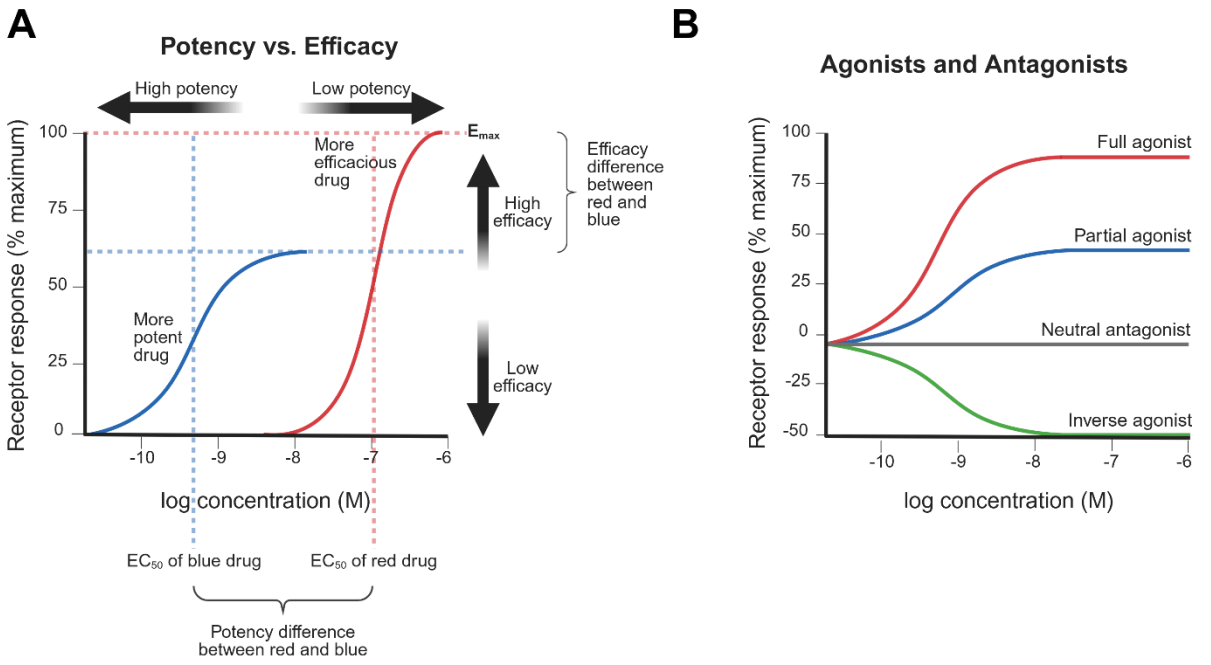

Figure 1. Pharmacological properties of ligands. (A) Visualization of potency and efficacy differences in dose-response curves. (B) Visualization of full agonism, partial agonism, inverse agonism, and neutral antagonism as dose-response curves. (A, B) Created with BioRender.com.

For instance, the nucleoside adenosine accumulates in the brain in the course of prolonged wakefulness, acts as the endogenous agonist at the adenosine A_1 and A_{2A} receptor subtypes in the brainstem and forebrain, and facilitates sleep initiation and consolidation through inhibition of excitatory neurons. Conversely, caffeine acts as an antagonist with inverse agonistic activity at adenosine A_1 and A_{2A} receptors, reduces signaling, prevents activation by adenosine, and in turn promotes wakefulness.[8; 9]

Apart from these orthosteric agonists and antagonists there are further ligands called allosteric modulators that bind to distinct sites and mediate receptor activation (positive allosteric modulators, PAMs) or inhibition (negative allosteric modulators, NAMs).[2]

Receptors can be categorized based on their location, structure, and mechanism of action. Intracellular receptors are located in the nucleus or the cytoplasm and can regulate gene expression by binding to DNA and altering transcription levels.[10] In contrast, cell-surface or membrane-bound receptors are typically embedded within the lipid bilayer and mediate the transduction of signals from extracellular to intracellular domains. Key types include ligand-gated

ion channels, which, upon activation, enable specific ions to cross the membrane;[11] and enzyme-linked receptors, such as receptor tyrosine kinases, which have an intracellular domain with enzymatic activity;[12] moreover, there are G protein-coupled receptors (GPCRs) (see **Figure 2**), which will be discussed in detail in the following chapter.

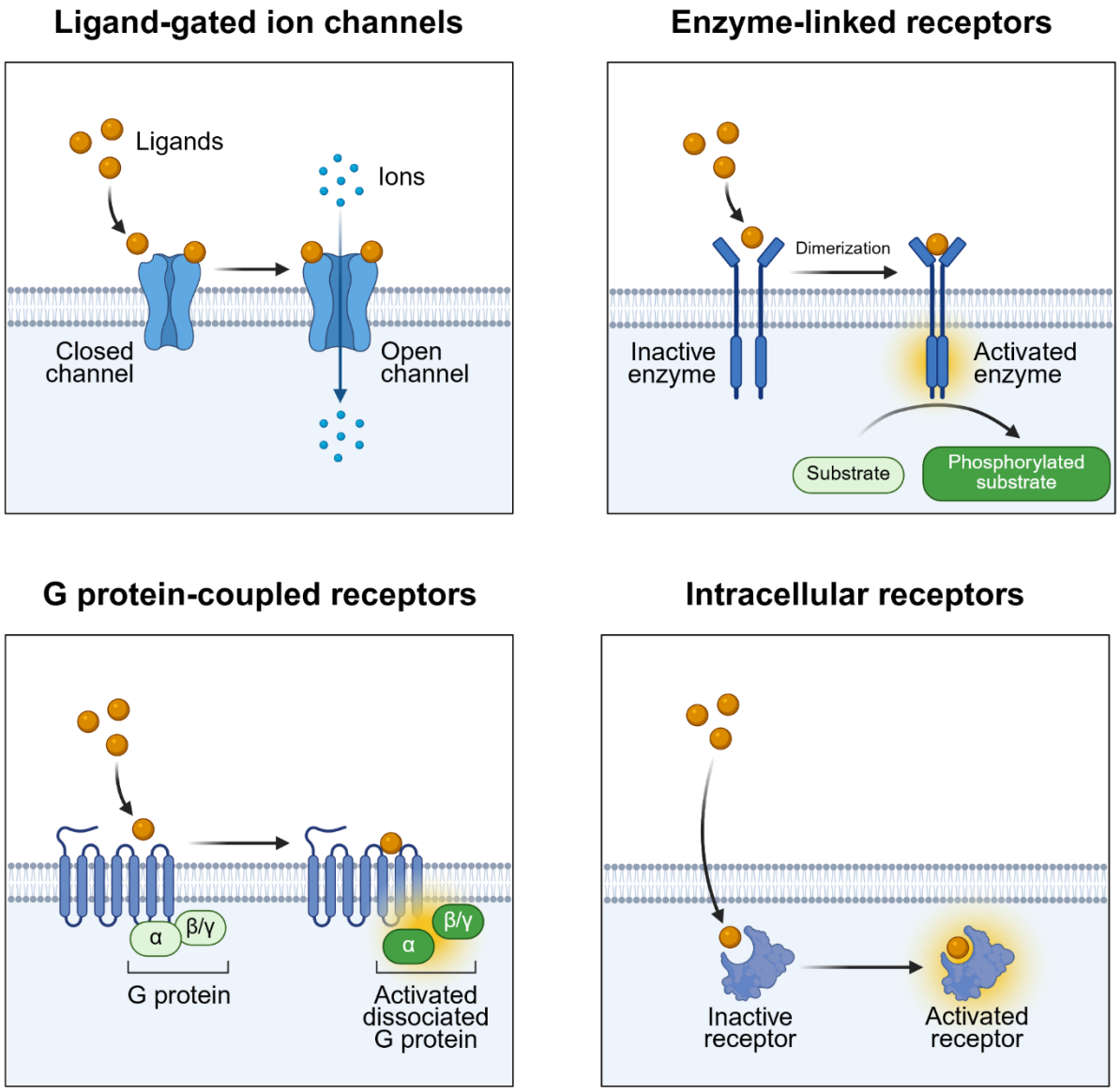

Figure 2. Different receptor types: ligand-gated ion channels, enzyme-linked receptors, G protein-coupled receptors (GPCRs), and intracellular receptors. Ligand-gated ion channels and GPCRs are typically membrane-bound, as depicted here, but there are also intracellular types. Created with BioRender.com.

2.2 G protein-coupled receptors

Among the various receptor families, GPCRs represent the largest group.[13; 14] They share a characteristic structure containing an extracellular N-terminus, an intracellular C-terminus, and

seven transmembrane (TM) helices connected by intracellular loops (ICLs) and extracellular loops (ECLs).[15] Therefore, they are also referred to as "7-TM receptors". GPCRs function by coupling to intracellular G proteins, which relay signals to downstream effectors.[16] They possess a wide variety of different ligands, e.g., biogenic amines such as adrenaline and dopamine, amino acids such as glutamate, γ-aminobutyric acid, lipids, peptides and proteins, nucleosides and nucleotides, and even calcium ions or – in the case of rhodopsin in the retina of the eye – light (see Figure 1).[17] These receptors are essential for many different processes in the human body, such as vision, smell, taste, heart, liver, lung, kidney, and brain functions, cell proliferation and migration, and many other processes.[15] In short, GPCRs are essential for life, and research on G proteins and GPCRs was honored by the awards of the Nobel Prize in Physiology or Medicine 1994 to Alfred G. Gilman and Martin Rodbell[18] and the Nobel Prize in Chemistry 2012 to Robert J. Lefkowitz and Brian Kobilka.[19]

GPCRs are at present one of the most important classes of targets for approved drugs and also for those in preclinical and clinical development. It is estimated that more than 30 % of all approved therapeutic drugs activate or inhibit GPCRs.[20] However, for only about 10 % of the more than 800 GPCRs present in human beings, drugs have been developed so far that are used as therapeutics to treat human diseases.[21]

2.2.1 Classification

There are two main classification schemes that have been proposed for this superfamily. The classical A-F system presented in 1994[22; 23] groups GPCRs from both vertebrates and invertebrates into six classes based on sequence homology: class A (rhodopsin-like), class B (secretin receptor family), class C (metabotropic glutamate/pheromone), class D (fungal mating pheromone receptors), class E (cyclic AMP receptors), and class F (frizzled/smoothened). Class D and E are not present in vertebrates but only in lower species. The alternative GRAFS system (glutamate, rhodopsin, adhesion, frizzled/taste2, secretin), focusing on GPCRs in vertebrates, distinguishes between secretin-like and adhesion-like receptors, and corresponds to the classical classes C, A, B2, F, and B.[24] Class A (or rhodopsin-like receptors), which is the largest class of GPCRs and represents nearly 85 % of GPCR genes, is further subdivided into four branches: α, β, γ, and δ. Of these, the α-branch, harboring biogenic amine and adenosine receptors, among others, is the best investigated one (see **Figure 3**).[25]

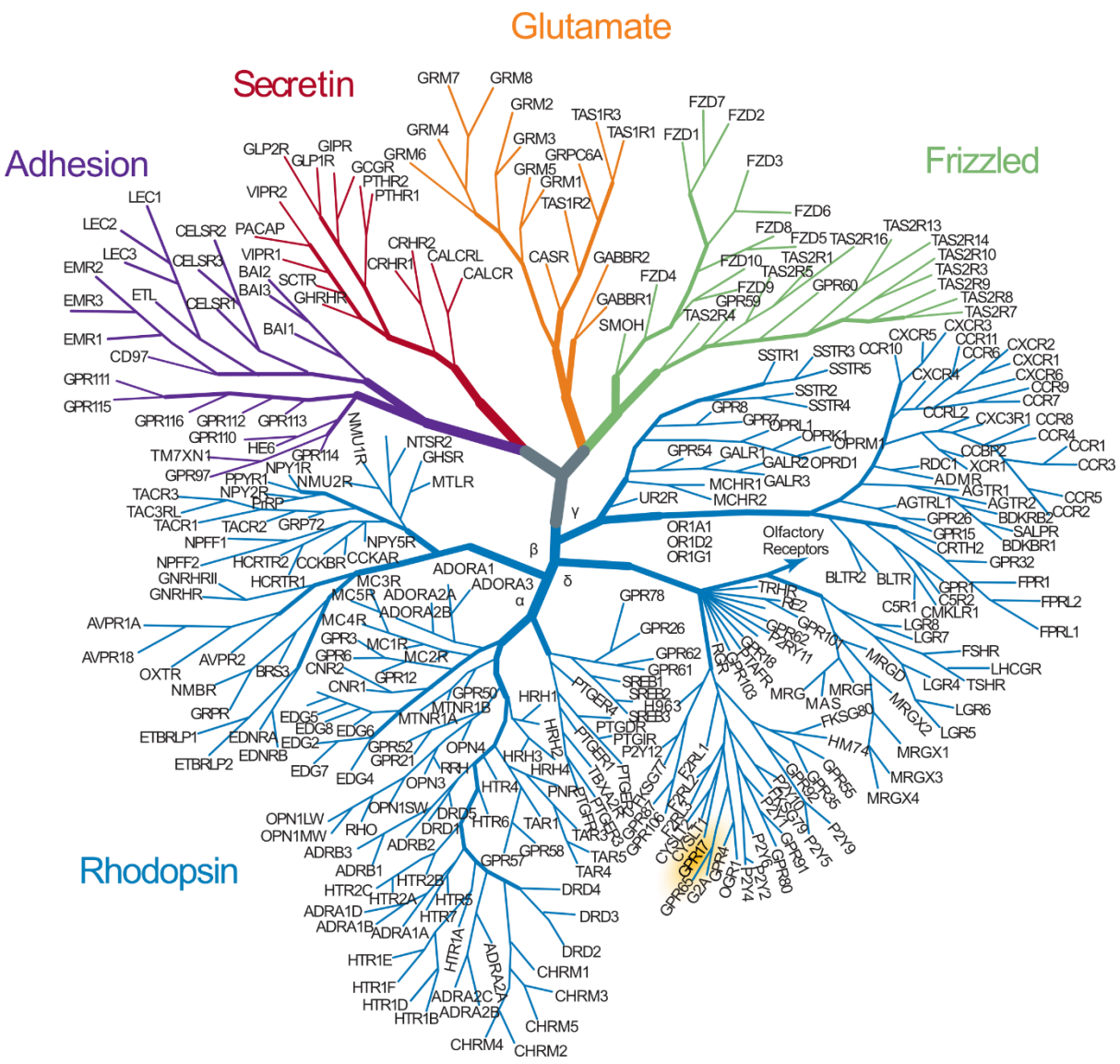

Figure 3. Phylogenetic tree showing GPCRs according to the GRAFS classification system. GPCRs are named according to their Uniprot entry name. The δ-branch class A orphan GPCR GPR17 is highlighted. Adapted with permission from Stevens et al.[26] Modified by Andhika B. Mahardhika and Michael Lewash.

GPCRs differ due to evolution, but still have characteristic amino acids at certain positions in their sequence. However, these positions are often slightly offset. The Ballesteros-Weinstein system makes the positions easier to compare by using two numbers. The most conserved amino acid X in transmembrane domain Y is defined as position 50 ($X^{Y.50}$). In the direction of the N-terminus, this number decreases by one with each amino acid, and in the direction of the C-terminus it increases accordingly.[27; 28]

2.2.2 Structure determination

The structural elucidation of GPCRs has been a monumental achievement in structural biology and has profoundly impacted on structure-based drug design. By revealing orthosteric ligand binding pockets and by providing insights into different receptor conformations, these structures are used, e.g., to guide compound structure design and optimize compound potency and efficacy in computer-aided modeling and docking studies.[29]

X-ray crystallography and the more recent cryo-electron microscopy (cryo-EM) are the two primary methods for determining macromolecular structures. X-ray crystallography relies on the highly ordered arrangement of molecules within crystals. X-rays interacting with the crystal generate a diffraction pattern that can be used to reconstruct a 3D electron density map and ultimately an atomic model.[30] For GPCRs, X-ray crystallography generally requires receptor stabilization and extensive condition optimization, making it more time-consuming. However, it has lower equipment costs, a traditionally higher achievable resolution, and a lower protein size threshold than cryo-EM, which is why it remains the gold standard for obtaining relatively small, inactive-state GPCR structures not in complex with signaling partners.[31] Cryo-EM, on the other hand, directly images macromolecules using transmission electron microscopy. Vitrification in amorphous ice preserves the sample and minimizes light-induced damage. Two-dimensional images from randomly oriented molecules are then computationally combined to generate a 3D reconstruction.[32] Recent advances in detector technology and processing algorithms – referred to as the "Resolution Revolution" – have significantly improved the resolution achievable with cryo-EM compared to its early days.[33] Due to its faster workflow, an increasing number of GPCR structures have been determined using cryo-EM in recent years, particularly active-state structures in complex with intracellular effectors such as G proteins.[31]

First insights into GPCR architecture started in the 1990s by employing X-ray crystallography. A major breakthrough was the determination of the first high-resolution (2.8 Å; a resolution below 3 Å is deemed high) crystal structure of rhodopsin in the year 2000.[34] The next significant milestone was the structure elucidation of the first human GPCRs, namely β2- and β1-adrenergic receptors, in 2007 and 2008, respectively.[35; 36] Since then, the number of determined GPCRs structures has grown exponentially due to improved protein expression and purification methods, receptor engineering techniques, and the aforementioned advancements in cryo-EM technologies. Today, over 450 structures of over 80 different GPCRs have been experimentally

determined.[37] Of these, more than 90 % employed cryo-EM.[37] Up to now, by far the best-investigated subclass of GPCRs are the biogenic amine receptors. However, other GPCR subfamilies can differ substantially, e.g., with regard to binding site and activation mechanism.[37] In contrast to intracellular receptors, which have an easier-to-simulate environment, the structural determination of membrane proteins such as GPCRs is particularly challenging because it requires extraction from their native membranes and purification, often leading to destabilization, conformational changes, and/or aggregation. Optimization for each specific receptor subtype is therefore required. Several techniques, especially for preparing proteins for crystallization, have been developed to overcome these obstacles:

- Single point mutations: Specific mutations, identified through experimental screening or computational methods based on existing structures, can enhance receptor thermostability and/or expression. A single S91$^{3.39}$K point mutation in the human adenosine A_{2A} receptor increased its melting temperature (T_M) by approximately 10°C compared to the unmutated construct and allowed structural determination of the receptor at 2.3 and 2.6 Å resolution, in complex with the preladenant conjugates PSB-2113 and PSB-2115, respectively, using X-ray crystallography.[38]
- Removal or replacement of flexible parts: N- and C-termini are often (partially) removed from constructs because they tend to be flexible and disordered. This intrinsic flexibility increases conformational heterogeneity, which can prevent crystallization and structure determination. Additionally, hydrophilic fusion proteins, such as the thermostabilized apocytochrome b_{562}RIL (BRIL) or T4 lysozyme, are often inserted into flexible regions including the N-terminus or the intracellular loop 3 (ICL3) to provide additional crystal contacts and enhance crystal and diffraction quality.[39; 40]
- Antibody or nanobody complex formation: Antibodies or antibody fragments (nanobodies) have been used to stabilize GPCRs especially in unstable active-state confromations.[41] The nanobody Nb35 was used to stabilize an intermediate complex of the A_{2A} receptor in combination with a heterotrimeric G protein and bound to small agonist 5'-*N*-ethylcarboxamidoadenosine (NECA) at 2.6 Å resolution using cryo-EM.[42]
- Stabilizing ligands: High-affinity ligands with slow dissociation rates and thus long residence times can reduce receptor flexibility and stabilize specific conformations.[43]

- Detergents and Lipidic Cubic Phase (LCP): Detergents are essential for solubilizing GPCRs from their native membranes. The LCP technique mimics the membrane environment further. It was pivotal in solving the structure of rhodopsin and has since been widely adopted for GPCR crystallization.[44]

Additionally, GPCR structures can be predicted by computational methods. DeepMind's neural network-based model, AlphaFold 2, made a major breakthrough in the 14th Critical Assessment of Structure Prediction (CASP14), demonstrating a median all-atom accuracy of 2.8 Å on the 58 protein domains of CASP14.[45] This success quickly led to the launch of the Alpha Fold Protein Structure Database in 2021, which now contains over 200 million protein structures.[46] This database has become an indispensable resource for diverse research purposes, from aiding experimental structure determination to accelerating drug discovery and mechanistic understanding. Recognizing their profound impact, Demis Hassabis and John Jumper of DeepMind were awarded one half of the 2024 Nobel Prize in Chemistry for their work on protein structure prediction.[47]

2.2.3 Signal transduction, receptor regulation, promiscuous coupling, and biased signaling

GPCRs transduce their signal via heterotrimeric guanine nucleotide-binding proteins, so-called G proteins, consisting of an α-, β-, and γ-subunit (see Figure 1 and Figure 3).[48] In the inactive state, the receptor is associated with a heterotrimeric G protein bound to guanosine diphosphate (GDP).[49; 50] Upon ligand binding and receptor activation, the GPCR undergoes a conformational shift from an equilibrium of inactive and active states toward an active conformation. Key to this process is the outward movement of transmembrane helix 6 (TM6), along with subtler movements of TM5 and TM7, creating a cavity on the intracellular side of the receptor.[51; 52] This movement is driven by conformational changes propagated from the ligand binding site through conserved microswitches like the sodium binding pocket at $D^{2.50}$ and $S^{3.39}$ and the DRY ($D^{3.49}$, $R^{3.50}$, $Y^{3.51}$) and NPxxY ($N^{7.49}$, $P^{7.50}$, $Y^{7.53}$) motifs. The C-terminal α5 helix of the Gα subunit can then insert into this pocket, which destabilizes the nucleotide binding site of the G protein, leading to the exchange of GDP for guanosine triphosphate (GTP).[50] Consequently, the Gα protein dissociates from the βγ-dimer and the receptor, thereby allowing both subunits to interact with downstream effector proteins, initiating the signal transduction cascade.[17] The G protein signaling cycle is eventually terminated by intrinsic GTPase activity of

the Gα subunit, which hydrolyzes GTP back to GDP, facilitating reassembly of the heterotrimeric complex with the receptor (see **Figure 4**). This process is accelerated by regulators of G protein signaling proteins, which act as GTPase-activating proteins, increasing the rate of GTP hydrolysis.

The human genome encodes 16 different Gα-subunits, which are subdivided into four families according to their protein sequence: $G\alpha_s$, $G\alpha_{i/o}$, $G\alpha_{q/11}$, and $G\alpha_{12/13}$.[53] Each family comprises several subtypes.[53] The different G proteins activate different second messenger systems, e.g., G_s proteins activate adenylate cyclase (AC) leading to increased intracellular cyclic adenosine-3',5'-monophosphate (cAMP) concentrations,[54] while G_i proteins inhibit AC leading to a reduction in cAMP formation in the cells. G_q proteins lead to an activation of phospholipase Cβ (PLC-β) that hydrolyzes phosphatidylinositol-4,5-bisphosphate (PIP_2) to generate diacylglycerol (DAG) and inositol trisphosphate (IP_3); then DAG triggers protein kinase C activation and IP_3 activates IP_3 receptors on the endoplasmic reticulum, resulting in a release of Ca^{2+} in the cells.[55] $G_{12/13}$ proteins regulate cytoskeletal dynamics via activation of Rho guanine nucleotide exchange factors (RhoGEFs), impacting cell morphology and migration.[56; 57]

The Gβγ dimer is composed of one of the five different Gβ proteins and of the 13 different Gγ proteins encoded by the genome.[53] Initially thought to be a passive participant, it is now recognized as an active signaling component, capable of modulating several effectors, including G protein-coupled inwardly rectifying potassium (GIRK) channels, voltage-gated calcium channels, phosphatidylinositol-3-kinase (PI3K), and mitogen-activated protein kinases (MAPKs).[58; 59] Furthermore, Gβγ subunits participate in the recruitment and activation of G protein-coupled receptor kinases (GRKs), which phosphorylate GPCRs primarily at their C-terminus and ICLs.[58; 59] This phosphorylation increases affinity for arrestin proteins, which, in addition to G proteins, can also bind to the intracellular cavity of activated GPCRs via a finger loop.[60; 61].

The human genome encodes four arrestins, namely arrestin-1, arrestin-2 (β-arrestin-1), arrestin-3 (β-arrestin-2), and arrestin-4, with arrestin-2 and -3 being widely expressed and interacting with numerous GPCRs.[62] While arrestins were originally thought to solely mediate receptor desensitization and internalization – they hinder the interaction between receptor and G proteins upon binding and connect the receptor with the endocytic machinery (such as clathrin and adaptor protein 2 complex), subsequently recycling the receptor back to the cell membrane or leading to degradation in proteasomes – emerging evidence suggests that they may also initiate distinct, G protein-independent signaling cascades.[63] Arrestin-mediated signaling has been im-

plicated in the activation of extracellular signal-regulated kinases (ERKs), which regulate cellular processes such as proliferation, differentiation, and apoptosis.[63] However, the extent to which arrestins function independently of G proteins remains a topic of ongoing debate, as some studies indicate that GPCR-induced signaling is abolished in the absence of active G proteins.[64–70]

GPCRs exhibit varying degrees of selectivity toward different G protein subtypes, with some receptors capable of coupling to multiple Gα proteins.[71–73] Recent large-scale studies have identified many GPCRs that activate multiple Gα protein families, with certain receptors, such as the B2 bradykinin receptor and the orexin 2 receptor, engaging all four Gα protein families.[71; 72] However, the functional relevance of such promiscuous coupling remains an open question, as receptor signaling is influenced by multiple factors, including spatiotemporal proximity of GPCRs and G proteins, expression levels, and ligand-dependent biases in signaling.

The ability of ligands to preferentially or solely activate specific signaling pathways, e.g., activation of G_i protein without inducing β-arrestin recruitment or vice versa, a phenomenon known as "biased signaling", is of particular interest in drug development.[74] This is expected to lead to favorable pharmacological outcomes in comparison with non-biased agonists while minimizing undesired effects. For example, it has been proposed that biased μ-opioid receptor agonists may have analgesic properties, but might exert less severe side effects than classical opioid analgesics, e.g., depression of breathing or addictive effects, and may therefore be safer than the currently applied analgesic opioid drugs.[75] However, these claims require further rigorous investigation.

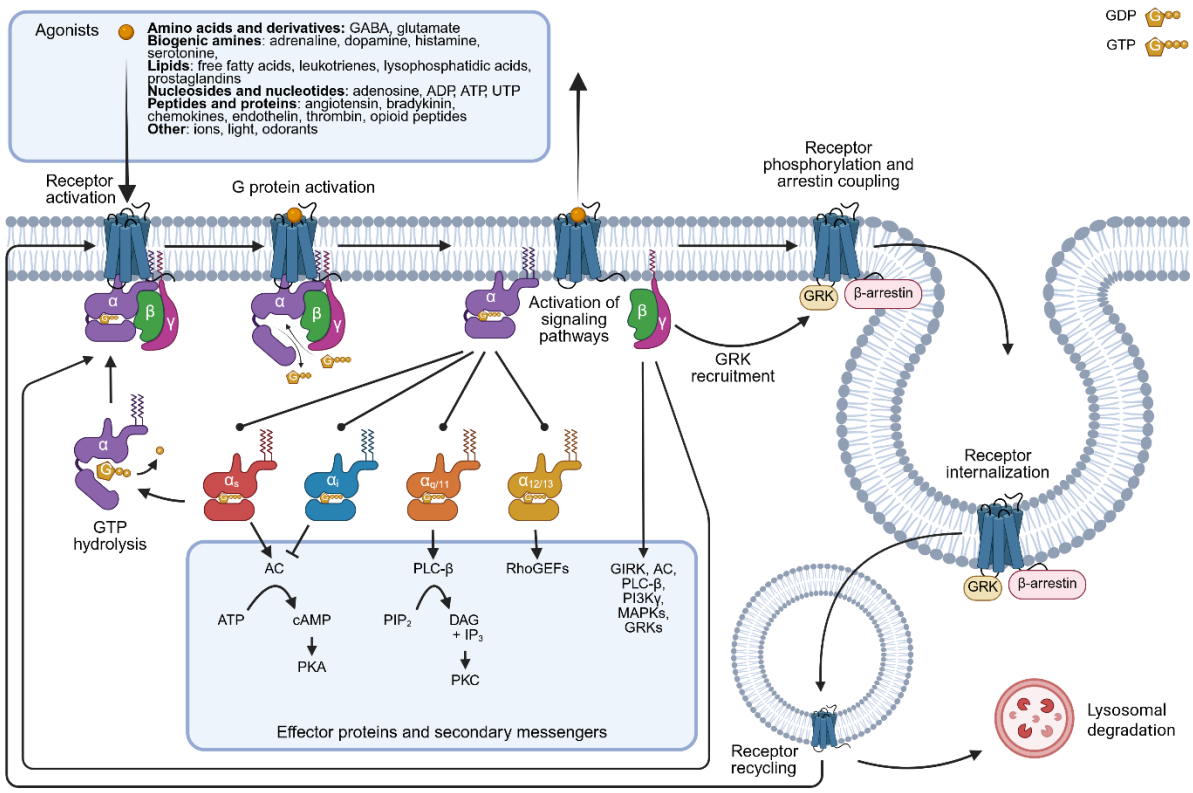

Figure 4. GPCR and G-protein activation cycle. The activation of a GPCR by its corresponding agonist (top left) triggers GDP-GTP exchange in the Gα protein subunit of the heterotrimeric G protein. Then, the Gα subunit dissociates from the βγ-subunit, both of which activate various effector proteins. Gβγ signaling leads to recruitment of GRKs, among others, which in turn phosphorylate the receptor and induce arrestin recruitment. Subsequently, the receptor is internalized and either degraded in the lysosome or recycled back to the cell membrane. The GTPase activity of the Gα subunit then leads to hydrolysis of GTP to GDP and the consequent rearrangement of the heterotrimeric G protein complex. Abbreviations: γ-aminobutyric acid (GABA), adenosine diphosphate (ADP), adenosine triphosphate (ATP), guanosine diphosphate (GDP), guanosine triphosphate (GTP), uridine triphosphate (UTP), adenylyl cyclase (AC), cyclic adenosine monophosphate (cAMP), protein kinase A (PKA), phospholipase Cβ (PLC-β), phosphatidylinositol 4,5-bisphosphate (PIP_2), diacyl glycerol (DAG), inositol 1,4,5-trisphosphate (IP_3), protein kinase C (PKC), Rho guanine nucleotide exchange factor (RhoGEF), G protein-coupled inwardly rectifying potassium channel (GIRK), phosphoinositide 3-kinase-γ (PI3Kγ), mitogen-activated protein kinase (MAPK), G protein-coupled receptor kinase (GRK). Created with BioRender.com.

2.3 The orphan G protein-coupled receptor GPR17

A significant subset of GPCRs remains classified as “orphan receptors”, i.e., their physiological agonist is yet unknown or unconfirmed.[76; 77] This presents both a challenge and an opportunity

for pharmacological research. The deorphanization of GPCRs, the process of identifying the cognate agonists of these receptors, has been a cornerstone of pharmacological discovery since the late 20th century. Early successes in the 1990s and 2000s, such as the deorphanization of the ghrelin receptor and the apelin receptor, demonstrated the potential of orphan GPCRs to unveil novel biological pathways and therapeutic targets. However, the pace of deorphanization has slowed in recent years, with over 100 GPCRs still awaiting ligand identification. Additionally, several reported ligand-receptor pairings have proven to be "false-positive": one or several physiological compounds have been proposed as cognate agonists for certain orphan GPCRs, but subsequent independent confirmation has not been successful, and therefore, the International Union of Pharmacology (IUPHAR) has not accepted them.[78]

The orphan GPCR GPR17 belongs to the δ-branch of the rhodopsin-like class A GPCR family (see **Figure 3**) which contains receptors for lipids, peptides, nucleotides (e.g., the nucleotide-activated P2Y receptors), and many further orphan receptors.[79] The human GPR17 protein (hGPR17) is encoded by the human *GPR17* gene located on chromosome 2q14.3.[80] It is highly conserved in vertebrates (the mouse and rat orthologs [mGPR17, rGPR17], encoded by the respective *Gpr17* genes, show 90 % amino acid sequence identity to hGPR17) which might indicate an important physiological role.

GPR17 is predominantly expressed in the central nervous system (CNS) by cells of the oligodendroglial cell line, particularly in late oligodendrocyte progenitor cells (OPCs) and pre-oligodendrocytes (pre-OLs)[81; 82] (collectively also termed "committed oligodendrocyte precursor cells" [COPs]) (see **Figure 5**).[83] The primary role of oligodendrocytes (OLs) is to form myelin sheaths around axons to allow transmission of electrical signals along the axon, leading to fast and efficient communication between neurons. Activation of GPR17 in OPCs inhibits their differentiation and maturation.[84–86]

In addition, GPR17 is expressed in the heart, the kidneys, and enteroendocrine cells in the intestine.[82; 85; 87]

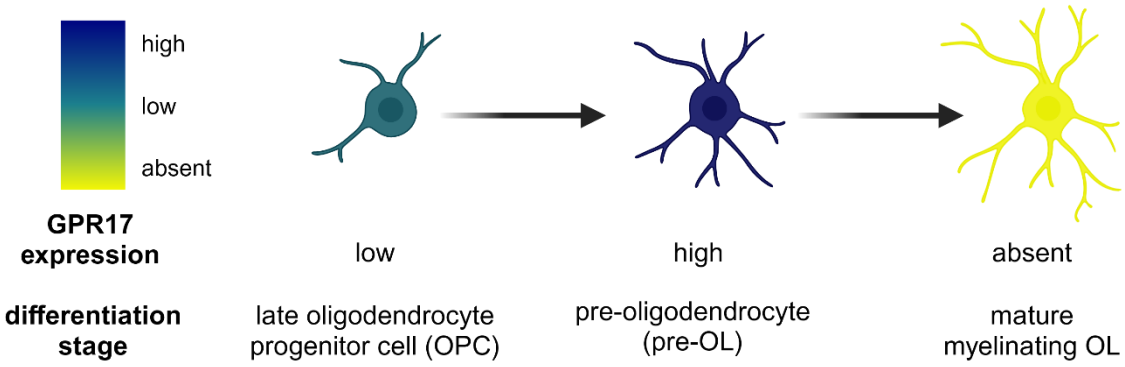

Figure 5. GPR17 expression during oligodendrocyte maturation. GPR17 is expressed in late oligodendrocyte precursor cells (OPCs) and, to a greater extent, in pre-oligodendrocytes (pre-OLs). In mature oligodendrocytes (OLs) GPR17 is downregulated.[81–83; 88] Adapted with permission from …

A comprehensive overview of GPR17 is provided in Chapter 3 and the accompanying review paper.[89] It discusses GPR17 classification, localization, isoforms, structure, signaling pathways, genetic variants, ligands, and its role in pathological conditions. This subchapter will fill in the gaps by providing more insight into the diseases in which GPR17 is involved and which could become future indications for GPR17 pharmacotherapy.

2.3.1 Therapeutic relevance of GPR17

GPR17 has emerged as a promising pharmacological target for the treatment of multiple sclerosis (MS) and further demyelinating or neurodegenerative diseases, diabetes and obesity, glioblastoma, and ischemic stroke.

2.3.2 Neurodegenerative diseases

Neurodegenerative diseases are a group of chronically progressing disorders characterized by progressive loss of function or structure of neurons, involving complex pathological processes including inflammation and the accumulation of abnormal protein aggregates. Examples include MS, Alzheimer's disease (AD), and Parkinson's disease (PD). Neurodegeneration often begins in definable areas of the brain and spreads over the course of the disease. PD begins with the death of dopaminergic neurons in the *substantia nigra* of the midbrain,[90] while in AD first signs of damage occur in the hippocampus.[91] Currently, there is no curative treatment for most NDs and available therapies only treat symptoms.[92] E.g., L-DOPA is metabolized to dopamine in the CNS and compensates for the dopamine deficiency in the treatment of PD. However, a continuous decrease in the effectiveness and duration of action of L-DOPA is observed

due to the constant death of dopaminergic neurons.[93] Hence, the development of new therapeutic options is required.

2.3.2.1 Multiple sclerosis

MS is a chronic inflammatory autoimmune disease affecting the CNS. It is characterized by infiltration of white and gray matter of the brain by immune cells, associated with inflammation and resulting in myelin sheath degradation.[94; 95]

However, exact causes of this inflammation and autoimmune reaction are still poorly understood.[96] It was suggested that the exposure to environmental factors in genetically predisposed individuals is required for development of MS and that each part alone is not sufficient.[97] Over 200 genes have been identified as potential contributors to MS risk.[98] The genetic trait with the greatest disease-association is the HLA-DRB1*15:01 haplotype within the human leukocyte antigen (HLA) complex.[97; 99; 100] Important environmental triggers are Epstein-Barr virus infection,[101] vitamin D deficiency, smoking, childhood/adolescence obesity, and exposure to organic solvents.[99; 100]

Since the demyelinating foci can occur throughout the CNS, MS can cause many different neurological symptoms, most commonly visual impairments in about one third of patients, but also sensory disturbances, motor weakness, spasticity, fatigue, pain, and cognitive dysfunction.[102]

The disease is currently incurable.[103] Existing therapeutic options focus on immune modulation,[104] symptom management,[105] and rehabilitation[103] to positively influence the course of the disease, reduce flare-ups, and prevent disability. However, these treatments lack efficacy in remyelination. Furthermore, a study found that even after prolonged stability, discontinuing disease-modifying therapy renewed inflammation in 18 % of patients within 15 months.[106]

Addressing demyelination is critical for reversing MS and GPR17 has emerged as a potential key target. Its chronic activation is thought to inhibit differentiation of OPCs into OLs and subsequent myelination (see **Figure 6**).[107–109]

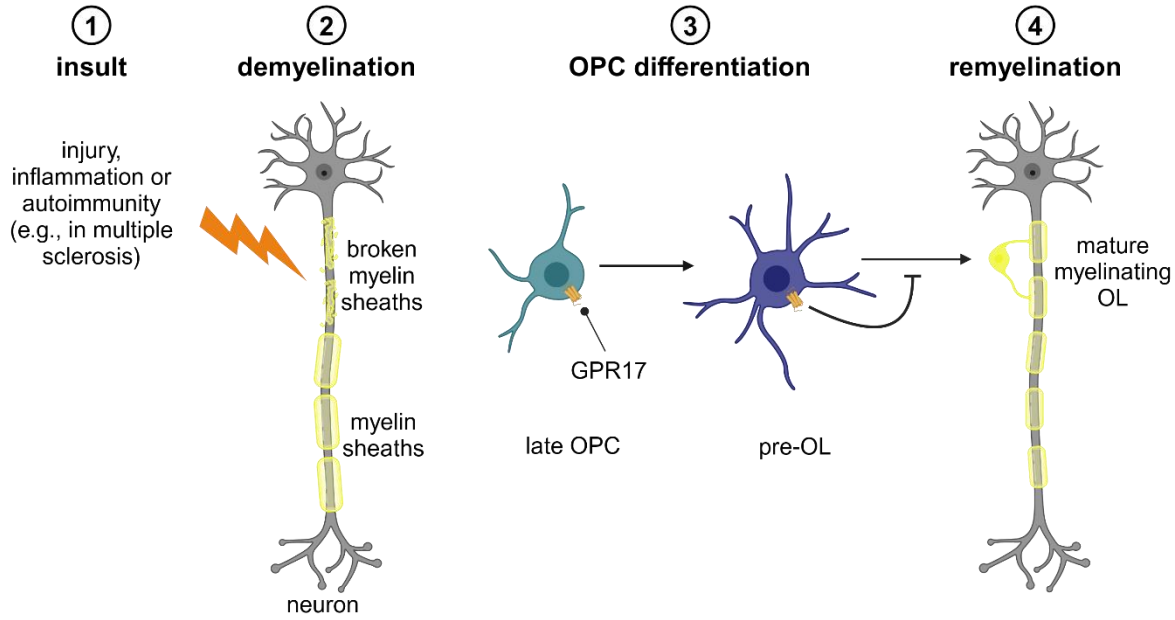

Figure 6. Myelin repair. GPR17 signaling downregulates OPC differentiation into OLs which in turn inhibits remyelination.[107–109] GPR17 has therefore been suggested as a target for the treatment of multiple sclerosis and other demyelinating diseases. Adapted with permission from Lewash et al.[89]

2.3.2.2 Alzheimer's disease

AD is a neurodegenerative disorder and the most common cause of dementia.[110] It is characterized by cognitive decline, behavioral abnormalities, and neuropsychiatric symptoms. The exact causes of AD remain unknown, although it is associated with the accumulation of β-amyloid (Aβ) plaques and hyperphosphorylated tau protein tangles in the brain as well as reduced activity of cholinergic neurons.[111; 112] AD is currently incurable and terminal.[113]

The development of AD is complex and not fully understood. Familial AD, a rare form accounting for less than 5 % of cases, is directly caused by inherited mutations in specific genes, primarily amyloid precursor protein (*APP*), presenilin 1 (*PSEN1*), and presenilin 2 (*PSEN2*), leading to excessive production of Aβ.[114; 115] The more prevalent sporadic AD is generally thought to result from a combination of genetic, lifestyle, and environmental factors. The most well-established risk factor is the ε4 allele of the apolipoprotein E gene (*APOE*).[115] Major lifestyle and environmental factors thought to contribute to AD risk include diabetes, obesity, hypertension, hypercholesterolemia, traumatic brain injury, depression, stress, sleep disturbances, smoking, lack of physical activity, hearing loss, and social isolation.[116]

GPR17 appears to be associated with Alzheimer's disease. It is upregulated in the hippocampus and frontal cortex of mouse brain in response to Aβ accumulation.[82; 117; 118]

2.3.3 Diabetes

Diabetes mellitus, in short diabetes, is a group of metabolic disorders. Type 2 diabetes mellitus (T2DM) is the most prevalent form, accounting for more than 90 % of cases.[119] It is caused by insulin resistance and subsequent relative lack of insulin, which leads to hyperglycemia.[119]
Lifestyle factors such as poor diet and physical inactivity are strongly associated with development of T2DM. Incidence and prevalence of this disease increases in parallel with the rates of obesity, which is a major contributor.[119] Additionally, T2DM has a significant familial clustering. Large-scale genetic studies have identified over 500 genetic variants associated with T2DM risk.[120] The most well-established genetic risk factor is a variant in the transcription factor 7-like 2 (*TCF7L2*) gene, which is closely associated with impaired insulin secretion.[121]
An important target for T2DM pharmacotherapy is the glucagon-like peptide-1 (GLP-1) receptor that stimulates glucose-dependent insulin release from β-cells of the pancreatic islets, the transcription of the insulin gene, and the proliferation of the pancreatic islets. It also inhibits glucagon production in the α-cells of the pancreatic islets, and induces satiety by binding to receptors in the area postrema in the medulla oblongata of the brainstem.[122; 123]
GPR17 is expressed in intestinal enteroendocrine cells (EECs) and functions as an inhibitory pathway for GLP-1 that is co-expressed by the cells.[124]

2.3.4 Glioblastoma

Glioblastoma is the most common malignant brain tumor in adults (almost 50 %) and among the most difficult cancers to treat. It originates from glial cells, which support and protect neurons in the brain.[125]
The majority of glioblastoma cases are sporadic.[126] Exposure to ionizing radiation is the only consistently established environmental cause.[127] Older age is also a significant risk factor, with most cases occurring in adults over the age of 40 and the incidence peaking between the ages of 75 and 84.[125]
GPR17 might be involved in glioblastoma development and cell signaling as it drives the modulation of mitochondrial electron transport chain complexes by increasing the production of reactive oxygen species (ROS).[128–130]

2.3.5 Ischemic stroke

Ischemic stroke is a neurological disease caused by a sudden reduction in blood flow and the resulting reduced supply of nutrients and oxygen to brain tissue.[131] Worldwide, it is the second leading cause of death (11.6 % of total deaths) after ischaemic heart disease.[132]

The primary mechanism behind this reduced blood flow is typically the constriction or blockage of one or more arteries supplying the brain, most commonly caused by atherosclerosis and/or embolism.[131] Atherosclerosis is a chronic inflammatory process in which deposits (plaque) consisting of cholesterol, fatty substances, cellular waste products, calcium, and fibrin form in the arterial walls. This plaque hardens and narrows the arteries. An embolism occurs when a thrombus or other debris in the body forms an embolus that enters the circulation, lodges in a smaller artery (e.g., in the brain), and blocks blood flow.

GPR17 appears to be associated with ischemic stroke.[84; 133]

3 GPR17 – orphan G protein-coupled receptor with therapeutic potential

Michael Lewash, Evi Kostenis, and Christa E. Müller

Trends Pharmacol. Sci. **2025**, *46*, 610–628, doi: 10.1016/j.tips.2025.05.001

3.1 Introduction

MS is a devastating demyelinating disease without curative treatment, as current therapies merely alleviate symptoms.[104] In the search for innovative therapies, GPR17 has moved into the focus of attention as a promising drug target for MS and other demyelinating diseases.[88] Blocking the receptor has been proposed to enable remyelination, which might therefore become a game-changer for MS patients. The first clinical trial of a GPR17 antagonist, PTD802, has recently been approved. In addition, truly potent and selective compounds have been developed in the past few years which will help in establishing the role of GPR17 as a new therapeutic target in further indications.[134–136]

To understand how this evolved, we provide a broad picture of the receptor. Since 2006, research on GPR17 has been characterized by ambiguities, irreproducible results, and contradictions. To date, only two reviews (in 2016 and 2020)[137; 138] have been published on the topic. In the present review, we provide a comprehensive and critical evaluation of the literature from a current perspective.

3.2 Summary

GPR17 is phylogenetically located between cysteinyl leukotriene receptors (CLTRs), free fatty acid receptors (FFARs), lysophosphatidic acid receptors (LPARs), P2Y receptors (P2YRs), protease-activated receptors (PARs), and other class A δ-branch orphan receptors. It is predominantly expressed in the CNS in late-stage OPCs and pre-OLs[81; 82] (collectively also termed COPs).[83] The human *GPR17* gene has two open reading frames that produce two isoforms that differ in their N-terminal length.[139] The short isoform (hGPR17-S) is predominantly expressed in the brain, whereas the long isoform (hGPR17-L) is preferentially expressed in peripheral tissues.[140; 141]

The recent cryo-EM structure determination at a resolution of 3.02 Å[46] proposed the same ligand-binding pocket previously found in docking studies.[134; 135] Notably, the structure highlights features such as the unique hairpin-like configuration of extracellular loop 2 (stabilized by a

disulfide bond, hydrogen bonds, and multiple hydrophilic interactions) and specific micro-switch motifs (e.g., the alteration of the NPxxY motif to DPxxY, which alters conformation of TM7, the DRY motif to DRF, which hypothetically impairs chemotaxis, and the CWxP motif to CFxP, which reduces flexibility of TM6), all of which possibly influence receptor activation and signaling pathways.[46]

The main signaling pathways of GPR17 linking the receptor to oligodendrocyte maturation control and thus its potential role in the treatment of MS, are mediated by G_i proteins: Inhibition of GPR17 leads to an increase in cAMP production and subsequent activation of protein kinase A (PKA) and exchange protein directly activated by cAMP 1 (EPAC1).[108; 109] PKA leads to OL differentiation by activating the extracellular-signal regulated kinase 1/2 (ERK1/2) signaling pathway and also more directly by translocation to the nucleus and phosphorylation of relevant transcription factors.[108] EPAC1 also leads to oligodendrocyte differentiation independently of PKA.[142–144] Furthermore, PKA leads to a decrease in OL apoptosis by inhibiting the X-linked inhibitor of apoptosis associated factor 1 (XAF1) pathway.[142] In addition, GPR17 also couples to G_q proteins and, at higher concentrations of the agonist, to G_s proteins (see **Figure 7**).[109]

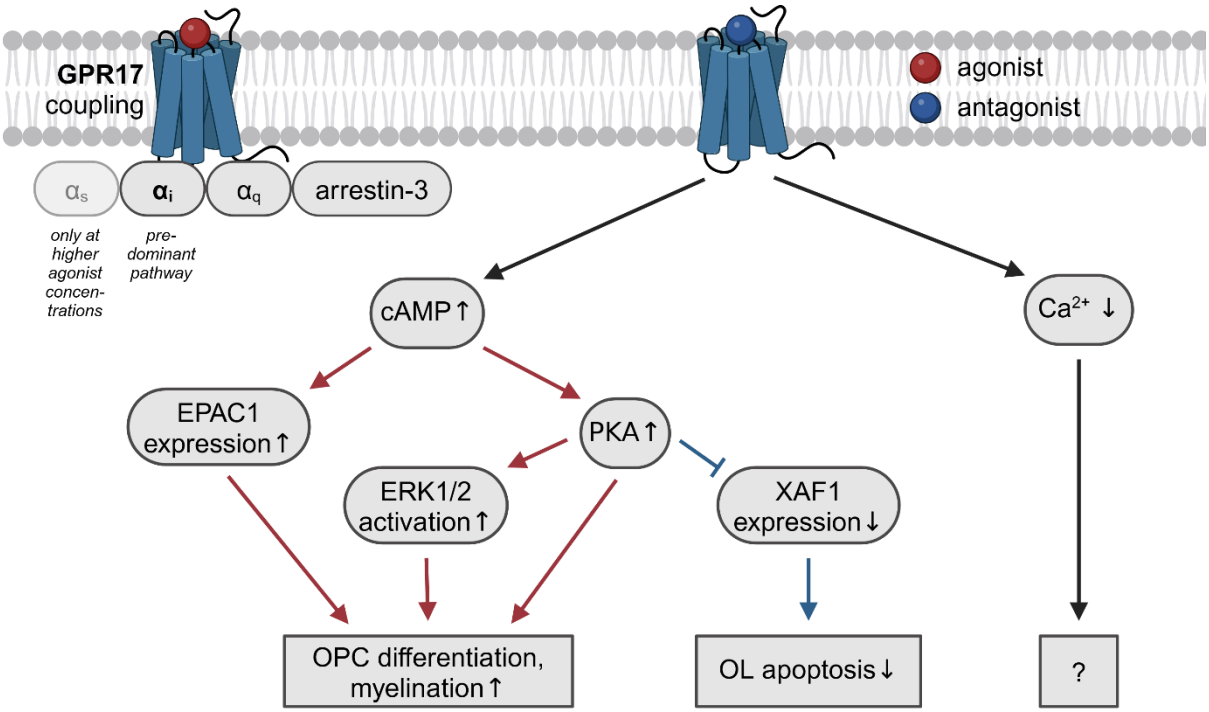

Figure 7. GPR17 coupling to different G-proteins, important signaling pathways and effects. The $G\alpha_i$ signaling cascade seems to be an important pathway that links GPR17 to oligodendrocyte maturation control.[87; 108; 142] The effect of $G\alpha_q$ and its downstream interacting molecules on oligodendrocyte maturation is not yet fully understood. Abbreviations: cAMP = cyclic adenosine monophosphate, ERK1/2 =

extracellular-signal regulated kinases 1/2, EPAC1 = exchange protein directly activated by cAMP 1, XAF1 = X-linked inhibitor of apoptosis associated factor 1. Adapted from Lewash et al.[89]

Attempts to deorphanize GPR17 have thus far failed.[46; 141; 145–150] MDL 29,951 (an *N*-methyl-D-aspartate (NMDA) receptor antagonist) is a robust and potent, but non-selective GPR17 agonist.[109; 134; 151] By replacing its chlorine atoms with fluorine (position 4) and bromine (position 6), respectively, PSB-18422 was synthesized, which is GPR17-selective and even more potent, making it an important tool compound for the receptor.[134] PSB-18183 is another selective indole scaffold-based agonist that uses a different binding mode compared to PSB-18422 due to its larger hexyloxy group at position 6 (see **Figure 8**).[134]

A collaboration between the Pharmaceutical Institute of the University of Bonn and UCB Pharma GmbH yielded multiple classes of potent and selective GPR17 antagonists: PSB-22269 and PSB-24040 are potent anthranilic acid scaffold-based antagonists (also see Chapter 4 for the related publication).[135] Most promising for therapeutic application are the potent, selective, and brain-permeable indolylsulfonamide scaffold-based antagonists, e.g., "I-116" (see **Figure 8**).[136; 151] A structurally related indolylsulfonamide derivative, PTD802, was recently authorized for the first clinical trial of a GPR17 antagonist. Several companies, including F. Hoffmann-La Roche AG, Rewind Therapeutics NV, Myrobalan Therapeutics Nanjing Co. Ltd, Nanjing Immunophage Biotech Co. Ltd, and Biogen Ma Inc. filed patents for very similar sulfonamide derivatives.[152–169]

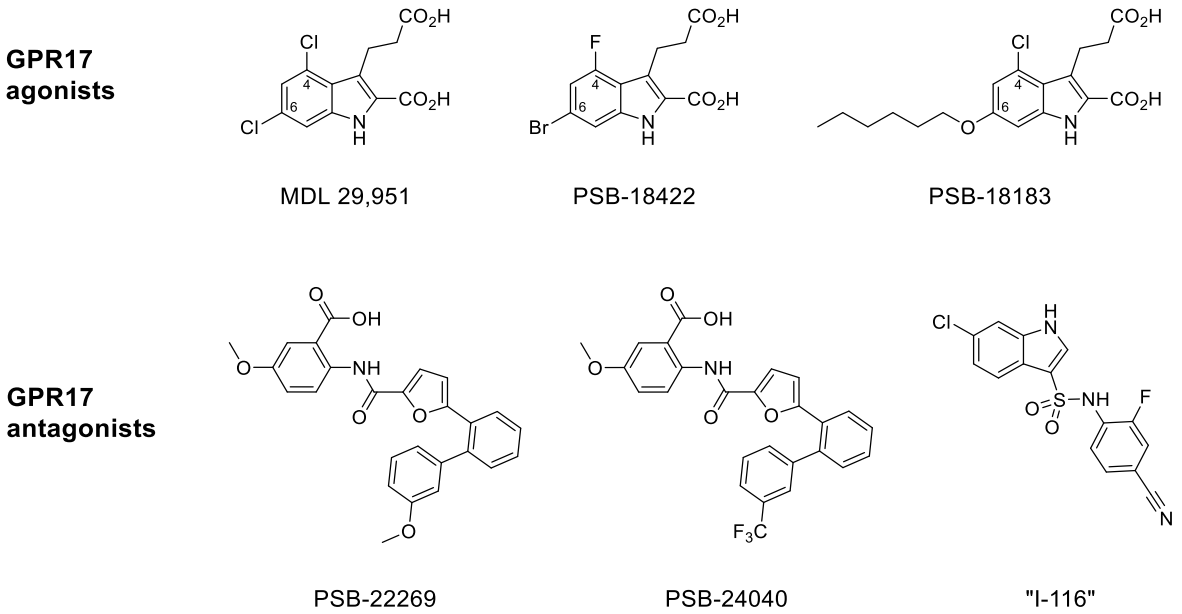

Figure 8. Important GPR17 agonists MDL 29,951, PSB-18422, and PSB-18183 as well as antagonists PSB-22269, PSB-24040, and "I-116".

GPR17 has been reported to affect neural development, myelination, and tissue repair, suggesting it as a target for the treatment of MS and other demyelinating and neurodegenerative diseases.

Gpr17 knockdown via small interfering RNA (siRNA), short hairpin RNA (shRNA), or antisense oligonucleotides led to OPC differentiation, remyelination, and damage mitigation after brain and spinal cord injury in multiple studies on mice and rats.[142; 133; 170; 171] These effects could be reproduced by pharmacological treatment: GPR17 antagonist montelukast induced OPC maturation after brain or optic nerve injury in mice[84; 172] and promoted neural development and cognitive abilities in rats.[117] On the other hand, GPR17 agonist MDL 29,951 impaired cognitive abilities in mice.[173]

Additionally, GPR17 has been implicated as potential drug target in further diseases, of which diabetes is the most promising one. GPR17 was suggested to be expressed in enteroendocrine cells[124] alongside incretin GLP-1, which stimulates insulin release and inhibits glucagon release, effectively lowering blood sugar levels. *Gpr17* knockdown in mice increased GLP-1 secretion, thereby improving insulin secretion and glucose tolerance as well as decreasing body weight and fat content.[124; 174] These effects could also be reproduced pharmacologically in a mouse enteroendocrine cell line: GPR17 expression decreased GLP-1 secretion, GPR17 agonist MDL 29,951 further decreased it, and GPR17 antagonist HAMI3379 reversed the decrease.[175]

3.3 Author contribution

I systemically and rigorously analyzed available research on GPR17 and critically evaluated and interpreted experimental findings. I wrote the manuscript in cooperation with Prof. Dr. Christa E. Müller, integrating my diverse insights into a coherent narrative.

4 Discovery of Anthranilic Acid Derivatives as Antagonists of the Pro-Inflammatory Orphan G Protein-Coupled Receptor GPR17

Nader M. Boshta,‖ Michael Lewash,‖ Meryem Köse, Vigneshwaran Namasivayam, Soumya Sarkar, Jan H. Voss, Andy J. Liedtke, Anna Junker, Maoqun Tian, Anne Stößel, Mahmoud Rashed, Ahmed Mahal, Nicole Merten, Cécile Pegurier, Jörg Hockemeyer, Evi Kostenis, and Christa E. Müller

‖ These authors contributed equally.

J. Med. Chem. **2024**, *67*, 19365–19394, doi: 10.1021/acs.jmedchem.4c01755

4.1 Introduction

Prior to this study, only few, weakly potent, and non-selective GPR17 antagonists had been described in literature, including CLTR1 antagonists montelukast and pranlukast as well as CLTR2 antagonist HAMI3379 (see **Figure 9**).

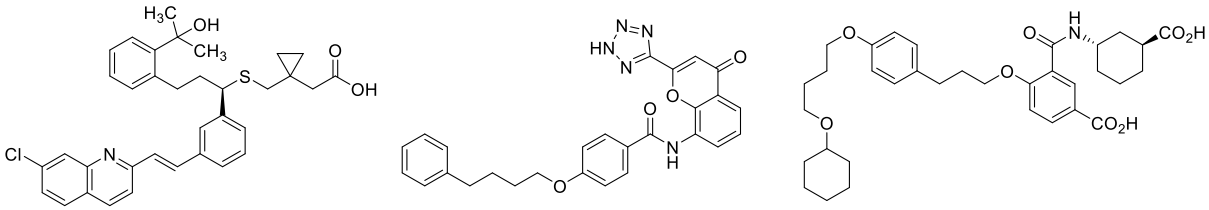

Figure 9. Non-selective GPR17 agonists montelukast, pranlukast, and HAMI3379.

This impeded research on GPR17, as it often times remained unclear whether the proposed effects were actually mediated by GPR17 or if the non-selective tool compounds used in the studies actually interacted with different receptors instead.

As mentioned above, the collaboration of the Pharmaceutical Institute of the University of Bonn with UCB Pharma GmbH has yielded several novel classes of potent and selective GPR17 antagonists, including the anthranilic acid derivatives described in this research article.

4.2 Summary

The starting point was a hit compound discovered during a high-throughput screening campaign. This hit, based on an anthranilic acid scaffold, was chemically modified in a systematic structure-activity relationship (SAR) study to improve its inhibitory potency.

The anthranilic acid core was retained throughout the series as its carboxylic acid function in position 2 was found to be critical for biological activity. Attempts to move the carboxylic acid residue to position 4 or to replace it with other acidic or non-acidic functions resulted in reduced potency or complete loss of activity. The central linking group in the hit compound, originally an enamine, was replaced by a more stable carboxamide group, which also provided a straightforward synthetic route. The original furan ring was partially substituted by other 5- or 6-membered heterocycles (including pyridine and thiazole derivatives), which did not increase potency. Additional structural diversity was introduced by modifying the substituents on the aromatic rings. Substitution of the anthranilic acid benzene ring did not increase potency, while substitution of the second benzene ring was generally well tolerated: Incorporation of biphenyl groups with specific substitutions – such as methoxy and trifluoromethyl groups – resulted in compounds with markedly improved potency. Notably, compounds PSB-22269 and its trifluoromethyl analog PSB-24040 emerged as lead candidates that displayed submicromolar inhibitory concentrations and high binding affinities (see **Figure 10**).

The comprehensive evaluation of the synthesized compounds included a variety of *in vitro* assays to characterize their pharmacological profiles. First, a screening campaign using calcium mobilization assays in Chinese hamster ovary (CHO) cells was performed to identify general trends. Selected antagonists were then re-investigated in calcium mobilization assays in human astrocytoma 1321N1 cells stably transfected with hGPR17 (1321N1-hGPR17 cells), in G protein activation assays, in cAMP accumulation assays, and in radioligand binding assays using a tritiated version of MDL 29,951 ([^{3}H]PSB-12150)[148] and membrane preparations from CHO Flp-In T-REx (FITR) cells stably transfected with hGPR17 (CHO-FITR-hGPR17 cells). Data across all performed functional assays were consistent, although G protein activation assays resulted in lower inhibitory potencies, possibly due to differences in the assay procedures (see **Figure 10**). In addition, the competitive antagonistic nature of the compounds was confirmed by performing shift assays – in this case calcium mobilization assays of MDL 29,951 against different concentrations of PSB-22269, yielding a curve shift from which the type of antagonism can be deduced.

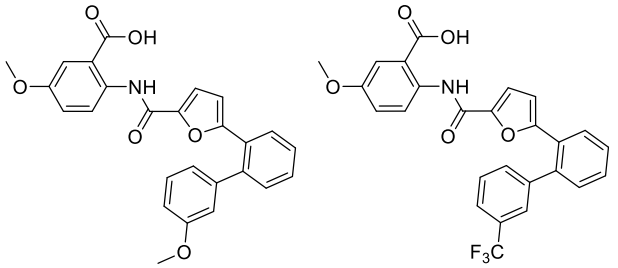

PSB-22269	**PSB-24040**
pIC_{50} = 6.90[a]	pIC_{50} = 7.48[a]
pIC_{50} = 7.71[b]	pIC_{50} = 8.10[b]
pIC_{50} = 6.31[c]	pIC_{50} = 6.53[c]
pK_i = 8.05[d]	pK_i = 7.08[d]

Figure 10. Anthranilic acid derivatives PSB-22269 and PSB-24040. [a]Potency in inhibiting calcium mobilization in 1321N1-hGPR17 cells, activated with MDL 29,951; three to four independent experiments were performed in duplicate. [b]Potency in inhibiting cAMP decrease induced by MDL 29,951 in the presence of 5 µM forskolin in CHO-FITR-hGPR17 cells; three independent experiments were performed in duplicate. [c]Potency in inhibiting the recruitment of the $G\alpha_{i2}$ effector Rap1GAP-RLucII to the membrane in GPR17-expressing human embryonic kidney 293 (HEK293) cells and activated with MDL 29,951; four independent experiments were performed in duplicate. [d]Binding affinity to GPR17, determined in agonist radioligand [^{3}H]PSB-12150 binding assays; three to five independent experiments were performed in duplicate.

In addition to biological assays, an inactive-state homology model of GPR17, based on the X-ray structure of the $P2Y_{12}$ receptor with insights from the cryo-EM and AlphaFold structures of GPR17, was constructed. The docking studies suggested the same binding site for the novel anthranilic acids as for the indole-based GPR17 agonists, e.g., PSB-18422. The anthranilic acid moiety of PSB-22269 is anchored in a binding pocket lined with positively charged arginine residues, the furan ring is involved in aromatic stacking, and the biphenyl group occupies a hydrophobic subpocket (see **Figure 11**).

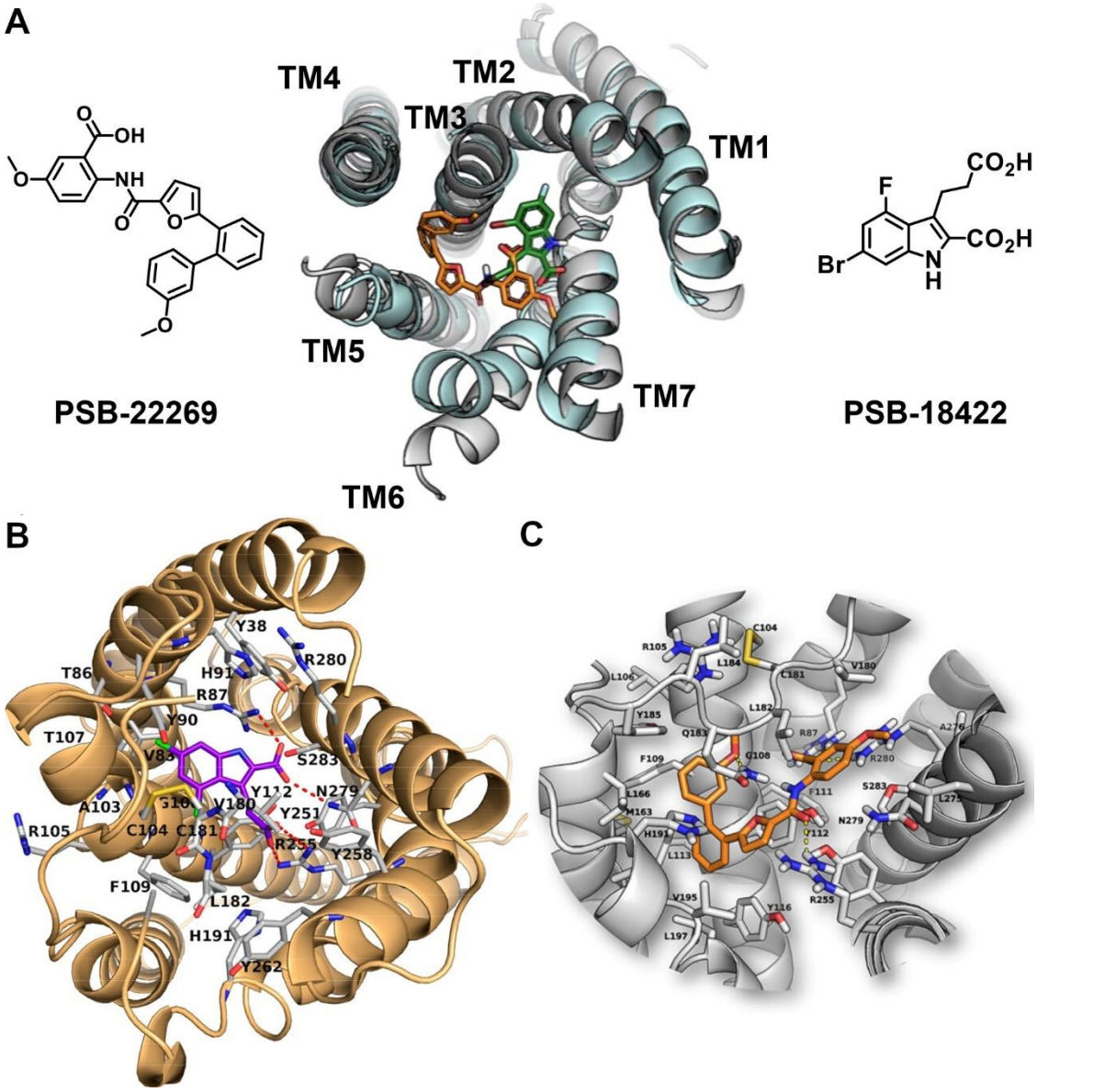

Figure 11. Proposed ligand binding and activation mechanism of GPR17. (A) Predicted binding poses of agonist PSB-18422 (green) and antagonist PSB-22269 (orange) in the putative binding pocket of GPR17 homology models for the active (blue) and inactive (gray) states. (B) Predicted binding pose of agonist MDL 29,951 in the putative binding pocket of GPR17 homology model for the active state. (C) Predicted binding pose of antagonist PSB-22269 in the putative binding pocket of GPR17 homology model for the inactive state. (B, C) Amino acid numbering corresponds to short isoform hGPR17-S. (A, C) Adapted with permission from Boshta, Lewash et al.[135] Copyright 2024 American Chemical Society. (B) Adapted with permission from Baqi et al.[134] Copyright 2018 American Chemical Society.

The discovery of the potent and selective tool compounds PSB-22269 and PSB-24040 will advance the exploration of GPR17 pharmacology and open up opportunities for the development of novel drug candidates, in particular for peripheral indications, such as diabetes and obesity.

4.3 Author contribution

I performed calcium mobilization assays and radioligand binding assays and compiled and interpreted all experimental results from various assay platforms. I drafted and edited the manuscript in cooperation with Prof. Dr. Christa E. Müller. Lastly, I coordinated the activities of all co-authors and integrated the data into the manuscript for the initial submission as well as the revision process.

5 Search for the endogenous ligand of GPR17

The identification of the endogenous agonist for GPR17 has been a subject of extensive investigations. However, all of the so-far suggested ligands have been disproved: Early studies suggested that pyrimidine nucleotides such as uridine diphosphate (UDP), UDP-glucose, and UDP-galactose, as well as leukotrienes, namely leukotriene C_4 (LTC_4) and leukotriene D_4 (LTD_4), could act as agonists of GPR17.[140] However, several laboratories could not reproduce the reported findings, and subsequent research could not confirm GPR17 activation by any of the aforementioned ligands, neither the short nor the long GPR17 isoform.[46; 141; 145–149] More recent studies have proposed that 24(*S*)-hydroxycholesterol acts as an endogenous agonist of GPR17,[151] but this too could not be confirmed by myself (see below) and others.[150]

5.1 24(*S*)-Hydroxycholesterol

Proposed physiological agonist 24(*S*)-hydroxycholesterol was tested alongside MDL 29,951 in calcium mobilization assays, radioligand agonist [^{3}H]PSB-12150 binding assays, and radioligand antagonist [^{3}H]PSB-1503 binding assays (see **Table 1** and **Figure 12**).

Table 1. Characterization of MDL 29,951 and 24(*S*)-hydroxycholesterol in calcium mobilization assays and radioligand binding assays.

Compound	**pEC_{50}** ± SEM Ca^{2+} assay[a]	**pK_i** ± SEM agonist radioligand binding[b]	**pK_i** ± SEM antagonist radioligand binding[c]
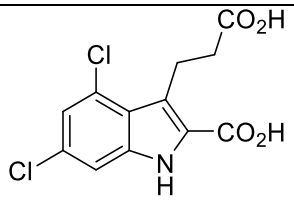 MDL 29,951	**6.82** ± 0.19 *(n=5)*[d]	**6.43** ± 0.23 *(n=5)*[d]	**4.83** ± 0.13 *(n=3)*[d]
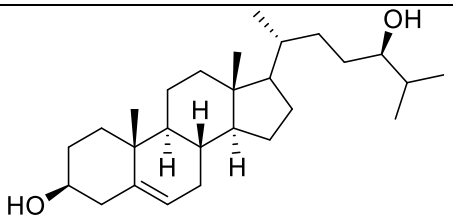 24(*S*)-Hydroxycholesterol	<**5** *(n=6)*[d]	<**5** *(n=7)*[d]	<**5** *(n=6)*[d]

[a]Potency in inducing calcium mobilization in GPR17-expressing 1321N1 astrocytoma cells. [b]Inhibition of binding of [^{3}H]PSB-12150 to GPR17 determined in radioligand binding assays. [c]Inhibition of binding of [^{3}H]PSB-1503 to GPR17 determined in radioligand binding assays. [d]Total number of independent experiments performed in duplicate are given in parentheses with italic font.

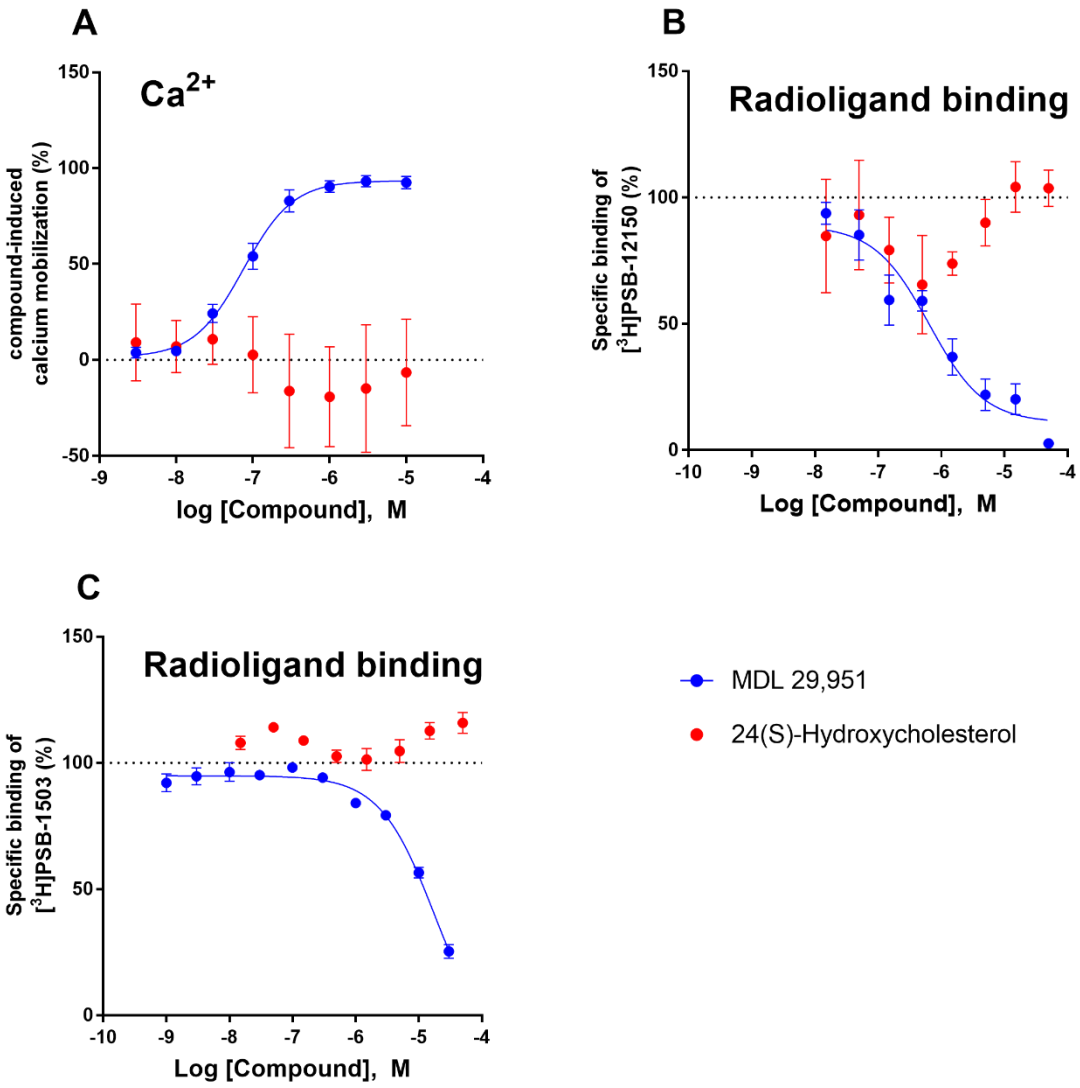

Figure 12. Characterization of 24(*S*)-hydroxycholesterol and MDL 29,951 in calcium mobilization and radioligand binding assays. (A) Characterization as GPR17 agonists in 1321N1-hGPR17 cells using calcium mobilization assays. Data points represent means ± SEM of 5 (MDL 29,951) or 6 (24(*S*)-hydroxycholesterol) independent experiments, performed in duplicate. (B) Characterization in membrane preparations of CHO-FITR-hGPR17 cells, determined in agonist radioligand [^{3}H]PSB-12150 binding assays. Data points represent means ± SEM of 5 (MDL 29,951) or 7 (24(*S*)-hydroxycholesterol) independent experiments, performed in duplicate. (C) Characterization in membrane preparations of CHO-FITR-hGPR17 cells, determined in antagonist radioligand [^{3}H]PSB-1503 binding assays. Data points

represent means ± SEM of 3 (MDL 29,951) or 6 (24(*S*)-hydroxycholesterol) independent experiments, performed in duplicate. (A-C) In some cases, SEM values are smaller than the symbols.

MDL 29,951 activated GPR17 at submicromolar activity with slightly higher potency than described previously.[134] Additionally, MDL 29,951 showed affinity in [^{3}H]PSB-12150 binding assays comparable to its potency but a 40-fold lower affinity in [^{3}H]PSB-1503 binding assays (see Subchapter 6.2.2 for discussion). 24(*S*)-Hydroxycholesterol showed no activity at GPR17 at the tested concentrations, which questions its proposed function as an endogenous agonist of GPR17.

5.2 Further potential endogenous ligands

Continuing the search for the endogenous ligand, multiple human metabolites with similar structures to MDL 29,951 and proposed endogenous ligands such as UDP and 24(*S*)-hydroxycholesterol were characterized at GPR17 in radioligand binding assays and/or calcium mobilization assays (see **Figure 13** and **Figure 14**).

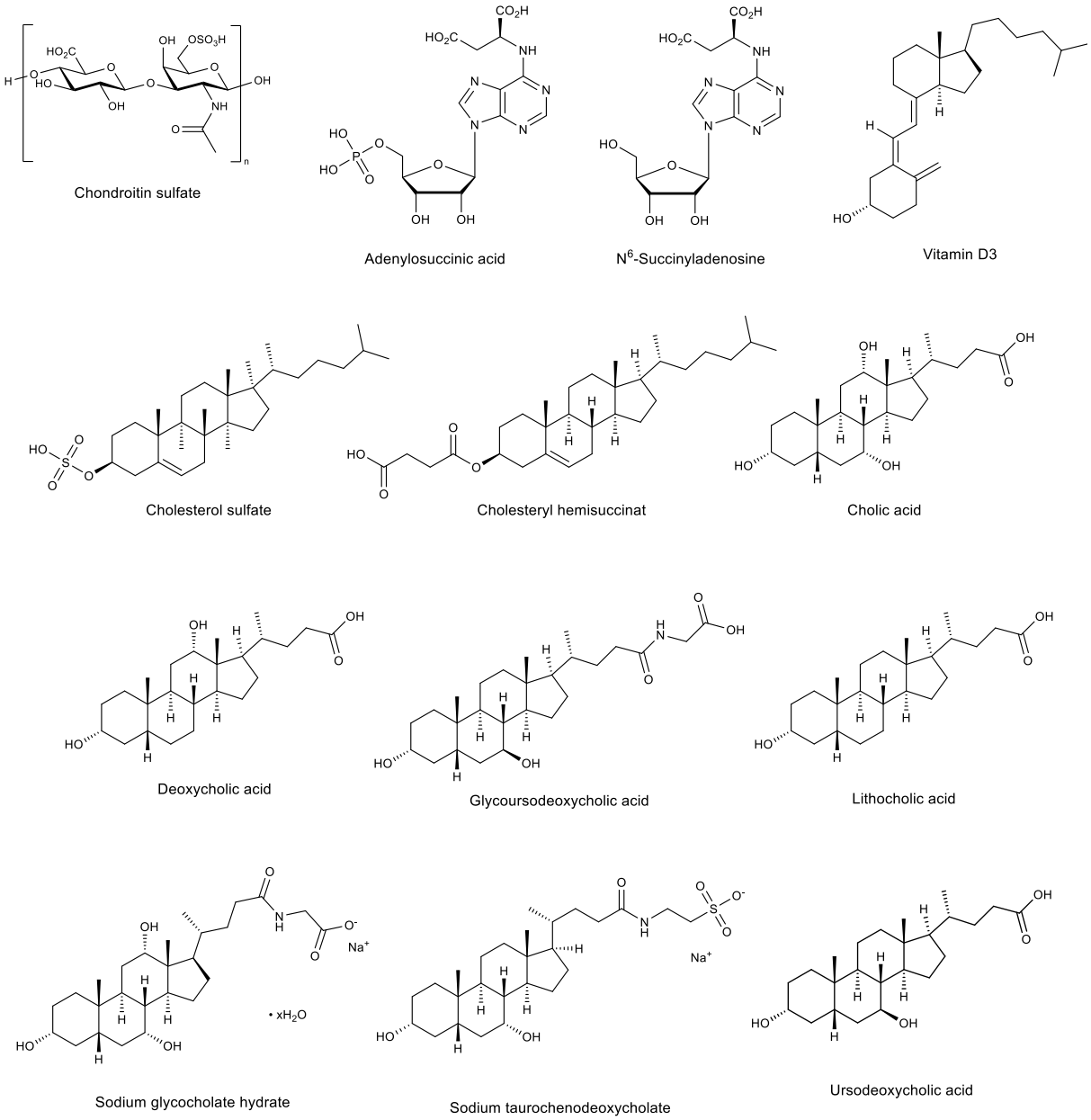

Figure 13. Human metabolites tested as potential endogenous ligands of GPR17 because of similar structure to known GPR17 agonists.

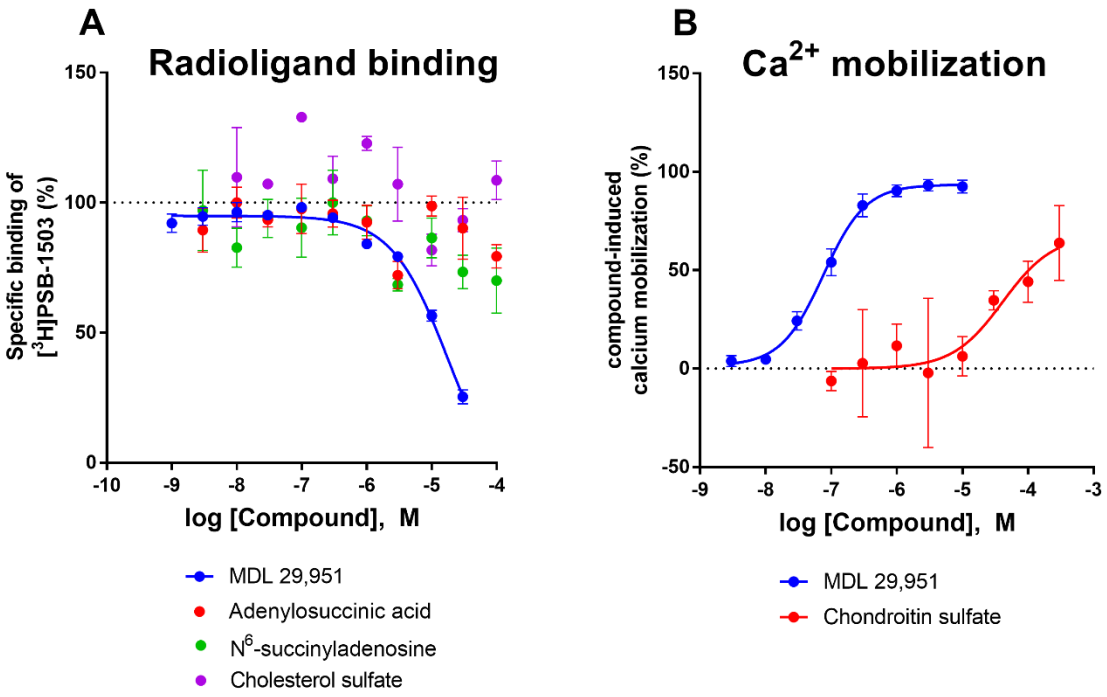

Figure 14. Characterization of selected potential endogenous ligands in calcium mobilization and radioligand binding assays. (A) Characterization in membrane preparations of CHO-FITR-hGPR17 cells, determined in antagonist radioligand [^{3}H]PSB-1503 binding assays. MDL 29,951 is shown as positive control. Data points represent means ± SEM of 1 (adenylosuccinic acid, N^6-succinyladenosine, and cholesterol sulfate) or 3 (MDL 29,951) independent experiments, performed in duplicate (MDL 29,951 and cholesterol sulfate) or quadruplicate (adenylosuccinic acid and N6-succinyladenosine). (B) Characterization in 1321N1-hGPR17 cells using calcium mobilization assays. Chondroitin sulfate data is expressed per monomer equivalent. The chondroitin sulfate curve was initially shifted downward but was later baseline corrected. MDL 29,951 is shown as positive control. Data points represent means ± SEM of 2 (chondroitin sulfate) or 5 (MDL 29,951) independent experiments, performed in duplicate. (A-B) In some cases, SEM values are smaller than the symbols.

Adenylosuccinic acid, N^6-succinyladenosine, and cholesterol sulfate did not show significant affinity for GPR17. Chondroitin sulfate appeared to be weakly potent and should be further investigated.

To further advance the search for the endogenous ligand, a virtual compound library was created. Based on insights from previous agonists,[134] it was hypothesized that the molecule would have a carboxy group and a lipophilic backbone. The search for a human metabolite with these properties, a molecular weight between 150 and 500 Da, and an estimated logP value of more than 2 yielded 783 results in the Human Metabolome Database (HMDB).[176] These 783 ligands

were prepared at pH 7.4 and docked twice into an agonist-bound GPR17 homology model based on the $P2Y_{12}$ receptor using induced fit docking and rigid receptor docking applying the MOE software. Based on their highest achieved binding score out of multiple poses, the 783 ligands were put into a diagram showing the binding scores (S values) of the 783 ligands in relation to their molecular weights. Lower S values represent a higher predicted binding affinity (see **Figure 15**).

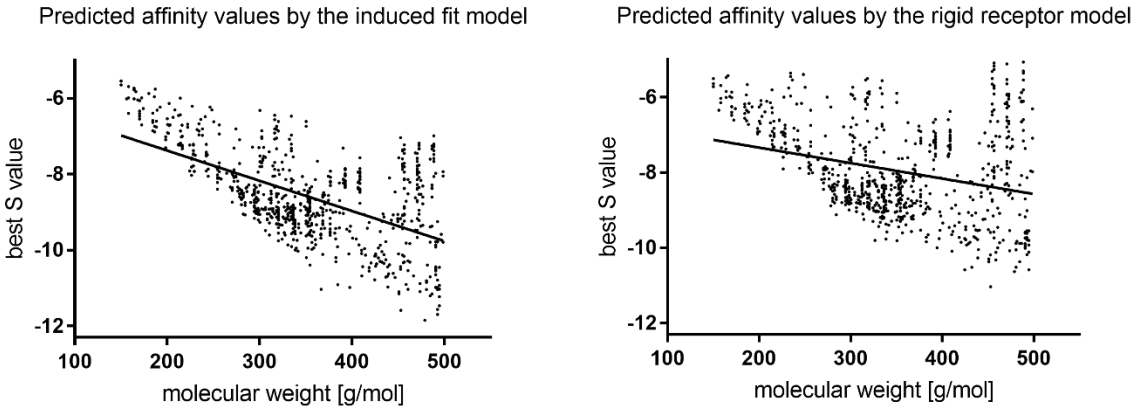

Figure 15. Docking results by MOE. Each ligand was docked multiple times into either the induced fit model (receptor conformation is flexible) or the rigid receptor model, trying to align its conformation to agonist MDL 29,951. For each pose an S value was calculated (lower S values represent a higher binding affinity). The S value of the best binding pose of each ligand was put into a diagram in relation to molecular weight.

On reconsideration, it was decided to leave out the logP value restriction and in turn add the property of having been predicted or even detected in the cerebrospinal fluid, as GPR17 is primarily expressed in the brain. This second search yielded 101 results, which were prepared at pH 7.4 and docked again into the same homology model using only the induced fit docking. This time, however, MOE should not try to align it to agonist MDL 29,951 already present in the model, but instead calculate the binding pocket without any restriction (see **Figure 16**).

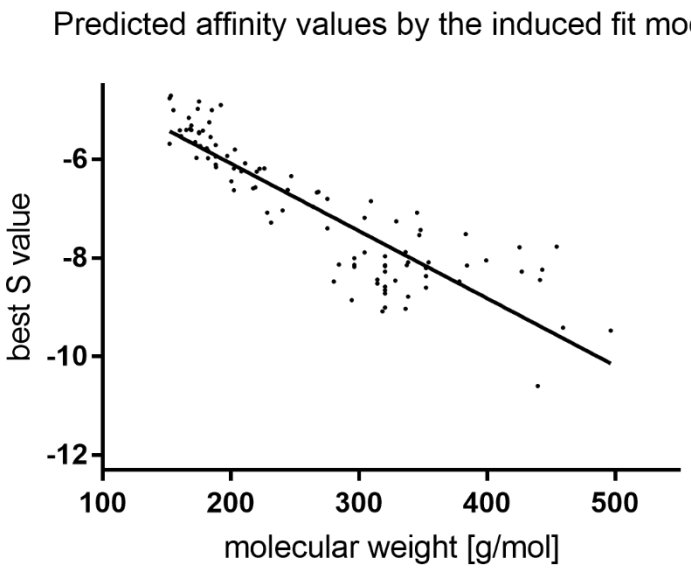

Figure 16. Docking results by MOE. Each ligand was docked multiple times into the induced fit model (receptor conformation is flexible), and for each pose an S value was calculated (lower S values represent a higher binding affinity). The S value of the best binding pose of each ligand was put into a diagram in relation to molecular weight.

While lower S values typically indicate higher predicted binding affinity, a common challenge in virtual screening is the intrinsic molecular weight bias of many scoring functions:[177; 178] Most of these functions are additive, i.e., they sum the contributions of individual atom-atom interactions. Large molecules tend to have more atoms that can interact nonspecifically with the receptor and thus generate lower S values. Therefore, optimizing for docking score alone can lead to the selection of larger molecules. To mitigate this bias and identify more candidates with different properties, it was decided to prioritize compounds that exhibited significantly more favorable (more negative) S values than predicted by their molecular weight. This was identified by selecting compounds showing large negative deviations from a regression line correlating S value with molecular weight across the entire docked library, rather than solely focusing on the lowest nominal S values. A total of 19 hit compounds were selected (see **Table 2**), two of which were excluded again based on previous negative findings (linoleic acid and leukotriene E_4).

Table 2. Selected potential endogenous agonists at GPR17 due to predicted high affinities

Compound	Structure	Molecular weight	S value of best pose
Symmetric dimethylarginine	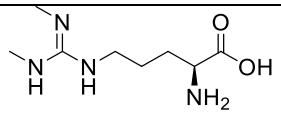	202.25	-6.63
γ-Aminobutyryl-lysine	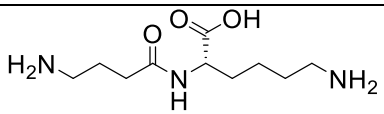	231.30	-7.29
Myristic acid	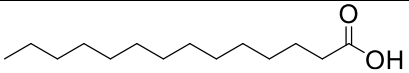	228.37	-7.08
Stearic acid	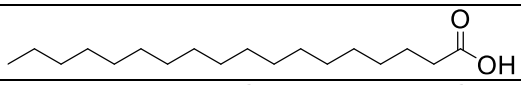	284.48	-8.13
9-OxoODE	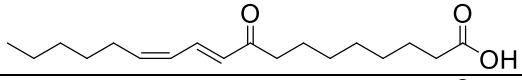	294.43	-8.86
13-HODE	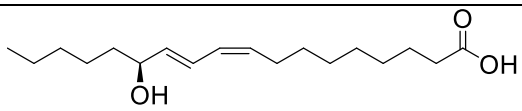	296.44	-8.18
9,10-Epoxyoctadecenoic acid	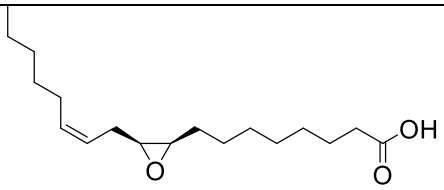	296.44	-8.14
9,10-DHOME	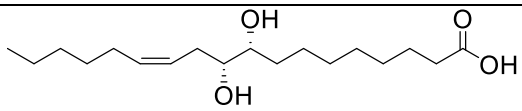	314.47	-8.45
12,13-DHOME	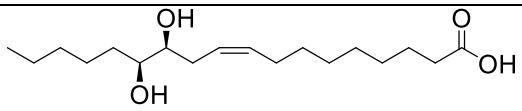	314.47	-8.52
15-KETE	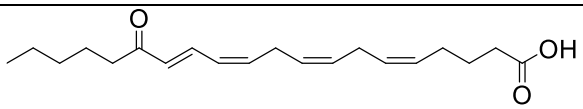	318.45	-9.08
8-HETE	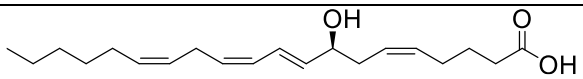	320.47	-8.59
14R,15S-EpETrE	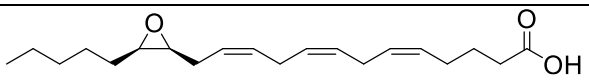	320.47	-9.01
9-HETE	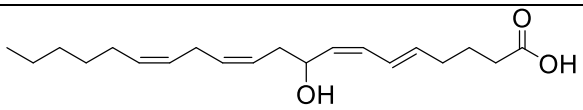	320.47	-8.66
15-HETE	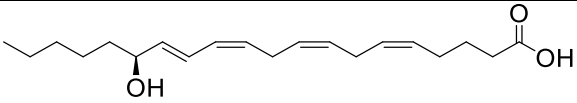	320.47	-8.72
Leukotriene B_4	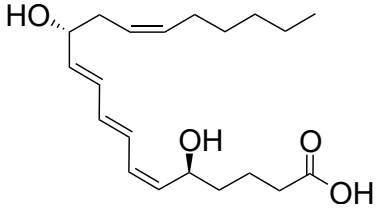	336.47	-9.03

11,12-DiHETrE	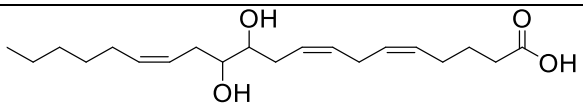	338.48	-8.09
14,15-DiHETrE	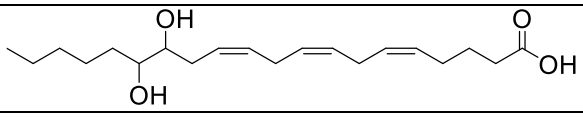	338.48	-8.79

Interestingly, even though 70 of the tested compounds were polar (logP < 2) and 31 tested compounds were apolar (logP > 2), only two of the 17 final hits were polar. On the one hand, this suggests a potential bias of virtual screening methods towards apolar substances, as has been reported in the literature.[178] On the other hand, a fatty acid-like structure for the endogenous ligand of GPR17 appears possible due to its phylogenetic relationship to FFARs (see Chapter 3), and may reflect an actual trend for this receptor. One notable hit was leukotriene B_4 (LTB_4), especially as other leukotrienes (LTC_4 and LTD_4) had previously been proposed as endogenous ligands of GPR17, although those findings could not be confirmed.

To put the S values in perspective, three well-studied GPR17 agonists were also docked using MOE (see **Table 3**).

Table 3. S values of three GPR17 agonists determined by docking in MOE.

Compound	**Structure**	**pEC_{50}**	**Molecular Weight**	**S value of best pose**
MDL 29,951	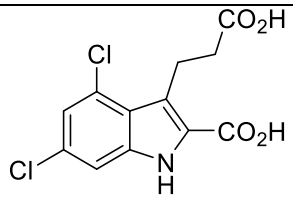	6.48[134]	302.11	-7.24
PSB-18422	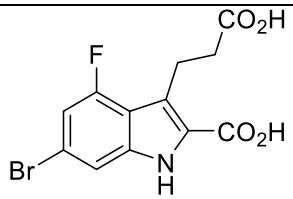	7.55[134]	328.97	-7.36
PZB10614096	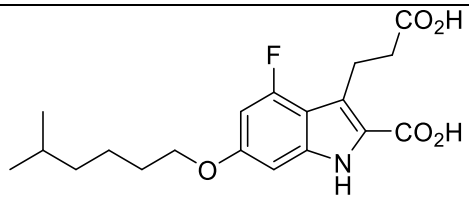	7.92 (Manuscript in preparation)	365.40	-8.24

Despite their known potency at GPR17, these compounds received average or below average (i.e., higher) S values than their molecular weights might suggest, possibly due to lipophilicity bias. However, virtual screening should primarily be regarded as a method for generating novel and diverse starting points, instead of identifying lead compounds with high affinity and/or

potency.[179] Therefore, based on availability, three identified compounds were selected for further experimental testing (see **Figure 17** and **Figure 18**).

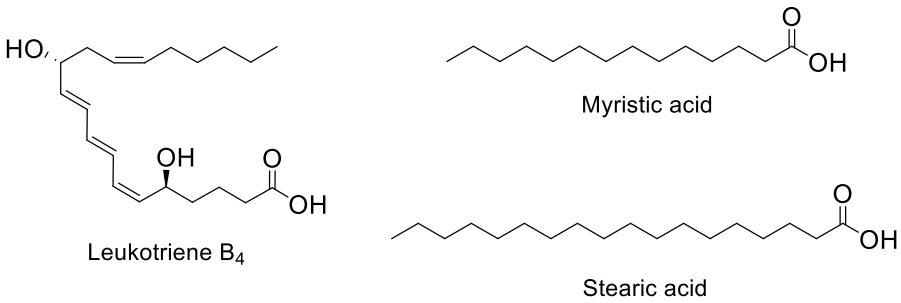

Figure 17. Human metabolites tested as potential endogenous ligands of GPR17 because of good performance in a virtual compound library screen.

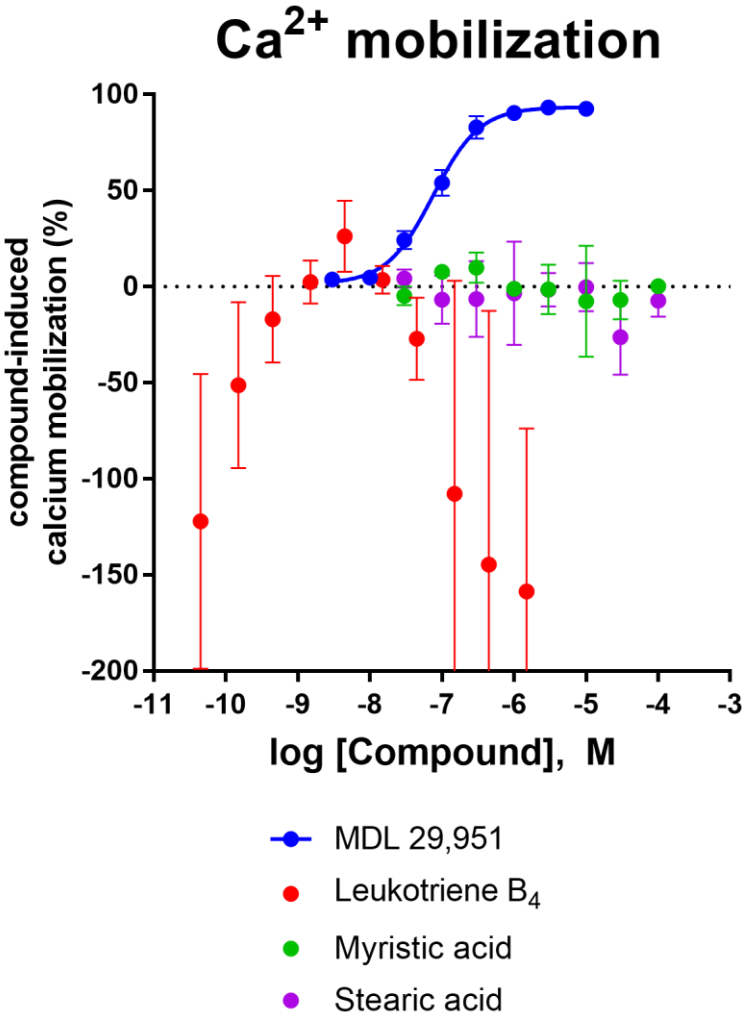

Figure 18. Characterization of selected potential endogenous ligands as GPR17 agonists in 1321N1-hGPR17 cells using calcium mobilization assays. MDL 29,951 is shown as positive control. Data points represent means ± SEM of 1 (myristic acid and stearic acid), 3 (leukotriene B_4), or 5 (MDL 29,951)

independent experiments, performed in duplicate. In some cases, SEM values are smaller than the symbols.

None of these compounds activated GPR17. Nonetheless, further testing of virtual screening hits – especially the best ones, such as 15-KETE – remains of interest. Prior to that, the screening method could be further validated and optimized using deorphanized receptors with known endogenous ligands. An alternative approach would be a broad screening of biological samples, e.g., with brain extracts, to investigate if the physiological agonist is present in the CNS, and to isolate, purify and characterize it subsequently.

6 Characterization of further GPR17 ligands

While the search for the endogenous agonist of GPR17 is still ongoing, multiple synthetic agonists and antagonists have been successfully discovered and optimized. Further research can reveal new optimized tool compounds to study the receptor and lead to the development of drugs for clinical testing.

6.1 Synthetic Agonists

The first identified compound capable of consistently activating GPR17 was indole scaffold-based MDL 29,951[109; 180] (pEC_{50} = 6.48).[134] MDL 29,951 had previously been developed as an *N*-methyl-D-aspartate (NMDA) receptor antagonist interacting with the glycine binding site.[181] All potent and selective GPR17 agonists published to date are based on the same indole scaffold.[134]

Efforts have been made to optimize the indole scaffold of MDL 29,951. PZB10614077, PZB10614096, PZB10618208, and PZB10618209 are further GPR17 agonists (data unpublished) similar to PSB-18183,[134] possessing a larger group than MDL 29,951 in position 6 that changes their binding mode.[134] JWS-15-90 is a structural variant that has an indazole instead of an indole scaffold and misses a carboxylic acid group in position 2 as the most notable changes. There is also interest in structurally different GPR17 agonists. One such agonist is the peptide mimetic amidocinnamic acid derivative PZB09412026. All compounds were investigated at GPR17 (see **Table 4** and **Figure 19**).

Table 4. Selected synthetic agonists and their characterization at GPR17 in calcium mobilization assays and radioligand binding assays.

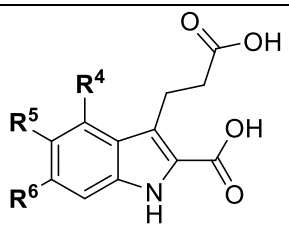

MDL 29,951, PZB10614077, PZB10614096, PZB10618208, PZB10618209

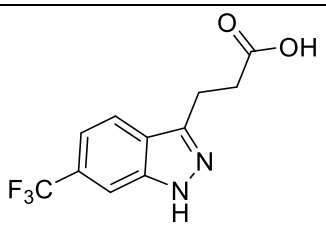

JWS-15-90

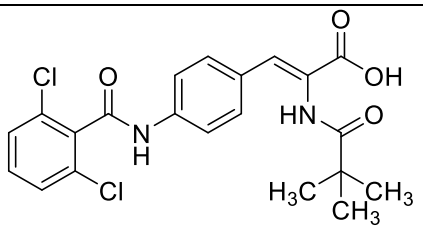

PZB09412026

Compound	R^4	R^5	R^6	$pK_i \pm$ SEM antagonist radioligand binding[a]	$pEC_{50} \pm$ SEM Ca^{2+} assay[b]
MDL 29,951	Cl	H	Cl	4.83 ± 0.13	6.82 ± 0.19
PZB10614077	Cl	H	3-phenylpropyloxy	5.05 ± 0.09	n.d.[c]
PZB10614096	F	H	5-methylhexyloxy	5.32 ± 0.03	n.d.[c]
PZB10618208	H	Cl	5-methylhexyloxy	5.17 ± 0.09	n.d.[c]
PZB10618209	H	F	5-methylhexyloxy	4.96 ± 0.34	n.d.[c]
JWS-15-90	*See structure above*			< 4	< 5
PZB09412026	*See structure above*			n.d.[c]	6.67 ± 0.24

[a]Inhibition of binding of [^{3}H]PSB-1503 to GPR17, determined in three independent radioligand binding assays performed in duplicate. [b]Potency in inducing calcium mobilization in GPR17-expressing 1321N1 astrocytoma cells, determined in two (JWS-15-90), five (MDL 29,951) or three (all other compounds) independent experiments, performed in duplicate. [c]n.d. = not determined

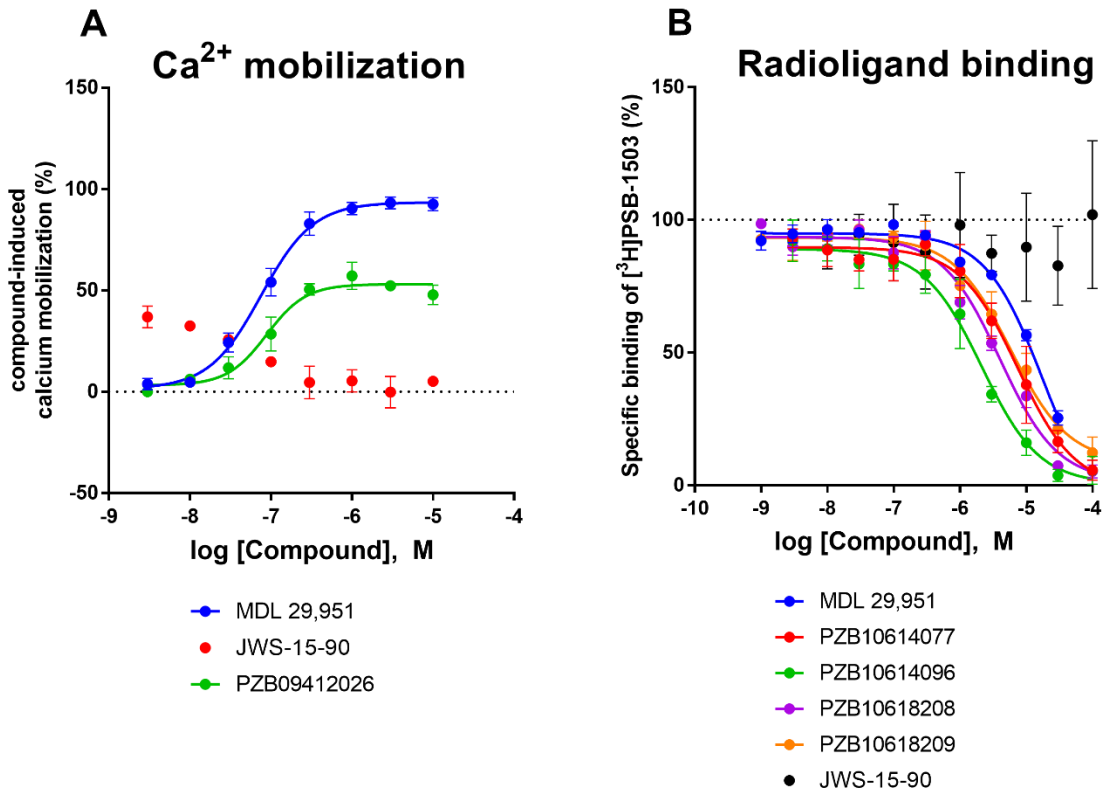

Figure 19. (A) Characterization of JWS-15-90 and PZB09412026 as GPR17 agonists in 1321N1-hGPR17 cells using calcium mobilization assays. MDL 29,951 is shown as positive control. Data points represent means ± SEM of 2 (JWS-15-90), 3 (PZB09412026), or 5 (MDL 29,951) independent experiments, performed in duplicate. (B) Characterization of JWS-15-90 in membrane preparations of CHO-FITR-hGPR17 cells, determined in antagonist radioligand [^{3}H]PSB-1503 binding assays. MDL 29,951

is shown as positive control. Data points represent means ± SEM of 3 independent experiments, performed in duplicate. (A-B) In some cases, SEM values are smaller than the symbols.

Indole derivatives showed moderate binding affinities with pK_i values between 4.83 and 5.32 determined vs. an antagonist radioligand. A bulkier substituent in position 6 increased affinity (compare MDL 29,951 vs. other indole derivatives). Shift of the halogen substituent from position 4 to position 5 decreases affinity (compare PZB10614096 vs. PZB10618209). The highest affinity was achieved by compound PZB10614096 (pK_i = 5.32), substituted with fluorine in position 4 and an aliphatic 5-methylhexyloxy substituent in position 6. As proposed by Baqi et al., both the indole scaffold and the carboxylic acid group in position 2 are vital for potency of indole derivatives at GPR17,[134] which is confirmed by the fact that the indazole derivative JWS-15-90 was inactive. Lastly, PZB09412026 was similarly potent (pEC_{50} = 6.67) as MDL 29,951, but showed partial agonistic activity, a valuable trait uncommon with previous GPR17 agonists.

6.2 GPR17 antagonists

The majority of tested compounds were synthetic antagonists at GPR17. First, there are indole scaffold-based antagonists. Additionally, the collaboration between the Pharmaceutical Institute of the University of Bonn and UCB Pharma GmbH has yielded several compound classes with inhibitory potency at GPR17, such as anthranilic acid derivatives (discussed in detail in Chapter 4) and indolylsulfonamide derivatives.

6.2.1 Indole derivatives

The affinity of nine indole derivatives was determined. These compounds possess the same indole scaffold as the indoles discussed in the previous chapter. However, the original carboxy group in position 2 is essential for agonistic activity[134] and its removal turned these compounds from agonists into antagonists (data unpublished) (see **Table 5** and **Figure 20**).

Table 5. Selected indole derivatives and their binding affinities (pK_i) at GPR17 determined in radioligand binding assays.

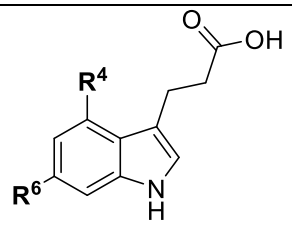

Compound	R^4	R^6	$pK_i \pm$ SEM antagonist radiolig-and binding[a]
PZB10618210	F	4-tolyl	5.09 ± 0.07
PZB10618218	Cl	5-methylhexyloxy	5.10 ± 0.09
PZB10618219	Cl	4-phenylbutyloxy	5.33 ± 0.18
PZB10618221	Cl	3-cyclopropylpropyloxy	5.45 ± 0.09
PZB10618225	F	octyloxy	5.64 ± 0.16
PZB10618226	F	heptyloxy	5.53 ± 0.13
PZB10618228	Cl	hexyloxy	5.04 ± 0.13
PZB10618231	Cl	4-methylpentyloxy	4.76 ± 0.07
PZB10618232	Cl	2-cyclopropylethoxy	4.95 ± 0.10

[a]Inhibition of binding of [^{3}H]PSB-1503 to GPR17, determined in three independent radioligand binding assays performed in duplicate.

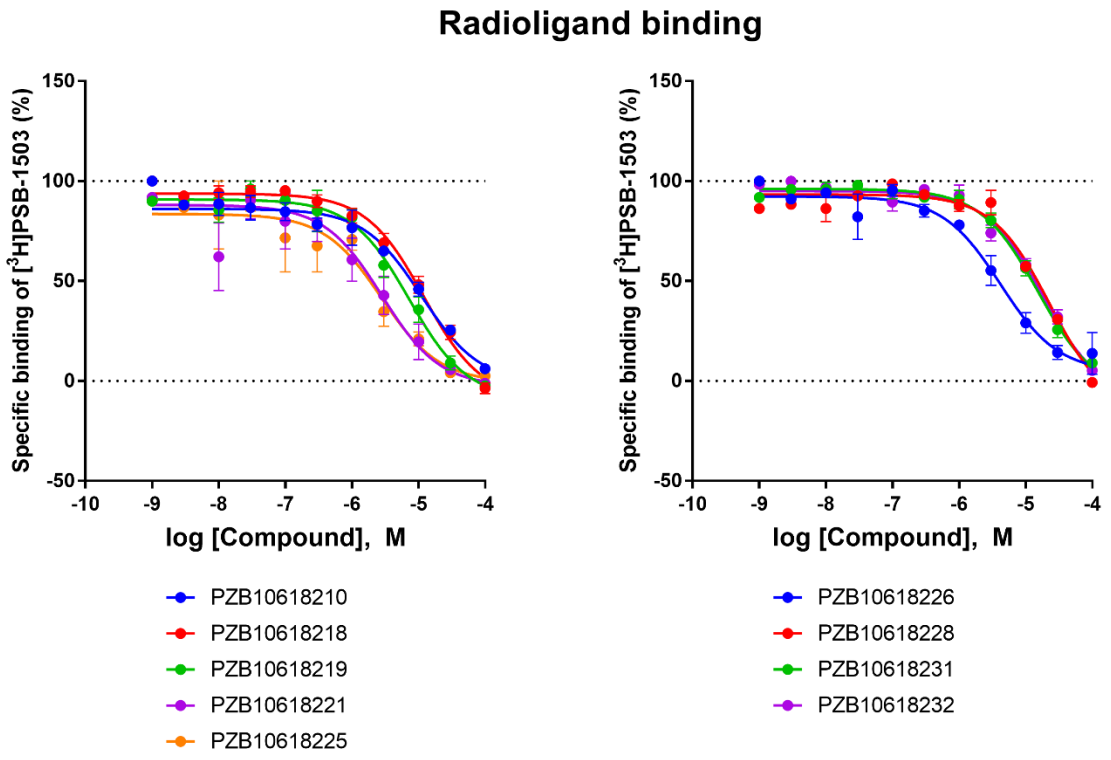

Figure 20. Characterization of selected indole derivatives in membrane preparations of CHO-FITR-hGPR17 cells, determined in radioligand binding assays vs. antagonist radioligand [^{3}H]PSB-1503. MDL 29,951 is shown as a positive control. Data points represent means ± SEM of 3 independent experiments, performed in duplicate. In some cases, SEM values are smaller than the symbols.

All nine compounds showed moderate binding affinities with pK_i values between 4.76 and 5.64. A large substituent in position 6 is well tolerated: Long aliphatic chains with eight carbon atoms yield compounds with the highest affinities (PZB10618221 and PZB10618225), while short aliphatic chains with 5 to 6 carbon atoms yielded compounds with the lowest affinities (PZB10618228, PZB10618231, and PZB10618232). Unbranched aliphatic chains lead to higher affinities than branched aliphatic chains (compare PZB10618228 vs. PZB10618231). Aromatic or mixed substituents in position 6 lie somewhere in between (PZB10618210 and PZB10618219) The highest affinity was achieved by compound PZB10618225 (pK_i = 5.64), substituted with fluorine in position 4 and a long unbranched octyloxy substituent in position 6.

6.2.2 Anthranilic acid derivatives

Another set of compounds with a previously determined antagonistic activity at human GPR17 are based on an anthranilic acid scaffold (see Chapter 4 for detailed discussion).

Prior to assessing the binding affinities of all compounds, four have been singled-out and tested utilizing both available radioligands (antagonist radioligand [^{3}H]PSB-1503 and agonist radioligand [^{3}H]PSB-12150) at membrane preparations from CHO-FITR-hGPR17 cells in order to select one of the radioligands for the experiments shown in the study (see **Table 6** and **Figure 21**).

Table 6. Normalized inhibition of binding of [^{3}H]PSB-12150 or [^{3}H]PSB-1503 to human GPR17 in CHO-FITR-hGPR17 cells by selected anthranilic acid derivatives.

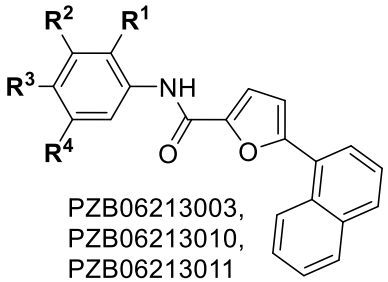

PZB06213003,
PZB06213010,
PZB06213011

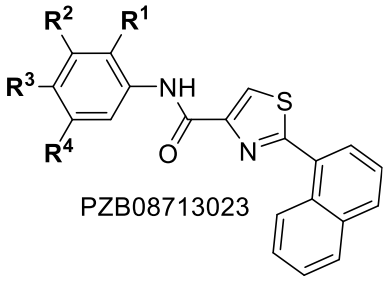

PZB08713023

Compound	R^1	R^2	R^3	R^4	pK_i ± SEM radioligand binding vs. agonist radioligand [^{3}H]PSB-12150[a]	pK_i ± SEM radioligand binding vs. antagonist radioligand [^{3}H]PSB-1503[a]
PZB06213003	carboxy	H	F	F	6.26 ± 0.12	5.34 ± 0.05
PZB06213010	carboxy	H	methoxy	H	6.22 ± 0.50	4.72 ± 0.03
PZB06213011	H	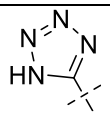	H	H	6.16 ± 0.32	5.41 ± 0.10
PZB08713023	carboxy	H	methoxy	H	6.81 ± 0.29	4.31 ± 0.13

[a]Inhibition of binding of specified radioligand to GPR17, determined in a single radioligand binding assay performed in duplicate.

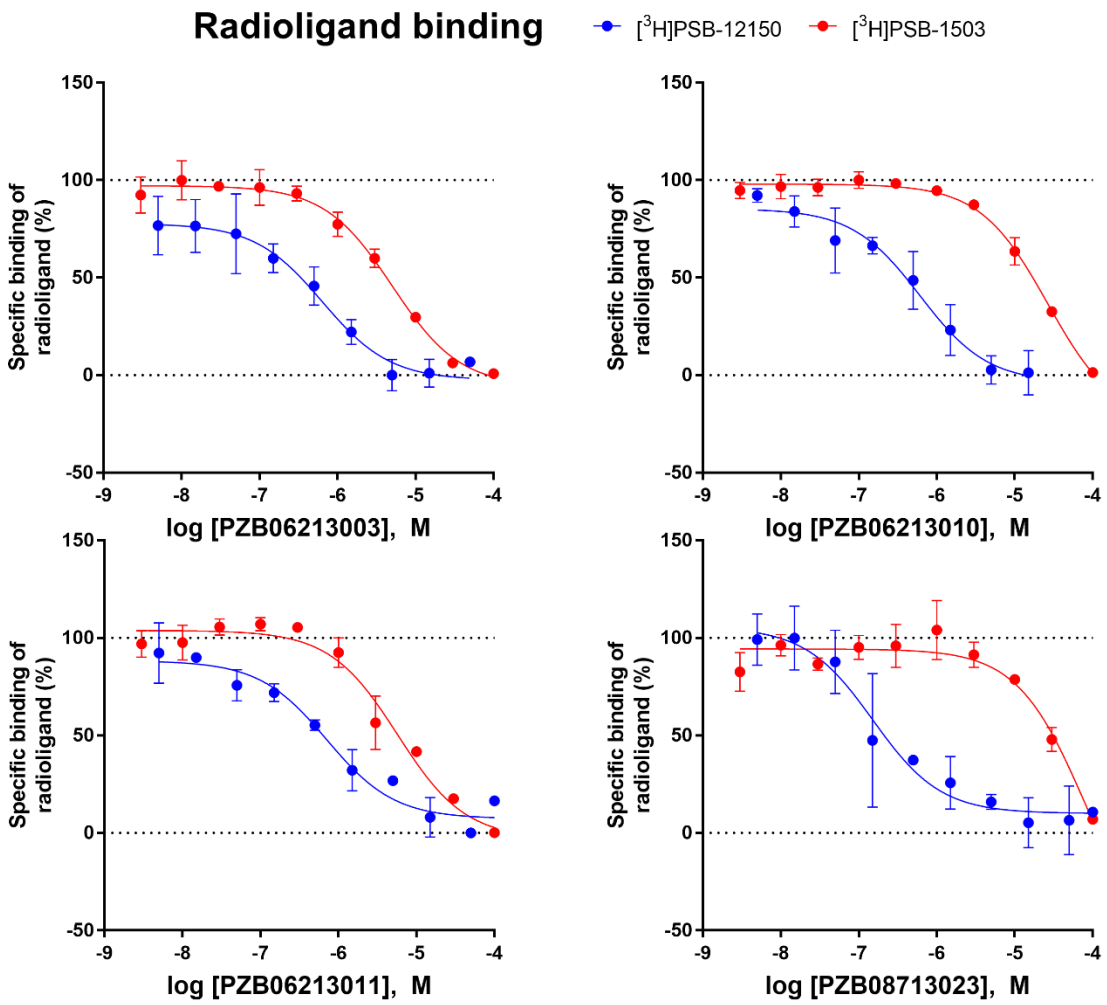

Figure 21. Characterization of selected anthranilic acid derivatives in radioligand binding assays vs. the agonist radioligand [^{3}H]PSB-12150 (MDL 29,951 derived) and vs. the antagonist radioligand [^{3}H]PSB-1503 (indolylsulfonamide derived). Membrane preparations of CHO-FITR-hGPR17 cells were used. Data points represent means ± SEM of a single experiment, performed in duplicate. In some cases, SEM values are smaller than the symbols.

The values determined vs. the antagonist radioligand [^{3}H]PSB-1503 were more precise (lower SEM). The values determined vs. the agonist radioligand [^{3}H]PSB-12150 were on average 1.42 pK_i units higher. Interestingly, there was a negative correlation: PZB087130123, the compound with the highest binding affinity determined in the [^{3}H]PSB-12150 binding assay was the compound with the lowest binding affinity determined in the [^{3}H]PSB-1503 binding assay.

It can be hypothesized that the radioligands utilize (partly) different binding pockets and that the anthranilic acids bind to the same pocket as the agonist radioligand, derived from MDL 29,951, explaining the higher measured affinities. Therefore, the agonist radioligand [^{3}H]PSB-12150 was chosen for the experiments detailed in Chapter 4.

6.2.3 Indolylsulfonamide derivatives

Another set of compounds with previously determined antagonistic activity at GPR17 are based on an indolylsulfonamide scaffold. Due to confidentiality agreements, the exact chemical structures are not disclosed. Because these compounds showed the highest pIC_{50} values at GPR17 in the past (determined in calcium mobilization assays),[136] they had the greatest potential to stabilize GPR17 for crystallization trials. It was hypothesized that from a group of highly affine indolylsulfonamide derivatives, the ligands with the longest residence time at GPR17 should have the greatest potential to stabilize it.

A kinetic binding assay employing the antagonist radioligand [^{3}H]PSB-1503 was established together with Lea Berger during her Master's thesis to evaluate the residence time of compounds at GPR17 (see Subchapter 10.4.4). After combining fixed concentrations of radioligand and unlabeled ligand, membrane protein is added in specific time intervals and results in different incubation durations. The resulting curve of the specific binding over time in combination with kinetic parameters of the radioligand allows determination of association and dissociation rates of the unlabeled ligand.

Seven compounds were tested for their residence time by Lea Berger. Subsequently, 18 more compounds were tested for their residence times (see **Table 7**, compounds tested by Lea Berger are shaded in grey).

Table 7. Residence times of selected indolylsulfonamide derivatives at GPR17 determined in kinetic radioligand binding assays. R^1 to R^3 cannot be disclosed for reasons of confidentiality.

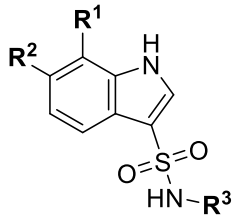

Compound	pIC_{50}[a]	Residence time [min][b]
PSB-23082	9.1	17.1 *(n=6)*
PZB00417001	8.4	< 1
PZB01415021	7.3	< 1
PZB01415041	9.4	< 1
PZB08615012	8.5	< 1
PZB08615073	8.9	< 1
PZB08615082	9.0	< 1
PZB08714044	8.1	< 1
PZB09616008	9.3	9.37
PZB13115016	9.2	1.26

PZB13115017	8.0	< 1
PZB13115018	8.9	< 1
PZB13115019	8.4	< 1
PZB13115023	8.9	< 1 *(n=4)*
PZB13115026	9.0	< 1
PZB13315021	7.6	1.29
PZB13315023	9.9	15.5
PZB13315024	9.6	10.8
PZB13315025	8.4	1.64
PZB13315026	7.7	1.68
PZB13315027	9.4	2.83
PZB13315028	9.0	< 1
PZB13315032	9.2	3.44
PZB16017003	8.6	< 1

[a]Potency in inhibiting calcium mobilization in CHO-FITR-hGPR17 cells, activated with MDL 29,951, determined in a single experiment by UCB Pharma GmbH. [b]Residence time at GPR17 determined in kinetic antagonist radioligand [^{3}H]PSB-1503 binding assays, three independent experiments (except where noted in italic brackets) were performed in duplicate.

PSB-23082 was found to be the compound with the longest residence time (17.1 min). It was tested further in thermostability assays alongside PZB13315023, which exhibited the second highest residence time (15.5 min) (see Chapter 7). However, assay results were poorly reproducible and should therefore be interpreted cautiously. In some cases, the difference in residence time from a single halogen exchange seemed too drastic. Furthermore, many compounds produced residence times of less than 1 min (and often even less than 1 s). Since such short residence times were deemed improbable for highly potent compounds, it was hypothesized that the assay was not able to produce accurate results for shorter residence times, and it was concluded that the assay in its current form is not suitable for determining residence times, at least for compounds with a faster kinetic than the radioligand (< 6.7 min). Further optimization is necessary, e.g., a lower temperature or a method for continuous measurement with a fluorescent conjugate.

Next, the previously unmodified indole nitrogen was substituted to explore the binding pocket's capacity for larger conjugates such as fluorescence tags. A total of 10 additional structurally similar compounds were characterized as antagonists in calcium mobilization assays (see **Table 8** and **Figure 22**).

Table 8. Inhibitory potencies (pIC_{50}) of selected indolylsulfonamide derivatives at GPR17 determined in calcium mobilization assays. R^1 and R^3 cannot be disclosed for reasons of confidentiality.

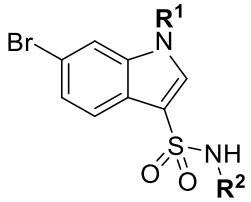

Compound	pIC_{50} ± SEM[a]
PZB00424004	5.45 ± 0.10
PZB00424005	5.56 ± 0.10
PZB00424006	6.35 ± 0.05
PZB00424007	7.09 ± 0.03
PZB00424009	5.03 ± 0.13
PZB00424010	5.54 ± 0.06
PZB00424011	5.72 ± 0.02
PZB00424013	5.49 ± 0.06
PZB00424014	5.14 ± 0.16
PZB00424015	6.79 ± 0.07

[a]Potency in inhibiting calcium mobilization in GPR17-expressing 1321N1 astrocytoma cells, activated with MDL 29,951 at its EC_{80} concentration, determined in three to five independent experiments, performed in duplicate.

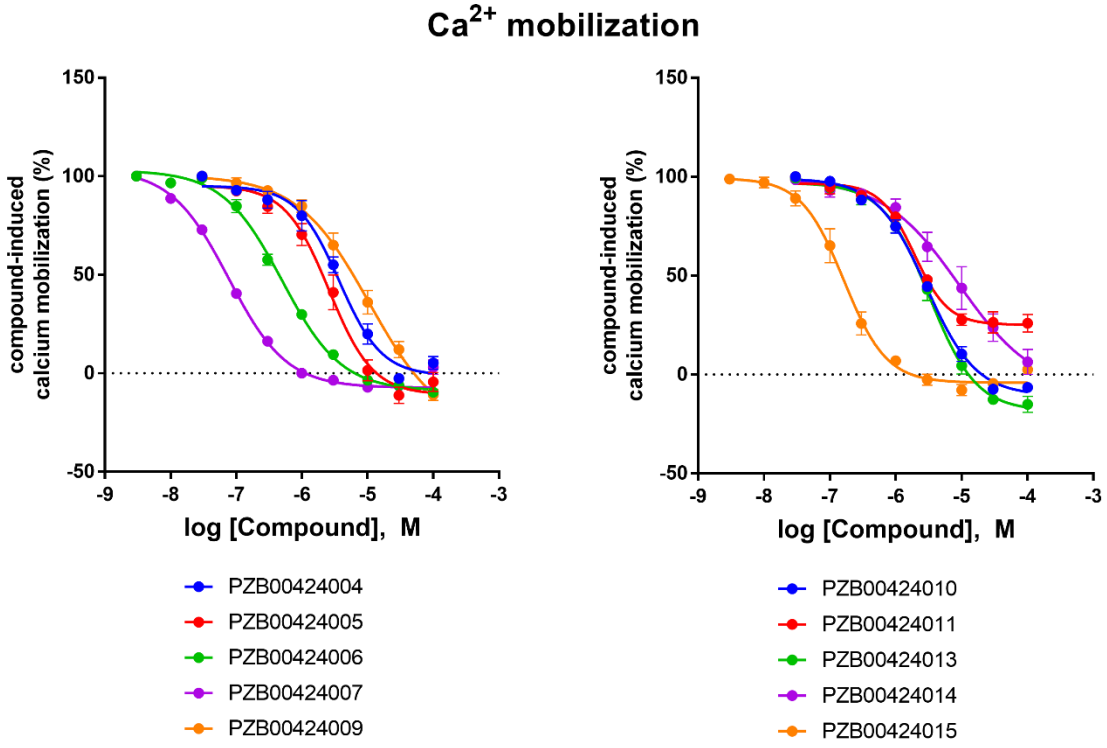

Figure 22. Characterization of selected indolylsulfonamide derivatives as GPR17 antagonists determined in 1321N1-hGPR17 cells. The receptor was activated with MDL 29,951 at its EC_{80} concentration. Data points represent means ± SEM of three independent experiments, performed in duplicate. In some cases, SEM values are smaller than the symbols.

Their inhibitory potencies range from pIC_{50} values of 4.83 to 7.04, the highest was achieved by PZB00424007. Interesting candidates would employ the indole nitrogen substituent of PZB00424007 with other substituents at its sulfonamide position.

7 Optimizing GPR17 thermostability and expression for structural studies

7.1 Construct design

The crystallization of GPCRs requires extensive receptor modifications to improve thermostability, expression, and other beneficial properties. More than 30 different receptor constructs have been designed, expressed, purified, and analyzed. For all constructs, a cleavable signal sequence derived from the influenza hemagglutinin (HA) protein was incorporated at the N-terminus to enhance expression, a FLAG-tag was appended downstream of the HA-tag to facilitate expression evaluation via flow cytometry, and a 10x His-tag was introduced at the C-terminus for protein purification (except for ML30, where it was relocated upstream of the N-terminus). The distinct GPR17 construct variants were further modified using the following strategies:

- Truncation of the N- and/or C-termini,
- Insertion of fusion partners
- Point mutations.

Additionally, in construct ML23, the polyhedrin promotor was replaced with a baculovirus *gp64* promotor. The following **Table 9** provides an overview over all designed constructs:

Table 9. GPR17 constructs overview.

Name	N-truncation	C-truncation	Fusion partner	Insertion Site	Mutation(s)	Other
17wt	1-28	-	-	-	-	-
17wtb	1-28	-	**BRIL**	L251-V253	-	-
ML1	**1-43**	**343-367**	-	-	-	-
ML2	1-43	343-367	BRIL	L251-V253	-	-
ML3	1-43	343-367	BRIL	L251-V253	**D321N**	-
ML4	1-43	343-367	BRIL	L251-V253	**F158Y**	-
ML5	1-43	343-367	BRIL	L251-V253	**S146K**	-
ML6	1-43	343-367	BRIL	L251-V253	**D321N, F158Y**	-
ML7	1-43	343-367	BRIL	L251-V253	**D321N, S146K**	-
ML8	1-43	343-367	BRIL	L251-V253	**F158Y, S146K**	-
ML9	1-43	343-367	BRIL	L251-V253	**A261D**	-
ML11	1-43	343-367	BRIL	L251-V253	**D105N**	-
ML12	1-43	343-367	BRIL	L251-V253	**A63P**	-

ML13	1-43	343-367	BRIL	L251-V253	**F65V**	-
ML14	1-43	343-367	BRIL	L251-V253	**A73G**	-
ML15	1-43	343-367	BRIL	L251-V253	**S107L**	-
ML16	1-43	343-367	BRIL	L251-V253	**S311L**	-
ML17	1-43	343-367	BRIL	L251-V253	**N204Q**	-
ML18	1-43	343-367	BRIL	L251-V253	**L269A**	-
ML19	1-43	343-367	BRIL	L251-V253	**Y240F**	-
ML20	1-43	343-367	BRIL	L251-V253	**D69V**	-
ML21	1-43	343-367	BRIL	L251-V253	**V75P**	-
ML22	1-43	343-367	BRIL	L251-V253	**K311T**	-
ML23	1-43	343-367	BRIL	L251-V253	-	***gp64* promo-tor**
ML24	**1-28**	343-367	BRIL	L251-V253	-	-
ML25	**1-51**	343-367	BRIL	L251-V253	-	-
ML27	1-43	343-367	BRIL	**L247-K255**	-	-
ML28	1-43	343-367	BRIL	**L251-K255**	-	-
ML30	1-43	343-367	BRIL	L251-V253	-	**N-terminal His-tag**
ML32	1-43	343-367	BRIL	**S246-K255**	-	-
ML33	1-43	343-367	BRIL	S246-K255	**D321N**	-
ML34	1-43	343-367	BRIL	S246-K255	**F158Y**	-
ML35	1-43	343-367	BRIL	S246-K255	**S146K**	-
ML36	1-43	343-367	BRIL	**L251-R252**	-	-

Figure 23 shows an example snake plot of GPR17 construct ML2.

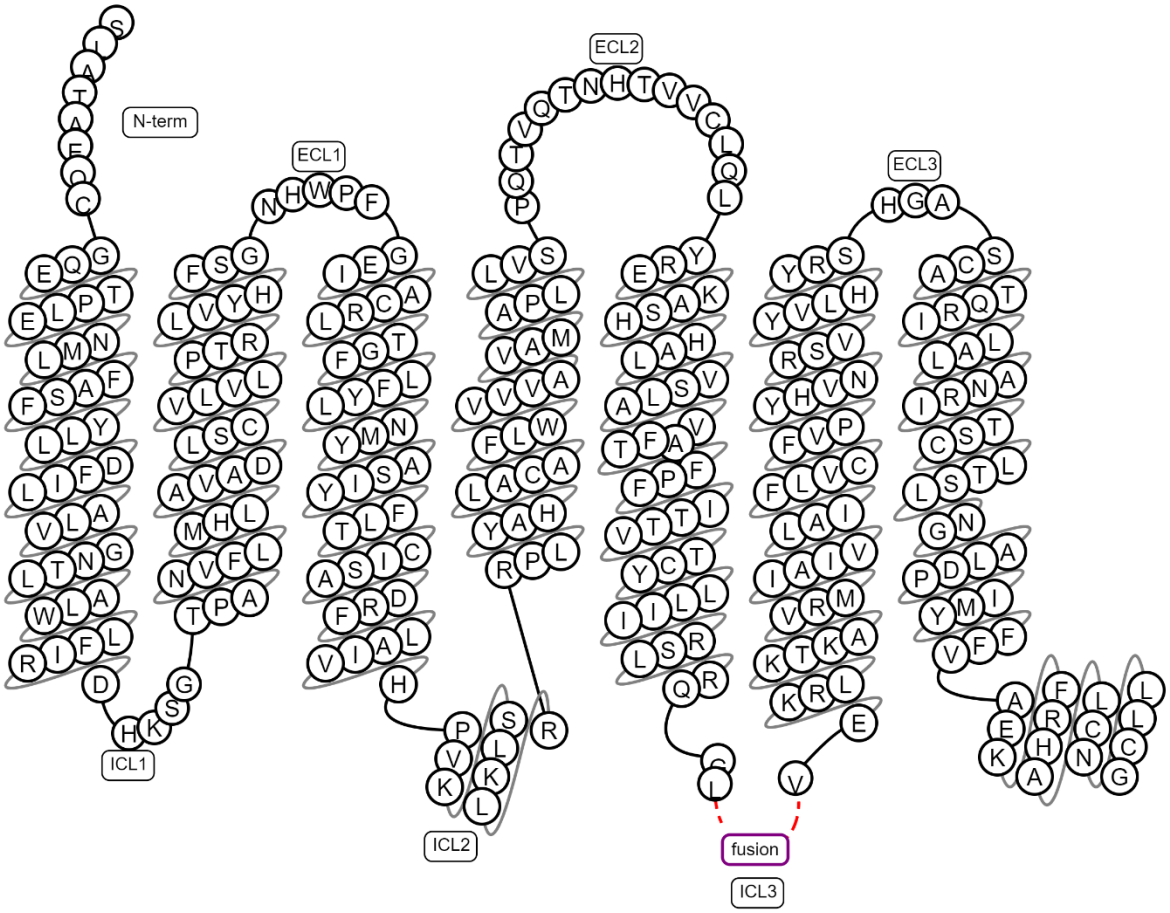

Figure 23. Snake plot of GPR17 construct ML2 with N-terminal truncation at S44, C-terminal truncation at G342, and insertion of fusion partner BRIL into ICL3 between residues L251 and V253. Generated by GPCRdb.[182]

In addition to construct sequence optimization, different protein expression and purification conditions were investigated as well:

- Type of expression system
- Passaging and amount of virus for the infection
- Expression of the apo state or in combination with ligands
- If in combination with ligands: addition of the ligand already during expression or only during purification
- Salt concentration in wash and elution buffers
- Additives during the solubilization and purification process (imidazole, $MgCl_2$, ATP)

7.2 Construct analysis

Expression and purification of GPR17 constructs were assessed using size-exclusion chromatography (SEC), a thermostability assay (TSA) based on *N*-[4-(7-diethylamino-4-methyl-3-coumarinyl)phenyl]maleimide (CPM), and sodium dodecyl sulfate-polyacrylamide gel electrophoresis (SDS-PAGE).

SEC was employed to evaluate overall protein yield, verify the identity of the purified protein sample based on elution time, estimate changes in protein quantity, and analyze the homogeneity of purified protein samples (see **Figure 24** for the complete elution profile of the 17wt construct from SEC analysis).

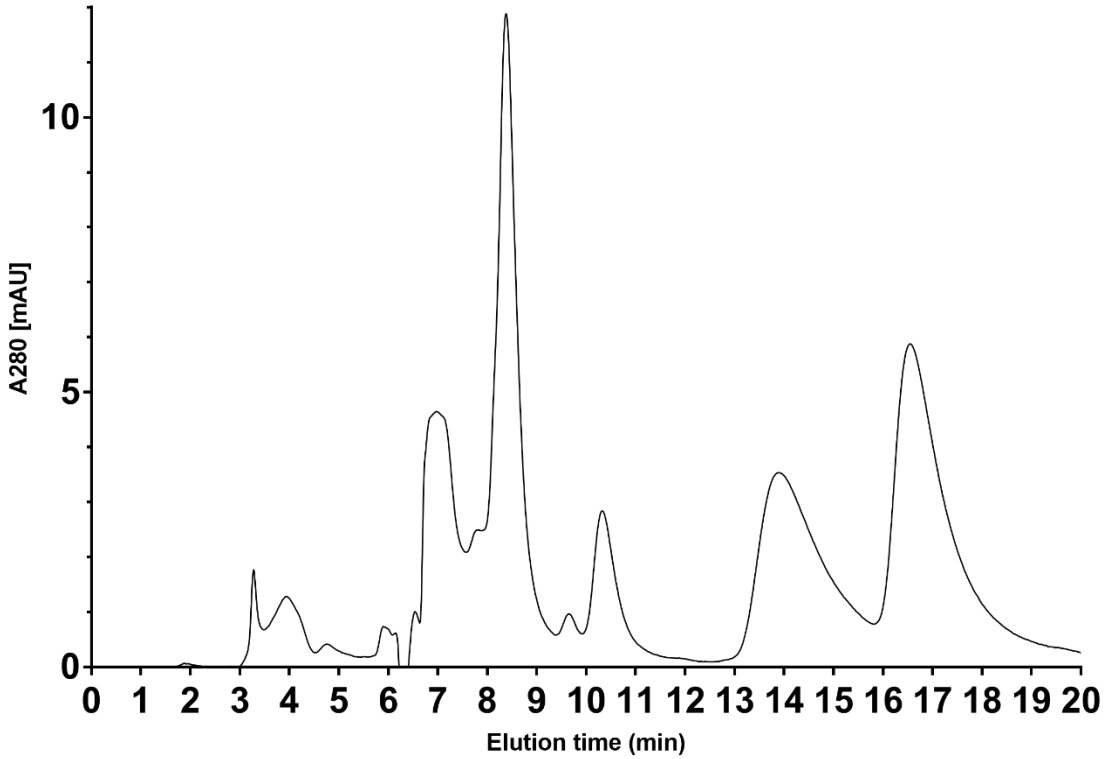

Figure 24. Complete elution profile of a SEC analysis of the GPR17 construct 17wt expressed in 40 mL of *Sf9* insect cells in the apo form.

The largest peak at approximately 8.4 min corresponds to imidazole, while the correctly folded GPR17 monomer can be observed at 3.8–3.9 min elution time. To improve interpretability, subsequent SEC chromatograms were truncated to display the retention time window between 2.5 and 5.0 min. Normalized SEC chromatograms were used to illustrate peak shape and assess

the presence of protein aggregates, which elute earlier due to their large size and precede the main protein peak.

The TSA was used to determine the "melting temperature" (T_M) of receptor constructs, providing insight into their thermostability. In this assay, protein unfolding upon heating exposes buried cysteine residues, which then react with the CPM dye, forming CPM-thiol adducts that increase fluorescence (see **Figure 25**). The T_M value is defined as the inflection point of the fluorescence curve, determined by nonlinear regression analysis.

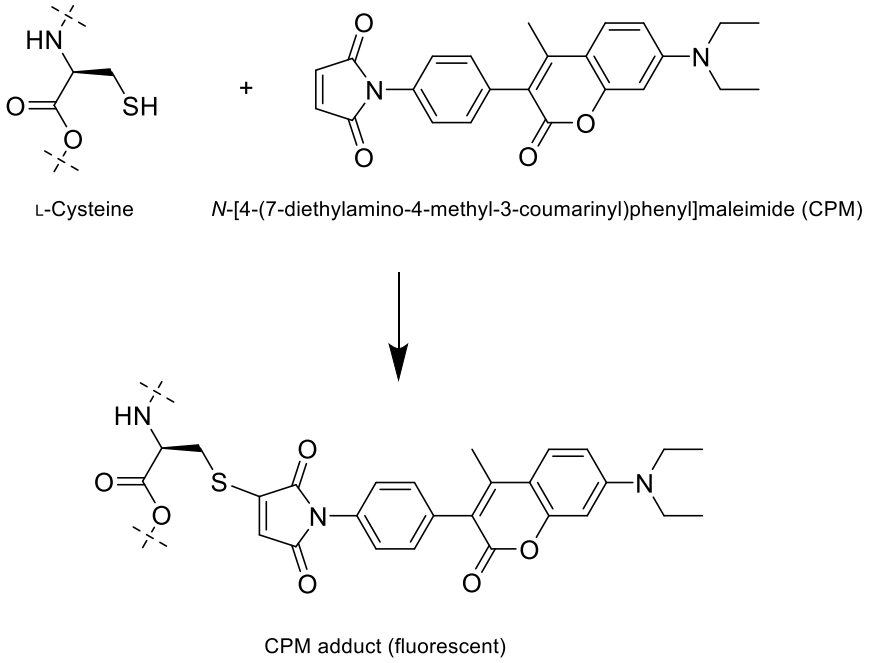

Figure 25. Chemistry of CPM adduct formation.

Due to a combination of low protein yield and low thermostability, the GPR17 constructs 17wt, 17wtb, ML1, ML3, ML4, and ML5 did not exhibit clear sigmoidal curves with distinct inflection points (see **Figure 26**). These results were characteristic of early construct optimization cycles performed with the receptor in the apo state. Therefore, TSA results are only shown for constructs bound to a stabilizing antagonist that increased thermostability and improved inflection point clarity.

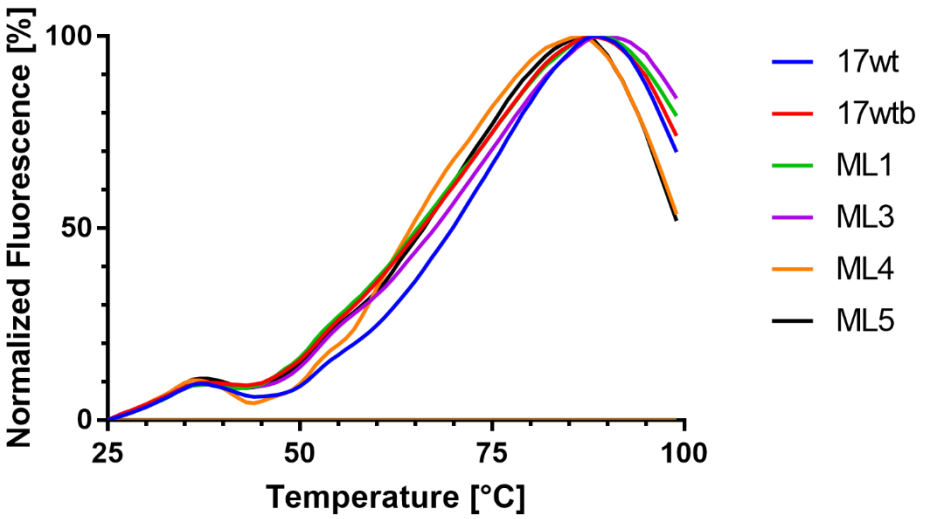

Figure 26. TSA analysis of GPR17 constructs 17wt, 17wtb, ML1, ML3, ML4, and ML5, all expressed in 40 mL of *Sf9* insect cells in the apo form. The assay was performed using CPM as a dye. For each construct separately, the largest fluorescence value was defined as 100 % normalized fluorescence, and the smallest fluorescence value as 0 % normalized fluorescence.

SDS-PAGE was performed to verify protein identity based on molecular weight and to assess purity by the amount of other proteins present in the sample (see **Figure 27** for the results of the first construction optimization cycle). SDS denatures proteins, thereby dissociating dimers and oligomers, which can result in a prominent main protein band that may overestimate actual protein concentration. The largely unmodified GPR17 construct 17wt is 43 kDa in size, the most commonly employed N- and C-terminal truncation removes 4 kDa, while the fusion protein BRIL adds 12 kDa, making construct 17wtb (untruncated termini and BRIL fusion) 55 kDa, ML1 (truncated termini and no fusion protein) 39 kDa, and most other constructs (truncated N-/C-termini and fusion with bRIL) 51 kDa. Lower molecular weight bands likely represent impurities, while higher molecular weight bands correspond to still present dimers and oligomers.

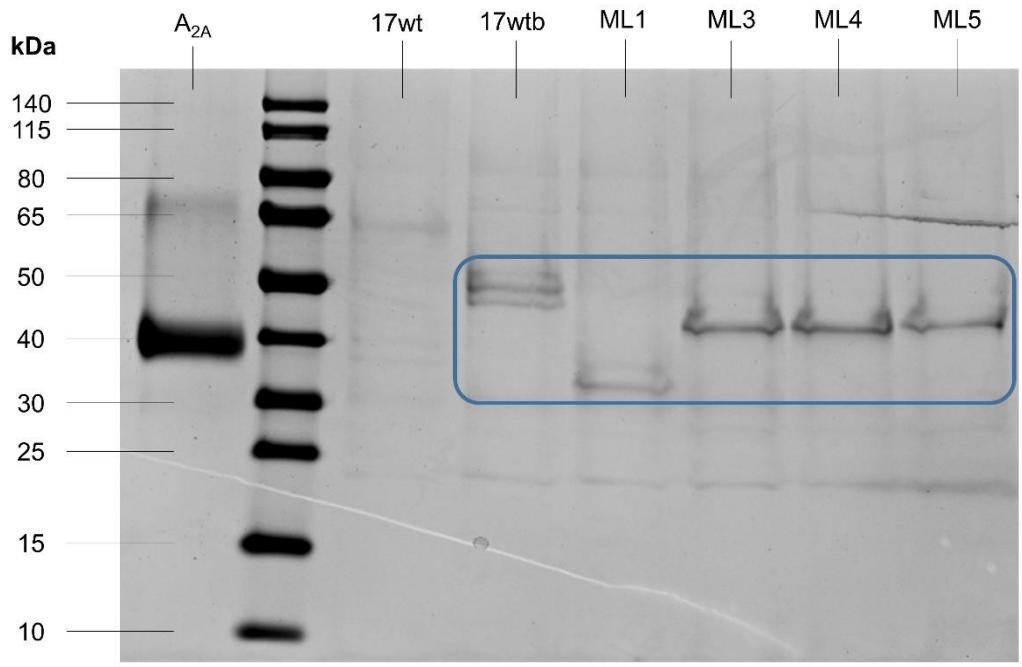

Figure 27. SDS-PAGE analysis of GPR17 constructs 17wt, 17wtb, ML1, ML3, ML4, and ML5, all expressed in 40 mL of *Sf9* insect cells in the apo form. Sample lanes were loaded with 22.5 µL protein solution or 4 µL of the A_{2A}-PSB1-BRIL construct as positive control. Bands representing the GPR17 constructs are circled in blue.

The SDS-PAGE analysis shows a very prominent control band of the A_{2A}-PSB1-BRIL construct and less prominent bands by GPR17 constructs. ML1 has a lower molecular weight than ML3, ML4, and ML5 due to the absence of the fusion protein bRIL, while 17wtb has a higher molecular weight due to no truncation of N- and C-termini. The absence of 17wt is probably due to an error in experimental procedure (it was present in the SEC analysis of the same protein sample, see **Figure 29**).

Small variations in experimental procedures, even for identical constructs, due to human error can accumulate over time and lead to slightly different results (see **Figure 28**). Therefore, in the following construct analysis, differences between samples should also be considered due to these inconsistencies.

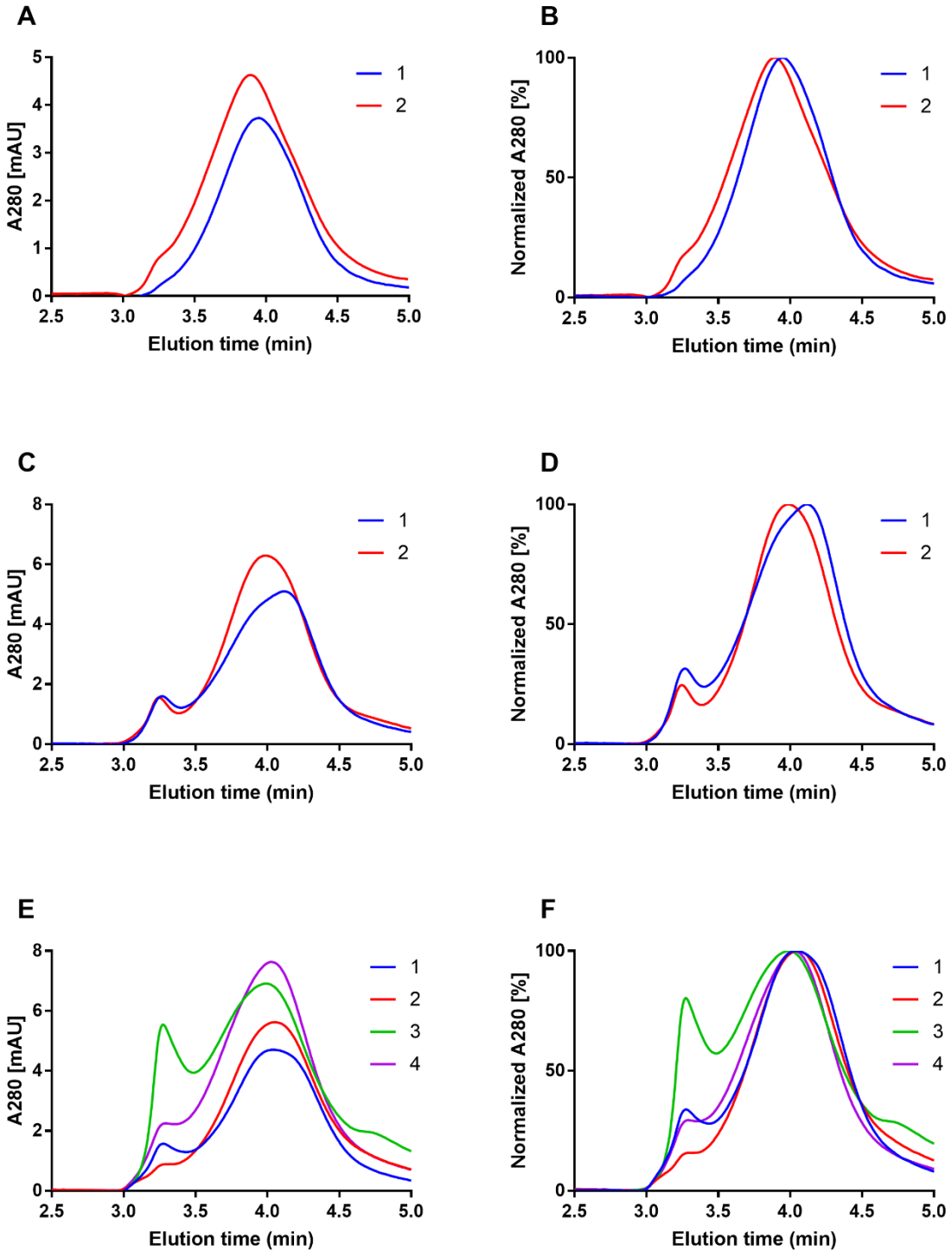

Figure 28. SEC analyses of GPR17 construct ML32 bound to GPR17 antagonist PSB-23082, shown each time as unscaled (A, C, E) and normalized data (B, D, F). Correctly folded protein monomer is suspected to be the peak at 3.8–3.9 min. (A, B) Protein was expressed in 40 mL of *Sf9* insect cells. (C, D) Protein was expressed in 40 mL of *Tni* insect cells. (E, F) Protein was expressed in 40 mL of *Tni* insect cells, and a higher salt concentration of 1000 nM was used in wash and elution buffers.

In the dataset of **Figure 28** – spanning multiple constructs, expression systems, and solubilization/purification conditions – the standard deviations for peak time and peak height were 0.042 and 0.94, respectively. Consequently, differences smaller than these values will be considered "non-significant", while larger differences will be deemed "significant".

7.3 Influence of N- and C-terminal truncation

The short isoform of GPR17 was used throughout the experiments, which is equivalent to a quasi-N-terminal truncation at M29 based on hGPR17-L amino acid numbering. For most constructs, the N-terminus was truncated even at S44 and the C-terminus was truncated (completely) at G342 (see **Figure 23**). These positions were chosen based on high occurrence in phylogenetically related receptors. Variants with an untruncated N-terminus and a completely truncated N-terminus (G52) were also tested.

First, the difference between truncated and untruncated GPR17 constructs was evaluated (see **Figure 29**).

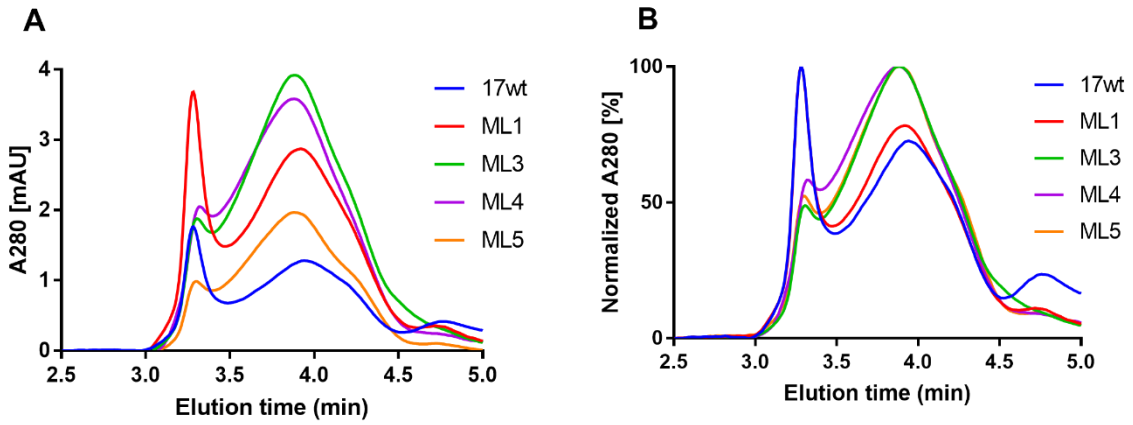

Figure 29. SEC analysis of GPR17 constructs 17wt, ML1, ML3, ML4, and ML5, all expressed in 40 mL of *Sf9* insect cells in the apo form, shown as unscaled (A) and normalized data (B).

SEC analysis showed that truncated constructs (ML1, ML3, ML4, ML5) exhibited higher protein yield than the untruncated construct (17wt). In addition, constructs that both fused with BRIL and contained point mutations (ML3, ML4, ML5) had a considerably lower aggregate peak at 3.3 min compared to unfused constructs (17wt, ML1), suggesting, because each construct possesses a different point mutation, that this effect was mediated by the fusion to BRIL

(which will be further discussed in the next subchapter). SDS-PAGE analysis of the same protein samples (see **Figure 27**) yielded similar results, with ML3 and ML4 displaying the most prominent bands.

Next, the effect of different N-terminal lengths was investigated (see **Figure 30**).

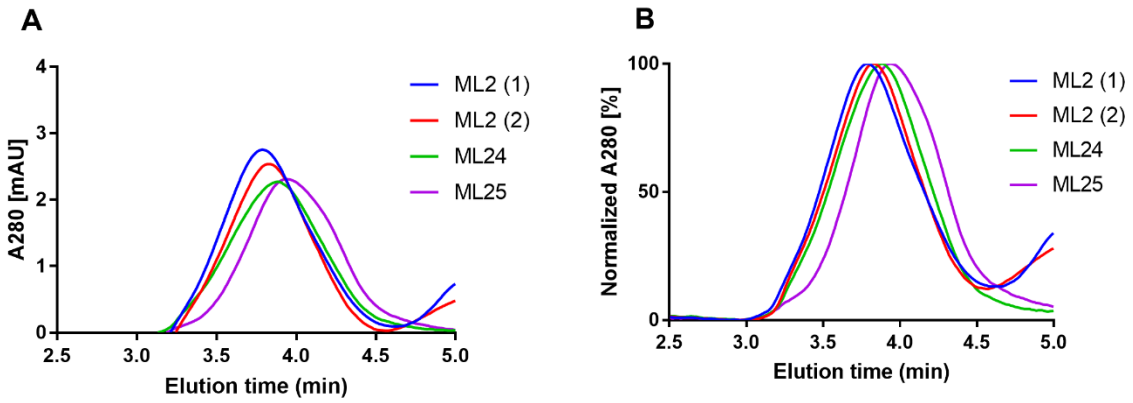

Figure 30. SEC analysis of constructs ML2 (tested twice), ML24, and ML25, all expressed in 40 mL of *Sf9* insect cells bound to GPR17 antagonist PSB-23082, shown as unscaled (A) and normalized data (B).

Here, the results did not differ significantly, albeit construct ML2 (N-terminus truncated to S44, C-terminus completely truncated) achieved a slightly higher protein yield than exclusive C-terminal truncation (ML24) or full truncation of both termini (ML25).

7.4 Influence of inserted fusion partners

Due to its successful use in crystallization of numerous phylogenetically related receptors, BRIL was selected as the fusion partner. As elucidated in the previous subchapter discussing **Figure 29**, fusion to BRIL seemed to reduce protein aggregation. In most constructs, BRIL was inserted into ICL3 between residues L251 and V253, a site chosen based on its frequent use in related receptors. Alternative BRIL insertion sites (e.g., K246-K255 and L251-K255) were also tested (see **Figure 31**).

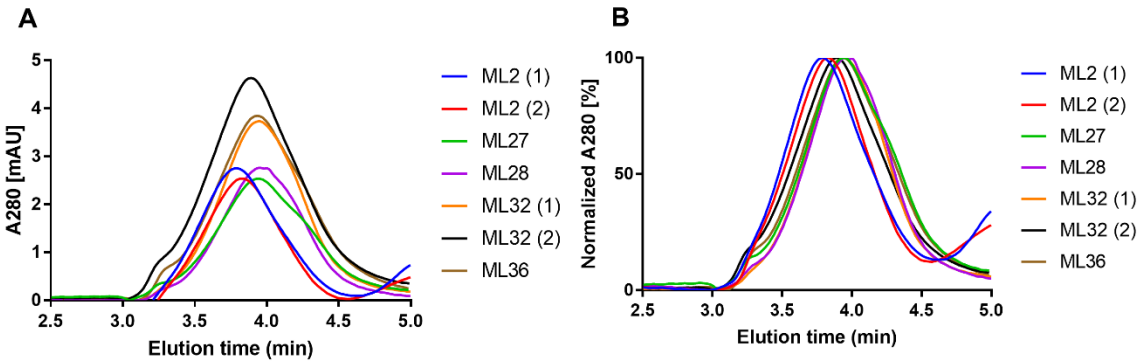

Figure 31. SEC analysis of GPR17 constructs ML2 (tested twice), ML27, ML28, ML32 (tested twice), and ML36, all bound to GPR17 antagonist PSB-23082 and expressed in 40 mL of *Sf9* insect cells, shown as unscaled (A) and normalized data (B).

Construct ML32 (insertion of BRIL between residues S246 and K255) showed the highest protein yield, followed by construct ML36 (insertion of BRIL between residues L251 and R252). Some of the samples were also investigated by SDS-PAGE (see **Figure 32**).

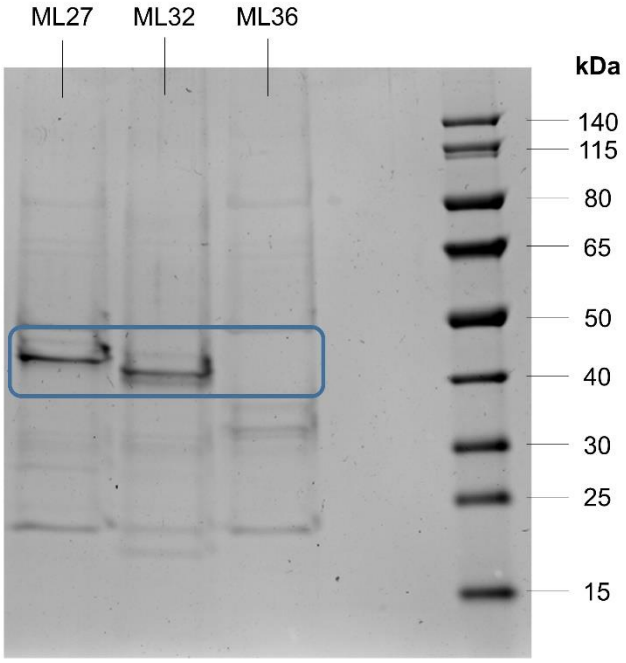

Figure 32. SDS-PAGE analysis of GPR17 constructs ML27, ML32, and ML36, expressed in 40 mL of *Sf9* insect cells, eluted in 110 µL, and bound to GPR17 antagonist PSB-23082. Sample lanes were loaded with 22.5 µL protein solution. Bands representing the GPR17 constructs are circled in blue.

Both ML27 and ML32 showed prominent bands, while ML36 displayed no band at all.

7.5 Influence of point mutations

Several point mutations were introduced. The selection of these point mutations was based on several strategies:

- Amino acids that were mutated in successful crystallization constructs of phylogenetically related receptors were mutated equally.
- Amino acids of GPR17 deviating from the conserved ones of phylogenetically related receptors were mutated to the conserved one.
- Amino acid mutations that were predicted as leading to the most stable mutants by LITiConDesign[183] and GPCRdb.[182]

The following **Table 10** lists all constructed point mutations of GPR17. The point mutations were partly applied in combinations. The GPR17 construct to which the point mutations were most commonly applied was ML2 (N-terminal truncation at S44, C-terminal truncation at G342, insertion of BRIL in ICL3 between L251 and V253).

Table 10. All employed point mutations for the generation of GPR17 constructs and their rationale.

Point mutation	GPCR residue number	Rationale
A63P	1.36	• $P^{1.36}$ occurs naturally in $CysLT_2$, $P2Y_1$, PAR1, PAR2, PAF, and $P2Y_{12}$ receptors
F65V	1.38	• $V^{1.38}$ occurs naturally in $CysLT_2$, $P2Y_1$, PAR1, PAR2, and PAF receptors, other hydrophobic aliphatic amino acids in 1.38 occur naturally in $CysLT_1$, $P2Y_{12}$, and FFA1 receptors
D69V	1.42	• $V^{1.42}$ occurs naturally in $P2Y_1$, PAR1, and PAR2 receptors, other hydrophobic aliphatic amino acids occur naturally at 1.42 in $CysLT_2$, $CysLT_1$, PAF, $P2Y_{12}$, and FFA1 receptors
A73G	1.46	• $G^{1.46}$ occurs naturally in $CysLT_2$, $P2Y_1$, $CysLT_1$, succinate, PAR2, PAF, $P2Y_{12}$, and FFA1 receptors
V75P	1.48	• $P^{1.48}$ occurs naturally in PAR1, PAR2, and FFA1 receptors
D105N	2.50	• used in the crystallization construct of the $CysLT_2$ receptor
S107L	2.52	• $L^{2.52}$ occurs naturally in $CysLT_2$, $P2Y_1$, $CysLT_1$, PAR1, PAR2, PAF, $P2Y_{12}$, and FFA1 receptors, another hydrophobic aliphatic amino acid occurs naturally in the succinate receptor

S146K	3.39	• used for stabilizing A_{2A}, A_{2B}, and A_3 receptors by colleagues in the same research group • presumably occupies the Na^+ binding site and exerts a stabilizing effect
F158Y	3.51	• used in the crystallization constructs of PAF and $CysLT_2$ receptors • $Y^{3.51}$ occurs naturally in $P2Y_1$, $P2Y_{12}$, PAR2, and FFA1 receptors • predicted improvement upon receptor expression by GPCRdb
Y240F	5.58	• used in the crystallization construct of the FFA1 receptor
L269A	6.41	• used in the crystallization construct of the PAR2 receptor
S311L	7.39	• $L^{7.39}$ occurs naturally $CysLT_2$, $CysLT_1$, PAR2, PAF, $P2Y_{12}$, and FFA1 receptors, another hydrophobic aliphatic amino acid occurs naturally in the PAR1 receptor
D321N	7.49	• used in the crystallization constructs of $P2Y_1$, $P2Y_{12}$, and PAF receptors • $N^{7.49}$ occurs naturally in $CysLT_2$ and PAF receptors • predicted thermostabilizing effect by GPCRdb
K311T	8.49	• K can impair the stability • $T^{8.49}$ occurs naturally in the $P2Y_1$ receptor
N204Q	ECL2	• used in the crystallization construct of the PAR2 receptor

Single point mutations in construct ML2 resulted in ML3 (D321N), ML4 (F158Y), and ML5 (S146K) (see **Figure 33**, also compare expression of ML3, ML4, and ML5 in *Sf9* insect cells in **Figure 29**).

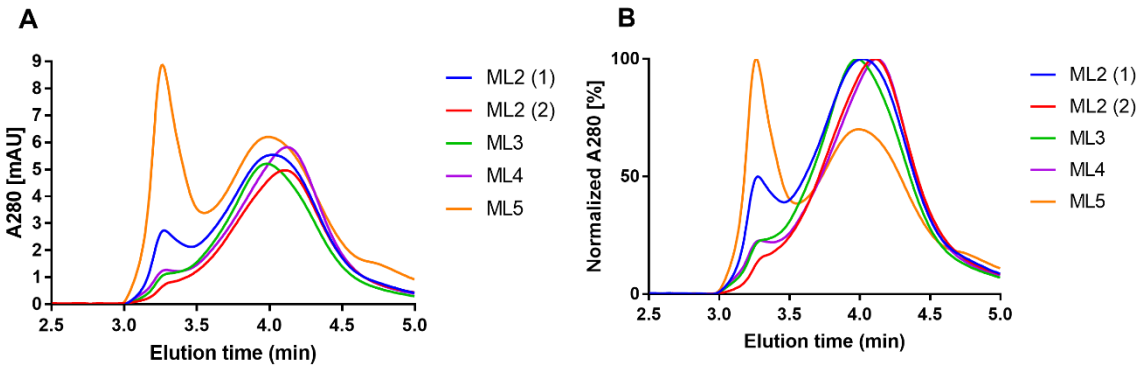

Figure 33. SEC analysis of GPR17 constructs ML2 (tested twice), ML3, ML4, and ML5, all bound to GPR17 antagonist PSB-23802 and expressed in 40 mL of *Tni* insect cells, shown as unscaled (A) and normalized data (B).

SEC analysis revealed that S146K improved protein yield significantly when expressed in *Tni* insect cells but also produced a large unwanted aggregate peak, which can be coincidental, as it was absent following *Sf9* insect cell expression (see **Figure 29**). It remains unclear why ML5 exhibited a higher yield in *Tni* insect cells but a lower yield in *Sf9* insect cells compared to ML3 and ML4.

Employing the same point mutations starting from construct ML32 (different position of BRIL compared to ML2) yielded ML33, ML34, and ML35 (D321N, F158Y, and S146K, respectively) (see **Figure 34**).

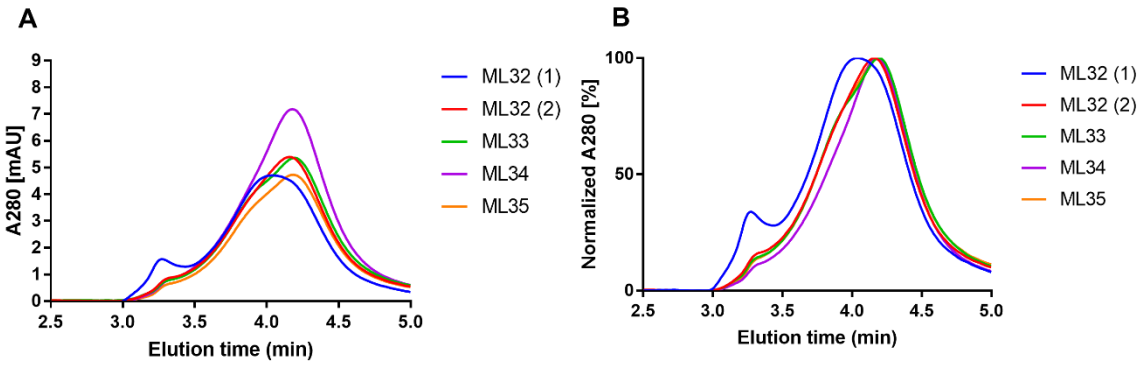

Figure 34. SEC analysis of constructs ML32 (tested twice), ML33, ML34, and ML35, all bound to GPR17 antagonist PSB-23802 and expressed in 40 mL of *Tni* insect cells, shown as unscaled (A) and normalized data (B).

Herein, F158Y mutation of GPR17 construct ML34 improved protein yield significantly, in line with the prediction by GPCRdb.

Next, ML32 and ML34 were again compared in a large-scale expression (see **Figure 35**).

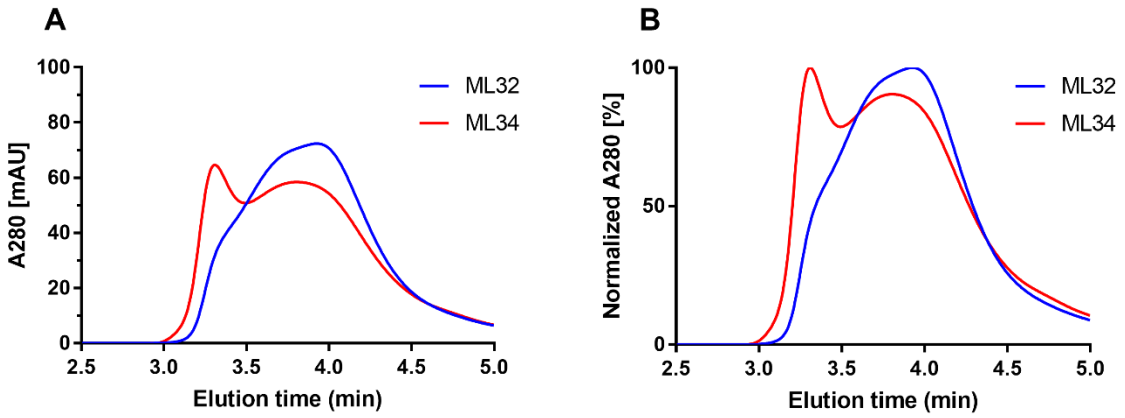

Figure 35. SEC analysis of constructs ML32 and ML34 bound to the antagonist PSB-23082, expressed in 450 mL of *Tni* insect cells and concentrated down to 200 µL after elution, shown as unscaled (A) and normalized data (B).

Needless to say, the total protein yield is higher in a large-scale expression. A measurement of protein concentration in these samples of ML32 and ML34 yielded results of 3.25 mg/mL and 1.90 mg/mL, respectively. This time, F158Y mutation was detrimental: it decreased the amount of correctly folded protein and increased the aggregate peak.

The negative effect can also be seen in the SDS-PAGE analysis of these protein samples (see **Figure 36**) and in the TSA analysis discussed in Subchapter 7.10.

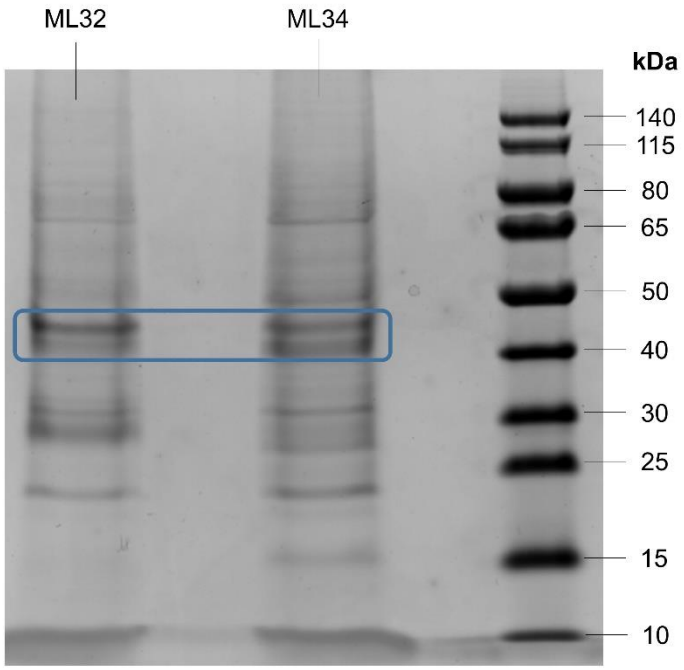

Figure 36. SDS-PAGE analysis of ML32 and ML34, each expressed in 450 mL of *Tni* insect cells, concentrated to 200 µL after elution, and bound to antagonist PSB-23082. Sample lanes were loaded with 22.5 µL protein solution. Bands representing the GPR17 constructs are circled in blue.

In addition to showing multiple bands, which suggest an unpure protein sample, construct ML34 showed a stronger band at a higher size of approx. 70 kDa when compared to ML32.

7.6 Influence of different promotors

The influence of different promotors was evaluated (see **Figure 37**).

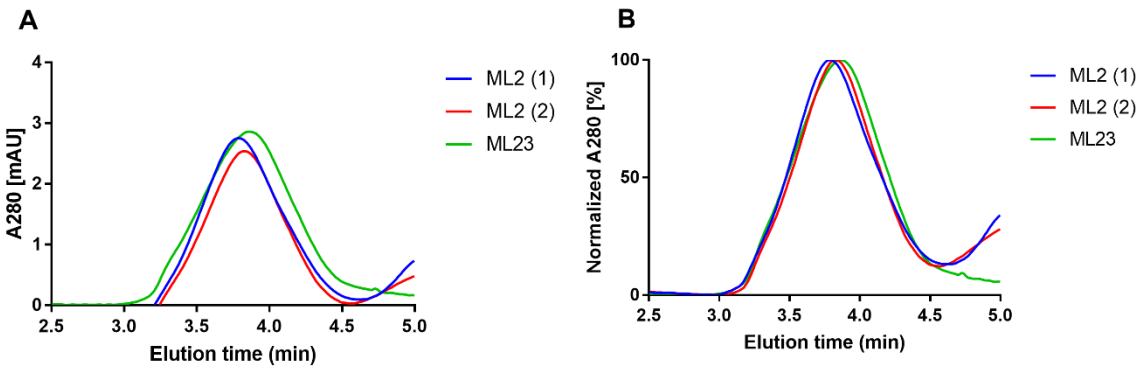

Figure 37. SEC analysis of constructs ML2 (tested twice) and ML23, expressed in 40 mL of *Sf9* insect cells and bound to the antagonist PSB-23082, shown as unscaled (A) and normalized data (B).

Exchange of the polyhedrin promotor to the *gp64* baculovirus promotor did not change protein yield significantly.

7.7 Influence of the expression system

The influence of the expression system on GPR17 constructs ML2 and ML25 was evaluated (see **Figure 38**).

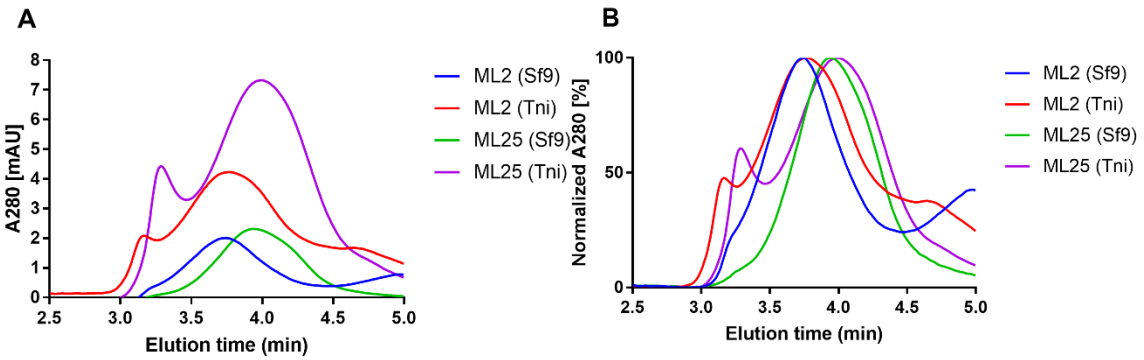

Figure 38. SEC analysis of constructs ML2 in the apo form and ML25 bound to the antagonist PSB-23082, expressed in 40 mL of either *Sf9* or *Tni* insect cells, shown as unscaled (A) and normalized data (B).

Changing the expression system from *Sf9* to *Tni* insect cells increased protein yield for constructs ML2 and ML25 two- to three-fold, although this also increased peak width and the relative height of the aggregate peak. ML2 samples were additionally investigated by SDS-PAGE (see **Figure 39**).

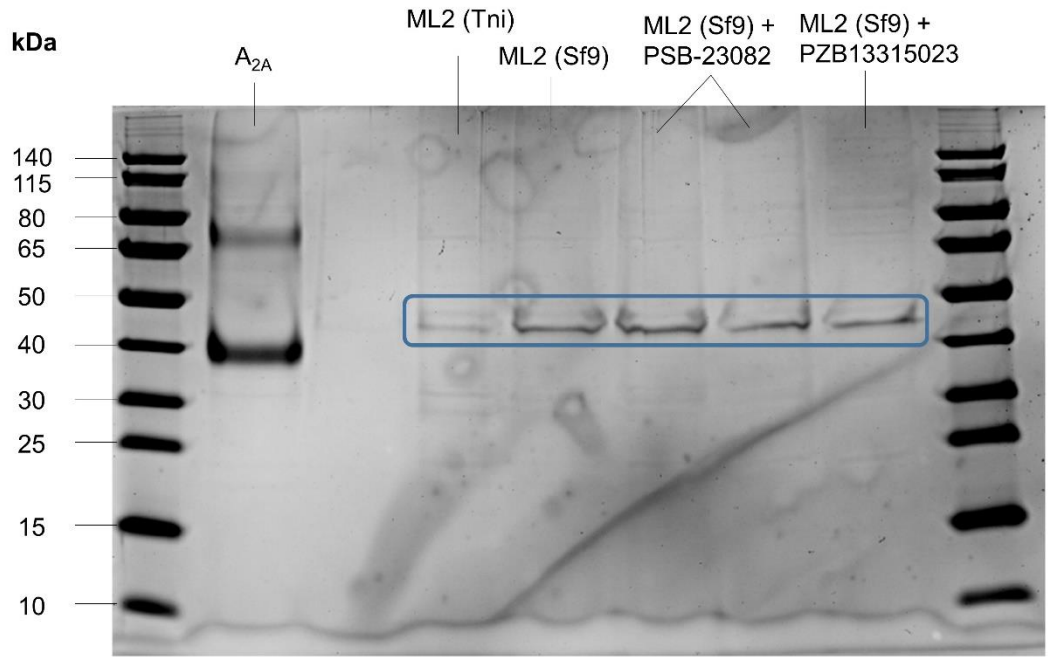

Figure 39. SDS-PAGE analysis of GPR17 construct ML2, expressed in 40 mL of either *Sf9* or *Tni* insect cells, eluted in 110 µL, either in the apo form or bound to antagonists PSB-23082 or PZB13315023. Sample lanes were loaded with 22.5 µL protein solution or 4 µL of the A_{2A}-PSB1-BRIL construct as positive control. Bands representing the GPR17 constructs are circled in blue.

Interestingly, SDS-PAGE analysis shows a lighter band for ML2 expressed in *Tni* insect cells than for the same construct expressed in *Sf9* insect cells. Additionally, presence of an antagonist did not change SDS-PAGE results.

Next, the influence of the expression system on GPR17 construct ML32 was investigated (see **Figure 40**).

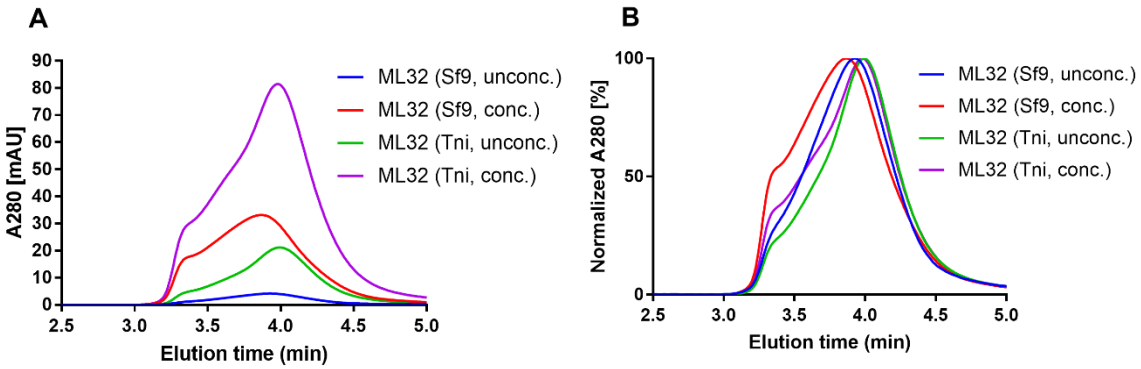

Figure 40. SEC analysis of construct ML32 bound to the antagonist PSB-23082, expressed in 450 mL of either *Sf9* or *Tni* cells, either eluted in 2 mL elution buffer (unconc.) or concentrated to 200 µL (conc.), shown as unscaled (A) and normalized data (B).

Changing the expression system from *Sf9* to *Tni* insect cells increased protein yield for ML32 five-fold (comparing the peak heights of unconcentrated protein samples) and, in contrast to constructs ML2 and ML25, reduced peak width. Interestingly, concentrating protein samples increased peak width.

These ML32 samples were additionally investigated by SDS-PAGE (see **Figure 41**).

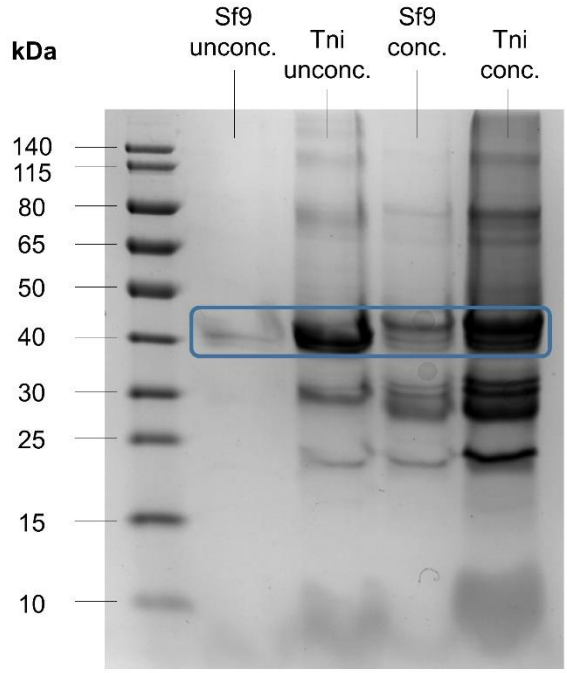

Figure 41. SDS-PAGE analysis of GPR17 construct ML32, expressed in 450 mL of either *Sf9* or *Tni* insect cells, eluted in 2 mL, either unconcentrated (unconc.) or concentrated to 200 µL (conc.), and bound to antagonist PSB-23082. Sample lanes were loaded with 22.5 µL protein solution. Bands representing the GPR17 constructs are circled in blue.

In concentrated samples, bands of lower molecular weight were especially prominent.

7.8 Influence of the virus on expression

Typically, 400 µL virus were used to infect freshly-grown *Sf9* or *Tni* cells at a concentration of 2-3 million cells per mL, after which cells would be incubated for 48 h. Different virus amounts (200 µL up to 1200 µL) and an infection duration of 72 h were investigated as well (see **Figure 42**).

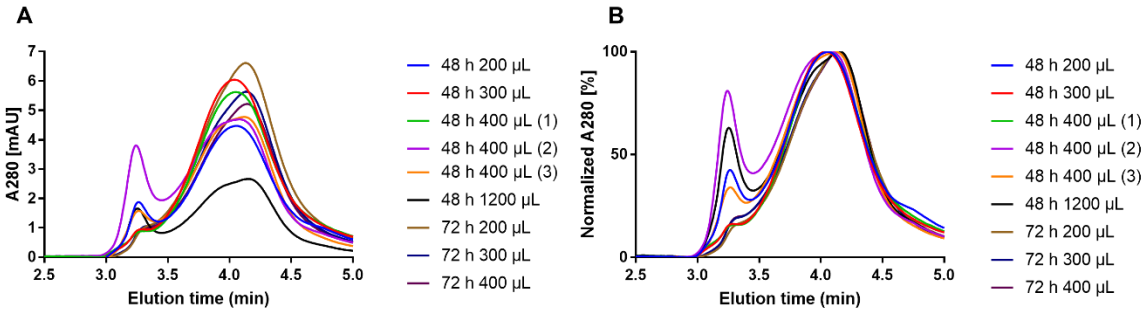

Figure 42. SEC analysis of construct ML32 expressed in 40 mL of *Tni* insect cells bound to the antagonist PSB-23082 with varying infection duration and virus amount, shown as unscaled (A) and normalized data (B).

When staying with the same infection duration, an increase in virus amount to 1200 µL lowered protein yield significantly, presumably due to overload of the cellular expression system, and a decrease to 200 µL lowered it slightly, meaning that the typical 400 µL were already close to the optimum. A slight decrease to 300 µL increased protein yield significantly. When prolonging infection duration, lower virus amounts seemed to be sufficient for achieving optimal results. The combination of 72 h infection time with 200 µL virus amount achieved the highest protein yield of all scenarios. In addition, prolonging of infection time from 48 h to 72 h shifted the peak significantly to a later elution time and reduced the aggregate peak, underscoring the advantage of longer infection time. However, differences in protein yield can also be caused by slightly different cell concentrations at the time of infection, which could not be controlled precisely.

7.9 Influence of salt concentration and additives during the solubilization and purification process

Sodium is thought to be important for stabilizing the protein. Typically, 800 mM NaCl were used in wash buffer 1, wash buffer 2, and elution buffer, but higher concentrations were investigated as well (see **Figure 43**).

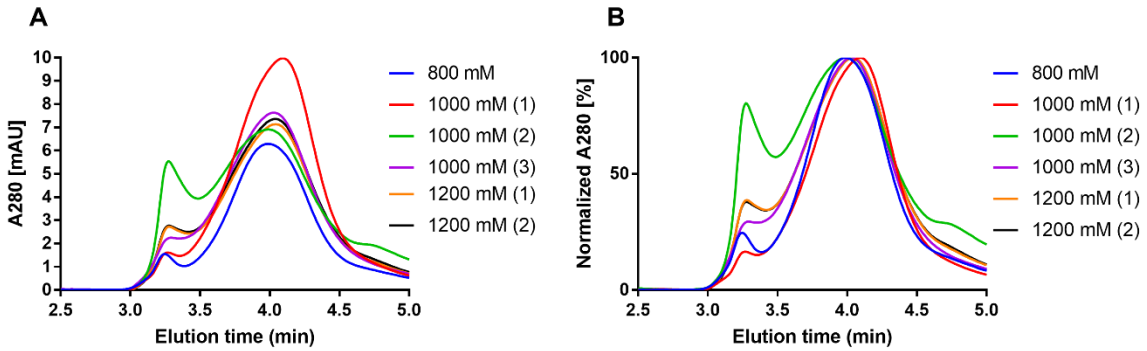

Figure 43. SEC analysis of construct ML32 expressed in 40 mL of *Tni* insect cells bound to the antagonist PSB-23082 using varying NaCl concentrations in wash buffer 1, wash buffer 2, and elution buffer, shown as unscaled (A) and normalized data (B).

An increase to 1000 mM NaCl significantly increased protein yield, while a further increase to 1200 mM decreased protein yield again compared to 1000 mM (protein yield was still significantly higher than at 800 mM NaCl).
Next, further differences in solubilization and elution conditions were investigated (see **Figure 44**).

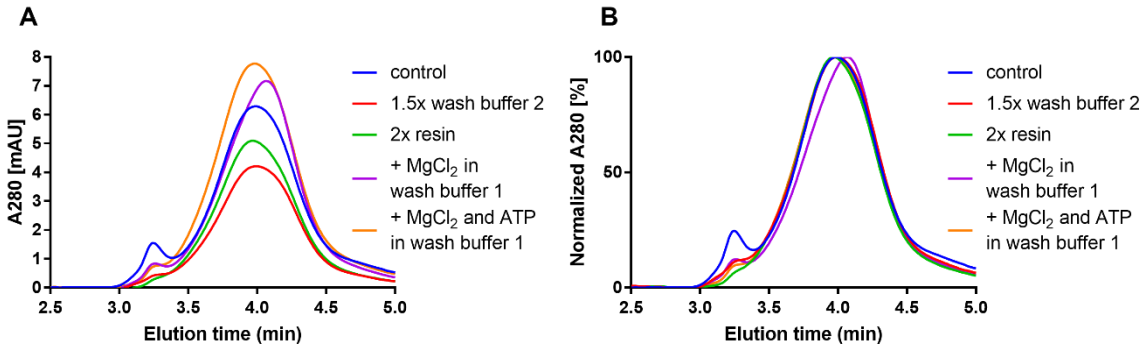

Figure 44. SEC analysis of construct ML32 expressed in 40 mL of *Tni* insect cells bound to the antagonist PSB-23082 under varying conditions, shown as unscaled (A) and normalized data (B).

Adding $MgCl_2$ in wash buffer 1 increased protein yield slightly, while adding a combination of $MgCl_2$ and ATP in wash buffer 1 increased it significantly. $MgCl_2$ and ATP are typically added to remove potential chaperones from the protein. It was suspected that adding these will help in improving purity of the protein, which can also be seen in the reduction of the aggregate peak and the significant shift of the peak to a later elution time (in the case of sole addition of $MgCl_2$). Using more wash buffer 2 was also assumed to potentially improve protein purity,

however, this reduced protein yield significantly. Lastly, using more TALON IMAC resin reduced protein yield significantly as well.

Imidazole is thought to interfere with protein binding and to elute proteins that bind weakly. Typically, imidazole is added at a concentration of 20 mM after solubilization, but double concentration (40 mM) was investigated as well (see **Figure 45**).

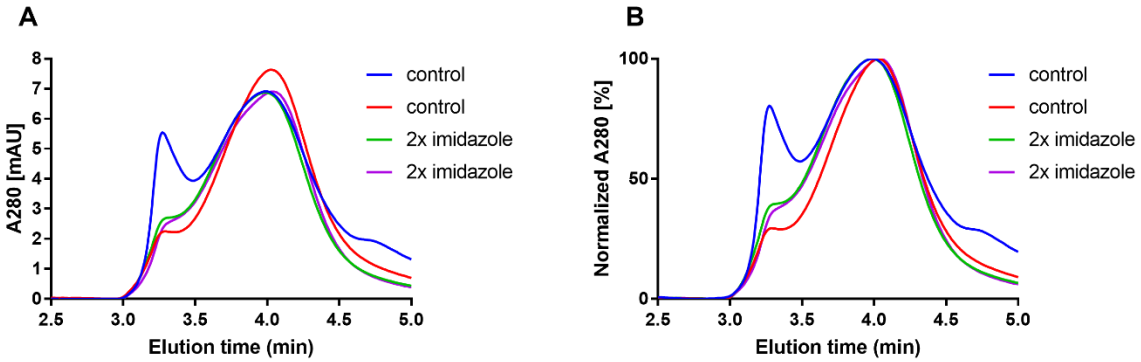

Figure 45. SEC analysis of construct ML32 expressed in 40 mL of *Tni* insect cells bound to the antagonist PSB-23082 under varying conditions, shown as unscaled (A) and normalized data (B).

Increased amount of imidazole decreased protein yield slightly and did not improve protein purity.

7.10 Influence of stabilizing antagonists

Prior to this work, out of several highly potent indolylsulfonamide-based GPR17 antagonists, the ones with the longest residence time, namely PSB-23082 and PZB13315023, were elucidated in radioligand binding assays (see Subchapter 6.2.3). Subsequently, the influence of these two antagonists in stabilizing GPR17 was investigated (see **Figure 46**).

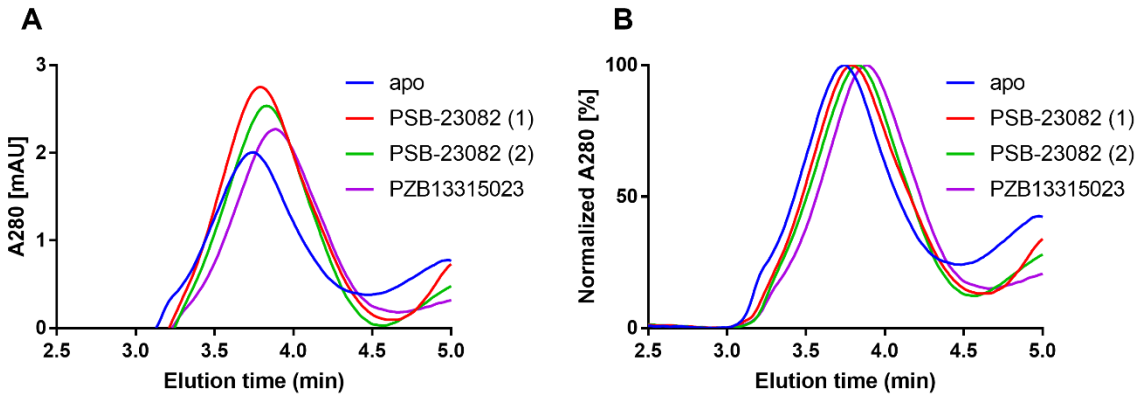

Figure 46. SEC analysis of construct ML2 expressed in 40 mL of *Sf9* insect cells, either in the apo state or bound to antagonists PSB-23082 or PZB13315023, shown as unscaled (A) and normalized data (B).

Protein yield of the construct in combination with an antagonist was slightly higher, especially when bound to PSB-23082, as compared to the apo state. Additionally, the peak was shifted to a significantly later elution time.

GPR17 constructs produced a visible inflection point in the TSA when combined with PSB-23082 (see **Figure 47**).

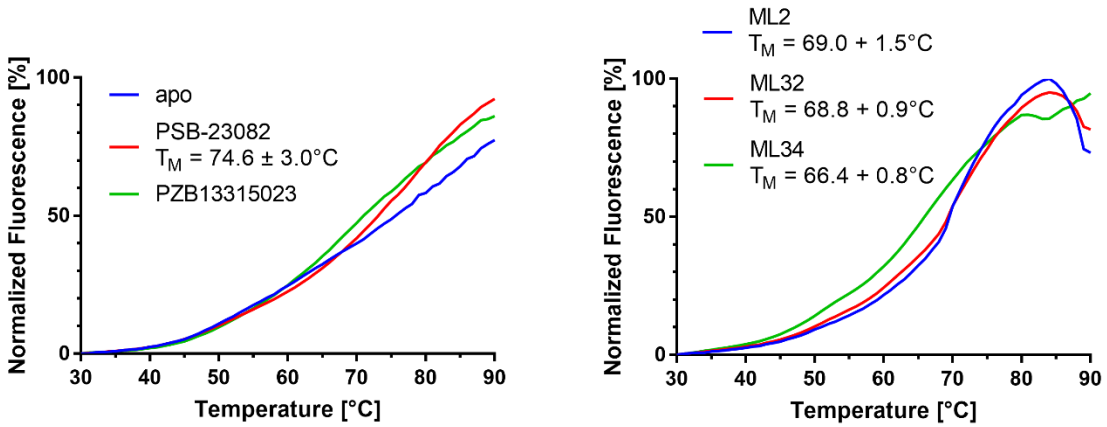

Figure 47. TSA analysis of construct ML2 expressed in *Sf9* insect cells, either in the apo form or bound to different antagonists (left) and of constructs ML2, ML32, and ML34 expressed in *Tni* insect cells and bound to antagonist PSB-23082 (right).

ML2 reached a higher T_M when expressed in *Sf9* cells (75°C) than when expressed in *Tni* cells (69°C). ML32 and ML34 expressed in *Tni* cells yielded T_M values of 69°C and 66°C, respectively.

Next, the influence of an earlier addition of PSB-23082 during the expression, instead of only adding it during solubilization and purification steps, was investigated (see **Figure 48**).

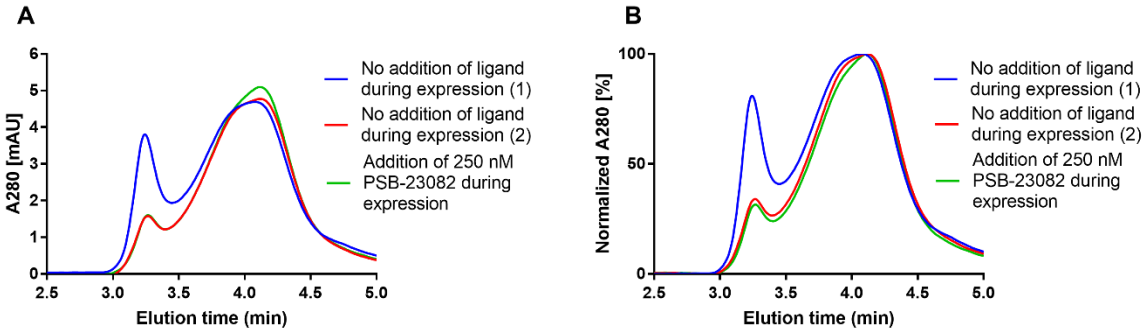

Figure 48. SEC analysis of construct ML32 expressed in 40 mL of *Tni* insect cells, shown as unscaled (A) and normalized data (B). Antagonist PSB-23082 was either added only in solubilization and purification steps or also during the expression already.

Co-expression of GPR17 and PSB-23082 increased protein yield slightly.

7.11 Conclusion of construct stabilization experiments

Extensive effort was put into design and analysis of different GPR17 constructs and optimization of expression and purification conditions.

Some modifications appear to be advantageous: Terminal truncation (at least of the C-terminus) increased protein yield. Fusion with BRIL decreased the amount of aggregated protein and, in particular, insertion of BRIL between residues S246 and K255 increased protein yield. A decrease in virus amount for expression from 400 µL to 300 µL (or even to 200 µL when combined with a longer infection time of 72 h) increased protein yield. Increase of NaCl concentration from 800 nM to 1000 nM in wash buffer 1, wash buffer 2, and elution buffer increased protein yield. Addition of $MgCl_2$ and ATP into wash buffer 1 increased protein yield. Lastly, GPR17 antagonist PSB-23082 increased thermostability to 66–75°C (depending on specific construct and expression system).

Other modifications produced mixed or unclear results: Medium N-terminal truncation of ML2 did not result in a protein yield significantly different to no N-terminal truncation (ML24) or full N-terminal truncation (ML25). Point mutations S146K and F158Y increased protein yield in some cases and decreased it and/or increased the amount of aggregated protein in other cases.

Exchange from polyhedrin to *gp64* promotor increased protein yield slightly but not significantly. Changing expression system from *Sf9* to *Tni* insect cells increased protein yield but, at least in some cases, decreased protein purity. Co-expression with antagonist PSB-23082 increased protein yield slightly but not significantly.

Taken together, the combination of the advantageous modifications allowed elucidation of antagonist-bound GPR17 constructs with a high yield of 3 mg/mL (expressed in 450 mL *Tni* insect cells, eluted in 2 mL buffer and concentrated to 200 µL, corresponding to 0.6 mg protein from 450 mL cells; construct ML32 and based on similar peak height in SEC analysis also extendable to construct ML2) and a high T_M of 69°C (constructs ML2 and ML32, expressed in *Tni* insect cells and bound to GPR17 antagonist PSB-23082). Further advancements in protein yield, protein stability, and especially protein purity would qualify GPR17 for crystallization trials in the future.

8 Summary & conclusions

This thesis presents research results from several subprojects, all related to orphan G protein-coupled receptor GPR17, ranging from ligand discovery and characterization to protein engineering for structural studies. The findings contribute to our understanding of GPR17 pharmacology and its potential as a therapeutic target. This section contains a detailed summary and discussion of the data obtained and provides an outlook on future experiments.

8.1 GPR17 – orphan G protein-coupled receptor with therapeutic potential

GPR17 has been reported to affect oligodendrocyte differentiation and myelination,[87; 107; 170] neural outgrowth and cognitive function,[86; 173] tissue repair,[84; 133; 171] and glucose metabolism,[124; 174; 175] making it an intriguing therapeutic target for multiple sclerosis, neurodegenerative diseases, diabetes, and obesity. Recently, suitable agonists and antagonists have been discovered and optimized,[134; 135] and several patents have been filed for antagonists.[136; 152–169] These will enable a broad exploration of GPR17 as a novel potential drug target. Future preclinical, and especially the outcome of the first, long-awaited clinical study with a potent, selective antagonist may open up new avenues for the curative treatment of demyelinating diseases.

Nonetheless, the current evidence is in most cases still unsatisfactory. Hence, we published a review article that discusses some contradictory findings reported in literature, identifies research gaps, and proposes future directions for exploiting the therapeutic potential of GPR17 (see Chapter 3).[89]

8.2 Search for the endogenous ligand of GPR17

The endogenous ligand of GPR17 is unknown. Identifying it is crucial, not only for elucidating its physiological role, but also for guiding the rational design of synthetic ligands with therapeutic potential.

In this thesis, multiple compounds, including adenosine derivatives and non-aromatic steroids, have been analyzed as potential endogenous ligands of GPR17, however, none displayed activity at the receptor. Contrasting previous findings,[151] 24(*S*)-hydroxycholesterol could not be confirmed as the endogenous ligand of GPR17, since it was found to be inactive. To further advance the search for the endogenous agonist, a comprehensive virtual high-throughput

screening campaign was performed using a curated library from the Human Metabolome Database and a docking approach using the MOE software. Although the *in silico* hit compounds tested to date have not shown any activity, this approach established a workflow that can be refined and reapplied. Key learnings included the limitations of molecular docking scoring functions, particularly their bias toward higher molecular weight and lipophilic compounds (see Chapter 5).

Therefore, GPR17 remains an orphan receptor. To identify its endogenous ligand, future efforts may focus on optimizing the virtual screening approach (e.g., reducing bias) or exploring alternative strategies, such as testing biological samples to identify its localization and subsequently characterize it.

8.3 Characterization of further GPR17 ligands

A diverse array of potential agonists and antagonists was investigated in this thesis using calcium mobilization assays and radioligand binding studies (see **Figure 49**).

Indole derivative MDL 29,951[109; 134] and peptide-mimetic PZB09412026 showed similar potency at GPR17 (pEC_{50} of 6.8 and 6.7, respectively), while exhibiting various degrees of efficacy – MDL 29,951 is a full agonist, while PZB09412026 behaves as a partial agonist in comparison. The discovery of partial agonists is notable, as these may allow more nuanced modulation of GPR17 activity. Affinities of indole-based agonists with a large substituent at position 6, utilizing a slightly different binding mode,[134] were also investigated. Indazole derivative JWS-15-90 did not show activity at GPR17.

On the antagonist side, in partial agreement with previous results,[109; 140] montelukast and pranlukast both showed inhibitory potency at GPR17 (pIC_{50} of 6.8 and 7.4, respectively). Decarboxylation of agonistic indole derivatives creates indole-based antagonists (data unpublished) that have moderate binding affinities at GPR17.

Further potent GPR17 antagonists, such as PSB-22269 and PSB-24040, are based on an anthranilic acid scaffold and can exhibit higher binding affinities of up to a pK_i of 8.1 (PSB-22269) determined in radioligand binding using radioligand agonist [^{3}H]PSB-12150 and potencies of up to pIC_{50} 7.2 (PSB-24040) determined in calcium mobilization assays. These findings were published (see Chapter 4).[135]

Finally, the most potent antagonists at GPR17 have an indolylsulfonamide structure, such as PZB00424007.[136; 151] It was hypothesized that the binding mode of indolylsulfonamides differs from that of indole agonists and anthranilic acids, since the latter two exhibit lower pK_i values

when tested against the indolylsulfonamide-based antagonist radioligand [^{3}H]PSB-1503 compared to the indole-based agonist radioligand [^{3}H]PSB-12150. The most potent GPR17 antagonists were also tested for their residence times at the receptor to find a compound suitable for stabilizing GPR17 for crystallization trials. In previous tests, indolylsulfonamide-based compound PSB-23082 achieved the highest residence time of 17.1 min. However, further testing showed that the kinetic radioligand binding assay is not a reliable method for determining residence times of these compounds, especially those with faster kinetics than that of the radioligand.

Exploration of further indolylsulfonamide modification is of high interest with the aim to create fluorescence labeled potent derivatives. Substitution at the indole nitrogen with a 3-ethoxy-3-oxopropyl group decreased potency (increase of pIC_{50} value by 1–2 units) compared to indolylsulfonamide derivatives that were unsubstituted at the indole nitrogen (see Chapter 6).

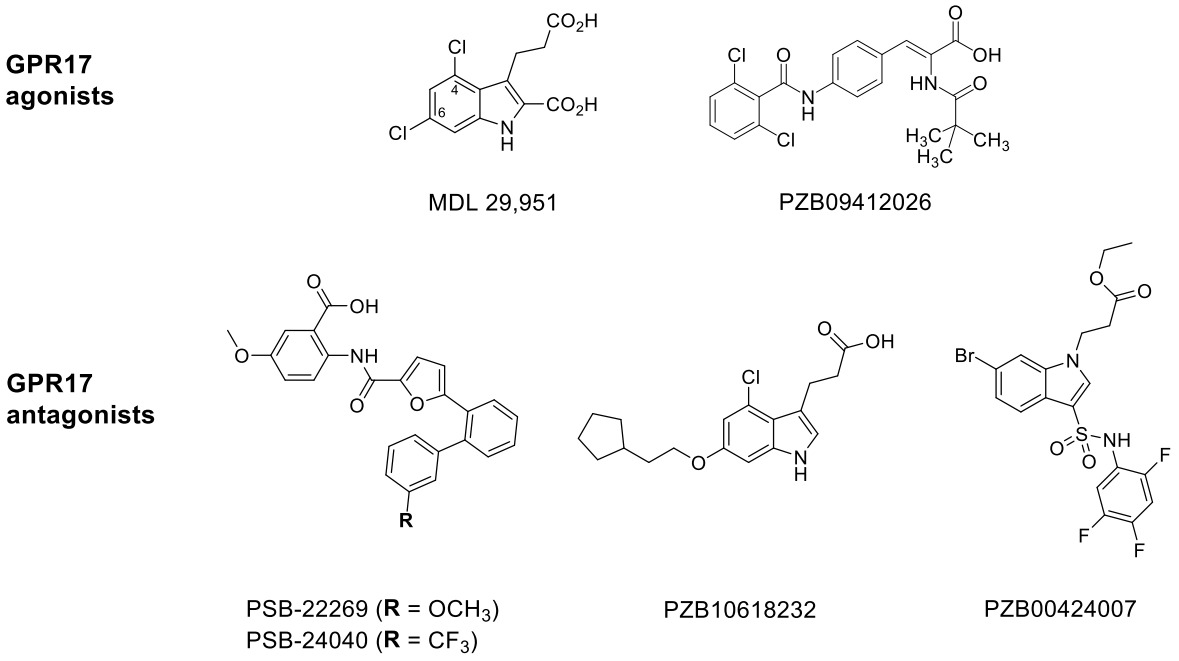

Figure 49. Selected GPR17 agonists and antagonists investigated and discussed in this thesis.

The elucidated structure-activity, structure-affinity, and structure-residence time relationships presented in this thesis and the related publication on anthranilic acid derivatives[135] will inform future drug discovery efforts targeting GPR17. Further research may focus on validating the therapeutic efficacy of lead compounds *in vivo* in different disease models. Investigation of biased signaling properties and the design of ligands with optimal signaling profiles would be of great interest. Finally, developing fluorescence labeled ligands would be most useful for a variety of studies, including imaging and mechanistic studies.

8.4 Optimizing GPR17 thermostability and expression for structural studies

Advances in high-resolution protein structure determination have transformed structure-based drug discovery, enabling optimization of hit and lead compounds through detailed molecular insights. However, structural elucidation of GPCRs remains a considerable challenge that requires specialized expertise and extensive protein engineering. In particular, the low inherent stability of GPCRs outside their native membrane environment complicates production of sufficient amounts of pure and stable protein. Additionally, each receptor often presents unique challenges, as evidenced by longstanding targets where structure determination has proven elusive. GPR17 has been elucidated by cryo-EM in the apo form and bound to a G protein,[46] whereas elucidation by X-ray crystallography and/or bound to a ligand (in particular an antagonist, since they are therapeutically more relevant) has not yet been achieved.

A major focus of this work was improving GPR17 expression, purification, and stabilization to enable future structural determination, especially by X-ray crystallography. Over 30 different GPR17 constructs have been designed and analyzed. They differed in the length of the N- and C-termini, whether and at which position they were fused with BRIL, whether they had one or more of several point mutations, and whether they had further modifications. These constructs were expressed in either *Sf9* or *Tni* insect cells. Some construct modifications appeared to be advantageous: Size exclusion chromatography and SDS-PAGE results showed that truncation of the C-terminus and fusion with BRIL, particularly between residues S246–K255, increased protein yield and decreased the amount of aggregated protein. Point mutations such as F158Y and S146K, however, variably influenced yield and stability dependent on construct design and expression system and did not show a clear trend. Modifying the expression, solubilization, and purification conditions also affects protein yield and purity: expression in *Tni* insect cells increased protein yield up to 5-fold compared to *Sf9* insect cells, a longer incubation time of 72 h and the addition of stabilizing GPR17 antagonist PSB-23082 during the infection period also appeared to be advantageous. A higher NaCl concentration of 1000 mM in wash and elution buffers increased protein yield as well (see **Figure 50**). Thermal shift assay results showed that the melting temperatures of the different constructs in the apo form all lie between 50 and 53°C. However, the inflection points are too indistinct to detect differences between various compounds. In the presence of PSB-23082, optimized GPR17 constructs ML2 and ML32 reached yields of 3 mg/mL and melting temperatures (T_M) of about 69°C, approaching thresholds required for crystallization (see Chapter 7).

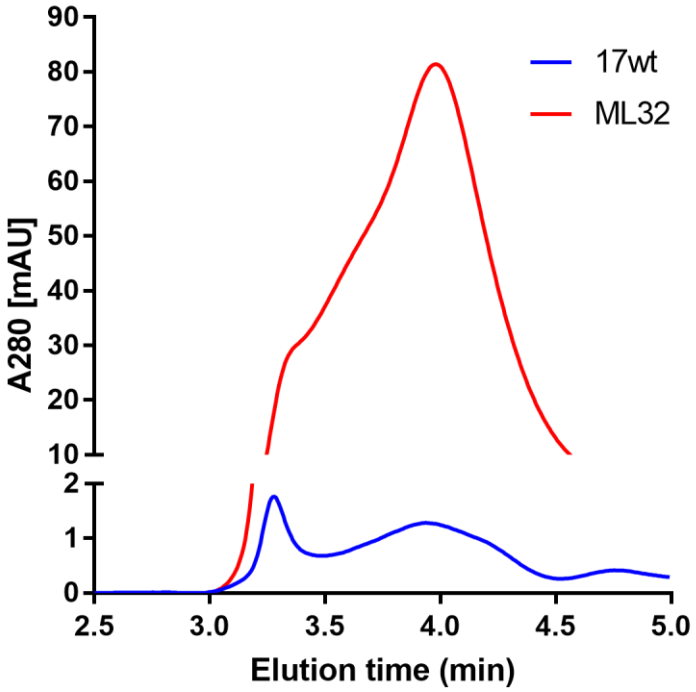

Figure 50. Size exclusion chromatography analysis of initial construct (17wt) in the apo form, expressed in 40 mL *Sf9* cells and eluted in 125 µL, and optimized construct (ML32) bound to GPR17 antagonist PSB-23082, expressed in 450 mL *Tni* cells, purified using an optimized protocol, and concentrated to 200 µL.

Low purity and suboptimal reproducibility are still the main reasons that complicate analysis of the results. Nonetheless, the advances in GPR17 thermostability and expression presented in this thesis lay the groundwork for future structural biology studies. These should focus on refining purification protocols, possibly incorporating other detergents and nanodiscs, exploring further thermostabilizing mutations, and attempting cryo-EM structure determination as a viable alternative.

9 Materials

9.1 Water specification

A Milli-Q® water purification system was used to obtain ultrapure water. PCR grade water was used for molecular and cell biological experiments.

9.2 Sterilization method

Heat stable materials, equipment, solutions, and media were autoclaved at 121°C for 21 min.

9.3 Chemicals

Table 11. Chemicals.

Name	Function	Source
Gel Loading Dye, Purple (6X)	Agarose gel electrophoresis	New England Biolabs GmbH, Frankfurt, Germany
GelRed® Nucleic Acid Gel Stain	Agarose gel electrophoresis	Biotium Inc., Fremont, US
GeneRuler 100 bp DNA Ladder	Agarose gel electrophoresis	Thermo Fisher Scientific GmbH, Dreieich, Germany
GeneRuler lambda DNA ladder	Agarose gel electrophoresis	Thermo Fisher Scientific GmbH, Dreieich, Germany
Lambda DNA/HindIII Marker	Agarose gel electrophoresis	Thermo Fisher Scientific GmbH, Dreieich, Germany
Buffer P1	Bacmid DNA preparation	QIAGEN GmbH, Hilden, Germany
Buffer P2	Bacmid DNA preparation	QIAGEN GmbH, Hilden, Germany
Buffer P3	Bacmid DNA preparation	QIAGEN GmbH, Hilden, Germany
Gentamicin sulfate	Bacmid DNA preparation	Carl Roth GmbH + Co. KG, Karlsruhe, Germany
Isopropyl-β-D-thiogalactopyranoside (IPTG)	Bacmid DNA preparation	Carl Roth GmbH + Co. KG, Karlsruhe, Germany
Kanamycin sulfate	Bacmid DNA preparation	Carl Roth GmbH + Co. KG, Karlsruhe, Germany
RNase A	Bacmid DNA preparation	QIAGEN GmbH, Hilden, Germany
Tetracycline	Bacmid DNA preparation	Carl Roth GmbH + Co. KG, Karlsruhe, Germany
5-Bromo-4-chloro-3-indolyl-β-D-galactopyranoside (X-gal)	Bacmid DNA preparation	VWR International GmbH, Darmstadt, Germany
Oregon Green™ 488 BAPTA-1	Calcium assay	Thermo Fisher Scientific GmbH, Dreieich, Germany

Pluronic® F-127, Product P2443	Calcium assay	Merck KGaA, Darmstadt, Germany
Deoxynucleotide (dNTP) Solution Mix (10 mM)	PCR	New England Biolabs GmbH, Frankfurt, Germany
Deoxynucleotide (dNTP) Solution Mix (2.5 mM)	PCR	New England Biolabs GmbH, Frankfurt, Germany
Dimethyl sulfoxide (DMSO), Sterile	PCR	New England Biolabs GmbH, Frankfurt, Germany
DpnI (20.0 U/mL)	PCR	New England Biolabs GmbH, Frankfurt, Germany
Magnesium chloride (50 mM)	PCR	New England Biolabs GmbH, Frankfurt, Germany
Phusion® GC Buffer (5X)	PCR	New England Biolabs GmbH, Frankfurt, Germany
Phusion® High-Fidelity DNA Polymerase (2.0 U/mL)	PCR	New England Biolabs GmbH, Frankfurt, Germany
Q5® High-Fidelity DNA Polymerase	PCR	New England Biolabs GmbH, Frankfurt, Germany
Q5® Reaction Buffer (5X)	PCR	New England Biolabs GmbH, Frankfurt, Germany
DNA Clean & Concentrator® Kit	PCR amplificate purification	Zymo Research Europe GmbH, Freiburg, Germany
Zymoclean Gel DNA Recovery Kit	PCR amplificate purification	Zymo Research Europe GmbH, Freiburg, Germany
LB broth powder	Plasmid and bacmid DNA preparation	Carl Roth GmbH + Co. KG, Karlsruhe, Germany
Ampicillin sodium	Plasmid DNA preparation	Cayman Chemical, Ann Arbor, US
ZR Plasmid Miniprep™-Classic Kit	Plasmid DNA preparation	Zymo Research Europe GmbH, Freiburg, Germany
Cholesteryl hemisuccinate (CHS)	Protein extraction and stabilization	Merck KGaA, Darmstadt, Germany
n-Dodecyl-β-D-maltopyranoside (DDM)	Protein extraction and stabilization	Anatrace Products LLC, Maumee, OH, US
cOmplete™ Protease Inhibitor Cocktail Tablets	Membrane preparation, protein purification	Roche Deutschland Holding GmbH, Grenzach-Wyhlen, Germany
Iodoacetamide	Protein purification	
TALON® Metal Affinity Resin	Protein purification	Takara Bio Europe SAS, Saint-Germain-en-Laye, France
[^{3}H]PSB-12150	Radioligand assay	Quotient Bioresearch Ltd., Fordham, UK
[^{3}H]PSB-1503	Radioligand assay	Quotient Bioresearch Ltd., Fordham, UK
MicroScint™-20	Radioligand assay	PerkinElmer LAS GmbH, Rodgau, Germany

ProSafe FC+ High Efficiency LSC cocktail	Radioligand assay	Meridian Biotechnologies Ltd, Waterfield, UK
Tris(hydroxymethyl)aminomethane (Tris)	Radioligand assay, buffer preparation	Carl Roth GmbH + Co. KG, Karlsruhe, Germany
Coomassie® Brilliant blue R-250	SDS-PAGE	AppliChem GmbH, Darmstadt, Germany
NuPAGE™ LDS Sample Buffer (4X)	SDS-PAGE	Thermo Fisher Scientific GmbH, Dreieich, Germany
PageRuler™ Prestained Protein Ladder	SDS-PAGE	Thermo Fisher Scientific GmbH, Dreieich, Germany
N-(4-(7-Diethylamino-4-methyl-3-coumarinyl)phenyl)maleimide (CPM)	Thermostability assay	Thermo Fisher Scientific GmbH, Dreieich, Germany

The TALON® Metal Affinity Resin solution was stored at a ratio of 1:1 (v/v) in 20 % ethanol. For preparation, it was washed six times with ultrapure water by centrifugation at 100 g for 5 min. After the last washing step, the resin was resuspended in the resin resuspension buffer. Compounds not listed in the table were produced in-house.

9.4 Buffers and solutions

Table 12. Buffers and solutions.

Name	Function	Composition
Krebs-Hepes buffer (KHB)	Calcium assay	118.6 mM NaCl, 11.7 mM D-Glucose, 10.0 mM HEPES, 4.7 mM KCl, 4.2 mM $NaHCO_3$, 1.3 mM $CaCl_2$, 1.2 mM KH_2PO_4, 1.2 mM $MgSO_4$; pH 7.4
Membrane prep buffer	Membrane preparation	25 mM Tris, 1 mM Na-EDTA, 0.32 M sucrose and cOmplete™ Protease Inhibitor Cocktail Tablets, pH 7.4
Scraping buffer	Membrane preparation	50 mM Tris and 2 mM Na-EDTA; pH 7.4
2X Solubilization buffer	Protein purification	100 mM HEPES pH 7.5, 1 M NaCl, 2 % DDM, 0.4 % CHS
High osmotic buffer	Protein purification	10 mM HEPES pH 7.5, 10 mM $MgCl_2$, 20 mM KCl, 1 M NaCl
Low osmotic buffer	Protein purification	10 mM HEPES pH 7.5, 10 mM $MgCl_2$, 20 mM KCl
Resin elution buffer	Protein purification	50 mM HEPES pH 7.5, 800 mM NaCl, 0.025 % DDM, 0.005 % CHS, 10 % glycerol, 220 mM imidazole
Resin resuspension buffer	Protein purification	50 mM HEPES pH 7.5, 500 mM NaCl, 10 % glycerol
Resin wash buffer I	Protein purification	50 mM HEPES pH 7.5, 800 mM NaCl, 0.1 % DDM, 0.02 % CHS, 10 % glycerol, 25 mM imidazole
Resin wash buffer II	Protein purification	50 mM HEPES pH 7.5, 800 mM NaCl, 0.05 % DDM, 0.01 % CHS, 10 % glycerol, 50 mM imidazole
Resuspension buffer	Protein purification	10 mM HEPES pH 7.5, 10 mM $MgCl_2$, 20 mM KCl, 30 % (v/v) glycerol

Coomassie® protein staining solution	SDS-PAGE	1.25 g Coomassie® Brilliant Blue R-250, 80 mL ethanol, 250 mL acetic acid, ad 1 L H_2O
SDS-PAGE running buffer	SDS-PAGE	50 mM MOPS, 50 mM Tris pH 7.4, 0.1 % SDS, 1 mM EDTA
HPLC buffer	Size exclusion chromatography	25 mM HEPES pH 7.5, 500 mM NaCl, 2 % glycerol, 0.05 % DDM, 0.01 % CHS

The resin buffers were freshly prepared before use.

9.5 Primers

All primers were designed by using the QuikChange® Primer Design Program by Agilent and subsequently synthesized by Invitrogen. The dried primer material was reconstituted to 100 µM and diluted to 5 µM with PCR-grade water. All primer solutions were stored at −20°C.

9.6 Plasmids

All plasmids were stored at −20°C.

Table 13. Plasmids.

Name	Source
hGPR17 in pCMV-Pro-Link 1	Produced in-house
hGPR17 in pLVX-IRES-mCherry	Research group of Prof. Dr. Evi Kostenis, Institute of Pharmaceutical Biology, University of Bonn, Germany
hGPR17 in pcDNA3.1 Zeo(+)	Produced in-house
hGPR17 in pFastBac1™	Produced in-house

9.7 Bacteria culture

9.7.1 Bacterial strains

All bacterial strains were stored at −80°C.

Table 14. Bacterial strains.

Name	Characteristics	Source
DH10Bac E. coli	Chemically competent E. coli cells suitable for transformation	Produced in the research group from an aliquot bought from Thermo Fisher Scientific GmbH, Dreieich, Germany
DH5α E. coli	Chemically competent E. coli cells suitable for transformation	Produced in the research group

9.7.2 Bacteria culture buffers, media, and supplements

LB medium was prepared by dissolving 25 g of LB broth powder in 1 L of demineralized water. The solution was autoclaved and stored at rt.

9.7.3 Agar plates

Agar plates were prepared by melting agar, cooling to about 60°C, and adding antibiotics and/or other additives. The still liquid agar was then poured onto Petri dishes where it cooled and hardened. The plates were stored at 4°C.
Ampicillin plates for DH5α E. coli were prepared by adding 100 µg/mL of ampicillin to molten agar.
3+2 plates for DH10Bac E. coli were prepared by adding 10 µg/mL gentamicin sulfate, 50 µg/mL kanamycin sulfate, 10 µg/mL tetracycline, 100 µg/mL X-gal, and 40 µg/mL IPTG to molten agar. Petri dishes were protected from light at all times.

9.8 Cell culture

9.8.1 Cell lines

All cells were stored at -150°C.

Table 15. Cell lines.

Name	Characteristics	Producer/Owner
CHO-FITR-hGPR17	Chinese hamster ovary (CHO) Flp-In™ T-REx™ (FITR) cells with a pLVX-IRES-mCherry plasmid containing the gene for human GPR17	Research group of Prof. Dr. Evi Kostenis, Institute of Pharmaceutical Biology, University of Bonn, Germany
1321N1-hGPR17	human brain astrocytoma 1321N1 cells with a pLVX-IRES-mCherry plasmid containing the gene for human GPR17	Research group of Prof. Dr. Evi Kostenis, Institute of Pharmaceutical Biology, University of Bonn, Germany
Sf9	Clonal isolate of *Spodoptera frugiperda* Sf21 cells (which are ovarian cells isolated from *Spodoptera frugiperda*)	Oxford Expression Technologies, Oxford, UK
Tni	Ovarian cells isolated from *Trichoplusia ni*	Oxford Expression Technologies, Oxford, UK

9.8.2 Cell culture buffers, media, and supplements

Table 16. Cell culture buffers, media, and supplements.

Name	Function	Source
Anti-FLAG™ FITC-conjugated antibody	Expression control	Gen Script Biotech Corporation, Leiden, Netherlands
Anti-gp64 PE-conjugated antibody	Infection control	Thermo Fisher Scientific GmbH, Dreieich, Germany
Dulbecco's Modified Eagle Medium (DMEM)	Human cell culture	Thermo Fisher Scientific GmbH, Dreieich, Germany
Dulbecco's Modified Eagle Medium / Ham's F-12 (DMEM/F-12)	Human cell culture	Thermo Fisher Scientific GmbH, Dreieich, Germany
Phosphate buffered saline (PBS)	Human cell culture	Thermo Fisher Scientific GmbH, Dreieich, Germany
ESF 921™ insect cell culture medium, protein-free	Insect cell culture	Expression Systems LLC, Davis, US
Transfection Medium	Insect cell culture	Oxford Expression Technologies, Oxford, UK
X-tremeGENE™ HP DNA transfection reagent	Insect cell culture	Sigma-Aldrich Chemie GmbH, Taufkirchen, Germany

9.9 Laboratory instruments and equipment

Table 17. Laboratory instruments and equipment.

Name	Function	Source
Agilent 1260 Infinity HPLC	Size exclusion chromatography	Agilent Technologies, Hamburg, Germany
Allegra X-30R centrifuge, F0685 rotor	Centrifugation	Beckman Coulter GmbH, Krefeld, Germany
Beckman Avanti J-20 High Capacity Centrifuge	DNA preparation, Bacmid preparation, Protein purification	Beckman Coulter GmbH, Krefeld, Germany
Centrifuge 5804, A-2-DWP Rotor	Deep well plate centrifugation	Eppendorf AG, Hamburg, Germany
ChemiDoc™ MP Imaging System	Gel visualization	Bio-Rad Laboratories GmbH, Munich, Germany
Colibri Microvolume Spectrometer	DNA quantification	Berthold Detection Systems GmbH, Pforzheim, Germany
Dounce Tissue Grinders	Protein purification	VWR International GmbH, Darmstadt, Germany
Guava easycyte 5-HT	Flow cytometry	Merck KGaA, Darmstadt, Germany
NanoFilm SEC-250 column	Size exclusion chromatography	Sepax Technologies, Inc., Newark, DE, US
peqSTAR 96X Universal Gradient	PCR	Peqlab Biotechnologie GmbH, Erlangen, Germany
Rotor-Gene Q 6plex	Thermostability assay	QIAGEN GmbH, Hilden, Germany
Sonopuls HD 2070	Protein purification	Bandelin electronic GmbH & Co. KG, Berlin, Germany

Name	Function	Source
Sonotrode MS 73 microtip	Protein purification	Bandelin electronic GmbH & Co. KG, Berlin, Germany
Thermomixer comfort	Transfection	Eppendorf AG, Hamburg, Germany
TopCount® NXT™	Scintillation Counter	Packard Bioscience GmbH, Dreieich, Germany
Tri-Carb® 2810TR Liquid Scintillation Analyzer	Scintillation Counter	PerkinElmer LAS GmbH, Rodgau, Germany
Tri-Carb® 2910TR Liquid Scintillation Analyzer	Scintillation Counter	PerkinElmer LAS GmbH, Rodgau, Germany
UltraTurrax®	Membrane preparation	IKA Labortechnik, Staufen, Germany
Vivaspin® 100 Centrifugal Concentrator	Protein purification	Vivaproducts, Inc., Littleton, MA, US

9.10 Software and web applications

Table 18. Software and web applications.

Software	Function	Source
Eurofins Genomics DNA sequencing	DNA sequencing	Eurofins Genomics, Ebersberg, Germany
GraphPad Prism 7.00	Graphical data analysis	GraphPad Software LLC, San Diego, US
QuikChange® Primer Design	Primer design	Agilent Technologies, Hamburg, Germany
SnapGene	Sequence design, sequence alignment	GSL Biotech LLC, San Diego, US

10 Methods

10.1 Cell culture

CHO-FITR-hGPR17 cells were cultured at 37°C and 5% CO_2 in DMEM/F-12, supplemented with 10% FCS, penicillin (100 U/mL), streptomycin (0.1 mg/mL), hygromycin B (300 µg/mL), blasticidin (30 µg/mL), and L-Glutamin (2 mM). 1321N1-hGPR17 cells were cultured at 37°C and 10% CO_2 in DMEM, supplemented with 10% FCS, penicillin (100 U/mL), streptomycin (0.1 mg/mL). At 70% confluency, CHO-FITR-hGPR17 and 1321N1-hGPR17 cells were washed with PBS and passaged by trypsination.

Sf9 and *Tni* insect cells were cultured at 27°C ESF 921™ insect cell culture medium. Cells were typically passaged twice a week to 0.8–1.0 × 10^6 cells/mL (*Sf9*) or 0.3 × 10^6 cells/mL (*Tni*), respectively.

10.2 Membrane preparation

CHO-FITR-hGPR17 cells were seeded under 1:10 dilution into 150 mm cell culture dishes and incubated to 70–90 % confluency. Approx. 48 h prior to the next step, doxycycline was added in a final concentration of 0.5 µg/mL to induce overexpression of *GPR17* using the tetracycline-dependent promoter of the cell line. After reaching the desired confluency, the medium was discarded, dishes were washed with 5 mL/dish PBS and subsequently frozen at −20°C overnight. The next day, dishes were thawed, 1 mL/dish of 50 mM Tris plus 2 mM Na-EDTA buffer at pH 7.4 was added, cells were detached with a rubber scraper and harvested. The suspension was centrifuged at 1000 g and 4°C for 10 min. The pellet was resuspended in 0.5 mL/dish membrane prep buffer and subsequently homogenized using an UltraTurrax for 1 min at level 5. Cell debris und nuclei were removed by centrifugation at 1000 g and 4°C for 10 min. The supernatant was then centrifuged again at 48000 g and 4°C for 30 min. The pellet was resuspended with 0.5 mL/dish of 50 mM Tris buffer at pH 7.4 and subsequently homogenized using an UltraTurrax for 30 s at level 3. These steps (centrifugation, resuspension, homogenization) were repeated three times while gradually decreasing the amount of Tris buffer used for resuspension to 0.1 mL/dish for the final repetition. This membrane preparation was aliquoted and stored at −80°C until further use.

10.3 Calcium mobilization assay

On the day of the experiment, confluent 1321N1-hGPR17 cells in two T175 flasks were washed with PBS, detached by trypsination, and volume adjusted to 30 ml with KHB in a falcon tube. Cells were incubated for 45 min at 37°C and 10% CO_2 and then centrifuged at 1200 rpm for 5 min. The cell pellet was resuspended in a mixture of 994 µL KHB with 3 µL of Oregon Green 488 BAPTA-1 und 3 µl Pluronic F-127. This was then incubated for 1 h in rotation and protected from light. After washing twice with KHB, cells were transferred to the wells of a clear bottomed 96 well plate, containing the antagonist dilution series in the case of antagonist testing. After incubation for 30 min, the plate was measured using a Novostar system, which pipetted an agonist dilution series (in the case of agonist testing) or MDL 29,951 to a final concentration of 10^{-6} M (in the case of antagonist testing) onto the wells of the clear bottomed 96 well plate. Data were analyzed using GraphPad PRISM 7.00.

10.4 Radioligand binding assay

Radioligand binding assays were performed with two different radioligands: the GPR17 antagonist radioligand [^{3}H]PSB-1503 and the GPR17 agonist radioligand [^{3}H]PSB-12150. Both were custom-labeled by Quotient Bioresearch Ltd., Fordham, UK. Membrane preparations from CHO-FITR-hGPR17 cells were used. Data were analyzed using GraphPad PRISM 7.00. Raw data were normalized to total binding (DMSO control) = 100% and nonspecific binding (unlabeled radioligand) = 0%.

10.4.1 Competition binding assay with [^{3}H]PSB-12150

$MgCl_2$ and ATP were freshly added to Tris buffer (50 mM, pH 7.4) to a final concentration of 10 mM and 100 µM, respectively, at the beginning of each experimental day. This buffer was used as the assay buffer. The [^{3}H]PSB-12150 DMSO solution was diluted to a final concentration of 25 nM with buffer. The membrane preparation was diluted to a final concentration of 200 mg/L with buffer. The compounds to be tested were dissolved in DMSO. In each vial 10 µL of a compound-DMSO solution, 100 µL of the radioligand buffer solution, 100 µL of the membrane preparation buffer solution, and 790 µL of the buffer were mixed.
The mixture was incubated for 1 h at rt. The membrane-bound radioligand was then separated from free radioligand by rapid filtration through grade GF/B glass microfiber filters. Each filter

unit was subsequently suspended in 3 mL ProSafe FC+ liquid scintillation cocktail and measured using liquid scintillation counting (Tri-Carb 2810TR or Tri-Carb 2910TR). Unlabeled PSB-12150 was used to measure nonspecific binding in a final concentration of 50 µM.

10.4.2 Competition binding assay with [^{3}H]PSB-1503

Phosphate buffer (50 mM, pH 7.4) was used as assay buffer and as wash buffer. The [^{3}H]PSB-1503 DMSO solution was diluted to a final concentration of 3 nM with buffer. The membrane preparation was diluted to a final concentration of 100 mg/L with buffer. The compounds to be tested were dissolved in DMSO. In each well of a 96 well deep well plate 10 µL of a compound-DMSO solution, 100 µL of the radioligand buffer solution, 100 µL of the membrane preparation buffer solution, and 290 µL of the buffer were mixed.
The mixture was incubated for 1 h at rt. The membrane-bound radioligand was then separated from free radioligand by rapid filtration through grade GF/B glass microfiber filters. To each well of the filter plate 50 µL of MicroScint-20 liquid scintillation cocktail was added and the plate was measured using liquid scintillation counting (TopCount NXT). Unlabeled PSB-1503 was used to measure nonspecific binding in a final concentration of 10 µM.

10.4.3 Determination of drug-receptor residence times by kinetic binding assays with [^{3}H]PSB-12150

$MgCl_2$ and ATP were freshly added to Tris buffer (50 nM, pH 7.4) to a final concentration of 10 mM and 100 µM, respectively, at the beginning of each experimental day. This buffer was used as the assay buffer. The [^{3}H]PSB-12150 DMSO solution was diluted to a final concentration of 25 nM with buffer. The membrane preparation was diluted to a final concentration of 200 mg/L with buffer. The compound to be tested was dissolved in DMSO. In each vial 10 µL of a compound-DMSO solution, 100 µL of the radioligand-buffer solution, and 790 µL of the buffer were mixed.
At different time points, from 3 h before harvest to immediately before, 100 µL of the membrane preparation-buffer solution was added to the vials and incubated at rt. The membrane-bound radioligand was then separated from free radioligand by rapid filtration through grade GF/B glass microfiber filters. Each filter unit was suspended in 3 mL ProSafe FC+ liquid scintillation cocktail and measured using liquid scintillation counting (Tri-Carb 2810TR or Tri-Carb 2910TR). Unlabeled PSB-12150 was used to measure nonspecific binding in a final concentration of 50 µM.

10.4.4 Determination of drug-receptor residence times by kinetic binding assays with [^{3}H]PSB-1503

Phosphate buffer (50 nM, pH 7.4) was used as assay buffer and as wash buffer. The [^{3}H]PSB-1503 DMSO solution was diluted to a final concentration of 3 nM with buffer. The membrane preparation was diluted to a final concentration of 100 mg/L with buffer. The compounds to be tested were dissolved in DMSO. In each vial 10 µL of a compound-DMSO solution, 100 µL of the radioligand-buffer solution, and 790 µL of the buffer were mixed.
At different time points, from 3 h before harvest to immediately before, 100 µL of the membrane preparation-buffer solution was added to the vials and incubated at rt. The membrane-bound radioligand was then separated from free radioligand by rapid filtration through grade GF/B glass microfiber filters. Each filter unit was suspended in 3 mL ProSafe FC+ liquid scintillation cocktail and measured using liquid scintillation counting (Tri-Carb 2810TR or Tri-Carb 2910TR). Unlabeled PSB-1503 was used to measure nonspecific binding in a final concentration of 10 µM.

10.5 Polymerase chain reaction (PCR)

PCR was used to isolate DNA fragments from genomic DNA by selective amplification of a specific region.

10.5.1 Mutagenesis PCR

Mutagenesis PCR was used to clone hGPR17 into the pFastBac1 plasmid and to further mutagenize recombinant pFastBac1-hGPR17 plasmid constructs. The following pipetting scheme was used to prepare the PCR samples.

Table 19. Mutagenesis PCR pipetting scheme.

Reagent	Amount
Phusion® GC buffer (5X)	5 µL
Deoxynucleotide (dNTP) Solution Mix (10 mM)	0.6 µL
DMSO	0.25 µL
Phusion® High-Fidelity DNA Polymerase (2.0 U/mL)	0.3 µL
PCR grade water	18.25 µL
Template DNA (c = 300-500 ng/µL)	0.3 µL
Forward Primer (5 µM)	0.6 µL
Reverse Primer (5 µM)	0.6 µL

The following thermocycler program was used for the PCR samples.

Table 20. Mutagenesis PCR thermocycler program.

	Temperature [°C]	**Time [s]**
Initial denaturation	98	180
(Denaturation	98	30
Annealing	58	45
Elongation	72	300) x 20
Final Elongation	72	600
Storage	12	∞
Lid temperature	105	∞

The PCR products were digested with DpnI for at least 1.5 h and stored at −20°C until transformation or further PCR.

10.5.2 Overlap extension PCR

Overlap extension PCR is a two-step PCR technique that was used to insert fusion partners into GPR17 constructs via intermediate mega-primers.

For the first step, primers were designed with 5' and 3' ends overlapping (20–25 bp) with the fusion partners and the insertion sites of GPR17 constructs, respectively. These primers were then used in a first PCR reaction with Q5® High-Fidelity DNA Polymerase to generate mega-primers containing the fusion partner and with 3' ends complementary to the insertion sites of the constructs. The following pipetting scheme was used to prepare the PCR samples for the first PCR.

Table 21. Mega-primer-generating PCR pipetting scheme.

Reagent	**Amount**
Q5® Reaction Buffer (5X)	10 µL
Deoxynucleotide (dNTP) Solution Mix (2.5 mM)	1 µL
Forward Primer (5 µM)	2 µL
Reverse Primer (5 µM)	2 µL
Template DNA	0.5 µL
Q5® High-Fidelity DNA Polymerase	0.5 µL
PCR grade water	34 µL

The following thermocycler program was used for the PCR samples.

Table 22. Mega-primer-generating PCR thermocycler program.

	Temperature [°C]	**Time [s]**
Initial denaturation	95	180
(Denaturation	95	30
Annealing	55	60

Elongation	68	90) x 30
Final Elongation	68	600
Storage	12	∞
Lid temperature	105	∞

The PCR products contained the mega-primers, which were extracted and purified from the mixture by agarose gel electrophoresis and then used in a second PCR together with Phusion® High-Fidelity DNA Polymerase. The following pipetting scheme was used to prepare the PCR samples for the second PCR.

Table 23. Overlap extension PCR pipetting scheme.

Reagent	Amount
Phusion® GC buffer (5X)	4 µL
Deoxynucleotide (dNTP) Solution Mix (10 mM)	0.6 µL
Magnesium chloride (50 mM)	0.2 µL
Template DNA	0.2 µL
Insert DNA	10 µL
Phusion® High-Fidelity DNA Polymerase (2.0 U/mL)	0.4 µL
PCR grade water	4.6 µL

The following thermocycler program was used for the PCR samples.

Table 24. Overlap extension PCR thermocycler program.

	Temperature [°C]	Time [s]
Initial denaturation	98	180
(Denaturation	95	30
Annealing	58	60
Elongation	72	300) x 25
Final Elongation	72	300
Storage	12	∞
Lid temperature	105	∞

The PCR products were digested with DpnI for at least 1.5 h and stored at −20°C until transformation or further PCR.

10.6 Agarose gel electrophoresis

Agarose gel electrophoresis was used to separate mixed DNA populations, either for the purification of specific DNA fragments or for in-process controls.

The gel was prepared by dissolving 0.5 g of agarose powder in 50 mL of TAE buffer by heating it in a microwave. 1 µL GelRed was added to the 1% (m/v) agarose gel solution to stain and visualize the DNA later. The gel solution was poured and allowed to stand for at least 20 min

to harden. DNA samples were mixed with Gel Loading Dye, Purple before transferring up to 30 µL into the gel wells. Different DNA ladders were used depending on the fragment size of the samples: Lambda DNA/HindIII Marker for fragment sizes between 564 and 21226 bp and Gene Ruler™ 100 bp DNA Ladder for fragment sizes between 100 and 1000 bp. Electrophoresis was performed horizontally with the gel completely immersed in the same TAE buffer (1X). The gel was typically run at 130 V for 30–60 min and afterward imaged in a ChemiDoc™ MP Imaging System. When purification of a DNA fragment was intended, the DNA fragment was cut out during brief irradiation with UV light and purified using the Zymoclean Gel DNA Recovery Kit.

10.7 Recombinant protein expression in insect cells

Modified protocols of the Invitrogen Bac-to-Bac Baculovirus Expression System were used to generate recombinant baculoviruses and subsequently express GPR17 constructs in *Sf9* or *Tni* insect cells. This approach is based on the transformation of a pFastBac plasmid containing a specific gene of interest into DH10Bac E. coli containing a baculovirus shuttle vector (bacmid). Subsequent transposition between the mini-Tn7 element on the pFastBac vector and the mini-*att*Tn7 target site on the bacmid generates the recombinant bacmid plasmid that is used to transfect insect cells and thereby generate recombinant baculoviruses containing the gene of interest. Finally, these baculoviruses are used to infect insect cells, which then express the protein of interest.

10.7.1 Cloning into the pFastBac1 vector

As starting material, hGPR17 DNA in a pcDNA3.1/Zeo(+) vector was used. The restriction sites for AscI and EcoRI were introduced by PCR. An in-house produced construct with a pFastBac1 vector and the same restriction sites as well as the PCR product were digested with AscI and EcoRI-HF in rCutSmart buffer and then separated into their fragments by agarose gel electrophoresis. The hGPR17 insert fragment and the pFastBac1 vector fragment were excised from the gel and subsequently purified using the DNA Clean & Concentrator Kit. Vector and insert fragments were ligated with T4 DNA Ligase in T4 DNA Ligase buffer at 16°C overnight.

10.7.2 Transformation into competent DH5α E. coli and purification of the plasmid DNA

For transformation, 5 µL of the plasmid were added to a 50 µL cell suspension of competent DH5α E. coli and incubated on ice for 30 min. Bacteria were then heat shocked in a water bath

at 42°C for 45 s and again placed on ice for 2 min. Next, 100 µL of LB medium at rt was added and the mixture was incubated for 1 h at 42°C and 350 rpm shaking in a thermocycler. The suspension was then spread on agar plates containing ampicillin (100 µg/mL) and incubated overnight for up to 18 h at 37°C.

The following day, single colonies were collected from each plate with a sterile filter tip and transferred into culture tubes containing a freshly prepared mixture of 5 mL LB medium and ampicillin (100 µg/mL). The tubes were incubated overnight at 37°C and 220 rpm in a shaker. The next day, plasmid DNA was purified by ethanol precipitation using the ZR Plasmid Miniprep-Classic Kit and taken up in 30 µL of PCR grade water. DNA concentration was measured using the Colibri Microvolume Spectrometer. Typical yields were between 300 and 500 ng/µL. Absorbance ratios of 1.8–2.0 for 260 nm/230 nm and 2.0–2.2 for 260nm/280nm were considered pure DNA. After restriction digestion, agarose gel electrophoresis was performed to ensure that transformation and purification were performed correctly and that DNA fragment length was as expected.

A portion of the purified plasmid DNA was diluted to 20 µL and a concentration between 50 and 100 ng/µL and then sent to Eurofins Genomics for sequencing. The following sequence primers were used:

- Forward primer: pBakPAC-FP
- Reverse primer: pFASTBAC-R

10.7.3 Transformation into competent DH10Bac E. coli and purification of the bacmid DNA

A quantity of 500 ng of the purified plasmid was added to a 50 µL cell suspension of competent DH10Bac E. coli and incubated on ice for 30 min. Then, the bacteria were heat shocked in a water bath at 42°C for 45 s and again placed on ice for 2 min. To that, 800 µL of LB medium at rt was added and the mixture was incubated for 4 h at 37°C and 350 rpm shaking in a thermocycler. The suspension was diluted 1:10 and 75 µL of the dilution was spread on a 3+2 agar plate containing tetracycline (10 µg/mL), gentamicin (7 µg/mL), kanamycin (50 µg/mL), IPTG (40 µg/mL), and X-gal (100 µg/mL). The plate was wrapped in aluminum foil and incubated at 37°C for at least 48 h.

Cells carrying the unmodified bacmid have a functional *lacZ* gene, one of the three genes of the *lac* operon. The gene product of *lacZ* is β-galactosidase, which cleaves lactose into glucose

and galactose. IPTG, a molecular mimic of a lactose metabolite, triggers *lac* operon transcription and therefore induces β-galactosidase expression. Then, β-galactosidase hydrolyzes X-gal, an analog of lactose, to galactose and 5-brom-4-chlor-3-indole. The latter then spontaneously dimerizes and is oxidized to 5,5'-dibromo-4,4'-dichloroindigo, an intensely blue colored product that leads to blue colonies. Successfully transformed DH10Bac E. coli can be identified by blue-white selection: the aforementioned transposition of the mini-Tn7 element of the pFastBac plasmid prevents the β-galactosidase expression by disrupting the reading frame of *lac*Z, leaving colonies white.[184; 185]

Thus, single white colonies were collected with a sterile filter tip and transferred to culture tubes containing a freshly prepared mixture of 5 mL of LB medium, tetracycline (10 µg/mL), gentamicin (7 µg/mL), and kanamycin (50 µg/mL). The tubes were incubated overnight at 37°C and 220 rpm in a shaker.

The following day, the bacmid DNA was purified by ethanol precipitation using QIAGEN Plasmid Buffers (P1, P2, P3). First, the cell suspension was centrifuged at 2500 g for 10 min. The supernatant was removed and 400 µL of Buffer P1 (resuspension buffer) was used to resuspend the pellet and transfer it to another tube. Next, 400 µL of Buffer P2 (lysis buffer) were added and the tube was carefully inverted repeatedly. Then, 400 µL of Buffer P3 (neutralization buffer) were added and the tube was again carefully and repeatedly inverted. The mixture was centrifuged at 14000 g and 4°C for 15 min. The supernatant containing the bacmid DNA was added to 800 µL isopropanol and gently inverted several times. The tube was stored at −20°C for at least 30 min. After centrifuging again at 14000 g and 4°C for 15 min, the pellet was washed twice with 500 µL of pre-chilled ethanol. The pellet was then dried in a laminar flow cabinet and dissolved in 30 µL of PCR grade water.

DNA concentration was measured using the Colibri Microvolume Spectrometer. Typical yields were between 2500 and 5000 ng/µL.

10.7.4 Bacmid verification test

PCR analysis was performed to verify the presence of bacmid DNA. The used M13/pUC forward and reverse primers are complementary to regions flanking the mini-*att*Tn7 site on the bacmid and thus also amplify the potentially inserted gene of interest. The following pipetting scheme was used to prepare the PCR samples.

Table 25. Bacmid verification test pipetting scheme.

Reagent	Amount
10x Standard Taq buffer	2.5 µL
10 mM dNTPs	0.5 µL
M13_forward 5 µM	0.5 µL
M13_reverse 5 µM	0.5 µL
Template (Bacmid)	1 µL
Taq Polymerase	0.15 µL
DEPC-treated H_2O	19.85 µL

The following thermocycler program was used for the PCR samples.

Table 26. Bacmid verification test thermocycler program.

	Temperature [°C]	Time [s]
Initial denaturation	95	30
(Denaturation	95	30
Annealing	58	60
Elongation	68	180) x 25
Final Elongation	72	300

The PCR products were then analyzed in agarose gel electrophoresis to verify the transposition of the pFastBac1 vectors into the bacmid vectors. The bacmid vector without a transposed construct has a band of 300 bp, while the bacmid vector with the correctly transposed construct has a band of approximately 3500 bp (2300 bp plus the size of the insert).

10.7.5 Bacmid transfection into *Sf9* insect cells

The transfection medium was prewarmed to rt, and the X-tremeGENE HP was prewarmed to 4°C and vortexed. For each transfection, 5 µL of the bacmid DNA was added to a mixture of 100 µL transfection medium and 3 µL X-tremeGENE HP. The mixture was mixed gently and incubated at rt for 15 min. The mixture was then added to 2.5 mL of *Sf9* cells at 10^6 cells/mL in a deep well plate. The plates were incubated at 27°C and 400 rpm for 96 h. A *gp64* assay was performed to confirm a successful transfection. The deep-well plate was then centrifuged at 2000 rpm for 15 min to harvest the supernatant containing the baculovirus (P1), which was then stored at 4°C.

10.7.6 Infection of insect cells

Baculovirus containing the gene of interest was used to infect insect cells for multiple reasons: First, the P1 virus was often amplified in a first round of infection to obtain a P2 virus with a

higher titer, which was subsequently used to infect insect cells, as insect cells produce low virus titers. Only *Sf9* insect cells can be used for this purpose since *Tni* insect cells do not produce virus. Higher virus passages are not recommended since the viruses are prone to recombination, which could mutate the gene of interest. Secondly, the infection was used to induce expression of the protein of interest in various levels. Hence, listed below are several infection options:

- 400 µL (except where noted) of P1 or P2 were used to infect 40 mL of freshly grown *Sf9* insect cells at 2−3 × 10^6 cells/mL (small-scale expression in *Sf9* insect cells)
- 400 µL (except where noted) of P2 were used to infect 40 mL of freshly grown *Tni* insect cells at 2−3 × 10^6 cells/mL (small-scale expression in *Tni* insect cells)
- 3–6 mL of P2 were used to infect 450–900 mL of freshly grown *Sf9* insect cells at 2−3 × 10^6 cells/mL (large-scale expression in *Sf9* insect cells)
- 3–6 mL of P2 were used to infect 450–900 mL of freshly grown *Tni* insect cells at 2−3 × 10^6 cells/mL (large-scale expression in *Tni* insect cells)

In all cases, the mixture was incubated at 27°C and 150 rpm for 48 h (except where noted). FLAG expression assay was performed to confirm successful infection. Small-scale expression batches were harvested by centrifugation at 4000 g for 15 min. Only for small-scale expression in *Sf9* insect cells, the baculovirus (P2) containing supernatant was recovered and stored at 4°C. Large-scale expression batches were harvested by centrifugation at 4000 g for 30 min. Cel pellets were then resuspended in 30 mL PBS and centrifuged again at 4000 g for 20 min. In all cases, the final obtained cell pellet was stored at −80°C.

10.7.7 Transfection and infection control via flow cytometry

Baculovirus-infected cells express glycoprotein 64 (*gp64*) on their surface, while expression of the protein of interest is accompanied by the expression of the N-terminal FLAG tag attached to each construct, making these structures viable targets for assessing transfection and infection success, respectively, via flow cytometry. Additionally, for infection control, total and surface expression levels were assessed individually with partial use of Triton X-100, a detergent that permeabilizes the cell membrane and allows detection of (misexpressed) intracellular FLAG-tags.

The phycoerythrin-conjugated anti-GP64 antibody stock solution (0.2 mg/mL) or the fluorescein-conjugated anti-FLAG antibody stock solution (0.5 mg/mL), respectively, was diluted 1:100 in TBS buffer supplemented with 4 % bovine serum albumin (BSA). Cell samples of

5 µL, containing approx. 1–1.5 × 10^4 cells, were mixed with 5 µL diluted antibody solution. For the FLAG-assay, cell samples were employed in duplicate so that Triton X-100 could be added to every second one. The mixture was incubated for 20 min at 4°C in the dark. Subsequently, 90 µL of TBS buffer was added to the mixture and it was analyzed using a Guava easyCyte HP flow cytometer (blue laser λ=488 nm, detection channel yellow fluorescence [for *gp64* assay] or green and red fluorescence [for FLAG assay]). Native *Sf9* insect cells lacking *gp64* and not expressing FLAG-tags were used as negative control to distinguish between transfected/infected and non-transfected/non-infected populations.

10.7.8 Insect cell membrane preparation and protein purification

Samples and buffers were stored on ice throughout the membrane preparation and protein purification process. All centrifugation and rocking steps were performed at 4°C.

10.7.8.1 Insect cell membrane preparation

Small-scale expression

The cell pellet was resuspended in 25 mL low osmotic buffer plus half a tablet of cOmplete Protease Inhibitor Cocktail and homogenized using a 15 mL Dounce homogenizer. The suspension was then centrifuged at 48000 g for 30 min. The supernatant was discarded and the cell pellet was resuspended in 25 mL high osmotic buffer and then homogenized and centrifuged again as described above. The washed cell pellet was resuspended in 3 mL resuspension buffer and homogenized using a 2 mL Dounce homogenizer. The membrane preparation was then frozen in liquid nitrogen and stored at −80°C.

Large-scale expression

The cell pellet was resuspended in 80–90 mL low osmotic buffer plus three tablets of cOmplete Protease Inhibitor Cocktail and homogenized using a 100 mL Dounce homogenizer. The suspension was then centrifuged at 48000 g for 30 min. The supernatant was discarded and the cell pellet was resuspended again in 80–90 mL low osmotic buffer plus two tablets of protease inhibitor cocktail. Subsequently, the cell pellet was resuspended in 80–90 mL high osmotic buffer and then homogenized and centrifuged again as described above. This was repeated two more times. The washed cell pellet was resuspended in 50 mL resuspension buffer and homogenized using a 40 mL Dounce homogenizer. Batches of 25 mL membrane preparation were then frozen in liquid nitrogen and stored at −80°C.

10.7.8.2 Preparation of the DDM/CHS stock solution

5 g of DDM were dissolved in 40 mL 250 mM Tris buffer at pH 8.0. Then, 1 g of CHS was added and the mixture was sonicated using a Sonopuls HD 2070 sonicator equipped with the Sonotrode MS 73 microtip at 95% power for approximately 15 min until CHS was completely dissolved. Subsequently, the volume was adjusted to 50 mL with water and rocked overnight at 4°C. The next day, the mixture was sterile-filtered and the resulting 10%/2% (w/v) DDM/CHS stock solution was stored at 4°C.

10.7.8.3 Solubilization and TALON binding

Small-scale expression

3 mL membrane preparation was thawed on ice. 2 mg/mL iodoacetamide was added and the sample was rocked for 30 min. If necessary, ligand was added to a final concentration of 1 µM and the sample was rocked for 30 min. 3 mL 2x solubilization buffer was added and the sample was rocked for 3 h. The solubilized membranes were then centrifuged at 10000 g for 30 min. The supernatant was added to 12.5 µL of washed TALON IMAC Cobalt (Co^{2+}) resin beads (corresponding to 25 µL slurry). Imidazole was added to a final concentration of 20 mM. The mixture was rocked overnight.

Large-scale expression

25 mL membrane preparation was thawed on ice. 2 mg/mL iodoacetamide was added and the sample was rocked for 30 min. If necessary, ligand was added to a final concentration of 1 µM and the sample was rocked for 30 min. 25 mL 2x solubilization buffer was added and the sample was rocked for 3 h. The solubilized membranes were then centrifuged at 10000 g for 30 min. The supernatant was added to 375–500 µL of washed TALON IMAC Co^{2+} resin beads (corresponding to 750–1000 µL slurry). Imidazole was added to a final concentration of 20 mM. The mixture was rocked overnight.

10.7.8.4 Purification and elution

Small-scale expression

The mixture was centrifuged at 100 g for 5 min to pellet the resin. Most of the supernatant was removed. The pellet was resuspended in the remaining buffer, pipetted into an empty gravity flow column, and briefly centrifuged. The column was washed with 750 µL wash buffer 1 and centrifuged briefly, then washed with 500 µL wash buffer 2 and briefly centrifuged again. The

washed protein was eluted by adding elution buffer to the column in three steps of 25, 50, and 50 µL; each step was incubated for 10 min and the elution fractions were combined.

Large-scale expression

The resin beads were pipetted into an empty gravity flow column and let settled down. The column was washed with 10–15 column volumes (CV) (1 CV is the volume of resin beads used) wash buffer 1. Then, the column was washed with 10 CV wash buffer 2. The washed protein was eluted by adding elution buffer in four steps of 500 µL and incubating 10 min between each elution step. The elution fractions were combined and concentrated to ~200 µL using Vivaspin 100 concentrators.

10.8 Protein analysis

The purified and eluted protein solution was used for SDS-PAGE, SEC, and TSA.

10.8.1 SDS-PAGE

SDS-PAGE was performed using Bis-Tris gels. The following scheme was used to prepare the resolving gel for four Bis-Tris gels.

Table 27. SDS-PAGE resolving gel pipetting scheme.

Reagent	Amount
1 M Bis-Tris pH 6.5–6.7	6.5 mL
30 % Acrylamide/bis-acrylamide (37.5:1)	6.5 mL
H_2O	6.5 mL
10 % APS	120 µL
N,N,N’,N’-tetramethylethylenediamine (TEMED)	48 µL

The resolving gel was immediately pipetted into each gel cassette and layered with 70 % isopropanol. After a polymerization time of 30 min, the isopropanol was drained. The following scheme was used to prepare the stacking gel.

Table 28. SDS-PAGE resolving gel pipetting scheme.

Reagent	Amount
1 M Bis-Tris pH 6.5–6.7	2.4 mL
30 % Acrylamide/bis-acrylamide (37.5:1)	1.6 mL
H_2O	5.6 mL
10 % APS	48 µL
N,N,N’,N’-tetramethylethylenediamine (TEMED)	32 µL

The stacking gel was pipetted onto the resolving gel and a 10-well comb was inserted. The gel was stored at 4°C or used directly for SDS-PAGE.

To prepare the samples, the reducing agent dithiothreitol was added to the purified protein solution to a final concentration of 200 mM to prevent formation of intra- and intermolecular disulfide bonds between cysteine residues and allow for better separation of proteins. The solution was then mixed with NuPAGE LDS Sample Buffer (4X) to a total volume of 30 µL and incubated for 30 min at 37°C. The gel was clamped into the electrophoresis module with a thick glass clamped on the other side. The buffer chambers were filled with SDS-PAGE running buffer. The samples and 5 µL of PageRuler Prestained Protein Ladder were loaded onto the gel. Electrophoresis was started at 50 V and increased to 120 V once the resolving gel was reached.

The gel was stained with Coomassie protein staining solution by heating in a microwave. The gel was destained by heating in the microwave with water and visualized using a ChemiDoc MP imaging system.

10.8.2 Size exclusion chromatography (SEC)

The sample was centrifuged for 10 min at 14000 g and 4°C to remove particles and moved to water-cooled HPLC vials. Then, 30 µL of the protein solution was injected via the autosampler into an Agilent Technologies 1260 Infinity HPLC system with a Sepax NanoFilm SEC-250 column (4.6x250 mm, 5 µm particle size, 250 Å pore size). The HPLC running buffer was precooled, the autosampler was run at 4°C, the flowrate was set to 0.5 mL/min, and the detection wavelength was set to 280 nm.

10.8.3 Thermostability assay (TSA)

A CPM stock solution in DMSO at 4 mg/mL was prepared. The stock solution was diluted 1:40 with HPLC running buffer. 1 µL of this CPM dilution was mixed with ~1 µg of protein and, in case of evaluating ligand-bound constructs, 1 µM final concentration of ligand and adjusted to 50 µL with HPLC running buffer. The sample was incubated for 10 min at 4°C in the dark. Then, the temperature-dependent fluorescence was analyzed using a Rotor-Gene Q real-time PCR cycler over a temperature range of 30 to 95°C in 1°C steps. The excitation wavelength was set to 365 nm, the detection wavelength was set to 460 nm, and the fluorescence gain was set to 1. The sample was incubated for 95 s in the first step and 10 s in each subsequent step.

11 List of abbreviations

Table 29. List of abbreviations.

Abbreviation	Description
1321N1-hGPR17 cells	Human brain astrocytoma 1321N1 cells stably transfected with hGPR17
Aβ	Amyloid beta
AC	Adenylate cyclase
AD	Alzheimer's disease
ADP	Adenosine diphosphate
APOE	Apolipoprotein E
APP	Amyloid precursor protein
APS	Ammonium persulfate
ATP	Adenosine triphosphate
Bis-tris	2-[Bis(2-hydroxyethyl)amino]-2-(hydroxymethyl)propane-1,3-diol
BRIL	Thermostabilized apocytochrome b_{562} RIL
cAMP	Cyclic adenosine monophosphate
Ca^{2+}	Calcium ion
CASP14	14th Critical Assessment of Structure Prediction
CHO	Chinese hamster ovary
CHO-FITR-hGPR17 cells	CHO-FITR cells stably transfected with hGPR17
CHS	Cholesteryl hemisuccinate
CLTR	Cysteinyl leukotriene receptors
CMV	Cytomegalovirus
CNS	Central nervous system
Co^{2+}	Cobalt ion
COP	Committed oligodendrocyte precursor cells
CPM	*N*-[4-(7-Diethylamino-4-methyl-3-coumarinyl)phenyl]maleimide
cryo-EM	Cryogenic electron microscopy
DAG	Diacylglycerol
DDM	n-Dodecyl-β-D-maltopyranoside
DMEM	Dulbecco's Modified Eagle Medium
DMSO	Dimethyl sulfoxide
DNA	Deoxyribonucleic acid
dNTP	Deoxynucleoside triphosphate
EAE	Experimental autoimmune encephalomyelitis
EC_{50}	Half-maximal effective concentration
ECL	Extracellular loop
EDTA	Ethylenediaminetetraacetic acid
EEC	Enteroendocrine cell
ERK	Extracellular signal-regulated kinase
ERK1/2	Extracellular signal-regulated kinase 1/2
EPAC1	Exchange protein directly activated by cAMP 1
FACS	Fluorescence-activated cell sorting

FFAR	Free fatty acid receptor
FITC	Fluorescein isothiocyanate
FITR	Flp-In T-REx
GABA	γ-Aminobutyric acid
GDP	Guanosine diphosphate
GIRK	G protein-coupled inwardly rectifying potassium
GLP-1	Glucagon-like peptide 1
gp64	Glycoprotein 64
GPCR	G protein-coupled receptor
GRK	G protein-coupled receptor kinase
GTP	Guanosine triphosphate
HEK293	Human embryonic kidney 293
HEPES	2-[4-(2-Hydroxyethyl)piperazin-1-yl]ethanesulfonic acid
hGPR17	Human GPR17
hGPR17-L	Human GPR17 (long isoform)
hGPR17-S	Human GPR17 (short isoform)
HLA	Human leukocyte antigen
HMDB	Human Metabolome Database
HPLC	High-performance liquid chromatography
IC_{50}	Half-maximal inhibitory concentration
ICL	Intracellular loop
IMAC	Immobilized metal affinity chromatography
IP_3	Inositol trisphosphate
IPTG	Isopropyl β-D-1-thiogalactopyranoside
IRES	Internal ribosomal entry site
IUPHAR	International Union of Pharmacology
K_d	Dissociation constant
KHB	Krebs-Hepes buffer
K_i	Inhibition constant
LB	Lysogeny broth
LCP	Lipidic cubic phase
LDS	Lithium dodecyl sulfate
LPAR	Lysophosphatidic acid receptor
LTB_4	Leukotriene B_4
LTC_4	Leukotriene C_4
LTD_4	Leukotriene D_4
LVX	Lily virus X
MAPK	Mitogen-activated protein kinase
mGPR17	Mouse GPR17
MOPS	3-(*N*-Morpholino)propanesulfonic acid
MS	Multiple sclerosis
NAM	Negative allosteric modulator
NECA	5'-*N*-Ethylcarboxamidoadenosine
NMDA	*N*-methyl-D-aspartate
OL	Oligodendrocyte
OPC	Oligodendrocyte progenitor cell

P2YR	P2Y receptor
PAGE	Polyacrylamide gel electrophoresis
PAM	Positive allosteric modulator
PAR	Protease-activated receptor
PCR	Polymerase chain reaction
PI3K	Phosphatidylinositol-3-kinase
PIP_2	Phosphatidylinositol-4,5-bisphosphate
PBS	Phosphate-buffered saline
PCR	Polymerase Chain Reaction
PD	Parkinson's disease
PKA	Protein kinase A
PKC	Protein kinase C
pre-OL	Pre-oligodendrocyte
PSEN1/2	Presenilin 1/2
rGPR17	Rat GPR17
RhoGEF	Rho guanine nucleotide exchange factors
ROS	Reactive oxygen species
rpm	Revolutions per minute
rt	Room temperature
SAR	Structure-activity relationship
SDS	Sodium dodecyl sulfate
SEC	Size exclusion chromatography
Sf	*Spodoptera frugiperda*
shRNA	Short hairpin RNA
siRNA	Small interfering RNA
T2DM	Type 2 diabetes mellitus
TAE	Tris-acetate-EDTA
TBS	Tris-buffered saline
TCF7L2	Transcription factor 7-like 2
TEMED	*N*,*N*,*N*',*N*'-Tetramethylethylenediamine
THTMP	2-(3,4-Dihydroquinolin-1(2*H*)-yl)(*p*-tolyl)methyl)phenol
TM	Transmembrane
T_M	Melting temperature
Tni	*Trichoplusia ni*
Tris	Tris(hydroxymethyl)aminomethane
TSA	Thermostability assay
UDP	Uridine diphosphate
UTP	Uridine triphosphate
X-gal	5-Bromo-4-chloro-3-indolyl-β-D-galactopyranoside

12 Danksagung

An erster Stelle möchte ich mich bei Prof. Dr. Christa Müller für die Aufnahme in ihren Arbeitskreis, das Vertrauen, die Betreuung sowie die wissenschaftliche und persönliche Unterstützung und Förderung über die gesamte Promotionszeit bedanken. Danke für deine Offenheit, die Freiheit, eigenständig zu forschen, und deine stets ermutigenden Worte, besonders bei Herausforderungen. Es war mir eine Freude, in einem inspirierenden Umfeld arbeiten zu dürfen.

Mein besonderer Dank gilt auch den Mitgliedern meiner Prüfungskommission für ihre Zeit und Mitwirkung: PD Dr. Anke Schiedel, Prof. Dr. Günther Weindl und Prof. Dr. Ulrich Ettinger.

Ich danke all den Kollegen, die mich wissenschaftlich begleitet und unterstützt haben. Hervorheben möchte ich Dr. Tobias Claff, Dr. Victoria Vaaßen, Dr. Jonathan Schlegel und Katharina Sylvester, für ihre Unterstützung bei der Einarbeitung in verschiedene Themenbereiche und ihre fachliche Expertise. Ebenso danke ich Lea Berger, deren Masterarbeit meine Forschung vorangebracht hat, sowie Dr. Jörg Hockemeyer, mit dem ich auf dem Weg zur Veröffentlichung des ersten Papers viele Höhen und Tiefen geteilt habe. Ich danke außerdem allen weiteren Kollegen für die tolle Arbeitsatmosphäre, hier nur eine unvollständige Liste: Dr. Andhika Mahardhika, Christiane Bous, Christin Vielmuth, Haneen Al-Hroub, Dr. Jan Voß, Dr. Jessica Nagel, Nicole Florin, Sophie Clemens, Sven Russell. Ein besonderer Dank geht an das wohl weltbeste Mensa-Team: Franka Westermann, Julia Dörner und Florian Schwermer, die nicht nur Kollegen geblieben sind, sondern zu denen ich auch tiefe Freundschaften knüpfen konnte.

Dank gebührt ebenfalls der Studienstiftung des deutschen Volkes für die finanzielle Förderung meiner Promotion sowie darüber hinaus für herausragende ideelle Förderung.

Nicht zuletzt danke ich meiner Familie, insbesondere meiner Mutter, für ihre stetige Unterstützung während meiner gesamten Ausbildungszeit.

Ein ganz besonderer Dank gilt meiner Frau, Sandra Lewash: für deinen Rückhalt, dein Verständnis und dein Mitfiebern in allen Phasen dieser Reise, die wir gemeinsam begangen haben und an der wir gemeinsam gewachsen sind. In diesem Sinne auch noch mal herzlichen Glückwunsch zum ersten Lewash et al. Paper. Da warst du schneller.

13 References

(1) Rang, H. P. The receptor concept: pharmacology's big idea. *Br. J. Pharmacol.* **2006**, *147*, S9–S16.

(2) Neubig, R. R.; Spedding, M.; Kenakin, T.; Christopoulos, A. International Union of Pharmacology Committee on Receptor Nomenclature and Drug Classification. XXXVIII. Update on terms and symbols in quantitative pharmacology. *Pharmacol. Rev.* **2003**, *55*, 597–606.

(3) Flanagan, C. A. GPCR-radioligand binding assays. *Methods Cell Biol.* **2016**, *132*, 191–215.

(4) Breen, C. J.; Raverdeau, M.; Voorheis, H. P. Development of a quantitative fluorescence-based ligand-binding assay. *Sci. Rep.* **2016**, *6*, 25769.

(5) Liu, K.; Southall, N.; Titus, S. A.; Inglese, J.; Eskay, R. L.; Shinn, P.; Austin, C. P.; Heilig, M. A.; Zheng, W. A multiplex calcium assay for identification of GPCR agonists and antagonists. *Assay Drug Dev. Technol.* **2010**, *8*, 367–379.

(6) Vasudevan, N. T. cAMP assays in GPCR drug discovery. *Methods Cell Biol.* **2017**, *142*, 51–57.

(7) Berg, K. A.; Clarke, W. P. Making sense of pharmacology: inverse agonism and functional selectivity. *Int. J. Neuropsychopharmacol.* **2018**, *21*, 962–977.

(8) Reichert, C. F.; Deboer, T.; Landolt, H.-P. Adenosine, caffeine, and sleep-wake regulation: state of the science and perspectives. *J. Sleep Res.* **2022**, *31*, e13597.

(9) Lazarus, M.; Oishi, Y.; Bjorness, T. E.; Greene, R. W. Gating and the need for sleep: dissociable effects of adenosine A1 and A2A receptors. *Front. Neurosci.* **2019**, *13*, 740.

(10) Kanneganti, T.-D. Intracellular innate immune receptors: life inside the cell. *Immunol. Rev.* **2020**, *297*, 5–12.

(11) Lemoine, D.; Jiang, R.; Taly, A.; Chataigneau, T.; Specht, A.; Grutter, T. Ligand-gated ion channels: new insights into neurological disorders and ligand recognition. *Chem. Rev.* **2012**, *112*, 6285–6318.

(12) Lemmon, M. A.; Schlessinger, J. Cell signaling by receptor tyrosine kinases. *Cell* **2010**, *141*, 1117–1134.

(13) Vass, M.; Kooistra, A. J.; Yang, D.; Stevens, R. C.; Wang, M.-W.; Graaf, C. de. Chemical diversity in the G protein-coupled receptor superfamily. *Trends Pharmacol. Sci.* **2018**, *39*, 494–512.

(14) Katritch, V.; Cherezov, V.; Stevens, R. C. Structure-function of the G protein-coupled receptor superfamily. *Annu. Rev. Pharmacol. Toxicol.* **2013**, *53*, 531–556.

(15) Rosenbaum, D. M.; Rasmussen, S. G. F.; Kobilka, B. K. The structure and function of G-protein-coupled receptors. *Nature* **2009**, *459*, 356–363.

(16) Milligan, G.; Kostenis, E. Heterotrimeric G-proteins: a short history. *Br. J. Pharmacol.* **2006**, *147*, S46–S55.

(17) Wingler, L. M.; Lefkowitz, R. J. Conformational basis of G protein-coupled receptor signaling versatility. *Trends Cell Biol.* **2020**, *30*, 736–747.

(18) Lefkowitz, R. J. Rodbell and Gilman win 1994 Nobel Prize for Physiology and Medicine. *Trends Pharmacol. Sci.* **1994**, *15*, 442–444.

(19) Schaffhausen, J. GPCRs signal a Nobel Prize. *Trends Pharmacol. Sci.* **2013**, *34*, 1.

(20) Hauser, A. S.; Attwood, M. M.; Rask-Andersen, M.; Schiöth, H. B.; Gloriam, D. E. Trends in GPCR drug discovery: new agents, targets and indications. *Nat. Rev. Drug Discov.* **2017**, *16*, 829–842.

(21) Sriram, K.; Insel, P. A. G protein-coupled receptors as targets for approved drugs: how many targets and how many drugs? *Mol. Pharmacol.* **2018**, *93*, 251–258.

(22) Kolakowski, L. F. GCRDb: a G-protein-coupled receptor database. *Recept. Channels* **1994**, *2*, 1–7.

(23) Attwood, T. K.; Findlay, J. B. Fingerprinting G-protein-coupled receptors. *Protein Eng.* **1994**, *7*, 195–203.

(24) Schiöth, H. B.; Fredriksson, R. The GRAFS classification system of G-protein coupled receptors in comparative perspective. *Gen. Comp. Endocrinol.* **2005**, *142*, 94–101.

(25) Spielman, S. J.; Kumar, K.; Wilke, C. O. Comprehensive, structurally-informed alignment and phylogeny of vertebrate biogenic amine receptors. *PeerJ* **2015**, *3*, e773.

(26) Lv, X.; Liu, J.; Shi, Q.; Tan, Q.; Wu, D.; Skinner, J. J.; Walker, A. L.; Zhao, L.; Gu, X.; Chen, N.; Xue, L.; Si, P.; Zhang, L.; Wang, Z.; Katritch, V.; Liu, Z.-J.; Stevens, R. C. In vitro expression and analysis of the 826 human G protein-coupled receptors. *Protein Cell* **2016**, *7*, 325–337.

(27) Ballesteros, J. A.; Weinstein, H. [19] Integrated methods for the construction of three-dimensional models and computational probing of structure-function relations in G protein-coupled receptors. *Methods in Neurosciences* **1995**, *25*, 366–428.

(28) Isberg, V.; Graaf, C. de; Bortolato, A.; Cherezov, V.; Katritch, V.; Marshall, F. H.; Mordalski, S.; Pin, J.-P.; Stevens, R. C.; Vriend, G.; Gloriam, D. E. Generic GPCR residue numbers - aligning topology maps while minding the gaps. *Trends Pharmacol. Sci.* **2015**, *36*, 22–31.

(29) Tautermann, C. S. GPCR structures in drug design, emerging opportunities with new structures. *Bioorg. Med. Chem. Lett.* **2014**, *24*, 4073–4079.

(30) Shi, Y. A glimpse of structural biology through X-ray crystallography. *Cell* **2014**, *159*, 995–1014.

(31) García-Nafría, J.; Tate, C. G. Structure determination of GPCRs: cryo-EM compared with X-ray crystallography. *Biochem. Soc. Trans.* **2021**, *49*, 2345–2355.

(32) Milne, J. L. S.; Borgnia, M. J.; Bartesaghi, A.; Tran, E. E. H.; Earl, L. A.; Schauder, D. M.; Lengyel, J.; Pierson, J.; Patwardhan, A.; Subramaniam, S. Cryo-electron microscopy--a primer for the non-microscopist. *FEBS J.* **2013**, *280*, 28–45.

(33) Kühlbrandt, W. Biochemistry. The resolution revolution. *Science* **2014**, *343*, 1443–1444.

(34) Palczewski, K.; Kumasaka, T.; Hori, T.; Behnke, C. A.; Motoshima, H.; Fox, B. A.; Le Trong, I.; Teller, D. C.; Okada, T.; Stenkamp, R. E.; Yamamoto, M.; Miyano, M. Crystal structure of rhodopsin: a G protein-coupled receptor. *Science* **2000**, *289*, 739–745.

(35) Rasmussen, S. G. F.; Choi, H.-J.; Rosenbaum, D. M.; Kobilka, T. S.; Thian, F. S.; Edwards, P. C.; Burghammer, M.; Ratnala, V. R. P.; Sanishvili, R.; Fischetti, R. F.; Schertler, G. F. X.; Weis, W. I.; Kobilka, B. K. Crystal structure of the human beta2 adrenergic G-protein-coupled receptor. *Nature* **2007**, *450*, 383–387.

(36) Warne, T.; Serrano-Vega, M. J.; Baker, J. G.; Moukhametzianov, R.; Edwards, P. C.; Henderson, R.; Leslie, A. G. W.; Tate, C. G.; Schertler, G. F. X. Structure of a beta1-adrenergic G-protein-coupled receptor. *Nature* **2008**, *454*, 486–491.

(37) Yang, D.; Zhou, Q.; Labroska, V.; Qin, S.; Darbalaei, S.; Wu, Y.; Yuliantie, E.; Xie, L.; Tao, H.; Cheng, J.; Liu, Q.; Zhao, S.; Shui, W.; Jiang, Y.; Wang, M.-W. G protein-coupled receptors: structure- and function-based drug discovery. *Signal Transduct. Target. Ther.* **2021**, *6*, 7.

(38) Claff, T.; Klapschinski, T. A.; Tiruttani Subhramanyam, U. K.; Vaaßen, V. J.; Schlegel, J. G.; Vielmuth, C.; Voß, J. H.; Labahn, J.; Müller, C. E. Single stabilizing point mutation enables high-resolution co-crystal structures of the adenosine A2A receptor with preladenant conjugates. *Angew. Chem. Int. Ed Engl.* **2022**, *61*, e202115545.

(39) Chun, E.; Thompson, A. A.; Liu, W.; Roth, C. B.; Griffith, M. T.; Katritch, V.; Kunken, J.; Xu, F.; Cherezov, V.; Hanson, M. A.; Stevens, R. C. Fusion partner toolchest for the stabilization and crystallization of G protein-coupled receptors. *Structure* **2012**, *20*, 967–976.

(40) Cherezov, V.; Rosenbaum, D. M.; Hanson, M. A.; Rasmussen, S. G. F.; Thian, F. S.; Kobilka, T. S.; Choi, H.-J.; Kuhn, P.; Weis, W. I.; Kobilka, B. K.; Stevens, R. C. High-resolution crystal structure of an engineered human beta2-adrenergic G protein-coupled receptor. *Science* **2007**, *318*, 1258–1265.

(41) Steyaert, J.; Kobilka, B. K. Nanobody stabilization of G protein-coupled receptor conformational states. *Curr. Opin. Struct. Biol.* **2011**, *21*, 567–572.

(42) Bi, M.; Wang, X.; Wang, J.; Xu, J.; Sun, W.; Adediwura, V. A.; Miao, Y.; Cheng, Y.; Ye, L. Structure and function of a near fully-activated intermediate GPCR-Gαβγ complex. *Nat. Commun.* **2025**, *16*, 1100.

(43) Hassell, A. M.; An, G.; Bledsoe, R. K.; Bynum, J. M.; Carter, H. L.; Deng, S.-J. J.; Gampe, R. T.; Grisard, T. E.; Madauss, K. P.; Nolte, R. T.; Rocque, W. J.; Wang, L.; Weaver, K. L.; Williams, S. P.; Wisely, G. B.; Xu, R.; Shewchuk, L. M. Crystallization of protein-ligand complexes. *Acta Crystallogr. D Biol. Crystallogr.* **2007**, *63*, 72–79.

(44) Li, D.; Caffrey, M. Structure and functional characterization of membrane integral proteins in the lipid cubic phase. *J. Mol. Biol.* **2020**, *432*, 5104–5123.

(45) Jumper, J.; Evans, R.; Pritzel, A.; Green, T.; Figurnov, M.; Ronneberger, O.; Tunyasuvunakool, K.; Bates, R.; Žídek, A.; Potapenko, A.; Bridgland, A.; Meyer, C.; Kohl, S. A. A.; Ballard, A. J.; Cowie, A.; Romera-Paredes, B.; Nikolov, S.; Jain, R.; Adler, J.; Back, T.; Petersen, S.; Reiman, D.; Clancy, E.; Zielinski, M.; Steinegger, M.; Pacholska, M.; Berghammer, T.; Bodenstein, S.; Silver, D.; Vinyals, O.; Senior, A. W.; Kavukcuoglu, K.; Kohli, P.; Hassabis, D. Highly accurate protein structure prediction with AlphaFold. *Nature* **2021**, *596*, 583–589.

(46) Ye, F.; Wong, T.-S.; Chen, G.; Zhang, Z.; Zhang, B.; Gan, S.; Gao, W.; Li, J.; Wu, Z.; Pan, X.; Du, Y. Cryo-EM structure of G-protein-coupled receptor GPR17 in complex with inhibitory G protein. *MedComm (2020)* **2022**, *3*, e159.

(47) Schlembach, M. C.; Wrublewski, D. T. Analysis for the science librarians of the 2024 nobel prize in chemistry: computational protein design and protein structure prediction. *Sci. Technol. Libr. (New York,. NY)* **2025**, 1–16.

(48) Duc, N. M.; Kim, H. R.; Chung, K. Y. Structural mechanism of G protein activation by G protein-coupled receptor. *Eur. J. Pharmacol.* **2015**, *763*, 214–222.

(49) Hilger, D.; Masureel, M.; Kobilka, B. K. Structure and dynamics of GPCR signaling complexes. *Nat. Struct. Mol. Biol.* **2018**, *25*, 4–12.

(50) Mahoney, J. P.; Sunahara, R. K. Mechanistic insights into GPCR-G protein interactions. *Curr. Opin. Struct. Biol.* **2016**, *41*, 247–254.

(51) Hilger, D. The role of structural dynamics in GPCR-mediated signaling. *FEBS J.* **2021**, *288*, 2461–2489.

(52) Venkatakrishnan, A. J.; Deupi, X.; Lebon, G.; Heydenreich, F. M.; Flock, T.; Miljus, T.; Balaji, S.; Bouvier, M.; Veprintsev, D. B.; Tate, C. G.; Schertler, G. F. X.; Babu, M. M. Diverse activation pathways in class A GPCRs converge near the G-protein-coupling region. *Nature* **2016**, *536*, 484–487.

(53) Syrovatkina, V.; Alegre, K. O.; Dey, R.; Huang, X.-Y. Regulation, signaling, and physiological functions of G-proteins. *J. Mol. Biol.* **2016**, *428*, 3850–3868.

(54) Qi, C.; Sorrentino, S.; Medalia, O.; Korkhov, V. M. The structure of a membrane adenylyl cyclase bound to an activated stimulatory G protein. *Science* **2019**, *364*, 389–394.

(55) Taylor, S. J.; Chae, H. Z.; Rhee, S. G.; Exton, J. H. Activation of the beta 1 isozyme of phospholipase C by alpha subunits of the Gq class of G proteins. *Nature* **1991**, *350*, 516–518.

(56) Suzuki, N.; Hajicek, N.; Kozasa, T. Regulation and physiological functions of G12/13-mediated signaling pathways. *Neurosignals.* **2009**, *17*, 55–70.

(57) Chen, Z.; Singer, W. D.; Sternweis, P. C.; Sprang, S. R. Structure of the p115RhoGEF rgRGS domain-Galpha13/i1 chimera complex suggests convergent evolution of a GTPase activator. *Nat. Struct. Mol. Biol.* **2005**, *12*, 191–197.

(58) Khan, S. M.; Sleno, R.; Gora, S.; Zylbergold, P.; Laverdure, J.-P.; Labbé, J.-C.; Miller, G. J.; Hébert, T. E. The expanding roles of Gβγ subunits in G protein-coupled receptor signaling and drug action. *Pharmacol. Rev.* **2013**, *65*, 545–577.

(59) Pfeil, E. M.; Brands, J.; Merten, N.; Vögtle, T.; Vescovo, M.; Rick, U.; Albrecht, I.-M.; Heycke, N.; Kawakami, K.; Ono, Y.; Ngako Kadji, F. M.; Hiratsuka, S.; Aoki, J.; Häberlein, F.; Matthey, M.; Garg, J.; Hennen, S.; Jobin, M.-L.; Seier, K.; Calebiro, D.; Pfeifer, A.; Heinemann, A.; Wenzel, D.; König, G. M.; Nieswandt, B.; Fleischmann, B. K.; Inoue, A.; Simon, K.; Kostenis, E. Heterotrimeric G protein subunit Gαq is a master switch for Gβγ-mediated calcium mobilization by Gi-coupled GPCRs. *Mol. Cell* **2020**, *80*, 940–954.

(60) Eichel, K.; Zastrow, M. von. Subcellular organization of GPCR signaling. *Trends Pharmacol. Sci.* **2018**, *39*, 200–208.

(61) Gurevich, V. V.; Gurevich, E. V. GPCR signaling regulation: the role of GRKs and arrestins. *Front. Pharmacol.* **2019**, *10*, 125.

(62) Caron, M. G.; Barak, L. S. A brief history of the β-arrestins. *Methods Mol. Biol.* **2019**, *1957*, 3–8.

(63) Wright, S. C.; Lukasheva, V.; Le Gouill, C.; Kobayashi, H.; Breton, B.; Mailhot-Larouche, S.; Blondel-Tepaz, É.; Antunes Vieira, N.; Costa-Neto, C.; Héroux, M.; Lambert, N. A.; Parreiras-E-Silva, L. T.; Bouvier, M. BRET-based effector membrane translocation assay monitors GPCR-promoted and endocytosis-mediated Gq activation at early endosomes. *Proc. Natl. Acad. Sci. U. S. A.* **2021**, *118*, e2025846118.

(64) Gurevich, V. V.; Gurevich, E. V. Arrestin-mediated signaling: is there a controversy? *World J. Biol. Chem.* **2018**, *9*, 25–35.

(65) Grundmann, M.; Merten, N.; Malfacini, D.; Inoue, A.; Preis, P.; Simon, K.; Rüttiger, N.; Ziegler, N.; Benkel, T.; Schmitt, N. K.; Ishida, S.; Müller, I.; Reher, R.; Kawakami, K.; Inoue, A.; Rick, U.; Kühl, T.; Imhof, D.; Aoki, J.; König, G. M.; Hoffmann, C.; Gomeza, J.; Wess, J.; Kostenis, E. Lack of beta-arrestin signaling in the absence of active G proteins. *Nat. Commun.* **2018**, *9*, 341.

(66) Gutkind, J. S.; Kostenis, E. Arrestins as rheostats of GPCR signalling. *Nat. Rev. Mol. Cell Biol.* **2018**, *19*, 615–616.

(67) Eichel, K.; Jullié, D.; Barsi-Rhyne, B.; Latorraca, N. R.; Masureel, M.; Sibarita, J.-B.; Dror, R. O.; Zastrow, M. von. Catalytic activation of β-arrestin by GPCRs. *Nature* **2018**, *557*, 381–386.

(68) Jean-Charles, P.-Y.; Kaur, S.; Shenoy, S. K. G protein-coupled receptor signaling through β-arrestin-dependent mechanisms. *J. Cardiovasc. Pharmacol.* **2017**, *70*, 142–158.

(69) Oligny-Longpré, G.; Corbani, M.; Zhou, J.; Hogue, M.; Guillon, G.; Bouvier, M. Engagement of β-arrestin by transactivated insulin-like growth factor receptor is needed for V2 vasopressin receptor-stimulated ERK1/2 activation. *Proc. Natl. Acad. Sci. U. S. A.* **2012**, *109*, E1028–E1037.

(70) Pandey, S.; Kumari, P.; Baidya, M.; Kise, R.; Cao, Y.; Dwivedi-Agnihotri, H.; Banerjee, R.; Li, X. X.; Cui, C. S.; Lee, J. D.; Kawakami, K.; Maharana, J.; Ranjan, A.; Chaturvedi, M.;

Jhingan, G. D.; Laporte, S. A.; Woodruff, T. M.; Inoue, A.; Shukla, A. K. Intrinsic bias at non-canonical, β-arrestin-coupled seven transmembrane receptors. *Mol. Cell* **2021**, *81*, 4605–4621.

(71) Avet, C.; Mancini, A.; Breton, B.; Le Gouill, C.; Hauser, A. S.; Normand, C.; Kobayashi, H.; Gross, F.; Hogue, M.; Lukasheva, V.; St-Onge, S.; Carrier, M.; Héroux, M.; Morissette, S.; Fauman, E. B.; Fortin, J.-P.; Schann, S.; Leroy, X.; Gloriam, D. E.; Bouvier, M. Effector membrane translocation biosensors reveal G protein and βarrestin coupling profiles of 100 therapeutically relevant GPCRs. *Elife* **2022**, *11*, e74101.

(72) Inoue, A.; Raimondi, F.; Kadji, F. M. N.; Singh, G.; Kishi, T.; Uwamizu, A.; Ono, Y.; Shinjo, Y.; Ishida, S.; Arang, N.; Kawakami, K.; Gutkind, J. S.; Aoki, J.; Russell, R. B. Illuminating G-protein-coupling selectivity of GPCRs. *Cell* **2019**, *177*, 1933–1947.

(73) Voss, J. H.; Mahardhika, A. B.; Inoue, A.; Müller, C. E. Agonist-dependent coupling of the promiscuous adenosine A2B receptor to Gα protein subunits. *ACS Pharmacol. Transl. Sci.* **2022**, *5*, 373–386.

(74) Smith, J. S.; Lefkowitz, R. J.; Rajagopal, S. Biased signalling: from simple switches to allosteric microprocessors. *Nat. Rev. Drug Discov.* **2018**, *17*, 243–260.

(75) Manglik, A.; Lin, H.; Aryal, D. K.; McCorvy, J. D.; Dengler, D.; Corder, G.; Levit, A.; Kling, R. C.; Bernat, V.; Hübner, H.; Huang, X.-P.; Sassano, M. F.; Giguère, P. M.; Löber, S.; Da Duan; Scherrer, G.; Kobilka, B. K.; Gmeiner, P.; Roth, B. L.; Shoichet, B. K. Structure-based discovery of opioid analgesics with reduced side effects. *Nature* **2016**, *537*, 185–190.

(76) Alavi, M. S.; Shamsizadeh, A.; Azhdari-Zarmehri, H.; Roohbakhsh, A. Orphan G protein-coupled receptors: The role in CNS disorders. *Biomed. Pharmacother.* **2018**, *98*, 222–232.

(77) Khan, M. Z.; He, L. Neuro-psychopharmacological perspective of Orphan receptors of Rhodopsin (class A) family of G protein-coupled receptors. *Psychopharmacology* **2017**, *234*, 1181–1207.

(78) Davenport, A. P.; Alexander, S. P. H.; Sharman, J. L.; Pawson, A. J.; Benson, H. E.; Monaghan, A. E.; Liew, W. C.; Mpamhanga, C. P.; Bonner, T. I.; Neubig, R. R.; Pin, J. P.; Spedding, M.; Harmar, A. J. International Union of Basic and Clinical Pharmacology. LXXXVIII. G protein-coupled receptor list: recommendations for new pairings with cognate ligands. *Pharmacol. Rev.* **2013**, *65*, 967–986.

(79) Laschet, C.; Dupuis, N.; Hanson, J. The G protein-coupled receptors deorphanization landscape. *Biochem. Pharmacol.* **2018**, *153*, 62–74.

(80) Seal, R. L.; Braschi, B.; Gray, K.; Jones, T. E. M.; Tweedie, S.; Haim-Vilmovsky, L.; Bruford, E. A. Genenames.org: the HGNC resources in 2023. *Nucleic Acids Res.* **2023**, *51*, D1003–D1009.

(81) Bernhardi, J. E. von; Dimou, L. Oligodendrogenesis is a key process for cognitive performance improvement induced by voluntary physical activity. *Glia* **2022**, *70*, 1052–1067.

(82) Rivera, A. D.; Chacon-De-La-Rocha, I.; Pieropan, F.; Papanikolau, M.; Azim, K.; Butt, A. M. Keeping the ageing brain wired: a role for purine signalling in regulating cellular metabolism in oligodendrocyte progenitors. *Pflugers Arch.* **2021**, *473*, 775–783.

(83) Fang, M.; Chen, L.; Tang, T.; Qiu, M.; Xu, X. The committed oligodendrocyte precursor cell, a newly-defined intermediate progenitor cell type in oligodendroglial lineage. *Glia* **2023**, *71*, 2499–2510.

(84) Wang, J.; He, X.; Meng, H.; Li, Y.; Dmitriev, P.; Tian, F.; Page, J. C.; Lu, Q. R.; He, Z. Robust myelination of regenerated axons induced by combined manipulations of GPR17 and microglia. *Neuron* **2020**, *108*, 876–886.

(85) Lecca, D.; Trincavelli, M. L.; Gelosa, P.; Sironi, L.; Ciana, P.; Fumagalli, M.; Villa, G.; Verderio, C.; Grumelli, C.; Guerrini, U.; Tremoli, E.; Rosa, P.; Cuboni, S.; Martini, C.; Buffo, A.; Cimino, M.; Abbracchio, M. P. The recently identified P2Y-like receptor GPR17 is a sensor of brain damage and a new target for brain repair. *PLoS One* **2008**, *3*, e3579.

(86) Braune, M.; Scherf, N.; Heine, C.; Sygnecka, K.; Pillaiyar, T.; Parravicini, C.; Heimrich, B.; Abbracchio, M. P.; Müller, C. E.; Franke, H. Involvement of GPR17 in neuronal fibre outgrowth. *Int. J. Mol. Sci.* **2021**, *22*, 11683.

(87) Lu, C.; Dong, L.; Zhou, H.; Li, Q.; Huang, G.; Bai, S. J.; Liao, L. G-protein-coupled receptor Gpr17 regulates oligodendrocyte differentiation in response to lysolecithin-induced demyelination. *Sci. Rep.* **2018**, *8*, 4502.

(88) Angelini, J.; Marangon, D.; Raffaele, S.; Lecca, D.; Abbracchio, M. P. The distribution of GPR17-expressing cells correlates with white matter inflammation status in brain tissues of multiple sclerosis patients. *Int. J. Mol. Sci.* **2021**, *22*, 4574.

(89) Lewash, M.; Kostenis, E.; Müller, C. E. GPR17 - orphan G protein-coupled receptor with therapeutic potential. *Trends Pharmacol. Sci.* **2025**, *46*, 610–628.

(90) Trist, B. G.; Hare, D. J.; Double, K. L. Oxidative stress in the aging substantia nigra and the etiology of Parkinson's disease. *Aging Cell* **2019**, *18*, e13031.

(91) Rao, Y. L.; Ganaraja, B.; Murlimanju, B. V.; Joy, T.; Krishnamurthy, A.; Agrawal, A. Hippocampus and its involvement in Alzheimer's disease: a review. *3 Biotech* **2022**, *12*, 55.

(92) Durães, F.; Pinto, M.; Sousa, E. Old drugs as new treatments for neurodegenerative diseases. *Pharmaceuticals (Basel)* **2018**, *11*, 44.

(93) Nagatsua, T.; Sawadab, M. L-dopa therapy for Parkinson's disease: past, present, and future. *Parkinsonism Relat. Disord.* **2009**, *15*, S3–S8.

(94) Lassmann, H.; van Horssen, J.; Mahad, D. Progressive multiple sclerosis: pathology and pathogenesis. *Nat. Rev. Neurol.* **2012**, *8*, 647–656.

(95) Ghasemi, N.; Razavi, S.; Nikzad, E. Multiple sclerosis: Pathogenesis, symptoms, diagnoses and cell-based therapy. *Cell J.* **2017**, *19*, 1–10.

(96) Dobson, R.; Giovannoni, G. Multiple sclerosis – a review. *Eur. J. Neurol.* **2019**, *26*, 27–40.

(97) Goodin, D. S.; Khankhanian, P.; Gourraud, P.-A.; Vince, N. The nature of genetic and environmental susceptibility to multiple sclerosis. *PLoS One* **2021**, *16*, e0246157.

(98) an Goris; Vandebergh, M.; McCauley, J. L.; Saarela, J.; Cotsapas, C. Genetics of multiple sclerosis: lessons from polygenicity. *Lancet Neurol.* **2022**, *21*, 830–842.

(99) Jacobs, B. M.; Noyce, A. J.; Bestwick, J.; Belete, D.; Giovannoni, G.; Dobson, R. Gene-Environment Interactions in Multiple Sclerosis: A UK Biobank Study. *Neurol. Neuroimmunol. Neuroinflamm.* **2021**, *8*, e1007.

(100) Barrie, W.; Yang, Y.; Irving-Pease, E. K.; Attfield, K. E.; Scorrano, G.; Jensen, L. T.; Armen, A. P.; Dimopoulos, E. A.; Stern, A.; Refoyo-Martinez, A.; Pearson, A.; Ramsøe, A.; Gaunitz, C.; Demeter, F.; Jørkov, M. L. S.; Møller, S. B.; Springborg, B.; Klassen, L.; Hyldgård, I. M.; Wickmann, N.; Vinner, L.; Korneliussen, T. S.; Allentoft, M. E.; Sikora, M.; Kristiansen, K.; Rodriguez, S.; Nielsen, R.; Iversen, A. K. N.; Lawson, D. J.; Fugger, L.; Willerslev, E. Elevated genetic risk for multiple sclerosis emerged in steppe pastoralist populations. *Nature* **2024**, *625*, 321–328.

(101) Bjornevik, K.; Münz, C.; Cohen, J. I.; Ascherio, A. Epstein-Barr virus as a leading cause of multiple sclerosis: mechanisms and implications. *Nat. Rev. Neurol.* **2023**, *19*, 160–171.

(102) Jasse, L.; Vukusic, S.; Durand-Dubief, F.; Vartin, C.; Piras, C.; Bernard, M.; Pélisson, D.; Confavreux, C.; Vighetto, A.; Tilikete, C. Persistent visual impairment in multiple sclerosis: prevalence, mechanisms and resulting disability. *Mult. Scler.* **2013**, *19*, 1618–1626.

(103) Iodice, R.; Aceto, G.; Ruggiero, L.; Cassano, E.; Manganelli, F.; Dubbioso, R. A review of current rehabilitation practices and their benefits in patients with multiple sclerosis. *Mult. Scler. Relat. Disord.* **2023**, *69*, 104460.

(104) Yang, J. H.; Rempe, T.; Whitmire, N.; Dunn-Pirio, A.; Graves, J. S. Therapeutic advances in multiple sclerosis. *Front. Neurol.* **2022**, *13*, 824926.

(105) Lakin, L.; Davis, B. E.; Binns, C. C.; Currie, K. M.; Rensel, M. R. Comprehensive approach to management of multiple sclerosis: addressing invisible symptoms-a narrative review. *Neurol. Ther.* **2021**, *10*, 75–98.

(106) Coerver, E. M. E.; Fung, W. H.; Beukelaar, J. de; Bouvy, W. H.; Canta, L. R.; Gerlach, O. H. H.; Hoitsma, E.; Hoogervorst, E. L. J.; Jong, B. A. de; Kalkers, N. F.; van Kempen, Z. L. E.; Lövenich, H.; van Munster, C. E. P.; van Oosten, B. W.; Smolders, J.; Vennegoor, A.; Zeinstra, E. M. P. E.; Barrantes-Cepas, M.; Kooij, G.; Schoonheim, M. M.; Lissenberg-Witte, B. I.; Teunissen, C. E.; Moraal, B.; Barkhof, F.; Uitdehaag, B. M. J.; Mostert, J.; Killestein, J.; Strijbis, E. M. M. Discontinuation of first-line disease-modifying therapy in patients with stable multiple sclerosis: the DOT-MS randomized clinical trial. *JAMA Neurol.* **2025**, *82*, 123–131.

(107) Chen, Y.; Wu, H.; Wang, S.; Koito, H.; Li, J.; Ye, F.; Hoang, J.; Escobar, S. S.; Gow, A.; Arnett, H. A.; Trapp, B. D.; Karandikar, N. J.; Hsieh, J.; Lu, Q. R. The oligodendrocyte-specific G protein-coupled receptor GPR17 is a cell-intrinsic timer of myelination. *Nat. Neurosci.* **2009**, *12*, 1398–1406.

(108) Simon, K.; Hennen, S.; Merten, N.; Blättermann, S.; Gillard, M.; Kostenis, E.; Gomeza, J. The orphan G protein-coupled receptor GPR17 negatively regulates oligodendrocyte differentiation via Gαi/o and its downstream effector molecules. *J. Biol. Chem.* **2016**, *291*, 705–718.

(109) Hennen, S.; Wang, H.; Peters, L.; Merten, N.; Simon, K.; Spinrath, A.; Blättermann, S.; Akkari, R.; Schrage, R.; Schröder, R.; Schulz, D.; Vermeiren, C.; Zimmermann, K.; Kehraus, S.; Drewke, C.; Pfeifer, A.; König, G. M.; Mohr, K.; Gillard, M.; Müller, C. E.; Lu, Q. R.; Gomeza, J.; Kostenis, E. Decoding signaling and function of the orphan G protein-coupled receptor GPR17 with a small-molecule agonist. *Sci. Signal.* **2013**, *6*, ra93.

(110) Knopman, D. S.; Amieva, H.; Petersen, R. C.; Chételat, G.; Holtzman, D. M.; Hyman, B. T.; Nixon, R. A.; Jones, D. T. Alzheimer disease. *Nat. Rev. Dis. Primers* **2021**, *7*, 33.

(111) Patil, P.; Thakur, A.; Sharma, A.; Flora, S. J. S. Natural products and their derivatives as multifunctional ligands against Alzheimer's disease. *Drug Dev. Res.* **2020**, *81*, 165–183.

(112) Chen, Z.-R.; Huang, J.-B.; Yang, S.-L.; Hong, F.-F. Role of cholinergic signaling in alzheimer's disease. *Molecules* **2022**, *27*, 1816.

(113) Dafre, R.; Wasnik, P. Current diagnostic and treatment methods of alzheimer's disease: a narrative review. *Cureus* **2023**, *15*, e45649.

(114) Wu, L.; Rosa-Neto, P.; Hsiung, G.-Y. R.; Sadovnick, A. D.; Masellis, M.; Black, S. E.; Jia, J.; Gauthier, S. Early-onset familial Alzheimer's disease (EOFAD). *Can. J. Neurol. Sci.* **2012**, *39*, 436–445.

(115) Andrade-Guerrero, J.; Santiago-Balmaseda, A.; Jeronimo-Aguilar, P.; Vargas-Rodríguez, I.; Cadena-Suárez, A. R.; Sánchez-Garibay, C.; Pozo-Molina, G.; Méndez-Catalá, C. F.; Cardenas-Aguayo, M.-D.-C.; Diaz-Cintra, S.; Pacheco-Herrero, M.; Luna-Muñoz, J.; Soto-Rojas, L. O. Alzheimer's Disease: An Updated Overview of Its Genetics. *Int. J. Mol. Sci.* **2023**, *24*.

(116) Zhang, X.-X.; Tian, Y.; Wang, Z.-T.; Ma, Y.-H.; Tan, L.; Yu, J.-T. The Epidemiology of Alzheimer's Disease Modifiable Risk Factors and Prevention. *J. Prev. Alzheimers. Dis.* **2021**, *8*, 313–321.

(117) Marschallinger, J.; Schäffner, I.; Klein, B.; Gelfert, R.; Rivera, F. J.; Illes, S.; Grassner, L.; Janssen, M.; Rotheneichner, P.; Schmuckermair, C.; Coras, R.; Boccazzi, M.; Chishty, M.; Lagler, F. B.; Renic, M.; Bauer, H.-C.; Singewald, N.; Blümcke, I.; Bogdahn, U.; Couillard-Despres, S.; Lie, D. C.; Abbracchio, M. P.; Aigner, L. Structural and functional rejuvenation of the aged brain by an approved anti-asthmatic drug. *Nat. Commun.* **2015**, *6*, 8466.

(118) Jin, S.; Wang, X.; Xiang, X.; Wu, Y.; Hu, J.; Li, Y.; Lin Dong, Y.; Tan, Y.; Wu, X. Inhibition of GPR17 with cangrelor improves cognitive impairment and synaptic deficits induced by Aβ1-42 through Nrf2/HO-1 and NF-κB signaling pathway in mice. *Int. Immunopharmacol.* **2021**, *101*, 108335.

(119) Ruze, R.; Liu, T.; Zou, X.; Song, J.; Chen, Y.; Xu, R.; Yin, X.; Xu, Q. Obesity and type 2 diabetes mellitus: connections in epidemiology, pathogenesis, and treatments. *Front. Endocrinol. (Lausanne)* **2023**, *14*, 1161521.

(120) DeForest, N.; Majithia, A. R. Genetics of Type 2 Diabetes: Implications from Large-Scale Studies. *Curr. Diab. Rep.* **2022**, *22*, 227–235.

(121) Del Bosque-Plata, L.; Martínez-Martínez, E.; Espinoza-Camacho, M. Á.; Gragnoli, C. The Role of TCF7L2 in Type 2 Diabetes. *Diabetes* **2021**, *70*, 1220–1228.

(122) Shi, Q.; Wang, Y.; Hao, Q.; Vandvik, P. O.; Guyatt, G.; Li, J.; Chen, Z.; Xu, S.; Shen, Y.; Ge, L.; Sun, F.; Li, L.; Yu, J.; Nong, K.; Zou, X.; Zhu, S.; Wang, C.; Zhang, S.; Qiao, Z.; Jian, Z.; Li, Y.; Zhang, X.; Chen, K.; Qu, F.; Wu, Y.; He, Y.; Tian, H.; Li, S. Pharmacotherapy for adults with overweight and obesity: a systematic review and network meta-analysis of randomised controlled trials. *Lancet* **2024**, *403*, e21–e31.

(123) Brown, E.; Heerspink, H. J. L.; Cuthbertson, D. J.; Wilding, J. P. H. SGLT2 inhibitors and GLP-1 receptor agonists: established and emerging indications. *Lancet* **2021**, *398*, 262–276.

(124) Yan, S.; Conley, J. M.; Reilly, A. M.; Stull, N. D.; Abhyankar, S. D.; Ericsson, A. C.; Kono, T.; Molosh, A. I.; Kubal, C. A.; Evans-Molina, C.; Ren, H. Intestinal Gpr17 deficiency improves glucose metabolism by promoting GLP-1 secretion. *Cell Rep.* **2022**, *38*, 110179.

(125) Grochans, S.; Cybulska, A. M.; Simińska, D.; Korbecki, J.; Kojder, K.; Chlubek, D.; Baranowska-Bosiacka, I. Epidemiology of glioblastoma multiforme-literature review. *Cancers (Basel)* **2022**, *14*, 2412.

(126) Pellerino, A.; Caccese, M.; Padovan, M.; Cerretti, G.; Lombardi, G. Epidemiology, risk factors, and prognostic factors of gliomas. *Clin. Transl. Imaging* **2022**, *10*, 467–475.

(127) McKinnon, C.; Nandhabalan, M.; Murray, S. A.; Plaha, P. Glioblastoma: clinical presentation, diagnosis, and management. *BMJ* **2021**, *374*, n1560.

(128) Mutharasu, G.; Murugesan, A.; Konda Mani, S.; Yli-Harja, O.; Kandhavelu, M. Transcriptomic analysis of glioblastoma multiforme providing new insights into GPR17 signaling communication. *J. Biomol. Struct. Dyn.* **2022**, *40*, 2586–2599.

(129) Liu, H.; Xing, R.; Ou, Z.; Zhao, J.; Hong, G.; Zhao, T.-J.; Han, Y.; Chen, Y. G-protein-coupled receptor GPR17 inhibits glioma development by increasing polycomb repressive complex 1-mediated ROS production. *Cell Death Dis.* **2021**, *12*, 610.

(130) Kari, S.; Kandhavelu, J.; Murugesan, A.; Thiyagarajan, R.; Kidambi, S.; Kandhavelu, M. Mitochondrial complex III bypass complex I to induce ROS in GPR17 signaling activation in GBM. *Biomed. Pharmacother.* **2023**, *162*, 114678.

(131) Feske, S. K. Ischemic stroke. *Am. J. Med.* **2021**, *134*, 1457–1464.

(132) Feigin, V. L.; Stark, B. A.; Johnson, C. O.; Roth, G. A.; Bisignano, C.; Abady, G. G.; Abbasifard, M.; Abbasi-Kangevari, M.; Abd-Allah, F.; Abedi, V.; Abualhasan, A.; Abu-Rmeileh, N. M. E.; Abushouk, A. I.; Adebayo, O. M.; Agarwal, G.; Agasthi, P.; Ahinkorah, B. O.; Ahmad, S.; Ahmadi, S.; Ahmed Salih, Y.; Aji, B.; Akbarpour, S.; Akinyemi, R. O.; Al

Hamad, H.; Alahdab, F.; Alif, S. M.; Alipour, V.; Aljunid, S. M.; Almustanyir, S.; Al-Raddadi, R. M.; Al-Shahi Salman, R.; Alvis-Guzman, N.; Ancuceanu, R.; Anderlini, D.; Anderson, J. A.; Ansar, A.; Antonazzo, I. C.; Arabloo, J.; Ärnlöv, J.; Artanti, K. D.; Aryan, Z.; Asgari, S.; Ashraf, T.; Athar, M.; Atreya, A.; Ausloos, M.; Baig, A. A.; Baltatu, O. C.; Banach, M.; Barboza, M. A.; Barker-Collo, S. L.; Bärnighausen, T. W.; Barone, M. T. U.; Basu, S.; Bazmandegan, G.; Beghi, E.; Beheshti, M.; Béjot, Y.; Bell, A. W.; Bennett, D. A.; Bensenor, I. M.; Bezabhe, W. M.; Bezabih, Y. M.; Bhagavathula, A. S.; Bhardwaj, P.; Bhattacharyya, K.; Bijani, A.; Bikbov, B.; Birhanu, M. M.; Boloor, A.; Bonny, A.; Brauer, M.; Brenner, H.; Bryazka, D.; Butt, Z. A.; Caetano dos Santos, Florentino Luciano; Campos-Nonato, I. R.; Cantu-Brito, C.; Carrero, J. J.; Castañeda-Orjuela, C. A.; Catapano, A. L.; Chakraborty, P. A.; Charan, J.; Choudhari, S. G.; Chowdhury, E. K.; Chu, D.-T.; Chung, S.-C.; Colozza, D.; Costa, V. M.; Costanzo, S.; Criqui, M. H.; Dadras, O.; Dagnew, B.; Dai, X.; Dalal, K.; Damasceno, A. A. M.; D'Amico, E.; Dandona, L.; Dandona, R.; Darega Gela, J.; Davletov, K.; La Cruz-Góngora, V. de; Desai, R.; Dhamnetiya, D.; Dharmaratne, S. D.; Dhimal, M. L.; Dhimal, M.; Diaz, D.; Dichgans, M.; Dokova, K.; Doshi, R.; Douiri, A.; Duncan, B. B.; Eftekharzadeh, S.; Ekholuenetale, M.; El Nahas, N.; Elgendy, I. Y.; Elhadi, M.; El-Jaafary, S. I.; Endres, M.; Endries, A. Y.; Erku, D. A.; Faraon, E. J. A.; Farooque, U.; Farzadfar, F.; Feroze, A. H.; Filip, I.; Fischer, F.; Flood, D.; Gad, M. M.; Gaidhane, S.; Ghanei Gheshlagh, R.; Ghashghaee, A.; Ghith, N.; Ghozali, G.; Ghozy, S.; Gialluisi, A.; Giampaoli, S.; Gilani, S. A.; Gill, P. S.; Gnedovskaya, E. V.; Golechha, M.; Goulart, A. C.; Guo, Y.; Gupta, R.; Gupta, V. B.; Gupta, V. K.; Gyanwali, P.; Hafezi-Nejad, N.; Hamidi, S.; Hanif, A.; Hankey, G. J.; Hargono, A.; Hashi, A.; Hassan, T. S.; Hassen, H. Y.; Havmoeller, R. J.; Hay, S. I.; Hayat, K.; Hegazy, M. I.; Herteliu, C.; Holla, R.; Hostiuc, S.; Househ, M.; Huang, J.; Humayun, A.; Hwang, B.-F.; Iacoviello, L.; Iavicoli, I.; Ibitoye, S. E.; Ilesanmi, O. S.; Ilic, I. M.; Ilic, M. D.; Iqbal, U.; Irvani, S. S. N.; Islam, S. M. S.; Ismail, N. E.; Iso, H.; Isola, G.; Iwagami, M.; Jacob, L.; Jain, V.; Jang, S.-I.; Jayapal, S. K.; Jayaram, S.; Jayawardena, R.; Jeemon, P.; Jha, R. P.; Johnson, W. D.; Jonas, J. B.; Joseph, N.; Jozwiak, J. J.; Jürisson, M.; Kalani, R.; Kalhor, R.; Kalkonde, Y.; Kamath, A.; Kamiab, Z.; Kanchan, T.; Kandel, H.; Karch, A.; Katoto, P. D.; Kayode, G. A.; Keshavarz, P.; Khader, Y. S.; Khan, E. A.; Khan, I. A.; Khan, M.; Khan, Moien AB; Khatib, M. N.; Khubchandani, J.; Kim, G. R.; Kim, M. S.; Kim, Y. J.; Kisa, A.; Kisa, S.; Kivimäki, M.; Kolte, D.; Koolivand, A.; Koulmane Laxminarayana, S. L.; Koyanagi, A.; Krishan, K.; Krishnamoorthy, V.; Krishnamurthi, R. V.; Kumar, G. A.; Kusuma, D.; La Vecchia, C.; Lacey, B.; Lak, H. M.; Lallukka, T.; Lasrado, S.; Lavados, P. M.; Leonardi, M.; Li, B.; Li, S.; Lin, H.; Lin, R.-T.; Liu, X.; Lo, W. D.; Lorkowski, S.; Lucchetti, G.; Lutzky Saute, R.; Magdy Abd El

Razek, Hassan; Magnani, F. G.; Mahajan, P. B.; Majeed, A.; Makki, A.; Malekzadeh, R.; Malik, A. A.; Manafi, N.; Mansournia, M. A.; Mantovani, L. G.; Martini, S.; Mazzaglia, G.; Mehndiratta, M. M.; Menezes, R. G.; Meretoja, A.; Mersha, A. G.; Miao Jonasson, J.; Miazgowski, B.; Miazgowski, T.; Michalek, I. M.; Mirrakhimov, E. M.; Mohammad, Y.; Mohammadian-Hafshejani, A.; Mohammed, S.; Mokdad, A. H.; Mokhayeri, Y.; Molokhia, M.; Moni, M. A.; Montasir, A. A.; Moradzadeh, R.; Morawska, L.; Morze, J.; Muruet, W.; Musa, K. I.; Nagarajan, A. J.; Naghavi, M.; Narasimha Swamy, S.; Nascimento, B. R.; Negoi, R. I.; Neupane Kandel, S.; Nguyen, T. H.; Norrving, B.; Noubiap, J. J.; Nwatah, V. E.; Oancea, B.; Odukoya, O. O.; Olagunju, A. T.; Orru, H.; Owolabi, M. O.; Padubidri, J. R.; Pana, A.; Parekh, T.; Park, E.-C.; Pashazadeh Kan, F.; Pathak, M.; Peres, M. F. P.; Perianayagam, A.; Pham, T.-M.; Piradov, M. A.; Podder, V.; Polinder, S.; Postma, M. J.; Pourshams, A.; Radfar, A.; Rafiei, A.; Raggi, A.; Rahim, F.; Rahimi-Movaghar, V.; Rahman, M.; Rahman, M. A.; Rahmani, A. M.; Rajai, N.; Ranasinghe, P.; Rao, C. R.; Rao, S. J.; Rathi, P.; Rawaf, D. L.; Rawaf, S.; Reitsma, M. B.; Renjith, V.; Renzaho, A. M. N.; Rezapour, A.; Rodriguez, J. A. B.; Roever, L.; Romoli, M.; Rynkiewicz, A.; Sacco, S.; Sadeghi, M.; Saeedi Moghaddam, S.; Sahebkar, A.; Saif-Ur-Rahman, K. M.; Salah, R.; Samaei, M.; Samy, A. M.; Santos, I. S.; Santric-Milicevic, M. M.; Sarrafzadegan, N.; Sathian, B.; Sattin, D.; Schiavolin, S.; Schlaich, M. P.; Schmidt, M. I.; Schutte, A. E.; Sepanlou, S. G.; Seylani, A.; Sha, F.; Shahabi, S.; Shaikh, M. A.; Shannawaz, M.; Shawon, M. S. R.; Sheikh, A.; Sheikhbahaei, S.; Shibuya, K.; Siabani, S.; Silva, D. A. S.; Singh, J. A.; Singh, J. K.; Skryabin, V. Y.; Skryabina, A. A.; Sobaih, B. H.; Stortecky, S.; Stranges, S.; Tadesse, E. G.; Tarigan, I. U.; Temsah, M.-H.; Teuschl, Y.; Thrift, A. G.; Tonelli, M.; Tovani-Palone, M. R.; Tran, B. X.; Tripathi, M.; Tsegaye, G. W.; Ullah, A.; Unim, B.; Unnikrishnan, B.; Vakilian, A.; Valadan Tahbaz, S.; Vasankari, T. J.; Venketasubramanian, N.; Vervoort, D.; Vo, B.; Volovici, V.; Vosoughi, K.; Vu, G. T.; Vu, L. G.; Wafa, H. A.; Waheed, Y.; Wang, Y.; Wijeratne, T.; Winkler, A. S.; Wolfe, C. D. A.; Woodward, M.; Wu, J. H.; Wulf Hanson, S.; Xu, X.; Yadav, L.; Yadollahpour, A.; Yahyazadeh Jabbari, S. H.; Yamagishi, K.; Yatsuya, H.; Yonemoto, N.; Yu, C.; Yunusa, I.; Zaman, M. S.; Zaman, S. B.; Zamanian, M.; Zand, R.; Zandifar, A.; Zastrozhin, M. S.; Zastrozhina, A.; Zhang, Y.; Zhang, Z.-J.; Zhong, C.; Zuniga, Y. M. H.; Murray, C. J. L. Global, regional, and national burden of stroke and its risk factors, 1990–2019: a systematic analysis for the Global Burden of Disease Study 2019. *Lancet Neurol.* **2021**, *20*, 795–820.

(133) Ceruti, S.; Villa, G.; Genovese, T.; Mazzon, E.; Longhi, R.; Rosa, P.; Bramanti, P.; Cuzzocrea, S.; Abbracchio, M. P. The P2Y-like receptor GPR17 as a sensor of damage and a new potential target in spinal cord injury. *Brain* **2009**, *132*, 2206–2218.

(134) Baqi, Y.; Pillaiyar, T.; Abdelrahman, A.; Kaufmann, O.; Alshaibani, S.; Rafehi, M.; Ghasimi, S.; Akkari, R.; Ritter, K.; Simon, K.; Spinrath, A.; Kostenis, E.; Zhao, Q.; Köse, M.; Namasivayam, V.; Müller, C. E. 3-(2-Carboxyethyl)indole-2-carboxylic acid derivatives: structural requirements and properties of potent agonists of the orphan G protein-coupled receptor GPR17. *J. Med. Chem.* **2018**, *61*, 8136–8154.

(135) Boshta, N. M.; Lewash, M.; Köse, M.; Namasivayam, V.; Sarkar, S.; Voss, J. H.; Liedtke, A. J.; Junker, A.; Tian, M.; Stößel, A.; Rashed, M.; Mahal, A.; Merten, N.; Pegurier, C.; Hockemeyer, J.; Kostenis, E.; Müller, C. E. Discovery of anthranilic acid derivatives as antagonists of the pro-inflammatory orphan G protein-coupled receptor GPR17. *J. Med. Chem.* **2024**, *67*, 19365–19394.

(136) Mueller, C. E.; Pegurier, C.; Deligny, M. L. R.; El-Tayeb, A.; Hockemeyer, J.; Ledecq, M.; Mercier, J.; Provins, L.; Boshta, N. M.; Bhattarai, S.; Namasivayam, V.; Funke, M.; Schwach, L.; Gollos, S.; Laufenberg, D. von; Barré, A. Aza(indole)-, benzothiophene-, and benzofuran-3-sulfonamides. WO 2018/122232 A1, 2022.

(137) Marucci, G.; Dal Ben, D.; Lambertucci, C.; Santinelli, C.; Spinaci, A.; Thomas, A.; Volpini, R.; Buccioni, M. The G protein-coupled receptor GPR17: overview and update. *ChemMedChem* **2016**, *11*, 2567–2574.

(138) Dziedzic, A.; Miller, E.; Saluk-Bijak, J.; Bijak, M. The GPR17 receptor—a promising goal for therapy and a potential marker of the neurodegenerative process in multiple sclerosis. *Int. J. Mol. Sci.* **2020**, *21*, 1852.

(139) Konda Mani, S.; Thiyagarajan, R.; Yli-Harja, O.; Kandhavelu, M.; Murugesan, A. Structural analysis of human G-protein-coupled receptor 17 ligand binding sites. *J. Cell. Biochem.* **2023**, *124*, 533–544.

(140) Ciana, P.; Fumagalli, M.; Trincavelli, M. L.; Verderio, C.; Rosa, P.; Lecca, D.; Ferrario, S.; Parravicini, C.; Capra, V.; Gelosa, P.; Guerrini, U.; Belcredito, S.; Cimino, M.; Sironi, L.; Tremoli, E.; Rovati, G. E.; Martini, C.; Abbracchio, M. P. The orphan receptor GPR17 identified as a new dual uracil nucleotides/cysteinyl-leukotrienes receptor. *EMBO J.* **2006**, *25*, 4615–4627.

(141) Benned-Jensen, T.; Rosenkilde, M. M. Distinct expression and ligand-binding profiles of two constitutively active GPR17 splice variants. *Br. J. Pharmacol.* **2010**, *159*, 1092–1105.

(142) Ou, Z.; Sun, Y.; Lin, L.; You, N.; Liu, X.; Li, H.; Ma, Y.; Cao, L.; Han, Y.; Liu, M.; Deng, Y.; Yao, L.; Lu, Q. R.; Chen, Y. Olig2-targeted G-protein-coupled receptor Gpr17 regulates oligodendrocyte survival in response to lysolecithin-induced demyelination. *J. Neurosci.* **2016**, *36*, 10560–10573.

(143) Liston, P.; Fong, W. G.; Kelly, N. L.; Toji, S.; Miyazaki, T.; Conte, D.; Tamai, K.; Craig, C. G.; McBurney, M. W.; Korneluk, R. G. Identification of XAF1 as an antagonist of XIAP anti-Caspase activity. *Nat. Cell Biol.* **2001**, *3*, 128–133.

(144) Gonsalvez, D.; Ferner, A. H.; Peckham, H.; Murray, S. S.; Xiao, J. The roles of extracellular related-kinases 1 and 2 signaling in CNS myelination. *Neuropharmacology* **2016**, *110*, 586–593.

(145) Maekawa, A.; Balestrieri, B.; Austen, K. F.; Kanaoka, Y. GPR17 is a negative regulator of the cysteinyl leukotriene 1 receptor response to leukotriene D4. *Proc. Natl. Acad. Sci. U. S. A.* **2009**, *106*, 11685–11690.

(146) Qi, A.-D.; Harden, T. K.; Nicholas, R. A. Is GPR17 a P2Y/leukotriene receptor? Examination of uracil nucleotides, nucleotide sugars, and cysteinyl leukotrienes as agonists of GPR17. *J. Pharmacol. Exp. Ther.* **2013**, *347*, 38–46.

(147) Nørregaard, K.; Benned-Jensen, T.; Rosenkilde, M. M. EBI2, GPR18 and GPR17--three structurally related, but biologically distinct 7TM receptors. *Curr. Top. Med. Chem.* **2011**, *11*, 618–628.

(148) Köse, M.; Ritter, K.; Thiemke, K.; Gillard, M.; Kostenis, E.; Müller, C. E. Development of (3)H2-Carboxy-4,6-dichloro-1H-indole-3-propionic acid ((3)HPSB-12150): a useful tool for studying GPR17. *ACS Med. Chem. Lett.* **2014**, *5*, 326–330.

(149) Simon, K.; Merten, N.; Schröder, R.; Hennen, S.; Preis, P.; Schmitt, N.-K.; Peters, L.; Schrage, R.; Vermeiren, C.; Gillard, M.; Mohr, K.; Gomeza, J.; Kostenis, E. The orphan receptor GPR17 is unresponsive to uracil nucleotides and cysteinyl leukotrienes. *Mol. Pharmacol.* **2017**, *91*, 518–532.

(150) Zhu, H.; Conley, J. M.; Karavadhi, S.; LaVigne, J. E.; Watts, V. J.; Sun, H.; Shen, M.; Hall, M. D.; Ren, H.; Patnaik, S. Discovery of novel and selective GPR17 antagonists as pharmacological tools for developing new therapeutic strategies in diabetes and obesity. *Eur. J. Med. Chem.* **2025**, *295*, 117794.

(151) Harrington, A. W.; Liu, C.; Phillips, N.; Nepomuceno, D.; Kuei, C.; Chang, J.; Chen, W.; Sutton, S. W.; O'Malley, D.; Pham, L.; Yao, X.; Sun, S.; Bonaventure, P. Identification and characterization of select oxysterols as ligands for GPR17. *Br. J. Pharmacol.* **2023**, *180*, 401–421.

(152) Pegurier, C.; Provins, L.; Cardenas, A.; Ledecq, M.; Mueller, C. E.; Hockemeyer, J.; El, T. A.; Boshta, N.; Rashed, M. Pyridinyl and pyrazinyl-(aza)indolsulfonamides. WO 2019/243303 A1, 2019.

(153) Pegurier, C.; Provins, L.; Isin, E. M.; Ledecq, M. Substituted alkoxypyridinyl indol-sulfonamides. WO 2019/243398 A1, 2019.

(154) Pegurier, C.; Lovera, S.; Mueller, C. E.; Hockemeyer, J.; Rashed, M.; El, T. A.; Zhang, Y. Q. N-(phenyl)-indole-3-sulfonamide derivatives and related compounds as GPR17 modulators for treating CNS disorders such as multiple sclerosis. WO 2020/254289 A1, 2020.

(155) Galley, G.; Gobbi, L.; Guba, W.; Mazunin, D.; Pinard, E.; Ricci, A. Novel pyrimidin-2-yl sulfonamide derivatives. WO 2022/180136 A1, 2022.

(156) Galley, G.; Gobbi, L.; Mazunin, D.; Pinard, E. Novel pyrimidinyl sulfonamide derivatives. WO 2024/153724 A1, 2024.

(157) Galley, G.; Gobbi, L.; Guba, W.; Mazunin, D.; Pinard, E.; Ricci, A. Novel imidazopyridine and pyrazolopyridine sulfonamide derivatives. WO 2024/017857 A1, 2024.

(158) Galley, G.; Gobbi, L.; Guba, W.; Mazunin, D.; Pinard, E.; Ricci, A. Novel isoquinolinone, pyrrolopyridinone and thienopyridinone sulfonamide derivatives. WO 2024/017856 A1, 2024.

(159) Galley, G.; Gobbi, L.; Guba, W.; Mazunin, D.; Pinard, E.; Ricci, A. Novel isothiazol-3-yl and isoxazol-3-yl sulfonamide compounds. WO 2024/017855 A1, 2024.

(160) Galley, G.; Gobbi, L.; Guba, W.; Mazunin, D.; Pinard, E.; Ricci, A. Novel naphthyl and isoquinoline sulfonamide derivatives. WO 2024/017858 A1, 2024.

(161) Galley, G.; Gobbi, L.; Guba, W.; Mazunin, D.; Pinard, E.; Ricci, A. Novel pyrimidinyl and triazinyl sulfonamide derivatives. WO 2024/017863 A1, 2024.

(162) Galley, G.; Gobbi, L.; Guba, W.; Mazunin, D.; Pinard, E. Novel 7-substituted indole sulfonamide derivatives. WO 2024/023129 A1, 2024.

(163) Galley, G.; Gobbi, L.; Guba, W.; Mazunin, D.; Pinard, E. Novel 7-substituted indole sulfonamide derivatives. WO 2024/023128 A1, 2024.

(164) Galley, G.; Gobbi, L.; Guba, W.; Mazunin, D.; Pinard, E. Novel deuterated pyrimidin-2-yl sulfonamide derivatives. WO 2024/042147 A2, 2024.

(165) Pinto, R. M. G. C.; Duvey, G. A. J.; Vanherck, J. C. A. L.; Marchand, A. D. M.; Pericolle, V. H. D. Fused pyrrolyl-sulfonamide compounds. WO 2024/115733 A1, 2024.

(166) Han, X.; Parker, N. F.; Ong, T. R.; Chen, Y. A.; Geng, B.; Wang, H.; Li, J.; Li, H.; Chen, H.; Zhang, E.; Ouyang, H.; Jiang, P.; Zhao, S.; Yang, M. GPR17 modulators and uses thereof. WO 2024/104462 A1, 2024.

(167) Xi, J.; Wu, Y.; Li, Y.; Jia, J.; Fan, G.; Wang, J. Compounds and their uses as GPR17 antagonists. WO 2024/153233 A1, 2024.

(168) Galley, G.; Gobbi, L. C.; Guba, W.; Mazunin, D.; Pinard, E. Novel deuterated pyrimidin-2-yl sulfonamide derivatives. US 2025/188061 A1, 2025.

(169) Capacci, A.; Evans, R.; Purgett, T.; Stein, Z.; Yousaf, Z. Indole and pyrrolopyridine derivatives as GPR17 modulators. WO 2025/038863, 2025.

(170) He, L.; Yang, H.; Feng, J.; Wei, T.; Huang, Y.; Zhang, X.; Wang, Z. Knockdown of G protein-coupled receptor-17 (GPR17) facilitates the regeneration and repair of myelin sheath post-periventricular leukomalacia (PVL). *Bioengineered* **2021**, *12*, 7314–7324.

(171) Zhao, B.; Zhao, C. Z.; Zhang, X. Y.; Huang, X. Q.; Shi, W. Z.; Fang, S. H.; Lu, Y. B.; Zhang, W. P.; Xia, Q.; Wei, E. Q. The new P2Y-like receptor G protein-coupled receptor 17 mediates acute neuronal injury and late microgliosis after focal cerebral ischemia in rats. *Neuroscience* **2012**, *202*, 42–57.

(172) Gelosa, P.; Bonfanti, E.; Castiglioni, L.; Delgado-Garcia, J. M.; Gruart, A.; Fontana, L.; Gotti, M.; Tremoli, E.; Lecca, D.; Fumagalli, M.; Cimino, M.; Aigner, L.; Abbracchio, M. P.; Sironi, L. Improvement of fiber connectivity and functional recovery after stroke by montelukast, an available and safe anti-asthmatic drug. *Pharmacol. Res.* **2019**, *142*, 223–236.

(173) Liang, Y.; Kang, X.; Zhang, H.; Xu, H.; Wu, X. Knockdown and inhibition of hippocampal GPR17 attenuates lipopolysaccharide-induced cognitive impairment in mice. *J. Neuroinflammation* **2023**, *20*, 271.

(174) Wargent, E. T.; Ahmad, S. J. S.; Lu, Q. R.; Kostenis, E.; Arch, J. R. S.; Stocker, C. J. Leanness and low plasma leptin in GPR17 knockout mice are dependent on strain and associated with increased energy intake that is not suppressed by exogenous leptin. *Front. Endocrinol. (Lausanne)* **2021**, *12*, 698115.

(175) Conley, J. M.; Jochim, A.; Evans-Molina, C.; Watts, V. J.; Ren, H. G protein-coupled receptor 17 inhibits glucagon-like peptide-1 secretion via a Gi/o-dependent mechanism in enteroendocrine cells. *Biomolecules* **2025**, *15*, 9.

(176) Wishart, D. S.; Guo, A.; Oler, E.; Wang, F.; Anjum, A.; Peters, H.; Dizon, R.; Sayeeda, Z.; Tian, S.; Lee, B. L.; Berjanskii, M.; Mah, R.; Yamamoto, M.; Jovel, J.; Torres-Calzada, C.; Hiebert-Giesbrecht, M.; Lui, V. W.; Varshavi, D.; Varshavi, D.; Allen, D.; Arndt, D.; Khetarpal, N.; Sivakumaran, A.; Harford, K.; Sanford, S.; Yee, K.; Cao, X.; Budinski, Z.; Liigand, J.; Zhang, L.; Zheng, J.; Mandal, R.; Karu, N.; Dambrova, M.; Schiöth, H. B.; Greiner, R.; Gautam, V. HMDB 5.0: the Human Metabolome Database for 2022. *Nucleic Acids Res.* **2022**, *50*, D622–D631.

(177) Reynolds, C. H.; Bembenek, S. D.; Tounge, B. A. The role of molecular size in ligand efficiency. *Bioorg. Med. Chem. Lett.* **2007**, *17*, 4258–4261.

(178) García-Ortegón, M.; Simm, G. N. C.; Tripp, A. J.; Hernández-Lobato, J. M.; Bender, A.; Bacallado, S. DOCKSTRING: Easy Molecular Docking Yields Better Benchmarks for Ligand Design. *J. Chem. Inf. Model.* **2022**, *62*, 3486–3502.

(179) Scior, T.; Bender, A.; Tresadern, G.; Medina-Franco, J. L.; Martínez-Mayorga, K.; Langer, T.; Cuanalo-Contreras, K.; Agrafiotis, D. K. Recognizing pitfalls in virtual screening: a critical review. *J. Chem. Inf. Model.* **2012**, *52*, 867–881.

(180) Kostenis, E.; Spinrath, A.; Hennen, S.; Peters, L.; Mueller, C. E.; Akkari, R.; Baqi, Y.; Ritter, K. GPR17 agonists and screening assay. EP 2 567 698 A1, 2013.

(181) Salituro, F. G.; Harrison, B. L.; Baron, B. M.; Nyce, P. L.; Stewart, K. T.; McDonald, I. A. 3-(2-carboxyindol-3-yl)propionic acid derivatives: antagonists of the strychnine-insensitive glycine receptor associated with the N-methyl-D-aspartate receptor complex. *J. Med. Chem.* **1990**, *33*, 2944–2946.

(182) Herrera, L. P. T.; Andreassen, S. N.; Caroli, J.; Rodríguez-Espigares, I.; Kermani, A. A.; Keserű, G. M.; Kooistra, A. J.; Pándy-Szekeres, G.; Gloriam, D. E. GPCRdb in 2025: adding odorant receptors, data mapper, structure similarity search and models of physiological ligand complexes. *Nucleic Acids Res.* **2025**, *53*, D425–D435.

(183) Bhattacharya, S.; Vaidehi, N. LITiCon: a discrete conformational sampling computational method for mapping various functionally selective conformational states of transmembrane helical proteins. *Methods Mol. Biol.* **2012**, *914*, 167–178.

(184) Juers, D. H.; Matthews, B. W.; Huber, R. E. LacZ β-galactosidase: structure and function of an enzyme of historical and molecular biological importance. *Protein Sci.* **2012**, *21*, 1792–1807.

(185) Chambers, A. C.; Aksular, M.; Graves, L. P.; Irons, S. L.; Possee, R. D.; King, L. A. Overview of the baculovirus expression system. *Curr. Protoc. Protein Sci.* **2018**, *91*, 5.4.1–5.4.6.

14 Appendix

14.1 Publication I. GPR17 – orphan G protein-coupled receptor with therapeutic potential

Reprinted with permission from Trends Pharmacol. Sci. 2025, 46, 610–628. Published by Elsevier Ltd. Access online: https://doi.org/10.1016/j.tips.2025.05.001

Trends in Pharmacological Sciences

CellPress OPEN ACCESS

Review

GPR17 – orphan G protein-coupled receptor with therapeutic potential

Michael Lewash [1], Evi Kostenis [2], and Christa E. Müller [1,*]

The orphan G protein-coupled receptor (GPCR) GPR17, whose physiological agonist remains unknown, has emerged as a promising drug target for multiple sclerosis (MS). Blockade of the receptor enables remyelination and may offer a novel therapeutic strategy for MS. Only recently, potent and selective tool compounds for GPR17 have become available, and patents on antagonists have surged, leading to the first clinical candidate, the GPR17 antagonist PTD802, which is to be developed for MS therapy. This may pave the way for further clinical studies exploring additional indications, such as neurodegenerative diseases. The newly determined cryo-electron microscopy (cryo-EM) structure of GPR17 is expected to facilitate future structure-based drug design efforts. This review presents and discusses these latest developments, providing a timely and comprehensive overview to guide future research in the field.

Highlights

The orphan G protein-coupled receptor GPR17 has emerged as a potential therapeutic target for multiple sclerosis (MS) and other demyelinating diseases.

By contrast with current MS therapeutics, GPR17 antagonists are expected to induce myelin repair which may result in a curative treatment for this debilitating chronic disease.

A recent cryo-electron microscopy (cryo-EM) study provided structural insights into the unliganded receptor.

Whereas its physiological agonist is still unknown, the development of potent and selective synthetic agonists and antagonists has enabled pharmacological research, including preclinical studies.

Several patents on GPR17 antagonists have been filed, and the results of the first clinical study are eagerly awaited.

GPR17 – a promising drug target for multiple sclerosis and beyond

GPR17 is a class A (rhodopsin-like), δ-branch **GPCR** (see Glossary). This branch comprises receptors that can be activated by nucleotides (P2Y receptors), lipids [cysteinyl-leukotriene (CysLT) receptors, platelet-activating factor receptor, free fatty acid receptors, lysophosphatidic acid receptors, prostaglandin receptors, and thromboxane receptors], small carboxylic acids (succinate receptor, oxoglutarate receptor), or peptides (e.g., proteinase-activated receptor 1). Dysregulation of GPR17 has been implicated in **MS** [1–6], a devastating **demyelinating** disease without curative treatment [7].

Different clinical phases and types of MS with different predominant symptoms exist [8,9]. These are subdivided into relapsing–remitting MS (RRMS), which can proceed to secondary-progressive MS (SPMS) with time, and primary-progressive MS (PPMS) characterized by less inflammation and more neurodegeneration. While disease-modifying therapies developed during the past decades have led to a decrease in relapses and disabilities by reducing neuroinflammation, they are particularly useful for treating RRMS; however, only a few treatment options for SPMS – and even fewer for PPMS – are available [8]. Remyelinating agents might fill this gap, potentially leading to substantial remission [7]. A promising target for **remyelination** is GPR17, based on the finding that knockdown of *Gpr17* in rats leads to myelin sheath regeneration [6]. Unfortunately, research on GPR17 has been hampered by confusion, irreproducible results, and contradictions. There are ongoing debates about its endogenous ligand [10–16] (Table 1), disputes about its activation or inhibition by certain nucleotides and leukotriene-based compounds [12,15,17,18] (Table 1), and disagreements about its expression on neurons, astrocytes, and microglia [1,5,10,19,20] (Table 2). This has been in part due to the lack of potent and selective tool compounds to study GPR17, but in the past few years suitable ligands have been discovered, optimized, and validated [21–23]. Additionally, several patents describing GPR17 antagonists, intended to be developed clinically, have been filed [24–40]. Moreover, the first GPR17-selective clinical candidate, the antagonist PTD802, was developed and will soon be investigated

[1]PharmaCenter Bonn, Pharmaceutical Institute, Pharmaceutical & Medicinal Chemistry, University of Bonn, An der Immenburg 4, D-53121 Bonn, Germany
[2]Pharmaceutical Biology, University of Bonn, Nußallee 6, D-53115 Bonn, Germany

*Correspondence: christa.mueller@uni-bonn.de (C.E. Müller).

clinically (https://phenotherapeutics.com/wp-content/uploads/2025/01/Pheno-CTA-approval-press-release-FINAL-10-01-2025.pdf). Further proposed remyelinating agents – the muscarinic M_1 receptor antagonist PIPE-307 (Phase 2), and the lysophosphatidic acid LPA_1 receptor antagonist PIPE-791 (Phase 1) – are currently being evaluated in clinical trials to assess their therapeutic potential (https://www.contineum-tx.com/programs/) in RRMS (M_1 antagonist) and in progressive MS (LPA_1 antagonist).

The first clinical trial of a GPR17 antagonist for MS is anticipated to spark interest in further indications. Evidence from preclinical studies indicates involvement of GPR17 in **neurodegenerative diseases** such as **Alzheimer's disease (AD)** and **Parkinson's disease (PD)** [41–44], glioblastoma [45–50], ischemic injury [20,51–57], bronchial asthma [58], and diabetes and obesity [59–61], indications that await future validation. Furthermore, a **cryo-electron microscopy (cryo-EM)** structure has revealed the receptor's three-dimensional arrangement and will allow rational drug development to be taken to the next level [62], supporting future drug development campaigns.

In this review we provide an overview of GPR17 expression and regulation, examine the first cryo-EM structure of the receptor, and evaluate GPR17 agonists and antagonists that enable biological studies including target validation. Relevant signaling pathways, genetic variants, and the role of GPR17 in pathological conditions are discussed. The potential role of GPR17 as a drug target for MS, neurodegenerative diseases such as AD and PD, ischemic injury, glioblastoma, bronchial asthma, diabetes, and obesity is critically reviewed.

GPR17 expression and regulation

GPR17 expression in brain and peripheral tissues

The human (h) *GPR17* gene, which is located on chromosome 2q21, has two open reading frames (ORFs), resulting in two receptor isoforms [63] that differ in the length of their extracellular N terminus: 23 amino acids in the short isoform hGPR17-S, 51 amino acids in the long isoform hGPR17-L, the following sequence being omitted in hGPR17-S: MSKRSWWAGSRKPPREMLKLSGSDSSQS. Interestingly, the closely related mouse $CysLT_1$ receptor also exists in two isoforms, but it is unknown whether they have different functions [64]. In contrast, the mouse (m) and rat (r) *Gpr17* genes code for only a single receptor isoform (mGPR17, rGPR17) corresponding to hGPR17-S.

Analysis of *hGPR17* gene expression by RT-PCR [10,15,65] revealed the **central nervous system (CNS)** to be the primary location of expression, which was confirmed by immunohistochemical GPR17 protein expression analysis in mice using commercially available anti-GPR17 antibodies (Cayman Chemicals, MI, USA) [4]. Analysis of hGPR17 protein expression in brain has only been performed using custom-made antibodies [5], and not yet been independently confirmed [66].

hGPR17 expression has also been reported in peripheral tissues, particularly in those that are susceptible to ischemic damage, including heart [10], intestine [60], kidney [10,65,67], liver [10,67], and lung [10] (Table 2). In addition, mGPR17 expression was reported in a population of cardiac-resident stromal cells in the heart using custom-made antibodies [2], and hGPR17 expression was reported in enteroendocrine cells in the intestine using commercially available anti-GPR17 antibodies (Novus Biologicals, Wiesbaden, Germany) [60].

hGPR17-S was reported to be the predominant form in the brain, whereas peripheral tissues appear to preferentially express hGPR17-L [65]. More extensive studies are needed to elucidate the differences between the isoforms. So far, most published work focused on the short isoform expressed in brain with the aim of elucidating its structure and function.

Glossary

Alzheimer's disease (AD): a neurodegenerative disorder resulting in the accumulation of β-amyloid (Aβ) and tau proteins in the brain. It is characterized by cognitive decline and memory loss.
Central nervous system (CNS): the brain and spinal cord.
Cryo-electron microscopy (cryo-EM): a structural biology technique for determining the 3D structure of biomolecules at near-atomic resolution.
Demyelination: the loss of or damage to the myelin sheaths that surround nerve fibers, impairing signal transmission and contributing to neurological disorders such as MS.
G protein-coupled receptor (GPCR): one of a family of membrane proteins which have seven transmembrane helices that transduce signals from extracellular to intracellular compartments mainly via G protein activation, and that are involved in regulating a wide range of physiological processes.
Multiple sclerosis (MS): a chronic inflammatory autoimmune disease affecting the CNS, characterized by demyelination and neuroinflammation.
Neurodegenerative diseases: a group of disorders characterized by progressive loss of function or structure of neurons, involving complex pathological processes including the accumulation of abnormal protein aggregates and inflammation. Examples include Alzheimer's and Parkinson's diseases.
Oligodendrocytes (OLs): myelin-producing cells of the CNS.
Orphan receptor: a receptor for which the endogenous agonist is still unknown.
Parkinson's disease (PD): a neurodegenerative disorder caused by the loss of dopamine-producing neurons in the substantia nigra. It is characterized by tremors, rigidity, bradykinesia, or even akinesia.
Potency: drug concentration required to produce an effect of specific intensity.
(Re-)myelination: the process of (re) generating (or restoring) myelin sheaths around (damaged) nerve fibers.

Table 1. Proposed agonists and antagonists of GPR17 with EC_{50} or IC_{50} values

Compound	EC_{50} or IC_{50} (μM)	Year proposed as GPR17 agonist or antagonist	Comments	Refs.
Agonists				
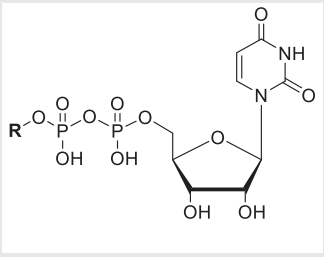 UDP (**R** = H) UDP-glucose (**R** = D-glucopyranosyl) UDP-galactose (**R** = D-galactopyranosyl)	UDP: 1.1 UDP-glucose: 12 UDP-galactose: 1.1[a]	2006	Could not be confirmed by other groups	[10–15]
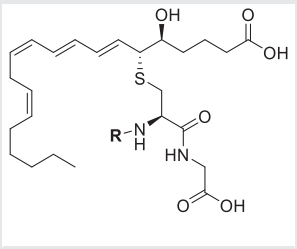 LTD_4 (**R** = H) LTC_4 (**R** = 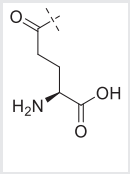	LTD_4: 7.2 LTC_4: 0.33[a]	2006	Could not be confirmed by other groups	[10,13,15]
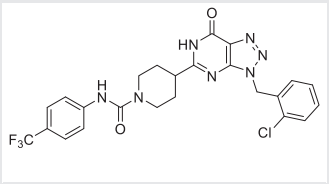 Asinex 1	0.00027[a]	2011	Could not be confirmed by other groups	[12,15,17]
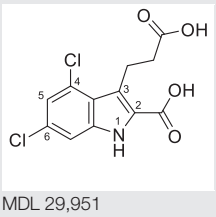 MDL 29,951	0.33[l] Range: 0.0071–6.6[a, b, c, d, e, f, g, h, i, j, k, l]	2013	Non-selective NMDA receptor antagonist (IC_{50} = 0.17 μM)	[21,12,15,104]

(continued on next page)

Table 1. (continued)

Compound	EC_{50} or IC_{50} (μM)	Year proposed as GPR17 agonist or antagonist	Comments	Refs.
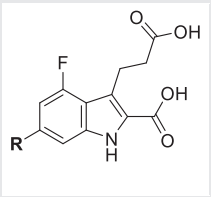 PSB-18422 (**R** = Br) PSB-18484 (**R** = I)	PSB-18422: 0.028[i] PSB-18484: 0.032[i]	2018	High potency (10-fold higher than MDL 29,951), high selectivity (EC_{50} at $P2Y_{1/2/4/6}$ > 50 μM)[a]	[21]
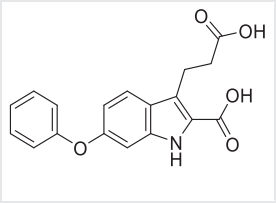 PSB-1837	0.27[i]	2018	Potency comparable to MDL 29,951, high selectivity (IC_{50} at NMDA receptor > 1000 μM)[a]	[21]
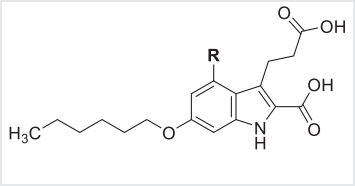 PSB-1867 (**R** = H) PSB-18183 (**R** = Cl)	PSB-1867: 0.12[i] PSB-18183: 0.067[i]	2018	High potency (3- to 5-fold higher than MDL 29,951), high selectivity (EC_{50} at $P2Y_{1/2/4/6/12/14}$ > 50 μM)[a]	[21]
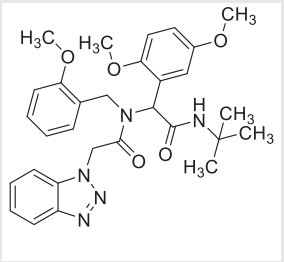 AC1MLNKK	23[b]	2018	Low potency, selectivity unknown	[88]
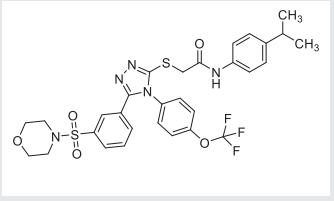 T0510.3657	16[b]	2018	Low potency, selectivity unknown; reported to induce cell death in GBM cells	[88,89]

Table 1. (continued)

Compound	EC_{50} or IC_{50} (μM)	Year proposed as GPR17 agonist or antagonist	Comments	Refs.
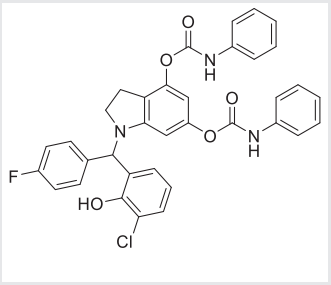 CHBC	19–60[b]	2021	Low potency, selectivity unknown, reported to induce cell death in GBM cells	[50,105]
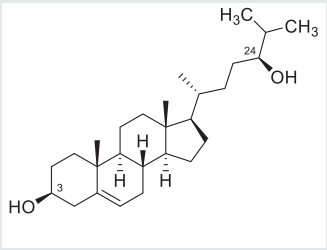 24(*S*)-Hydroxycholesterol	3.9–4.8[h, k] >10[l]	2023	Could not be confirmed by other groups	[15,16]
Antagonists				
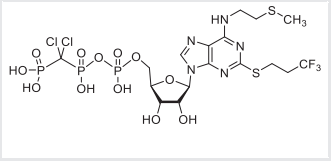 Cangrelor	0.00070[m]	2006	$P2Y_{12}$ receptor antagonist (IC_{50} = 0.82 nM), could not be confirmed by other groups [15,18]	[10,15,18,106]
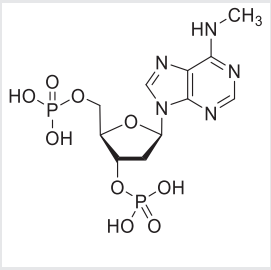 MRS2179	0.51[m]	2006	Nonselective $P2Y_1$ receptor antagonist (IC_{50} = 3.5 μM)[s]	[10,107]
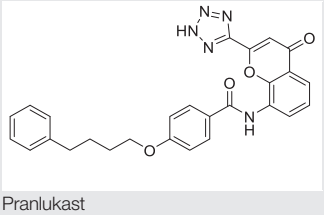 Pranlukast	0.011–0.11[m, p, q] 2.7–4.5[n, o]	2006	Nonselective $CysLT_1$ receptor antagonist (IC_{50} = 5.8 nM[s] or 3.8 nM[r])	[10,12,23,108,109]

(continued on next page)

Table 1. (continued)

Compound	EC_{50} or IC_{50} (μM)	Year proposed as GPR17 agonist or antagonist	Comments	Refs.
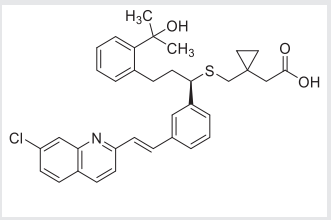 Montelukast	0.035–0.060[m, p] >10[n, o]	2006	Nonselective $CysLT_1$ receptor antagonist (IC_{50} = 3.4 nM)[s]; promoted neuronal outgrowth in dopaminergic organotypic slice co-cultures [42]	[10,12,23,42,108]
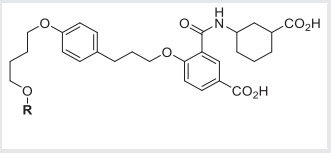 HAMI3379 (**R** = cyclohexyl) $BayCysLT_2$ (**R** = phenyl)	0.1–10[n, o, p, y, z]	2018	Nonselective $CysLT_2$ receptor antagonists (HAMI3379 IC_{50} = 3.8 nM[w], $BayCysLT_2$ IC_{50} = 53 nM[x])	[18,110,111]
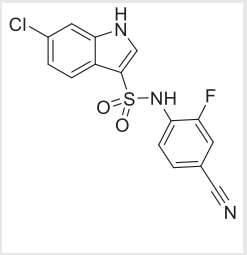 I-116	0.0041–0.033[t, u, v]	2017 / 2023	High potency, indolyl-sulfonamide scaffold	[15,24]
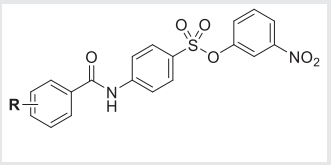 14a (**R** = H) 14f (**R** = *m*-CF_3) 14l (**R** = *p*-Cl) 14m (**R** = *o*-Cl)	14a: 3.2[p] 14f: 3.8[p] 14l: 3.4[p] 14m: 1.7[p]	2020	Suramin-derived scaffold, 14a and 14f are selective ($P2Y_2$ IC_{50} > 10), while 14l and 14m are dual antagonists (similar $P2Y_2$ IC_{50})	[22]
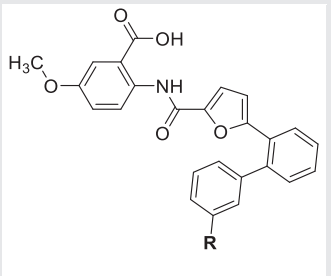 PSB-22269 (**R** = OCH_3) PSB-24040 (**R** = CF_3)	PSB-22269: 0.0089–0.13[p, aa, ab, ac] PSB-24040: 0.0079–0.30[p, aa, ab, ac]	2024	High potency, anthranilic acid scaffold	[23]

Table 2. Overview of GPR17 expression in human organs and tissues

Organ/tissue	Expression level	Predominant isoform	Refs
Brain: • late oligodendrocyte progenitor cells (OPCs), pre-oligodendrocytes (pre-OLs) • could not be confirmed by other groups: astrocytes, neurons, microglia	Highest	Short	[1,3,5,10,19,20,57,75]
Heart: cardiac-resident stromal cells	High	Long	[2,10]
Kidney	High	Long	[10,67]
Intestine: enteroendocrine cells	Moderate	n.d.[a]	[60]
Liver: hepatocytes	Low	n.d.[a]	[10,67]
Lung	Low	n.d.[a]	[10]

[a]n.d., not determined.

Dynamic regulation of GPR17 in oligodendrocytes

In the brain, GPR17 is moderately expressed in a subset of **oligodendrocyte (OL)** progenitor (precursor) cells (OPCs), also known as neural/glial antigen 2 (NG2) cells due to the presence of the chondroitin sulfate proteoglycan NG2 in their later, morphologically more complex stages, and to a greater extent in pre-oligodendrocytes (pre-OLs) (Table 2 and Figure 1) [68,69]. In a recently introduced nomenclature for OL lineage cells, these GPR17-expressing cells are termed 'committed OL precursor cells' (or COPs), corresponding to late-stage OPCs and pre-OLs, which represent a transitional stage between early GPR17^{-} OPCs and newly formed OLs (NFOs, also known as immature OLs) [70]. *mGpr17* expression in COPs is upregulated by OL transcription factor 2 (Olig2) [71], which appears to be affected by mammalian target of rapamycin (mTOR) and WNT signaling [72,73], with high WNT activity suppressing *Gpr17* expression and vice versa, as observed in mouse brain [73].

Notes to Table 1.
[a]EC_{50} value determined in [^{35}S]GTPγS binding assays using membrane preparation from 1321N1 astrocytoma cells transfected with hGPR17.
[b]EC_{50} value determined in cAMP assays in HEK293 cells transfected with hGPR17.
[c]EC_{50} value determined in cAMP assays in CHO-K1 cells transfected with hGPR17.
[d]EC_{50} value determined in cAMP assays in 1321N1 astrocytoma cells transfected with hGPR17.
[e]EC_{50} value determined in [^{35}S]GTPγS binding assays using membrane preparation from HEK293 cells transfected with hGPR17.
[f]EC_{50} value determined in [^{35}S]GTPγS binding assays using membrane preparations from CHO-K1 cells transfected with hGPR17.
[g]EC_{50} value determined in calcium mobilization assays in HEK293 cells transfected with hGPR17.
[h]EC_{50} value determined in calcium mobilization assays in CHO-K1 cells transfected with hGPR17.
[i]EC_{50} value determined in calcium mobilization assays in 1321N1 astrocytoma cells transfected with hGPR17.
[j]EC_{50} value determined in [^{35}S]GTPγS binding assays using membrane preparation from COS7 cells transfected with hGPR17.
[k]EC_{50} value determined in cAMP assays in SK-N-MC cells transfected with hGPR17.
[l]EC_{50} value determined in calcium mobilization assays in SK-N-MC cells transfected with hGPR17.
[m]IC_{50} value determined in [^{35}S]GTPγS binding assays using membrane preparation from 1321N1 astrocytoma cells transfected with hGPR17.
[n]IC_{50} value determined in IP_1 assays versus agonist MDL 29,951 in HEK293 cells transfected with hGPR17.
[o]IC_{50} value determined in calcium mobilization assays versus agonist MDL 29,951 in HEK293 cells transfected with hGPR17.
[p]IC_{50} value determined in calcium mobilization assays versus agonist MDL 29,951 in 1321N1 astrocytoma cells transfected with hGPR17.
[q]IC_{50} value determined in [^{3}H]LTD_4 binding assays using membrane preparation from COS7 cells transfected with $CysLT_1$ receptor.
[r]IC_{50} value determined in IP_1 assays versus $CysLT_1$ receptor agonist LTD_4 in HEK293 cells transfected with $CysLT_1$ receptor.
[s]IC_{50} value determined in platelet aggregation assay versus agonist ADP in platelets purified from human blood.
[t]IC_{50} value determined in [^{35}S]GTPγS binding assays using membrane preparation from COS7 cells transfected with hGPR17.
[u]IC_{50} value determined in cAMP inhibition assays versus agonist MDL 29,951 in SK-N-MC cells transfected with hGPR17.
[v]IC_{50} value determined in calcium mobilization assays versus agonist MDL 29,951 in SK-N-MC cells transfected with hGPR17.
[w]IC_{50} value determined in calcium mobilization assay versus $CysLT_2$ receptor agonist LTD_4 in CHO cells transfected with $CysLT_2$ receptor.
[x]IC_{50} value determined in β-arrestin assay versus $CysLT_2$ receptor agonist LTD_4 in C2C12 myoblast cells transfected with $CysLT_2$ receptor.
[y]IC_{50} value determined in β-arrestin assay versus agonist MDL 29,951 in HEK293 cells transfected with hGPR17.
[z]IC_{50} value determined in calcium mobilization assays versus agonist MDL 29,951 in CHO cells transfected with hGPR17.
[aa]IC_{50} value determined in cAMP inhibition assays versus agonist MDL 29,951 in CHO-FITR cells transfected with hGPR17.
[ab]IC_{50} value determined in G protein effector membrane translocation assays versus agonist MDL 29,951 in HEK293 cells transfected with hGPR17.
[ac]IC_{50} value determined in [^{3}H]PSB-12150 binding assays using membrane preparation from CHO-FITR cells transfected with hGPR17.

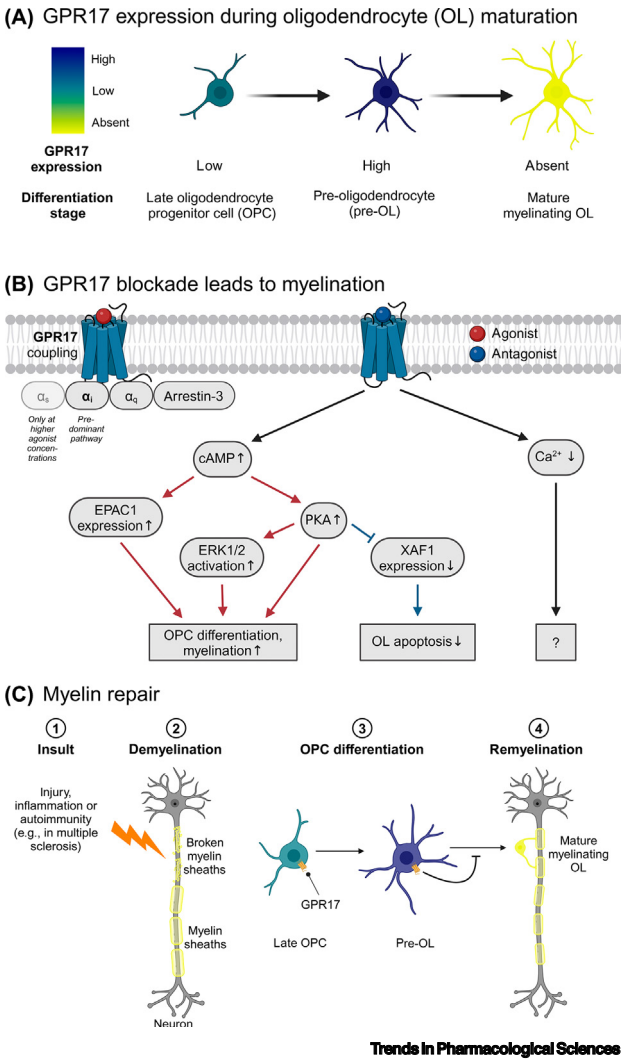

Figure 1. Role of GPR17 in oligodendrocyte maturation and myelin repair. (A) G protein-coupled receptor 17 (GPR17) expression during oligodendrocyte (OL) maturation: GPR17 is expressed in late OL progenitor cells (OPCs) and, to a greater extent, in pre-OLs. In mature OLs GPR17 is downregulated [5,68–70]. (B) GPR17 coupling to different G proteins, important signaling pathways and effects: the $G\alpha_i$ signaling cascade seems to be the predominant pathway that links GPR17 to OL maturation control [3,71,93]. The effect of $G\alpha_q$ and its downstream interacting molecules on OL maturation is not yet understood. Abbreviations: cAMP, cyclic adenosine monophosphate; EPAC1, exchange protein directly activated by cAMP 1; ERK1/2, extracellular-signal-regulated kinases 1/2; PKA, protein kinase A; XAF1, X-linked inhibitor of apoptosis associated factor 1. (C) Myelin repair: GPR17 signaling downregulates OPC differentiation into OLs which in turn inhibits remyelination [1,12,93]. GPR17 has therefore been suggested as a target for the treatment of multiple sclerosis and other demyelinating diseases. Figure created with BioRender.

Downregulation of GPR17 correlates with subsequent cell maturation into myelinating OLs [5], possibly mediated or modulated by increased lactate release [74]. This process can be inhibited by activated microglia [55]. However, the exact role of GPR17 in OL lineage progression remains controversial. Fang *et al.* proposed that GPR17 expression marks a population of COPs that exit the proliferation cycle, downregulating NG2, and proceeding to differentiation into myelinating OLs [70]. By contrast, Miralles *et al.* reported that, under physiological conditions, the $NG2^{+}GPR17^{-}$ OPCs, and not the GPR17-expressing subset, differentiate into myelinating OLs [75]. They propose that GPR17 expression plays a regulatory role in maintaining the OPC pool, since *Gpr17* knockdown led to premature OPC differentiation and impaired their proliferation [75]. These conflicting findings suggest that GPR17 may exert context-dependent roles in balancing proliferation and differentiation of oligodendroglial cells.

Cryo-electron microscopy structure of GPR17

GPR17, like other GPCRs, consists of a single polypeptide chain forming seven transmembrane (TM) helices, three extracellular loops (ECLs), and three intracellular loops (ICLs), with an extracellular N- terminus and an intracellular C terminus. Human GPR17 is highly homologous with its mouse and rat orthologs (90% sequence identity), while mouse and rat GPR17s are almost identical (99% identity).

The recent determination of the cryo-EM structure of hGPR17 in its apo form (no ligand bound) in complex with G_i protein at a resolution of 3.02 Å provided insights into its three-dimensional architecture. The ECL2 was observed to form a hairpin-like structure that is stabilized by a disulfide bridge with a cysteine residue in TM3, and by two hydrogen bonds with residues in TM7, in addition to multiple polar interactions (Figure 2). The authors hypothesized that the ECL2 occupies the (orthosteric) binding pocket [62].

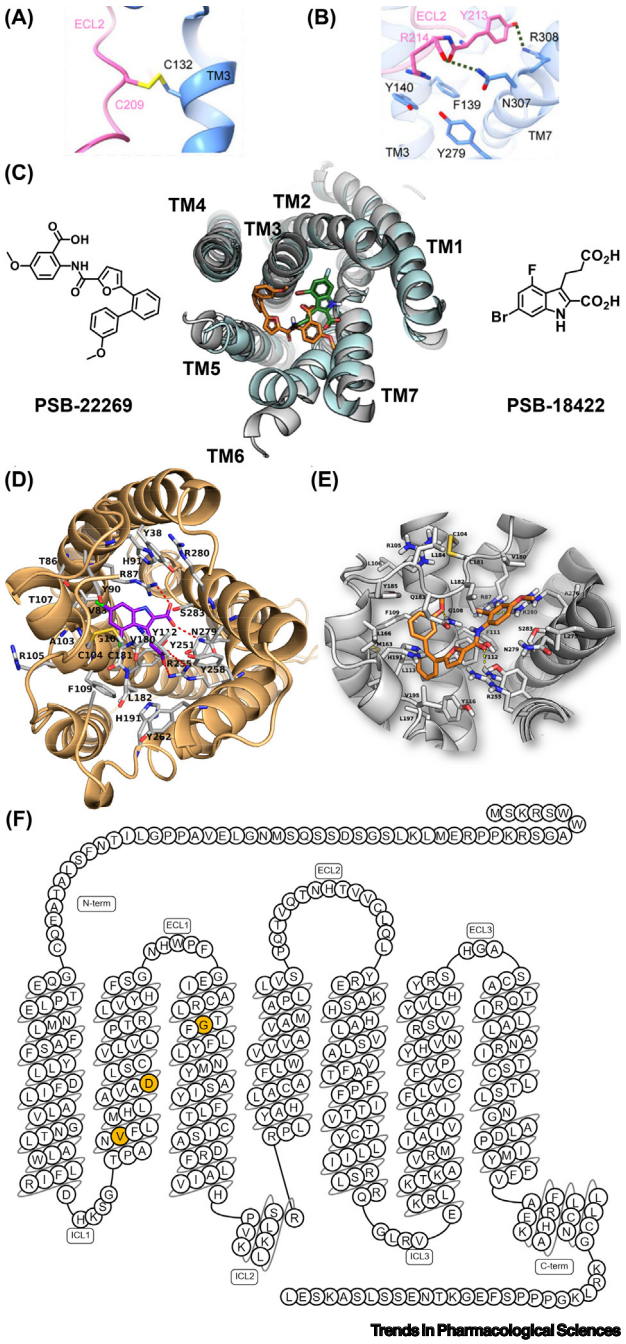

Figure 2. Proposed ligand binding and activation mechanism of GPR17. (A,B) Cryo-electron microscopy (cryo-EM) structure of the putative binding pocket of G protein-coupled receptor 17 (GPR17) (blue) occupied by extracellular loop 2 (ECL2, pink). (A) Disulfide bond (yellow) between ECL2 and transmembrane domain 3 (TM3). (B) Hydrogen bonds between ECL2 and transmembrane domain 7 (TM7). (C) Predicted binding poses of agonist PSB-18422 (green) and antagonist PSB-22269 (orange) in the putative binding pocket of GPR17 homology models for the active (blue) and inactive (gray) states. (D) Predicted binding pose of agonist MDL 29,951 in the putative binding pocket of GPR17 homology model for the active state. (E) Predicted binding pose of antagonist PSB-22269 in the putative binding pocket of GPR17 homology model for the inactive state. (F) Snake plot of the full sequence of hGPR17-L. The positions of genetic variants V96M, D105N, and G136S are highlighted in yellow. (A,B,D–F) Amino acid numbering in (A), (B), and (F) corresponds to long isoform hGPR17-L, while numbering in (D) and (E) corresponds to short isoform hGPR17-S. Shown amino acids in A and B correspond to F111, F112, C104, C181, Y185, R186, N279, and R280 in hGPR17-S numbering (subtract 28 to go from hGPR17-L numbering to hGPR17-S numbering). (A) and (B) adapted with permission from Ye *et al.*, 2022 [62]. (C) and (E) adapted with permission from Boshta *et al.* [23]. Copyright 2024 American Chemical Society. (D) Adapted with permission from Baqi *et al.* [21]. Copyright 2018 American Chemical Society. (F) Generated by GPCRdb [85].

Molecular modeling and docking studies of agonists and antagonists were performed using active- and inactive-state comparative models of GPR17 based on X-ray crystal structures of the phylogenetically related $P2Y_{12}$ receptor, an AlphaFold prediction, and the cryo-EM structure, respectively. Docking of an agonist (PSB-18422) and an antagonist (PSB-22269) suggested a binding site dominated by interactions with basic amino acid residues, similar to the putative orthosteric binding site that was predicted based on the cryo-EM structure (Figure 2) [23].

GPR17 features a combination of unique microswitches. The NPxxY motif present in many related GPCRs is mutated to DPxxY in GPR17, which alters the conformation of TM7 [62]. The DRY motif is changed to a DRF, which is also found on the phylogenetically similar C-X-C chemokine receptor 6 (CXCR6) (37% amino acid sequence similarity/19% identity), in which mutation to DRY led to an increase in calcium signaling and migratory responses. It has therefore been hypothesized that the DRF motif impairs chemotaxis, at least in chemokine receptors [76]. The CWxP motif is replaced by CFxP in GPR17, which reduces the flexibility of TM6 [62]. Agonist binding typically induces a change in receptor conformation of GPCRs, which induces intracellular signaling events, while antagonists block receptor activation.

Synthetic agonists and antagonists enable biological studies, including target validation

The identification of endogenous agonist(s) for GPR17 has been a subject of extensive investigations (Table 1). Early studies suggested that pyrimidine nucleotides, such as uridine diphosphate (UDP), UDP-glucose, and UDP-galactose, as well as leukotrienes – namely leukotriene C_4 (LTC_4) and LTD_4 – could act as agonists of GPR17 [10]. The compounds were thought to induce GPR17-mediated calcium mobilization and activation of downstream signaling pathways in various cell types expressing GPR17 [10]. Based on these data, it was hypothesized that GPR17 may be a dual receptor, phylogenetically located between nucleotide P2Y and CysLT receptors, and responsive to both classes of ligands, nucleotides, and cysteinyl leukotrienes [10].

However, several laboratories have failed to reproduce the reported findings, and subsequent research could not confirm activation of GPR17, neither the short nor the long GPR17 isoforms, by any of the aforementioned ligands [11,13,14,62,65,77]. The general classification of GPR17 as phylogenetically located between CysLT and P2Y receptors [10] overlooks its close relationship with some other GPCR family members. Our re-analysis using NGPhylogeny.fr/iTOL [78–84] and GPCRdb [85] revealed that the GPCRs most closely related to GPR17 are not limited to the $P2Y_1$ (43% similarity/24% identity) and the $CysLT_2$ receptor (41%/25%), but also include lysophosphatidic acid receptor subtypes LPA_6 (43%/24%) and LPA_4 (39%/24%), the oxoglutarate receptor (42%/22%), and the **orphan receptor** GPR87 (39%/22%) (Figure 3). Thus, a broader view might be helpful to enable the discovery of the physiological agonist for GPR17.

More recent studies have proposed 24(*S*)-hydroxycholesterol to acts as an endogenous agonist of GPR17 [15], however, this could not be independently confirmed [16].

Since the physiological agonist of GPR17 is still unknown, the identification of an efficient synthetic agonist has played a crucial role for the subsequent identification of GPR17 antagonists (Table 1). The purine analog Asinex 1 (also known as GPR17 ligand-5) [17] was proposed as an agonist of GPR17, but this could not be confirmed [12,15]. Previous studies from the Kostenis group identified the first compound capable of consistently activating GPR17: MDL 29,951 [12,86] (EC_{50} value: 0.33 μM in calcium mobilization assays [21], with similar **potency** on

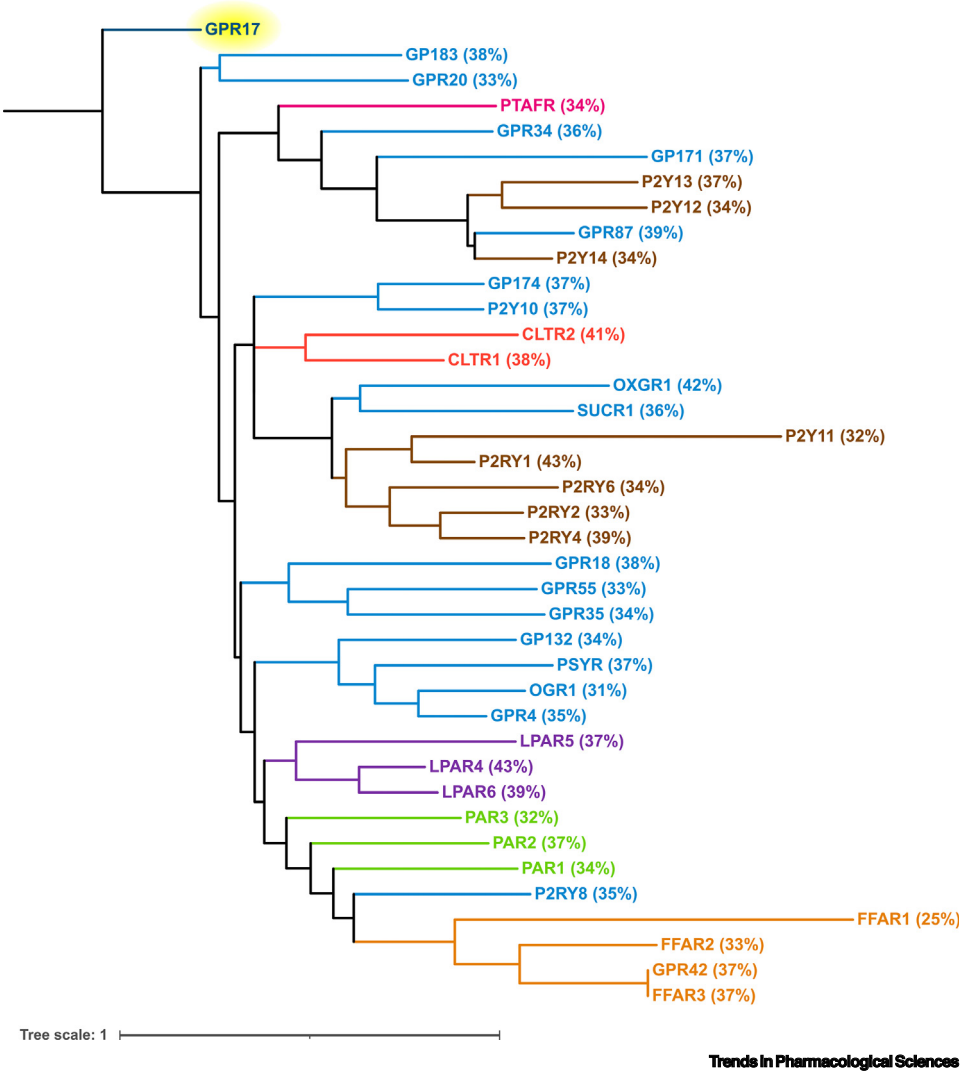

Figure 3. Phylogenetic relationships between the human G protein-coupled receptor 17 (GPR17) and 38 closely related human class A, δ-branch GPCRs. Receptors are labeled by their UniProt names. Receptor families are highlighted in different colors: orphan GPCRs (including GPR17) in blue, cysteinyl-leukotriene receptors (CLTR) in red, the nucleotide-activated P2Y receptors (P2RY) in brown, the platelet-activated receptor (PTAFR) in pink, lysophosphatidic acid receptors (LPARs) in purple, protease-activated receptors (PARs) in green, and free fatty acid receptors (FFARs) in yellow. Other abbreviations: OGR1, ovarian cancer G protein-coupled receptor 1 (also known as GPR68); OXGR1, 2-oxoglutarate receptor 1; PSYR, psychosine receptor (also known as GPR65); SUCR1, succinate receptor. Unbroken horizontal lines reflect the phylogenetic distance, that is, the longer the distance between two receptors, the less related they are. The phylogenetic tree was generated using NGPhylogeny.fr and iTol [78–84]. Phylogenetic distance does not correlate directly with amino acid sequence similarity. Therefore, sequence similarity (where similar is defined as BLOSUM62 score [112] >0) to GPR17 was additionally calculated by GPCRdb [85], shown in brackets for each receptor.

hGPR17, rGPR17, and mGPR17 [12]). MDL 29,951 had previously been developed as an *N*-methyl-D-aspartate (NMDA) receptor antagonist interacting with the glycine binding site [87]. Kostenis and coworkers showed that activation of GPR17 by MDL 29,951 results in the arrest of OLs at an immature stage [12]. We subsequently prepared the first radioligand for GPR17, a tritium-labeled form of MDL 29,951 [14], and investigated the structure–activity relationships of

the indole-based agonist, recognizing that the indole scaffold requires an unsubstituted nitrogen atom and a propanoic acid residue at the indole 3-position for high potency. Replacement of the chlorine atoms of MDL 29,951 by fluorine (position 4), and bromine (position 6) yielded compound PSB-18422, which exhibits a tenfold higher potency (EC_{50} value of 0.028 μM in calcium mobilization assays) (Table 1), and increased GPR17 selectivity versus $P2Y_{1/2/4/6}$ receptors as compared with MDL 29,951 [21]. Further noteworthy agonists based on the indole scaffold include PSB-1837, PSB-1867, and PSB-18484 (also known as PSB2 and incorrectly as PSB-16484) [21,42]. Interestingly, while the compounds with a small substituent at position 6 were only slightly more potent at hGPR17 compared with rGPR17 or mGPR17, those with large lipophilic residues were about 40-fold more potent, suggesting a larger binding pocket in the human receptor as compared with a smaller pocket in the rodent receptors [21,42]. Both classes of GPR17 agonists were proposed to display different binding modes [21]. Interestingly, derivatives with a long residue in the indole 6-position did no longer interact with NMDA receptors.

GPR17 agonists based on more complex heterocyclic scaffolds – namely AC1MLNKK, T0510.3657 (also known as T0), and CHBC – have been reported (Table 2) [50,88,89]. These agonists are weakly potent (EC_{50} values in the range 16–60 μM, determined in cAMP assays) [50,88]. By contrast with MDL 29,951, CHBC showed cytotoxic effects on glioblastoma multiforme (GBM) cells in cell growth inhibition assays [50]. A virtual screening approach suggested several heterocyclic compounds, mostly with a triazole ring, as potent GPR17 agonists. They were studied in GTPγS binding assays, and selected compounds were further evaluated [90]. However, the observed effects are not clearly due to GPR17 activation, but may result from other activities.

Regarding antagonists, the first reported compounds able to consistently inhibit the activation of GPR17 were the $CysLT_1$ receptor antagonists montelukast and pranlukast (Table 2) [62,91]. In previous studies, the Kostenis group reported that the $CysLT_2$ receptor antagonists HAMI3379 and Bay$CysLT_2$ block GPR17 activation with moderate potency [18]. By contrast, the proposed purine-nucleotide-based P2Y receptor antagonists cangrelor and MRS2179 could not be confirmed by other groups [10,15,18].

A major breakthrough in the development of potent, selective, brain-permeable antagonists that are suitable for clinical application was achieved with the discovery of indolylsulfonamide derivatives (e.g., I-116), invented by scientists at the Pharmaceutical Institute, University of Bonn, Germany (Müller and coworkers), in collaboration with UCB Pharma within a government-funded project (BioPharma Neuroallianz) (Table 2) [24]. I-116 was later re-synthesized by a different group for investigating GPR17 in GTPγS binding, cAMP inhibition, and calcium mobilization assays [15]. Pheno Therapeutics recently obtained clinical trial authorization for the orally bioavailable, brain-permeable GPR17 antagonist PTD802 (structurally related to the indolylsulfonamide I-116, but its concrete structure has not been disclosed). Recently, several companies – including UCB Pharma GmbH, F. Hoffmann-La Roche AG, Rewind Therapeutics NV, Myrobalan Therapeutics Nanjing Co. Ltd, Nanjing Immunophage Biotech Co. Ltd, and Biogen Ma Inc. – filed patents claiming structurally very similar sulfonamide derivatives as potent GPR17 antagonists [25–40]. This class of compounds has suitable properties to validate GPR17 as a drug target in brain diseases in preclinical and clinical trials.

Previous studies from our groups also described moderately potent suramin-derived antagonists 14a, 14f, 14l, and 14m, which are either GPR17-selective or dual blockers of GPR17 and $P2Y_2$ receptors [22]. Additionally, we recently described new potent antagonists, PSB-22269 and PSB-24040, based on an anthranilic acid scaffold [23] (Table 1).

In summary, the most potent GPR17 agonist published to date is PSB-18422 due to its high potency (EC_{50} = 0.028 μM in calcium mobilization assays) and high selectivity (EC_{50} at $P2Y_{1/2/4/6}$ >50 μM) [21]. It is structurally derived from MDL 29,951, which has been shown in numerous studies to be an effective and undisputed GPR17 agonist [12,15,21], confirming the reproducibility of our initial findings. The most potent GPR17 antagonists published to date are the indolylsulfonamide scaffold-based I-116 [15,24] and the anthranilic acid scaffold-based PSB-24040 [23]. These and other tool compounds, in combination with knockout approaches, have enabled the evaluation of GPR17 as a potential drug target.

Role of GPR17 in pathological conditions: regulation of myelination and more

Receptor signaling: promiscuous G protein coupling and links to myelination

G proteins are heterotrimeric proteins composed of three subunits, α, β, and γ. The Gα subunit is further subdivided into four families: $G\alpha_i$ proteins inhibit adenylyl cyclases (AC) which catalyze the conversion of ATP to cyclic adenosine monophosphate (cAMP). $G\alpha_s$ proteins activate AC. $G\alpha_{q/11}$ proteins activate phospholipase C (PLC) which cleaves phosphatidylinositol 4,5-bisphosphate (PIP_2) into diacylglycerol (DAG) and inositol-1,4,5-trisphosphate (IP_3), inducing the intracellular mobilization of calcium ions from the endoplasmic reticulum. The fourth class of Gα proteins, $G\alpha_{12/13}$, activate intracellular protein kinases.

The signaling pathways associated with GPR17 activation are diverse and context-dependent. GPR17 can couple with different classes of G proteins; while coupling with $G_{i/o}$ and $G_{q/11}$ is already observed at low agonist concentrations, as reported by different groups in various assays [12,92], G_s coupling induced by the GPR17 agonist MDL 29,951 requires 50–75-fold higher concentrations, and its (patho)physiological relevance remains questionable [12].

Regulation of the myelination process by GPR17 is believed to be linked to the G_i signaling pathway induced by the receptor (Figure 1). GPR17 activation reduces intracellular cAMP production and subsequently protein kinase A (PKA) and exchange protein directly activated by cAMP 1 (EPAC1) activity, which have been proposed to inhibit OPC differentiation [12,93], although the exact role of EPAC in myelination remains elusive [94]. *Gpr17* knockout in mice resulted in elevated *Epac1* expression, downregulation of X-linked inhibitor of apoptosis associated factor 1 (*Xaf1*), a proapoptotic tumor suppressor, and activation of the extracellular-signal-regulated kinase 1/2 (ERK1/2) signaling pathway, which was previously reported to increase OPC differentiation and myelin thickness [71,95,96]. Moreover, GPR17 overexpression *in vitro* increased *Xaf1* expression, whereas GPR17 inhibition by the antagonist pranlukast or cAMP supplementation with the membrane-permeable dibutyryl-cAMP decreased *Xaf1* expression [71].

GPR17 can additionally recruit arrestin-3 (β-arrestin-2) [12,97]. It has been proposed that arrestins can initiate signaling pathways by activating ERK1/2 independently of G proteins. However, recent studies have questioned this hypothesis by demonstrating that ERK1/2 activation is undetectable in the absence of active G protein α-subunits, leading to the assumption that arrestin recruitment modulates G protein-controlled activation of ERK1/2 but may not induce signaling by itself [98].

A total of 18 different genetic variants of GPR17 have been identified, each with a frequency of less than 0.5% in the general population, and up to 1% in patients with metabolic disease. Three of those are of particular interest as they may affect the downstream signaling profile of GPR17 (Figure 2). V96 is located in TM2 at the putative coupling site to GPR17 transducers; the V96M mutation impairs coupling to G_q proteins as well as arrestin recruitment. D105 is an essential residue of the sodium-binding pocket that is highly conserved in class A GPCRs. The

D105N mutation impairs coupling with both G_q and G_i proteins but preserves arrestin recruitment. G136 is located near the proposed binding pocket of the GPR17 agonist MDL 29,951. The G136S mutation was reported to prevent GPR17 agonist-mediated cAMP and Ca^{2+} signaling and arrestin recruitment [97].

Role of GPR17 in multiple sclerosis: a novel target for remyelination

Current MS therapeutics reduce or prevent inflammation and immune activation, but are unable to restore damaged myelin sheaths [7]. GPR17 has attracted much attention as a potential MS target because of its negative role in OL differentiation and myelination. The receptor is expressed by oligodendroglial cells in human MS tissues [5]. *Gpr17* has also been reported to be upregulated in adult C57BL/6 mice after demyelination induced in three different mouse models of MS – the immune-mediated experimental autoimmune encephalitis (EAE) model [1,54] and the chemically induced cuprizone [4,54] and the lysophosphatidylcholine (LPC) models [3,4] – suggesting a potential negative impact on OL myelination (Figure 1). *Gpr17*-overexpressing mice showed severe demyelination, while knockout animals exhibited increased myelination [1,3]. In a post-periventricular leukomalacia (PVL) rat model, *Gpr17* overexpression led to myelin sheath degradation, while *Gpr17* knockdown resulted in its regeneration [6] (Table 3).

There is compelling evidence to propose GPR17 as a drug target to induce myelin repair and thus provide a disease-modifying therapeutic option for MS and potentially other demyelinating diseases. However, current animal models are used primarily to assess the potency of pharmacological interventions to accelerate myelin repair rather than their ability to induce remyelination

Table 3. Potential of GPR17 as a drug target

Disease	Evidence	Agonist or antagonist desired for therapeutic effect	Refs
Multiple sclerosis (MS)	GPR17/*Gpr17* was found to be upregulated in human MS tissues and demyelinating mouse models; *Gpr17* overexpressing mice showed increased demyelination, while *Gpr17* knockout mice showed increased myelination; *Gpr17* overexpression led to myelin sheath degradation in a PVL rat model, while *Gpr17* knockdown led to its regeneration	Antagonist	[1,3–6,54]
Neurodegenerative diseases (e.g., Alzheimer's disease, Parkinson's disease)	LPS-induced cognitive deficit coincided with increased GPR17 expression in mice. Treatment with GPR17 agonist MDL 29,951 induced cognitive deficits, and *Gpr17* knockdown prevented LPS-induced cognitive deficits. The GPR17 antagonist montelukast increased hippocampal neurogenesis and restored memory and learning in rats, while such effects were not measured in *Gpr17* knockout mouse neurospheres. The GPR17 antagonist montelukast promoted neural outgrowth in rat-brain slice cultures while the selective GPR17 agonist PSB-18484 decreased it	Antagonist	[41,42,44]
Ischemic damage, stroke, and injury	*Gpr17* antisense oligonucleotide reduced tissue damage in a mouse model of spinal cord injury; GPR17-expressing OPCs proliferated and amplified the myelination process in a mouse model of stroke	Unclear	[51,53]
Diabetes and obesity	*Gpr17* knockout 129 mice showed increased energy expenditure and energy intake, lower body weight, lower fat content, and resistance to high-fat-diet-induced glucose intolerance, in *Gpr17* knockout C57BL/6 mice only female animals showed lower body weight. *Gpr17* knockout mice showed improved glucose tolerance and insulin secretion and increased GLP-1 secretion, GPR17 expression in a murine enteroendocrine cell line constitutively decreased GLP-1 secretion which was potentiated by GPR17 agonist MDL 29,951 and reduced by GPR17 agonist HAMI3379	Antagonist	[59–61]
Bronchial asthma	*Gpr17* knockout mice showed elevated expression of $CysLT_1$ and Th2/Th17, and elevated levels of IgE and specific IgG1 after exposure to house dust mite	Unclear	[58]
Glioblastoma	GPR17 agonist CHBC led to apoptosis of GBM cells (unclear whether mediated by GPR17)	Agonist	[50]

from scratch, which limits their predictive power for human therapies [99]. Furthermore, evaluating the effect of a treatment in a clinical setting may be difficult, since identifying and objectively measuring remyelination in MS patients presents significant challenges [100,101]. And even if remyelination succeeds, it does not necessarily prevent disease progression in MS in animals, suggesting that promoting remyelination alone is unlikely to be sufficient as a therapeutic strategy [99]. Thus, combination therapies may be required: for example, combinations of remyelinating agents and disease-modifying, anti-inflammatory MS drugs.

Two other GPCR antagonists which have been claimed to induce remyelination are being clinically evaluated: the M_1-selective muscarinic acetylcholine receptor antagonist PIPE-307, which blocks the $G_{q/11}$-coupled M_1 receptor, is in Phase 2 clinical trials for RRMS, while the LPA_1 receptor antagonist PIPE-791, currently being evaluated in a Phase 1 trial, is being developed for the so far difficult-to-treat progressive types of MS [102] (www.contineum-tx.com/programs/). Interestingly, LPA_1 is coupled to G_i and $G_{q/11}$, like GPR17, in addition to $G_{12/13}$ proteins. It may be speculated that activation of both G_q and G_i protein contributes to the effects, perhaps acting synergistically.

Neurodegenerative diseases: GPR17 blockade enhances neurogenesis and cognitive function

GPR17 may contribute to the pathogenesis of neurodegenerative diseases. The receptor is upregulated in the hippocampus and cortex of mouse brain in response to an injection of $A\beta_{1-42}$, the main toxic β-amyloid (Aβ) peptide, and to inflammatory lipopolysaccharide (LPS) [43,44]. The GPR17 antagonist montelukast promoted neural outgrowth in organotypic rat-brain slice cultures, directly and through increased mRNA-expression of relevant genes. By contrast, the selective GPR17 agonist PSB-18484 decreased direct neural outgrowth [42]. In an *in vivo* study, oral treatment with montelukast increased hippocampal neurogenesis, reduced inflammation, and restored memory and learning in old Fisher 344 rats [41]. By contrast with wild-type cells, neurospheres isolated from *Gpr17* knockout mice did not proliferate in response to montelukast treatment [41]. Moreover, the GPR17 agonist MDL 29,951 induced cognitive impairment in mice [44]. In a recent clinical safety trial, montelukast was found to be well tolerated in PD patients [103] (Table 3).

The exact mechanisms underlying the observed effects, and the question of whether these results can be translated to humans, remain unclear [41,44]. Both MDL 29,951 and montelukast are non-selective, and results are likely confounded by their activation of NMDA, or $CysLT_1$ receptors, respectively.

The dual role of GPR17 in brain injury: damage propagation and repair mediation

GPR17 was reported to play a role in brain injury and ischemic damage. GPR17-expressing OPCs have been observed to accumulate at the periphery of ischemic regions, with their density increasing over time following the onset of the ischemic event [57]. The exact function of the receptor in this process is unclear. Some studies suggested that GPR17 expression contributes to the damage: in a mouse model of spinal cord injury, a *Gpr17* antisense oligonucleotide reduced tissue damage and associated deficits [51]. In an acute neuronal injury model in rat brain, *Gpr17* knockdown with small interfering RNA (siRNA) reduced damage and inhibited microgliosis [20]. In a rat subarachnoid hemorrhage model, short hairpin RNA (shRNA)-mediated *Gpr17* knockdown promoted OPC differentiation [56]. In a cellular optic nerve injury model, administration of the GPR17 antagonist montelukast stimulated the differentiation of OPCs [55]. However, other studies suggest that the subset of $GPR17^+$ OPCs may even contribute to repair processes such as remyelination. In a mouse model of stroke, $GPR17^+$ OPCs (which differentiate slowly under physiological conditions), after triggering by a sufficiently strong stimulus, migrated towards the injury site, proliferated rapidly, and even enhanced the myelination process [52–54]. $GPR17^+$ OPCs have thus been suggested to act as a 'reserve pool' of OPCs for

mediating cell death and inducing repair mechanisms [52]. A study examining the differentiation capabilities of GPR17$^+$ OPCs in two different mouse models (EAE and the cuprizone model) suggested that the specific environments of different models are likely responsible for the different behavior of GPR17$^+$ OPCs [54]. More research is required using human models (e.g., organoid cultures, and, in particular, clinical trials) to clarify the potential of GPR17 as a drug target (Table 3). Potent GPR17 antagonists – including a clinical candidate – are now available to shed light on the receptor's role in brain injuries.

GPR17 and GLP-1: implications for diabetes and obesity treatment

GPR17 is expressed in human and rodent intestinal enteroendocrine cells [60]. *Gpr17* knockout mice of an investigated strain (129 mice) displayed increased energy expenditure and energy intake, lower body weight, lower fat content, and resistance to high-fat-diet-induced glucose intolerance, compared to wild-type mice [59]. It has been suggested, however, that the metabolic effects of GPR17 deletion may vary depending on the genetic background of the animals, which complicates the interpretation of the results; in *Gpr17* knockout C57BL/6 mice, only female animals showed reduced body weight, while no other differences were found compared to wild-type mice [59]. GPR17 may function as part of an inhibitory pathway for glucagon-like peptide-1 (GLP-1) which is produced and released by enteroendocrine cells [60]. GLP-1 plays an important role in glucose metabolism and has emerged as a validated drug target for type 2 diabetes and obesity. Knockdown of *Gpr17* in intestinal cells of tamoxifen-inducible intestine-specific *Gpr17* knockout C57BL/6 mice increased GLP-1 secretion, which in turn improved glucose tolerance and insulin secretion [60]. In a murine enteroendocrine cell line stably expressing hGPR17-L, receptor expression constitutively reduced GLP-1 secretion when compared with control cells, which was further potentiated by the agonist MDL 29,951, and reduced by the antagonist HAMI3379 [61]. This effect was proposed to be mediated via $G_{i/o}$ signaling [60,61]. GPR17 antagonists may thus have potential for the treatment of diabetes and obesity by increasing GLP-1 secretion, perhaps in combination with dipeptidylpeptidase-4 (DPP4) inhibitors to prevent GLP-1 degradation (Table 3). Translation of these findings into therapeutic application will require sustained GLP-1 secretion, which will have to be demonstrated in further studies.

GPR17 in bronchial asthma: deficiency exacerbates allergic lung inflammation

In a mouse model of allergic lung inflammation, GPR17 was reported to exhibit a beneficial effect. *Gpr17* knockout resulted in elevated $CysLT_1R$ expression, Th2/Th17 cytokine release, and serum levels of immunoglobins IgE and specific IgG1 after house dust mite exposure, compared to wild-type mice [58]. The effects of GPR17 antagonists have not yet been investigated in this context, and studies in human cells have not been performed. Thus, the current evidence is still limited, and further studies are required (Table 3).

GPR17 in glioblastoma: involvement via reactive oxygen species (ROS) and cell cycle regulation

GPR17 has been reported to be expressed in GBM and to be involved in GBM initiation and progression through various GBM signaling pathways [45,46,49]. G_i protein signaling of GPR17 inhibits the transcription of ring finger protein 2 (RNF2), and the subsequent formation of poly-comb repressive complex 1 (PRC1) catalyzes histone H2A mono-ubiquitination on the kruppel-like factor 9 (KLF9) promotor. This in turn leads to an elevated expression of KLF9, and subsequently to a rise in ROS which ultimately induces apoptosis and inhibits cell proliferation [47,48]. In the human GBM cell lines LN229 and SNB19, the low-potency GPR17 agonist CHBC exhibited cell cycle arrest and cytotoxicity by reducing the mitochondrial membrane potential and by activating proapoptotic caspase 3/7 (Table 3) [50]. However, whether the observed effects are actually mediated by GPR17 remains to be demonstrated. The newly developed tool compounds will eventually allow the study of the proposed effects of GPR17 in glioblastomas.

Concluding remarks and future perspectives

GPR17 is expressed in various tissues, with prominent expression in the CNS on OPCs and pre-OLs. The receptor has been reported to affect neural development, myelination, and tissue repair. Dysregulation of GPR17 contributes to neurological and inflammatory diseases, which makes GPR17 an intriguing therapeutic target. Nonetheless, the current evidence is in most cases still unsatisfactory and sometimes even contradictory (see Outstanding questions). In addition to the fact that the physiological agonist of GPR17 is still unknown, a major obstacle in elucidating GPR17 functions has long been the lack of suitable tools. Although a cryo-EM structure of the receptor has been determined, it was obtained only in the apo-form, and not in complex with a ligand. Only recently, suitable agonists and antagonists have been discovered and optimized, and several patents describing antagonists have been filed. These will enable a broad exploration of GPR17 as a novel potential drug target. Future preclinical studies – and especially the outcome of the first, long-awaited clinical study evaluating a potent, selective antagonist – may open up new avenues for the potentially curative treatment of demyelinating diseases, including the so far difficult-to-treat progressive forms of MS, and spark up studies on further therapeutic indications.

Outstanding questions

What is the cognate agonist of GPR17?

How do GPR17 agonists and antagonists bind to the receptor and how is it activated?

What is the functional difference between the short and the long GPR17 isoforms?

How does GPR17 activation contribute to neurodegeneration and cognitive impairment in neurodegenerative diseases?

Will GPR17 antagonists induce myelin repair in patients?

Author contributions

The manuscript was written through contributions of all authors. All authors have given approval to the final version of the manuscript.

Acknowledgments

M.L. received a doctoral scholarship from the Studienstiftung des deutschen Volkes (German National Academic Foundation). C.E.M. and E.K. were supported by the BMBF (German Federal Ministry for Education and Research) within the BioPharma initiative 'Neuroallianz, Project T3', collaborative project with UCB Pharma.

Declaration of interests

E.K. and C.E.M. are coinventors of the patent 'GPR17 agonists and screening assay' [86]. C.E.M. is coinventor of the patents 'pyridinyl and pyrazinyl-(aza)indolsulfonamides' and '*N*-phenyl-indole-3-sulfonamide derivatives and related compounds as GPR17 modulators for treating CNS disorders such as multiple sclerosis' [25,27].

References

1. Chen, Y. *et al.* (2009) The oligodendrocyte-specific G protein-coupled receptor GPR17 is a cell-intrinsic timer of myelination. *Nat. Neurosci.* 12, 1398–1406
2. Cosentino, S. *et al.* (2014) Expression of dual nucleotides/cysteinyl-leukotrienes receptor GPR17 in early trafficking of cardiac stromal cells after myocardial infarction. *J. Cell. Mol. Med.* 18, 1785–1796
3. Lu, C. *et al.* (2018) G-protein-coupled receptor Gpr17 regulates oligodendrocyte differentiation in response to lysolecithin-induced demyelination. *Sci. Rep.* 8, 4502
4. Nyamoya, S. *et al.* (2019) G-protein-coupled receptor Gpr17 expression in two multiple sclerosis remyelination models. *Mol. Neurobiol.* 56, 1109–1123
5. Angelini, J. *et al.* (2021) The distribution of GPR17-expressing cells correlates with white matter inflammation status in brain tissues of multiple sclerosis patients. *Int. J. Mol. Sci.* 22, 4574
6. He, L. *et al.* (2021) Knockdown of G protein-coupled receptor-17 (GPR17) facilitates the regeneration and repair of myelin sheath post-periventricular leukomalacia (PVL). *Bioengineered* 12, 7314–7324
7. Yang, J.H. *et al.* (2022) Therapeutic advances in multiple sclerosis. *Front. Neurol.* 13, 824926
8. McGinley, M.P. *et al.* (2021) Diagnosis and treatment of multiple sclerosis: a review. *JAMA* 325, 765–779
9. Kuhlmann, T. *et al.* (2023) Multiple sclerosis progression: time for a new mechanism-driven framework. *Lancet Neurol.* 22, 78–88
10. Ciana, P. *et al.* (2006) The orphan receptor GPR17 identified as a new dual uracil nucleotides/cysteinyl-leukotrienes receptor. *EMBO J.* 25, 4615–4627
11. Maekawa, A. *et al.* (2009) GPR17 is a negative regulator of the cysteinyl leukotriene 1 receptor response to leukotriene D4. *Proc. Natl. Acad. Sci. U. S. A.* 106, 11685–11690
12. Hennen, S. *et al.* (2013) Decoding signaling and function of the orphan G protein-coupled receptor GPR17 with a small-molecule agonist. *Sci. Signal.* 6, ra93
13. Qi, A-D. *et al.* (2013) Is GPR17 a P2Y/leukotriene receptor? Examination of uracil nucleotides, nucleotide sugars, and cysteinyl leukotrienes as agonists of GPR17. *J. Pharmacol. Exp. Ther.* 347, 38–46
14. Köse, M. *et al.* (2014) Development of (3)H2-Carboxy-4,6-dichloro-1H-indole-3-propionic acid ((3)HPSB-12150): a useful tool for studying GPR17. *ACS Med. Chem. Lett.* 5, 326–330
15. Harrington, A.W. *et al.* (2023) Identification and characterization of select oxysterols as ligands for GPR17. *Br. J. Pharmacol.* 180, 401–421
16. Zhu, H. *et al.* (2024) Discovery of novel and selective GPR17 antagonists as pharmacological tools for developing new therapeutic strategies in diabetes and obesity. *bioRxiv*, Published online December 07, 2024. https://doi.org/10.1101/2024.12.04.626849
17. Eberini, I. *et al.* (2011) *In silico* identification of new ligands for GPR17: a promising therapeutic target for neurodegenerative diseases. *J. Comput. Aided Mol. Des.* 25, 743–752
18. Merten, N. *et al.* (2018) Repurposing HAM13379 to block GPR17 and promote rodent and human oligodendrocyte differentiation. *Cell Chem. Biol.* 25, 775–786.e5
19. Cahoy, J.D. *et al.* (2008) A transcriptome database for astrocytes, neurons, and oligodendrocytes: a new resource for understanding brain development and function. *J. Neurosci.* 28, 264–278

20. Zhao, B. *et al.* (2012) The new P2Y-like receptor G protein-coupled receptor 17 mediates acute neuronal injury and late microgliosis after focal cerebral ischemia in rats. *Neuroscience* 202, 42–57
21. Baqi, Y. *et al.* (2018) 3-(2-Carboxyethyl)indole-2-carboxylic acid derivatives: structural requirements and properties of potent agonists of the orphan G protein-coupled receptor GPR17. *J. Med. Chem.* 61, 8136–8154
22. Pillaiyar, T. *et al.* (2020) Design, synthesis and biological evaluation of suramin-derived dual antagonists of the proinflammatory G protein-coupled receptors P2Y2 and GPR17. *Eur. J. Med. Chem.* 186, 111789
23. Boshta, N.M. *et al.* (2024) Discovery of anthranilic acid derivatives as antagonists of the pro-inflammatory orphan G protein-coupled receptor GPR17. *J. Med. Chem.* 67, 19365–19394
24. Mueller, C.E. *et al.* UCB Pharma GmbH. (Aza)indole-, benzothiophene-, and benzofuran-3-sulfonamides, WO 2018/122232 A1
25. Pegurier, C. *et al.* UCB Pharma GmbH. Pyridinyl and pyrazinyl-(aza)indolsulfonamides, WO 2019/243303 A1
26. Pegurier, C. *et al.* UCB Pharma GmbH. Substituted alkoxypyridinyl indolsulfonamides, WO 2019/243398 A1
27. Pegurier, C. *et al.* UCB Pharma GmbH. N-(phenyl)-indole-3-sulfonamide derivatives and related compounds as GPR17 modulators for treating CNS disorders such as multiple sclerosis, WO 2020/254289 A1
28. Galley, G. *et al.* Novel pyrimidin-2-yl sulfonamide derivatives, WO 2022/180136 A1
29. Galley, G. *et al.* Novel imidazopyridine and pyrazolopyridine sulfonamide derivatives, WO 2024/017857 A1
30. Galley, G. *et al.* Novel isoquinolinone, pyrrolopyridinone and thienopyridinone sulfonamide derivatives, WO 2024/017856 A1
31. Galley, G. *et al.* Novel isothiazol-3-yl and isoxazol-3-yl sulfonamide compounds, WO 2024/017855 A1
32. Galley, G. *et al.* Novel naphthyl and isoquinoline sulfonamide derivatives, WO 2024/017858 A1
33. Galley, G. *et al.* Novel pyrimidinyl and triazinyl sulfonamide derivatives, WO 2024/017863 A1
34. Galley, G. *et al.* Novel 7-substituted indole sulfonamide derivatives, WO 2024/023129 A1
35. Galley, G. *et al.* Novel 7-substituted indole sulfonamide derivatives, WO 2024/023128 A1
36. Galley, G. *et al.* Novel deuterated pyrimidin-2-yl sulfonamide derivatives, WO 2024/042147 A2
37. Pinto, R.M.G.C. *et al.* Rewind Therapeutics NV. Fused pyrrolyl-sulfonamide compounds, WO 2024/115733 A1
38. Han, X. *et al.* Myrobalan Therapeutics Nanjing Co. Ltd. GPR17 modulators and uses thereof, WO 2024/104462 A1
39. Xi, J. *et al.* Nanjing Immunophage Biotech Co. Ltd. Compounds and their uses as GPR17 antagonists, WO 2024/153233 A1
40. Capacci, A. *et al.* Biogen Ma Inc. [US]. Indole and pyrrolopyridine derivatives as GPR17 modulators, WO 2025/038863
41. Marschallinger, J. *et al.* (2015) Structural and functional rejuvenation of the aged brain by an approved anti-asthmatic drug. *Nat. Commun.* 6, 8466
42. Braune, M. *et al.* (2021) Involvement of GPR17 in neuronal fibre outgrowth. *Int. J. Mol. Sci.* 22, 11683
43. Jin, S. *et al.* (2021) Inhibition of GPR17 with cangrelor improves cognitive impairment and synaptic deficits induced by Aβ1-42 through Nrf2/HO-1 and NF-κB signaling pathway in mice. *Int. Immunopharmacol.* 101, 108335
44. Liang, Y. *et al.* (2023) Knockdown and inhibition of hippocampal GPR17 attenuates lipopolysaccharide-induced cognitive impairment in mice. *J. Neuroinflammation* 20, 271
45. Dougherty, J.D. *et al.* (2012) Candidate pathways for promoting differentiation or quiescence of oligodendrocyte progenitor-like cells in glioma. *Cancer Res.* 72, 4856–4868
46. Johnson, R.M. *et al.* (2020) Development of a gene expression-based prognostic signature for IDH wild-type glioblastoma. *Neuro-Oncology* 22, 1742–1756
47. Barbour, H. *et al.* (2020) Polycomb group-mediated histone H2A monoubiquitination in epigenome regulation and nuclear processes. *Nat. Commun.* 11, 5947
48. Liu, H. *et al.* (2021) G-protein-coupled receptor GPR17 inhibits glioma development by increasing polycomb repressive complex 1-mediated ROS production. *Cell Death Dis.* 12, 610
49. Mutharasu, G. *et al.* (2022) Transcriptomic analysis of glioblastoma multiforme providing new insights into GPR17 signaling communication. *J. Biomol. Struct. Dyn.* 40, 2586–2599
50. Nguyen, P. *et al.* (2022) GPR17 signaling activation by CHBC agonist induced cell death via modulation of MAPK pathway in glioblastoma. *Life Sci.* 291, 120307
51. Ceruti, S. *et al.* (2009) The P2Y-like receptor GPR17 as a sensor of damage and a new potential target in spinal cord injury. *Brain* 132, 2206–2218
52. Viganò, F. *et al.* (2016) GPR17 expressing NG2-Glia: oligodendrocyte progenitors serving as a reserve pool after injury. *Glia* 64, 287–299
53. Bonfanti, E. *et al.* (2017) The role of oligodendrocyte precursor cells expressing the GPR17 receptor in brain remodeling after stroke. *Cell Death Dis.* 8, e2871
54. Coppolino, G.T. *et al.* (2018) Differential local tissue permissiveness influences the final fate of GPR17-expressing oligodendrocyte precursors in two distinct models of demyelination. *Glia* 66, 1118–1130
55. Wang, J. *et al.* (2020) Robust myelination of regenerated axons induced by combined manipulations of GPR17 and microglia. *Neuron* 108, 876–886.e4
56. Wang, Y. *et al.* (2023) Inhibition of GPR17/ID2 axis improve remyelination and cognitive recovery after SAH by mediating OPC differentiation in rat model. *Transl. Stroke Res.* 16, 178–193
57. Raffaele, S. *et al.* (2025) Characterisation of GPR17-expressing oligodendrocyte precursors in human ischaemic lesions and correlation with reactive glial responses. *J. Pathol.* 265, 226–243
58. Maekawa, A. *et al.* (2010) GPR17 regulates immune pulmonary inflammation induced by house dust mites. *J. Immunol.* 185, 1846–1854
59. Wargent, E.T. *et al.* (2021) Leanness and low plasma leptin in GPR17 knockout mice are dependent on strain and associated with increased energy intake that is not suppressed by exogenous leptin. *Front. Endocrinol. (Lausanne)* 12, 698115
60. Yan, S. *et al.* (2022) Intestinal Gpr17 deficiency improves glucose metabolism by promoting GLP-1 secretion. *Cell Rep.* 38, 110179
61. Conley, J.M. *et al.* (2025) G protein-coupled receptor 17 inhibits glucagon-like peptide-1 secretion via a Gi/o-dependent mechanism in enteroendocrine cells. *Biomolecules* 15, 9
62. Ye, F. *et al.* (2022) Cryo-EM structure of G-protein-coupled receptor GPR17 in complex with inhibitory G protein. *MedComm* 3, e159
63. Konda Mani, S. *et al.* (2023) Structural analysis of human G-protein-coupled receptor 17 ligand binding sites. *J. Cell. Biochem.* 124, 533–544
64. Maekawa, A. *et al.* (2001) Identification in mice of two isoforms of the cysteinyl leukotriene 1 receptor that result from alternative splicing. *Proc. Natl. Acad. Sci. U. S. A.* 98, 2256–2261
65. Benned-Jensen, T. and Rosenkilde, M.M. (2010) Distinct expression and ligand-binding profiles of two constitutively active GPR17 splice variants. *Br. J. Pharmacol.* 159, 1092–1105
66. Michel, M.C. *et al.* (2009) How reliable are G-protein-coupled receptor antibodies? Naunyn Schmiedebergs. *Arch. Pharmacol.* 379, 385–388
67. Spellman, M. *et al.* (2024) Signaling of GPR17 in hepatic and renal tissues. *Physiology*, Published online May 21, 2024. https://doi.org/10.1152/physiol.2024.39.S1.1524
68. Rivera, A.D. *et al.* (2021) Keeping the ageing brain wired: a role for purine signalling in regulating cellular metabolism in oligodendrocyte progenitors. *Pflugers Arch.* 473, 775–783
69. von Bernhardi, J.E. and Dimou, L. (2022) Oligodendrogenesis is a key process for cognitive performance improvement induced by voluntary physical activity. *Glia* 70, 1052–1067
70. Fang, M. *et al.* (2023) The committed oligodendrocyte precursor cell, a newly-defined intermediate progenitor cell type in oligodendroglial lineage. *Glia* 71, 2499–2510
71. Ou, Z. *et al.* (2016) Olig2-targeted G-protein-coupled receptor Gpr17 regulates oligodendrocyte survival in response to lysolecithin-induced demyelination. *J. Neurosci.* 36, 10560–10573
72. Fumagalli, M. *et al.* (2015) The ubiquitin ligase Mdm2 controls oligodendrocyte maturation by intertwining mTOR with G

protein-coupled receptor kinase 2 in the regulation of GPR17 receptor desensitization. *Glia* 63, 2327–2339
73. Boccazzi, M. *et al.* (2023) G protein-coupled receptor 17 is regulated by WNT pathway during oligodendrocyte precursor cell differentiation. *Neurobiol. Dis.* 187, 106315
74. Marangon, D. *et al.* (2022) Rewiring of glucose and lipid metabolism induced by G protein-coupled receptor 17 silencing enables the transition of oligodendrocyte progenitors to myelinating cells. *Cells* 11, 2369
75. Miralles, A.J. *et al.* (2023) Analysis of the GPR17 receptor in NG2-glia under physiological conditions unravels a new subset of oligodendrocyte progenitor cells with distinct functions. *Glia* 71, 1536–1552
76. Koenen, A. *et al.* (2017) The DRF motif of CXCR6 as chemokine receptor adaptation to adhesion. *PLoS One* 12, e0173486
77. Simon, K. *et al.* (2017) The orphan receptor GPR17 is unresponsive to uracil nucleotides and cysteinyl leukotrienes. *Mol. Pharmacol.* 91, 518–532
78. Lemoine, F. *et al.* (2019) NGPhylogeny.fr: new generation phylogenetic services for non-specialists. *Nucleic Acids Res.* 47, W260–W265
79. Junier, T. and Zdobnov, E.M. (2010) The Newick utilities: high-throughput phylogenetic tree processing in the UNIX shell. *Bioinformatics* 26, 1669–1670
80. Katoh, K. and Standley, D.M. (2013) MAFFT multiple sequence alignment software version 7: improvements in performance and usability. *Mol. Biol. Evol.* 30, 772–780
81. Criscuolo, A. and Gribaldo, S. (2010) BMGE (Block Mapping and Gathering with Entropy): a new software for selection of phylogenetic informative regions from multiple sequence alignments. *BMC Evol. Biol.* 10, 210
82. Guindon, S. *et al.* (2010) New algorithms and methods to estimate maximum-likelihood phylogenies: assessing the performance of PhyML 3.0. *Syst. Biol.* 59, 307–321
83. Lemoine, F. *et al.* (2018) Renewing Felsenstein's phylogenetic bootstrap in the era of big data. *Nature* 556, 452–456
84. Letunic, I. and Bork, P. (2024) Interactive Tree of Life (iTOL) v6: recent updates to the phylogenetic tree display and annotation tool. *Nucleic Acids Res.* 52, W78–W82
85. Herrera, L.P.T. *et al.* (2025) GPCRdb in 2025: adding odorant receptors, data mapper, structure similarity search and models of physiological ligand complexes. *Nucleic Acids Res.* 53, D425–D435
86. Kostenis, E. *et al.* Rheinische Friedrich-Wilhelms-Universität Bonn. GPR17 agonists and screening assay, EP 2 567 698 A1
87. Salituro, F.G. *et al.* (1990) 3-(2-carboxyindol-3-yl)propionic acid derivatives: antagonists of the strychnine-insensitive glycine receptor associated with the N-methyl-D-aspartate receptor complex. *J. Med. Chem.* 33, 2944–2946
88. Saravanan, K.M. *et al.* (2018) Identification of novel GPR17-agonists by structural bioinformatics and signaling activation. *Int. J. Biol. Macromol.* 106, 901–907
89. Doan, P. *et al.* (2021) Alkylaminophenol and GPR17 agonist for glioblastoma therapy: a combinational approach for enhanced cell death activity. *Cells* 10, 1975
90. Parravicini, C. *et al.* (2020) Development of the first in vivo GPR17 ligand through an iterative drug discovery pipeline: a novel disease-modifying strategy for multiple sclerosis. *PLoS One* 15, e0231483
91. Pugliese, A.M. *et al.* (2009) Functional characterization of two isoforms of the P2Y-like receptor GPR17: 35SGTPgammaS binding and electrophysiological studies in 1321N1 cells. *Am. J. Physiol. Cell Physiol.* 297, C1028–C1040
92. Inoue, A. *et al.* (2019) Illuminating G-protein-coupling selectivity of GPCRs. *Cell* 177, 1933–1947.e25
93. Simon, K. *et al.* (2016) The orphan G protein-coupled receptor GPR17 negatively regulates oligodendrocyte differentiation via Gαi/o and its downstream effector molecules. *J. Biol. Chem.* 291, 705–718
94. Gao, Z-Z. *et al.* (2020) EPAC negatively regulates myelination via controlling proliferation of oligodendrocyte precursor cells. *Neurosci. Bull.* 36, 639–648
95. Liston, P. *et al.* (2001) Identification of XAF1 as an antagonist of XIAP anti-caspase activity. *Nat. Cell Biol.* 3, 128–133
96. Gonsalvez, D. *et al.* (2016) The roles of extracellular related-kinases 1 and 2 signaling in CNS myelination. *Neuropharmacology* 110, 586–593
97. Conley, J.M. *et al.* (2021) Human GPR17 missense variants identified in metabolic disease patients have distinct downstream signaling profiles. *J. Biol. Chem.* 297, 100881
98. Wess, J. *et al.* (2023) β-arrestins: structure, function, physiology, and pharmacological perspectives. *Pharmacol. Rev.* 75, 854–884
99. Kipp, M. (2016) Remyelination strategies in multiple sclerosis: a critical reflection. *Expert. Rev. Neurother.* 16, 1–3
100. Plemel, J.R. *et al.* (2017) Remyelination therapies: a new direction and challenge in multiple sclerosis. *Nat. Rev. Drug Discov.* 16, 617–634
101. Neumann, B. *et al.* (2020) Problems and pitfalls of identifying remyelination in multiple sclerosis. *Cell Stem Cell* 26, 617–619
102. Chen, K. *et al.* (2025) Enhancing remyelination in multiple sclerosis via M1 muscarinic acetylcholine receptor. *Mol. Pharmacol.* 107, 100027
103. Wallin, J. *et al.* (2025) Effects of montelukast on neuroinflammation in Parkinson's disease: an open label safety and tolerability trial with CSF markers and 11CPBR28 PET. *Mov. Disord.* 40, 739–744
104. Heppenstall, P.A. and Fleetwood-Walker, S.M. (1997) The glycine site of the NMDA receptor contributes to neurokinin1 receptor agonist facilitation of NMDA receptor agonist-evoked activity in rat dorsal horn neurons. *Brain Res.* 744, 235–245
105. Nguyen, P. *et al.* (2021) Synthesis and preclinical validation of novel indole derivatives as a GPR17 agonist for glioblastoma treatment. *J. Med. Chem.* 64, 10908–10918
106. Kaza, E.A. *et al.* (2017) P2Y12 receptor function and response to cangrelor in neonates with cyanotic congenital heart disease. *JACC Basic Transl. Sci.* 2, 465–476
107. Grasa, L. *et al.* (2009) P2Y(1) receptors mediate inhibitory neuromuscular transmission in the rat colon. *Br. J. Pharmacol.* 158, 1641–1652
108. Lynch, K.R. *et al.* (1999) Characterization of the human cysteinyl leukotriene CysLT1 receptor. *Nature* 399, 789–793
109. Gusach, A. *et al.* (2019) Structural basis of ligand selectivity and disease mutations in cysteinyl leukotriene receptors. *Nat. Commun.* 10, 5573
110. Ni, N.C. *et al.* (2011) A selective cysteinyl leukotriene receptor 2 antagonist blocks myocardial ischemia/reperfusion injury and vascular permeability in mice. *J. Pharmacol. Exp. Ther.* 339, 768–778
111. Wunder, F. *et al.* (2010) Pharmacological characterization of the first potent and selective antagonist at the cysteinyl leukotriene 2 (CysLT(2)) receptor. *Br. J. Pharmacol.* 160, 399–409
112. Ashrafzadeh, S. *et al.* (2024) Scoring alignments by embedding vector similarity. *Brief. Bioinform.* 25, bbae178

14.2 Publication II. Discovery of Anthranilic Acid Derivatives as Antagonists of the Pro-Inflammatory Orphan G Protein-Coupled Receptor GPR17

Journal of Medicinal Chemistry

pubs.acs.org/jmc

Article

Discovery of Anthranilic Acid Derivatives as Antagonists of the Pro-Inflammatory Orphan G Protein-Coupled Receptor GPR17

Nader M. Boshta,[‖] Michael Lewash,[‖] Meryem Köse, Vigneshwaran Namasivayam, Soumya Sarkar, Jan H. Voss, Andy J. Liedtke, Anna Junker, Maoqun Tian, Anne Stößel, Mahmoud Rashed, Ahmed Mahal, Nicole Merten, Cécile Pegurier, Jörg Hockemeyer, Evi Kostenis, and Christa E. Müller*

Cite This: *J. Med. Chem.* 2024, 67, 19365−19394

Read Online

ACCESS | Metrics & More | Article Recommendations | Supporting Information

ABSTRACT: The G protein-coupled receptor 17 (GPR17) is an orphan receptor involved in inflammatory diseases. GPR17 antagonists have been proposed for the treatment of multiple sclerosis due to their potential to induce remyelination. Potent, selective antagonists are required to enable target validation. In the present study, we describe the discovery of a novel class of GPR17 antagonists based on an anthranilic acid scaffold. The compounds' potencies were evaluated in calcium mobilization and radioligand binding assays, and structure−activity relationships were analyzed. Selected antagonists were additionally studied in cAMP and G protein activation assays. The most potent antagonists were 5-methoxy-2-(5-(3′-methoxy-[1,1′-biphenyl]-2-yl)furan-2-carboxamido)benzoic acid (**52**, PSB-22269, K_i 8.91 nM) and its 3′-trifluoromethyl analog (**54**, PSB-24040, K_i 83.2 nM). Receptor−ligand docking studies revealed that the compounds' binding site is characterized by positively charged arginine residues and a lipophilic pocket. These findings yield valuable insights into this poorly characterized receptor providing a basis for future drug development.

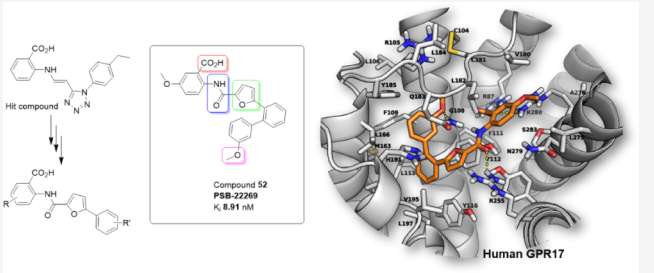

INTRODUCTION

G protein-coupled receptors (GPCRs), the largest family of cell membrane receptors, are involved in the transduction of extracellular signals to the cytosolic compartment.[1] They constitute an important class of drug targets, as more than 30% of all approved drugs interact with GPCRs, and many more are in preclinical or clinical development.[2] For a significant number of the more than 800 human GPCRs, the physiological agonist is still unknown or unconfirmed. Many of these orphan receptors belong to the δ-branch of the rhodopsin-like class A GPCR subfamily, which contains nucleotide-, peptide-, and lipid-activated receptors involved in inflammation and immunity. They are considered promising targets for future drugs. GPR17 belongs to this receptor subfamily and has great potential as a novel drug target. Synthetic agonists of GPR17 were identified which have enabled screening campaigns in the search for antagonists.[3−5] The receptor is mainly coupled to G_q and G_i proteins mediating intracellular calcium mobilization via phospholipase C activation and a decrease in cAMP concentrations by inhibition of adenylate cyclase. At higher agonist concentrations, G_s coupling can also be observed, then resulting in an increase in intracellular cAMP concentrations.[3]

GPR17 is highly conserved in vertebrates (the mouse and rat orthologs are identical and show 93% amino acid sequence identity to the human ortholog). The most closely related GPCRs based on sequence similarity are the cysteinylleukotriene receptors $CysLT_1$ and $CysLT_2$, the lysophosphatidic acid receptors LPA_4, LPA_5, and LPA_6, the nucleotide-activated $P2Y_1$ receptor, the oxoglutarate receptor, and the orphan receptors GPR65 and GPR183 (all with an amino acid sequence similarity of 50−55%).

GPR17 is highly expressed in the central nervous system (CNS) and, to a lower extent, in heart and kidneys. Transient expression has been observed in specific maturation stages of oligodendrocytes, namely, in oligodendrocyte precursor cells (OPCs) and in preoligodendrocytes (pre-OLs). Oligodendrocytes form the myelin sheath around axons, and GPR17 has been reported to play a role in the myelination process.[6−11]

GPR17 is involved in inflammatory diseases. GPR17 upregulation was observed in human multiple sclerosis (MS) plaques, and in animal models of MS, a disease characterized by demyelination, insufficient remyelination, and axon degeneration.[6,11−16] The receptor also seems to be involved in $CysLT_1$-mediated allergic inflammation and cytokine

Received: July 27, 2024
Revised: October 2, 2024
Accepted: October 8, 2024
Published: November 1, 2024

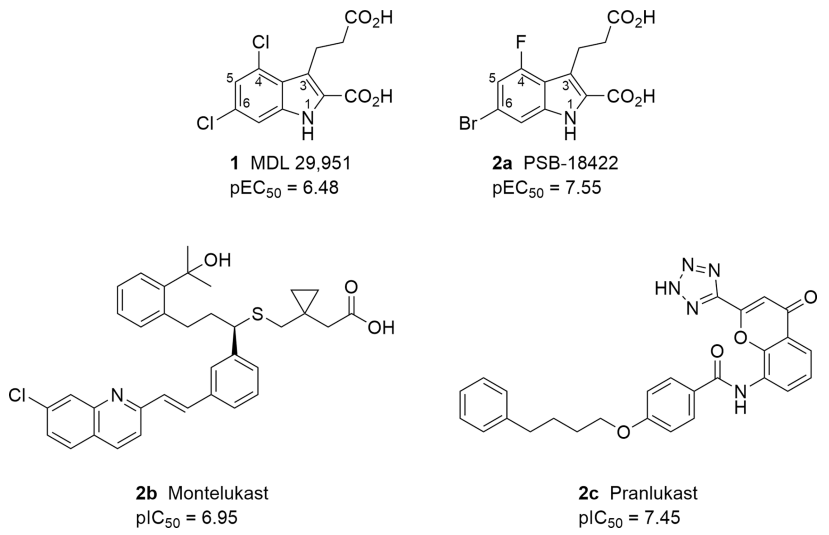

Figure 1. First synthetic GPR17 agonist MDL 29,951 and optimized, highly potent analog PSB-18422.[3,4] Synthetic antagonists montelukast and pranlukast.[12,27,30,31] pEC_{50} and pIC_{50} values were determined using calcium mobilization assays in 1321N1 astrocytoma cells stably transfected with the human GPR17 (for **2b** and **2c**, see Figure S45).

expression in lung.[17] GPR17 was reported to be upregulated after ischemic or traumatic CNS injury, a state in which axon remyelination is needed.[18] Moreover, GPR17 was reported to inhibit tumor growth by increasing the production of reactive oxygen species in glioblastoma multiforme,[19−21] and to increase appetite and to reduce metabolism as an effector of the forkhead box protein O1 (FOXO1) in agouti-related peptide neurons.[22] Therefore, pharmacological interventions aimed at modulating GPR17 activity hold significant therapeutic potential.

Several studies have proposed physiological agonists for GPR17, including nucleotides (UDP, UDP-glucose, UDP-galactose), and lipids (LTC_4, LTD_4, 24-(*S*)-hydroxycholesterol).[12,23−25] None of them has been unambiguously confirmed so far; in fact, several groups, including ours, have not been able to reproduce these published results.[3,24,26,27] Therefore, GPR17 remains an orphan receptor.

Meanwhile, synthetic surrogate agonists have been discovered: the first one was the indole derivative MDL 29,951 (**1**, EC_{50} = 0.331 μM),[3] which had previously been developed as an *N*-methyl-D-aspartate (NMDA) receptor antagonist (see Figure 1).[28] Köse et al. developed the corresponding radioligand [^{3}H]PSB-12150, which allowed the determination of binding affinities of GPR17 ligands.[29] Baqi et al. studied structure−activity relationships of **1** and identified PSB-18422 (**2a**, EC_{50} = 0.0279 μM), a GPR17 agonist showing increased potency (Figure 1).[4]

Only few, weakly potent GPR17 antagonists have been described so far, e.g., the $CysLT_1$ receptor antagonists montelukast (**2b**) and pranlukast (**2c**) (Figure 1).[12,27,30,31]

In the present study, we describe the discovery of a novel class of GPR17 antagonists based on an anthranilic acid scaffold. In a high-throughput-screening campaign, the commercially available anthranilic acid derivative (*E*)-2-((2-(1-(4-ethylphenyl)-1*H*-tetrazol-5-yl)vinyl)amino)benzoic acid (**3**, CAS: 329762−07−4, see Figure 2) was discovered to block GPR17, showing 65% inhibition at a concentration of 5 μM determined in a fluorescence-based calcium mobilization assay in a recombinant GPR17-expressing cell line. Structural variations of hit compound **3** were performed, and the compounds were evaluated in radioligand binding and functional assays to study the structure−activity relationships (SARs) of this class of compounds.

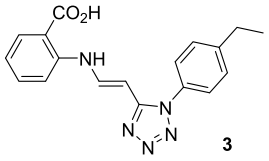

Figure 2. GPR17 antagonist hit compound **3**.

Moreover, we investigated the novel antagonists' binding mode by performing docking studies based on a homology model and a recently described cryo-electron microscopy (cryo-EM) structure of GPR17.[32]

RESULTS AND DISCUSSION

Design. The structure of hit compound **3** can be divided into four parts (see Figure 3): the anthranilic acid moiety (red), the enamine moiety (blue), the tetrazole ring (green), and the aromatic moiety attached to the heterocycle (black). Optimization with the goal to improve potency led to novel anthranilic acid derivatives described by general formula **I** (Figure 3). In most of the derivatives, the (substituted) anthranilic acid moiety was preserved. Replacement of the carboxylic acid was also tried in order to reduce polarity and thereby potentially improve physicochemical and pharmacokinetic properties. In all derivatives, the central enamine group was exchanged by an amide group, which was expected to be more stable[33,34] and discovered to be well tolerated. Among several linking heterocycles, a furan moiety substituted at positions 2 and 5 led to the best results and was therefore present in most of the targeted compounds (general formula **II**). Finally, the terminal phenyl ring, attached to the central heterocycle (i.e., the furan ring in **II**) was replaced by (substituted) phenyl, biphenyl, or naphthyl residues.

Chemistry. Novel anthranilic acid *N*-carboxamide derivatives were synthesized as depicted in Schemes 1−6 . All new compounds (**7−25, 31−49, 51−60, 64−70, 74−76, 79−84**) were fully characterized and biologically evaluated as GPR17

https://doi.org/10.1021/acs.jmedchem.4c01755
J. Med. Chem. 2024, 67, 19365−19394

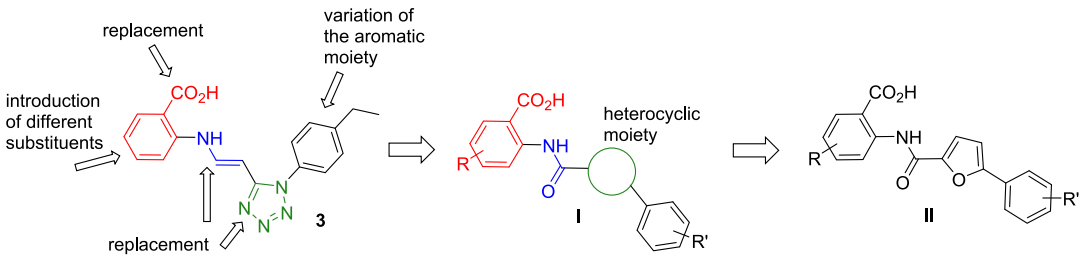

Figure 3. Compound design based on hit compound **3**.

Scheme 1. Synthesis of 2-(5-Phenylfuran-2-carboxamido)- and 5-Methoxy-2-(5-phenylfuran-2-carboxamido)benzoic Acid Derivatives 7−25[a]

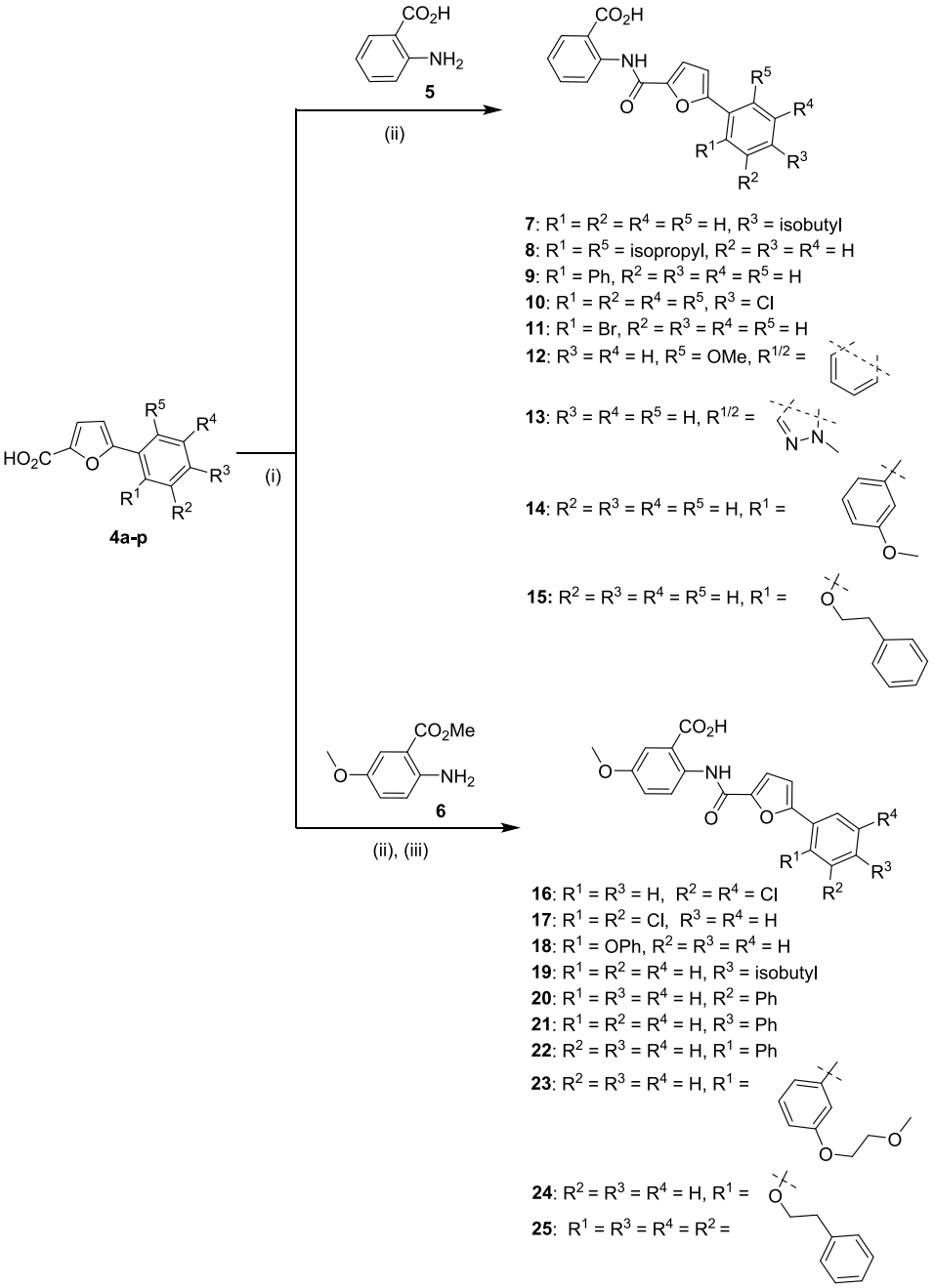

[a]Reagents and conditions: (i) $SOCl_2$, DCM, reflux, 3 h; (ii) diisopropylethylamine (DIPEA), DCM, rt, 16 h; (iii) THF/MeOH/H_2O (2:1:2), NaOH, 35 °C, 12 h.

https://doi.org/10.1021/acs.jmedchem.4c01755
J. Med. Chem. 2024, 67, 19365−19394

Scheme 2. Synthesis of 2-(Furan-2-carboxamido)benzoic Acid Derivatives Bearing a Naphthalene-1-yl or a 2-Isopropylphenyl Residue at the Furan 5-Position (31−49)[a]

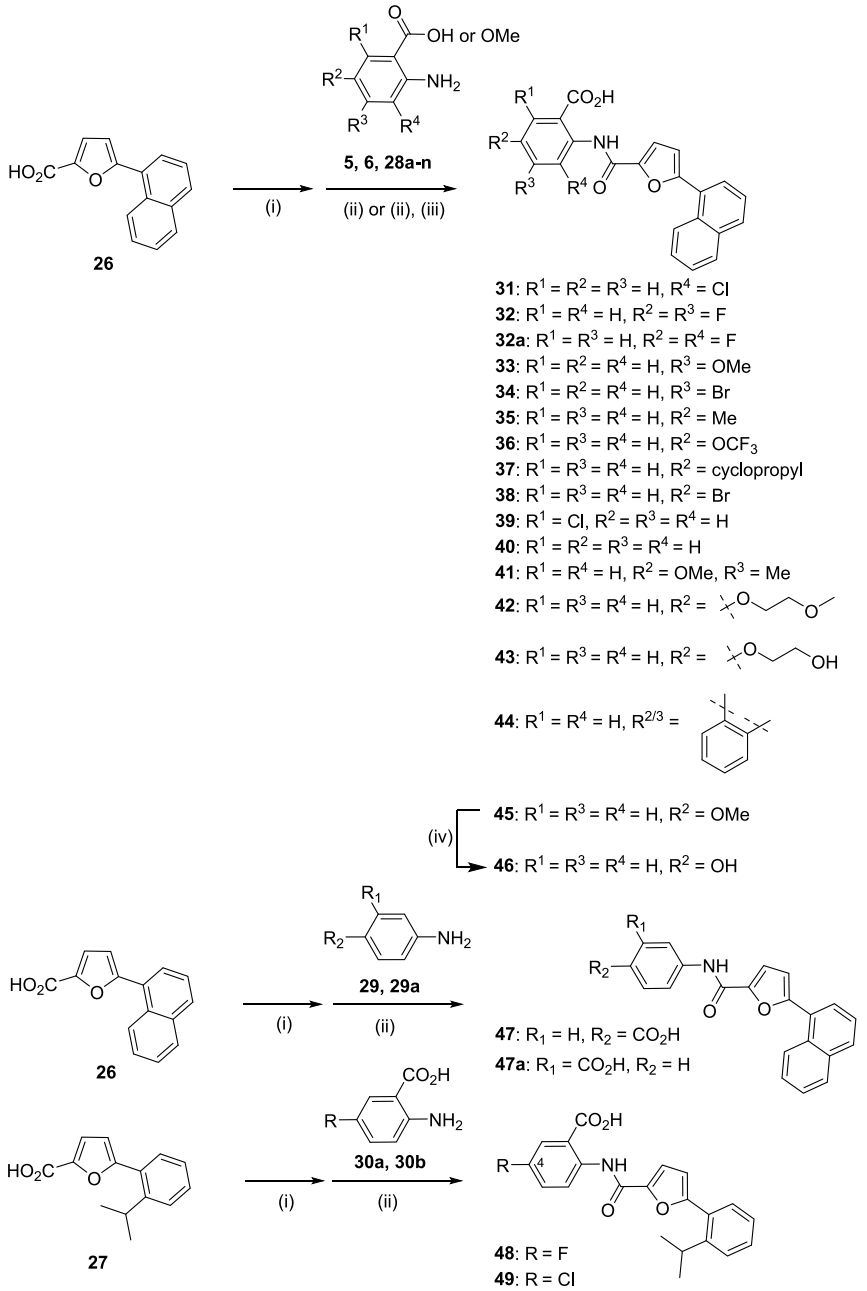

[a]Reagents and conditions: (i) $SOCl_2$, DCM, reflux, 3 h; (ii) DIPEA, DCM, rt, 16 h; (iii, only when the methyl esters were used) THF/MeOH/H_2O (2:1:2), NaOH, 35 °C, 12 h; (iv) BBr3, DCM, rt, 16 h.

antagonists. Most of the final anthranilic acid *N*-carboxamides were synthesized by reaction of an appropriately substituted carboxylic acid chloride (formed in situ from the corresponding free acid) with an anthranilic acid derivative in the presence of a base. Employing the free anthranilic acid generally led to good yields. When a methyl ester of the anthranilic acid was used, saponification to the final product was performed. A series of anthranilic acid furan-(5-phenyl)carboxamides was synthesized to explore the substitution pattern on the phenyl moiety. The furan-(5-phenyl)carboxylic acids (**4a**−**p**) were synthesized by various procedures (Scheme 1).

Starting from 5-(naphthalen-1-yl)furan-2-carboxylic acid (**26**), a large number of derivatives was synthesized with the aim to explore the optimal substitution pattern of the anthranilic acid moiety (Scheme 3). The carboxylic acid **26** was converted to its acid chloride and subsequently reacted with various substituted anthranilic acids or their methyl esters (**28**), respectively, in the presence of a base. When methyl ester-protected anthranilic acids were used, the final products could be obtained after hydrolysis, followed by purification by column chromatography on silica gel. Derivative **46** bearing a free OH group at the 5-position of the anthranilic acid moiety was obtained from its methoxy derivative, compound **45**, by demethylation using boron tribromide in DCM at rt. Starting from 5-(2-isopropylphenyl)furan-2-carboxylic acid (**27**), two anthranilic acid derivatives were prepared, bearing either a

https://doi.org/10.1021/acs.jmedchem.4c01755
J. Med. Chem. 2024, 67, 19365−19394

Scheme 3. Synthesis of 2-(5-([1,1′-Biphenyl]-2-yl)furan-2-carboxamido)-5-methoxybenzoic Acid Derivatives (51−60)[a]

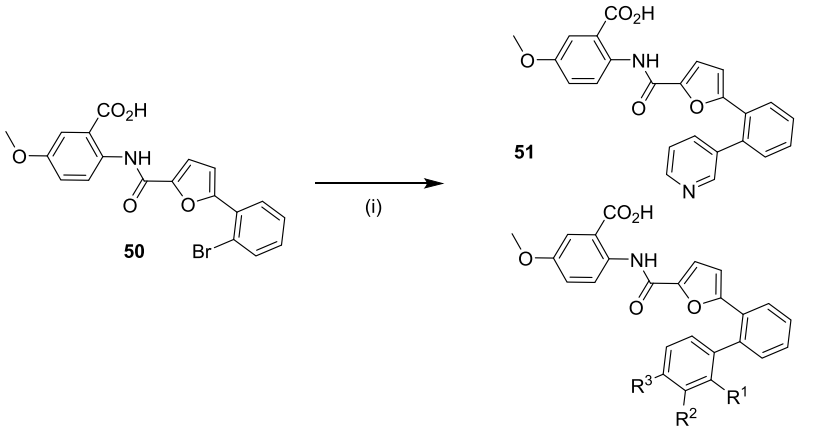

52: $R^1 = R^3 = H$, $R^2 = OCH_3$
53: $R^1 = R^3 = H$, $R^2 = CN$
54: $R^1 = R^3 = H$, $R^2 = CF_3$
55: $R^1 = R^3 = H$, R^2 = isopropyl
56: $R^1 = R^3 = H$, R^2 = cyclopropoxy
57: $R^1 = R^2 = H$, $R^3 = OCH_3$
58: $R^1 = OCH_3$, $R^2 = R^3 = H$
59: $R^1 = R^3 = H$, $R^2 = CH_2OH$
60: $R^1 = R^3 = H$, $R^2 = SO_2Me$

[a]Reagents and conditions: (i) Aryl boronic acid (1.2 equiv), Na_2CO_3 (2.0 equiv), $Pd(PPh_3)_4$ (0.05 equiv), DME/H_2O, Ar, 80 °C, 16 h.

fluorine or a chlorine atom at the 5-position of the anthranilic acid moiety (compounds **48** and **49**). Again, amide formation was achieved by reaction of the anthranilic acid derivative **30** with the furan carboxylic acid chloride in the presence of diisopropylethylamine (DIPEA) (Scheme 2).

A different synthetic pathway was pursued to obtain compounds **51−60,** characterized by a 5-methoxy-substituted anthranilic acid moiety and differently substituted biphenyl residues attached to the 5-position of the 2-furancarboxylic acid. Compound **50** was reacted with the appropriate aryl boronic acid derivative in the presence of a base and tetrakis(triphenylphosphine)palladium(0) as a catalyst in DME/H_2O at 80 °C. Moderate to good yields of the final products **51−60** were obtained (Scheme 3).

Next, the central furan moiety of the scaffold was replaced by 5- or 6-membered heterocycles to further explore the SARs (Scheme 4). A series of pyridine derivatives (**64−67**) was synthesized by condensation of 6-(naphthalen-1-yl)picolinic acid (**61**) or 6-(naphthalen-1-yl)nicotinic acid (**61a**), respectively, via their acid chlorides, with appropriate anthranilic acid derivatives (**6**, **28b**, **30a**, **30b**, or **63**) under basic conditions at rt. Furthermore, one derivative bearing a central saturated piperidine moiety was synthesized starting from the acid chloride of 1-(naphthalen-1-yl)piperidine-4-carboxylic acid (**61b**) and the anthranilic acid methyl ester **30a** in the presence of a base at rt yielding compound **67a** after final saponification.

Moreover, anthranilic acid derivatives with a central thiazole ring were synthesized (Scheme 4). Acid chlorides prepared from the appropriate thiazole carboxylic acids, bearing a naphthalen-1-yl moiety at the 2-position of the central thiazole ring (**62**), were coupled at rt with 5-substituted anthranilic acids (**6, 28h, 30a**) in the presence of a base. After purification by column chromatography on silica gel compounds **64−70** were obtained in yields of 27 to 83%.

Several derivatives were synthesized, in which the carboxyl group of the anthranilic acid moiety was replaced by an NH-acidic 5-membered heterocycle. To this end, 3-(2-aminophenyl)-1,2,4-oxadiazol-5(4*H*)-one[35] (**71**) and 2-(2*H*-tetrazol-5-yl)aniline[36] (**72**) were reacted with the acid chlorides of the 5-arylfuran-2-carboxylic acid derivative **4h** or **73**, respectively, in the presence of a base at rt yielding products **74−76** (Scheme 5).

Compounds bearing a neutral substituent as a replacement for the carboxylic acid were synthesized as described above by reaction of compounds **77** and **78a−c** with the carboxylic acid derivatives **4c** and **26** resulting in the final products **79−82**. Compounds **83** and **84** were both obtained by oxidation of **82** using *m*-chloroperbenzoic acid (1.4 equiv for **83**, 4.5 equiv for **84**) (Scheme 6).

Pharmacological Evaluation. The new anthranilic acid derivatives were initially screened for their potency to inhibit GPR17-induced Gq protein-mediated calcium mobilization. A Chinese hamster ovary (CHO) cell line stably expressing the human GPR17 under the control of a tetracycline-inducible promoter was employed that was previously generated using the Flp-In T-REx (FITR) system (CHO-FITR-hGPR17 cells).[37] Compounds exhibiting pIC_{50} values of around 7 or higher and also those of particular interest for structure−activity relationships were subsequently investigated in calcium mobilization assays using 1321N1 astrocytoma cells stably transfected with the human GPR17 as previously described.[38] Selected potent compounds were further investigated in cAMP assays and in G protein effector-membrane translocation assays (GEMTA) to investigate inhibition of GPR17-mediated $G\alpha_{i/o/z}$ protein activation.[39] Finally, the compounds were investigated in radioligand binding assays to determine their GPR17 affinity. Competition experiments were performed using the GPR17 agonist radioligand [^{3}H]PSB-12150 and membrane preparations of CHO-FITR-hGPR17 cells.[29]

https://doi.org/10.1021/acs.jmedchem.4c01755
J. Med. Chem. 2024, 67, 19365−19394

Scheme 4. Synthesis of 2-(6-(Naphthalen-1-yl)picolinic Acid Amides and 2-(2-(Naphthalen-1-yl)thiazole-4-carboxamides (64−70)[a]

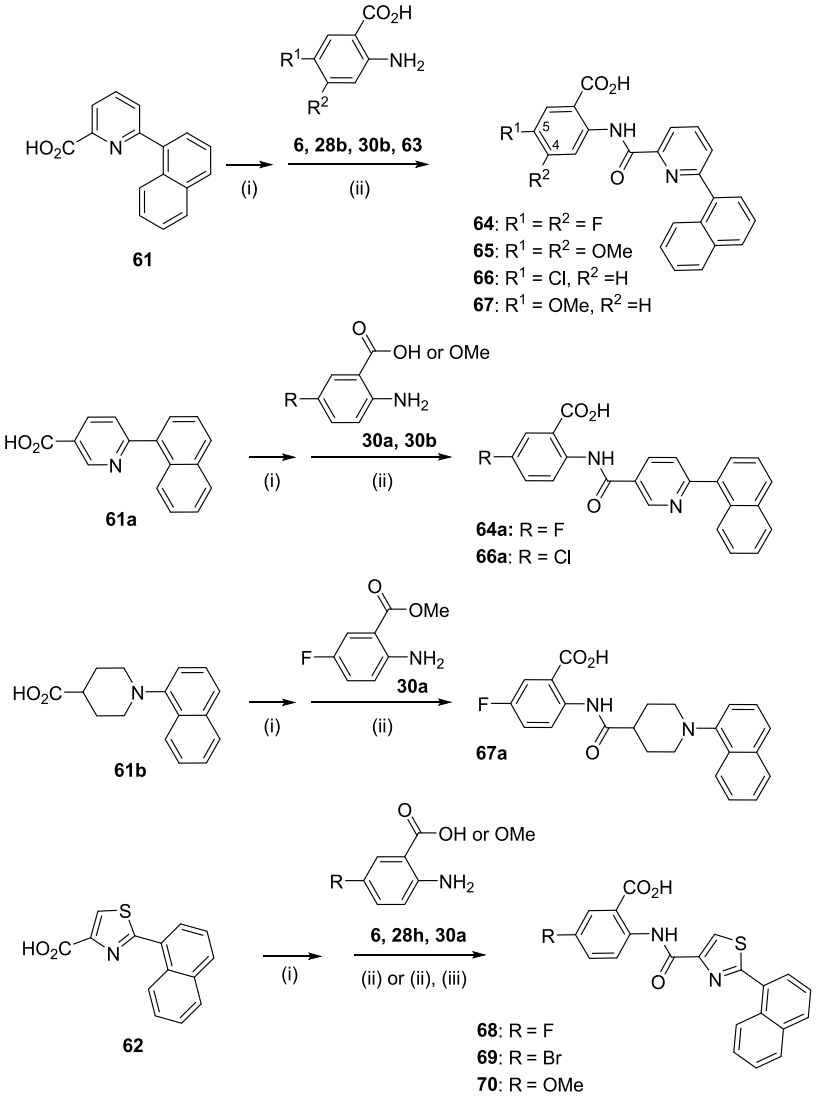

[a]Reagents and conditions: (i) $SOCl_2$, DCM, reflux, 3 h; (ii) DIPEA, DCM, rt, 16 h; (iii) THF/MeOH/H_2O (2:1:2), NaOH, 35 °C, 12 h.

Preliminary Screening of GPR17 Antagonists in Calcium Mobilization Assays. On the basis of screening hit **3** novel anthranilic acid derivatives were designed, synthesized, and tested. First, the enamine moiety of **3** was replaced by a carboxamide group. The test results indicated that this replacement is well accepted and even beneficial for GPR17-antagonistic activity. The carboxamide was expected to be more stable than the enamine linker, and due to the straightforward formation of amide bonds from readily available carboxylic acids and amines, this modification offers the possibility for broad exploration of SARs.[33,34] As a next step, the central 1,2-disubstituted tetrazole of hit compound **3** was replaced by other 5- or 6-membered heteroaromatic moieties. Preliminary screening in functional assays indicated that other aromatic heterocycles were generally well tolerated. Most of the subsequently synthesized compounds entailed a 2,5-disubstituted furan ring. The test results for **70**, containing a central 2,4-disubstituted thiazole moiety (pIC_{50} = 7.1), and for **67**, harboring a central 2,6-disubstituted pyridine ring (pIC_{50} = 6.9), indicated that these variations were also well tolerated, even slightly better than the 2,5-disubstituted furan (compared to analog **45**, pIC_{50} = 6.7). On the other hand, **64a**, containing a 2,5-disubstituted pyridine moiety (pIC_{50} = 5.6) and **67a**, entailing a 1,4-disubstituted piperidine ring (pIC_{50} = 5.4), were less potent inhibitors (see Table 1).

The 5-position of 2,5-disubstituted furan 2-carboxamides was broadly explored by introducing substituted phenyl rings. The test results revealed that substitution at the R^1 position on the phenyl ring at the furan-5-position (e.g., with Br in **11**, pIC_{50} = 6.8) led to higher potency than substitution of the phenyl ring at the R^2 or R^3 positions (compare, e.g., **10**, pIC_{50} = 6.1; **17**, pIC_{50} = 6.3). Best results were obtained for biphenyl derivatives containing a phenyl residue in the R^1 position of the phenyl ring (e.g., **9**, pIC_{50} = 7.1). In comparison, phenyl at position R^2 (**20**, pIC_{50} = 6.4) or R^3 (**21**, pIC_{50} = 5.8) resulted in derivatives with reduced potency. Isopropyl at the R^1 position was tolerated by GPR17 (e.g., **48**, pIC_{50} = 6.7), while a large phenethyloxy substituent at the same position was less well accepted (**15**, pIC_{50} = 6.6) (see Table 2).

https://doi.org/10.1021/acs.jmedchem.4c01755
J. Med. Chem. 2024, 67, 19365−19394

Scheme 5. Synthesis of Derivatives Bearing an Acidic 5-Membered Heterocyclic Moiety as a Carboxylic Acid Replacement (74−76)[a]

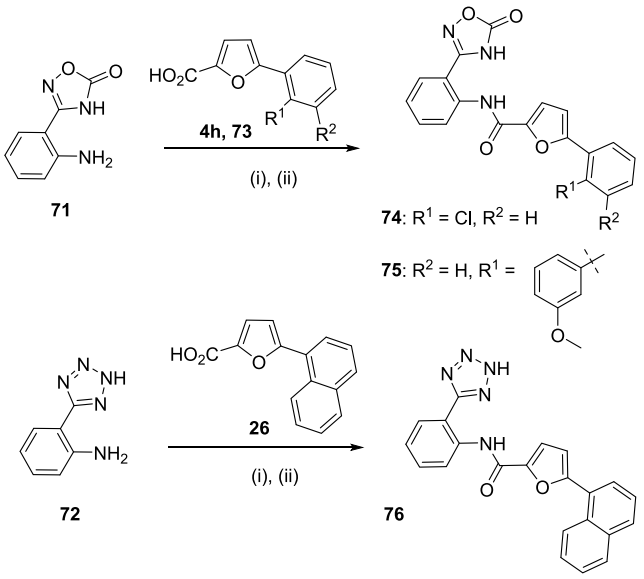

[a]Reagents and conditions: (i) $SOCl_2$, DCM, reflux, 3 h. (ii) DIPEA, DCM, rt, 16 h.

Scheme 6. Synthesis of Derivatives Bearing a Neutral Substituent Instead of a Carboxylic Acid Group (79−84)[a]

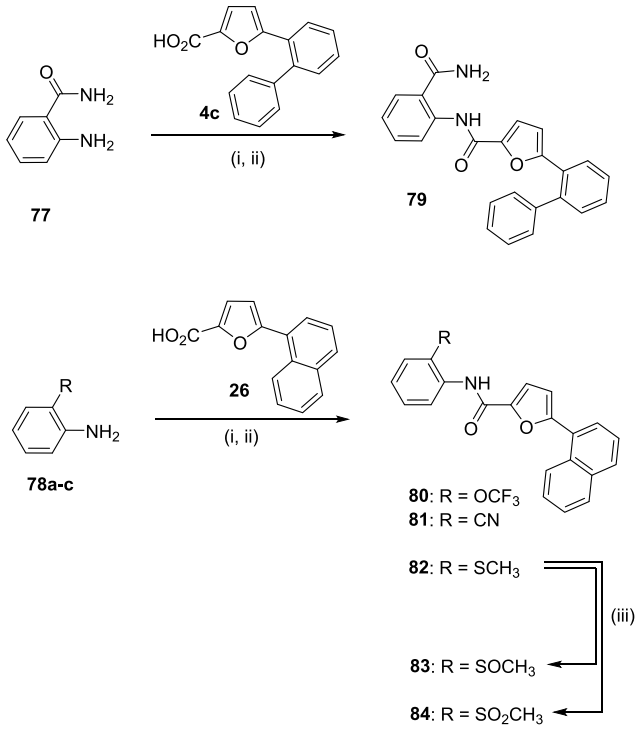

[a]Reagents and conditions: (i) $SOCl_2$, DCM, reflux, 3 h. (ii) DIPEA, DCM, rt, 16 h. (iii) *m*-chloroperbenzoic acid, DCM, rt, 1 h.

An α-naphthyl residue was also introduced at the furan 2-carboxamide position 5 leading to submicromolar potencies in the calcium assay (e.g., **37**, pIC_{50} = 6.7). The furan-5-(naphth-1-yl) moiety was kept constant for the exploration of the anthranilic acid substitution pattern of related carboxamides (see below). The test results revealed that substitution tended to lead to less potent inhibitors when compared to the unsubstituted derivative (**40**, pIC_{50} = 6.9). This was especially true for substitution at R^1 or R^4 (e.g., **31**, pIC_{50} = 5.3; **39**, pIC_{50} = 5.0). Substitution at R^2 or R^3 did not affect potency or reduced it only slightly (e.g., **34**, pIC_{50} = 6.2; **38**, pIC_{50} = 6.3) (see Table 3).

Because of these promising preliminary results, an extensive exploration and evaluation of 5-(2-biphenyl)-substituted furan-2-carboxamides, prepared by a Suzuki cross-coupling reaction, was performed (compounds **52−60**). In this series, compounds bearing a 5-methoxy group at the anthranilic acid moiety were investigated (see Table 4).

Finally, the substitution pattern of the anthranilic acid moiety was studied. Compounds bearing a neutral substituent instead of a carboxylic acid moiety (**79−84**) lost all activity, emphasizing the importance of the acidic moiety for interaction with GPR17. Replacement of the carboxylate group by a 5-membered acidic heterocyclic moiety (compounds **74−76**) resulted in reduced potency. A 1,2,4-oxadiazol-5(4*H*)-one moiety as a replacement for carboxylate (e.g., in **75**, pIC_{50} = 6.4) was better tolerated than a tetrazolate (**76**, pIC_{50} = 5.9). A shift of the carboxylic group to the *para*-position (compound **47**, pIC_{50} = 6.1) or *meta*-position (compound **47a**, pIC_{50} = 5.8) led to a decrease in potency (see Table 5).

Comprehensive Evaluation of Selected GPR17 Antagonists. Compounds that had displayed a pIC_{50} value of around 7 or higher in preliminary screening assays, or those that were structurally interesting for SAR analysis were subsequently fully characterized. To this end, their inhibitory potency was determined in calcium mobilization assays, an effect downstream of G_q coupling, using a different cell line, namely, 1321 N1 astrocytoma cells stably transfected with the human GPR17. Next, the inhibitory potency of selected antagonists was reassessed in orthogonal functional assays measuring effects on intracellular cAMP production, and determining G protein activation by an effector membrane translocation assay, respectively.[39] In all assays, compound **1** was employed as the standard agonist for testing due to its widespread use in GPR17 research, its commercial availability, and the comparability with previous results. Finally, GPR17 affinity of the compounds was determined in radioligand binding assays.

Calcium Mobilization Assays. Inhibitory potency of selected compounds in G_q protein-dependent calcium mobilization assays using 1321N1 astrocytoma cells was determined versus an EC_{80} concentration of GPR17 agonist **1** (corresponding to 1 μM in this assay). All investigated antagonists potently blocked GPR17-mediated calcium mobilization with submicromolar potency ranging from pIC_{50} values of 6.1 to 7.5 (see Figures 5, 6 and Table 6), confirming that they act as potent GPR17 antagonists.

cAMP Accumulation Assays. The inhibitory potency of four selected compounds, **22**, **52**, **54**, and **57**, was additionally determined in cAMP accumulation assays using CHO-FITR-hGPR17 cells. All four antagonists potently blocked the GPR17-mediated decrease in intracellular cAMP induced by agonist **1** (employed at its EC_{90} concentration) in the presence of forskolin. The antagonists displayed nanomolar potencies ranging from pIC_{50} values of 7.7 to 8.1 (see Figures 5, 6 and Table 6), confirming that they act as potent GPR17 antagonists.

https://doi.org/10.1021/acs.jmedchem.4c01755
J. Med. Chem. 2024, 67, 19365−19394

Table 1. Synthesized 2-Carboxamidobenzoic Acid Derivatives 38, 45, 64−70 and Effects of Different 5- and 6-membered Heterocyclic Aromatic Moieties on the Compounds' Potency as GPR17 Antagonists Determined in Calcium Mobilization Assays

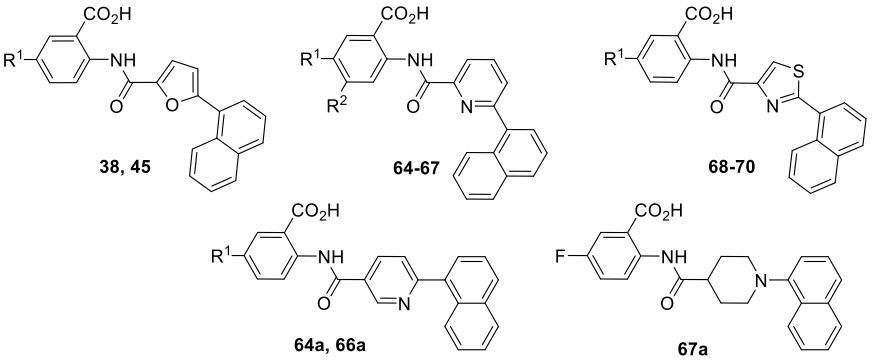

Compd.	R^1	R^2	pIC_{50} at human GPR17[a]
38	Br	-	6.3
45	OCH_3	-	6.7
64	F	F	6.7
64a	F	-	5.6
65	OCH_3	OCH_3	5.8
66	Cl	H	6.7
66a	Cl	-	5.7
67	OCH_3	H	6.9
67a	*for structure see above*		5.4
68	F	-	6.7
69	Br	-	6.3
70	OCH_3	-	7.1

[a]Potency in inhibiting calcium mobilization in CHO-FITR-hGPR17 cells, activated with 1, determined in a single preliminary screening experiment.

Effector Membrane Translocation Assays Measuring G Protein Activation. Direct G protein activation was measured by the G protein effector-membrane translocation assay (GEMTA).[39] Upon agonist-induced receptor activation of a recombinantly expressed Gα protein subunit, a renilla luciferase(RLucII)-tagged effector protein is recruited to the plasma membrane, which is saturated with a membrane-anchored renilla green fluorescent protein (rGFP-CAAX).[39]

GPR17 is preferably coupled to G_q and $G_{i/o}$ proteins. Thus, in initial experiments, we determined GPR17-induced activation of $G\alpha_{i/o}$ protein family members by the GPR17 agonist MDL 29,951 (**1**). Cells, cotransfected with the human GPR17 and either $G\alpha_{i2}$, $G\alpha_{oA}$, or $G\alpha_z$, were stimulated with **1** (see Figure 4) resulting in an increased BRET ratio between the RLuc-II-tagged $G\alpha_{i/o}$ effector Rap1 GTPase-activating protein (Rap1GAP-RLucII) and the membrane-tethered rGFP-CAAX. Agonist **1** showed high potency in activating $G\alpha_{i2}$ (pEC_{50} = 7.40) and $G\alpha_z$ (pEC_{50} = 7.38), while somewhat lower potency was observed in activating $G\alpha_{oA}$ (pEC_{50} = 6.67). The largest signal-to-noise ratio was observed in the $G\alpha_{i2}$ protein activation assay (see Figure 4). Thus, the novel GPR17 inhibitors were subsequently investigated for inhibition of GPR17 agonist-induced $G\alpha_{i2}$ activation in the GEMTA assays.

The inhibitory potency of selected antagonists was determined by testing multiple compound concentrations at cells stimulated with an EC_{80} concentration of agonist **1** (corresponding to 200 nM in this assay). All investigated compounds potently blocked GPR17-mediated recruitment of the $G\alpha_{i2}$ effector Rap1GAP-RLucII to the membrane with pIC_{50} values ranging from 6.0 to 6.5 (see Figures 5, 6 and Table 6).

Radioligand Binding Assays. Finally, selected potent compounds were tested in competition binding assays for their GPR17 affinity using the agonist radioligand [^{3}H]PSB-12150 and membrane preparations of cells recombinantly expressing the human GPR17. All tested compounds showed a concentration-dependent displacement of the radioligand which was complete at high antagonist concentrations, indicating that they likely act as competitive antagonists with regard to the employed agonist radioligand. All investigated antagonists potently bound to GPR17, ranging from pK_i values of 6.1 to 8.1 (see Figures 5, 6 and Table 6) confirming their high-affinity interaction with GPR17.

Concentration−response curves and binding competition curves for selected anthranilic acid derivatives (**22**, **52**, **54**, **57**) are provided in Figure 5 (for others, see Figures S46−S48).

Correlation of Data Obtained in Different Assays. Data for the most potent antagonists determined in the two functional assays were consistent, although GEMTA assays generally resulted in somewhat lower pIC_{50} values (see Table 6, Figures 5 and S50). It should be noted that GEMTA assay data are determined in a highly artificial system. Measurements of the second messenger cAMP revealed potent inhibition for the tested antagonists in these G_i protein-dependent assays, confirming results obtained in the Gq protein-dependent calcium mobilization assays.

The determined pK_i values of all compounds except for **52** were comparable to the pIC_{50} values obtained from the

https://doi.org/10.1021/acs.jmedchem.4c01755
J. Med. Chem. 2024, 67, 19365−19394

Table 2. Synthesized 2-(5-Arylfuran-2-carboxamido)benzoic Acid Derivatives 7−25, 48, 49, 51 and Effects of Differently Substituted 5-Arylfuran Moieties on the Potency at GPR17 Determined in Calcium Mobilization Assays[a]

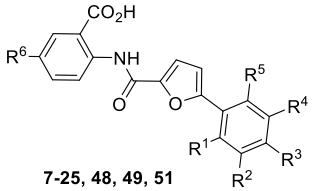

7-25, 48, 49, 51

Compd.	R^1	R^2	R^3	R^4	R^5	R^6	pIC_{50} at human GPR17[a]
7	H	H	isobutyl	H	H	H	6.3
8	isopropyl	H	H	H	isopropyl	H	5.7
9	phenyl	H	H	H	H	H	7.1
10	H	H	Cl	H	H	H	6.1
11	Br	H	H	H	H	H	6.8
12			H	H	OCH_3	H	6.2
13			H	H	H	H	5.6
14	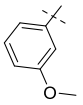	H	H	H	H	H	7.0
15	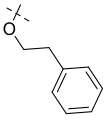	H	H	H	H	H	6.6
16	H	Cl	H	Cl	H	OCH_3	6.5
17	Cl	Cl	H	H	H	OCH_3	6.3
18	phenyloxy	H	H	H	H	OCH_3	6.7
19	H	H	isobutyl	H	H	OCH_3	6.3
20	H	phenyl	H	H	H	OCH_3	6.4
21	H	H	phenyl	H	H	OCH_3	5.8
22	phenyl	H	H	H	H	OCH_3	7.1
23	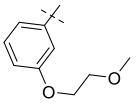	H	H	H	H	OCH_3	7.2
24	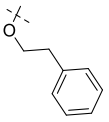	H	H	H	H	OCH_3	6.4
25	H	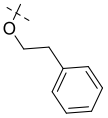	H	H	H	OCH_3	6.1
48	isopropyl	H	H	H	H	F	6.7
49	isopropyl	H	H	H	H	Cl	6.1
51		H	H	H	H	OCH_3	6.0

[a]Potency in inhibiting calcium mobilization in CHO-FITR-hGPR17 cells, activated with **1**, determined in a single preliminary screening experiment.

calcium mobilization assays, ranging from 6.10 to 7.08 (see Table 6, Figures 5 and S48). Compound **52**, however, showed a high pK_i value of 8.05 (Table 6, Figure 5), corresponding to 8.91 nM, in the radioligand binding assay. This discrepancy might be attributed to slow dissociation kinetics of **52**.

The observed, mostly minor, differences between functional and binding data may be explained by different binding

https://doi.org/10.1021/acs.jmedchem.4c01755
J. Med. Chem. 2024, 67, 19365−19394

Table 3. Synthesized 2-(5-(Naphth-1-yl)furan-2-carboxamido)benzoic Acid Derivatives 31−46 and Effects of Differently Substituted Benzoic Acid Moieties on the Inhibitory Potency at GPR17 Determined in Calcium Mobilization Assays[a]

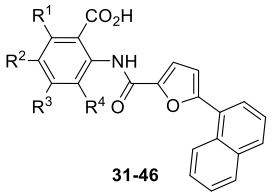

31-46

Compd.	R^1	R^2	R^3	R^4	pIC_{50} at human GPR17[a]
31	H	H	H	Cl	5.3
32	H	F	F	H	6.6
32a	H	F	H	F	5.3
33	H	H	OCH_3	H	6.7
34	H	H	Br	H	6.2
35	H	CH_3	H	H	6.9
36	H	OCF_3	H	H	6.2
37	H	cyclopropyl	H	H	6.7
38	H	Br	H	H	6.3
39	Cl	H	H	H	5.0
40	H	H	H	H	6.9
41	H	OCH_3	CH_3	H	6.4
42	H	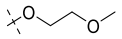	H	H	6.5
43	H	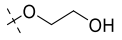	H	H	6.3
44	H			H	6.4
45	H	OCH_3	H	H	6.7
46	H	OH	H	H	6.4

[a]Potency in inhibiting calcium mobilization in CHO-FITR-hGPR17 cells, activated with **1**, determined in a single preliminary screening experiment.

kinetics, and variations in assay conditions. Radioligand binding studies, conducted under equilibrium conditions, involve a 1-hour incubation of membrane preparation, radioligand, and antagonist. In contrast, the GEMTA assays have significantly shorter incubation times (5 min for the full mixture), while in the calcium mobilization assay, the signal is immediately observed after addition of the agonist. Because therapeutic drugs are in a state of equilibrium when administered multiple times, the radioligand binding studies might be more informative with regard to binding kinetics and residence time. On the other hand, cell-based assays with living cells are closer to the in vivo situation. Taken together, we have characterized the new antagonists in a broad range of different assays all of which confirm their potency in binding to GPR17 and thereby blocking the different GPR17-coupled signaling pathways.

To further confirm that the compounds act as competitive GPR17 antagonists, concentration−response curves for agonist **1** in calcium assays were performed in the presence of several different concentrations of antagonist **52**. Increasing concentrations of **52** produced a parallel rightward shift of the curve without significantly changing the Hill slope (see Figure 7). This suggests that **52** is a competitive antagonist at GPR17 binding to the same site as agonist **1**.

Structure−Activity Relationships. Figure 8 summarizes the observed structure−activity relationships of the synthesized anthranilic acid derivatives. The central anthranilic acid moiety was found to be essential for the activity. Moving the carboxylic acid group from 2-position to 4-position reduced the potency of the compounds, substitution with a tetrazole moiety decreased potency as well, other acidic and nonacidic groups (OCF_3, CN, SCH_3, $SOCH_3$, SO_2CH_3) led to inactive compounds. Substitution in positions 3 and 6 generally decreased potency while substitution in positions 4 or 5 was tolerated, although it did not increase the potency. The replacement of the 5-membered heteroaromatic furan ring was investigated as well. Some heteroaromatic moieties like 2,4-disubstituted thiazole and 2,6-disubstituted pyridine led to equally active compounds, while a 2,5-disubstituted pyridine or a 1,4-disubstituted piperidine decreased potency. Lastly, substitution of the second benzene ring was studied which was tolerated in all positions. The most potent compounds all contain a phenyl, *meta*-methoxyphenyl or *para*-methoxyphenol group in position 2'.

Homology Model of the Inactivate-State Human GPR17. Initially, we developed a homology model of the human GPR17 in its active state based on the crystal structure of the human $P2Y_{12}$ receptor in complex with the agonist 2-methylthio-ADP (Figure 9A).[4] This model contributed to the identification of the binding site of indole derivatives that act as GPR17 agonists. Very recently, a cryo-EM structure of the human GPR17 in its active apo-state, bound to a G_i

https://doi.org/10.1021/acs.jmedchem.4c01755
J. Med. Chem. 2024, 67, 19365−19394

Table 4. Synthesized 2-(5-(2-Biphenyl)furan-2-carboxamido)benzoic Acid Derivatives 22, 23, 52−60 and the Effect of Differently Substituted Biphenyl Moieties on the Potency at GPR17 Determined in Calcium Mobilization Assays[a]

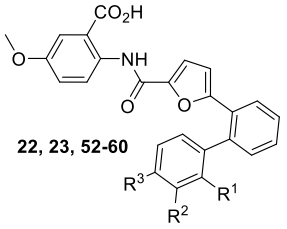

Compd.	R^1	R^2	R^3	pIC_{50} at human GPR17[a]
22	H	H	H	7.1
23	H	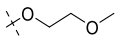	H	7.2
52 PSB-22269	H	OCH_3	H	7.0
53	H	CN	H	6.8
54 PSB-24040	H	CF_3	H	7.0
55	H	isopropyl	H	6.9
56	H	cyclopropoxy	H	6.7
57	H	H	OCH_3	7.1
58	OCH_3	H	H	6.5
59	H	CH_2OH	H	6.1
60	H	SO_2CH_3	H	5.5

[a]Potency in inhibiting calcium mobilization in CHO-FITR-hGPR17 cells, activated with **1**, determined in a single preliminary screening experiment.

protein, was published (Figure 9B).[32] Comparing the structures (Figure 9C), we observed substantial similarity between our active-state $P2Y_{12}$-based homology model and the cryo-EM structure, with a root-mean-square deviation (RMSD) of approximately 3.8 Å for the backbone Cα atoms. The transmembrane helices (TM) 1, 2, 3, and 7 aligned well, each showing an average RMSD between 1.0 and 2.0 Å. However, intracellular loops (ICL) 2 and 3, extracellular loops (ECL) 2 and 3, and TM5 showed poor alignment with average RMSD values between 4.7 and 6.5 Å. Twelve amino acids exhibited deviations of more than 8 Å in the homology model compared to the cryo-EM structure: L170 in ICL2, L212-K216 in ECL2 and TM5, S246-Q249 in TM5, V253 in ICL3, and R263 in TM6. These discrepancies were primarily due to the flexible intracellular and extracellular loops, and the outer part of TM5, while the proposed binding pocket is very similar in both structures (see Figure 9).

Given the high similarity of our homology model and the cryo-EM structure of GPR17 in its active conformation, we generated a new homology model of the inactive state of GPR17 for the docking of antagonists. The model was developed based on the X-ray structure of the human $P2Y_{12}$ receptor in complex with the antagonist AZD1283 (PDB 4NTJ).[40] Comparison of the active and inactive state homology models of GPR17 resulted in an RMSD value of 3.1 Å. The main structural differences (>5 Å) were found for the following amino acid residues: G122 in TM2, V165−K169 in ICL2, L251-L257 in ICL3 and TM6, V287-R291 in TM6, V328-A329 in TM7 and TM8, and K331-F332 in TM8 (see Figure 10). The refined inactive-state homology model thus provides a robust framework for docking studies of antagonists, allowing us to explore the binding site and interactions of the developed anthranilic acid derivatives.

Molecular Docking Studies. In order to gain a deeper understanding of the binding mode and interactions of anthranilic acid derivatives, the potent antagonist **52** was docked into the binding site of the inactive-state GPR17 homology model (see Figure 11). Docking results suggest that antagonist **52** occupies the same binding site as agonists **1** (MDL 29,951) and **2a** (PSB-18422) and is anchored through a combination of polar and hydrophobic interactions (see Figure S51). This is confirmed by competitive binding of the anthranilic acid-based antagonists versus the agonist radioligand [^{3}H]PSB-12150 (tritiated version of compound **1**). Specifically, the acidic group of the anthranilic acid core is expected to establish a strong interaction with Arg87. It is positioned at a distance of approximately 3 Å from Arg280 and may thus form additional interactions with this basic residue. This is confirmed by compound **79**, where its replacement by a carboxamido group results in loss of activity (see Figure S52). The carbonyl group of the amide likely forms an interaction with Arg255, and the amino group possibly forms a water-mediated interaction with the backbone carbonyl group of Gly108. The furan ring of antagonist **52** is proposed to be involved in aromatic stacking with Tyr112, or with Tyr251, respectively. This could contribute to a stabilization of the antagonist in the binding pocket. Replacing the furan ring with pyridine (**64a**) or thiazole (**70**) is tolerated. The biphenyl group is expected to occupy a subpocket formed by Phe109, Leu113, Met163, Leu166, Asn183, Tyr185, His191, Leu194, Val195, and Leu197. This subpocket also accommodates naphthyl (**64a**) or substituted benzene rings (**15**). It mainly consists of hydrophobic residues, and resulting hydrophobic

https://doi.org/10.1021/acs.jmedchem.4c01755
J. Med. Chem. 2024, 67, 19365−19394

Table 5. Synthesized 2-Arylcarboxamidofuran Derivatives (40, 47, 47a, 74−76, 79−84) and the Effect of the Replacement of the Carboxylic Acid Moiety on the Potency at GPR17 Determined in Calcium Mobilization Assays[a]

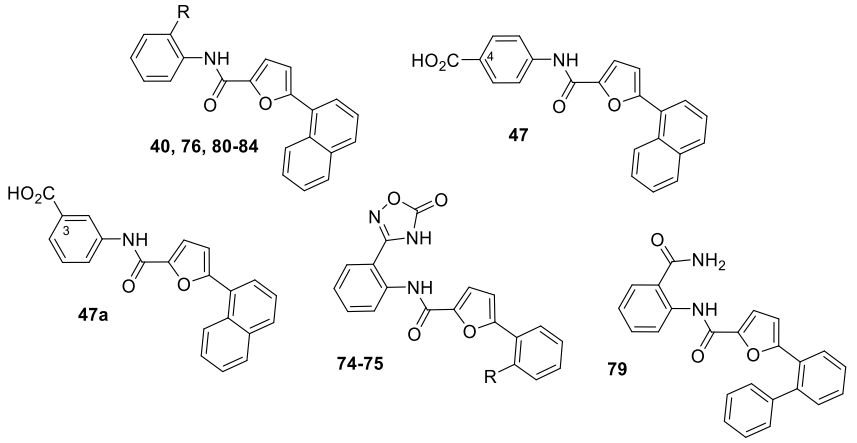

Compd.	R	pIC$_{50}$ at human GPR17[a]
40	COOH	6.9
47	*for structure see above*	6.1
47a	*for structure see above*	5.8
74	Cl	6.3
75	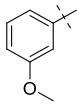	6.4
76		5.9
79	*for structure see above*	< 4
80	OCF_3	< 4
81	CN	< 4
82	SCH_3	< 4
83	$SOCH_3$	< 4
84	SO_2CH_3	< 4

[a]Potency in inhibiting calcium mobilization in CHO-FITR-hGPR17 cells, activated with **1**, determined in a single preliminary screening experiment.

interactions may significantly contribute to the high binding affinity of the antagonist. The methoxy group in the *meta*-position of the biphenyl ring system of **52** is oriented toward the disulfide bridge formed between Cys104 and Cys181. Its orientation in the docked pose suggests that it could be involved in additional stabilizing interactions with Gln183 located in the extracellular loop, which might affect the conformation of the binding pocket.

CONCLUSIONS

In conclusion, we discovered and optimized potent GPR17 antagonists derived from an anthranilic acid scaffold. A total of 64 differently substituted 2-carboxamidobenzoic acid derivatives and analogs were synthesized and evaluated in calcium mobilization and radioligand binding assays. Selected potent antagonists were further studied in an orthogonal assay measuring direct G protein activation. Derivatives of 2-(5-(2-biphenyl)furan-2-carboxamido)benzoic acid showed high GPR17-antagonistic activity. Replacement of the biphenyl moiety by other lipophilic, aromatic moieties, e.g., naphthyl or *ortho*-isopropylphenyl, also resulted in potent antagonists. The carboxy group of the anthranilic acid core structure was found to be essential. A refined homology model of the human inactive-state GPR17 was developed, which enables docking studies with antagonists. It was employed to rationalize interactions of the potent anthranilic acid derivate **52** within the proposed binding site that is lined by several positively charged arginine residues and by a highly lipophilic subpocket. The most potent antagonists were 5-methoxy-2-(5-(3′-methoxy-[1,1′-biphenyl]-2-yl)furan-2-carboxamido)benzoic acid (**52**, PSB-22269, pK_i 8.05, pIC$_{50}$ 6.90) and 5-methoxy-2-(5-(3′-(trifluoromethyl)-[1,1′-biphenyl]-2-yl)furan-2-carboxamido)benzoic acid (**54**, PSB-24040, pK_i 7.08, pIC$_{50}$ 7.48). These novel GPR17 antagonists are suggested as tool compounds to study GPR17 pharmacology, and as new lead structures for further optimization and for the development of potential drug candidates.

EXPERIMENTAL SECTION

Biological Assays. *Calcium (Ca^{2+}) Mobilization Assays for Preliminary Compound Screening.* CHO-FITR-hGPR17 cells were defrosted and seeded at a density of 20,000 cells per well into black 384-well plates with clear bottom. Cells were incubated overnight at 37 °C in a humidified atmosphere of

https://doi.org/10.1021/acs.jmedchem.4c01755
J. Med. Chem. 2024, 67, 19365−19394

Table 6. Inhibitory Potencies (pIC_{50}) and Binding Affinities (pK_i) of Selected Compounds, Determined in Calcium Mobilization Assays, GEMTA (G Protein Effector Membrane Translocation) Assays, cAMP Accumulation Assays, and Radioligand Binding Assays

Compd.	Structure	Inhibition of GPR17-induced calcium mobilization $pIC_{50} \pm SEM$[a]	Inhibition of GPR17 agonist-induced cAMP decrease $pIC_{50} \pm SEM$[b]	Inhibition of GPR17 agonist-induced G protein activation $pIC_{50} \pm SEM$[c]	Inhibition of [^{3}H]PSB-12150 binding to GPR17 $pK_i \pm SEM$[d]
9	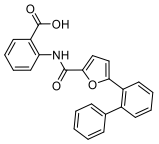	6.88 ± 0.07	n.d.[e]	6.62 ± 0.04	6.33 ± 0.21
14	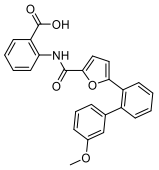	6.59 ± 0.04	n.d.	6.37 ± 0.04	6.24 ± 0.23
15	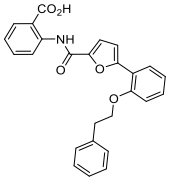	6.45 ± 0.10	n.d.	n.d.	6.10 ± 0.16
22	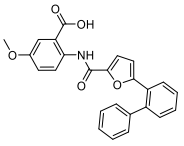	7.05 ± 0.10	8.14 ± 0.06	6.43 ± 0.05	6.59 ± 0.58
23	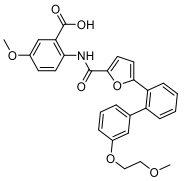	6.12 ± 0.01	n.d.	5.99 ± 0.04	6.60 ± 0.35
33	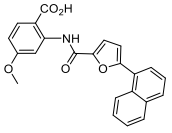	6.45 ± 0.03	n.d.	6.02 ± 0.07	6.11 ± 0.42
37	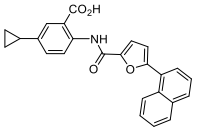	6.79 ± 0.12	n.d.	6.50 ± 0.05	6.32 ± 0.33
48	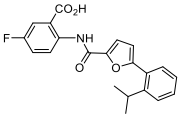	6.26 ± 0.24	n.d.	6.30 ± 0.09	6.86 ± 0.28
52 PSB-22269	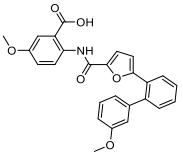	6.90 ± 0.08	7.71 ± 0.07	6.31 ± 0.03	8.05 ± 0.41

https://doi.org/10.1021/acs.jmedchem.4c01755
J. Med. Chem. 2024, 67, 19365−19394

Table 6. continued

Compd.	Structure	Inhibition of GPR17-induced calcium mobilization $pIC_{50} \pm SEM^a$	Inhibition of GPR17 agonist-induced cAMP decrease $pIC_{50} \pm SEM^b$	Inhibition of GPR17 agonist-induced G protein activation $pIC_{50} \pm SEM^c$	Inhibition of [^{3}H]PSB-12150 binding to GPR17 $pK_i \pm SEM^d$
54 PSB-24040	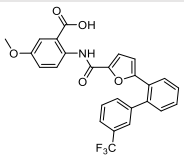	7.48 ± 0.32	8.10 ± 0.06	6.53 ± 0.07	7.08 ± 0.14
57	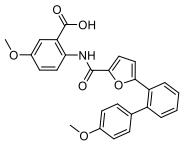	6.72 ± 0.11	7.74 ± 0.06	6.45 ± 0.08	7.05 ± 0.28
67	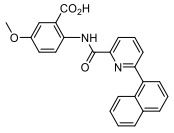	6.33 ± 0.15	n.d.	6.05 ± 0.12	6.60 ± 0.10
70	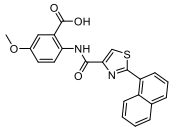	6.38 ± 0.07	n.d.	6.10 ± 0.08	6.30 ± 0.38

[a]Potency in inhibiting calcium mobilization in 1321N1 astrocytoma cells stably transfected with the human GPR17, activated with **1**, determined in three to four independent experiments, performed in duplicates. [b]Potency in inhibiting cAMP decrease induced by **1** in the presence of 5 μM forskolin in CHO-FITR-hGPR17 cells, determined in three independent experiments, performed in duplicates. [c]Potency in inhibiting the recruitment of the $G\alpha_{i2}$ effector Rap1GAP-RLucII to the membrane in HEK293 cells stably transfected with the human GPR17 and activated with **1**. Four independent experiments were performed in duplicates. [d]Binding affinity to human GPR17, determined in radioligand binding assays; three to five independent experiments were performed in duplicates. [e]n.d., not determined.

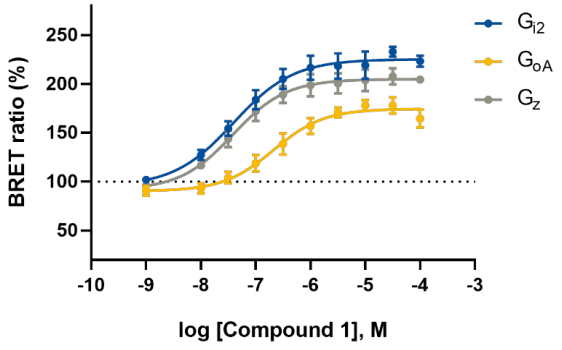

	Potency ($pEC_{50} \pm SEM$)	Maximal effect (BRET ratio in % ± SEM)
$G\alpha_{i2}$	7.40 ± 0.05	233 ± 6
$G\alpha_{oA}$	6.67 ± 0.08	184 ± 3
$G\alpha_z$	7.38 ± 0.10	214 ± 8

Figure 4. Concentration-dependent activation of GPR17 by agonist **1** determined in G protein effector membrane translocation assays (GEMTA). $G\alpha_{i2}$ (blue), $G\alpha_{oA}$ (yellow), and $G\alpha_z$ proteins (gray). Basal activation = 100%. Data are means ± SEM of three independent experiments, each performed in duplicate.

5% CO_2. Sixteen to 20 hours after seeding, CHO-FITR-hGPR17 cells were loaded for 60 min with Calcium 5 dye (Molecular Devices, San José, CA, USA), a fluorescent Ca^{2+} indicator dye, according to manufacturer's instructions. The fluorescence signal, which corresponds to the cytosolic Ca^{2+} concentration, was recorded over time at room temperature in a FLIPR Tetra reader (Molecular Devices, San José, CA, USA). Cells were first incubated for 30 min at room temperature in Hank's Balanced Salt Solution (HBSS) 4-(2-hydroxyethyl)-1-piperazineethanesulfonic acid (HEPES) buffer pH 7.4 containing increasing concentrations of test compound (typically 10^{-11} M to 10^{-6} M). Then, **1** was added to the cells to a final concentration of 50 nM. Inhibitory effects of varying concentration test compounds were measured, and resulting pIC_{50} values were determined. All incubations were performed in duplicate, and results were compared to a concentration response curve of GPR17 agonists and antagonist reference compounds. Analysis and curve fitting were performed in ActivityBase XE (IDBS, Woking, UK) using the XLfit 4-parameter logistic equation $y = A + ((B - A)/(1 + ((C/x)^D)))$ where A, B, C, and D stand for minimum y, maximum y, IC_{50}, and slope, respectively.

Calcium (Ca^{2+}) Mobilization Assays of Subsequent Experiments. pLVX-IRES-hGPR17wt expressing 1321N1 astrocytoma cells were cultured in Dulbecco's modified Eagle Medium (DMEM), supplemented with 10% fetal calf serum (FCS), 0.1 mg/mL streptomycin, and 100 U/ml penicillin, at 37 °C and 10% CO_2. On the day of the experiment, the

https://doi.org/10.1021/acs.jmedchem.4c01755
J. Med. Chem. 2024, 67, 19365−19394

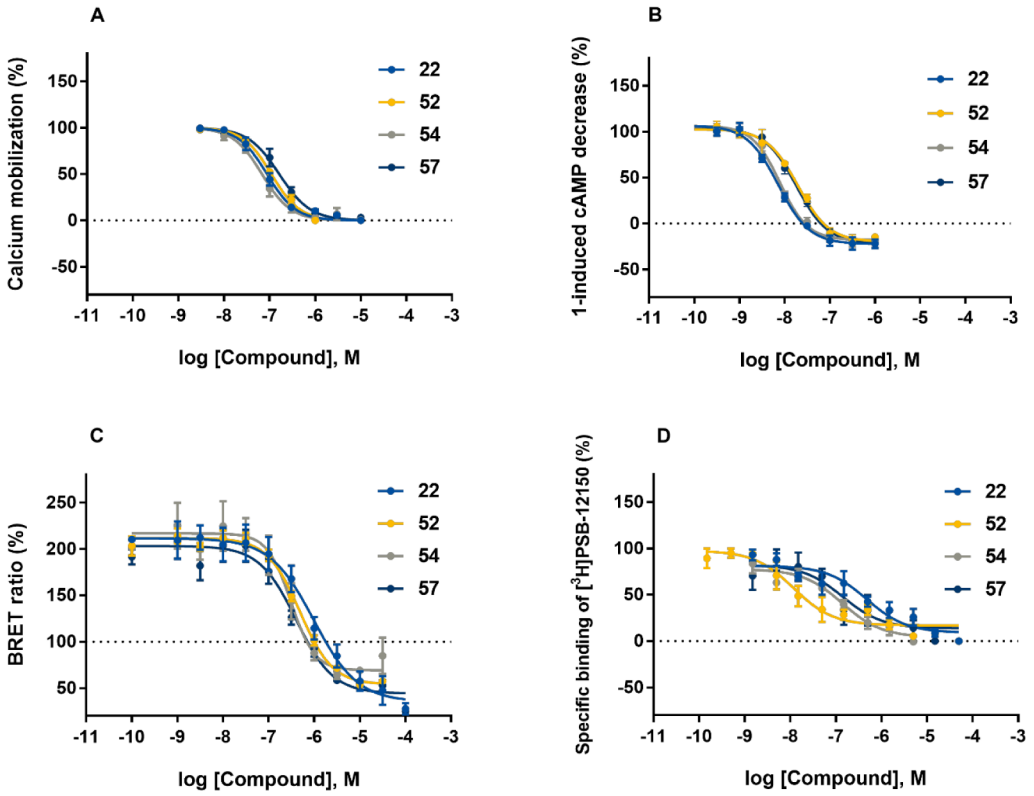

Figure 5. (A) Concentration-inhibition curves of selected anthranilic acid derivatives determined in calcium mobilization assays performed with 1321N1-hGPR17 cells. The receptor was activated with agonist **1** at its EC_{80} concentration. Data points represent means ± SEM from three independent experiments performed in duplicate. For pIC_{50} values see Table 6. (B) Concentration-dependent inhibition by selected anthranilic acid derivatives of GPR17-mediated decrease in cAMP accumulation induced by GPR17 agonist **1** (10 nM, EC_{90}) in the presence of 5 μM forskolin, performed with CHO-FITR-hGPR17 cells. Data points represent means ± SEM from three independent experiments performed in duplicate. For pIC_{50} values, see Table 6. (C) Concentration-inhibition curves of selected anthranilic acid derivatives in G protein effector-membrane translocation assays performed with HEK293-hGPR17 cells. GPR17 was activated by an EC_{80} concentration of agonist **1**. Basal activation = 100%. Data points represent means ± SEM from four independent experiments performed in duplicate. For pIC_{50} values, see Table 6. (D) Competition binding curves of selected anthranilic acid derivatives versus [^{3}H]PSB-12150 at human GPR17 in a membrane preparation of CHO-FITR-hGPR17 cells. Data points represent means ± SEM from three to five independent experiments performed in duplicate. For pK_i values, see Table 6.

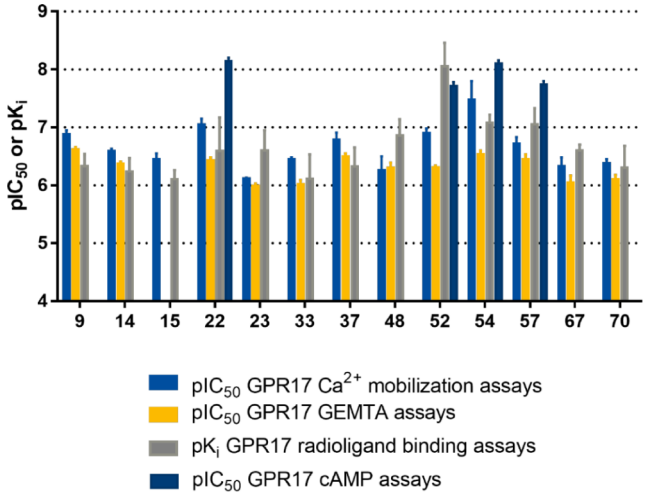

Figure 6. Comparison of data obtained for selected anthranilic acid derivatives as GPR17 antagonists, determined in calcium mobilization assays, GEMTA assays, radioligand binding assays, and cAMP assays at human GPR17.

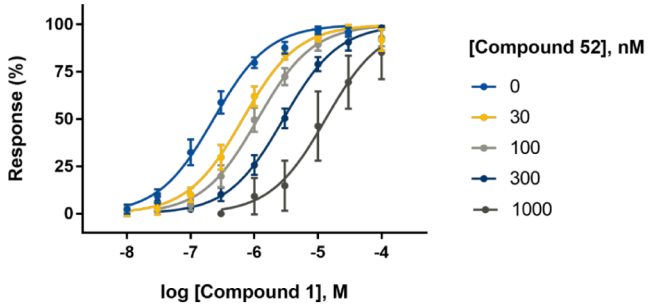

[Compound **52**], nM	pEC_{50} ± SEM	pK_B[a]
0	6.63 ± 0.10	
30	6.20 ± 0.11	
100	5.95 ± 0.11	7.46
300	5.51 ± 0.10	
1000	4.88 ± 0.17	

Figure 7. Concentration-dependent activation of GPR17 by agonist **1** in the presence of different concentrations of antagonist **52** determined in calcium mobilization assays. Data are means ± SEM of four independent experiments, performed in duplicate. [a]The pK_B value is the negative logarithm of the equilibrium dissociation constant of receptor inhibitors.

confluent cells in 2 T175 flasks were washed with phosphate buffered saline (PBS), detached by trypsination and taken up

https://doi.org/10.1021/acs.jmedchem.4c01755
J. Med. Chem. 2024, 67, 19365−19394

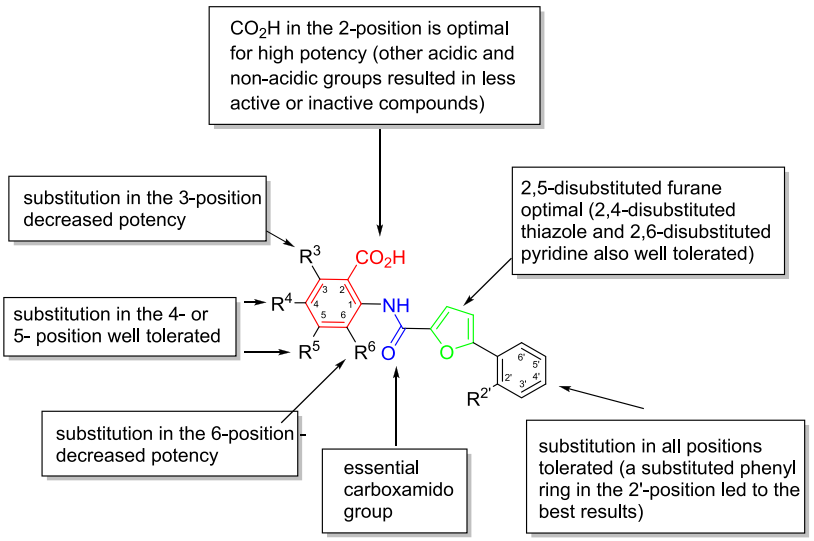

Figure 8. Summary of structure–activity relationships of anthranilic acid derivatives as GPR17 antagonists.

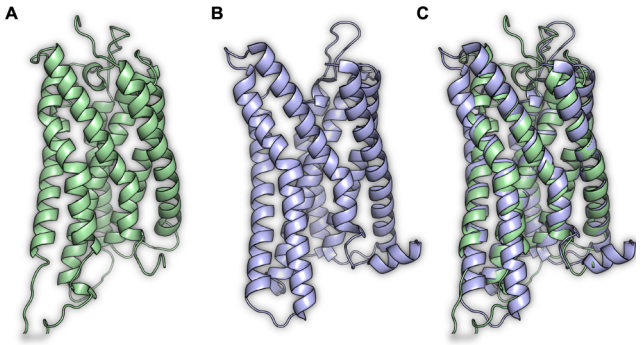

Figure 9. Comparison of the homology model of the human GPR17 and the experimentally determined cryo-EM structure in an active conformation.[4,32] (A) Homology model of the human GPR17 based on the active-state human $P2Y_{12}$ receptor crystal structure (PDB 4PXZ) represented in cartoon and colored in green. (B) Cryo-EM structure of the human GPR17 (PDB 7Y89) represented in cartoon and colored in light blue. (C) Superimposed human GPR17 structures. RMSD: 3.8 Å.

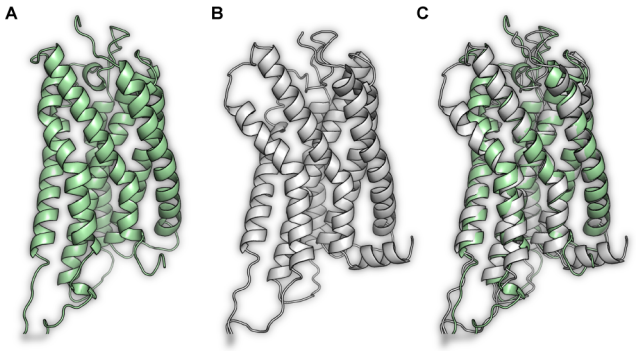

Figure 10. Comparison of different homology models of the human GPR17. (A) Homology model of the human GPR17 deduced from the active-state human $P2Y_{12}$ receptor crystal structure (PDB 4PXZ) shown in cartoon representation and colored in green. (B) Homology model of the human GPR17 deduced from the inactive-state human $P2Y_{12}R$ crystal structure (PDB 4NTJ) shown in cartoon representation and colored in gray. (C) Superimposed human GPR17 structures. RMSD: 3.1 Å.

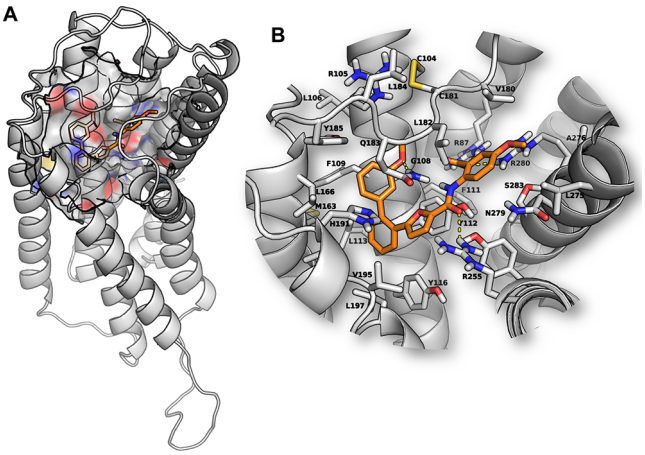

Figure 11. (A) Docked pose of antagonist **52** in the homology model of the human GPR17 (inactive state). The anthranilic acid derivative **52** is shown as stick model (colored in orange) and the receptor in cartoon representation (colored gray). (B) Putative binding pose of **52** with the important amino acids (shown in stick representation and colored in gray) in the binding pocket of the GPR17 model. Electrostatic interactions between the antagonist and the receptor are depicted as yellow dotted lines.

in medium to a total volume of 30 mL in a falcon tube. The cells were incubated for 45 min and then centrifuged at 1200 rpm for 5 min. The cell pellet was resuspended in a mixture of 994 μL potassium hydrogen phthalate buffer (HPB) with 3 μL of Oregon Green 488 BAPTA-1 and 3 μL Pluronic F-127. This was then incubated for 1 h in rotation and protected from light. After washing twice with HPB, the cells were transferred to the wells of a clear bottomed 96 well plate, containing a dilution series of the antagonist in DMSO (2% final DMSO concentration). After incubation for 30 min, the plate was measured using a Novostar system, which pipetted either a constantly concentrated solution of **1** in DMSO and HPB (in the majority of cases) or a dilution series (in the case of the shift assay shown in Figure 7) onto the wells of the clear bottomed 96 well plate. Controls with the same amount of DMSO but without agonist or antagonists as well as controls with DMSO and **1** (no antagonist) were measured as well. The data were obtained from three to four independent experi-

https://doi.org/10.1021/acs.jmedchem.4c01755
J. Med. Chem. 2024, 67, 19365–19394

ments, each performed in duplicate. The data were analyzed with GraphPad PRISM 7.00 (GraphPad, San Diego, CA, USA) using the "[Agonist] vs normalized response", "[Antagonist] vs. normalized response -- Variable slope", and "Gaddum/Schild EC_{50} shift" models.

G Protein Effector Membrane Translocation Assay (GEMTA). GEMTA assays were performed similar to the previously published protocol.[39] HEK293 cells were cultured in Dulbecco's modified Eagle Medium (DMEM) (supplemented with 10% fetal calf serum (FCS), 0.1 mg mL^{-1} streptomycin, and 100 U ml^{-1} penicillin) at 37 °C and 5% CO_2. To transfect the cells, the cells were washed with phosphate buffered saline (PBS), detached by trypsination, and the cell number was adjusted to 350,000 cells per ml in culture medium. The following cDNA mixture was prepared (amounts per 350,000 cells; in pcDNA3.1(+) plasmids): 200 ng GPR17, 20 ng Gα cDNA (10 ng in case of Gα_z), 10 ng Rap1GAP-RLucII, 500 ng rGFP-CAAX, salmon sperm DNA ad 1 μg. A 3-fold amount of polyethylenimine (PEI, dissolved in PBS) was added and acted as transfection reagent. The DNA-PEI mixture was incubated at room temperature for 30 min before it was added to the cells. Cells were incubated with the transfection mixture for 48 h. Subsequently, the media containing the transfection mixture was aspirated, and cells were washed with PBS, and incubated with Tyrode's buffer (137 mM NaCl, 0.9 mM KCl, 1 mM $MgCl_2$, 11.9 mM $NaHCO_3$, 3.6 mM NaH_2PO_4, 25 mM HEPES, 5.5. mM glucose, 1 mM $CaCl_2$, pH adjusted to 7.4 with NaOH) for 15 min at 37 °C before the addition of the GPR17 agonist **1**. The agonist incubated for 5 min prior to the addition of the luciferase substrate (5 μM Coelenterazine 400a, BioMol, Hamburg, Germany). In experiments testing GPR17 antagonists, these were incubated for 20 min before addition of the agonist **1**. RLucII-emission (395 nm) and GFP fluorescence (510 nm) were measured in a Mithras LB940 plate reader. The rGFP/RLucII-BRET ratios were analyzed in GraphPad PRISM 8.4.0 (GraphPad, San Diego, CA, USA) using the "(log) agonist vs. response − Variable slope (four parameters)" model. Data were expressed as percent of basal BRET ratio and were to this end normalized to a BRET ratio of 0 = 0%, buffer signal = 100%. All data are presented as mean ± SEM of three or four independent experiments, each performed in duplicate.

cAMP Accumulation Assays. CHO-FITR-hGPR17 cells were cultivated in DMEM with nutrient mixture F-12 (DMEM/F12) supplemented with 10% (v/v) FCS, penicillin (100 U/ml), streptomycin (0.1 mg/mL), hygromycin B (500 μg/mL), and blasticidin (30 μg/mL). Expression of hGPR17 was induced by treatment with doxycycline (1 μg/mL) for 16−24 h. The cAMP assays were performed in white, low-volume 384-well plates with 5,000 CHO-FITR-hGPR17 cells per well. Cells were preincubated for 30 min with varying concentrations of test compound or vehicle solution (final DMSO concentration 0.7%) at room temperature. Then a fixed concentration of 10 nM GPR17 agonist **1** (EC_{90}) was added in a final volume of 20 μL HBSS supplemented with 20 mM HEPES (pH 7.4) in the presence of 5 μM forskolin and 0.1 mM of the phosphodiesterase inhibitor isobutylmethylxanthine (IBMX). After 60 min of incubation, the reaction was terminated by addition of cAMP-d2 reagent and anti-cAMP antibody, and the plate was incubated for 60 min at room temperature according to the manufacturer's instructions of the HTRF cAMP dynamic 2 kit from Cisbio Bioassays (Revvity, Waltham, MA, USA). Changes of cAMP were determined by measuring the fluorescence ratio (665 nm/620 nm) using a Mithras LB 940 reader (Berthold Technologies, Bad Wildbad, Germany). Three independent experiments were performed in duplicates, and data were normalized to the effect induced by forskolin.

Radioligand Binding Assays. Radioligand binding assays were performed with the GPR17 agonist radioligand [^{3}H]PSB-12150 (17 Ci/mmol), a tritiated version of **1**. It was custom-labeled by Quotient Bioresearch Ltd., Fordham, UK. Membrane preparations from CHO-FITR-hGPR17 cells were used. $MgCl_2$ and ATP were freshly added to Tris buffer (50 mM, pH 7.4) to a final concentration of 10 mM and 100 μM, respectively, at the beginning of each experimental day. This buffer was used as the assay buffer. The [^{3}H]PSB-12150 DMSO solution was diluted to a final concentration of 25 nM with buffer. The membrane preparation was diluted to a final concentration of 200 mg/L with buffer. The substances to be tested were dissolved in DMSO. Ten μL of a substance-DMSO solution, 100 μL of the radioligand-buffer solution, and 100 μL of the membrane preparation buffer solution were mixed in 790 μL of the buffer in each vial. The mixture was incubated for 1 h at rt. The membrane-bound radioligand was then separated from free radioligand by rapid filtration through grade GF/B glass microfiber filters (Whatman, Dassel, Germany). Each filter unit was subsequently suspended in 3 mL ProSafe FC+ liquid scintillation cocktail (Meridian Biotechnologies Ltd., Epsom, UK) and measured using liquid scintillation counting (Tri-Carb 2810TR or Tri-Carb 2910 TR, PerkinElmer, Inc., Waltham, MA, USA). Unlabeled PSB-12150 was used to measure nonspecific binding in a final concentration of 100 μM. Data were analyzed using GraphPad Prism Version 7.00 (GraphPad, San Diego, CA, USA). Data are presented as mean pK_i ± SEM of three to five independent experiments, each performed in duplicate.

Structural Modeling of the Human GPR17 Receptor. An inactive state of the human GPR17 model was generated using the X-ray structure of the human $P2Y_{12}$ receptor as a template. The crystal structure of the human $P2Y_{12}$ receptor complexed with the antagonist AZD1283 (PDB 4NTJ)[40] was obtained from the Research Collaboratory for Structural Bioinformatics (RCSB) Protein Data Bank (PDB). The amino acid sequences of human GPR17 (accession number Q13304) retrieved from the UniProt database (http://www.uniprot.org/.) were aligned with the human $P2Y_{12}$ receptor (accession number Q9H244).[41] Sequence alignment between the template and target sequences was performed using Clustal Omega,[42] and manual adjustments were made to optimize the alignment. This refined alignment was then used to generate homology models of human GPR17 with MODELER 9.12.[43] From the 500 models generated, those with the best Discrete Optimized Protein Energy (DOPE) scores were selected.

Docking Studies. The generated model of the human GPR17 inactive state was prepared using the protein preparation tool implemented in the Molecular Operating Environment (MOE 2020.01)[44] and protonation using the Protonate 3D. Then the atomic partial charges were added, and a three-dimensional energy scoring grid was computed using AutoDockTools, defining a box of 60 × 60 × 60 points with a spacing of 0.375 Å. The prepared human GPR17 receptor model was utilized for flexible molecular docking using AutoDock4.2.[45] The selected anthranilic acid derivative **52** was docked into the binding site of the receptor. Fifty independent docking calculations were executed using the

https://doi.org/10.1021/acs.jmedchem.4c01755
J. Med. Chem. 2024, 67, 19365−19394

varCPSO-ls algorithm from PSO@Autodock within AutoDock4.2.[46] Termination criteria were set at 50,000 evaluation steps, with cognitive (c1) and social (c2) coefficients of the varCPSO-ls algorithm set at 6.05, and a swarm size of 60 particles. For the remaining parameters, the default values were applied. The docking poses were visually inspected based on docking scores, and the top-ranked pose was selected as the putative binding pose.

Chemistry. All commercially available reagents were used as purchased from different companies. Solvents were used without additional purification. Thin-layer chromatography was performed using TLC aluminum sheets silica gel 60 F_{254} (Merck, Darmstadt, Germany). Column chromatography was performed with silica gel (0.060−0.200 mm, Acros or 0.040−0.063 mm, Merck). Final compounds were dried at 60 °C under normal pressure and/or under vacuum (0.08−0.12 mbar) at rt. ^{1}H- and ^{13}C NMR data were recorded on a Bruker Avance 500 MHz NMR or on a Bruker AV-600 MHz spectrometer. Chemical shifts are reported in parts per million (ppm) relative to the deuterated solvent, i.e., DMSO, δ ^{1}H: 2.49 ppm; ^{13}C: 39.7 ppm. Coupling constants J are given in Hertz. For multiplicities, the following abbreviations were used: s (singlet), d (doublet), t (triplet), q (quartet), m (multiplet), and br (broad). The purities of isolated products were determined by HPLC coupled with ESI-MS and UV-detector using the following procedure: The compounds were dissolved in water/methanol = 1:1 (containing 2 mM ammonium acetate, concentration ca. 0.5 mg/mL). A 10 μL volume of the solution was injected into an HPLC column (Phenomenex Luna 3 μm C18, 50 mm × 2.00 mm), and elution was performed using a gradient of water/methanol (containing 2 mM ammonium acetate) from 90:10 to 0:100. The gradient was immediately started at a flow rate of 250 μL L/min for 15 min, followed by washing with 100% methanol for another 15 min. UV absorption was detected from 200 to 950 nm using a diode array detector (DAD). The purity of the compounds was determined by HPLC-UV-MS and proved to be ≥95% (except for **17**, **59**, and **69**, which were obtained with purities of 94.2, 91.4, and 90.5%, respectively).

The synthesis of 5-arylfuran-2-carboxylic acids (**4a**−**p**) was performed according to various procedures (either described in the literature or in the Supporting Information). All boronic acid and most anthranilic acid derivatives which were used as building blocks were purchased from different companies. The synthesis of more complex anthranilic acid derivatives or their analogs which were used as starting materials is described in the Supporting Information. A total of 64 final products **7**−**25**, **31**−**49**, **51**−**60**, **64**−**70**, **74**−**76**, **79**−**84** were synthesized and analyzed as described below.

*Preparation of Anthranilic Acid N-Carboxamide Derivatives **7**−**25**, **31**−**49**, **64**−**70**, **74**−**76** (General Procedure A).* To a solution of the heterocyclic carboxylic acid derivative (e.g., 0.25 mmol) in DCM (5 mL) $SOCl_2$ (2 mmol) was added. The solution was refluxed 3 h and subsequently concentrated under reduced pressure. The resulting acid chloride was directly used without further purification. The acid chloride was dissolved in DCM (10 mL) and treated with a mixture of the appropriate free anthranilic acid (0.35 mmol) or the methyl anthranilate, respectively, and DIPEA (5 mmol) in DCM (10 mL) at rt. After stirring at rt for 18 h, volatile components were removed under reduced pressure and the resulting crude was purified by column chromatography on silica gel (eluent: DCM/MeOH = 9.5:0.5, if not otherwise noted) to afford the corresponding amide derivative. When methyl anthranilates were used as starting materials the crude intermediate was dissolved in a mixture of THF, MeOH, and H_2O (2:1:2), treated with NaOH (5 mmol) and stirred at 35 °C for 12 h. The solvents were removed under reduced pressure, and water (15 mL) was added to the residue. Subsequently, the pH was adjusted to 1−2 with 1 N HCl and the precipitate was filtered under reduced pressure, washed with water, dried at 60 °C, and purified by column chromatography on silica gel 60 (eluent: eluent: DCM/MeOH = 9.5:0.5, if not otherwise noted).

*2-(5-(4-Isobutylphenyl)furan-2-carboxamido)benzoic Acid (**7**).* Compound **7** was synthesized according to the general procedure **A** starting from 5-(4-isobutylphenyl)furan-2-carboxylic acid (**4a**, 0.92 mmol) and 2-aminobenzoic acid (**5**, 1.50 mmol). Yield: 63%; colorless solid; ^{1}H NMR (500 MHz, DMSO-d_6): δ 12.48 (s, 1H, CO_2H), 8.75 (dd, J = 8.4, 1.0 Hz, 1H), 8.08 (dd, J = 7.9, 1.6 Hz, 1H), 7.84 (d, J = 8.2 Hz, 2H), 7.66 (ddd, J = 8.7, 7.4, 1.7 Hz, 1H), 7.37 (d, J = 3.6 Hz, 1H, furan-H), 7.27 (d, J = 8.3 Hz, 2H), 7.22−7.18 (m, 1H), 7.16 (d, J = 3.6 Hz, 1H, furan-H), 2.51−2.48 (m, 2H, CH_2CH), 1.87 (dq, J = 13.6, 6.8 Hz, 1H, CH_2CH), 0.88 (d, J = 6.6 Hz, 6H, $(CH_3)_2$). ^{13}C NMR (126 MHz, DMSO-d_6): δ 169.9, 155.5, 155.4, 146.1, 142.3, 140.8, 134.3, 131.3, 129.5, 126.7, 124.1, 122.8, 119.4, 117.6, 116.0, 107.8, 44.2, 29.4, 22.0. LC-MS (m/z): positive mode 364.2 $[M + H]^+$; purity by HPLC UV (254 nm)-ESI-MS: 98.3%.

*2-(5-(2,6-Diisopropylphenyl)furan-2-carboxamido)-benzoic Acid (**8**).* Compound **8** was synthesized according to the general procedure **A** starting from 5-(2,6-diisopropylphenyl)furan-2-carboxylic acid (**4b**, 0.37 mmol) and 2-aminobenzoic acid (**5**, 0.63 mmol). Yield: 57%; colorless solid; ^{1}H NMR (600 MHz, DMSO-d_6): δ 12.78 (s, 1H, CO_2H), 8.69 (d, J = 8.4 Hz, 1H), 8.01 (dd, J = 7.9, 1.6 Hz, 1H), 7.60 (t, J = 7.8 Hz, 1H), 7.47 (t, J = 7.8 Hz, 1H), 7.39 (d, J = 3.4 Hz, 1H, furan-H), 7.28 (d, J = 7.8 Hz, 2H), 7.15 (t, J = 8.1 Hz, 1H), 6.73 (d, J = 3.4 Hz, 1H, furan-H), 2.66−2.57 (m, 2H, $(CH)_2$), 1.13 (d, J = 6.9 Hz, 12H, $(CH_3)_4$). ^{13}C NMR (151 MHz, DMSO-d_6): δ 169.7, 155.8, 154.1, 149.0, 146.9, 140.7, 131.1, 130.3, 127.3, 122.6, 119.3, 116.1, 112.6, 30.5, 23.94. LC-MS (m/z): positive mode 392.3 $[M + H]^+$; purity by HPLC UV (254 nm)-ESI-MS: 99.8%.

*2-(5-([1,1′-Biphenyl]-2-yll)furan-2-carboxamido)benzoic Acid (**9**).* Compound **9** was synthesized according to the general procedure **A** starting from 5-([1,1′-biphenyl]-2-yl)-furan-2-carboxylic acid (**4c**, 0.37 mmol) and 2-aminobenzoic acid (**5**, 0.63 mmol). Yield: 68%; colorless solid; ^{1}H NMR (600 MHz, DMSO-d_6): δ 13.87 (s, 1H, CO_2H), 12.31 (s, 1H, NH), 8.69 (d, J = 8.3 Hz, 1H), 8.08−8.02 (m, 2H), 7.67−7.60 (m, 1H), 7.54 (td, J = 7.6, 1.3 Hz, 1H), 7.51−7.47 (m, 1H), 7.47−7.38 (m, 3H,), 7.36−7.32 (m, 1H), 7.31−7.28 (m, 2H), 7.19 (t, J = 8.0 Hz, 1H), 7.12 (d, J = 3.7 Hz, 1H, furan-H). ^{13}C NMR (151 MHz, DMSO-d_6): δ 134.3, 131.3, 130.7, 128.8, 128.7, 128.5, 128.0, 127.7, 127.4, 126.8, 122.8, 119.5, 116.9, 116.0, 111.5. LC-MS (m/z): positive mode 384.0 $[M + H]^+$; purity by HPLC UV (254 nm)-ESI-MS: 99.7%.

*2-(5-(4-Chlorophenyl)furan-2-carboxamido)benzoic Acid (**10**).* Compound **10** was synthesized according to general procedure **A** starting from 5-(4-chlorophenyl)furan-2-carboxylic acid (**4d**, 0.44 mmol) and 2-aminobenzoic acid (**5**, 0.6 mmol). Yield: 20% over two steps; colorless solid; ^{1}H NMR (500 MHz, DMSO-d_6): δ 13.93 (s br, 1H, CO_2H), 12.45 (s, 1H, NH), 8.71 (d, J = 8.4 Hz, 1H), 8.07 (d, J = 9.3 Hz, 1H),

https://doi.org/10.1021/acs.jmedchem.4c01755
J. Med. Chem. 2024, 67, 19365−19394

7.95−7.89 (m, 2H), 7.68−7.61 (m, 1H), 7.59−7.51 (m, 2H), 7.38 (d, J = 3.6 Hz, 1H, furan-H), 7.27 (d, J = 3.7 Hz, 1H, furan-H), 7.20 (m, 1H). ^{13}C NMR (126 MHz, DMSO-d_6): δ 170.1, 155.6, 154.1, 147.0, 140.8, 134.5, 133.7, 131.6, 129.3, 128.1, 126.0, 123.1, 119.7, 117.8, 116.4, 109.4. LC-MS (m/z): positive mode 342.1 $[M + H]^+$; purity by HPLC UV (254 nm)-ESI-MS: 98.8%.

*2-(5-(2-Bromophenyl)furan-2-carboxamido)-5-methoxybenzoic Acid (**11**).* Compound **11** was synthesized according to the general procedure **A** starting from 5-(2-bromophenyl)-furan-2-carboxylic acid (**4e**, 1.87 mmol) and 2-aminobenzoic acid (**5**, 2.87 mmol). Yield: 91%; Colorless solid; ^{1}H NMR (600 MHz, DMSO-d_6): δ 13.95 (s br, 1H, CO_2H), 12.15 (s, 1H, NH), 8.61 (d, J = 9.2 Hz, 1H), 8.00 (d, J = 7.6 Hz, 1H), 7.81 (d, J = 8.0 Hz, 1H), 7.56−7.51 (m, 2H), 7.40−7.34 (m, 3H), 7.28 (d, J = 9.1 Hz, 1H), 3.79 (s, 3H, OCH_3) ppm. 13C-NMR (151 MHz, DMSO-d_6) δ: 169.6, 155.3, 154.6, 152.5, 147.1, 134.5, 134.1, 130.7, 129.6, 129.4, 128.4, 121.6, 120.6, 119.8, 118.0, 116.8, 115.3, 113.2, 55.6 (OCH_3) ppm. LC-MS (m/z): positive mode 416.0 $[M + H]^+$; purity by HPLC UV (254 nm)-ESI-MS: 98.6%.

*2-(5-(2-Methoxynaphthalen-1-yl)furan-2-carboxamido)-benzoic Acid (**12**).* Compound **12** was synthesized according to the general procedure **A** starting from 5-(2-methoxynaphthalen-1-yl)furan-2-carboxylic acid (**4f**, 0.37 mmol) and 2-aminobenzoic acid (**5**, 0.63 mmol). Yield: 72%; colorless solid; ^{1}H NMR (500 MHz, DMSO-d_6): δ 13.57 (s, 1H, CO_2H), 12.29 (s, 1H, NH), 8.73 (d, J = 8.5 Hz, 1H), 8.12 (d, J = 9.1 Hz, 1H), 8.02 (dd, J = 7.9, 1.6 Hz, 1H), 7.95 (d, J = 8.1 Hz, 1H), 7.82 (d, J = 8.6 Hz, 1H), 7.68−7.62 (m, 1H), 7.59 (d, J = 9.2 Hz, 1H), 7.56−7.50 (m, 1H), 7.48 (d, J = 3.5 Hz, 1H, furan-H), 7.45−7.39 (m, 1H), 7.21−7.16 (m, 1H), 6.91 (d, J = 3.5 Hz, 1H, furan-H), 3.94 (s, 1H, OCH_3). ^{13}C NMR (126 MHz, DMSO-d_6): δ 169.7, 155.9, 155.8, 151.3, 146.8, 140.7, 134.2, 132.6, 131.8, 131.1, 128.3, 128.1, 127.6, 124.0, 123.9, 122.8, 119.6, 116.6, 116.0, 114.3, 113.8, 111.8, 56.6. LC-MS (m/z): positive mode 388.3 $[M + H]^+$; purity by HPLC UV (254 nm)-ESI-MS: 99.1%.

*2-(5-(1-Methyl-1H-indazol-4-yl)furan-2-carboxamido)-benzoic Acid (**13**).* Compound **13** was synthesized according to the general procedure **A** starting from 5-(1-methyl-1*H*-indazol-4-yl)furan-2-carboxylic acid (**4g**, 0.35 mmol) and 2-aminobenzoic acid (**5**, 0.61 mmol). Yield: 81%; colorless solid; ^{1}H NMR (500 MHz, DMSO-d_6): δ 13.94 (s, 1H, CO_2H), 12.41 (s, 1H, NH), 8.75 (dd, J = 8.4, 0.9 Hz, 1H), 8.69 (d, J = 0.9 Hz, 1H), 8.09 (dd, J = 7.9, 1.5 Hz, 1H), 7.77 (dd, J = 7.2, 0.5 Hz, 1H), 7.72 (d, J = 8.5 Hz, 1H), 7.67 (td, J = 8.7, 8.0, 1.6 Hz, 1H), 7.50 (dd, J = 8.4, 7.3 Hz, 1H), 7.47−7.49 (m, 2H, furan-H), 7.24−7.20 (m, 1H), 4.11 (s, 3H, NCH_3). ^{13}C NMR (126 MHz, DMSO-d_6): δ 169.9, 155.5, 154.5, 146.9, 140.7, 140.1, 134.3, 131.9, 131.3, 126.0, 122.9, 121.4, 119.7, 118.5, 117.9, 117.4, 116.1, 110.6, 35.5 (NCH_3). LC-MS (m/z): positive mode 362.40 $[M + H]^+$; purity by HPLC UV (254 nm)-ESI-MS: 99.7%.

*2-(5-(3′-Methoxy-[1,1′-biphenyl]-2-yl)furan-2-carboxamido)benzoic Acid (**14**).* Compound **14** was synthesized according to general procedure **A** starting from 5-(3′-methoxy-[1,1′-biphenyl]-2-yl)furan-2-carboxylic acid (**4h**, 1.50 mmol) and 2-aminobenzoic acid (**5**, 1.65 mmol). Yield: 33%; colorless solid; ^{1}H NMR (500 MHz, DMSO-d_6): δ 13.84 (s br, 1H), 12.31 (s, 1H), 8.68 (d, J = 7.9 Hz, 1H), 8.05 (ddd, J = 9.3, 7.6, 1.5 Hz, 2H), 7.64 (ddd, J = 8.8, 7.5, 1.7 Hz, 1H), 7.51 (dtd, J = 21.4, 7.5, 1.5 Hz, 2H), 7.37−7.31 (m, 2H), 7.21−7.17 (m, 1H), 7.14 (d, J = 3.6 Hz, 1H, furan-H), 6.99−6.95 (m, 1H), 6.86−6.83 (m, 2H), 5.69 (d, J = 3.6 Hz, 1H, furan-H), 3.72 (s, 3H, OCH_3). ^{13}C NMR (126 MHz, DMSO-d_6): δ 170.0, 159.5, 155.7, 154.2, 146.1, 142.4, 140.8, 140.1, 134.5, 131.5, 130.8, 129.9, 129.0, 128.2, 127.6, 126.9, 123.1, 121.2, 119.7, 117.2, 116.2, 114.4, 113.5, 111.7, 55.3 (OCH_3). LC-MS (m/z): positive mode 414.2 $[M + H]^+$; purity by HPLC UV (254 nm)-ESI-MS: 98%.

*2-(5-(2-Phenethoxyphenyl)furan-2-carboxamido)benzoic Acid (**15**).* Compound **15** was synthesized according to the general procedure **A** starting from 5-(2-phenethoxyphenyl)-furan-2-carboxylic acid (**4i**, 0.16 mmol) and 2-aminobenzoic acid (**5**, 0.18 mmol). Yield: 84%; colorless solid; ^{1}H NMR (500 MHz, DMSO-d_6): δ 13.87 (s br, 1H, CO_2H), 12.45 (s, 1H, NH), 8.73 (d, J = 8.2 Hz, 1H), 8.05 (ddd, J = 14.9, 7.9, 1.6 Hz, 3H), 7.65 (ddd, J = 8.5, 7.4, 1.6 Hz, 2H), 7.41−7.30 (m, 6H), 7.29 (d, J = 3.6 Hz, 1H, furan-H), 7.26−7.15 (m, 3H), 7.10−7.02 (m, 1H), 6.92 (d, J = 3.6 Hz, 1H, furan-H), 4.41 (t, J = 6.7 Hz, 2H, OCH_2CH_2Ph), 3.19 (t, J = 6.7 Hz, 2H, OCH_2CH_2Ph). ^{13}C NMR (126 MHz, DMSO-d_6): δ 170.1, 155.7, 155.3, 151.9, 145.51, 141.0, 138.4, 134.5, 131.5, 130.3, 129.0, 128.5, 126.5, 125.8, 123.0, 120.9, 119.6, 117.8, 117.7, 116.2, 112.9, 112.7, 68.9 (OCH_2), 35.0 (CH_2Ph). LC-MS (m/z): positive mode 428.3 $[M + H]^+$; purity by HPLC UV (254 nm)-ESI-MS: 99.1%.

*2-(5-(3,5-Dichlorophenyl)furan-2-carboxamido)-5-methoxybenzoic Acid (**16**).* Compound **HR 16** was synthesized according to the general procedure **A** starting from 5-(3,5-dichlorophenyl)furan-2-carboxylic acid (**4j**, 0.42 mmol) and 2-amino-5-methoxybenzoic acid methyl ester (**6**, 0.6 mmol). Yield: 17.6%; pale yellow solid; ^{1}H NMR (500 MHz, DMSO-d_6): δ 12.69 (s, 1H, CO_2H), 8.53 (d, J = 9.1 Hz, 1H), 7.94 (d, J = 1.3 Hz, 2H), 7.60 (t, J = 1.9 Hz, 1H), 7.55 (d, J = 3.1 Hz, 1H), 7.42 (d, J = 3.6 Hz, 1H, furan-H), 7.32 (d, J = 3.6 Hz, 1H, furan-H), 7.20 (dd, J = 9.1, 3.2 Hz, 1H), 3.79 (s, 3H, OCH_3). ^{13}C NMR (126 MHz, DMSO-d_6): δ 169.5, 155.1, 154.6, 151.90, 148.1, 135.1, 133.9, 132.5, 128.0, 122.7, 121.5, 120.1, 119.6, 117.0, 115.4, 111.1, 55.5 (OCH_3). LC-MS (m/z): positive mode 406.1 $[M + H]^+$; purity by HPLC UV (254 nm)-ESI-MS: 99%.

*2-(5-(2,3-Dichlorophenyl)furan-2-carboxamido)-5-methoxybenzoic Acid (**17**).* Compound **17** was synthesized according to general procedure **A** starting from 5-(2,3-dichlorophenyl)furan-2-carboxylic acid (**4k**, 0.14 mmol) and 2-amino-5-methoxybenzoic acid methyl ester (**6**, 0.15 mmol). Yield: 43%; off-white solid; ^{1}H NMR (500 MHz, DMSO-d_6): δ 13.89 (s br, 1H, CO_2H), 12.15 (s, 1H, NH), 8.60 (d, J = 9.1 Hz, 1H), 8.01 (dd, J = 8.0, 1.5 Hz, 1H), 7.70 (dd, J = 8.1, 1.6 Hz, 1H), 7.52 (d, J = 3.1 Hz, 1H), 7.49 (t, J = 8.0 Hz, 1H), 7.42−7.36 (m, 2H), 7.27 (dd, J = 9.2, 3.1 Hz, 1H), 3.79 (s, 3H, OCH_3). ^{13}C NMR (126 MHz, DMSO-d_6): δ 169.6, 155.1, 154.6, 150.7, 147.4, 134.0, 133.5, 130.7, 129.9, 128.8, 128.2, 127.3, 121.6, 120.5, 118.1, 116.9, 115.3, 114.4, 55.6 (OCH_3). LC-MS (m/z): positive mode 406.3 $[M + H]^+$; purity by HPLC UV (254 nm)-ESI-MS: 94.2%.

*5-Methoxy-2-(5-(2-phenoxyphenyl)furan-2-carboxamido)benzoic Acid (**18**).* Compound **18** was synthesized according to general procedure **A** starting from 5-(2-phenoxyphenyl)furan-2-carboxylic acid (**4l**, 0.50 mmol) and 2-amino-5-methoxybenzoic acid methyl ester (**6**, 0.55 mmol). Yield: 78%; colorless solid; ^{1}H NMR (600 MHz, DMSO-d_6): δ 14.02 (s br, 1H, CO_2H), 12.22 (s, 1H, NH), 8.64 (d, J = 9.2 Hz, 1H), 8.16 (d, J = 7.7 Hz, 1H), 7.54 (d, J = 3.1 Hz, 1H),

https://doi.org/10.1021/acs.jmedchem.4c01755
J. Med. Chem. 2024, 67, 19365−19394

7.45−7.38 (m, 3H), 7.34−7.25 (m, 3H), 7.16 (t, J = 7.4 Hz, 1H), 7.07−6.99 (m, 4H), 3.79 (s, 3H, OCH_3). ^{13}C NMR (151 MHz, DMSO-d_6) δ = 169.8, 156.2, 155.3, 154.5, 152.9, 150.9, 146.3, 134.3, 130.5, 130.4, 126.5, 124.5, 123.9, 121.4, 121.0, 120.7, 120.0, 118.2, 117.7, 117.5, 115.3, 112.8, 55.6 (OCH_3). LC-MS (m/z): positive mode 430.1 $[M + H]^+$; purity by HPLC UV (254 nm)-ESI-MS: 99.6%.

*2-(5-(4-Isobutylphenyl)furan-2-carboxamido)-5-methoxybenzoic Acid (**19**).* Compound **19** was synthesized according to the general procedure **A** starting from 5-(4-isobutylphenyl)-furan-2-carboxylic acid (**4a**, 0.92 mmol) and 2-amino-5-methoxybenzoic acid methyl ester (**6**, 1.50 mmol). Yield: 87%; colorless solid; ^1H NMR (500 MHz, DMSO-d_6): δ 13.96 (s, 1H, CO_2H), 12.17 (s, 1H, NH), 8.66 (d, J = 9.2 Hz, 1H), 7.82 (d, J = 8.2 Hz, 2H), 7.55 (d, J = 3.1 Hz, 1H), 7.32 (d, J = 3.6 Hz, 1H), 7.30−7.24 (m, 3H), 7.14 (d, J = 3.6 Hz, 1H), 3.80 (s, 3H, OCH_3), 2.50−2.52 (m, 2H, CH_2), 1.87 (dq, J = 13.5, 6.7 Hz, 1H, CH), 0.87 (s, 6H, $(CH_3)_2$). ^{13}C NMR (126 MHz, DMSO-d_6) δ = 169.5, 155.2, 154.2, 146.3, 142.2, 134.2, 129.5, 126.7, 124.0, 121.1, 120.4, 117.3, 117.2, 115.0, 107.7, 55.3 (OCH_3), 44.2, 29.4, 22.0. LC-MS (m/z): positive mode 394.5 $[M + H]^+$; purity by HPLC UV (254 nm)-ESI-MS: 100%.

*2-(5-([1,1′-Biphenyl]-3-yl)furan-2-carboxamido)-5-methoxybenzoic Acid (**20**).* Compound **20** was synthesized according to general procedure **A** starting from 5-([1,1′-biphenyl]-3-yl)furan-2-carboxylic acid (**4m**, 0.50 mmol) and 2-amino-5-methoxybenzoic acid methyl ester (**6**, 0.55 mmol). Yield: 27%; beige solid; ^1H NMR (500 MHz, DMSO-d_6): δ 13.90 (s br, 1H, CO_2H), 12.17 (s, 1H, NH), 8.63 (d, J = 9.1 Hz, 1H), 8.18 (t, J = 1.9 Hz, 1H), 7.92 (dt, J = 7.6, 0.9 Hz, 1H), 7.79−7.76 (m, 2H), 7.69 (ddd, J = 7.7, 1.9, 1.1 Hz, 1H), 7.58 (t, J = 7.7 Hz, 1H), 7.55−7.49 (m, 3H), 7.44−7.39 (m, 1H), 7.36 (s, 2H), 7.27 (dd, J = 9.2, 3.1 Hz, 1H), 3.80 (s, 3H, OCH_3). ^{13}C NMR (126 MHz, DMSO-d_6): δ 169.7, 155.4, 155.0, 154.5, 146.9, 141.2, 139.6, 134.2, 130.0, 129.9, 129.2, 128.0, 127.4, 127.0, 123.1, 122.8, 121.5, 120.6, 117.9, 117.4, 115.3, 109.1, 55.6 (OCH_3). LC-MS (m/z): positive mode 414.2 $[M + H]^+$; purity by HPLC UV (254 nm)-ESI-MS: 98.8%.

*2-(5-([1,1′-Biphenyl]-4-yl)furan-2-carboxamido)-5-methoxybenzoic Acid (**21**).* Compound **21** was synthesized according to general procedure **A** starting from 5-([1,1′-biphenyl]-4-yl)furan-2-carboxylic acid (**4n**, 0.4 mmol) and 2-amino-5-methoxybenzoic acid methyl ester (**6**, 0.54 mmol). Yield: 54%; Colorless solid; ^1H NMR (600 MHz, DMSO-d_6): δ 13.89 (s, 1H, CO_2H), 8.61 (d, J = 9.0 Hz, 1H), 8.02 (d, J = 8.3 Hz, 2H), 7.75 (d, J = 8.2 Hz, 2H), 7.69 (d, J = 7.5 Hz, 2H), 7.64 (d, J = 3.2 Hz, 1H), 7.51−7.43 (m, 2H), 7.41−7.35 (m, 1H), 7.28 (d, J = 3.6 Hz, 1H, furan-H), 7.21 (d, J = 3.6 Hz, 1H, furan-H), 7.09 (dd, J = 9.0, 3.2 Hz, 1H), 3.76 (s, 3H, OCH_3). ^{13}C NMR (151 MHz, DMSO-d_6): δ 170.4, 155.6, 154.9, 154.6, 148.0, 140.6, 139.7, 134.6, 129.5, 128.8, 128.3, 127.6, 127.1, 125.3, 123.1, 120.8, 118.3, 116.9, 116.1, 108.8, 55.7 (OCH_3). LC-MS (m/z): positive mode 414.5 $[M + H]^+$; purity by HPLC UV (254 nm)-ESI-MS: 99.9%.

*2-(5-([1,1′-Biphenyl]-2-yl)furan-2-carboxamido)-5-methoxybenzoic Acid (**22**).* Compound **22** was synthesized according to the general procedure **A** starting from 5-([1,1′-biphenyl]-2-yl)furan-2-carboxylic acid (**4c**, 0.38 mmol) and 2-amino-5-methoxybenzoic acid methyl ester (**6**, 0.58 mmol). Yield: 68%; colorless solid; ^1H NMR (600 MHz, DMSO-d_6): δ 13.76 (s, 1H, CO_2H), 12.00 (s, 1H, NH), 8.60 (d, J = 9.1 Hz, 1H), 8.03 (d, J = 7.5 Hz, 1H), 7.56−7.47 (m, 3H), 7.45−7.41 (m, 3H), 7.34 (d, J = 7.3 Hz, 1H), 7.29 (d, J = 6.8 Hz, 2H), 7.28−7.23 (m, 1H), 7.08 (d, J = 3.3 Hz, 1H, furan-H), 5.57 (d, J = 3.3 Hz, 1H, furan-H), 3.79 (s, 3H, OCH_3). ^{13}C NMR (151 MHz, DMSO-d_6): δ 169.4, 155.1, 154.3, 153.9, 146.0, 140.8, 139.9, 134.0, 130.7, 128.8, 128.7, 128.5, 127.9, 127.6, 127.5, 126.7, 121.2, 120.4, 117.4, 116.5, 115.0, 111.4, 55.4 (OCH_3). LC-MS (m/z): positive mode 414.1 $[M + H]^+$; purity by HPLC UV (254 nm)-ESI-MS: 100%.

*5-Methoxy-2-(5-(3″-(2-methoxyethoxy)-[1,1′:2′,1″-terphenyl]-2-yl)furan-2-carboxamido)benzoic Acid (**23**).* Compound **23** was synthesized according to general procedure **A** starting from 5-(3″-(2-methoxyethoxy)-[1,1′:2′,1″-terphenyl]-2-yl)furan-2-carboxylic acid (**4o**, 0.5 mmol) and 2-amino-5-methoxybenzoic acid methyl ester (**6**, 0.3 mmol). Yield: 2%; pale yellow solid; ^1H NMR (500 MHz, DMSO-d_6): δ 13.42 (s, 1H, CO_2H), 8.55 (d, J = 9.0 Hz, 1H), 8.08 (d, J = 7.8 Hz, 1H), 7.59 (d, J = 3.2 Hz, 1H), 7.51 (t, J = 7.5 Hz, 1H), 7.45 (t, J = 7.5 Hz, 1H), 7.37−7.29 (m, 2H), 7.10 (dd, J = 9.0, 3.2 Hz, 1H), 7.03 (d, J = 3.6 Hz, 1H, furan-H), 6.98 (dd, J = 7.7, 2.5 Hz, 1H), 6.88−6.81 (m, 2H), 5.60 (d, J = 3.6 Hz, 1H, furan-H), 4.11−3.98 (m, 2H, $OCH_2CH_2OCH_3$), 3.77 (s, 3H, $OCH_2CH_2OCH_3$), 3.61 (dd, J = 5.7, 3.4 Hz, 2H, $OCH_2CH_2OCH_3$), 3.27 (s, 3H, OCH_3). ^{13}C NMR (126 MHz, DMSO-d_6): δ 169.7, 158.7, 155.2, 154.3, 153.7, 146.8, 142.5, 139.8, 134.2, 130.7, 129.9, 128.7, 128.2, 127.7, 127.0, 121.3, 120.6, 118.5, 116.0, 115.6, 114.8, 114.2, 111.4, 70.5, 67.1, 58.3, 55.4. LC-MS (m/z): positive mode 488.1 $[M + H]^+$; purity by HPLC UV (254 nm)-ESI-MS: 98.9%.

*5-Methoxy-2-(5-(2-phenethoxyphenyl)furan-2-carboxamido)benzoic Acid (**24**).* Compound **24** was synthesized according to the general procedure **A** starting from 5-(2-phenethoxyphenyl)furan-2-carboxylic acid (**4i**, 0.16 mmol) and 2-amino-5-methoxybenzoic acid methyl ester (**6**, 0.18 mmol). Yield: 95%; beige solid; ^1H NMR (500 MHz, DMSO-d_6): δ 13.95 (s br, 1H, CO_2H), 12.17 (s, 1H, NH), 8.65 (d, J = 9.2 Hz, 1H), 8.02 (dd, J = 7.8, 1.6 Hz, 1H), 7.54 (d, J = 3.1 Hz, 1H), 7.40−7.20 (m, 9H), 7.10−7.01 (m, 1H), 6.91 (d, J = 3.6 Hz, 1H, furan-H), 4.41 (t, J = 6.7 Hz, 2H, OCH_2CH_2Ph), 3.79 (s, 3H, OCH_3), 3.19 (t, J = 6.7 Hz, 2H, OCH_2CH_2Ph). ^{13}C NMR (126 MHz, DMSO-d_6): δ 169.8, 155.4, 155.3, 154.5, 151.7, 145.7, 138.4, 134.4, 130.2, 129.0, 128.5, 126.5, 125.8, 121.4, 121.0, 120.7, 117.8, 117.6, 117.3, 115.2, 112.9, 112.6, 69.0 (OCH_2), 55.6 (OCH_3), 35.0 (CH_2Ph). LC-MS (m/z): positive mode 458.5 $[M + H]^+$; purity by HPLC UV (254 nm)-ESI-MS: 97.5%.

*5-Methoxy-2-(5-(3-phenethoxyphenyl)furan-2-carboxamido)benzoic Acid (**25**).* Compound **25** was synthesized according to the general procedure **A** starting from 5-(3-phenethoxyphenyl)furan-2-carboxylic acid (**4p**, 0.13 mmol) and 2-amino-5-methoxybenzoic acid methyl ester (**6**, 0.14 mmol). Yield: 99%; colorless solid; ^1H NMR (500 MHz, DMSO-d_6): δ 13.91 (s br, 1H, CO_2H), 12.13 (s, 1H, NH), 8.62 (d, J = 9.2 Hz, 1H), 7.54 (d, J = 3.1 Hz, 1H), 7.52−7.48 (m, 1H), 7.46−7.44 (m, 1H), 7.38 (t, J = 8.0 Hz, 1H), 7.36−7.26 (m, 6H), 7.25 (d, J = 3.7 Hz, 1H, furan-H), 7.24−7.20 (m, 1H), 6.98 (dd, J = 8.2, 2.5 Hz, 1H), 4.30 (t, J = 6.8 Hz, 2H, OCH_2CH_2Ph), 3.79 (s, 3H, OCH_3), 3.07 (t, J = 6.8 Hz, 2H, OCH_2CH_2Ph). ^{13}C NMR (126 MHz, DMSO-d_6): δ 169.7, 159.1, 155.4, 155.0, 154.5, 146.8, 138.4, 134.3, 130.6, 130.4, 129.1, 128.5, 126.4, 121.5, 120.6, 117.7, 117.3, 116.6, 115.4, 115.3, 110.6, 109.0, 68.5 (OCH_2), 55.6 (OCH_3), 35.0

https://doi.org/10.1021/acs.jmedchem.4c01755
J. Med. Chem. 2024, 67, 19365−19394

(CH_2Ph). LC-MS (m/z): positive mode 458.5 $[M + H]^+$; purity by HPLC UV (254 nm)-ESI-MS: 98.6%.

*3-Chloro-2-(5-(naphthalen-1-yl)furan-2-carboxamido)-benzoic Acid (**31**).* Compound **31** was synthesized according to general procedure **A** starting from 5-(naphthalen-1-yl)furan-2-carboxylic acid (**26**, 0.44 mmol) and methyl 2-amino-3-chlorobenzoate (**28a**, 0.65 mmol). Yield: 54%; colorless solid; ^1H NMR (500 MHz, DMSO-d_6): δ 12.47 (s, 1H, CO_2H), 8.50 (d, J = 8.5 Hz, 1H), 8.28 (d, J = 7.5 Hz, 1H), 8.03 (d, J = 8.1 Hz, 2H), 8.00 (d, J = 7.3 Hz, 1H), 7.71−7.58 (m, 3H), 7.40 (d, J = 3.6 Hz, 1H, furan-H), 7.22 (t, J = 8.1 Hz, 1H), 7.18 (d, J = 3.5 Hz, 1H, furan-H), 7.08 (d, J = 7.2 Hz, 1H). ^{13}C NMR (126 MHz, DMSO-d_6): δ 167.5, 155.6, 154.9, 147.6, 137.9, 133.7, 131.6, 129.8, 129.7, 129.4, 128.8, 128.3, 127.7, 127.0, 126.6, 126.4, 125.6, 125.1, 124.8, 118.2, 116.4, 112.0. LC-MS (m/z): positive mode 392.1 $[M + H]^+$; purity by HPLC UV (254 nm)-ESI-MS: 99.8%.

*4,5-Difluoro-2-(5-(naphthalen-1-yl)furan-2-carboxamido)benzoic Acid (**32**).* Compound **32** was synthesized according to general procedure **A** starting from 5-(naphthalen-1-yl)furan-2-carboxylic acid (**26**, 0.25 mmol) and methyl 2-amino-4,5-difluorobenzoate (**28b**, 0.4 mmol). Yield: 33%; colorless solid; ^1H NMR (500 MHz, DMSO-d_6): δ 15.22 (s, 1H, CO_2H), 8.62 (dd, J = 13.6, 7.6 Hz, 1H), 8.51 (d, J = 8.5 Hz, 1H), 8.04−7.95 (m, 4H), 7.69−7.57 (m, 3H), 7.40 (d, J = 3.5 Hz, 1H, furan-H), 7.19 (d, J = 3.5 Hz, 1H, furan-H). ^{13}C NMR (126 MHz, DMSO-d_6): δ 167.9, 156.0, 154.8, 150.0 (dd, J = 246, 13.0 Hz), 144.1 (dd, J = 241, 12.9 Hz), 137.7 (d, J = 9.6 Hz), 133.7, 129.8, 129.4, 128.8, 127.7, 126.9, 126.6, 126.5, 125.7, 125.1, 121.6, 119.5 (d, J = 17.7 Hz), 116.5, 112.1, 107.4 (d, J = 23.0 Hz). LC-MS (m/z): positive mode 394.2 $[M + H]^+$; purity by HPLC UV (254 nm)-ESI-MS: 99.1%.

*3,5-Difluoro-2-(5-(naphthalen-1-yl)furan-2-carboxamido)benzoic Acid (**32a**).* Compound **32a** was synthesized according to general procedure **A** starting from 5-(naphthalen-1-yl)furan-2-carboxylic acid (**26**, 0.44 mmol) and 2-amino-3,5-difluorobenzoic acid (**28n**, 0.6 mmol). Yield: 52%; colorless solid; ^1H NMR (500 MHz, DMSO-d_6): δ 12.93 (s, 1H, COOH), 8.51 (dd, J = 8.5, 1.1 Hz, 1H), 8.06−7.99 (m, 2H), 7.94 (dd, J = 7.3, 1.2 Hz, 1H), 7.69−7.57 (m, 3H), 7.52 (ddd, J = 9.1, 3.1, 1.3 Hz, 1H), 7.41 (d, J = 3.5 Hz, 1H, furan-H), 7.30 (ddd, J = 10.4, 8.6, 3.0 Hz, 1H), 7.16 (d, J = 3.6 Hz, 1H, furan-H). ^{13}C NMR (126 MHz, DMSO-d_6): δ 167.5, 157.9 (dd, J = 242.9, 11.9 Hz), 155.7, 155.3 (dd, J = 252.3, 12.0 Hz), 155.0, 147.8, 133.7, 133.5 (d, J = 5.0 Hz), 129.8, 129.5, 128.8, 127.7, 127.0, 126.7, 126.5, 125.6, 125.1, 123.1 (d, J = 12.4 Hz), 116.7, 112.2 (d, J = 21.9 Hz), 111.9, 106.0−105.0 (m). LC-MS (m/z): positive mode 394.2 $[M + H]^+$; purity by HPLC UV (254 nm)-ESI-MS: 99.3%.

*4-Methoxy-2-(5-(naphthalen-1-yl)furan-2-carboxamido)-benzoic Acid (**33**).* Compound **33** was synthesized according to general procedure **A** starting from 5-(naphthalen-1-yl)furan-2-carboxylic acid (**26**, 0.78 mmol) and 2-amino-4-methoxybenzoic acid (**28c**, 1 mmol). Yield: 59%; colorless solid; ^1H NMR (500 MHz, DMSO-d_6): δ 13.22 (s, 1H, CO_2H), 8.51 (d, J = 8.5 Hz, 1H), 8.38 (d, J = 2.6 Hz, 1H), 8.05−7.96 (m, 4H), 7.73−7.66 (m, 1H), 7.65−7.56 (m, 2H), 7.45 (d, J = 3.6 Hz, 1H, furan-H), 7.20 (d, J = 3.5 Hz, 1H, furan-H), 6.74 (dd, J = 8.8, 2.7 Hz, 1H), 3.84 (s, 3H, OCH_3). ^{13}C NMR (126 MHz, DMSO-d_6): δ 170.1, 163.2, 156.0, 155.1, 147.4, 142.7, 133.7, 133.2, 129.9, 129.4, 128.8, 127.8, 126.9, 126.54, 126.51, 125.6, 125.0, 117.2, 112.4, 108.6, 104.6, 55.6 (OCH_3). LC-MS (m/z): positive mode 388.4 $[M + H]^+$; purity by HPLC UV (254 nm)-ESI-MS: 99.1%.

*4-Bromo-2-(5-(naphthalen-1-yl)furan-2-carboxamido)-benzoic Acid (**34**).* Compound **34** was synthesized according to general procedure **A** starting from 5-(naphthalen-1-yl)furan-2-carboxylic acid (**26**, 0.42 mmol) and 2-amino-4-bromobenzoic acid (**28d**, 0.59 mmol). Yield: 55%; colorless solid; ^1H NMR (500 MHz, DMSO-d_6): δ 14.63 (s, 1H, CO_2H), 8.88 (d, J = 2.0 Hz, 1H), 8.51 (d, J = 8.5 Hz, 1H), 8.04−7.99 (m, 4H), 7.69−7.65 (m, 1H), 7.64−7.56 (m, 2H), 7.43 (d, J = 3.6 Hz, 1H, furan-H), 7.27 (dd, J = 8.4, 2.0 Hz, 1H), 7.19 (d, J = 3.6 Hz, 1H, furan-H). ^{13}C NMR (126 MHz, DMSO-d_6): δ 169.4, 156.1, 155.0, 147.6, 141.9, 133.7, 133.3, 129.8, 129.4, 128.8, 127.7, 126.9, 126.6, 126.5, 125.6, 125.0, 124.9, 124.7, 121.3, 116.8, 112.2. LC-MS (m/z): positive mode 436.0 $[M + H]^+$; purity by HPLC UV (254 nm)-ESI-MS: 97.9%.

*5-Methyl-2-(5-(naphthalen-1-yl)furan-2-carboxamido)-benzoic Acid (**35**).* Compound **35** was synthesized according to the general procedure **A** starting from 5-(naphthalen-1-yl)furan-2-carboxylic acid (**26**, 0.38 mmol) and 2-amino-5-methylbenzoic acid (**28e**, 0.50 mmol). Yield: 58%; colorless solid. ^1H NMR (500 MHz, DMSO-d_6): δ 12.58 (s, 1H), 8.62 (d, J = 8.4 Hz, 1H), 8.51 (d, J = 8.7 Hz, 1H), 8.03 (d, J = 8.2 Hz, 2H), 7.97 (dd, J = 6.9, 0.7 Hz, 1H), 7.87 (d, J = 2.2 Hz, 1H), 7.73−7.66 (m, 1H), 7.64−7.57 (m, 2H), 7.45−7.42 (m, 2H), 7.20 (d, J = 3.6 Hz, 1H), 2.32 (s, 3H, CH_3). ^{13}C NMR (126 MHz, DMSO-d_6): δ 170.1, 155.7, 154.9, 147.4, 138.5, 134.7, 133.7, 132.1, 131.5, 129.9, 129.4, 128.8, 127.8, 126.9, 126.5, 125.6, 125.1, 119.8, 117.1, 117.0, 112.4, 20.4 (CH_3). LC-MS (m/z): positive mode 372.1 $[M + H]^+$; purity by HPLC UV (254 nm)-ESI-MS: 99.9%.

*2-(5-(naphthalen-1-yl)furan-2-carboxamido)-5-(trifluoromethoxy)benzoic Acid (**36**).* Compound **36** was synthesized according to general procedure **A** starting from 5-(naphthalen-1-yl)furan-2-carboxylic acid (**26**, 0.41 mmol) and 2-amino-5-(trifluoromethoxy)benzoic acid (**28f**, 0.56 mmol). Yield: 24%; colorless solid; ^1H NMR (500 MHz, DMSO-d_6): δ 15.34 (s, 1H, CO_2H), 8.70 (d, J = 9.0 Hz, 1H), 8.51 (d, J = 8.5 Hz, 1H), 8.03 (d, J = 8.0 Hz, 3H), 7.98 (d, J = 3.0 Hz, 1H), 7.64 (tt, J = 14.0, 7.4 Hz, 3H), 7.39 (d, J = 3.6 Hz, 1H, furan-H), 7.37 (dd, J = 9.1, 3.1 Hz, 1H), 7.19 (d, J = 3.5 Hz, 1H, furan-H). ^{13}C NMR (126 MHz, DMSO-d_6): δ 168.3, 156.0, 154.6, 148.1, 142.6, 139.8, 133.7, 129.7, 129.4, 128.8, 127.6, 126.9, 126.7, 126.4, 125.6, 125.0, 123.4, 123.1, 120.1, 119.9 (q, J = 257 Hz), 116.2, 112.0. LC-MS (m/z): positive mode 442.4 $[M + H]^+$; purity by HPLC UV (254 nm)-ESI-MS: 98.0%.

*5-Cyclopropyl-2-(5-(naphthalen-1-yl)furan-2-carboxamido)benzoic Acid (**37**).* Compound **37** was synthesized according to general procedure **A** starting from 5-(naphthalen-1-yl)furan-2-carboxylic acid (**26**, 0.42 mmol) and methyl 2-amino-5-cyclopropylbenzoic acid (**28g**, 0.59 mmol). Yield: 46% over two steps; colorless solid; ^1H NMR (600 MHz, DMSO-d_6): δ 14.18 (s br, 1H, CO_2H), 8.53 (d, J = 8.5 Hz, 1H), 8.50 (d, J = 8.5 Hz, 1H), 8.04−7.98 (m, 3H), 7.81 (d, J = 2.4 Hz, 1H), 7.69−7.65 (m, 1H), 7.64−7.56 (m, 2H), 7.38 (d, J = 3.5 Hz, 1H, furan-H), 7.17 (dd, J = 10.2, 3.0 Hz, 2H), 1.91 (ddd, J = 13.5, 8.5, 5.1 Hz, 1H, cyclopropyl-H), 0.95−0.89 (m, 2H, (cyclopropyl-H)$_2$), 0.67−0.60 (m, 2H, (cyclopropyl-H)$_2$). ^{13}C NMR (151 MHz, DMSO-d_6): δ 170.6, 155.6, 154.6, 148.1, 138.4, 137.3, 133.7, 129.7, 129.4, 128.9, 128.8, 128.4, 127.7, 126.9, 126.7, 126.5, 125.7, 125.1, 121.8, 119.2, 116.1, 112.1, 14.8, 9.1. LC-MS (m/z): positive mode

https://doi.org/10.1021/acs.jmedchem.4c01755
J. Med. Chem. 2024, 67, 19365−19394

398.4 [M + H]$^+$; purity by HPLC UV (254 nm)-ESI-MS: 95.2%.

*5-Bromo-2-(5-(naphthalen-1-yl)furan-2-carboxamido)-benzoic Acid (**38**).* Compound **38** was synthesized according to general procedure **A** starting from 5-(naphthalen-1-yl)furan-2-carboxylic acid (**26**, 0.42 mmol) and methyl 2-amino-5-bromobenzoic acid (**28h**, 0.59 mmol). Yield: 22% over two steps; colorless solid; ^{1}H NMR (600 MHz, DMSO-d_6): δ 14.72 (s, 1H, CO_2H), 8.60 (d, J = 8.8 Hz, 1H), 8.51 (d, J = 8.5 Hz, 1H), 8.18 (d, J = 2.5 Hz, 1H), 8.02 (t, J = 6.5 Hz, 3H), 7.69−7.64 (m, 1H), 7.64−7.57 (m, 3H), 7.40 (d, J = 3.6 Hz, 1H, furan-H), 7.19 (d, J = 3.6 Hz, 1H, furan-H). ^{13}C NMR (126 MHz, DMSO-d_6): δ 168.5, 162.5, 155.9, 154.7, 147.9, 140.0, 133.8, 133.6, 129.8, 129.4, 128.9, 127.7, 126.9, 126.7, 126.5, 125.7, 125.1, 121.0, 116.5, 113.9, 112.1. LC-MS (m/z): positive mode 436.0 [M + H]$^+$; purity by HPLC UV (254 nm)-ESI-MS: 98.5%.

*2-Chloro-6-(5-(naphthalen-1-yl)furan-2-carboxamido)-benzoic Acid (**39**).* Compound **39** was synthesized according to general procedure **A** starting from 5-(naphthalen-1-yl)furan-2-carboxylic acid (**26**, 0.65 mmol) and methyl 2-amino-6-chlorobenzoic acid (**28i**, 1 mmol). Yield: 57%; colorless solid; ^{1}H NMR (500 MHz, DMSO-d_6): δ 13.12 (s br, 1H, CO_2H), 10.59 (s, 1H, NH), 8.45 (d, J = 8.4 Hz, 1H), 8.04 (d, J = 8.1 Hz, 2H), 7.99 (dd, J = 7.2, 0.9 Hz, 1H), 7.82 (dd, J = 7.8, 1.5 Hz, 1H), 7.74 (dd, J = 8.1, 1.4 Hz, 1H), 7.68−7.57 (m, 3H), 7.51 (d, J = 3.5 Hz, 1H, furan-H), 7.40 (t, J = 7.9 Hz, 1H), 7.16 (d, J = 3.5 Hz, 1H, furan-H). ^{13}C NMR (126 MHz, DMSO-d_6): δ 166.9, 156.4, 154.8, 147.3, 134.2, 133.7, 132.7, 132.4, 132.0, 129.8, 129.5, 129.2, 128.9, 127.6, 127.1, 126.7, 126.5, 125.6, 125.0, 116.8, 111.9. LC-MS (m/z): positive mode 392.1 [M + H]$^+$; purity by HPLC UV (254 nm)-ESI-MS: 97.7%.

*2-(5-(Naphthalen-1-yl)furan-2-carboxamido)benzoic Acid (**40**).* Compound **40** was synthesized according to the general procedure **A** starting from 5-(naphthalen-1-yl)furan-2-carboxylic acid (**26**, 0.42 mmol) and 2-aminobenzoic acid (**5**, 0.69 mmol). Yield: 78%; colorless solid; ^{1}H NMR (500 MHz, DMSO-d_6): δ 12.83 (s, 1H, CO_2H), 8.79−8.71 (m, 1H), 8.53 (d, J = 8.6 Hz, 1H), 8.08 (dd, J = 7.9, 1.5 Hz, 1H), 8.03 (d, J = 8.0 Hz, 2H), 7.99 (dd, J = 7.2, 1.0 Hz, 1H), 7.73−7.67 (m, 1H), 7.66−7.57 (m, 3H), 7.47 (d, J = 3.6 Hz, 1H, furan-H), 7.23−7.16 (m, 2H). ^{13}C NMR (126 MHz, DMSO-d_6): δ 169.9, 155.7, 154.8, 147.2, 140.7, 133.7, 133.5, 131.3, 129.7, 129.2, 128.6, 127.6, 126.7, 126.3, 125.4, 124.8, 122.7, 119.5, 117.2, 117.0, 112.2. LC-MS (m/z): positive mode 358.2 [M + H]$^+$; purity by HPLC UV (254 nm)-ESI-MS: 99.8%.

*5-Methoxy-4-methyl-2-(5-(naphthalen-1-yl)furan-2-carboxamido)benzoic Acid (**41**).* Compound **41** was synthesized according to general procedure **A** starting from 5-(naphthalen-1-yl)furan-2-carboxylic acid (**26**, 0.29 mmol) and 2-amino-5-methoxy-4-methylbenzoic acid (**28j**, 0.29 mmol). Yield: 21%; light brown solid; ^{1}H NMR (500 MHz, DMSO-d_6): δ 12.30 (br s, 1H, CO_2H), 8.56 (s, 1H), 8.51 (d, J = 8.6 Hz, 1H), 8.04 (d, J = 8.2 Hz, 2H), 7.97 (d, J = 7.2 Hz, 1H), 7.72−7.67 (m, 1H), 7.65−7.59 (m, 2H), 7.49 (s, 1H), 7.42 (d, J = 3.6 Hz, 1H, furan-H), 7.19 (d, J = 3.6 Hz, 1H, furan-H), 3.81 (s, 3H, OCH_3), 2.24 (s, 3H, CH_3). ^{13}C NMR (125 MHz, DMSO-d_6): δ 169.8, 155.5, 154.8, 152.7, 147.5, 134.4, 133.7, 133.0, 129.9, 129.5, 128.9, 127.8, 126.9, 126.6, 126.5, 125.6, 125.0, 122.2, 117.0, 115.3, 112.4, 111.6, 55.6 (OCH_3), 16.8 (CH_3). LC-MS (m/z): positive mode 402.4 [M + H]$^+$; purity by HPLC UV (254 nm)-ESI-MS: 99.7%.

*5-(2-Methoxyethoxy)-2-(5-(naphthalen-1-yl)furan-2-carboxamido)benzoic Acid (**42**).* Compound **42** was synthesized according to general procedure **A** starting from 5-(naphthalen-1-yl)furan-2-carboxylic acid (**26**, 0.5 mmol), 2-amino-5-(2-methoxyethoxy)benzoic acid (**28k**, 0.73 mmol, for synthesis see Supporting Information). Yield: 67%; colorless solid; ^{1}H NMR (500 MHz, DMSO-d_6): δ 12.52 (s, 1H, CO_2H), 8.64 (d, J = 9.1 Hz, 1H), 8.51 (d, J = 8.6 Hz, 1H), 8.03 (d, J = 8.3 Hz, 2H), 7.97 (dd, J = 7.3, 1.2 Hz, 1H), 7.69 (ddd, J = 8.4, 6.7, 1.4 Hz, 1H), 7.64−7.58 (m, 2H), 7.55 (d, J = 3.1 Hz, 1H), 7.43 (d, J = 3.6 Hz, 1H, furan-H), 7.26 (dd, J = 9.2, 3.2 Hz, 1H), 7.19 (d, J = 3.6 Hz, 1H, furan-H), 4.16−4.03 (m, 2H, $OCH_2CH_2OCH_3$), 3.72−3.57 (m, 2H, $OCH_2CH_2OCH_3$), 3.31 (s, 3H, $OCH_2CH_2OCH_3$). ^{13}C NMR (126 MHz, DMSO-d_6): δ 169.7, 155.5, 154.8, 153.7, 147.6, 134.4, 133.7, 129.9, 129.4, 128.8, 127.8, 126.9, 126.6, 126.5, 125.6, 125.1, 121.4, 120.6, 118.9, 116.9, 116.1, 112.4, 70.5, 67.5, 58.3. LC-MS (m/z): positive mode 432.5 [M + H]$^+$; purity by HPLC UV (254 nm)-ESI-MS: 99.1%.

*5-(2-Hydroxyethoxy)-2-(5-(naphthalen-1-yl)furan-2-carboxamido)benzoic Acid (**43**).* Compound **43** was synthesized according to the general procedure **A** starting from 5-(naphthalen-1-yl)furan-2-carboxylic acid (**26**, 0.5 mmol) and 2-acetoxyethyl 5-(2-acetoxyethoxy)-2-aminobenzoate (**28l**, 0.55 mmol, for synthesis see Supporting Information). Yield: 19%; colorless solid; ^{1}H NMR (500 MHz, DMSO-d_6): δ 13.82 (s, 1H), 12.15 (s, 1H), 8.65 (d, J = 9.2 Hz, 1H), 8.50 (d, J = 8.5 Hz, 1H), 8.04 (d, J = 8.1 Hz, 2H), 7.97 (d, J = 7.3 Hz, 1H), 7.72−7.67 (m, 1H), 7.66−7.59 (m, 2H), 7.54 (d, J = 3.1 Hz, 1H), 7.45 (d, J = 3.6 Hz, 1H), 7.29 (dd, J = 9.2, 3.1 Hz, 1H), 7.20 (d, J = 3.6 Hz, 1H), 4.85 (s, 1H, OH), 4.02 (t, J = 5.0 Hz, 2H, OCH_2CH_2OH), 3.72 (t, J = 4.9 Hz, 2H, OCH_2CH_2OH). ^{13}C NMR (126 MHz, DMSO-d_6): δ 169.6, 155.5, 154.9, 154.0, 147.4, 134.3, 133.7, 129.9, 129.5, 128.9, 127.8, 126.9, 126.5, 125.6, 125.0, 121.6, 121.1, 117.7, 117.1, 116.0, 112.4, 70.2, 59.7. LC-MS (m/z): positive mode 418.5 [M + H]$^+$; purity by HPLC UV (254 nm)-ESI-MS: 99.9%.

*3-(5-(Naphthalen-1-yl)furan-2-carboxamido)-2-naphthoic Acid (**44**).* Compound **44** was synthesized according to general procedure **A** starting from 5-(naphthalene-1-yl)furan-2-carboxylic acid (**26**, 0.41 mmol) and 3-amino-2-naphthoic acid (**28m**, 0.58 mmol). Yield: 15%; colorless solid; ^{1}H NMR (500 MHz, DMSO-d_6): δ 13.18 (s, 1H, CO_2H), 9.15 (s, 1H), 8.75 (s, 1H), 8.54 (d, J = 8.6 Hz, 1H), 8.06−8.00 (m, 4H), 7.90 (d, J = 8.2 Hz, 1H), 7.73−7.67 (m, 1H), 7.66−7.57 (m, 3H), 7.51−7.45 (m, 2H), 7.22 (d, J = 3.6 Hz, 1H, furan-H). ^{13}C NMR (126 MHz, DMSO-d_6): δ 170.0, 155.9, 154.9, 147.7, 136.5, 135.5, 133.7, 133.2, 129.9, 129.5, 129.1, 129.0, 128.8, 128.5, 127.8, 127.2, 126.9, 126.6, 126.5, 125.6, 125.5, 125.1, 119.1, 116.9, 116.2, 112.4. LC-MS (m/z): positive mode 478.4 [M + H]$^+$; purity by HPLC UV (254 nm)-ESI-MS: 98.0%.

*5-Methoxy-2-(5-(naphthalen-1-yl)furan-2-carboxamido)-benzoic Acid (**45**).* Compound **45** was synthesized according to general procedure **A** starting from 5-(naphthalen-1-yl)furan-2-carboxylic acid (**26**, 0.5 mmol), 2-amino-5-methoxybenzoic acid methyl ester (**6**, 0.7 mmol). Yield: 23%; colorless solid; ^{1}H NMR (500 MHz, DMSO-d_6): δ 14.83 (s, 1H, CO_2H), 8.55 (d, J = 8.9 Hz, 1H), 8.50 (d, J = 8.5 Hz, 1H), 8.05−7.98 (m, 3H), 7.69−7.56 (m, 4H), 7.34 (d, J = 3.5 Hz, 1H, furan-H), 7.15 (d, J = 3.4 Hz, 1H, furan-H), 6.98 (dd, J = 9.0, 3.2 Hz, 1H), 3.74 (s, 3H, OCH_3). ^{13}C NMR (126 MHz, DMSO-d_6): δ 170.3, 155.4, 154.2, 154.1, 148.5, 134.3, 133.7, 129.6, 129.4,

https://doi.org/10.1021/acs.jmedchem.4c01755
J. Med. Chem. 2024, 67, 19365−19394

128.8, 127.6, 126.8, 126.4, 125.9, 125.7, 125.1, 120.0, 116.3, 116.1, 115.4, 111.9, 55.3 (OCH_3). LC-MS (m/z): positive mode 388.5 $[M + H]^+$; purity by HPLC UV (254 nm)-ESI-MS: 99.0%.

*5-Hydroxy-2-(5-(naphthalen-1-yl)furan-2-carboxamido)-benzoic Acid (**46**).* To a stirred solution of compound **45** (0.16 mmol) in DCM (30 mL) was added boron tribromide (0.15 mL, 1.6 mmol). The mixture was stirred at rt for 16 h. Subsequently, the solution was quenched with a saturated solution of $NaHCO_3$. The crude product was extracted with additional DCM (2 × 50 mL). The combined organic extracts were dried over $MgSO_4$, filtered and concentrated. The residue was purified by silica gel column chromatography (DCM/MeOH = 9:1). Yield: 42%; colorless solid; ^{1}H NMR (500 MHz, DMSO-d_6): δ 14.54 (s, 1H, CO_2H), 9.22 (s, 1H, OH), 8.49 (d, J = 8.5 Hz, 1H), 8.43 (d, J = 8.8 Hz, 1H), 8.04−7.98 (m, 3H), 7.69−7.57 (m, 3H), 7.52 (d, J = 3.6 Hz, 1H), 7.31 (d, J = 3.5 Hz, 1H), 7.14 (d, J = 4.1 Hz, 1H), 6.82 (dd, J = 8.9, 3.0 Hz, 1H). ^{13}C NMR (126 MHz, DMSO-d_6): δ 170.6, 155.2, 154.2, 152.3, 148.6, 133.7, 132.8, 129.6, 129.4, 128.8, 127.6, 126.82, 126.80, 126.4, 125.7, 125.1, 120.1, 117.8, 117.6, 115.3, 111.9. LC-MS (m/z): positive mode 374.5 $[M + H]^+$; purity by HPLC UV (254 nm)-ESI-MS: 95.2%.

*4-(5-(Naphthalen-1-yl)furan-2-carboxamido)benzoic Acid (**47**).* Compound **47** was synthesized according to the general procedure **A** starting from 5-(naphthalen-1-yl)furan-2-carboxylic acid (**26**, 0.41 mmol) and 4-aminobenzoic acid (**29**, 0.58 mmol). Yield: 47%; colorless solid. ^{1}H NMR (600 MHz, DMSO-d_6): δ 12.74 (s, 1H), 10.47 (s, 1H), 8.40 (d, J = 8.4 Hz, 1H), 8.07−8.03 (m, 2H), 7.98 (dd, J = 7.2, 1.0 Hz, 1H), 7.96−7.89 (m, 4H), 7.67−7.60 (m, 4H), 7.17 (d, J = 3.5 Hz, 1H). ^{13}C NMR (151 MHz, DMSO-d_6): δ 167.1, 156.5, 155.2, 147.0, 142.8, 133.7, 130.4, 129.9, 129.6, 128.9, 127.6, 127.3, 126.8, 126.5, 125.6, 125.0, 119.8, 117.2, 112.0. LC-MS (m/z): positive mode 358.2 $[M + H]^+$; purity by HPLC UV (254 nm)-ESI-MS: 98.5%.

*3-(5-(Naphthalen-1-yl)furan-2-carboxamido)benzoic Acid (**47a**).* Compound **47a** was synthesized according to general procedure A starting from 5 (naphthalen-1-yl)furan-2-carboxylic acid (**26**, 0.40 mmol) and 3-aminobenzoic acid (**29a**, 0.70 mmol). Yield: 32%; beige solid; ^{1}H NMR (600 MHz, DMSO-d_6) δ 12.96 (s br, 1H, CO_2H), 10.49 (s, 1H, NH), 8.40 (d, J = 8.4 Hz, 1H), 8.38 (s, 1H), 8.08−8.02 (m, 3H), 7.99 (d, J = 7.2 Hz, 1H), 7.72−7.60 (m, 4H), 7.59 (d, J = 3.8 Hz, 1H), 7.48 (t, J = 7.9 Hz, 1H), 7.16 (d, J = 3.6 Hz, 1H). ^{13}C NMR (151 MHz, DMSO-d_6) δ 167.5, 156.5, 155.1, 147.1, 139.0, 133.7, 131.8, 129.9, 129.6, 129.1, 128.9, 127.6, 127.3, 126.9, 126.5, 125.7, 125.0, 124.7, 124.6, 121.4, 116.9, 112.0. LC-MS (m/z): positive mode 358.2 $[M + H]^+$; purity by HPLC UV (254 nm)-ESI-MS: 95.0%.

*5-Fluoro-2-(5-(2-isopropylphenyl)furan-2-carboxamido)-benzoic Acid (**48**).* Compound **48** was synthesized according to the general procedure **A** starting from 5-(2-isopropylphenyl)-2-furancarboxylic acid (**27**, 0.42 mmol) and methyl 2-amino-5-fluorobenzoate (**30a**, 0.59 mmol). Yield: 51%; colorless solid; ^{1}H NMR (500 MHz, DMSO-d_6): δ 14.42 (s, 1H, CO_2H), 8.63 (dd, J = 9.1, 5.3 Hz, 1H), 7.78 (dd, J = 9.8, 3.2 Hz, 1H), 7.68 (d, J = 6.8 Hz, 1H), 7.48 (d, J = 7.4 Hz, 1H), 7.42 (t, J = 7.0 Hz, 1H), 7.32−7.23 (m, 3H), 6.79 (d, J = 3.5 Hz, 1H, furan-H), 3.38 (h, J = 6.8 Hz, CH-isopropyl), 1.22 (d, J = 6.8 Hz, 6H, $(CH_3)_2$). ^{13}C NMR (126 MHz, DMSO-d_6): δ 168.7, 162.4, 157.0 (d, J = 239.2 Hz), 155.3 (d, J = 104.0 Hz), 147.1 (d, J = 123.2 Hz), 137.1, 129.5, 129.0, 128.2, 126.1, 125.3, 120.6 (d, J = 6.9 Hz), 117.8 (d, J = 21.9 Hz), 117.2 (d, J = 22.6 Hz), 116.0, 111.2, 29.3, 23.8. LC-MS (m/z): positive mode 468.4 $[M + H]^+$; purity by HPLC UV (254 nm)-ESI-MS: 96.6%.

*5-Chloro-2-(5-(2-isopropylphenyl)furan-2-carboxamido)-benzoic Acid (**49**).* Compound **49** was synthesized according to the general procedure **A** starting from 5-(2-isopropylphenyl)-2-furancarboxylic acid (**27**, 0.42 mmol) and methyl 2-amino-5-chlorobenzoate (**30b**, 0.59 mmol). Yield: 78%; colorless solid; ^{1}H NMR (500 MHz, DMSO-d_6): δ 14.59 (s, 1H, CO_2H), 8.62 (d, J = 8.9 Hz, 1H), 8.03 (d, J = 2.7 Hz, 1H), 7.68 (dd, J = 7.8, 1.2 Hz, 1H), 7.49−7.39 (m, 3H), 7.32−7.28 (m, 2H), 6.79 (d, J = 3.6 Hz, 1H, furan-H), 3.38 (h, J = 6.8 Hz, 1H, CH-isopropyl), 1.22 (d, J = 6.8 Hz, 6H, $(CH_3)_2$). ^{13}C NMR (126 MHz, DMSO-d_6): δ 168.5, 155.9, 155.1, 147.5, 146.6, 139.6, 130.9, 130.8, 129.5, 129.0, 128.1, 126.1, 125.8, 125.1, 120.6, 116.3, 111.3, 29.3, 23.9. LC-MS (m/z): positive mode 484.1 $[M + H]^+$; purity by HPLC UV (254 nm)-ESI-MS: 99.1%.

*4,5-Difluoro-2-(6-(naphthalen-1-yl)picolinamido)benzoic Acid (**64**).* Compound **64** was synthesized according to the general procedure **A** starting from 6-(naphthalen-1-yl)picolinic acid (**61**, 0.41 mmol, for synthesis see Supporting Information) and 2-amino-4,5-difluorobenzoic acid (**28b**, 0.57 mmol). Yield: 77%; colorless solid; ^{1}H NMR (500 MHz, DMSO-d_6): δ 14.61 (s, 1H, CO_2H), 8.82 (dd, J = 13.9, 7.7 Hz, 1H), 8.23−8.15 (m, 2H), 8.10−8.01 (m, 3H), 7.97 (dd, J = 11.8, 9.6 Hz, 1H), 7.91−7.84 (m, 2H), 7.67−7.61 (m, 1H), 7.59−7.50 (m, 2H). ^{13}C NMR (126 MHz, DMSO-d_6): δ 167.3, 163.5, 157.2, 150.7, 150.2 (dd, J = 247.0, 13.8 Hz), 144.2 (dd, J = 242.0, 12.6 Hz), 138.5, 137.4 (d, J = 10.2 Hz), 137.2, 133.5, 130.5, 129.1, 128.5, 128.4, 128.3, 127.0, 126.2, 125.7, 125.1, 121.2, 119.7 (d, J = 17.8 Hz), 108.2 (d, J = 23.0 Hz). LC-MS (m/z): positive mode 405.4 $[M + H]^+$; purity by HPLC UV (254 nm)-ESI-MS: 99.6%.

*5-Fluoro-2-(6-(naphthalen-1-yl)nicotinamido)benzoic Acid (**64a**).* Compound 64a was synthesized according to the general procedure A starting from 6-(naphthalen-1-yl)nicotinic acid (**61a**, 0.26 mmol) and methyl 2-amino-5-fluorobenzoate (**30a**, 0.39 mmol). Yield: 44%; colorless solid; ^{1}H NMR (600 MHz, DMSO-d_6): δ 14.06 (s br, 1H, CO_2H), 12.00 (s, 1H), 9.28 (d, J = 2.4 Hz, 1H), 8.62 (dd, J = 9.1, 5.1 Hz, 1H), 8.44 (dd, J = 8.1, 2.4 Hz, 1H), 8.10 (d, J = 8.3 Hz, 1H), 8.06 (d, J = 8.1 Hz, 1H), 8.04 (dd, J = 8.2, 1.5 Hz, 1H), 7.90 (d, J = 8.1 Hz, 1H), 7.78 (dd, J = 9.2, 3.2 Hz, 1H), 7.70 (dd, J = 7.0, 1.3 Hz, 1H), 7.66−7.62 (m, 1H), 7.61−7.52 (m, 3H). ^{13}C NMR (151 MHz, DMSO-d_6): δ 168.7 (d, J = 2.2 Hz), 163.3, 161.5, 157.5 (d, J = 242.0 Hz), 148.1, 137.2, 137.0 (d, J = 2.5 Hz), 136.0, 133.6, 130.5, 129.6, 128.6 (d, J = 3.8 Hz), 128.1, 127.0, 126.3, 125.6, 125.4, 125.1, 123.2 (d, J = 7.3 Hz), 121.1 (d, J = 22.2 Hz), 120.2 (d, J = 6.7 Hz), 117.3 (d, J = 24.0 Hz). LC-MS (m/z): positive mode 387.1 $[M + H]^+$; purity by HPLC UV (254 nm)-ESI-MS: 98.2%.

*4,5-Dimethoxy-2-(6-(naphthalen-1-yl)picolinamido)-benzoic Acid (**65**).* Compound **65** was synthesized according to the general procedure **A** starting from 6-(naphthalen-1-yl)picolinic acid (**61**, 0.41 mmol) and 2-amino-4,5-dimethoxybenzoic acid (**63**, 0.57 mmol). Yield: 48%; off-white solid; ^{1}H NMR (500 MHz, DMSO-d_6): δ 13.37 (s, 1H, CO_2H), 8.67 (s, 1H), 8.26−8.19 (m, 2H), 8.07−8.01 (m, 3H), 7.89 (d, J = 7.5 Hz, 1H), 7.81 (d, J = 7.0 Hz, 1H), 7.68−7.63 (m, 1H), 7.59−7.51 (m, 2H), 7.48 (s, 1H), 3.88 (s, 3H, OCH_3), 3.76 (s, 3H, OCH_3). ^{13}C NMR: (126 MHz, DMSO-d_6): δ 168.9, 162.8,

https://doi.org/10.1021/acs.jmedchem.4c01755
J. Med. Chem. 2024, 67, 19365−19394

157.3, 152.7, 150.3, 143.9, 138.7, 137.2, 136.0, 133.5, 130.5, 129.2, 128.5, 128.4, 128.2, 127.0, 126.2, 125.7, 125.1, 121.0, 113.4, 109.9, 103.6, 55.73 (OCH_3), 55.71 (OCH_3). LC-MS (m/z): positive mode 429.3 $[M + H]^+$; purity by HPLC UV (254 nm)-ESI-MS: 97.5%.

*5-Chloro-2-(6-(naphthalen-1-yl)picolinamido)benzoic Acid (**66**).* Compound **66** was synthesized according to the general procedure **A** starting from 6-(naphthalen-1-yl)picolinic acid (**61**, 1.0 mmol) and 2-amino-5-chlorobenzoic acid (**30b**, 1.1 mmol). Yield: 54%; colorless solid. ^{1}H NMR (600 MHz, DMSO-d_6): δ 13.82 (s, 1H), 13.15 (s, 1H), 8.92 (d, J = 9.0 Hz, 1H), 8.29−8.25 (m, 1H), 8.25−8.21 (m, 1H), 8.09−8.01 (m, 3H), 7.95−7.90 (m, 2H), 7.79 (d, J = 7.0 Hz, 1H), 7.74 (d, J = 9.6 Hz, 1H), 7.69−7.63 (m, 1H), 7.60−7.51 (m, 2H). ^{13}C NMR (151 MHz, DMSO-d_6): δ 167.9, 163.1, 157.4, 149.6, 139.4, 138.9, 137.2, 133.8, 133.6, 130.6, 130.5, 129.3, 128.8, 128.5, 128.1, 127.1, 126.8, 126.3, 125.7, 125.1, 121.9, 121.3, 119.2. LC-MS (m/z): positive mode 403.2 $[M + H]^+$; purity by HPLC UV (254 nm)-ESI-MS: 96.3%.

*5-Chloro-2-(6-(naphthalen-1-yl)nicotinamido)benzoic (**66a**).* Compound **66a** was synthesized according to the general procedure **A** starting from 6-(naphthalen-1-yl)nicotinic acid (**61a**, 0.26 mmol) and 2-amino-5-chlorobenzoic acid (**30b**, 0.38 mmol). Yield: 61%; colorless solid. ^{1}H NMR (600 MHz, DMSO-d_6): δ 12.16 (s, 1H), 9.28 (d, J = 2.4 Hz, 1H), 8.66 (d, J = 8.9 Hz, 1H), 8.44 (dd, J = 8.2, 2.4 Hz, 1H), 8.10 (d, J = 8.4 Hz, 1H), 8.07 (d, J = 8.2 Hz, 1H), 8.04 (dd, J = 8.0, 1.4 Hz, 1H), 8.01 (d, J = 2.7 Hz, 1H), 7.91 (d, J = 8.3 Hz, 1H), 7.77 (dd, J = 8.9, 2.7 Hz, 1H), 7.72−7.69 (m, 1H), 7.66−7.63 (m, 1H), 7.60−7.53 (m, 2H). ^{13}C NMR (151 MHz, DMSO): δ 169.1, 163.8, 162.0, 148.4, 139.8, 137.5, 136.3, 134.3, 133.9, 130.9, 130.8, 129.9, 128.9, 128.8, 128.4, 127.6, 127.3, 126.6, 125.9, 125.7, 122.9, 120.1. LC-MS (m/z): positive mode 403.2 $[M + H]^+$; purity by HPLC UV (254 nm)-ESI-MS: 99.1%.

*5-Methoxy-2-(6-(naphthalen-1-yl)picolinamido)benzoic Acid (**67**).* Compound **67** was synthesized according to the general procedure **A** starting from 6-(naphthalen-1-yl)picolinic acid (**61**, 1.0 mmol) and 2-amino-5-methoxybenzoic acid (**6**, 1.1 mmol). Yield: 75%; beige solid; ^{1}H NMR (600 MHz, DMSO-d_6): δ 13.51 (s br, 1H, CO_2H), 12.87 (s, 1H), 8.82 (d, J = 9.2 Hz, 1H), 8.26 (dd, J = 7.7, 1.0 Hz, 1H), 8.21 (t, J = 7.7 Hz, 1H), 8.06 (d, J = 8.2 Hz, 2H), 8.04 (dd, J = 8.1, 1.5 Hz, 1H), 7.90 (dd, J = 7.6, 1.0 Hz, 1H), 7.78 (dd, J = 7.0, 0.9 Hz, 2H), 7.66 (dd, J = 8.0, 7.2 Hz, 1H), 7.60−7.51 (m, 2H), 7.47 (d, J = 3.1 Hz, 1H), 7.28 (dd, J = 9.2, 3.1 Hz, 1H), 3.78 (s, 3H, OCH_3). ^{13}C NMR (151 MHz, DMSO-d_6): δ 168.8, 162.6, 157.3, 154.6, 150.0, 138.9, 137.3, 134.0, 133.6, 130.6, 129.3, 128.6, 128.5, 128.1, 127.1, 126.3, 125.7, 125.2, 121.9, 121.1, 120.3, 118.5, 115.2, 55.6 (OCH_3). LC-MS (m/z): positive mode 399.1 $[M + H]^+$; purity by HPLC UV (254 nm)-ESI-MS: 99.7%.

*5-Fluoro-2-(1-(naphthalen-1-yl)piperidine-4-carboxamido)benzoic Acid (**67a**).* Compound **67a** was synthesized according to the general procedure **A** starting from 1-(naphthalen-1-yl)piperidine-4-carboxylic acid (**61b**, 0.38 mmol) and methyl 2-amino-5-fluorobenzoate (**30a**, 0.59 mmol). Yield: 16%; colorless solid; ^{1}H NMR (600 MHz, DMSO-d_6): δ 13.90 (s, 1H), 11.09 (s, 1H), 8.51 (dd, J = 9.2, 5.0 Hz, 1H), 8.10 (d, J = 8.2 Hz, 1H), 7.87 (d, J = 7.9 Hz, 1H), 7.70 (dd, J = 9.1, 2.9 Hz, 1H), 7.61−7.45 (m, 4H), 7.45−7.37 (m, 1H), 7.12 (d, J = 7.4 Hz, 1H), 3.41−3.33 (m, 2H), 2.88−2.73 (m, 2H), 2.57 (tt, J = 10.9, 4.2 Hz, 1H), 2.14−1.84 (m, 4H). ^{13}C NMR (151 MHz, DMSO-d_6): δ 173.7, 168.9, 157.3 (d, J = 241.1 Hz), 150.3, 128.8 (d, J = 5.7 Hz), 126.5, 126.3, 125.9, 123.8, 123.5, 123.0 (d, J = 6.8 Hz), 121.3 (d, J = 22.3 Hz), 119.5 (d, J = 6.9 Hz), 117.3 (d, J = 23.9 Hz), 115.3, 53.1 (NCH_2), 44.1 (CH), 29.5 (CH_2). LC-MS (m/z): positive mode 393.1 $[M + H]^+$; purity by HPLC UV (254 nm)-ESI-MS: 97.1%.

*5-Fluoro-2-(2-(naphthalen-1-yl)thiazole-4-carboxamido)-benzoic Acid (**68**).* Compound **68** was synthesized according to the general procedure **A** starting from 2-(naphthalen-1-yl)thiazole-4-carboxylic acid (**62**, 0.40 mmol, for synthesis see Supporting Information) and methyl 2-amino-5-fluorobenzoate (**30a**, 0.64 mmol). Yield: 83%; colorless solid; ^{1}H NMR (500 MHz, DMSO-d_6): δ 13.87 (s, 1H, CO_2H), 12.75 (s, 1H, NH), 9.19 (d, J = 8.6 Hz, 1H), 8.90 (dd, J = 9.3, 5.2 Hz, 1H), 8.68 (s, 1H, thiazole-H), 8.15 (d, J = 8.3 Hz, 1H), 8.09−8.02 (m, 2H), 7.81−7.75 (m, 2H), 7.69−7.63 (m, 2H), 7.61−7.55 (m, 1H). ^{13}C NMR (126 MHz, DMSO-d_6): δ 168.2, 167.6, 159.2, 157.0 (d, J = 242 Hz), 150.4, 137.4, 133.8, 131.4, 129.5, 129.2, 129.0, 128.6, 128.4, 126.8 (d, J = 3.8 Hz), 125.5, 122.1 (d, J = 7.2 Hz), 121.2 (d, J = 22.1 Hz), 118.6 (d, J = 6.6 Hz), 117.26 (d, J = 23.6 Hz). LC-MS (m/z): positive mode 393.1 $[M + H]^+$; purity by HPLC UV (254 nm)-ESI-MS: 99.6%.

*5-Bromo-2-(2-(naphthalen-1-yl)thiazole-4-carboxamido)-benzoic Acid (**69**).* Compound **69** was synthesized according to the general procedure **A** starting from 2-(naphthalen-1-yl)thiazole-4-carboxylic acid (**62**, 0.27 mmol) and methyl 2-amino-5-bromobenzoate (**28h**, 0.43 mmol). Yield: 77%; brownish solid; ^{1}H NMR (500 MHz, DMSO-d_6): δ 14.21 (s, 1H, CO_2H), 9.33 (d, J = 9.0 Hz, 1H), 8.76 (d, J = 8.9 Hz, 1H), 8.59 (s, 1H, thiazole-H), 8.18 (d, J = 2.6 Hz, 1H), 8.12 (d, J = 8.3 Hz, 1H), 8.07 (dd, J = 7.2, 1.1 Hz, 1H), 8.03 (d, J = 8.1 Hz, 1H), 7.83−7.78 (m, 1H), 7.69 (dd, J = 8.9, 2.6 Hz, 1H), 7.66−7.61 (m, 1H), 7.60−7.56 (m, 1H). ^{13}C NMR (126 MHz, DMSO-d_6): δ 167.8, 167.3, 159.2, 151.0, 139.6, 134.1, 133.5, 133.5, 131.1, 129.3, 128.9, 128.3, 128.2, 126.5, 126.2, 125.9, 125.2, 121.3, 114.0. LC-MS (m/z): positive mode 453.1 $[M + H]^+$; purity by HPLC UV (254 nm)-ESI-MS: 90.5%.

*5-Methoxy-2-(2-(naphthalen-1-yl)thiazole-4-carboxamido)benzoic Acid (**70**).* Compound **70** was synthesized according to the general procedure **A** starting from 2-(naphthalen-1-yl)thiazole-4-carboxylic acid (**62**, 0.29 mmol) and 2-amino-5-methoxybenzoic acid methyl ester (**6**, 0.45 mmol). Yield: 27%; colorless solid; ^{1}H NMR (600 MHz, DMSO-d_6): δ 13.63 (s, 1H, CO_2H), 12.63 (s, 1H, NH), 9.20 (d, J = 8.6 Hz, 1H), 8.80 (d, J = 9.2 Hz, 1H), 8.64 (s, 1H, thiazole-H), 8.15 (d, J = 8.2 Hz, 1H), 8.09−8.04 (m, 2H), 7.80 (t, J = 8.3 Hz, 1H), 7.70−7.62 (m, 2H), 7.55 (d, J = 3.1 Hz, 1H), 7.31 (dd, J = 9.2, 3.1 Hz, 1H), 3.81 (s, 3H, OCH_3). LC-MS (m/z): positive mode 405.2 $[M + H]^+$; purity by HPLC UV (254 nm)-ESI-MS: 98%.

*5-(2-Chlorophenyl)-N-(2-(5-oxo-4,5-dihydro-1,2,4-oxadiazol-3-yl)phenyl)furan-2-carboxamide (**74**).* Compound **74** was synthesized according to the general procedure **A** starting from 5-(2-chlorophenyl)furan-2-carboxylic acid **73** (0.45 mmol) and 3-(2-aminophenyl)-1,2,4-oxadiazol-5(4*H*)-one (**71**, 0.45 mmol, for synthesis see Supporting Information).[35] The reaction mixture was concentrated under vacuum and the residue was purified by silica gel column chromatography (DCM/ethyl acetate/AcOH = 90:8:2). The resulting material was treated with diethyl ether and filtered. Yield: 23%; colorless solid; ^{1}H NMR (600 MHz, DMSO-d_6): δ 12.8 (s br, 1H, NH-oxadiazole), 11.49 (s, 1H, NH-amide), 8.52 (d, J = 8.3 Hz, 1H), 8.29 (d, J = 7.9 Hz, 1H), 7.81 (d, J = 7.8 Hz, 1H),

https://doi.org/10.1021/acs.jmedchem.4c01755
J. Med. Chem. 2024, 67, 19365−19394

7.63−7.55 (m, 2H), 7.52 (t, J = 7.6 Hz, 1H), 7.44 (t, J = 7.9 Hz, 1H), 7.39 (dd, J = 28.8, 3.1 Hz, 3H), 7.29 (t, J = 7.6 Hz, 1H). ^{13}C NMR (151 MHz, DMSO-d_6): δ 163.2, 160.3, 155.8, 151.5, 146.7, 136.9, 132.0, 131.0, 130.3, 129.9, 129.1, 128.4, 128.1, 127.4, 124.2, 121.5, 117.3, 114.6, 113.4. LC-MS (m/z): positive mode 382.1 $[M + H]^+$; purity by HPLC UV (254 nm)-ESI-MS: 96.2%.

*5-(3′-Methoxy-[1,1′-biphenyl]-2-yl)-N-(2-(5-oxo-4,5-dihydro-1,2,4-oxadiazol-3-yl)phenyl)furan-2-carboxamide (**75**).* Compound **75** was synthesized according to the general procedure **A** starting from 5-(3′-methoxy-[1,1′-biphenyl]-2-yl)furan-2-carboxylic acid (**4h**, 0.34 mmol) and 3-(2-aminophenyl)-1,2,4-oxadiazol-5(4*H*)-one (**71**, 0.30 mmol). The reaction mixture was concentrated under vacuum and the residue was purified by silica gel column chromatography (DCM/ethyl acetate = 70:30 + 0.3% TFA). Recrystallization was performed using ethyl acetate. Yield: 73%; pale orange solid; ^{1}H NMR (500 MHz, DMSO-d_6): δ 13.05 (s br, 1H, NH-oxadiazol), 10.68 (s, 1H, NH-amide), 8.44 (d, J = 8.2 Hz, 1H), 8.10 (d, J = 8.0 Hz, 1H), 7.76 (dd, J = 7.9, 1.3 Hz, 1H), 7.66−7.60 (m, 1H), 7.58−7.45 (m, 2H), 7.37−7.31 (m, 3H), 7.17 (d, J = 3.5 Hz, 1H, furan-H), 6.96 (dd, J = 8.5, 2.4 Hz, 1H), 6.86−6.80 (m, 2H), 5.72 (d, J = 3.6 Hz, 1H, furan-H), 3.72 (s, 3H, OCH_3). ^{13}C NMR (126 MHz, DMSO-d_6): δ 159.52, 159.48, 157.9, 155.8, 154.4, 145.7, 142.4, 139.9, 136.8, 132.7, 130.8, 129.8, 129.0, 128.8, 128.1, 127.5, 127.3, 124.3, 121.9, 121.1, 117.3, 114.5, 113.4, 113.1, 111.5, 55.3 (OCH_3). LC-MS (m/z): positive mode 454.4 $[M + H]^+$; purity by HPLC UV (254 nm)-ESI-MS: 97.9%.

*N-(2-(2H-Tetrazol-5-yl)phenyl)-5-(naphthalen-1-yl)furan-2-carboxamide (**76**).* Compound **76** was synthesized according to the general procedure **A** starting from 5-(naphthalen-1-yl)furan-2-carboxylic acid (**26**, 0.50 mmol) and 2-(2*H*-tetrazol-5-yl)aniline (**72**, 0.75 mmol).[36] The crude compound was purified by silica gel column chromatography (DCM/MeOH = 90:10). Yield: 24%; pale yellow solid; ^{1}H NMR (600 MHz, DMSO-d_6): δ 12.00 (s, 1H, tetrazole-H), 8.66 (d, J = 8.5 Hz, 1H), 8.54 (d, J = 8.5 Hz, 1H), 8.25 (d, J = 7.2 Hz, 1H), 8.10−8.02 (m, 3H), 7.72−7.67 (m, 2H), 7.66−7.60 (m, 2H), 7.54 (d, J = 3.8 Hz, 1H, furan-H), 7.40−7.35 (m, 1H), 7.28 (d, J = 3.7 Hz, 1H, furan-H). ^{13}C NMR (151 MHz, DMSO-d_6): δ 156.1, 155.0, 147.0, 136.9, 133.8, 132.0, 130.0, 129.3, 129.0, 128.7, 127.9, 127.2, 126.53, 126.45, 125.8, 124.8, 124.3, 121.5, 117.5, 113.0, 112.5. LC-MS (m/z): positive mode 382.5 $[M + H]^+$; purity by HPLC UV (254 nm)-ESI-MS: 99.4%.

Preparation of Compounds 51−60 (General Procedure B). In a sealed tube, a mixture of compound **50** (0.2 mmol), the appropriate arylboronic acid derivative (0.24 mmol), sodium carbonate (0.4 mmol) and tetrakis-(triphenylphosphine)palladium(0) ($Pd(PPh_3)_4$, 0.01 mmol) in a mixture of dimethoxyethan (DME) and water (8 mL/2 mL) was stirred for 16 h at 80 °C. Subsequently, the reaction mixture was cooled to room temperature and filtered on a Celite pad. The Celite pad was washed with additional ethyl acetate (15 mL) and the obtained solution was concentrated under reduced pressure. The residue was quenched with water (30 mL) and extracted with ethyl acetate (3 × 50 mL). The combined organic layers were washed with brine, dried over magnesium sulfate, filtered and concentrated under reduced pressure. The residue was purified by column chromatography using (eluent: DCM/MeOH = 98:2) affording the final products **51**−**60**.

*5-Methoxy-2-(5-(2-(pyridin-3-yl)phenyl)furan-2-carboxamido)benzoic Acid (**51**).* Compound **51** was synthesized according to the general procedure **B** starting from **50** (0.24 mmol) and pyridin-3-ylboronic acid (0.36 mmol). Yield: 47%; colorless solid; ^{1}H NMR (600 MHz, DMSO-d_6): δ 11.94 (s, 1H, NH), 8.61−8.56 (m, 2H), 8.49 (s, 1H), 8.01 (d, J = 7.5 Hz, 1H), 7.75 (d, J = 7.8 Hz, 1H), 7.62−7.53 (m, 2H), 7.53 (d, J = 3.1 Hz, 1H), 7.47−7.41 (m, 2H), 7.26 (dd, J = 9.2, 3.0 Hz, 1H), 7.14 (d, J = 3.6 Hz, 1H, furan-H), 5.81 (d, J = 3.6 Hz, 1H, furan-H), 3.80 (s, 3H, OCH_3). ^{13}C NMR (126 MHz, DMSO-d_6): δ 169.5, 155.2, 154.5, 154.0, 149.2, 148.8, 146.6, 136.7, 136.6, 134.1, 131.3, 129.4, 128.8, 128.1, 127.7, 123.7, 121.5, 120.6, 117.7, 116.7, 115.2, 111.9, 55.6. LC-MS (m/z): positive mode 415.2 $[M + H]^+$; purity by HPLC UV (254 nm)-ESI-MS: 98.6%.

*5-Methoxy-2-(5-(3′-methoxy-[1,1′-biphenyl]-2-yl)furan-2-carboxamido)benzoic Acid (**52**, PSB-22269).* Compound **52** was synthesized according to the general procedure **B** starting from **50** (0.24 mmol) and (3-methoxyphenyl)boronic acid (0.36 mmol). Yield: 51%; colorless solid; ^{1}H NMR (500 MHz, DMSO-d_6): δ 13.92 (s, 1H, CO_2H), 12.01 (s, 1H, NH), 8.60 (d, J = 9.2 Hz, 1H), 8.03 (dd, J = 7.8, 1.2 Hz, 1H), 7.57−7.46 (m, 3H), 7.38−7.30 (m, 2H), 7.26 (dd, J = 9.2, 3.1 Hz, 1H), 7.11 (d, J = 3.6 Hz, 1H, furan-H), 7.00−6.95 (m, 1H), 6.87−6.83 (m, 2H), 5.68 (d, J = 3.6 Hz, 1H, furan-H), 3.80 (s, 3H, OCH_3), 3.73 (s, 3H, OCH_3). ^{13}C NMR (126 MHz, DMSO-d_6): δ 169.3, 159.3, 155.1, 154.3, 153.8, 146.0, 142.2, 139.8, 134.0, 130.6, 129.6, 128.7, 127.9, 127.4, 126.6, 121.2, 121.0, 120.4, 117.5, 116.6, 115.0, 114.1, 113.3, 111.4, 55.4 (OCH_3), 55.0 (OCH_3). LC-MS (m/z): positive mode 444.2 $[M + H]^+$; purity by HPLC UV (254 nm)-ESI-MS: 97.6%.

*2-(5-(3′-Cyano-[1,1′-biphenyl]-2-yl)furan-2-carboxamido)-5-methoxybenzoic Acid (**53**).* Compound **53** was synthesized according to the general procedure **B** starting from **50** (0.24 mmol) and (3-cyanophenyl)boronic acid (0.36 mmol). Yield: 39%; colorless solid; ^{1}H NMR (600 MHz, DMSO-d_6): δ 13.91 (s, 1H, CO_2H), 11.92 (s, 1H, NH), 8.58 (d, J = 9.1 Hz, 1H), 7.98 (d, J = 7.6 Hz, 1H), 7.87−7.79 (m, 1H), 7.63−7.57 (m, 3H), 7.52−7.54 (m, 2H), 7.42 (d, J = 7.4 Hz, 1H), 7.26 (dd, J = 9.1, 2.8 Hz, 1H), 7.14 (d, J = 3.4 Hz, 1H, furan-H), 5.86 (d, J = 3.4 Hz, 1H, furan-H), 3.79 (s, 3H, OCH_3). ^{13}C NMR (151 MHz, DMSO-d_6): δ 169.3, 155.0, 154.3, 153.7, 146.4, 141.8, 137.8, 133.9, 133.8, 132.3, 131.4, 130.8, 129.6, 129.1, 128.6, 127.6, 127.5, 121.3, 120.3, 118.4, 117.5, 116.5, 115.0, 111.7, 111.7, 55.4 (OCH_3). LC-MS (m/z): positive mode 439.2 $[M + H]^+$; purity by HPLC UV (254 nm)-ESI-MS: 95.5%.

*5-Methoxy-2-(5-(3′-(trifluoromethyl)-[1,1′-biphenyl]-2-yl)-furan-2-carboxamido)benzoic Acid (**54**, PSB-24040).* Compound **54** was synthesized according to the general procedure **B** starting from **50** (0.24 mmol) and (3-(trifluoromethyl)-phenyl)boronic acid (0.36 mmol). Yield: 47%; colorless solid; ^{1}H NMR (600 MHz, DMSO-d_6): δ 13.91 (s, 1H, CO_2H), 11.90 (s, 1H, NH), 8.57 (d, J = 9.1 Hz, 1H), 7.99 (d, J = 7.5 Hz, 1H), 7.73 (d, J = 7.6 Hz, 1H), 7.67−7.53 (m, 6H), 7.52 (d, J = 3.0 Hz, 1H, Furan-H), 7.44 (d, J = 7.1 Hz, 1H), 7.25 (dd, J = 9.2, 3.1 Hz, 1H), 7.13 (d, J = 3.6 Hz, 1H, furan-H), 5.83 (d, J = 3.6 Hz, 1H, furan-H), 3.79 (s, 3H, OCH_3). ^{13}C NMR (151 MHz, DMSO-d_6): δ 169.5, 155.2, 154.5, 154.0, 146.6, 141.8, 138.5, 134.1, 133.2, 129.8, 129.6, 129.4, 128.7, 127.9, 127.7, 125.5 (q, J = 3.4 Hz), 124.4 (q, J = 3.7 Hz), 124.2 (q, J = 273 Hz), 121.4, 120.5, 117.6, 116.6, 115.2, 111.7, 55.6

https://doi.org/10.1021/acs.jmedchem.4c01755
J. Med. Chem. 2024, 67, 19365−19394

ppm. LC-MS (m/z): positive mode 482.2 $[M + H]^+$; purity by HPLC UV (254 nm)-ESI-MS: 96.3%.

*2-(5-(3′-Isopropyl-[1,1′-biphenyl]-2-yl)furan-2-carboxamido)-5-methoxybenzoic Acid (**55**).* Compound **55** was synthesized according to the general procedure **B** starting from **50** (0.24 mmol) and (3-isopropylphenyl)boronic acid (0.36 mmol). Yield: 27%; colorless solid; ^{1}H NMR (600 MHz, DMSO-d_6): δ 13.92 (s, 1H, CO_2H), 11.98 (s, 1H, NH), 8.58 (d, J = 9.1 Hz, 1H), 8.00 (d, J = 7.1 Hz, 1H), 7.54−7.46 (m, 3H), 7.38−7.32 (m, 2H), 7.25 (dd, J = 9.2, 3.0 Hz, 2H), 7.13−7.10 (m, 2H), 7.09 (d, J = 3.6 Hz, 1H, furan-H), 5.63 (d, J = 3.6 Hz, 1H, furan-H), 3.79 (s, 3H), 2.87 (hept, J = 6.8 Hz, 1H), 1.14 (d, J = 6.9 Hz, 6H). ^{13}C NMR (151 MHz, DMSO-d_6): δ 169.6, 155.3, 154.5, 154.3, 148.8, 146.2, 140.9, 140.5, 134.2, 130.9, 129.1, 128.8, 128.0, 127.8, 127.1, 127.0, 126.3, 125.8, 121.4, 120.6, 117.7, 116.7, 115.2, 111.5, 55.6 (OCH_3), 33.5, 23.9. LC-MS (m/z): positive mode 456.4 $[M + H]^+$; purity by HPLC UV (254 nm)-ESI-MS: 93.9%.

*2-(5-(3′-(Cyclopropoxy)-[1,1′-biphenyl]-2-yl)furan-2-carboxamido)-5-methoxybenzoic Acid (**56**).* Compound **56** was synthesized according to the general procedure **B** starting from **50** (0.24 mmol) and (3-cyclopropoxyphenyl)boronic acid (0.36 mmol). Yield: 28%; colorless solid; ^{1}H NMR (600 MHz, DMSO-d_6): δ 13.94 (s, 1H, CO_2H), 12.11 (s, 1H, NH), 8.60 (d, J = 9.1 Hz, 1H), 8.02 (d, J = 7.7 Hz, 1H), 7.56−7.45 (m, 3H), 7.36−7.30 (m, 2H), 7.26 (dd, J = 9.1, 3.0 Hz, 1H), 7.11 (d, J = 3.6 Hz, 1H, furan-H), 6.95 (dd, J = 8.3, 2.2 Hz, 1H), 6.83 (d, J = 8.2 Hz, 2H), 5.70 (d, J = 3.6 Hz, 1H, furan-H), 3.79 (s, 3H, OCH_3), 3.77 (d, J = 7.0 Hz, 2H, OCH_2), 1.23−1.10 (m, 1H, cyclopropyl-CH), 0.57−0.49 (m, 2H, cyclopropyl-CH_2), 0.31−0.23 (m, 2H, cyclopropyl-CH_2). ^{13}C NMR (151 MHz, DMSO-d_6) δ = 169.6, 158.9, 155.3, 154.5, 154.0, 146.3, 142.4, 140.1, 134.2, 130.8, 129.8, 128.9, 128.2, 127.7, 126.9, 121.4, 121.1, 120.5, 118.0, 116.8, 115.3, 114.8, 114.3, 111.6, 72.2, 55.6 (OCH_3), 10.2, 3.2. LC-MS (m/z): positive mode 484.4 $[M + H]^+$; purity by HPLC UV (254 nm)-ESI-MS: 96.8%.

*5-Methoxy-2-(5-(4′-methoxy-[1,1′-biphenyl]-2-yl)furan-2-carboxamido)benzoic Acid (**57**).* Compound **57** was synthesized according to the general procedure **B** starting from **50** (0.24 mmol) and (4-methoxyphenyl)boronic acid (0.36 mmol). Yield: 37%; colorless solid; ^{1}H NMR (500 MHz, DMSO-d_6): δ 13.91 (s, 1H, CO_2H), 12.01 (s, 1H, NH), 8.61 (d, J = 9.2 Hz, 1H), 8.02 (d, J = 7.3 Hz, 1H), 7.54 (d, J = 3.0 Hz, 1H), 7.45−7.52 (m, 2H), 7.32 (d, J = 6.8 Hz, 1H), 7.26 (dd, J = 9.1, 3.0 Hz, 1H), 7.21 (d, J = 8.5 Hz, 2H), 7.11 (d, J = 3.6 Hz, 1H, furan-H), 7.00 (d, J = 8.5 Hz, 2H), 5.64 (d, J = 3.7 Hz, 1H, furan-H), 3.79 (s, 3H, OCH_3), 3.77 (s, 3H, OCH_3). ^{13}C NMR (126 MHz, DMSO-d_6): δ 169.4, 158.8, 155.1, 154.2, 154.0, 145.9, 139.7, 134.0, 133.0, 131.0, 129.9, 128.7, 127.6, 126.7, 121.2, 120.3, 117.5, 116.6, 115.0, 114.0, 111.3, 55.4 (OCH_3), 55.0 (OCH_3). LC-MS (m/z): positive mode 444.1 $[M + H]^+$; purity by HPLC UV (254 nm)-ESI-MS: 97.8%.

*5-Methoxy-2-(5-(2′-methoxy-[1,1′-biphenyl]-2-yl)furan-2-carboxamido)benzoic Acid (**58**).* Compound **58** was synthesized according to the general procedure **B** starting from **50** (0.24 mmol) and (2-methoxyphenyl)boronic acid (0.36 mmol). Yield: 87%; colorless solid; ^{1}H NMR (500 MHz, DMSO-d_6): δ 13.96 (s, 1H, CO_2H), 12.04 (s, 1H, NH), 8.61 (d, J = 9.2 Hz, 1H), 8.07 (d, J = 1.4 Hz, 1H), 7.54 (d, J = 3.1 Hz, 1H), 7.53−7.40 (m, 3H), 7.30−7.23 (m, 2H,), 7.18 (dd, J = 7.4, 1.8 Hz, 1H), 7.12−7.04 (m, 3H), 5.50 (d, J = 3.7 Hz, 1H, furan-H), 3.80 (s, 3H, OCH_3), 3.56 (s, 3H, OCH_3). ^{13}C NMR (126 MHz, DMSO-d_6): δ 169.4, 156.1, 155.1, 154.2, 145.8, 136.4, 134.0, 131.2, 130.2, 129.6, 128.5, 128.3, 127.7, 125.8, 121.2, 120.9, 120.4, 117.5, 116.7, 115.0, 111.5, 109.8, 55.4 (OCH_3), 55.3 (OCH_3). LC-MS (m/z): positive mode 444.3 $[M + H]^+$; purity by HPLC UV (254 nm)-ESI-MS: 98.9%.

*2-(5-(3′-(Hydroxymethyl)-[1,1′-biphenyl]-2-yl)furan-2-carboxamido)-5-methoxybenzoic Acid (**59**).* Compound **59** was synthesized according to the general procedure **B** starting from **50** (0.24 mmol) and (3-(hydroxymethyl)phenyl)boronic acid (0.36 mmol). Yield: 47%; colorless solid; ^{1}H NMR (600 MHz, DMSO-d_6): δ 12.18 (s, 1H, CO_2H), 8.61 (d, J = 9.1 Hz, 1H), 8.06 (d, J = 7.8 Hz, 1H), 7.65−7.59 (m, 2H), 7.57−7.51 (m, 3H), 7.50−7.46 (m, 1H), 7.42−7.35 (m, 1H), 7.34−7.31 (m, 1H), 7.27−7.23 (m, 1H), 7.15 (d, J = 7.0 Hz, 1H), 7.08 (d, J = 3.6 Hz, 1H, furan-H), 5.57 (d, J = 3.6 Hz, 1H, furan-H), 4.53 (s, 2H, CH_2), 3.79 (s, 3H, OCH_3). ^{13}C NMR (151 MHz, DMSO-d_6): δ 169.4, 157.2, 155.1, 154.2, 153.8, 146.0, 144.0, 143.0, 140.6, 140.1, 134.0, 133.0, 132.3, 131.9, 131.4, 130.7, 128.9, 128.3, 127.9, 127.4, 127.0, 126.6, 125.7, 121.2, 120.2, 117.8, 116.8, 116.5, 115.1, 113.4, 113.2, 111.4, 62.6 (CH_2), 55.3 (OCH_3). LC-MS (m/z): positive mode 444.27 $[M + H]^+$; purity by HPLC UV (254 nm)-ESI-MS: 91.4%.

*5-Methoxy-2-(5-(3′-(methylsulfonyl)-[1,1′-biphenyl]-2-yl)-furan-2-carboxamido)benzoic Acid (**60**).* Compound **60** was synthesized according to the general procedure **B** starting from **50** (0.24 mmol) and (3-(methylsulfonyl)phenyl)boronic acid (0.36 mmol). Yield: 54%; colorless solid; ^{1}H NMR (500 MHz, DMSO-d_6): δ 13.89 (s br, 1H, CO_2H), 11.92 (s, 1H, NH), 8.56 (d, J = 9.1 Hz, 1H), 8.00 (dd, J = 7.8, 1.6 Hz, 1H), 7.94 (dt, J = 6.7, 2.1 Hz, 1H), 7.80 (t, J = 1.7 Hz, 1H), 7.73−7.67 (m, 2H), 7.57 (dtd, J = 18.8, 7.5, 1.4 Hz, 2H), 7.51 (d, J = 3.1 Hz, 1H), 7.45 (dd, J = 7.3, 1.6 Hz, 1H), 7.25 (dd, J = 9.2, 3.1 Hz, 1H), 7.11 (d, J = 3.6 Hz, 1H, furan-H), 5.78 (d, J = 3.6 Hz, 1H, furan-H), 3.78 (s, 3H, OCH_3), 3.17 (s, 3H, SO_2CH_3). ^{13}C NMR (126 MHz, DMSO-d_6): δ 169.5, 155.2, 154.5, 153.8, 146.6, 141.9, 141.3, 138.2, 134.3, 134.1, 131.1, 129.9, 129.4, 128.9, 127.8, 127.7, 127.3, 126.2, 121.5, 120.6, 117.7, 116.7, 115.2, 112.0, 55.6 (OCH_3), 43.6 (SO_2CH_3). LC-MS (m/z): positive mode 492.3 $[M + H]^+$; purity by HPLC UV (254 nm)-ESI-MS: 97.3%.

*5-([1,1′-Biphenyl]-2-yl)-N-(2-carbamoylphenyl)furan-2-carboxamide (**79**).* Compound **79** was synthesized according to the general procedure **A** starting from 5-([1,1′-biphenyl]-2-yl)furan-2-carboxylic acid (**4c**, 0.38 mmol) and 2-aminobenzamide (**77**, 0.57 mmol). Yield: 18%; colorless solid; ^{1}H NMR (500 MHz, DMSO-d_6) δ: 12.96 (s, 1H, NH), 8.61 (dd, J = 8.4, 1.1 Hz, 1H), 8.36 (s, 1H, $CONH_2$), 8.07 (dd, J = 7.9, 1.4 Hz, 1H), 7.89 (dd, J = 8.0, 1.5 Hz, 1H), 7.86 (s br, 1H, $CONH_2$), 7.57−7.37 (m, 6H), 7.35−7.28 (m, 3H), 7.19−7.13 (m, 1H), 7.06 (d, J = 3.6 Hz, 1H, furan-H), 5.57 (d, J = 3.7 Hz, 1H, furan-H). ^{13}C NMR (126 MHz, DMSO-d_6) δ: 171.1 ($CONH_2$), 155.6, 154.1, 146.3, 141.0, 140.2, 139.7, 132.6, 130.9, 128.94, 128.90, 128.7, 128.1, 127.8, 127.7, 127.1, 122.8, 120.0, 119.3, 116.7, 111.5. MS (m/z): positive mode 383.2 $[M + H]^+$; purity by HPLC UV (254 nm)-ESI-MS: 96%.

*5-(Naphthalen-1-yl)-N-(2-(trifluoromethoxy)phenyl)-furan-2-carboxamide (**80**).* Compound **80** was synthesized according to general procedure **A** starting from 5-(naphthalen-1-yl)furan-2-carboxylic acid (**26**, 0.50 mmol) and 2-(trifluoromethoxy)aniline (**78a**, 0.70 mmol). Yield: 57%; colorless solid; ^{1}H NMR (600 MHz, DMSO-d_6): δ 10.03 (s, 1H, NH), 8.44−8.38 (m, 1H), 8.04 (dd, J = 7.5, 2.5 Hz, 2H),

https://doi.org/10.1021/acs.jmedchem.4c01755
J. Med. Chem. 2024, 67, 19365−19394

7.97 (dd, J = 7.2, 1.1 Hz, 1H), 7.77 (dd, J = 7.9, 1.4 Hz, 1H), 7.67−7.59 (m, 3H), 7.55 (d, J = 3.5 Hz, 1H, furan-H), 7.49−7.42 (m, 2H), 7.40−7.34 (m, 1H), 7.16 (d, J = 3.5 Hz, 1H, furan-H). ^{13}C NMR (126 MHz, DMSO-d_6): δ 156.4, 155.1, 146.9, 142.2, 133.7, 130.1, 129.9, 129.6, 128.9, 127.8, 127.6, 127.5, 127.2, 127.1, 126.7, 126.5, 125.6, 124.9, 121.5, 117.0, 111.9 (OCF_3 could not be observed). LC-MS (m/z): positive mode 398.1 $[M + H]^+$; purity by HPLC UV (254 nm)-ESI-MS: 99.3%.

*N-(2-Cyanophenyl)-5-(naphthalen-1-yl)furan-2-carboxamide (**81**).* Compound **81** was synthesized according to general procedure **A** starting from 5-(naphthalen-1-yl)furan-2-carboxylic acid (**26**, 0.42 mmol) and 2-aminobenzonitrile (**78b**, 0.59 mmol). Yield: 25%; colorless solid; ^{1}H NMR (500 MHz, DMSO-d_6): δ 10.55 (s, 1H, NH), 8.42 (d, J = 8.4 Hz, 1H), 8.08−8.02 (m, 2H), 8.00 (dd, J = 7.2, 1.0 Hz, 1H), 7.89 (dd, J = 7.8, 1.3 Hz, 1H), 7.79−7.73 (m, 1H), 7.69−7.60 (m, 4H), 7.58 (d, J = 3.6 Hz, 1H, furan-H), 7.47−7.41 (m, 1H), 7.19 (d, J = 3.6 Hz, 1H, furan-H). ^{13}C NMR (151 MHz, DMSO-d_6): δ 156.5, 155.3, 146.6, 139.7, 134.0, 133.7, 133.3, 130.0, 129.6, 128.9, 127.6, 127.3, 126.9, 126.7, 126.6, 126.5, 125.6, 125.0, 117.6, 117.0, 112.1, 109.2. LC-MS (m/z): positive mode 339.3 $[M + H]^+$; purity by HPLC UV (254 nm)-ESI-MS: 98.5%.

*N-(2-(Methylthio)phenyl)-5-(naphthalen-1-yl)furan-2-carboxamide (**82**).* Compound **82** was synthesized according to general procedure **A** starting from 5-(naphthalen-1-yl)furan-2-carboxylic acid (**26**, 0.84 mmol) and 2-(methylthio)aniline (**78c**, 1.26 mmol). Yield: 68%; colorless solid; ^{1}H NMR (500 MHz, $CDCl_3$): δ 9.57 (s, 1H, NH), 8.54 (dd, J = 8.2, 1.3 Hz, 1H), 8.52−8.47 (m, 1H), 7.93−7.90 (m, 2H), 7.82 (dd, J = 7.3, 1.2 Hz, 1H), 7.60−7.51 (m, 4H), 7.43 (d, J = 3.5 Hz, 1H, furan-H), 7.39−7.32 (m, 1H), 7.09 (td, J = 7.6, 1.4 Hz, 1H), 6.89 (d, J = 3.5 Hz, 1H, furan-H), 2.38 (s, 3H, SCH_3). ^{13}C NMR (126 MHz, $CDCl_3$): δ 156.1, 155.9, 147.5, 138.4, 134.0, 133.6, 130.2, 129.9, 129.3, 128.8, 127.2, 127.1, 127.0, 126.3, 125.31, 125.28, 125.2, 124.4, 120.3, 117.1, 111.8, 19.1 (SCH_3). LC-MS (m/z): positive mode 360.1 $[M + H]^+$; purity by HPLC UV (254 nm)-ESI-MS: 99.0%.

*N-(2-(Methylsulfinyl)phenyl)-5-(naphthalen-1-yl)furan-2-carboxamide (**83**).* A solution of *N*-(2-(methylthio)phenyl)-5-(naphthalen-1-yl)furan-2-carboxamide (**82**, 0.11 mmol) and *m*-chloroperbenzoic acid (mCPBA, 0.15 mmol) in DCM (5 mL) was stirred at rt for 1 h. Subsequently a saturated aqueous solution of $NaHCO_3$ (25 mL) was added and the product was extracted with additional DMM (2 × 30 mL). The combined organic extracts were dried over $MgSO_4$, filtered and concentrated. The residue was purified by column chromatography on silica gel (eluent: DCM/AcOEt = 9.5:0.5). Yield: 85%, resin-like beige solid. ^{1}H NMR (600 MHz, $CDCl_3$): δ 11.52 (s, 1H, NH), 8.66 (d, J = 8.3 Hz, 1H), 8.47 (d, J = 8.5 Hz, 1H), 7.99−7.92 (m, 1H), 7.91−7.84 (m, 2H), 7.60−7.48 (m, 4H), 7.43 (d, J = 3.5 Hz, 1H, furan-H), 7.32 (dd, J = 7.7, 1.4 Hz, 1H), 7.18−7.12 (m, 1H), 6.90 (d, J = 3.5 Hz, 1H, furan-H), 2.94 (s, 3H, $S(O)CH_3$). ^{13}C NMR (151 MHz, $CDCl_3$): δ 156.7, 156.1, 146.9, 140.0, 133.9, 132.7, 130.0, 129.7, 128.7, 128.1, 127.1, 127.0, 126.1, 125.8, 125.4, 125.1, 123.7, 122.9, 117.2, 111.7, 41.0. LC-MS (m/z): positive mode 376.1 $[M + H]^+$; purity by HPLC UV (254 nm)-ESI-MS: 99.0%.

*N-(2-(Methylsulfonyl)phenyl)-5-(naphthalen-1-yl)furan-2-carboxamide (**84**).* Compound **84** was prepared as described above for compound **83** starting from *N*-(2-(methylthio)-phenyl)-5-(naphthalen-1-yl)furan-2-carboxamide (**82**, 0.11 mmol) and an excess of *m*-chloroperbenzoic acid (mCPBA, 0.50 mmol). Yield: 64%, beige resin-like solid. ^{1}H NMR (600 MHz, $CDCl_3$) δ: 10.65 (s, 1H, NH), 8.68 (dd, J = 8.4, 1.0 Hz, 1H), 8.48−8.46 (m, 1H), 7.98−7.93 (m, 2H), 7.92−7.89 (m, 2H), 7.70−7.66 (m, 1H), 7.63−7.52 (m, 3H), 7.46 (d, J = 3.5 Hz, 1H, furan-H), 7.31−7.26 (m, 1H), 6.94 (d, J = 3.6 Hz, 1H, furan-H), 3.09 (s, 3H, SO_2CH_3). ^{13}C NMR (151 MHz, $CDCl_3$) δ: 156.3, 146.5, 136.9, 135.4, 134.0, 130.0, 129.4, 128.8, 127.4, 127.3, 127.1, 126.8, 126.3, 125.5, 125.0, 124.2, 122.7, 118.0, 111.9, 44.3 (SO_2CH_3). MS (m/z): positive mode 392.1 $[M + H]^+$; purity by HPLC UV (254 nm)-ESI-MS: 96%.

■ ASSOCIATED CONTENT

Supporting Information

The Supporting Information is available free of charge at https://pubs.acs.org/doi/10.1021/acs.jmedchem.4c01755.

Synthesis of intermediates (**4a−4p**, **26−27**, **28k−28l**, **61−62**, **71−72**); ^{1}H NMR spectra, ^{13}C NMR spectra and LC/MS data sets of selected compounds (**9**, **14**, **20**, **22-23**, **25**, **32-33**, **37**, **40**, **42**, **45**, **48**, **51-52**, **54**, **55**, **57**, **65**, **67**, **70**, **75**); concentration−response curves of known antagonists (**2a−2b**); concentration−response curves and inhibition of binding curves of selected compounds (**9**, **14−15**, **22−23**, **33**, **37**, **48**, **52**, **54**, **57**, **67**, **70**), correlation of data obtained for selected compounds (**9**, **14−15**, **22−23**, **33**, **37**, **48**, **52**, **54**, **57**, **67**, **70**) (PDF)

Inactive-state model of GPR17 (PDB)

Apo-form and in complex with antagonist **52** (PDB)

Molecular formula strings (CSV)

■ AUTHOR INFORMATION

Corresponding Author

Christa E. Müller − *PharmaCenter Bonn, Pharmaceutical Institute, Pharmaceutical & Medicinal Chemistry, University of Bonn, Bonn D-53121, Germany;* orcid.org/0000-0002-0013-6624; Phone: +49-228-73-2301; Email: christa.mueller@uni-bonn.de; Fax: +49-228-73-2567

Authors

Nader M. Boshta − *PharmaCenter Bonn, Pharmaceutical Institute, Pharmaceutical & Medicinal Chemistry, University of Bonn, Bonn D-53121, Germany;* Present Address: Chemistry Department, Faculty of Science, Manoufia University, Gamal Abdel-Nasser Street, Shebin El-Kom 32511, Egypt

Michael Lewash − *PharmaCenter Bonn, Pharmaceutical Institute, Pharmaceutical & Medicinal Chemistry, University of Bonn, Bonn D-53121, Germany;* orcid.org/0009-0009-1383-4745

Meryem Köse − *PharmaCenter Bonn, Pharmaceutical Institute, Pharmaceutical & Medicinal Chemistry, University of Bonn, Bonn D-53121, Germany*

Vigneshwaran Namasivayam − *PharmaCenter Bonn, Pharmaceutical Institute, Pharmaceutical & Medicinal Chemistry, University of Bonn, Bonn D-53121, Germany;* orcid.org/0000-0003-3031-3377

Soumya Sarkar − *PharmaCenter Bonn, Pharmaceutical Institute, Pharmaceutical & Medicinal Chemistry, University*

of Bonn, Bonn D-53121, Germany; orcid.org/0009-0000-4240-1812

Jan H. Voss − *PharmaCenter Bonn, Pharmaceutical Institute, Pharmaceutical & Medicinal Chemistry, University of Bonn, Bonn D-53121, Germany;* orcid.org/0000-0003-0595-4607

Andy J. Liedtke − *PharmaCenter Bonn, Pharmaceutical Institute, Pharmaceutical & Medicinal Chemistry, University of Bonn, Bonn D-53121, Germany;* orcid.org/0009-0001-1430-7869

Anna Junker − *PharmaCenter Bonn, Pharmaceutical Institute, Pharmaceutical & Medicinal Chemistry, University of Bonn, Bonn D-53121, Germany;* orcid.org/0000-0001-5151-0930

Maoqun Tian − *PharmaCenter Bonn, Pharmaceutical Institute, Pharmaceutical & Medicinal Chemistry, University of Bonn, Bonn D-53121, Germany*

Anne Stößel − *PharmaCenter Bonn, Pharmaceutical Institute, Pharmaceutical & Medicinal Chemistry, University of Bonn, Bonn D-53121, Germany*

Mahmoud Rashed − *PharmaCenter Bonn, Pharmaceutical Institute, Pharmaceutical & Medicinal Chemistry, University of Bonn, Bonn D-53121, Germany;* Present Address: On leave from: Pharmaceutical Medicinal Chemistry & Drug Design Department, Faculty of Pharmacy (Boys), Al-Azhar University, Cairo, 11884, Egypt; orcid.org/0000-0003-0706-1044

Ahmed Mahal − *PharmaCenter Bonn, Pharmaceutical Institute, Pharmaceutical & Medicinal Chemistry, University of Bonn, Bonn D-53121, Germany;* orcid.org/0000-0002-6977-3752

Nicole Merten − *Pharmaceutical Biology, University of Bonn, Bonn D-53115, Germany;* orcid.org/0000-0002-8487-6805

Cécile Pegurier − *UCB, Chemin du Foriest, Braine-l'alleud BE-1420, Belgium*

Jörg Hockemeyer − *PharmaCenter Bonn, Pharmaceutical Institute, Pharmaceutical & Medicinal Chemistry, University of Bonn, Bonn D-53121, Germany*

Evi Kostenis − *Pharmaceutical Biology, University of Bonn, Bonn D-53115, Germany;* orcid.org/0000-0001-8284-5514

Complete contact information is available at: https://pubs.acs.org/10.1021/acs.jmedchem.4c01755

Author Contributions

[‖]N.M.B and M.L. contributed equally to this work. The manuscript was written through contributions of all authors. All authors have given approval to the final version of the manuscript.

Funding

M.L. was supported by the Studienstiftung des deutschen Volkes (German National Academic Foundation) which provided a doctoral scholarship. C.E.M. and E.K. were supported by the BMBF (German Federal Ministry for Education and Research) within the BioPharma initiative "Neuroallianz".

Notes

The authors declare no competing financial interest.

■ ACKNOWLEDGMENTS

We thank Katharina Sylvester, Marion Schneider, Christiane Bous, Christin Vielmuth, Hamid Radjainia, and Roland Drews for expert technical assistance. We are most grateful to Michel Bouvier and his research group for providing the biosensors for the GEMTA assays.

■ ABBREVIATIONS

CHO, Chinese hamster ovary; DAD, diode array detector; DIPEA, diisopropylethylamine; EMTA, effector-membrane translocation assay; FITR, Flp-In T-REx; FCA, furan-carboxylic acid; GEMTA, G protein effector-membrane translocation assay.

■ REFERENCES

(1) Davenport, A. P.; Alexander, S. P. H.; Sharman, J. L.; Pawson, A. J.; Benson, H. E.; Monaghan, A. E.; Liew, W. C.; Mpamhanga, C. P.; Bonner, T. I.; Neubig, R. R.; Pin, J. P.; Spedding, M.; Harmar, A. J. International Union of Basic and Clinical Pharmacology. LXXXVIII. G protein-coupled receptor list: recommendations for new pairings with cognate ligands. *Pharmacol. Rev.* **2013**, *65*, 967−986.

(2) Hauser, A. S.; Attwood, M. M.; Rask-Andersen, M.; Schiöth, H. B.; Gloriam, D. E. Trends in GPCR drug discovery: new agents, targets and indications. *Nat. Rev. Drug Discovery* **2017**, *16*, 829−842.

(3) Hennen, S.; Wang, H.; Peters, L.; Merten, N.; Simon, K.; Spinrath, A.; Blättermann, S.; Akkari, R.; Schrage, R.; Schröder, R.; Schulz, D.; Vermeiren, C.; Zimmermann, K.; Kehraus, S.; Drewke, C.; Pfeifer, A.; König, G. M.; Mohr, K.; Gillard, M.; Müller, C. E.; Lu, Q. R.; Gomeza, J.; Kostenis, E. Decoding Signaling and Function of the Orphan G Protein−Coupled Receptor GPR17 with a Small-Molecule Agonist. *Sci. Sign.* **2013**, *6* (298), ra93.

(4) Baqi, Y.; Pillaiyar, T.; Abdelrahman, A.; Kaufmann, O.; Alshaibani, S.; Rafehi, M.; Ghasimi, S.; Akkari, R.; Ritter, K.; Simon, K.; Spinrath, A.; Kostenis, E.; Zhao, Q.; Köse, M.; Namasivayam, V.; Müller, C. E. 3-(2-Carboxyethyl)indole-2-carboxylic Acid Derivatives: Structural Requirements and Properties of Potent Agonists of the Orphan G Protein-Coupled Receptor GPR17. *J. Med. Chem.* **2018**, *61*, 8136−8154.

(5) Nguyen, P.; Doan, P.; Murugesan, A.; Ramesh, T.; Rimpilainen, T.; Candeias, N. R.; Yli-Harja, O.; Kandhavelu, M. GPR17 signaling activation by CHBC agonist induced cell death via modulation of MAPK pathway in glioblastoma. *Life Sci.* **2022**, *291*, 120307.

(6) Chen, Y.; Wu, H.; Wang, S.; Koito, H.; Li, J.; Ye, F.; Hoang, J.; Escobar, S. S.; Gow, A.; Arnett, H. A.; Trapp, B. D.; Karandikar, N. J.; Hsieh, J.; Lu, Q. R. The oligodendrocyte-specific G protein-coupled receptor GPR17 is a cell-intrinsic timer of myelination. *Nat. Neurosci.* **2009**, *12*, 1398−1406.

(7) Fumagalli, M.; Daniele, S.; Lecca, D.; Lee, P. R.; Parravicini, C.; Fields, R. D.; Rosa, P.; Antonucci, F.; Verderio, C.; Trincavelli, M. L.; Bramanti, P.; Martini, C.; Abbracchio, M. P. Phenotypic changes, signaling pathway, and functional correlates of GPR17-expressing neural precursor cells during oligodendrocyte differentiation. *J. Biol. Chem.* **2011**, *286*, 10593−10604.

(8) Lu, C.; Dong, L.; Zhou, H.; Li, Q.; Huang, G.; Bai, S. J.; Liao, L. G-Protein-Coupled Receptor Gpr17 Regulates Oligodendrocyte Differentiation in Response to Lysolecithin-Induced Demyelination. *Sci. Rep.* **2018**, *8* (1), 4502.

(9) Rivera, A. D.; Chacon-De-La-Rocha, I.; Pieropan, F.; Papanikolau, M.; Azim, K.; Butt, A. M. Keeping the ageing brain wired: a role for purine signalling in regulating cellular metabolism in oligodendrocyte progenitors. *Pflugers Arch.* **2021**, *473*, 775−783.

(10) Marucci, G.; Dal Ben, D.; Lambertucci, C.; Santinelli, C.; Spinaci, A.; Thomas, A.; Volpini, R.; Buccioni, M. The G Protein-Coupled Receptor GPR17: Overview and Update. *ChemMedchem* **2016**, *11*, 2567−2574.

(11) Fumagalli, M.; Lecca, D.; Coppolino, G. T.; Parravicini, C.; Abbracchio, M. P. Pharmacological Properties and Biological

Functions of the GPR17 Receptor, a Potential Target for Neuro-Regenerative Medicine. *Adv. Exp. Med. Biol.* **2017**, *1051*, 169−192.
(12) Ciana, P.; Fumagalli, M.; Trincavelli, M. L.; Verderio, C.; Rosa, P.; Lecca, D.; Ferrario, S.; Parravicini, C.; Capra, V.; Gelosa, P.; Guerrini, U.; Belcredito, S.; Cimino, M.; Sironi, L.; Tremoli, E.; Rovati, G. E.; Martini, C.; Abbracchio, M. P. The orphan receptor GPR17 identified as a new dual uracil nucleotides/cysteinyl-leukotrienes receptor. *Embo J.* **2006**, *25*, 4615−4627.
(13) Nyamoya, S.; Leopold, P.; Becker, B.; Beyer, C.; Hustadt, F.; Schmitz, C.; Michel, A.; Kipp, M. G-Protein-Coupled Receptor Gpr17 Expression in Two Multiple Sclerosis Remyelination Models. *Mol. Neurobiol.* **2019**, *56*, 1109−1123.
(14) Coppolino, G. T.; Marangon, D.; Negri, C.; Menichetti, G.; Fumagalli, M.; Gelosa, P.; Dimou, L.; Furlan, R.; Lecca, D.; Abbracchio, M. P. Differential local tissue permissiveness influences the final fate of GPR17-expressing oligodendrocyte precursors in two distinct models of demyelination. *Glia* **2018**, *66*, 1118−1130.
(15) Fumagalli, M.; Lecca, D.; Abbracchio, M. P. CNS remyelination as a novel reparative approach to neurodegenerative diseases: The roles of purinergic signaling and the P2Y-like receptor GPR17. *Neuropharmacology* **2016**, *104*, 82−93.
(16) Bonfanti, E.; Bonifacino, T.; Raffaele, S.; Milanese, M.; Morgante, E.; Bonanno, G.; Abbracchio, M. P.; Fumagalli, M. Abnormal Upregulation of GPR17 Receptor Contributes to Oligodendrocyte Dysfunction in SOD1 G93A Mice. *Int. J. Mol. Sci.* **2020**, *21* (7), 2395.
(17) Maekawa, A.; Xing, W.; Austen, K. F.; Kanaoka, Y. GPR17 regulates immune pulmonary inflammation induced by house dust mites. *J. Immunol.* **2010**, *185*, 1846−1854.
(18) Lecca, D.; Trincavelli, M. L.; Gelosa, P.; Sironi, L.; Ciana, P.; Fumagalli, M.; Villa, G.; Verderio, C.; Grumelli, C.; Guerrini, U.; Tremoli, E.; Rosa, P.; Cuboni, S.; Martini, C.; Buffo, A.; Cimino, M.; Abbracchio, M. P. The recently identified P2Y-like receptor GPR17 is a sensor of brain damage and a new target for brain repair. *PLoS One* **2008**, *3*, No. e3579.
(19) Mutharasu, G.; Murugesan, A.; Konda Mani, S.; Yli-Harja, O.; Kandhavelu, M. Transcriptomic analysis of glioblastoma multiforme providing new insights into GPR17 signaling communication. *J. Biomol. Struct. Dyn.* **2022**, *40*, 2586−2599.
(20) Kari, S.; Kandhavelu, J.; Murugesan, A.; Thiyagarajan, R.; Kidambi, S.; Kandhavelu, M. Mitochondrial complex III bypass complex I to induce ROS in GPR17 signaling activation in GBM. *Biomed. Pharmacother.* **2023**, *162*, 114678.
(21) Liu, H.; Xing, R.; Ou, Z.; Zhao, J.; Hong, G.; Zhao, T.-J.; Han, Y.; Chen, Y. G-protein-coupled receptor GPR17 inhibits glioma development by increasing polycomb repressive complex 1-mediated ROS production. *Cell Death Dis* **2021**, *12* (6), 610.
(22) Ren, H.; Cook, J. R.; Kon, N.; Accili, D. Gpr17 in AgRP Neurons Regulates Feeding and Sensitivity to Insulin and Leptin. *Diabetes* **2015**, *64*, 3670−3679.
(23) Simon, K.; Merten, N.; Schröder, R.; Hennen, S.; Preis, P.; Schmitt, N.-K.; Peters, L.; Schrage, R.; Vermeiren, C.; Gillard, M.; Mohr, K.; Gomeza, J.; Kostenis, E. The Orphan Receptor GPR17 Is Unresponsive to Uracil Nucleotides and Cysteinyl Leukotrienes. *Mol. Pharmacol.* **2017**, *91*, 518−532.
(24) Qi, A.-D.; Harden, T. K.; Nicholas, R. A. Is GPR17 a P2Y/leukotriene receptor? examination of uracil nucleotides, nucleotide sugars, and cysteinyl leukotrienes as agonists of GPR17. *J. Pharmacol. Exp. Ther.* **2013**, *347*, 38−46.
(25) Harrington, A. W.; Liu, C.; Phillips, N.; Nepomuceno, D.; Kuei, C.; Chang, J.; Chen, W.; Sutton, S. W.; O'Malley, D.; Pham, L.; Yao, X.; Sun, S.; Bonaventure, P. Identification and characterization of select oxysterols as ligands for GPR17. *Br. J. Pharmacol.* **2023**, *180*, 401−421.
(26) Maekawa, A.; Balestrieri, B.; Austen, K. F.; Kanaoka, Y. GPR17 is a negative regulator of the cysteinyl leukotriene 1 receptor response to leukotriene D4. *Proc. Natl. Acad. Sci. U. S. A* **2009**, *106*, 11685−11690.
(27) Benned-Jensen, T.; Rosenkilde, M. M. Distinct expression and ligand-binding profiles of two constitutively active GPR17 splice variants. *Br. J. Pharmacol.* **2010**, *159*, 1092−1105.
(28) Baron, B. M.; Harrison, B. L.; McDonald, I. A.; Meldrum, B. S.; Palfreyman, M. G.; Salituro, F. G.; Siegel, B. W.; Slone, A. L.; Turner, J. P.; White, H. S. Potent indole- and quinoline-containing N-methyl-D-aspartate antagonists acting at the strychnine-insensitive glycine binding site. *J. Pharmacol. Exp. Ther.* **1992**, *262*, 947−956.
(29) Köse, M.; Ritter, K.; Thiemke, K.; Gillard, M.; Kostenis, E.; Müller, C. E. Development of (3)H2-Carboxy-4,6-dichloro-1H-indole-3-propionic Acid ((3)HPSB-12150): A Useful Tool for Studying GPR17. *ACS Med. Chem. Lett.* **2014**, *5*, 326−330.
(30) Pugliese, A. M.; Trincavelli, M. L.; Lecca, D.; Coppi, E.; Fumagalli, M.; Ferrario, S.; Failli, P.; Daniele, S.; Martini, C.; Pedata, F.; Abbracchio, M. P. Functional characterization of two isoforms of the P2Y-like receptor GPR17: 35SGTPgammaS binding and electrophysiological studies in 1321N1 cells. *Am. J. Physiol. Cell Physiol.* **2009**, *297*, C1028−40.
(31) Braune, M.; Scherf, N.; Heine, C.; Sygnecka, K.; Pillaiyar, T.; Parravicini, C.; Heimrich, B.; Abbracchio, M. P.; Müller, C. E.; Franke, H. Involvement of GPR17 in Neuronal Fibre Outgrowth. *Int. J. Mol. Sci.* **2021**, *22* (21), 11683.
(32) Ye, F.; Wong, T.-S.; Chen, G.; Zhang, Z.; Zhang, B.; Gan, S.; Gao, W.; Li, J.; Wu, Z.; Pan, X.; Du, Y. Cryo-EM structure of G-protein-coupled receptor GPR17 in complex with inhibitory G protein. *MedComm* **2022**, *3* (4), No. e159.
(33) Castro-Alvarez, A.; Carneros, H.; Costa, A. M.; Vilarrasa, J. Computer-Aided Insight into the Relative Stability of Enamines. *Synthesis* **2017**, *49*, 5285−5306.
(34) Kumari, S.; Carmona, A. V.; Tiwari, A. K.; Trippier, P. C. Amide Bond Bioisosteres: Strategies, Synthesis, and Successes. *J. Med. Chem.* **2020**, *63*, 12290−12358.
(35) Lee, W. M. *Novel nitrile and amidoxime compounds and methods of preparation*. US 2,008,026,038,9 A1. 2008, 20081029.
(36) Koguro, K.; Oga, T.; Mitsui, S.; Orita, R. Novel Synthesis of 5-Substituted Tetrazoles from Nitriles. *Synthesis* **1998**, *1998* (6), 910−914.
(37) Ward, R. J.; Alvarez-Curto, E.; Milligan, G. Using the Flp-In T-Rex system to regulate GPCR expression. *Methods Mol. Biol.* **2011**, *746*, 21−37.
(38) Hillmann, P.; Ko, G.-Y.; Spinrath, A.; Raulf, A.; Kügelgen, I. V.; Wolff, S. C.; Nicholas, R. A.; Kostenis, E.; Höltje, H.-D.; Müller, C. E. Key Determinants of Nucleotide-Activated G Protein-Coupled P2Y 2 Receptor Function Revealed by Chemical and Pharmacological Experiments, Mutagenesis and Homology Modeling. *J. Med. Chem.* **2009**, *52* (9), 2762−2775.
(39) Avet, C.; Mancini, A.; Breton, B.; Le Gouill, C.; Hauser, A. S.; Normand, C.; Kobayashi, H.; Gross, F.; Hogue, M.; Lukasheva, V.; St-Onge, S.; Carrier, M.; Héroux, M.; Morissette, S.; Fauman, E. B.; Fortin, J.-P.; Schann, S.; Leroy, X.; Gloriam, D. E.; Bouvier, M. Effector membrane translocation biosensors reveal G protein and βarrestin coupling profiles of 100 therapeutically relevant GPCRs. *Elife* **2022**, *11*, No. e74101.
(40) Zhang, K.; Zhang, J.; Gao, Z.-G.; Zhang, D.; Zhu, L.; Han, G. W.; Moss, S. M.; Paoletta, S.; Kiselev, E.; Lu, W.; Fenalti, G.; Zhang, W.; Müller, C. E.; Yang, H.; Jiang, H.; Cherezov, V.; Katritch, V.; Jacobson, K. A.; Stevens, R. C.; Wu, B.; Zhao, Q. Structure of the human P2Y12 receptor in complex with an antithrombotic drug. *Nature* **2014**, *509*, 115−118.
(41) UniProt Consortium. UniProt: a hub for protein information. *Nucleic Acids Res.* **2015**, *43*, D204−12.
(42) Sievers, F.; Wilm, A.; Dineen, D.; Gibson, T. J.; Karplus, K.; Li, W.; Lopez, R.; McWilliam, H.; Remmert, M.; Söding, J.; Thompson, J. D.; Higgins, D. G. Fast, scalable generation of high-quality protein multiple sequence alignments using Clustal Omega. *Mol. Syst. Biol.* **2011**, *7* (1), 539.
(43) Webb, B.; Sali, A. Protein Structure Modeling with MODELLER. *Methods Mol. Biol.* **2021**, *2199*, 239−255.

https://doi.org/10.1021/acs.jmedchem.4c01755
J. Med. Chem. 2024, 67, 19365−19394

(44) Ulc, C. C. Molecular operating environment (MOE), 2020.09. In *Chemical Computing Group ULC*; McGill University: Canada Montreal, QC, 2020.
(45) Morris, G. M.; Huey, R.; Lindstrom, W.; Sanner, M. F.; Belew, R. K.; Goodsell, D. S.; Olson, A. J. AutoDock4 and AutoDockTools4: Automated docking with selective receptor flexibility. *J. Comput. Chem.* **2009**, *30*, 2785−2791.
(46) Namasivayam, V.; Günther, R. pso@autodock: a fast flexible molecular docking program based on Swarm intelligence. *Chem. Biol. Drug Des.* **2007**, *70*, 475−484.

https://doi.org/10.1021/acs.jmedchem.4c01755
J. Med. Chem. 2024, 67, 19365−19394

Supporting Information

Discovery of anthranilic acid derivatives as antagonists of the pro-inflammatory orphan G protein-coupled receptor GPR17

*Nader M. Boshta,[‡a§] Michael Lewash,[‡a] Meryem Köse,[a] Vigneshwaran Namasivayam,[a] Soumya Sarkar,[a] Jan H. Voss,[a] Andy J. Liedtke,[a] Anna Junker,[a] Maoqun Tian,[a] Anne Stößel,[a] Mahmoud Rashed,[a†] Ahmed Mahal,[a] Nicole Merten,[b] Cécile Pegurier,[c] Jörg Hockemeyer,[a] Evi Kostenis[b], and Christa E. Müller[a]**

[‡]These authors contributed equally.

[a]PharmaCenter Bonn, Pharmaceutical Institute, Pharmaceutical & Medicinal Chemistry, University of Bonn, An der Immenburg 4, D-53121 Bonn, Germany

[b]Pharmaceutical Biology, University of Bonn, Nußallee 6, D-53115 Bonn, Germany

[c]UCB, Chemin du Foriest, Braine-l'alleud BE-1420, Belgium

[§]Present address: Chemistry Department, Faculty of Science, Manoufia University, Gamal Abdel-Nasser Street, Shebin El-Kom 32511, Egypt

[†]On leave from: Pharmaceutical Medicinal Chemistry & Drug Design Department, Faculty of Pharmacy (Boys), Al-Azhar University, Cairo, 11884, Egypt

*Corresponding author email address: christa.mueller@uni-bonn.de

Table of contents

Synthesis of 5-Arylfuran-2-carboxylic acids and anthranilic acid analogs

General procedures to 5-arylfuran-2-carboxylic acids (4a-4p, 26-27, 61-62)

General procedure A to obtain 5-arylfuran-2-carboxylic acids

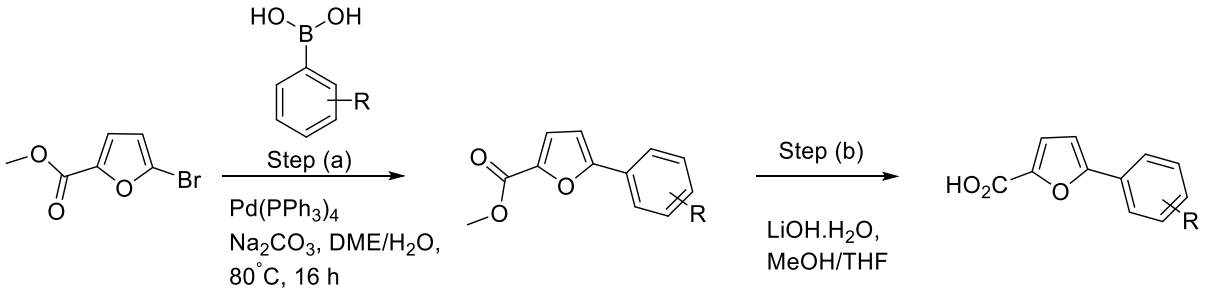

Step (a): A suspension of methyl 5-bromofuran-2-carboxylate (6.1 mmol), arylboronic acid (5.6 mmol), tetrakis(triphenylphosphine)palladium(0) (0.3 mmol) and Na_2CO_3 (11 mmol) in a mixture of dimethoxyethane (DME) and water (4:1, 50 mL) was reacted under argon atmosphere for 18 h at 80°C. Subsequently, the DME was evaporated under reduced pressure. The residue was treated with brine (50 mL) and extracted with DCM (3 x 30 mL). The combined organic extracts were dried over $MgSO_4$, filtered, evaporated and purified by silica gel column chromatography (eluent: EtOAc:petroleum ether = 10:90). The methyl 5-(2-aryl)furan-2-carboxylates thus obtained were only characterized by LC/MS and directly used for the following hydrolyzation step.

Step (b): A slurry of the methyl 5-arylfuran-2-carboxylate (5 mmol) and NaOH (60 mmol) in a mixture of MeOH (25 mL), THF (45 mL) and water (45 mL) was stirred for 1 h at rt (TLC control, eluent: EtOAc:petroleum ether = 10:90). Subsequently, the organic solvents were evaporated and the resulting aqueous phase was slowly treated with HCl (1N, 60 mL) under vigorous stirring. The resulting solid was filtered under reduced pressure, washed with water (100 mL) and dried under vacuum to give the free 5-arylfuran-2-carboxylic acid.

General procedure B to obtain 5-arylfuran-2-carboxylic acids

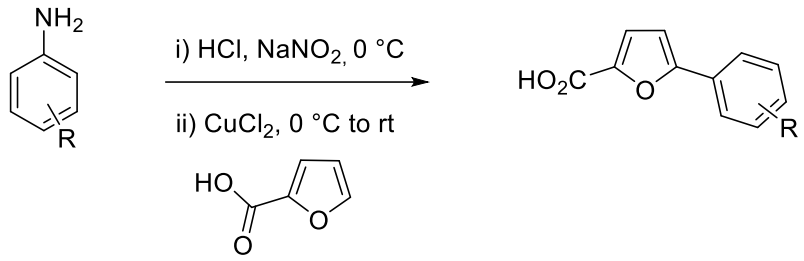

A solution of an appropriately substituted aniline derivative (20 mmol) in a mixture of H_2O (10 mL) and diluted HCl (ca. 18%, 8 mL) was cooled to 0 °C. At this temperature, a solution of sodium nitrite (1.4 g, 20 mmol) in H_2O (10 mL) was added, and the mixture was stirred for additional 20 min. To the resulting solution was added a solution of 2-furoic acid (1.46 g, 13.0 mmol) in acetone (7 mL), followed by the addition of a solution of copper(II) chloride (523 mg, 3.9 mmol) in H_2O (5 mL). The mixture was stirred for 6 h at rt. After evaporation of acetone, the mixture was diluted with brine (50 mL) and extracted with ethyl acetate (3 × 30 mL). The combined organic phases were dried over $MgSO_4$, filtered, and concentrated. The residue was washed with petroleum ether and finally recrystallized (EtOAc:petroleum ether = 1:1) yielding 5-arylfuran-2-carboxylic acids.

Synthesis of 5-([1,1'-biphenyl]-3-yl)furan-2-carboxylic acid (4m)

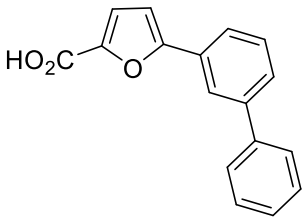

Starting from methyl 5-bromofuran-2-carboxylate and [1,1'-biphenyl]-3-ylboronic acid, compound **4m** was prepared according to the **general procedure A**. Yield: 47% over two steps.

^{1}H-NMR (500 MHz, DMSO-d_6) δ = 13.10 (s, 1H), 8.04 (t, *J* = 1.9 Hz, 1H), 7.80 (dt, *J* = 7.7, 1.5 Hz, 1H), 7.76-7.71 (m, 2H), 7.68 (dt, *J* = 7.7, 1.5 Hz, 1H), 7.57 (t, *J* = 7.8 Hz, 1H), 7.49 (dd, *J* = 8.4, 7.0 Hz, 2H), 7.44-7.38 (m, 1H), 7.34 (d, *J* = 3.5 Hz, 1H), 7.27 (d, *J* = 3.7 Hz, 1H) ppm. ^{13}C-NMR (126 MHz, DMSO) δ = 159.4, 156.3, 144.4, 141.2, 139.7, 130.0, 129.9, 129.1, 128.0, 127.5, 127.0, 123.5, 122.7, 120.0, 108.5 ppm.

Synthesis of 5-([1,1'-biphenyl]-4-yl)furan-2-carboxylic acid (4n)

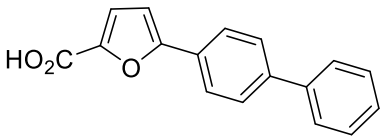

Starting from methyl 5-bromofuran-2-carboxylate and [1,1'-biphenyl]-4-ylboronic acid, compound **4n** was prepared according to the **general procedure A**. Yield: 68% over two steps. The product was only characterized by LC/MS and directly used to synthesized the final anthranilic acid derivative.

Synthesis of 5-([1,1'-Biphenyl]-2-yl)furan-2-carboxylic acid (4c)

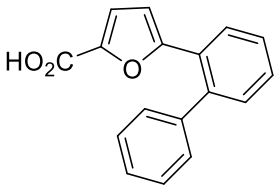

Starting from methyl 5-bromofuran-2-carboxylate and [1,1'-biphenyl]-2-ylboronic acid, compound **4c** was prepared according to the **general procedure A**. Yield: 53% over two steps. ^{1}H-NMR (500 MHz, DMSO-d_6) δ = 12.96 (s, 1H), 7.82-7.79 (m, 1H), 7.50 (dtd, *J* = 17.3, 7.5,

1.6 Hz, 2H), 7.43-7.37 (m, 3H), 7.34 (dd, *J* = 7.5, 1.5 Hz, 1H), 7.26-7.23 (m, 2H), 7.06 (d, *J* = 3.5 Hz, 1H), 5.68 (d, *J* = 3.5 Hz, 1H) ppm. ^{13}C-NMR (126 MHz, DMSO) δ = 159.3, 155.6, 143.8, 140.9, 140.2, 130.9, 129.2, 128.9, 128.7, 128.1, 127.84, 127.75, 127.6, 119.2, 111.1 ppm.

Synthesis of 5-(3,5-dichlorophenyl)furan-2-carboxylic acid (4j)

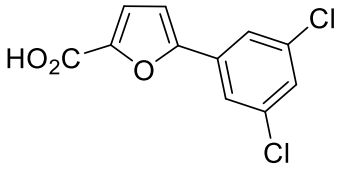

Starting from methyl 5-bromofuran-2-carboxylate and 3,5-dichlorophenylboronic acid, compound **4j** was prepared according to the **general procedure A**. Yield: 54% over two steps. ^{1}H NMR (600 MHz, DMSO-d_6) δ = 7.80 (d, *J* = 2.0 Hz, 2H), 7.57 (d, *J* = 2.0 Hz, 1H), 7.31 (d, *J* = 3.6 Hz, 1H), 7.19 (d, *J* = 3.6 Hz, 1H) ppm. ^{13}C-NMR (151 MHz, DMSO-d_6) δ = 159.8, 152.1, 147.6, 135.1, 132.8, 127.7, 122.6, 118.2, 110.5 ppm.

Synthesis of 5-(4-chlorophenyl)furan-2-carboxylic acid (4d)

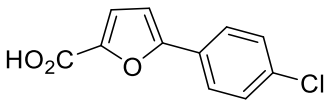

Starting from 4-chlorobenzenediazonium hydrochloride and 2-furoic acid, compound **4d** was synthesized according to the **general procedure B**. The product was only characterized by LC/MS and directly used to synthesized the final anthranilic acid derivative.

Synthesis of 5-(2,3-dichlorophenyl)furan-2-carboxylic acid (4k)

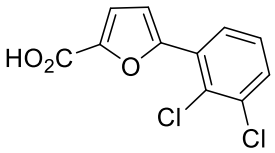

Starting from methyl 5-bromofuran-2-carboxylate and 2,3-dichlorophenylboronic acid, compound **4k** was prepared according to the **general procedure A**. Yield: 11% over two steps. The product was only characterized by LC/MS and directly used to synthesized the final anthranilic acid derivative.

Synthesis of 5-(2-phenoxyphenyl)furan-2-carboxylic acid (4l)

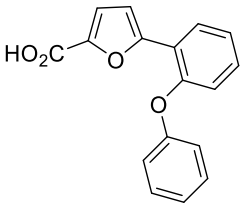

Starting from methyl 5-bromofuran-2-carboxylate and 2-phenoxybenzeneboronic acid, compound **4l** was prepared according to the **general procedure A**. Yield: 73% over two steps. ^{1}H-NMR (500 MHz, DMSO-d_6) δ = 13.11 (s, 1H), 7.93 (dd, *J* = 7.9, 1.8 Hz, 1H), 7.41-7.37 (m, 3H), 7.31 (td, *J* = 7.6, 1.2 Hz, 1H), 7.26 (d, *J* = 3.6 Hz, 1H), 7.16-7.12 (m, 1H), 7.04-6.99 (m, 3H), 6.94 (d, *J* = 3.6 Hz, 1H) ppm. ^{13}C-NMR (126 MHz, DMSO) δ = 159.3, 156.2, 152.8, 152.1, 143.9, 130.5, 130.3, 127.0, 124.6, 123.8, 121.1, 120.1, 119.9, 118.1, 112.1 ppm.

Synthesis of 5-(4-isobutylphenyl)furan-2-carboxylic acid (4a)

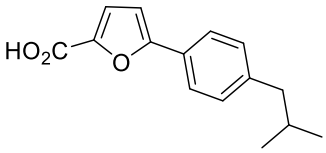

Starting from methyl 5-bromofuran-2-carboxylate and (4-isobutylphenyl)boronic acid, compound **4a** was prepared according to the **general procedure A**. Yield: 82% over two steps. The product was only characterized by LC/MS and directly used to synthesized the final anthranilic acid derivative.

Synthesis of 5-(2-isopropylphenyl)-2-furancarboxylic acid (27)

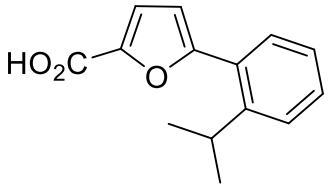

Starting from methyl 5-bromofuran-2-carboxylate and (2-isopropylphenyl)boronic acid, compound **27** was prepared according to the **general procedure A**. Yield: 80% over two steps. ^{1}H-NMR (500 MHz, DMSO-d_6): δ 13.03 (s, 1H, CO_2H), 7.53-7.45 (m, 2H), 7.42 (m, 1H), 7.31 (d, J = 3.5 Hz, 1H), 7.30-7.22 (m, 1H), 6.76 (d, J = 3.5 Hz, 1H), 3.29 (hept, J = 6.7 Hz, 1H), 1.20 (d, J = 6.8 Hz, 6H) ppm. ^{13}C-NMR (126 MHz, DMSO-d_6) δ = 159.4, 156.7, 146.8, 144.4, 129.8, 129.2, 128.2, 126.2, 126.1, 119.3, 110.9, 29.5, 23.9 ppm.

Synthesis of 5-(naphthalen-1-yl)furan-2-carboxylic acid (26)

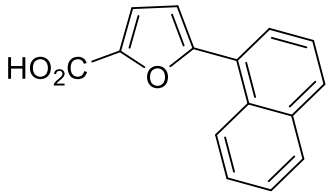

Starting from methyl 5-bromofuran-2-carboxylate and naphthalene-1-boronic acid, compound **26** was prepared according to the **general procedure A**. Yield: 77% over two steps. ^{1}H-NMR (500 MHz, DMSO-d_6) δ = 13.17 (s, 1H), 8.38 (d, *J* = 8.3 Hz, 1H), 8.03 (dt, *J* = 8.4, 1.9 Hz, 2H), 7.85 (d, *J* = 7.1 Hz, 1H), 7.67-7.57 (m, 3H), 7.41 (d, *J* = 3.5 Hz, 1H), 7.10 (d, *J* = 3.5 Hz, 1H) ppm.

Synthesis of 5-(2-bromophenyl)furan-2-carboxylic acid (4e)

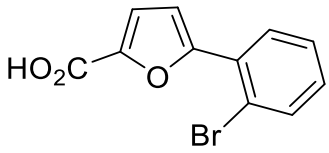

Starting from 2-Bromobenzenediazonium hydrochloride and 2-furoic acid, compound **4e** was synthesized according to the **general procedure B**. Yield: 38%. The product was only characterized by LC/MS and directly used to synthesized the final anthranilic acid derivative.

Synthesis of 5-(3'-methoxy-[1,1'-biphenyl]-2-yl)furan-2-carboxylic acid (4h)

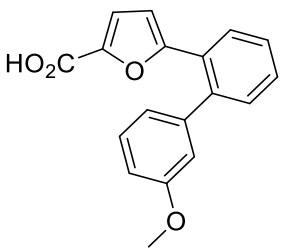

Compound **4h** was prepared following the first step of the **general procedure A** starting from 5-(2-bromophenyl)furan-2-carboxylic acid and 3-methoxyphenylboronic acid. The crude product was recrystallized from EtOAc. Yield: 21%. ^{1}H-NMR (500 MHz, DMSO-d_6) δ = 12.95 (s, 1H), 7.79 (dd, *J* = 7.6, 1.6 Hz, 1H), 7.49 (dtd, *J* = 18.7, 7.4, 1.5 Hz, 2H), 7.37-7.27 (m, 2H), 7.08 (d, *J* = 3.6 Hz, 1H), 6.98-6.93 (m, 1H), 6.82-6.78 (m, 2H), 5.76 (d, *J* = 3.8 Hz, 1H), 3.72 (s, 3H, OCH_3) ppm. ^{13}C-NMR (126 MHz, DMSO-d_6) δ = 159.4, 159.3, 155.5, 143.8, 142.3, 140.0, 130.8, 129.8, 129.1, 128.2, 127.8, 127.6, 121.2, 119.3, 114.3, 113.5, 111.1, 55.2 ppm.

Synthesis of 5-(3'-(2-methoxyethoxy)-[1,1'-biphenyl]-2-yl)furan-2-carboxylic acid (4o)

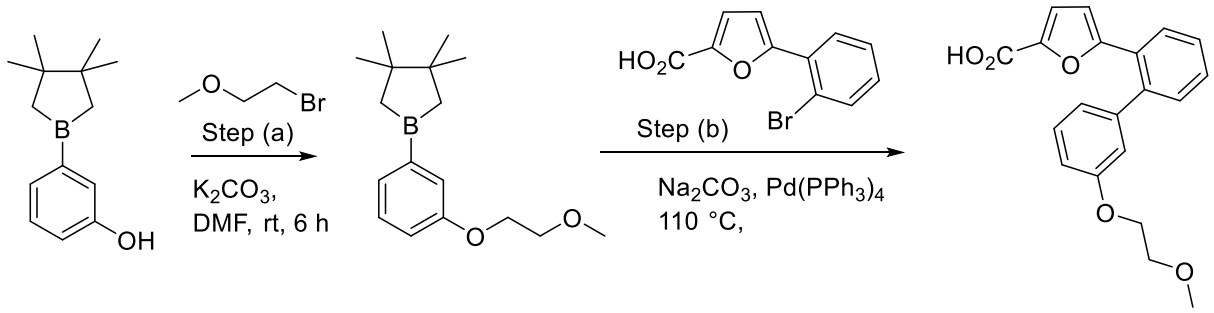

Step (a): 1-(3-(2-methoxyethoxy)phenyl)-3,3,4,4-tetramethylborolane: A mixture of 3-(3,3,4,4-tetramethylborolan-1-yl)phenol (5 mmol), 1-bromo-2-methoxyethane, K_2CO_3 (10 mmol) in DMF (7 mL) was stirred at rt for 6 h. After evaporation of volatile materials, the residue was purified by flash column chromatography (eluent: EtOAc:petroleum ether = 1:10) yielding a yellow oil which was directly used for the next step.

Step (b): Compound 4o: A suspension of 1-(3-(2-methoxyethoxy)phenyl)-3,3,4,4-tetramethylborolane (1 mmol), 5-(2-bromophenyl)furan-2-carboxylic acid (1 mmol), Na_2CO_3 (2 mmol) and tetrakis(triphenylphosphine) palladium(0) (50 mg) in a mixture of DME and water (4:1, 8 mL) was stirred at 110°C for 8 h. After colling to rt the mixture was extracted with

DCM (3 x 50 mL). The combined organic extracts were dried over $MgSO_4$, filtered and evaporated. The residue was purified by column chromatography (eluent: DCM:MeOH = 9:1). The product was only characterized by LC/MS and directly used to synthesized the final anthranilic acid derivative.

Synthesis of 5-(1-methyl-1*H*-indazol-4-yl)furan-2-carboxylic acid (4g)

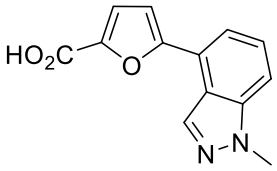

Starting from methyl 5-bromofuran-2-carboxylate and (1-methyl-*1H*-indazol-4-yl)boronic acid, compound **4g** was prepared according to the **general procedure A**. Yield: 73% over two steps. The product was only characterized by LC/MS and directly used to synthesized the final anthranilic acid derivative.

Synthesis of 2-(naphthalen-1-yl)thiazole-4-carboxylic acid (62)

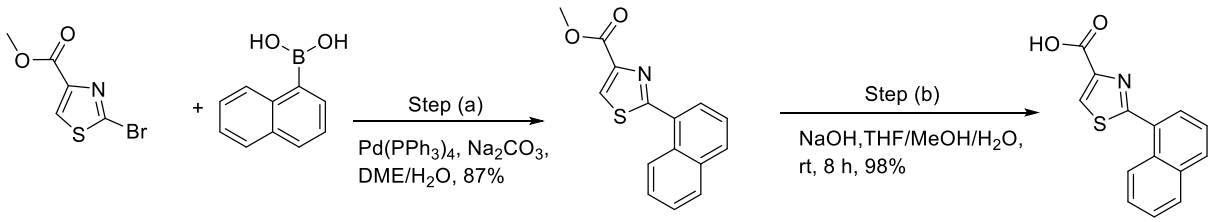

Step (a): A mixture of methyl 2-bromothiazole-4-carboxylate (1.35 mmol), naphthalen-1-ylboronic acid (1.48 mmol), tetrakis(triphenylphosphine)palladium(0) (78 mg) and Na_2CO_3 (287 mg) in a mixture of DME and water (4:1, 20 mL) was reacted under argon atmospherbe for 19 h at 80°C. After evaporation of DME, the residue was treated with additional water (50

mL) and extracted with EtOAc (3 x 50 mL) and subsequently with DCM (3 x 150 mL). The combined organic extracts were dried over $MgSO_4$, filtered, evaporated and purified by silica gel column chromatography (EtOAc:petroleum ether = 10:90). The obtained light-yellow oil (which slowly crystallized) was only characterized by LC/MS and directly used for the next step. Yield: 87%.

Step (b): The obtained methyl 2-(naphthalen-1-yl)thiazole-4-carboxylate (0.75 mmol) and NaOH (310 mg) were suspended in a mixture of MeOH (2 mL), THF (4 mL) and water (4 mL). The slurry was stirred for 8 h at rt (TLC control, eluent: EtOAc:petroleum ether = 20:80). Subsequently, MeOH and THF were evaporated and the resulting aqueous phase was slowly treated with 1N HCl until an oily precipitate was observed. The mixture was extracted with EtOAc (3 x 50 mL). The combined organic extracts were dried over $MgSO_4$, filtered and evaporated. Yield: 98%.

Synthesis of 6-(naphthalen-1-yl)picolinic acid (61)

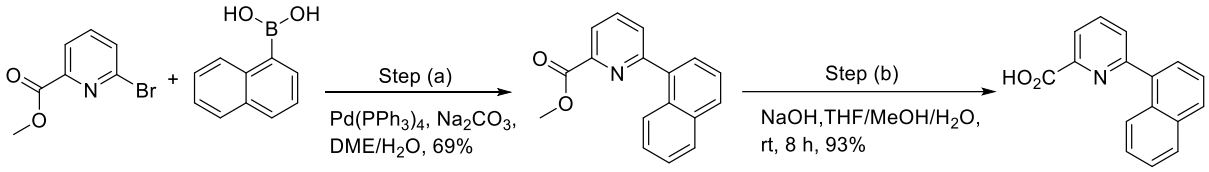

Step (a): A mixture of methyl 6-bromopicolinate (22 mmol), naphthalen-1-ylboronic acid (25 mmol), tetrakis(triphenylphosphine)palladium(0) (1.1 mmol) and Na_2CO_3 (45 mmol) in a mixture of DME and water (4:1, 200 mL) was reacted under argon atmosphere for 19 h at 80°C. After evaporation of DME, the residue was treated with additional water (100 mL) and extracted with EtOAc (3 x 100 mL) and subsequently with DCM (3 x 100 mL). The combined organic extracts were dried over $MgSO_4$, filtered, evaporated and purified by silica gel column

chromatography (EtOAc:petroleum ether = 20:80). The obtained light-yellow oil (which slowly crystallized) was only characterized by LC/MS and directly used for the next step. Yield: 69%.

Step (b): The obtained methyl 6-(naphthalen-1-yl)picolinate (15 mmol) and NaOH (150 mmol) were suspended in a mixture of MeOH (63 mL), THF (125 mL) and water (125 mL). The slurry was stirred for 8 h at rt (TLC control, eluent: EtOAc:petroleum ether = 20:80). Subsequently, MeOH and THF were evaporated and the resulting aqueous phase was slowly treated with 1N HCl until an oily precipitate was observed. The mixture was extracted with EtOAc (3 x 50 mL). The combined organic extracts were dried over $MgSO_4$, filtered and evaporated yielding a light beige solid. Yield: 93%. ^{1}H NMR (500 MHz, DMSO-d_6) δ = 13.18 (s br, 1H), 8.17-8.08 (m, 2H), 8.07-7.97 (m, 3H), 7.87 (dd, *J* = 7.5, 1.4 Hz, 1H), 7.66-7.61 (m, 2H), 7.58-7.48 (m, 2H) ppm. ^{13}C-NMR (126 MHz, DMSO) δ = 166.4, 158.4, 148.4, 138.4, 137.4, 133.6, 130.7, 129.2, 128.5, 128.1, 127.9, 126.8, 126.2, 125.5, 125.4, 123.3 ppm.

Synthesis of 5-(3-phenethoxyphenyl)furan-2-carboxylic acid (4p) and 5-(2-phenethoxyphenyl)furan-2-carboxylic acid (4i)

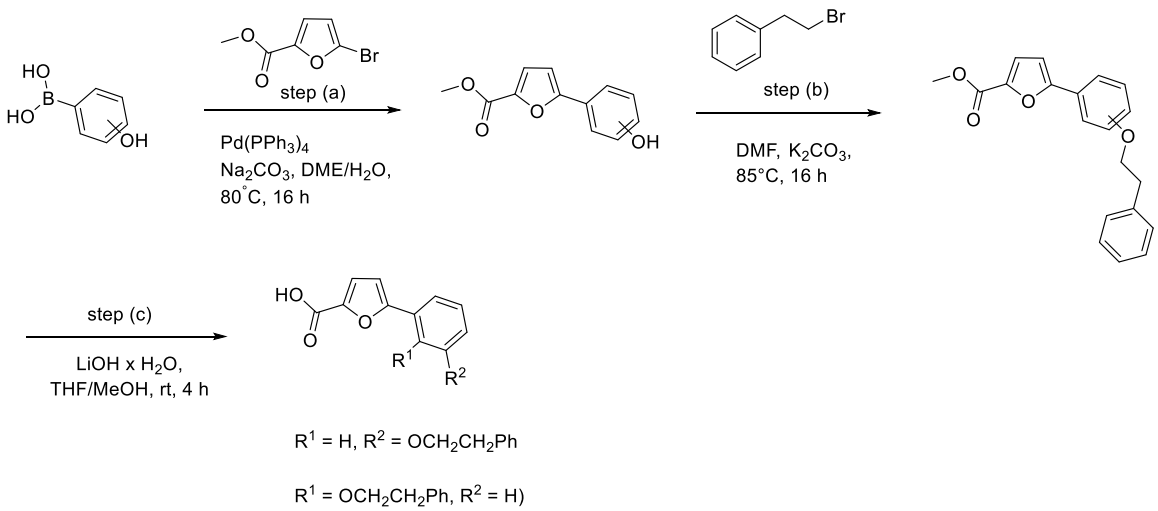

Step (a): Starting from methyl 5-bromofuran-2-carboxylate and 2- or 3-, resp., hydroxyphenylboronic acid, the intermediates methyl 5-(3-hydroxyphenyl)furan-2-carboxylate (yield: 51%) and methyl 5-(2-hydroxyphenyl)furan-2-carboxylate (yield: 85%) synthesized according to the **general procedure A** omitting the hydrolyzation step. The products were only characterized by LC/MS and directly used for the following step.

Step (b): **Synthesis of compound 4p and compound 4i:** A mixture of the appropriate methyl 5-(hydroxyphenyl)furan-2-carboxylate (1.4 mmol), (2-bromoethyl)benzene (1.5 mmol) and K_2CO_3 (3 mmol) in DMF (6 mL) was stirred at 85°C for 48 h. The mixture was treated with water (75 mL) and extracted with diethyl ether (3 x 50 mL). The combined organic extracts were dried over $MgSO_4$, filtered and concentrated. The crude products were purified by purified by column chromatography on silica gel 60 (eluent: DCM:MeOH = 9:1) to afford the desired intermediates. **Methyl 5-(2-phenethoxyphenyl)furan-2-carboxylate**: ^{1}H-NMR (500 MHz, DMSO-d_6): δ = 7.77 (dd, *J* = 7.8, 1.7 Hz, 1H), 7.37-7.34 (m, 3H), 7.32-7.28 (m, 2H), 7.31 (d, *J* = 3.6 Hz, 1H), 7.24-7.17 (m, 2H), 7.09-7.04 (m, 1H), 6.85 (d, *J* = 3.6 Hz, 1H), 4.38 (t, *J* = 6.7 Hz, 2H, OC*H*$_2$CH$_2$Ph), 3.82 (s, 3H, OCH_3), 3.16 (t, *J* = 6.7 Hz, 2H, OCH_2CH_2Ph) ppm.

Step (c): A mixture of 0.25 mmol of the appropriate methyl 5-(phenethoxyphenyl)furan-2-carboxylate (0.25 mmol), lithium hydroxide monohydrate (0.62 mmol) in MeOH (15 mL)was stirred at rt for 4 h. After completion of the reaction as indicated by TLC, the reaction mixture was concentrated under reduced pressure, diluted with H_2O (70 mL) and acidified with diluted hydrochloric acid. The mixture was extracted with EtOAc (3 x 50 mL). The combined organic extracts were dried over $MgSO_4$, filtered and concentrated. The oily residue was treated with a mixture of diethyl ether/petroleum ether (1:1) yielding **compound 4p -** or **compound 4i**, respectively, which were only characterized by LC/MS and directly used for the synthesis of the final anthranilic acid derivatives.

Synthesis 2-amino-5-(2-hydroxyethoxy)benzoic acid (28l)

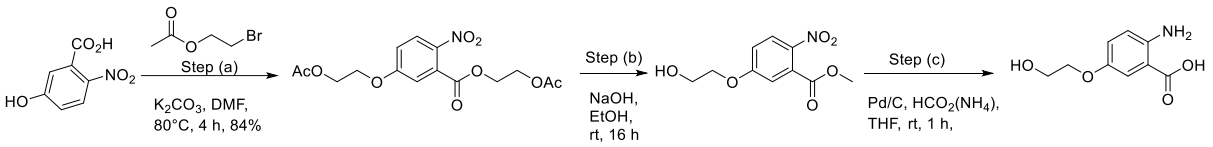

Step (a): 2-Acetoxyethyl 5-(2-acetoxyethoxy)-2-nitrobenzoate: A mixture of commercially available 5-hydroxy-2-nitrobenzoic acid (5.5 mmol), 2-bromoethyl acetate (21 mmol) and K_2CO_3 (13 mmol) in DMF (5 mL) was heated at 80°C for 4 h (TLC control, eluent: DCM:MeOH = 90:10). Subsequently, water was added (100 mL) and the mixture was extracted with DCM (3 x 50 mL). The combined organic extracts were dried over $MgSO_4$, filtered and concentrated. The purification was done using silica gel column chromatography (DCM:MeOH = 90:10) to afford the desired intermediate. Yield: 84%.

Step (b): 5-(2-Hydroxyethoxy)-2-nitrobenzoic acid: A mixture of the obtained 2-acetoxyethyl 5-(2-acetoxyethoxy)-2-nitrobenzoate from step (a)), 4N NaOH (3 mL) and EtOH (10 mL) was stirred for 16 h at rt. Subsequently, EtOH was evaporated and the residue was diluted with 1N HCl (50 mL). The mixture was extracted with DCM (3 x 40 mL) and the combined organic extracts were dried over $MgSO_4$, filtered and evaporated leading to 0.32 g (86%) of a yellowish solid.

Step (c): 2-Amino-5-(2-hydroxyethoxy)benzoic acid: A suspension of 5-(2-hydroxyethoxy)-2-nitrobenzoic acid (1.1 mmol) and Pd/C (10%) (100 mg) in THF (8 mL) was stirred under hydrogen atmosphere (50 psi) for 1 h. The mixture was filtrated over celite and washed with additional THF (15 mL), the solvent was removed under reduced pressure yielding a colorless solid. Yield: 98%. The product was only characterized by LC/MS and directly used to synthesized the final anthranilic acid.

Synthesis of 2-amino-5-(2-methoxyethoxy)benzoic acid (28k)

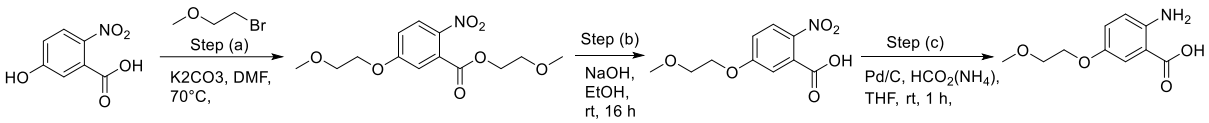

Step (a): 2-Methoxyethyl 5-(2-methoxyethoxy)-2-nitrobenzoate: A mixture of commercially available 5-hydroxy-2-nitrobenzoic acid (3.8 mmol), 1-bromo-2-methoxyethane (13.4 mmol) and K_2CO_3 (9 mmol) in DMF (5 mL) was heated at 70°C for 3 h (TLC control, eluent: DCM:MeOH = 90:10). Subsequently, water was added (100 mL) and the mixture was extracted with DCM (3 x 50 mL). The combined organic extracts were dried over $MgSO_4$, filtered and concentrated. The purification by column chromatography (DCM:MeOH = 90:10) afforded the desired intermediate which was directly used for the next step without further characterization.

Step (b): 5-(2-methoxyethoxy)-2-nitrobenzoic acid: A mixture of the obtained 2-methoxyethyl 5-(2-methoxyethoxy)-2-nitrobenzoate from step (a), 4N NaOH (3 mL) and EtOH (10 mL) was stirred for 16 h at rt. Subsequently, EtOH was evaporated and the residue was diluted with 1N HCl (50 mL). The mixture was extracted with DCM (3 x 40 mL) and the combined organic extracts were dried over $MgSO_4$, filtered and evaporated. The residue was directly used for the following step.

Step (c): 2-Amino-5-(2-methoxyethoxy)benzoic acid: A suspension of **5-(2-methoxyethoxy)-2-nitrobenzoic acid** (1.2 mmol) and Pd/C (10%) (100 mg) in THF (8 mL) was stirred under hydrogen atmosphere (50 psi) for 1 h. The mixture was filtered over celite, washed with additional THF (15 mL) and concentrated. The product was only characterized by LC/MS and directly used to synthesized the final anthranilic acid.

Synthesis of 3-(2-aminophenyl)-1,2,4-oxadiazol-5(4*H*)-one (71)

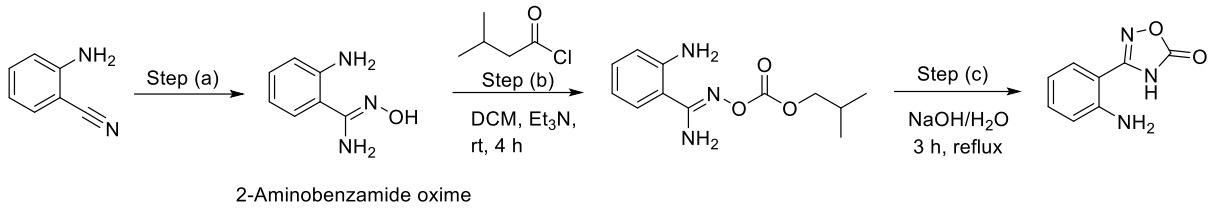

Step (a): 2-Aminobenzamide oxime: Commercially available 2 aminobenzonitrile was reacted to 2-aminobenzamide oxime according to a reported procedure (Lee, W. M. Novel nitrile and amidoxime compounds and methods of preparation. US20080260389 20081029, 2008).

Step (b): 2-Amino-*N*'-((isobutoxycarbonyl)oxy)benzimidamide: To a mixture of 2-aminobenzamide oxime (6.6 mmol) and trimethylamine (1 mL) in DCM (15 mL) was slowly added isobutylchloroformate (6.6 mmol). After stirring at rt for 4 h the mixture was poured into water and extracted with DCM (2 x 50 mL). The organic extracts were dried over $MgSO_4$, filtered and evaporated. Recrystallization of the residue using DCM/petroleum ether yielded a colorless solid. Yield: 95%. 1H-NMR (600 MHz, $CDCl_3$) δ = 7.33-7.23 (m, 1H), 7.20-7.10 (m, 1H), 6.73-6.62 (m, 2H), 5.10 (s, 2H), 4.30 (s br, 2H), 4.00 (d, *J* = 6.7 Hz, 2H), 2.00 (dt, *J* = 13.4, 6.7 Hz, 1H), 0.95 (d, *J* = 6.8 Hz, 6H) ppm.

Step (c): 3-(2-Aminophenyl)-1,2,4-oxadiazol-5(4*H*)-one: A suspension of 2-amino-*N*'-((isobutoxycarbonyl)oxy)benzimidamide (4.0 mmol) in a 2% aqueous solution of NaOH (25 mL) was refluxed for 3 h. Subsequently the mixture was cooled to rt, neutralized with diluted HCl (pH 4-5) and extracted with ethyl acetate (3 x 50 mL). The combined organic layers were washed with brine, dried over $MgSO_4$ and concentrated. The residue was purified by silica gel column chromatography (DCM:EtOAc = 80:20). Recrystallization was performed using

DCM/petroleum ether yielding a yellow solid. Yield: 82%. The product was only characterized by LC/MS and directly used to synthesized the final anthranilic acid derivative.

Synthesis 2-(2*H*-tetrazol-5-yl)aniline (72)

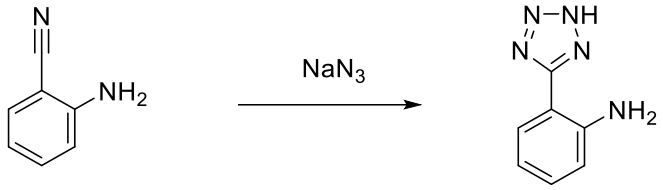

2-(2*H*-Tetrazol-5-yl)aniline was synthesized according to a reported procedure starting from commercially available 2-aminobenzonitrile and sodium azide.[35]

^{1}H-NMR spectra, ^{13}C-NMR spectra, and LC/MS data sets of selected final (potent) derivatives

^{1}H- and ^{13}C-NMR spectra of 5-(3'-methoxy-[1,1'-biphenyl]-3-yl)-N-(2-(5-oxo-4,5-dihydro-1,2,4-oxadiazol-3-yl)phenyl)furan-2-carboxamide (75)

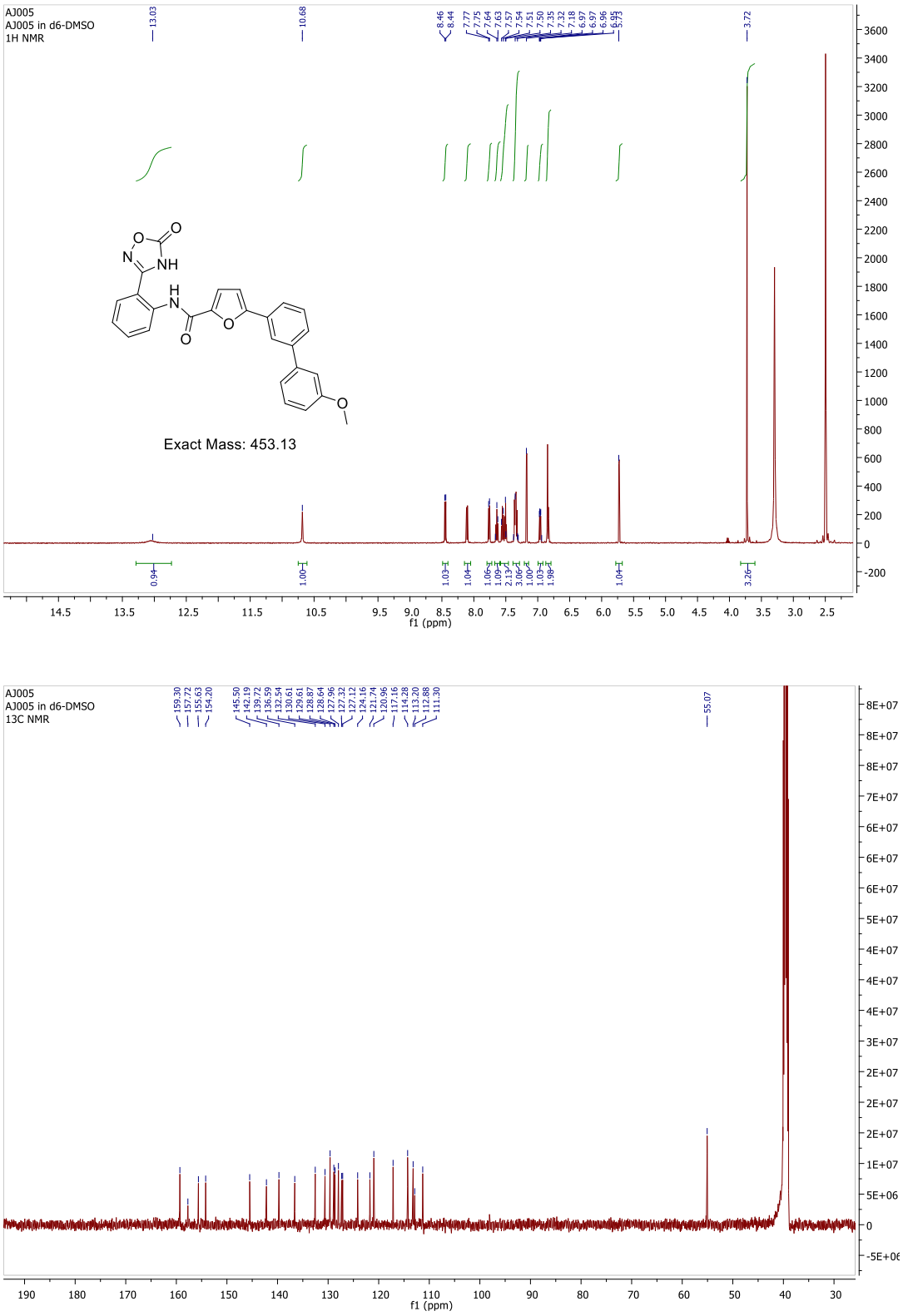

Figure S1. ^{1}H- and ^{13}C-NMR spectra of compound **75**

LC/MS data set of 5-(3'-methoxy-[1,1'-biphenyl]-3-yl)-N-(2-(5-oxo-4,5-dihydro-1,2,4-oxadiazol-3-yl)phenyl)furan-2-carboxamide (75)

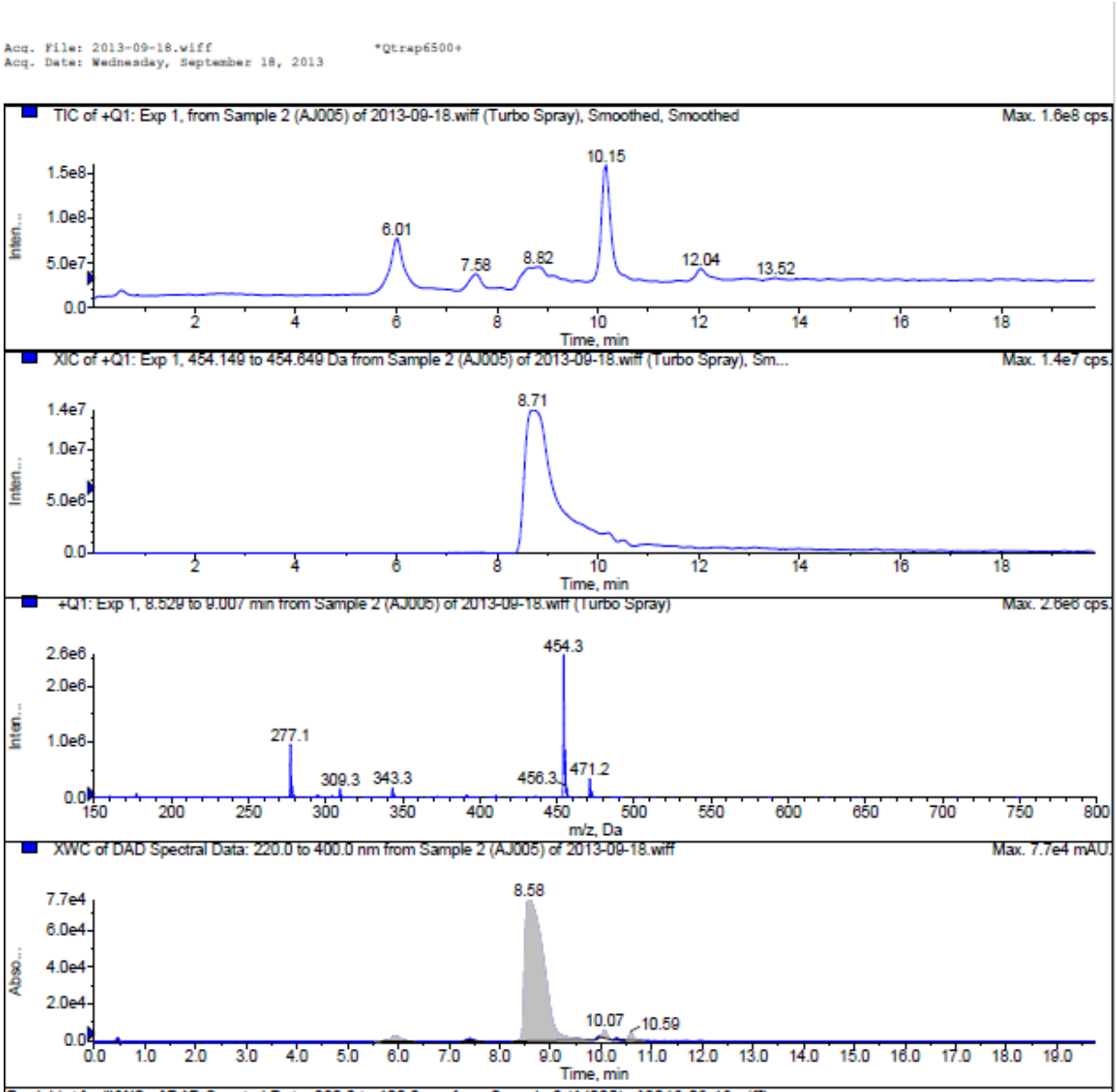

Peak List for "XWC of DAD Spectral Data: 220.0 to 400.0 nm from Sample 2 (AJ005) of 2013-09-18.wiff"

	Time (min)	Area (mAU x min)	% Area	Height (mAU)	% Height	Width (min)	Baseline Type
1	0.4657	7989.0268	0.3968	2304.3940	2.4636	0.1333	Base to Base
2	5.9379	3.7239e4	1.8497	2877.2366	3.0761	0.7533	Base to Base
3	7.4128	1.1372e4	0.5648	1312.4671	1.4032	0.4267	Base to Base
4	8.5784	1.9056e6	94.6534	7.7213e4	82.5494	1.5800	Base to Base
5	9.9588	2447.0093	0.1215	622.3920	0.6654	0.1067	Base to Base
6	10.0689	2.1301e4	1.0580	4269.2791	4.5643	0.2000	Base to Base
7	10.3123	5029.2472	0.2498	884.4090	0.9455	0.2533	Base to Base
8	10.5905	2.2265e4	1.1059	4052.4056	4.3325	0.3533	Base to Base

Polarity/Scan Type: Positive Q1 MS Analyst Version: 1.7.2

Figure S2. LC/MS data set of compound **75**

^{1}H- and ^{13}C-NMR spectra of 5-methoxy-2-(5-(3-phenethoxyphenyl)furan-2-carboxamido)benzoic acid (25)

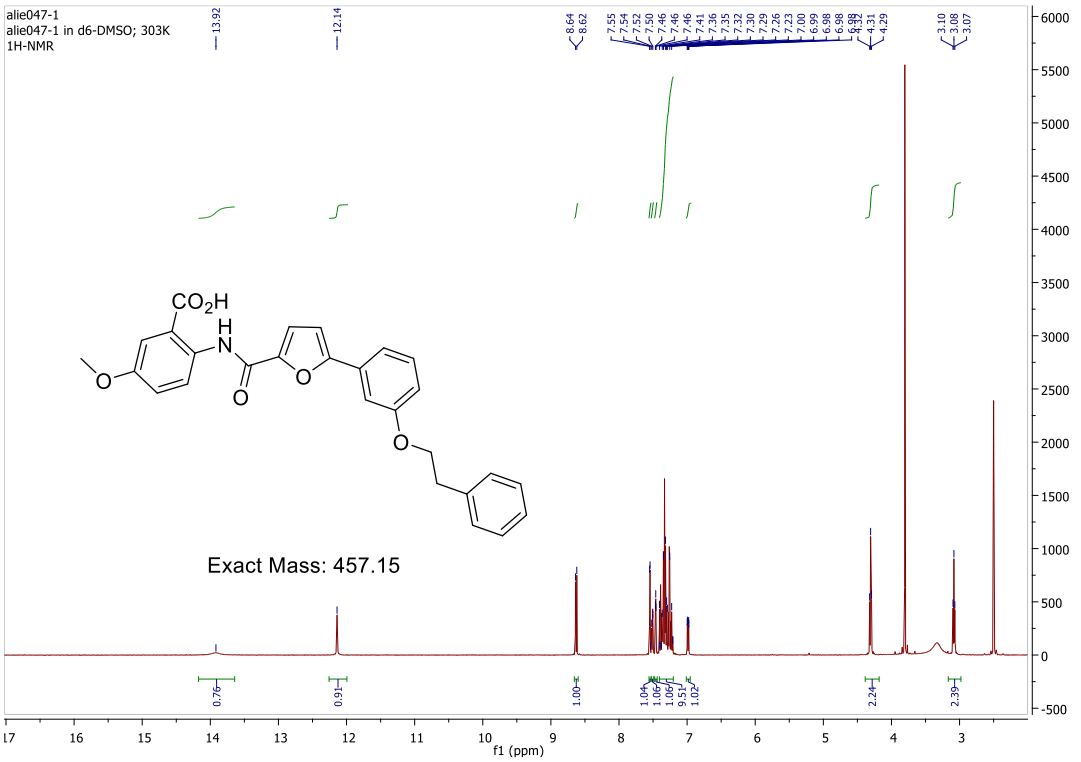

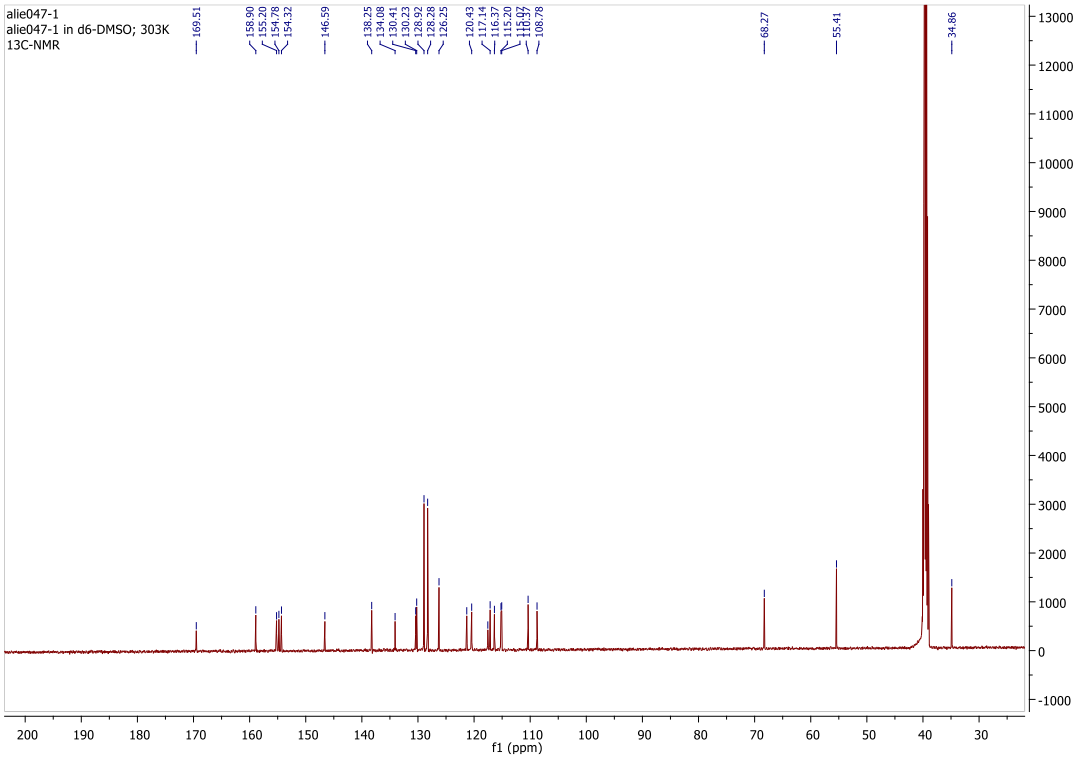

Figure S3. ^{1}H- and ^{13}C-NMR spectra of compound **25**

LC/MS data set of 5-methoxy-2-(5-(3-phenethoxyphenyl)furan-2-carboxamido)benzoic acid (25)

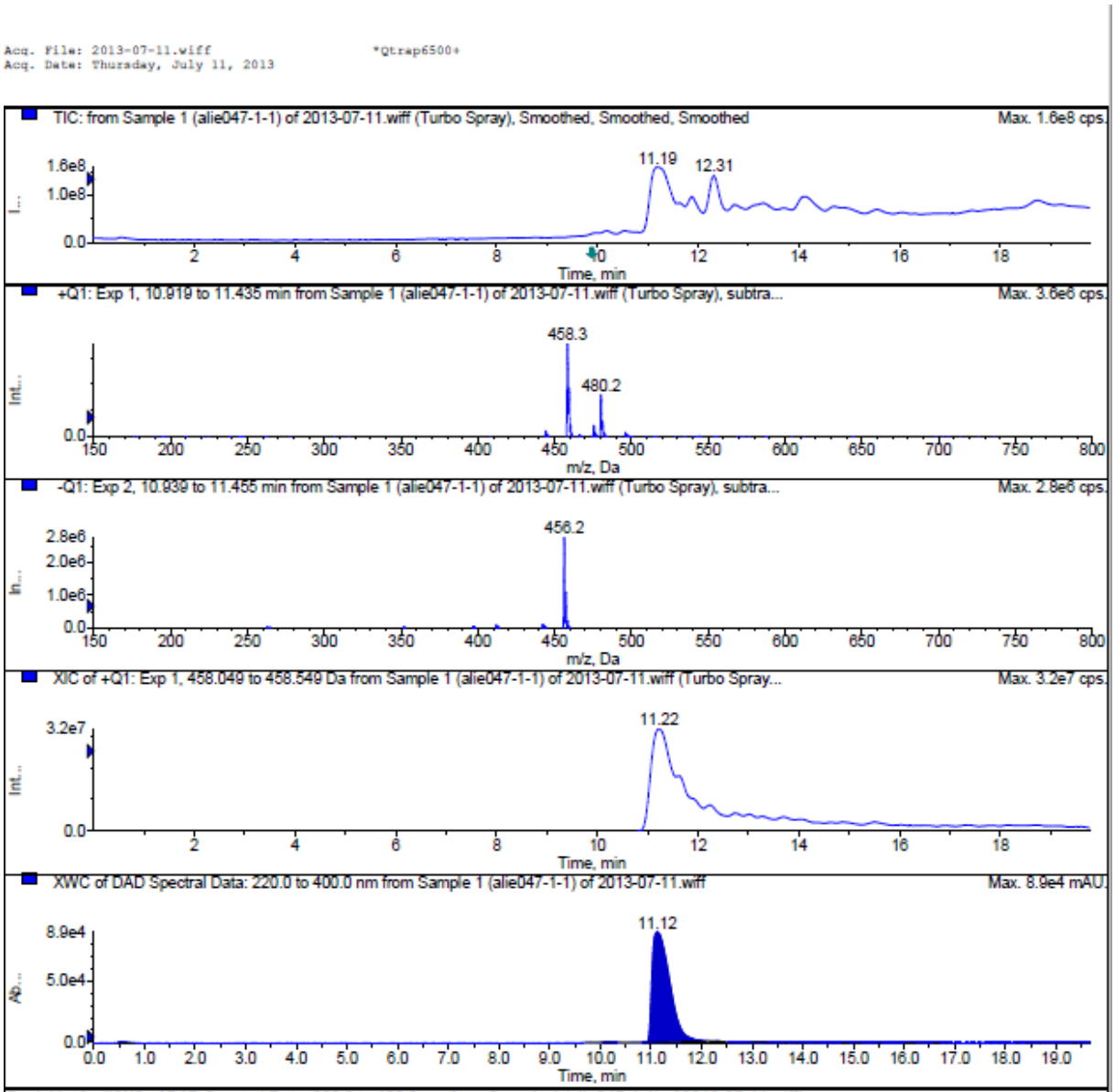

Peak List for "XWC of DAD Spectral Data: 220.0 to 400.0 nm from Sample 1 (alie047-1-1) of 2013-07-11.wiff"

	Time (min)	Area (mAU x min)	% Area	Height (mAU)	% Height	Width (min)	Baseline Type
1	0.5156	1.4144e4	0.6545	1497.1826	1.6066	0.3600	Base to Base
2	9.8807	2351.8007	0.1088	277.4763	0.2978	0.3333	Base to Base
3	10.1248	2236.4434	0.1035	331.9716	0.3562	0.2600	Base to Base
4	10.4680	6113.2352	0.2829	710.1015	0.7620	0.4200	Base to Base
5	11.1232	2.1237e6	98.2705	8.8833e4	95.3243	1.2333	Base to Base
6	12.2157	1.0816e4	0.5005	1340.5815	1.4385	0.3400	Base to Base
7	13.0910	1715.1761	0.0794	199.9825	0.2148	0.3000	Base to Base

Polarity/Scan Type: Positive Q1 MS, ... Analyst Version: 1.7.2

Figure S4. LC/MS data set of compound **25**

^{1}H- and ^{13}C-NMR spectra of 4,5-difluoro-2-(5-(naphthalen-1-yl)furan-2-carboxamido)benzoic acid (32)

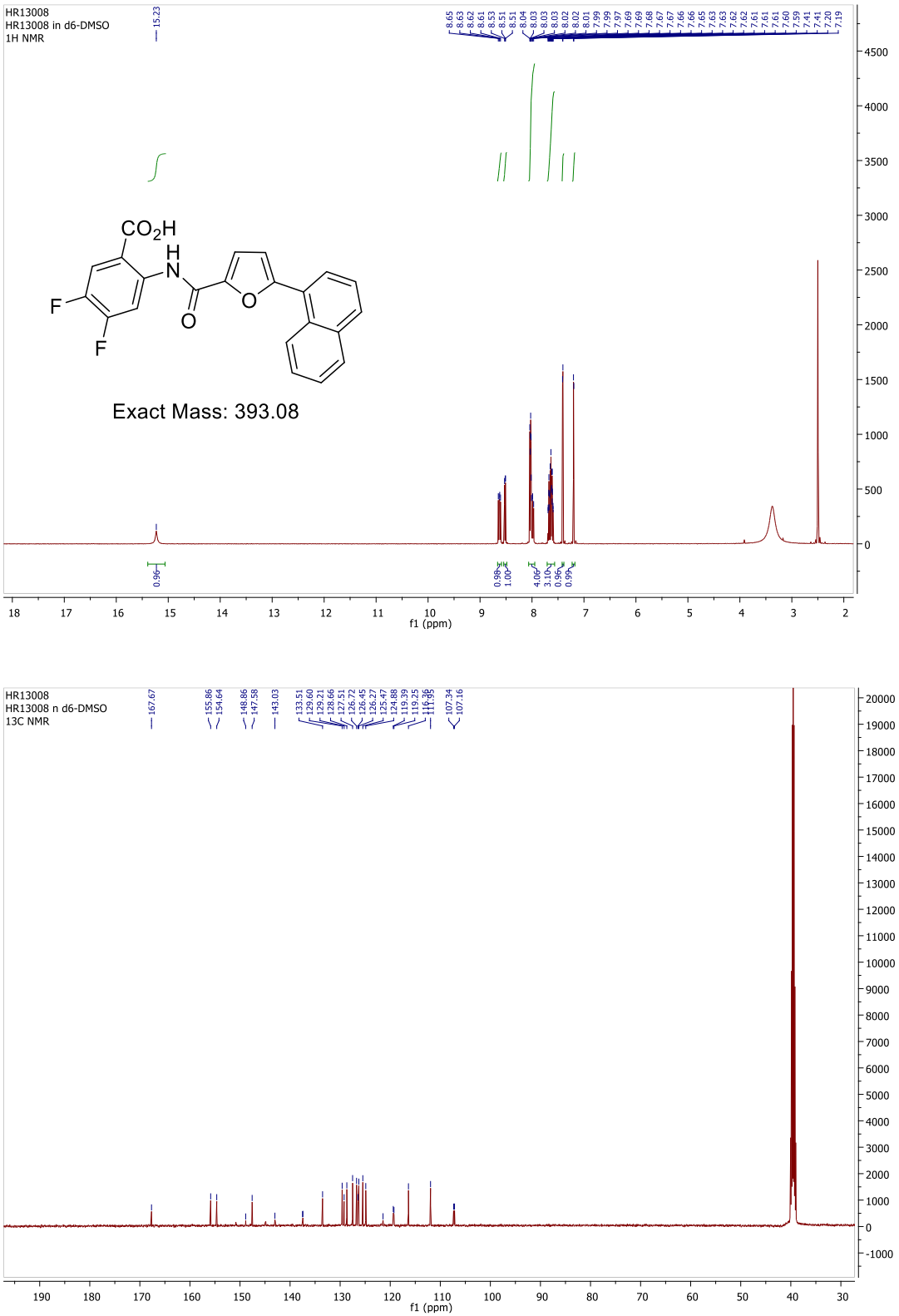

Figure S5. ^{1}H- and ^{13}C-NMR spectra of compound **32**

LC/MS data set of 4,5-difluoro-2-(5-(naphthalen-1-yl)furan-2-carboxamido)benzoic acid (32)

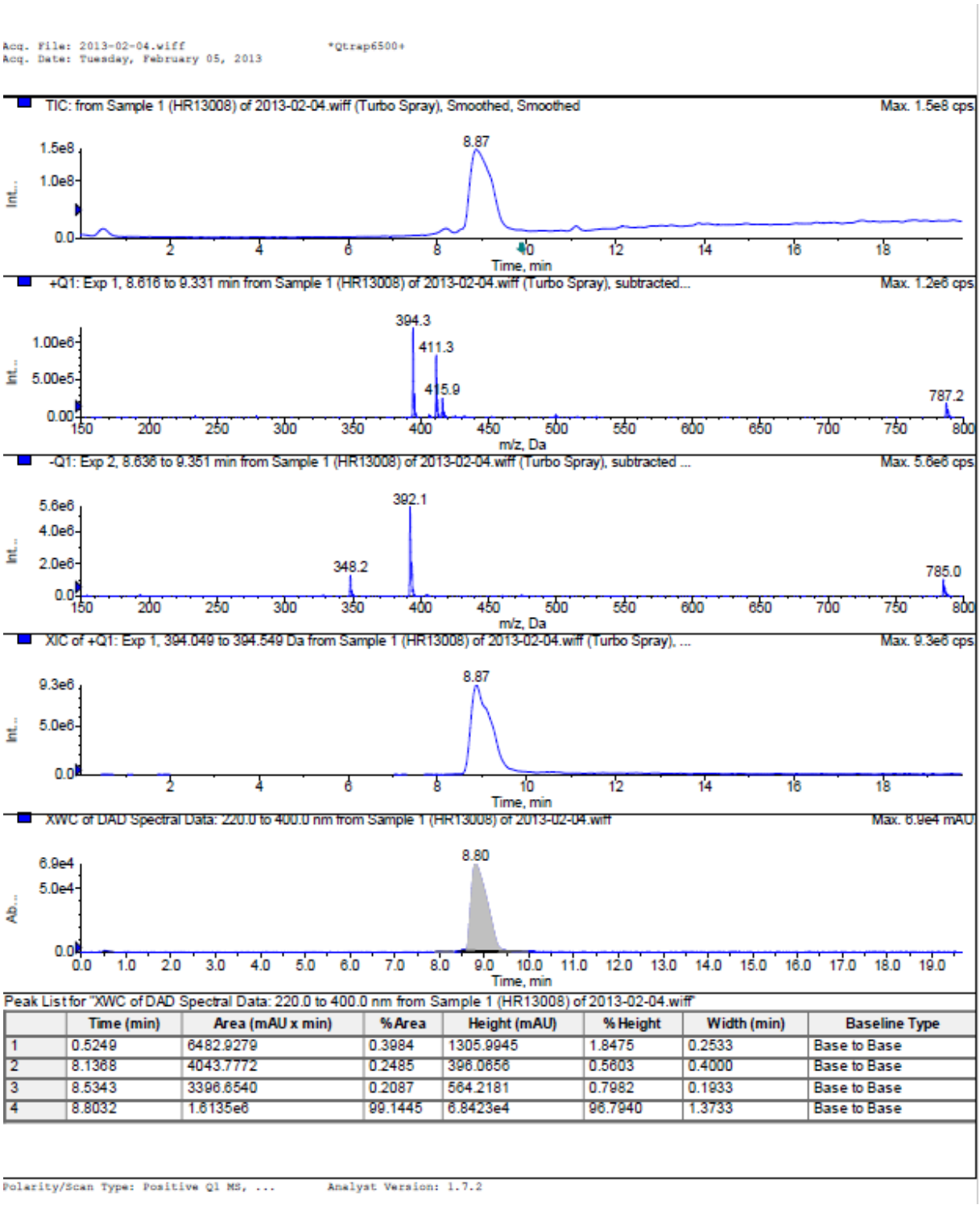

	Time (min)	Area (mAU x min)	% Area	Height (mAU)	% Height	Width (min)	Baseline Type
1	0.5249	6482.9279	0.3984	1305.9945	1.8475	0.2533	Base to Base
2	8.1368	4043.7772	0.2485	396.0656	0.5603	0.4000	Base to Base
3	8.5343	3396.6540	0.2087	564.2181	0.7982	0.1933	Base to Base
4	8.8032	1.6135e6	99.1445	6.8423e4	96.7940	1.3733	Base to Base

Figure S6. LC/MS data set of compound **32**

^{1}H- and ^{13}C-NMR spectra of 5-methoxy-2-(5-(naphthalen-1-yl)furan-2-carboxamido)benzoic (45)

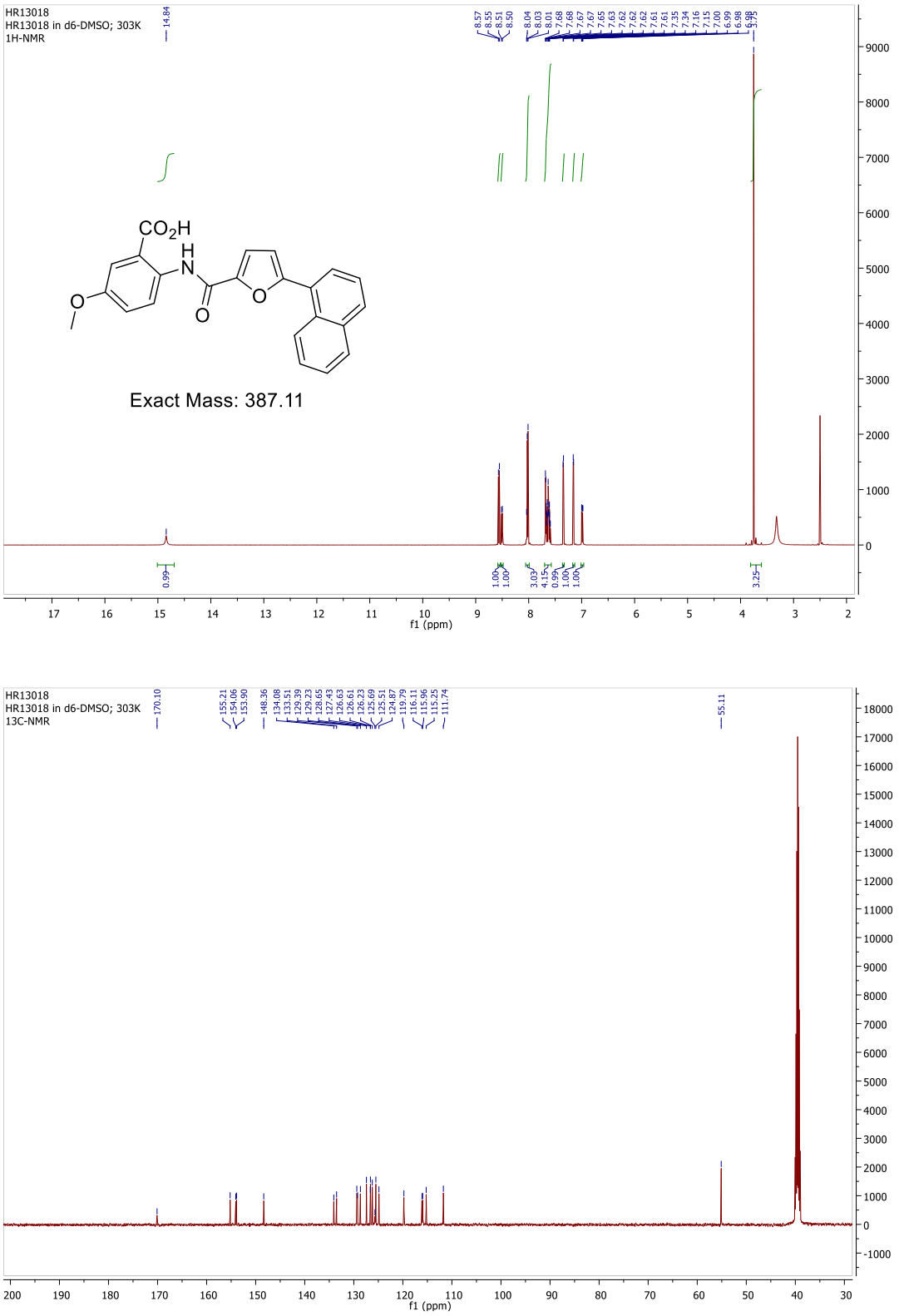

Figure S7. ^{1}H- and ^{13}C-NMR spectra of compound **45**

LC/MS data set of 5-methoxy-2-(5-(naphthalen-1-yl)furan-2-carboxamido)benzoic (45)

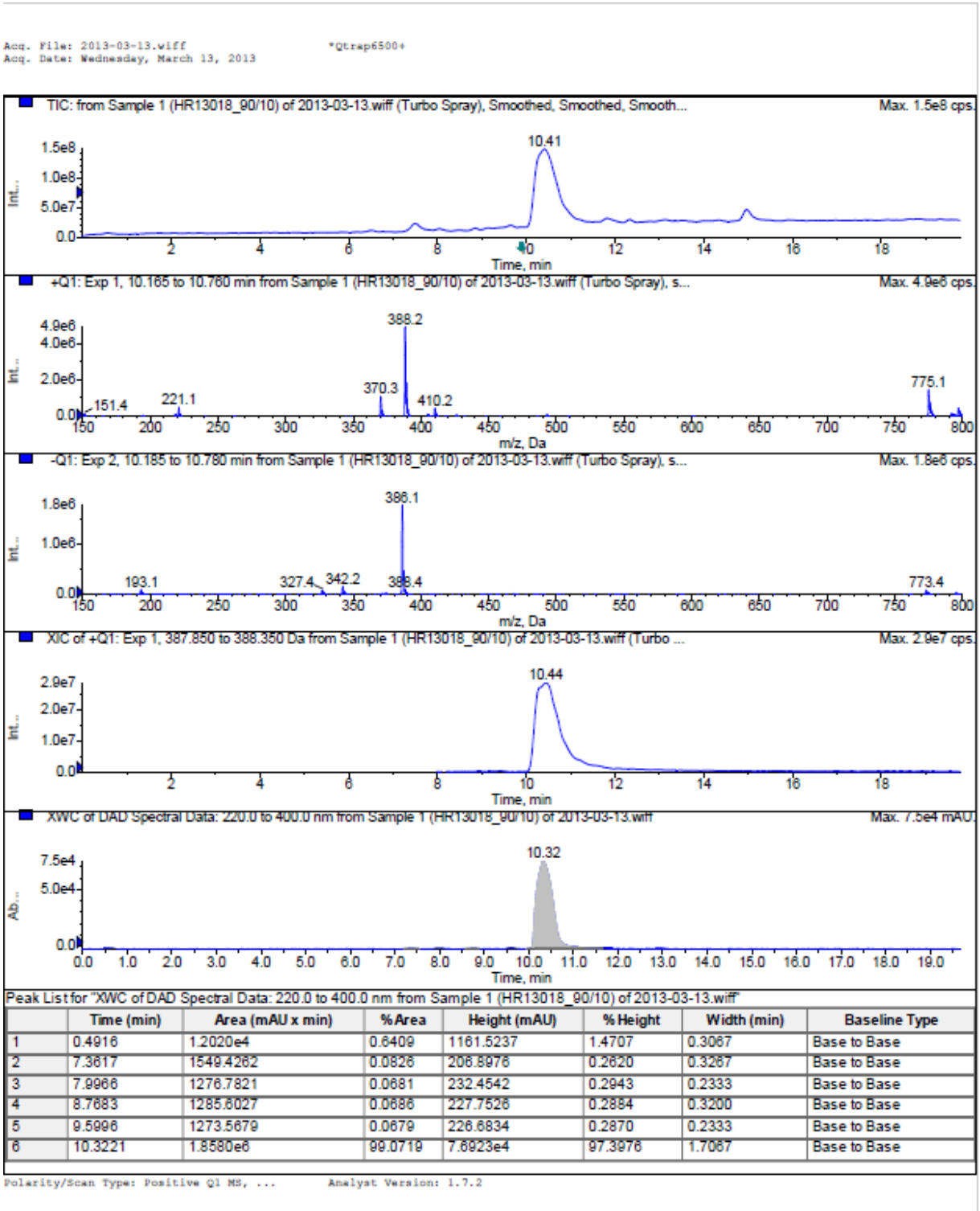

	Time (min)	Area (mAU x min)	% Area	Height (mAU)	% Height	Width (min)	Baseline Type
1	0.4916	1.2020e4	0.6409	1161.5237	1.4707	0.3067	Base to Base
2	7.3617	1549.4262	0.0826	206.8976	0.2620	0.3267	Base to Base
3	7.9966	1276.7821	0.0681	232.4542	0.2943	0.2333	Base to Base
4	8.7683	1285.6027	0.0686	227.7526	0.2884	0.3200	Base to Base
5	9.5996	1273.5679	0.0679	226.6834	0.2870	0.2333	Base to Base
6	10.3221	1.8580e6	99.0719	7.6923e4	97.3976	1.7067	Base to Base

Figure S8. LC/MS data set of compound **45**

^{1}H- and ^{13}C-NMR spectra of 4-methoxy-2-(5-(naphthalen-1-yl)furan-2-carboxamido)benzoic acid (33)

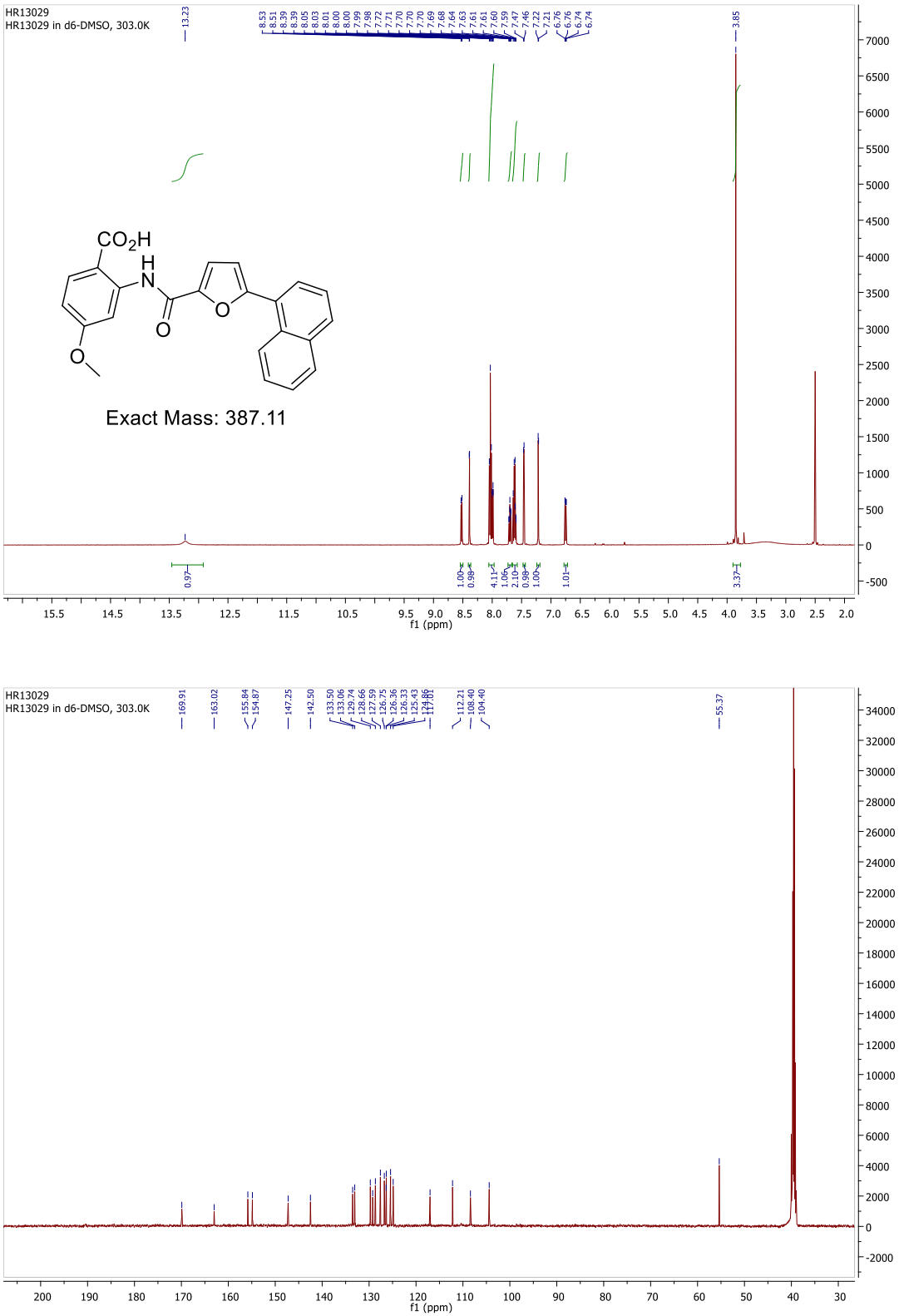

Figure S9. ^{1}H- and ^{13}C-NMR spectra of compound **33**

LC/MS data set of 4-methoxy-2-(5-(naphthalen-1-yl)furan-2-carboxamido)benzoic acid (33)

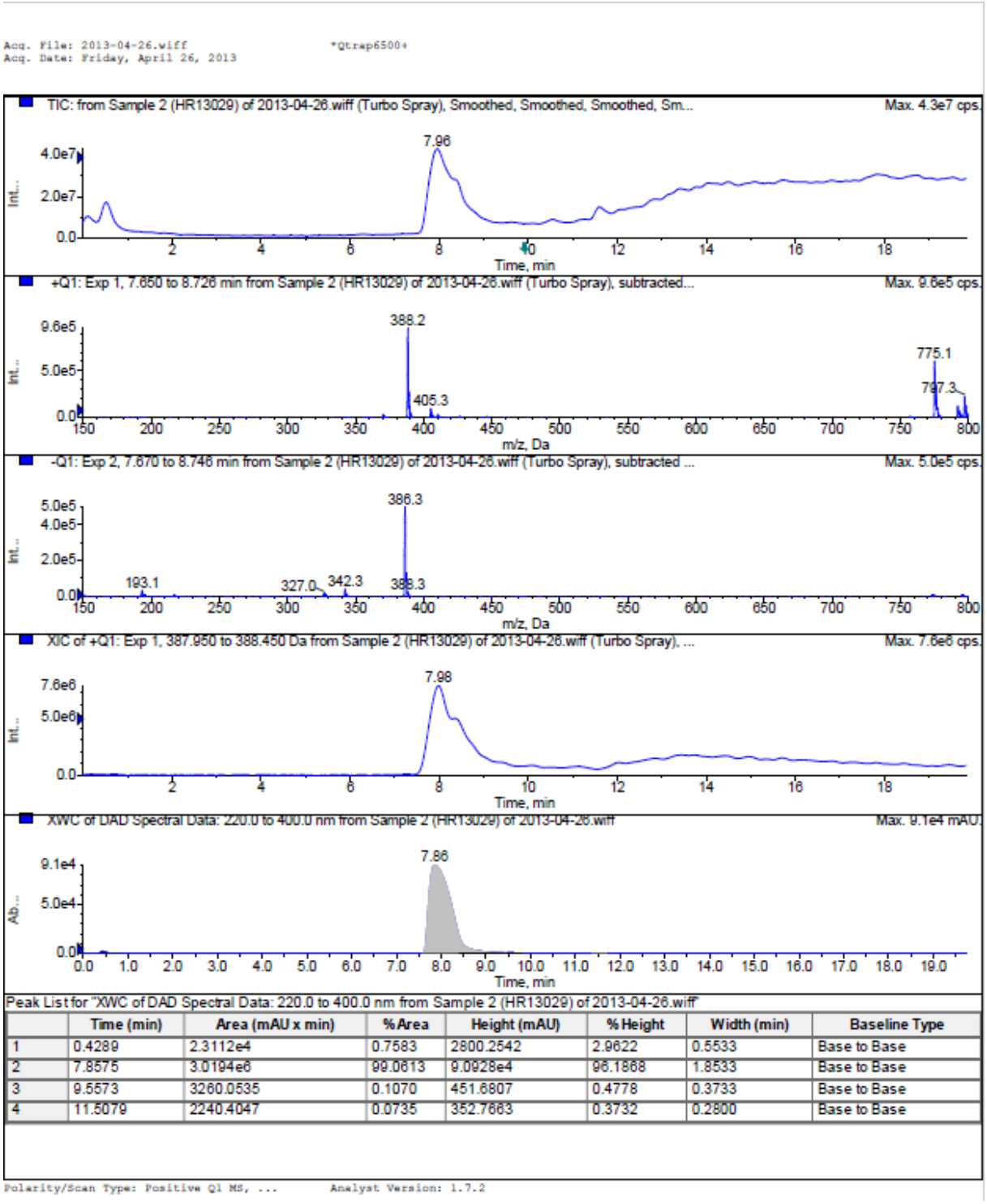

Peak List for "XWC of DAD Spectral Data: 220.0 to 400.0 nm from Sample 2 (HR13029) of 2013-04-26.wiff"

	Time (min)	Area (mAU x min)	% Area	Height (mAU)	% Height	Width (min)	Baseline Type
1	0.4289	2.3112e4	0.7583	2800.2542	2.9622	0.5533	Base to Base
2	7.8575	3.0194e6	99.0613	9.0928e4	96.1868	1.8533	Base to Base
3	9.5573	3260.0535	0.1070	451.6807	0.4778	0.3733	Base to Base
4	11.5079	2240.4047	0.0735	352.7663	0.3732	0.2800	Base to Base

Polarity/Scan Type: Positive Q1 MS, ... Analyst Version: 1.7.2

Figure S10. LC/MS data set of compound **33**

^{1}H- and ^{13}C-NMR spectra of 5-(2-methoxyethoxy)-2-(5-(naphthalen-1-yl)furan-2-carboxamido)benzoic acid (42)

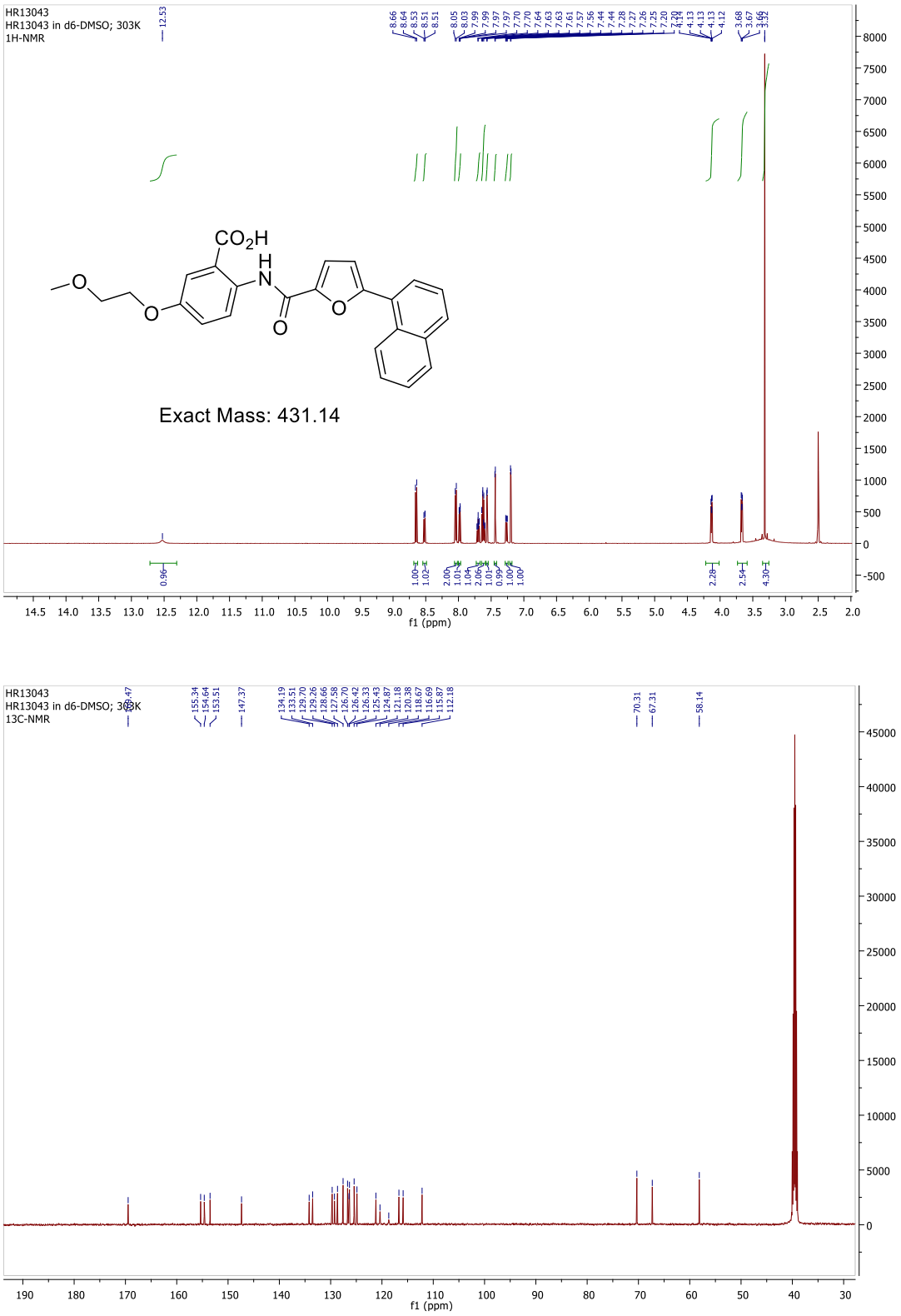

Figure S11. ^{1}H- and ^{13}C-NMR spectra of compound **42**

LC/MS data set of 5-(2-methoxyethoxy)-2-(5-(naphthalen-1-yl)furan-2-carboxamido)benzoic acid (42)

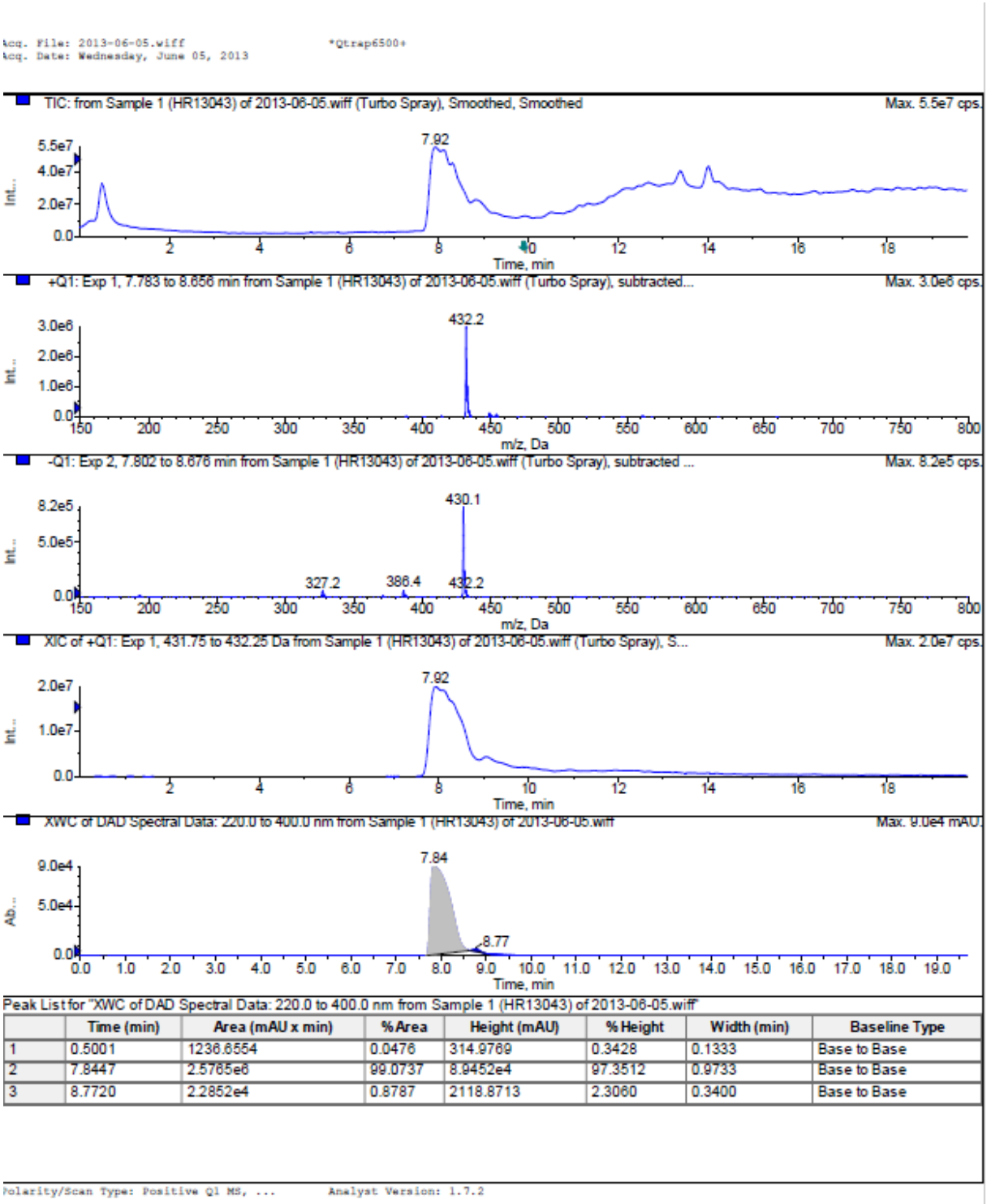

	Time (min)	Area (mAU x min)	% Area	Height (mAU)	% Height	Width (min)	Baseline Type
1	0.5001	1236.6554	0.0476	314.9769	0.3428	0.1333	Base to Base
2	7.8447	2.5765e6	99.0737	8.9452e4	97.3512	0.9733	Base to Base
3	8.7720	2.2852e4	0.8787	2118.8713	2.3060	0.3400	Base to Base

Figure S12. LC/MS data set of compound **42**

^{1}H- and ^{13}C-NMR spectra of 5-methoxy-2-(5-(3'-(2-methoxyethoxy)-[1,1'-biphenyl]-2-yl)furan-2-carboxamido)benzoic acid (23)

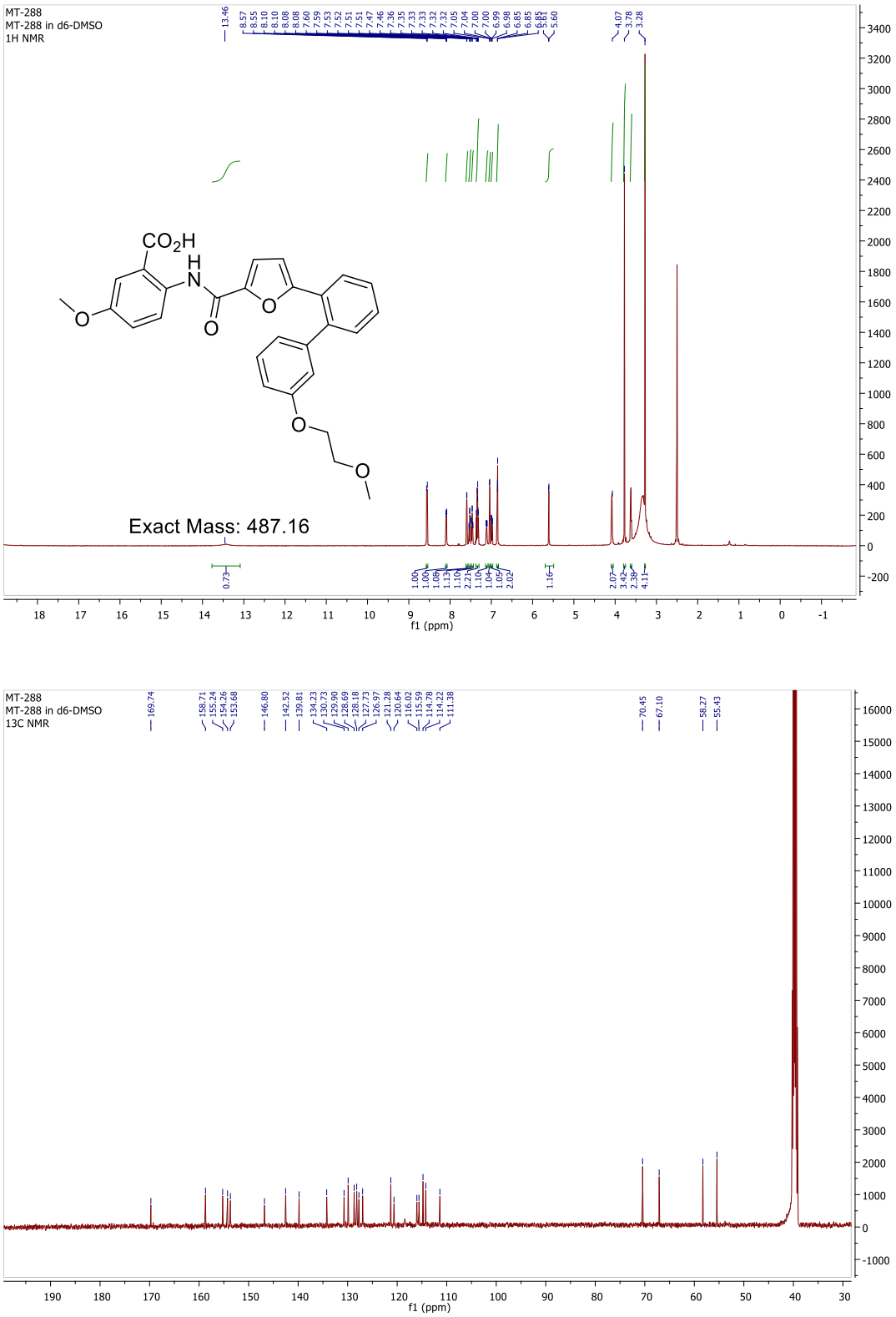

Figure S13. ^{1}H- and ^{13}C-NMR spectra of compound **23**

LC/MS data set of 5-methoxy-2-(5-(3'-(2-methoxyethoxy)-[1,1'-biphenyl]-2-yl)furan-2-carboxamido)benzoic acid (23)

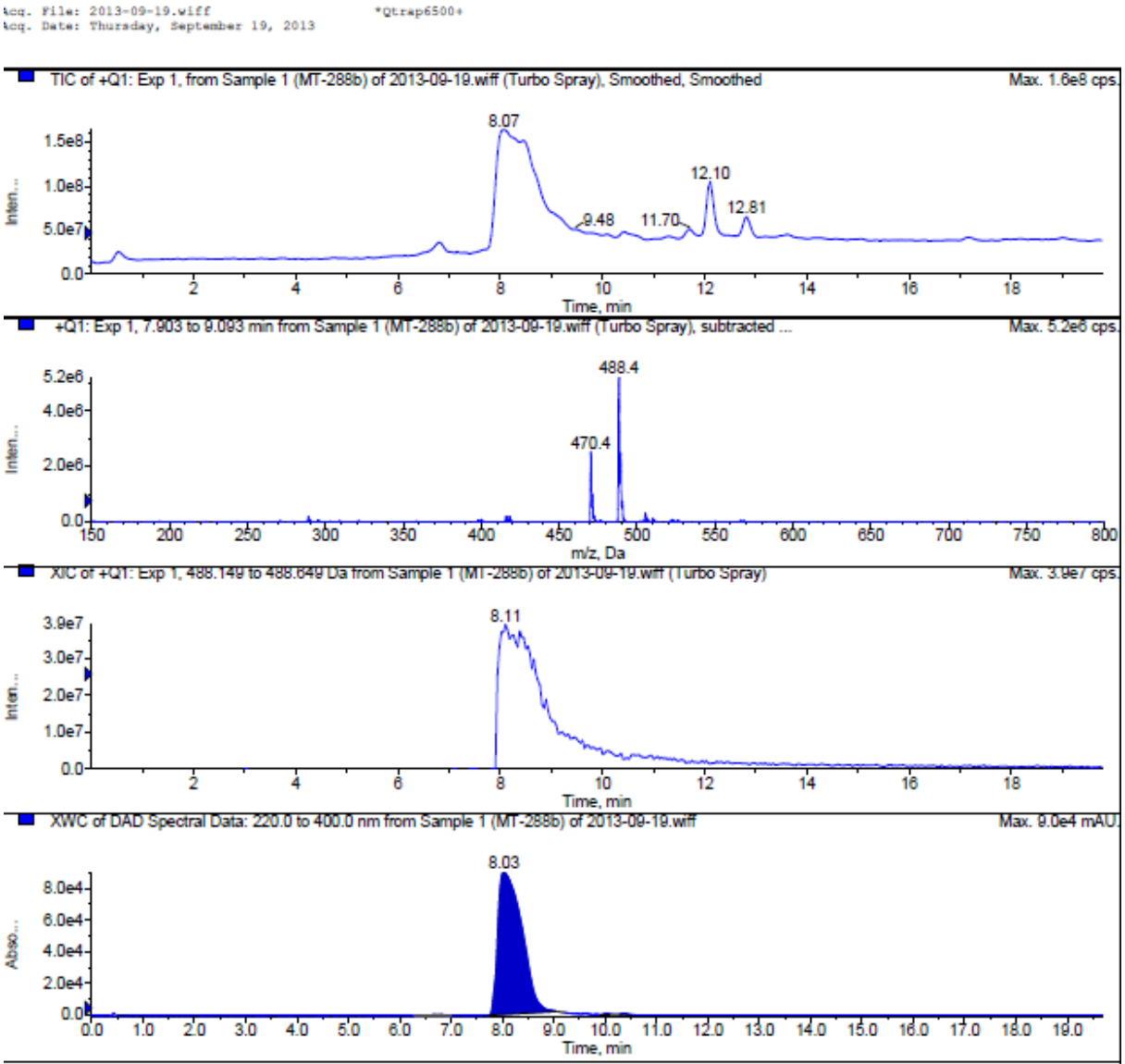

Peak List for "XWC of DAD Spectral Data: 220.0 to 400.0 nm from Sample 1 (MT-288b) of 2013-09-19.wiff"

	Time (min)	Area (mAU x min)	%Area	Height (mAU)	%Height	Width (min)	Baseline Type
1	0.5341	2550.2029	0.0876	544.3405	0.5798	0.1467	Base to Base
2	6.7424	1.4762e4	0.5068	1353.0035	1.4411	0.7067	Base to Base
3	8.0301	2.8848e6	99.0402	8.9923e4	95.7777	1.3200	Base to Base
4	9.0960	1443.1229	0.0495	240.0991	0.2557	0.1467	Base to Base
5	10.0314	2624.4511	0.0901	505.8776	0.5388	0.2267	Base to Base
6	10.2081	1639.4198	0.0563	371.4346	0.3956	0.1533	Base to Base
7	10.3675	4935.9200	0.1695	949.4611	1.0113	0.2133	Base to Base

Polarity/Scan Type: Positive Q1 MS Analyst Version: 1.7.2

Figure S14. LC/MS data set of compound **23**

^{1}H-NMR spectrum of 5-methoxy-2-(2-(naphthalen-1-yl)thiazole-4-carboxamido)benzoic acid (70)

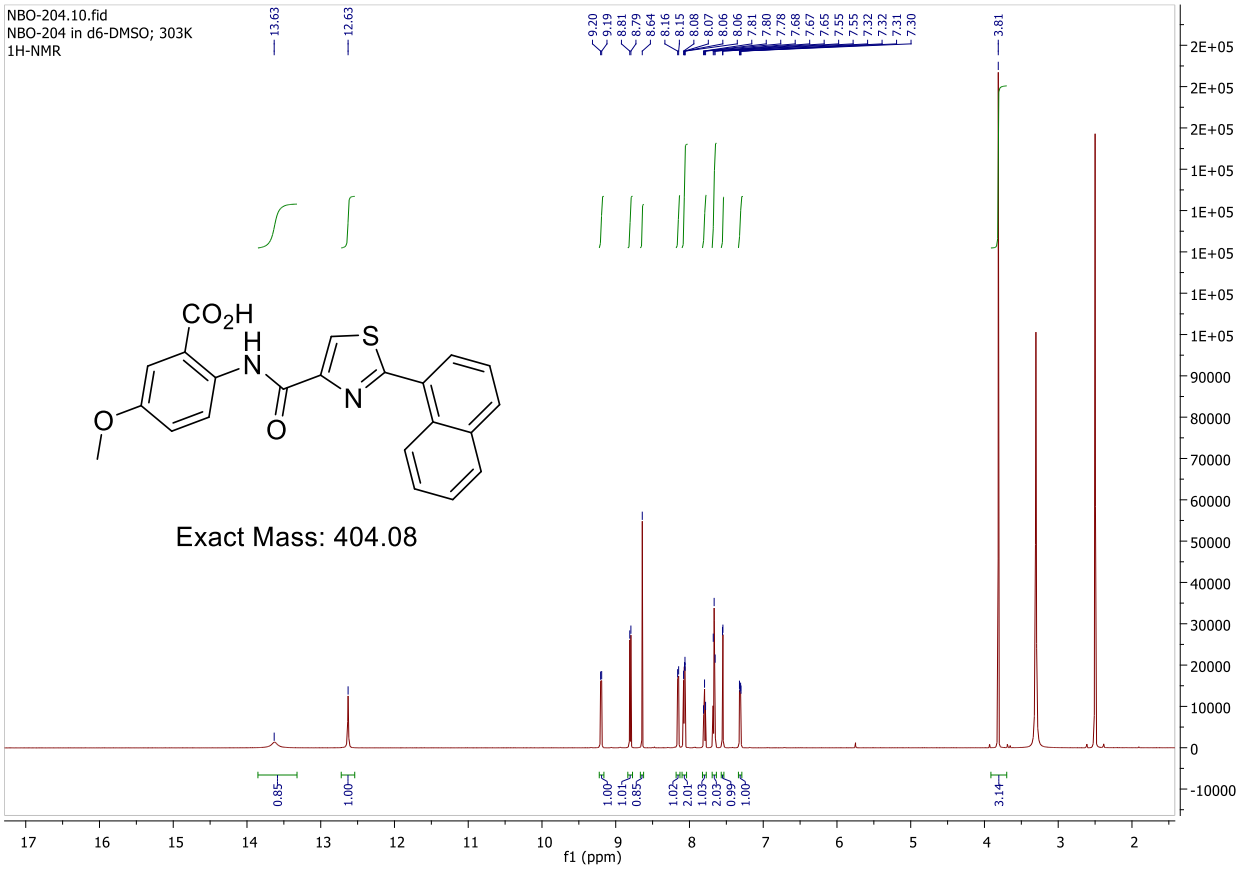

Figure S15. ^{1}H-NMR spectrum of compound **70**

LC/MS data set of 5-methoxy-2-(2-(naphthalen-1-yl)thiazole-4-carboxamido)benzoic acid (70)

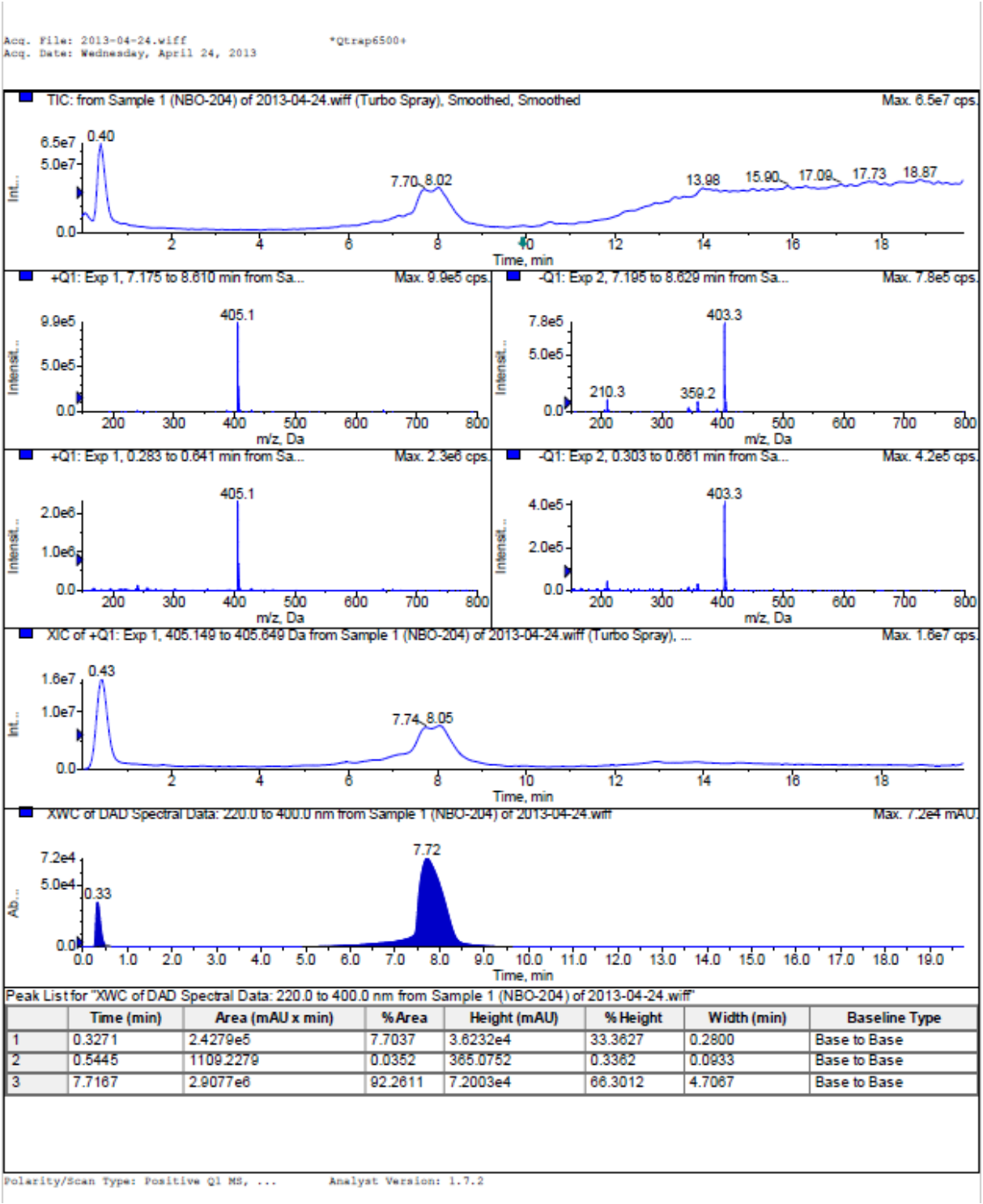

	Time (min)	Area (mAU x min)	% Area	Height (mAU)	% Height	Width (min)	Baseline Type
1	0.3271	2.4279e5	7.7037	3.6232e4	33.3627	0.2800	Base to Base
2	0.5445	1109.2279	0.0352	365.0752	0.3362	0.0933	Base to Base
3	7.7167	2.9077e6	92.2611	7.2003e4	66.3012	4.7067	Base to Base

Figure S16. LC/MS data set of compound **70**

^{1}H- and ^{13}C-NMR spectra of 2-(5-(naphthalen-1-yl)furan-2-carboxamido)benzoic acid (40)

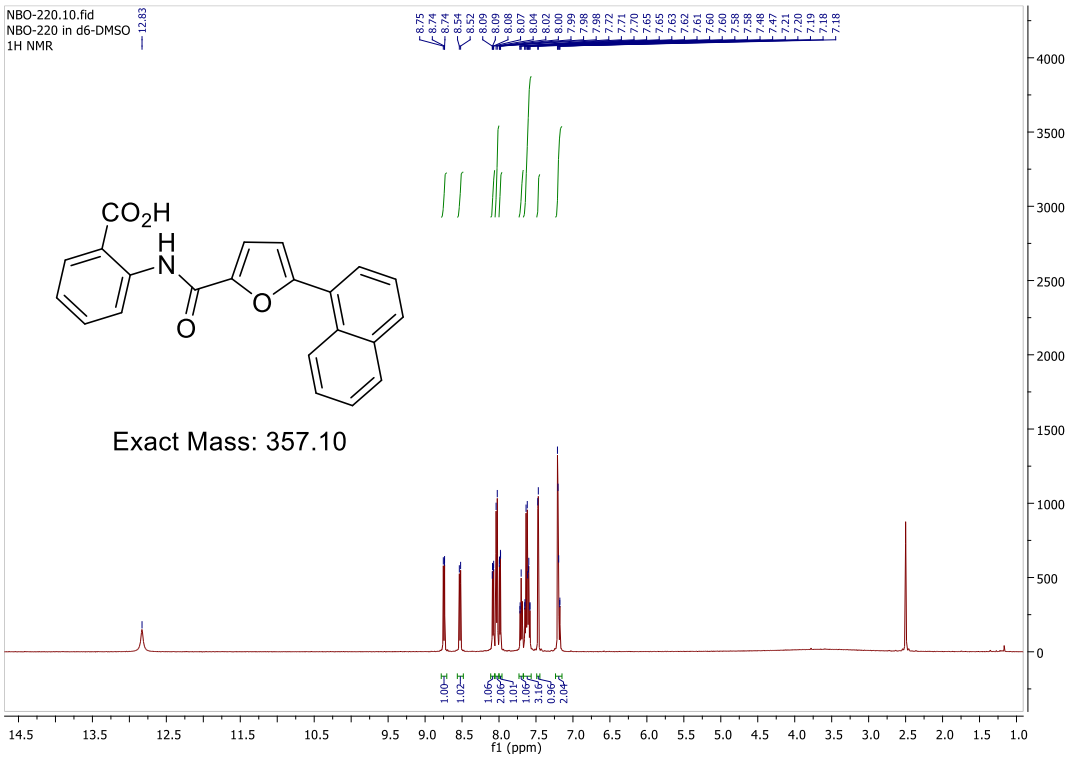

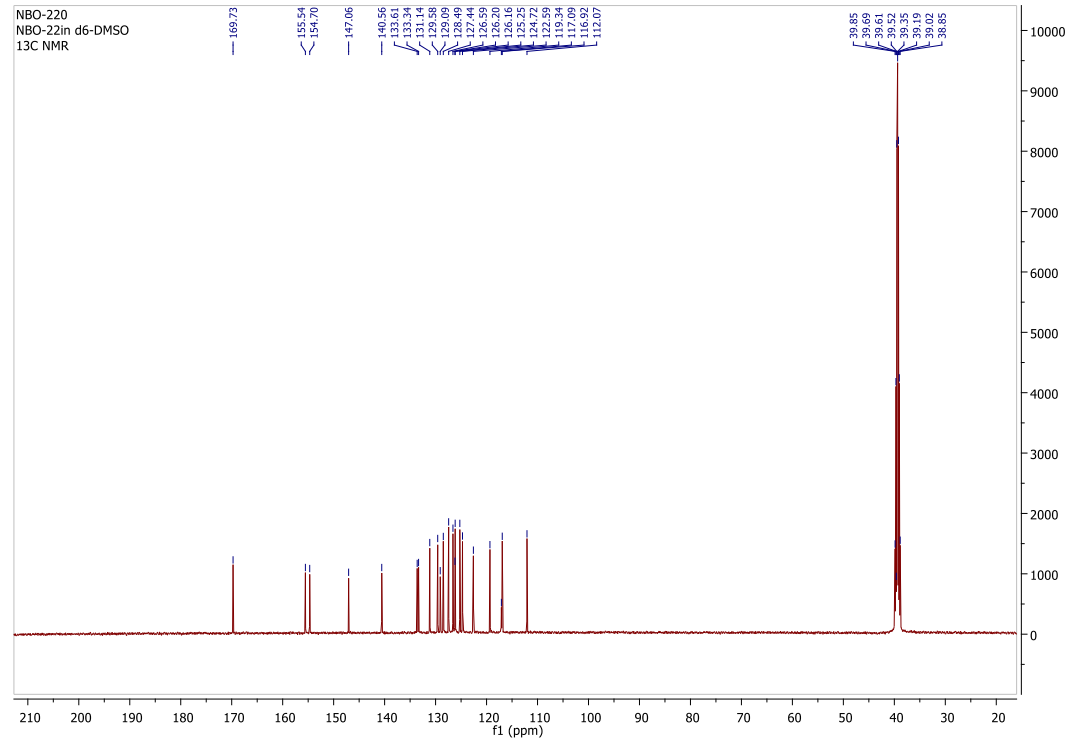

Figure S17. ^{1}H- and ^{13}C-NMR spectra of compound **40**

LC/MS data set of 2-(5-(naphthalen-1-yl)furan-2-carboxamido)benzoic acid (40)

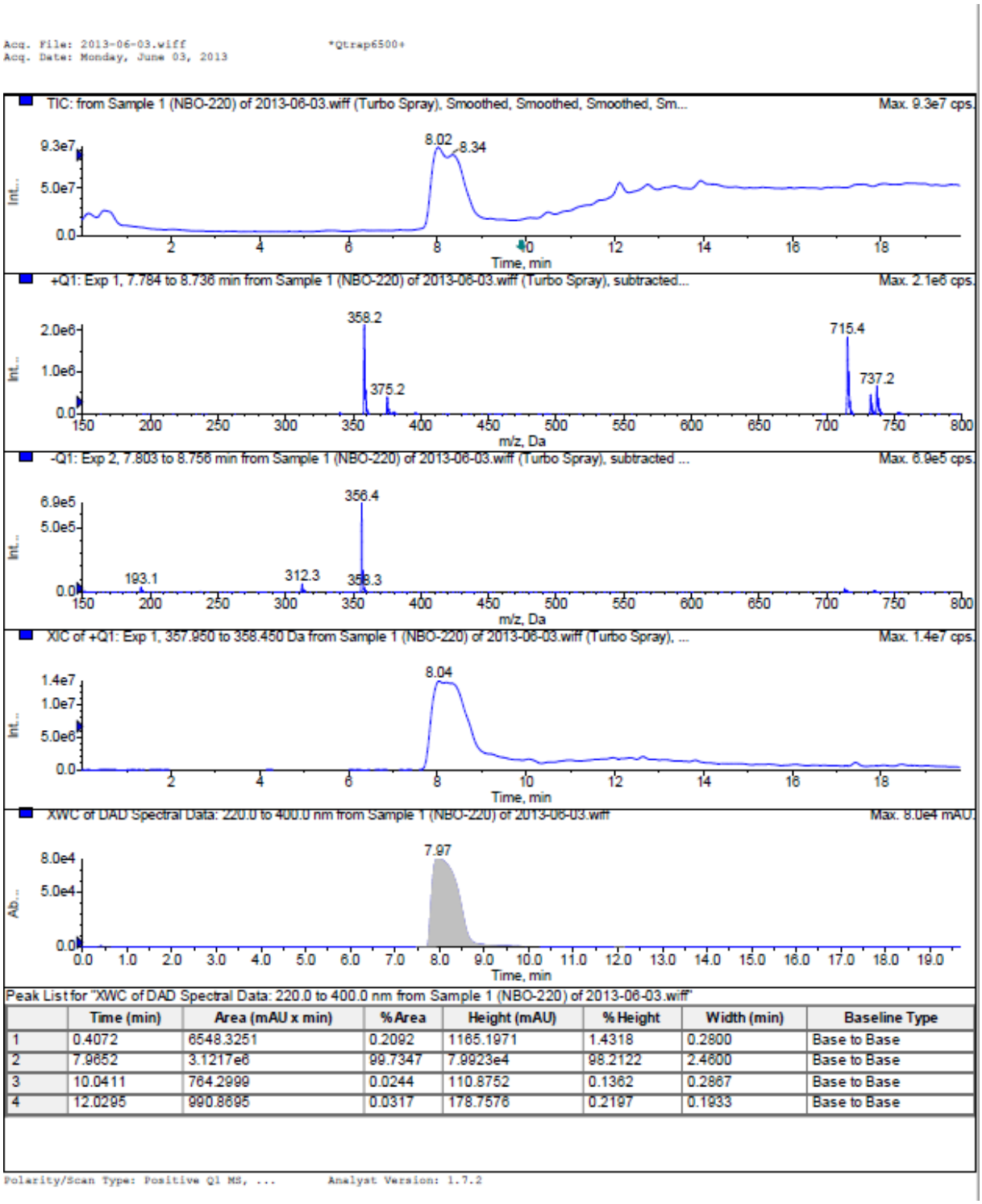

	Time (min)	Area (mAU x min)	% Area	Height (mAU)	% Height	Width (min)	Baseline Type
1	0.4072	6548.3251	0.2092	1165.1971	1.4318	0.2800	Base to Base
2	7.9652	3.1217e6	99.7347	7.9923e4	98.2122	2.4600	Base to Base
3	10.0411	764.2999	0.0244	110.8752	0.1362	0.2867	Base to Base
4	12.0295	990.8695	0.0317	178.7576	0.2197	0.1933	Base to Base

Figure S18. LC/MS data set of compound **40**

^{1}H- and ^{13}C-NMR spectra of 2-(5-([1,1'-biphenyl]-2-yl)furan-2-carboxamido)-5-methoxybenzoic acid (22)

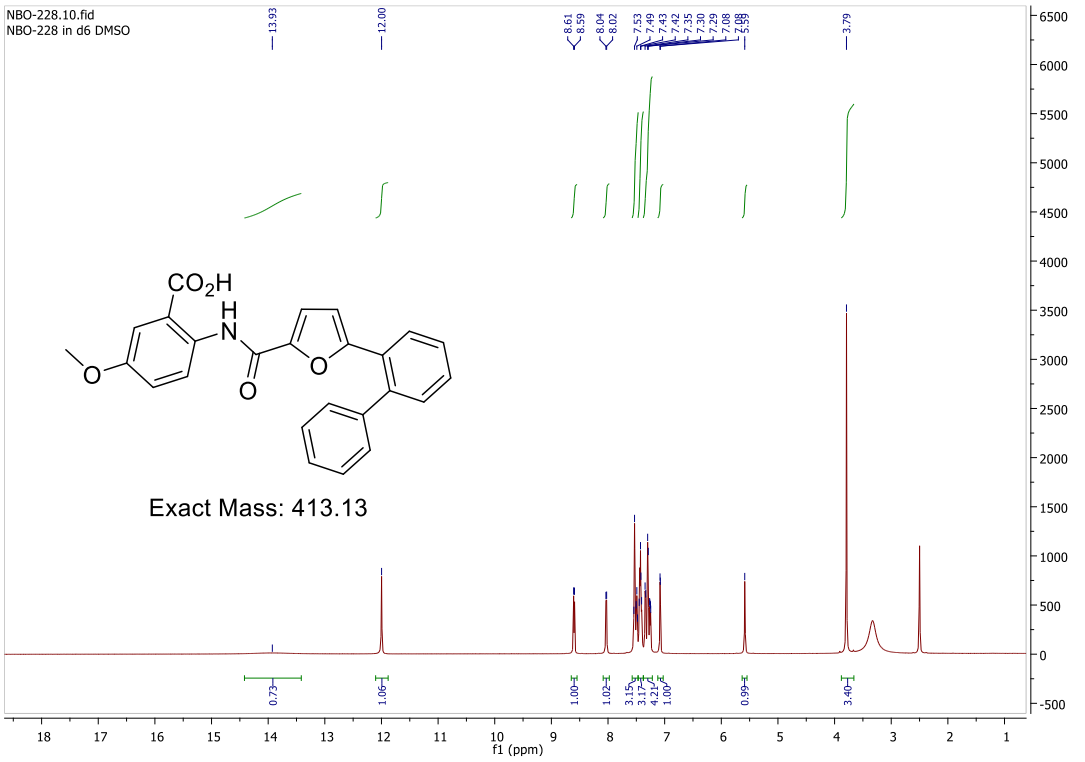

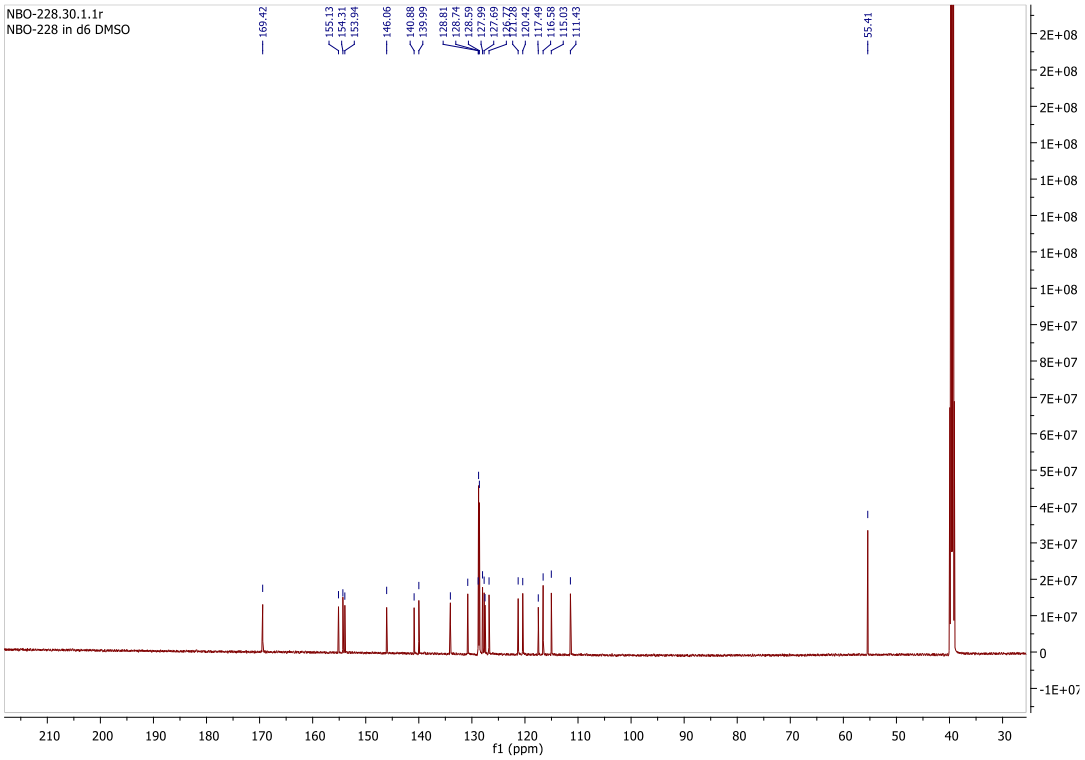

Figure S19. ^{1}H- and ^{13}C-NMR spectra of compound **22**

LC/MS data set of 2-(5-([1,1'-biphenyl]-2-yl)furan-2-carboxamido)-5-methoxybenzoic acid (22)

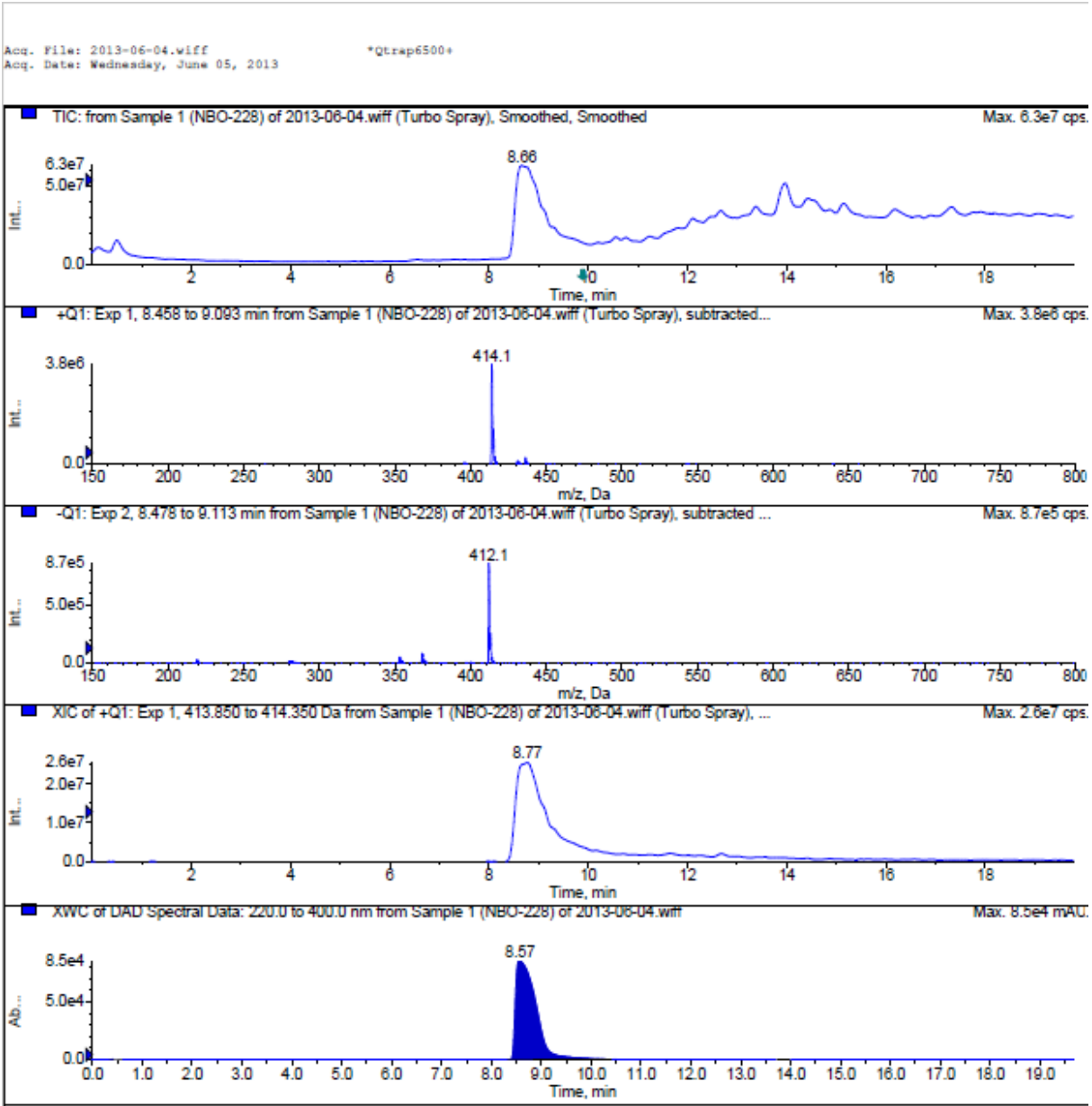

Peak List for "XWC of DAD Spectral Data: 220.0 to 400.0 nm from Sample 1 (NBO-228) of 2013-06-04.wiff"

	Time (min)	Area (mAU x min)	% Area	Height (mAU)	% Height	Width (min)	Baseline Type
1	0.4039	2457.0145	0.1037	894.7588	1.0295	0.0933	Base to Base
2	0.4948	1291.8237	0.0545	310.9313	0.3577	0.1400	Base to Base
3	8.5674	2.3627e6	99.7486	8.5373e4	98.2243	2.0667	Base to Base
4	13.8250	2207.0193	0.0932	337.7142	0.3886	0.2467	Base to Base

Figure S20. LC/MS data set of compound **22**

^{1}H- and ^{13}C-NMR spectra of 2-(5-([1,1'-biphenyl]-2-yl)furan-2-carboxamido)benzoic acid (9)

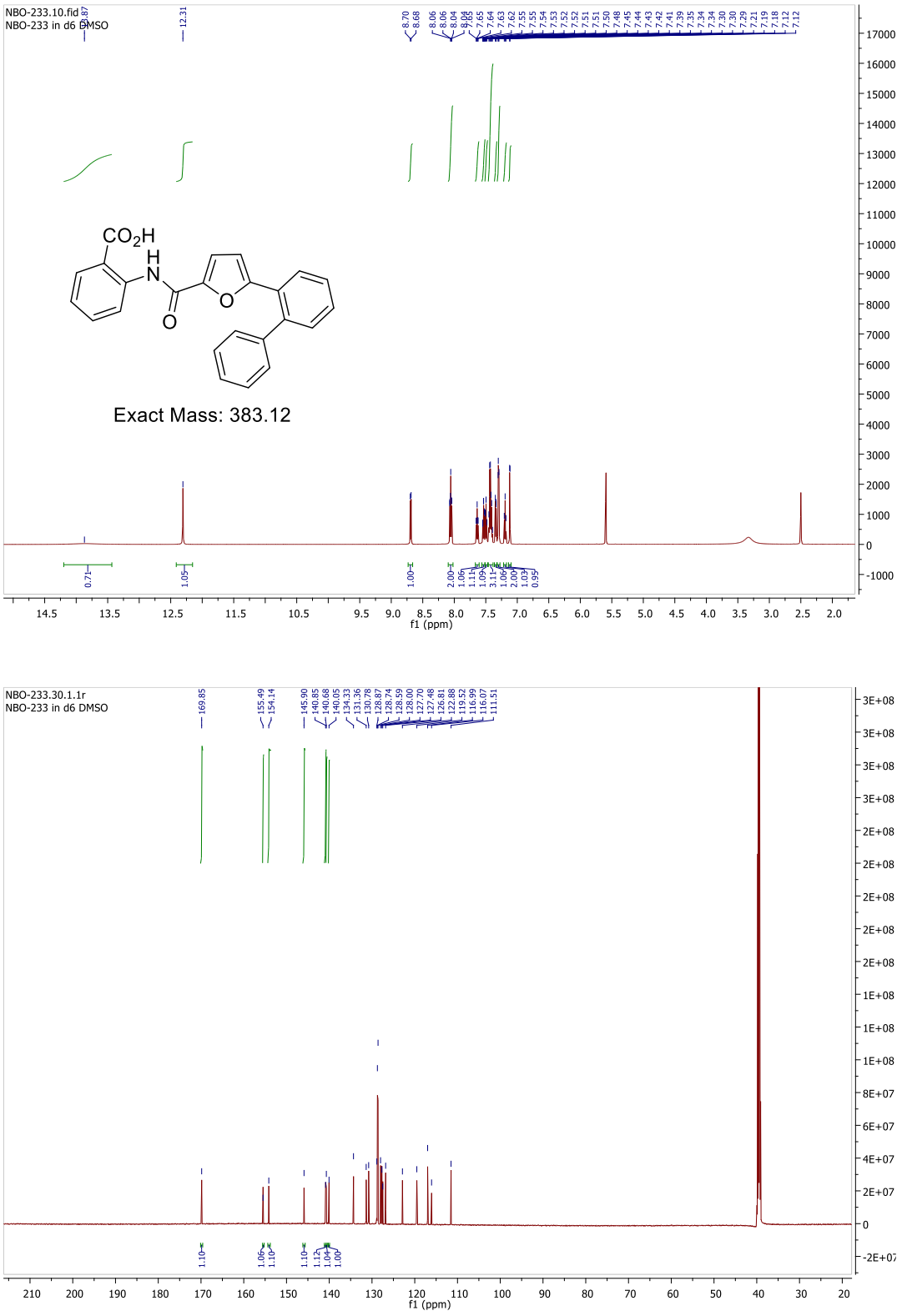

Figure S21. ^{1}H- and ^{13}C-NMR spectra of compound **9**

LC/MS data set of 2-(5-([1,1'-biphenyl]-2-yl)furan-2-carboxamido)benzoic acid (9)

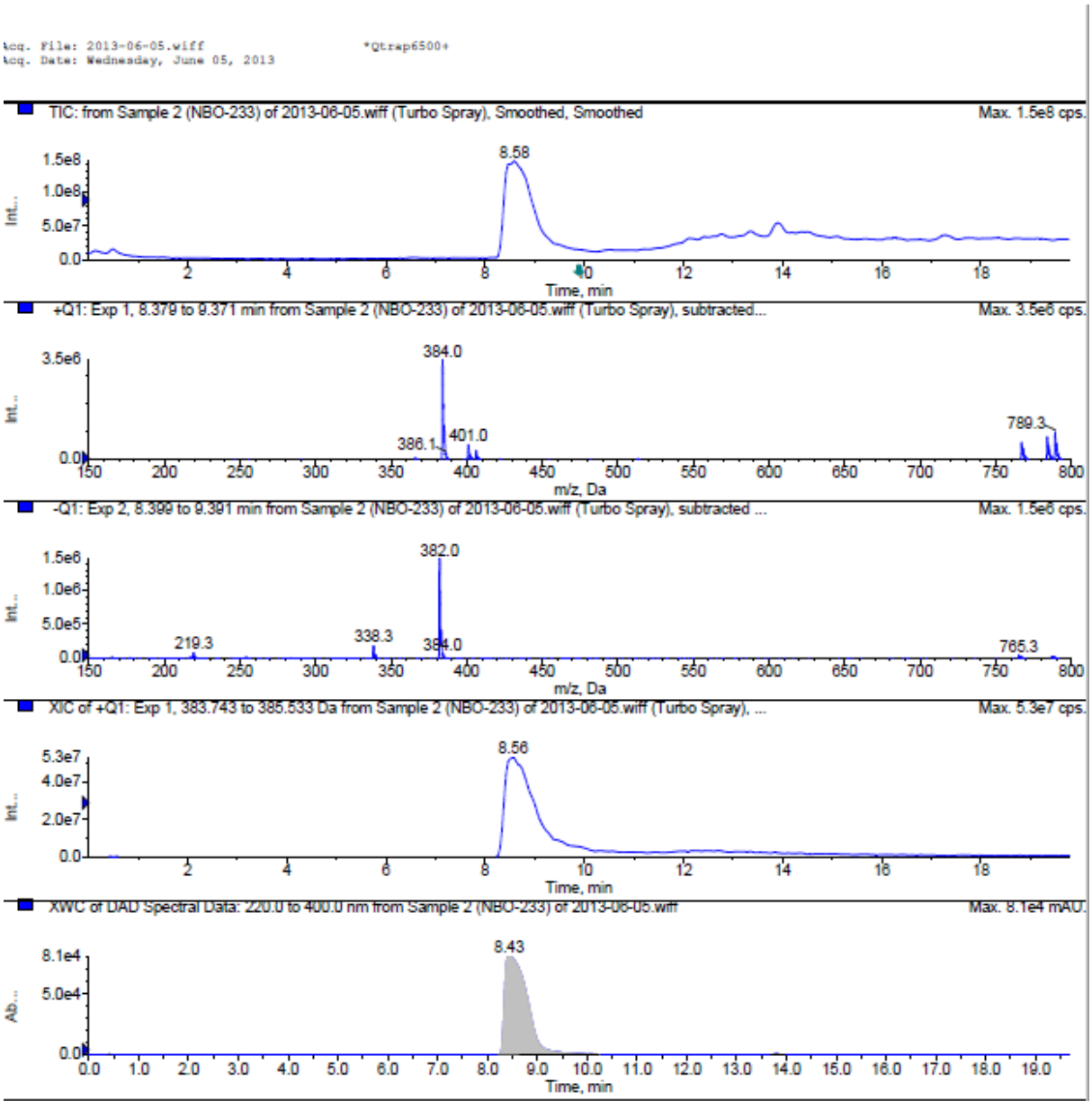

	Time (min)	Area (mAU x min)	% Area	Height (mAU)	% Height	Width (min)	Baseline Type
1	0.4117	2718.9904	0.1082	998.0363	1.2035	0.0933	Base to Base
2	8.4321	2.5063e6	99.7366	8.1320e4	98.0598	2.0400	Base to Base
3	13.7955	3900.7712	0.1552	610.9647	0.7367	0.2800	Base to Base

Figure S22. LC/MS data set of compound **9**

^{1}H- and ^{13}C-NMR spectra of 5-methoxy-2-(5-(3'-methoxy-[1,1'-biphenyl]-2-yl)furan-2-carboxamido)benzoic acid (52)

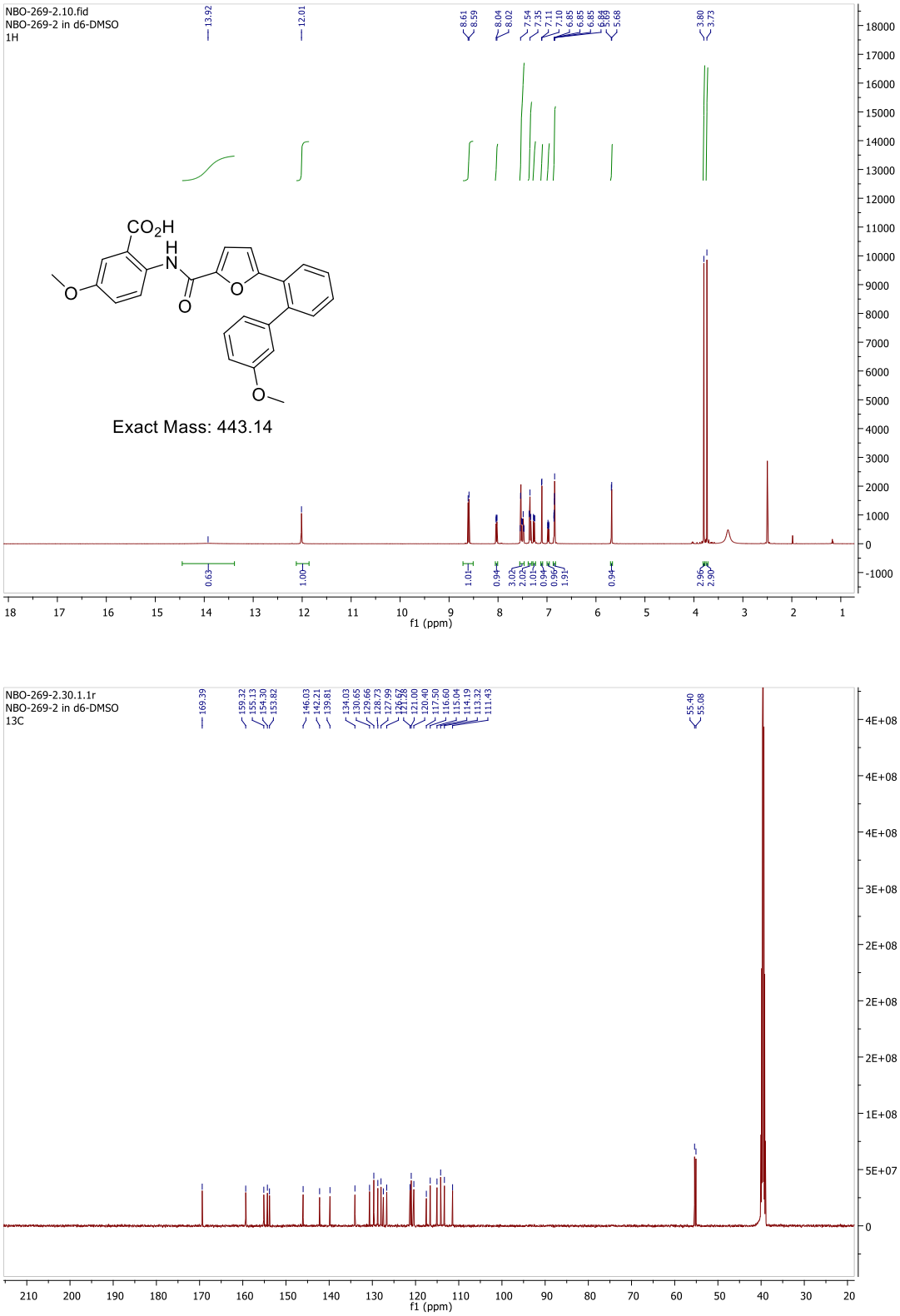

Figure S23. ^{1}H- and ^{13}C-NMR spectra of compound **52**

LC/MS data set of of 5-methoxy-2-(5-(3'-methoxy-[1,1'-biphenyl]-2-yl)furan-2-carboxamido)benzoic acid (52)

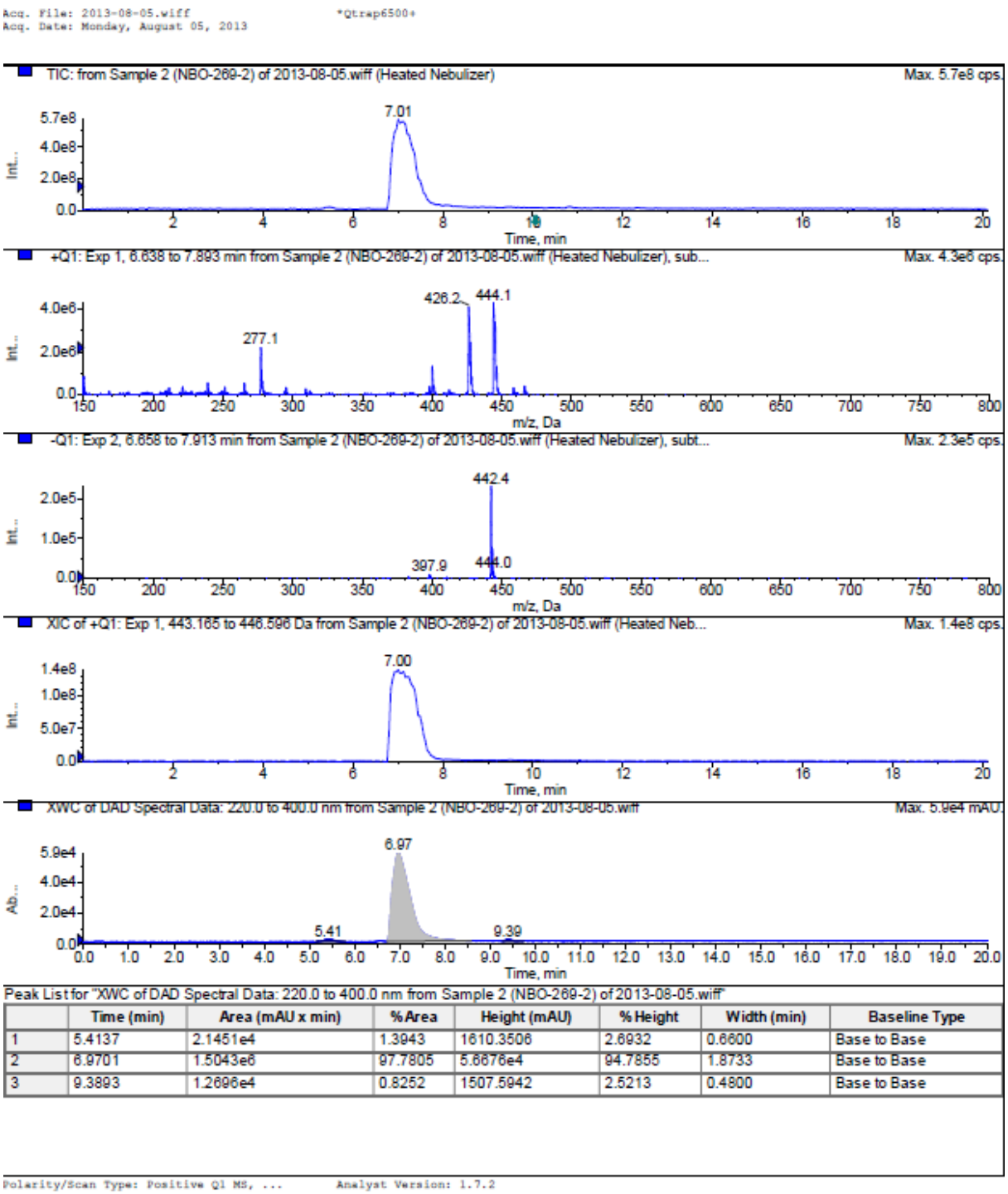

	Time (min)	Area (mAU x min)	% Area	Height (mAU)	% Height	Width (min)	Baseline Type
1	5.4137	2.1451e4	1.3943	1610.3506	2.6932	0.6600	Base to Base
2	6.9701	1.5043e6	97.7805	5.6676e4	94.7855	1.8733	Base to Base
3	9.3893	1.2696e4	0.8252	1507.5942	2.5213	0.4800	Base to Base

Figure S24. LC/MS data set of compound **52**

^{1}H- and ^{13}C-NMR spectra of 5-methoxy-2-(5-(4'-methoxy-[1,1'-biphenyl]-2-yl)furan-2-carboxamido)benzoic acid (57)

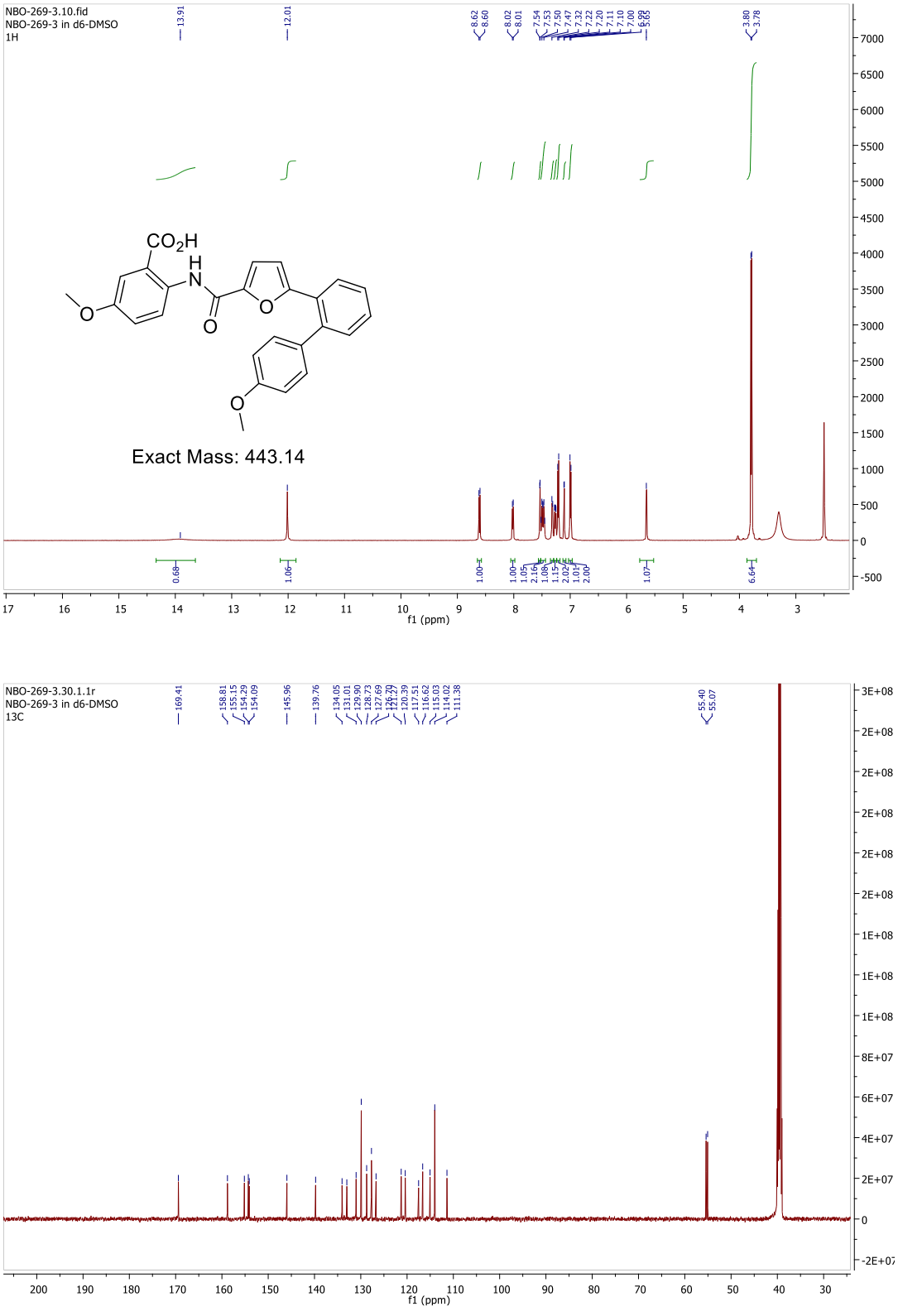

Figure S25. ^{1}H- and ^{13}C-NMR spectra of compound **57**

LC/MS data set of 5-methoxy-2-(5-(4'-methoxy-[1,1'-biphenyl]-2-yl)furan-2-carboxamido)benzoic acid (57)

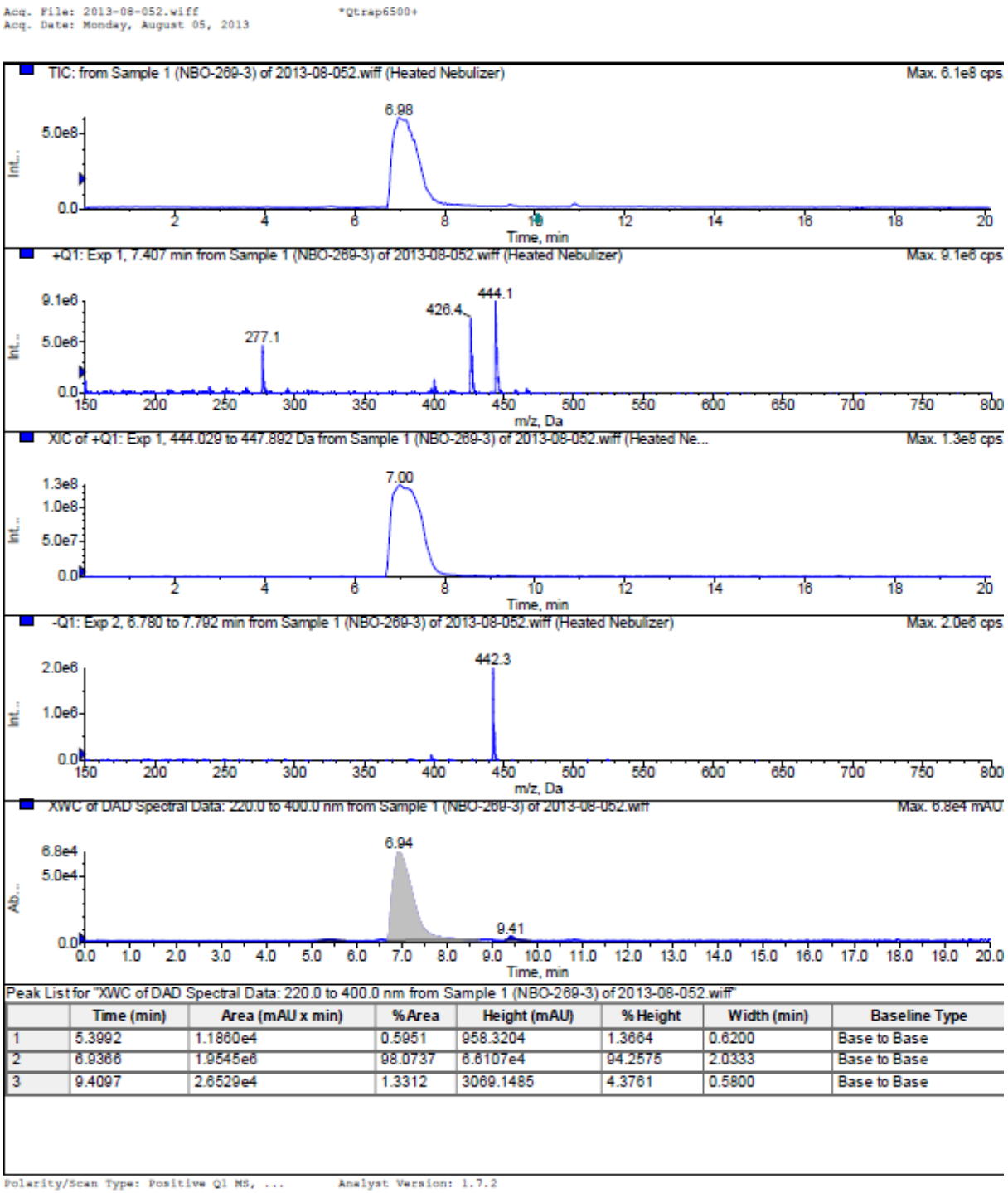

	Time (min)	Area (mAU x min)	%Area	Height (mAU)	%Height	Width (min)	Baseline Type
1	5.3992	1.1860e4	0.5951	958.3204	1.3664	0.6200	Base to Base
2	6.9366	1.9545e6	98.0737	6.6107e4	94.2575	2.0333	Base to Base
3	9.4097	2.6529e4	1.3312	3069.1485	4.3761	0.5800	Base to Base

Figure S26. LC/MS data set of compound **57**

^{1}H-NMR spectrum of 5-methoxy-2-(5-(2-(pyridin-3-yl)phenyl)furan-2-carboxamido)benzoic acid (51)

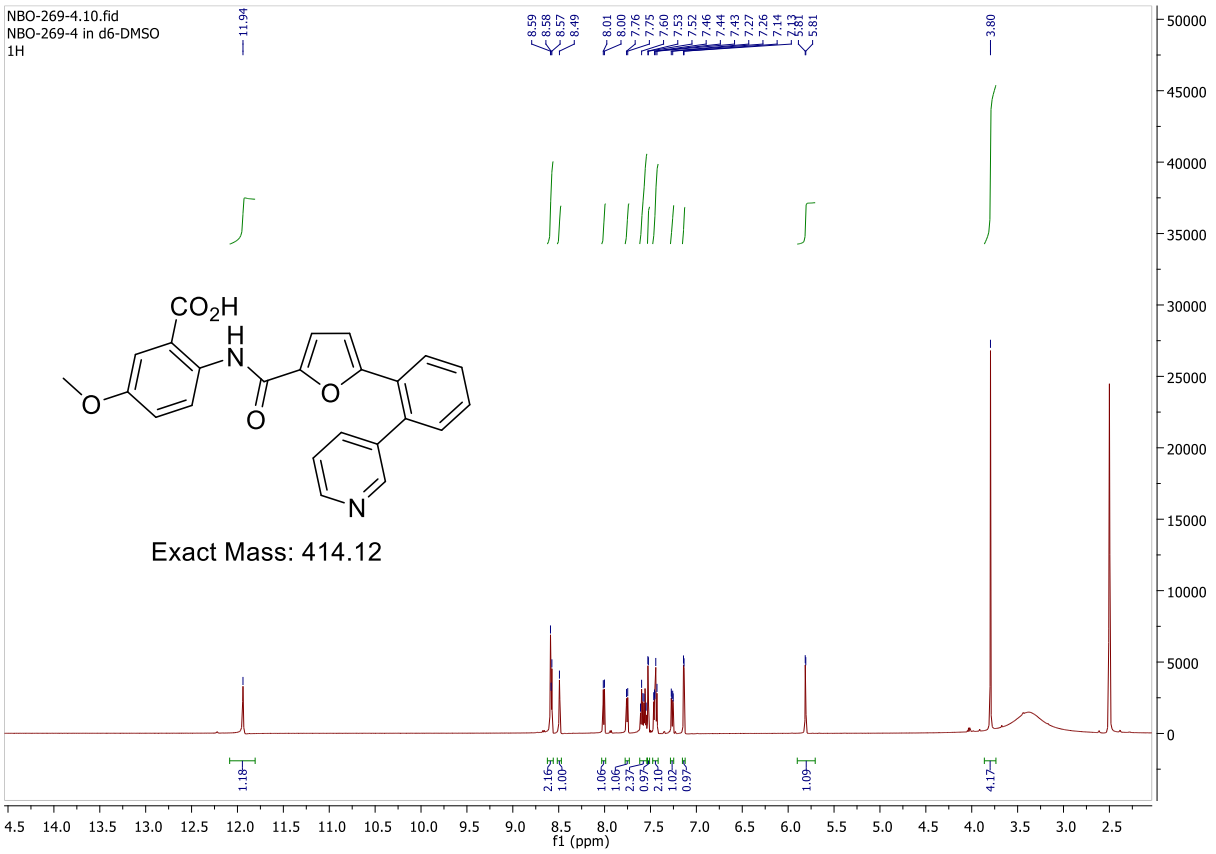

Figure S27. ^{1}H-NMR spectrum of compound **51**

LC/MS data set of 5-methoxy-2-(5-(2-(pyridin-3-yl)phenyl)furan-2-carboxamido)benzoic acid (51)

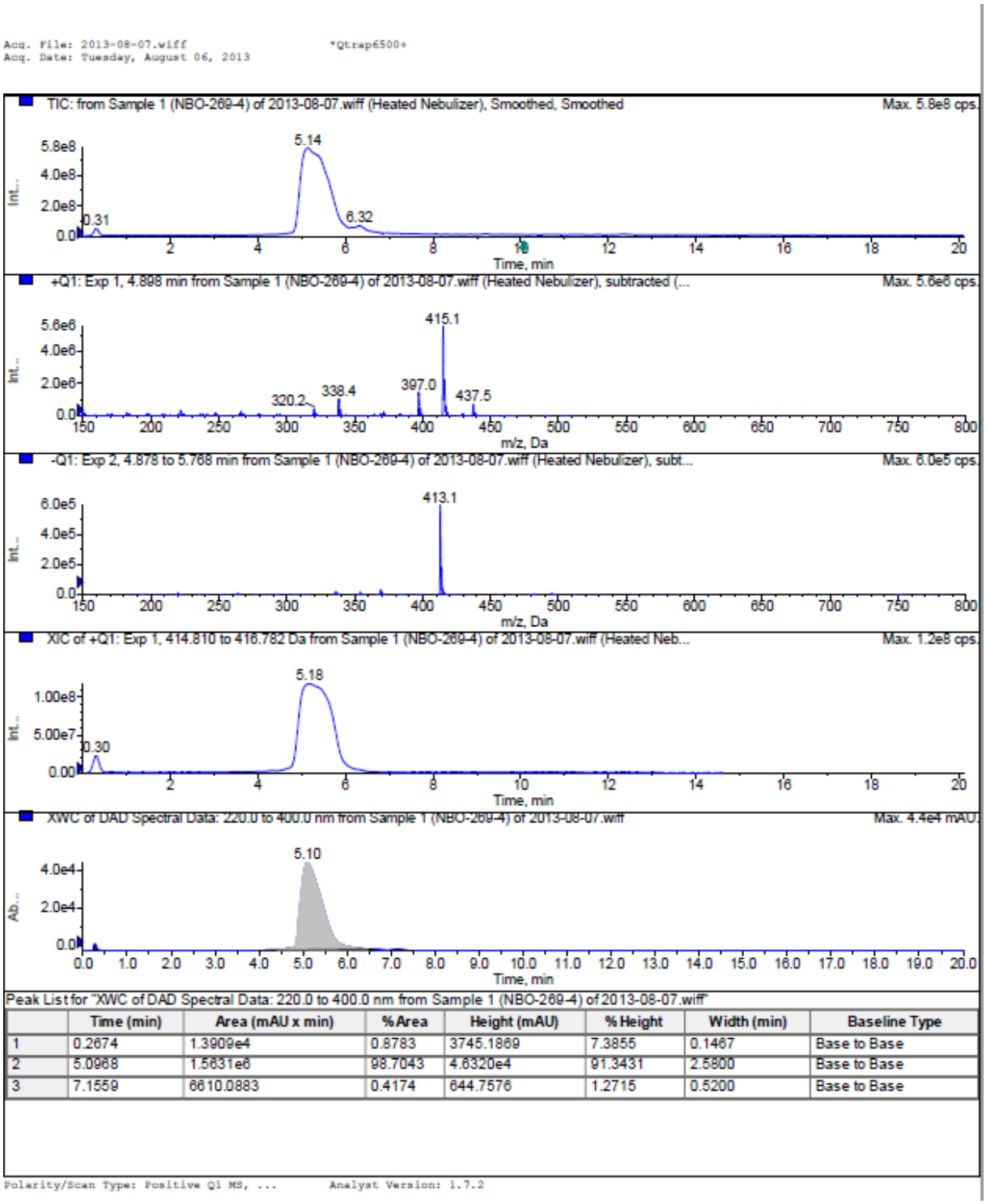

	Time (min)	Area (mAU x min)	% Area	Height (mAU)	% Height	Width (min)	Baseline Type
1	0.2674	1.3909e4	0.8783	3745.1869	7.3855	0.1467	Base to Base
2	5.0968	1.5631e6	98.7043	4.6320e4	91.3431	2.5800	Base to Base
3	7.1559	6610.0883	0.4174	644.7576	1.2715	0.5200	Base to Base

Figure S28. LC/MS data set of compound **51**

^{1}H-NMR spectrum of 2-(5-(3'-isopropyl-[1,1'-biphenyl]-2-yl)furan-2-carboxamido)-5-methoxybenzoic acid (55)

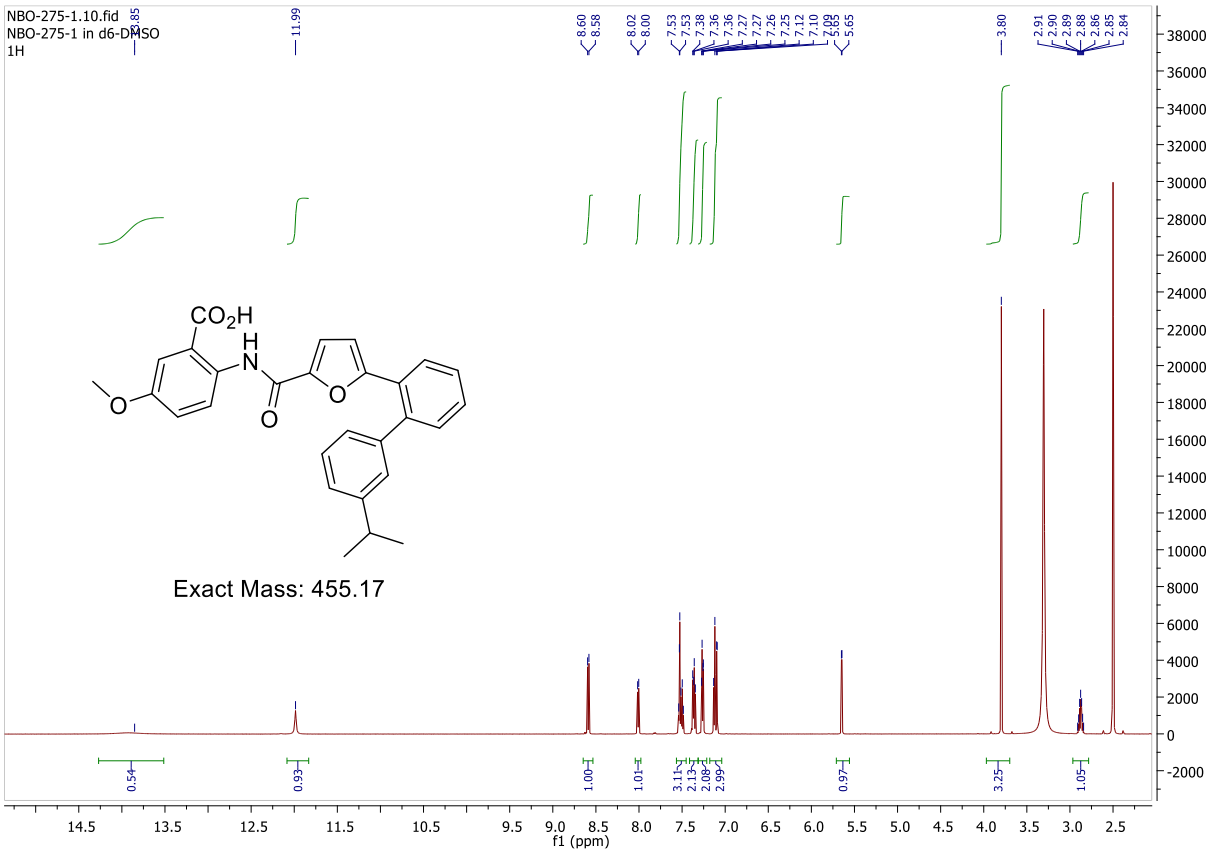

Figure S29. ^{1}H-NMR spectrum of compound **55**

LC/MS data set of 2-(5-(3'-isopropyl-[1,1'-biphenyl]-2-yl)furan-2-carboxamido)-5-methoxybenzoic acid (55)

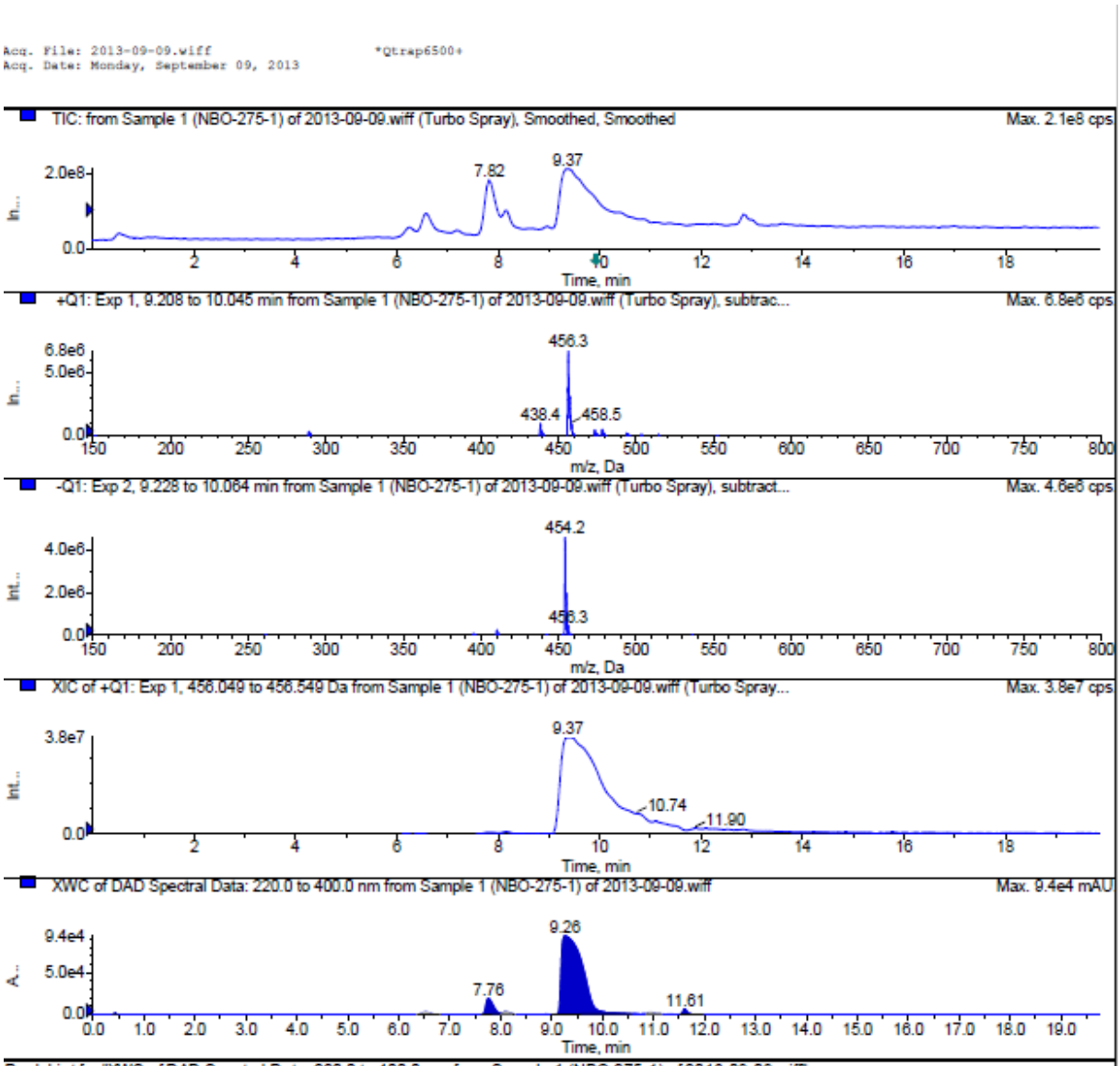

Peak List for "XWC of DAD Spectral Data: 220.0 to 400.0 nm from Sample 1 (NBO-275-1) of 2013-09-09.wiff"

	Time (min)	Area (mAU x min)	% Area	Height (mAU)	% Height	Width (min)	Baseline Type
1	0.4362	5805.6253	0.2007	2073.5889	1.6162	0.1000	Base to Base
2	6.5267	2.4597e4	0.8505	2838.3457	2.2123	0.4467	Base to Base
3	7.7597	1.7631e5	6.0959	1.8637e4	14.5261	0.3933	Base to Base
4	8.1016	1.5396e4	0.5323	3013.4176	2.3488	0.2467	Base to Base
5	9.2629	2.6291e6	90.9039	9.3589e4	72.9462	1.5733	Base to Base
6	10.9376	9099.1518	0.3146	1945.6787	1.5165	0.2933	Base to Base
7	11.6129	3.1872e4	1.1020	6201.8554	4.8339	0.4600	Base to Base

Polarity/Scan Type: Positive Q1 MS, ... Analyst Version: 1.7.2

Figure S30. LC/MS data set of compound **55**

^{1}H- and ^{13}C-NMR spectra of 5-methoxy-2-(5-(3'-(trifluoromethyl)-[1,1'-biphenyl]-2-yl)furan-2-carboxamido)benzoic acid (54)

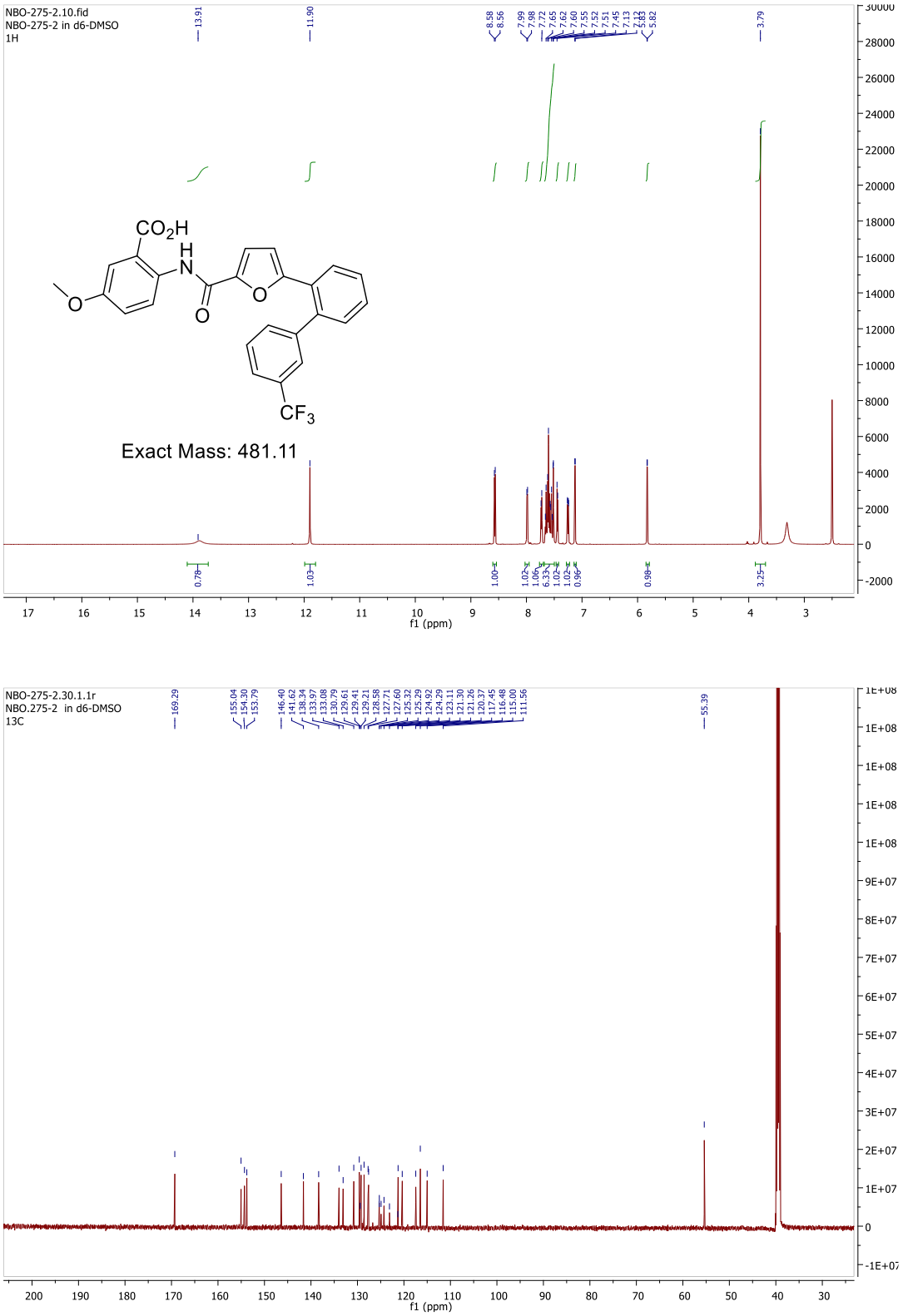

Figure S31. ^{1}H- and ^{13}C-NMR spectra of compound **54**

LC/MS data set of 5-methoxy-2-(5-(3'-(trifluoromethyl)-[1,1'-biphenyl]-2-yl)furan-2-carboxamido)benzoic acid (54)

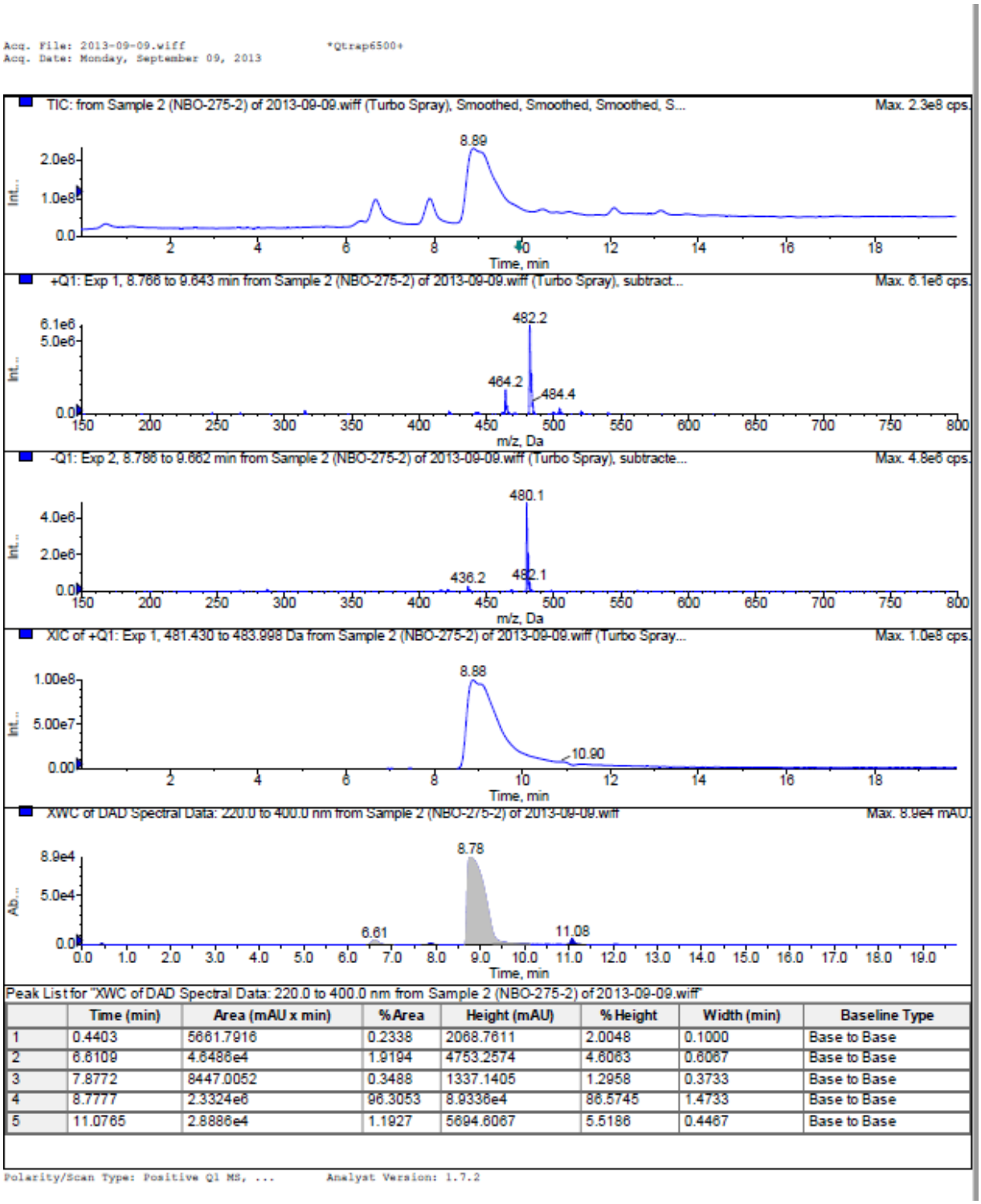

Peak List for "XWC of DAD Spectral Data: 220.0 to 400.0 nm from Sample 2 (NBO-275-2) of 2013-09-09.wiff"

	Time (min)	Area (mAU x min)	% Area	Height (mAU)	% Height	Width (min)	Baseline Type
1	0.4403	5661.7916	0.2338	2068.7611	2.0048	0.1000	Base to Base
2	6.6109	4.6486e4	1.9194	4753.2574	4.6063	0.6067	Base to Base
3	7.8772	8447.0052	0.3488	1337.1405	1.2958	0.3733	Base to Base
4	8.7777	2.3324e6	96.3053	8.9336e4	86.5745	1.4733	Base to Base
5	11.0765	2.8886e4	1.1927	5694.6067	5.5186	0.4467	Base to Base

Polarity/Scan Type: Positive Q1 MS, ... Analyst Version: 1.7.2

Figure S32. LC/MS data set of compound **54**

^{1}H- and ^{13}C-NMR spectra of 5-methoxy-2-(6-(naphthalen-1-yl)picolinamido)benzoic acid (67)

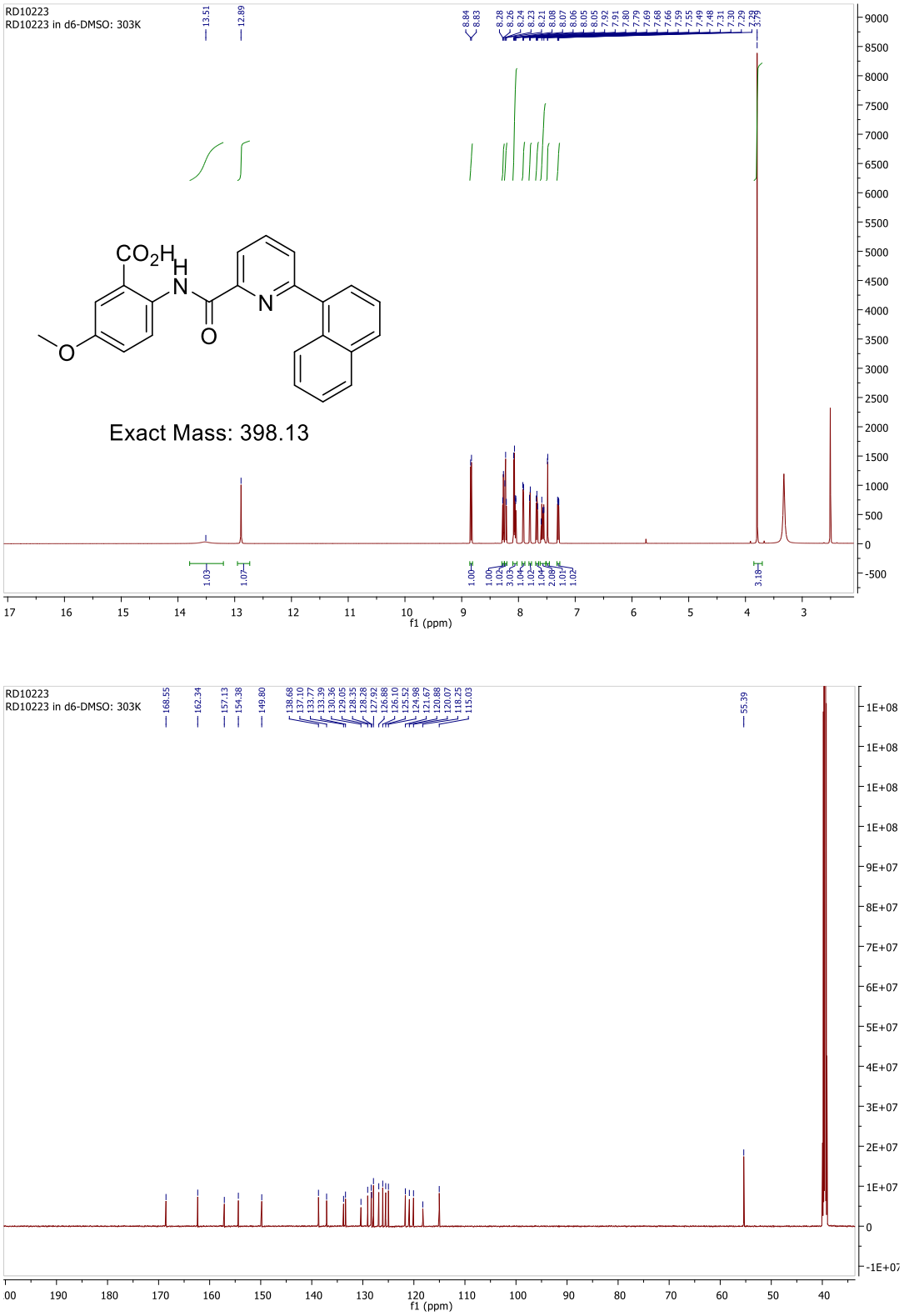

Figure S33. ^{1}H- and ^{13}C-NMR spectra of compound **67**

LC/MS data set of 5-methoxy-2-(6-(naphthalen-1-yl)picolinamido)benzoic acid (67)

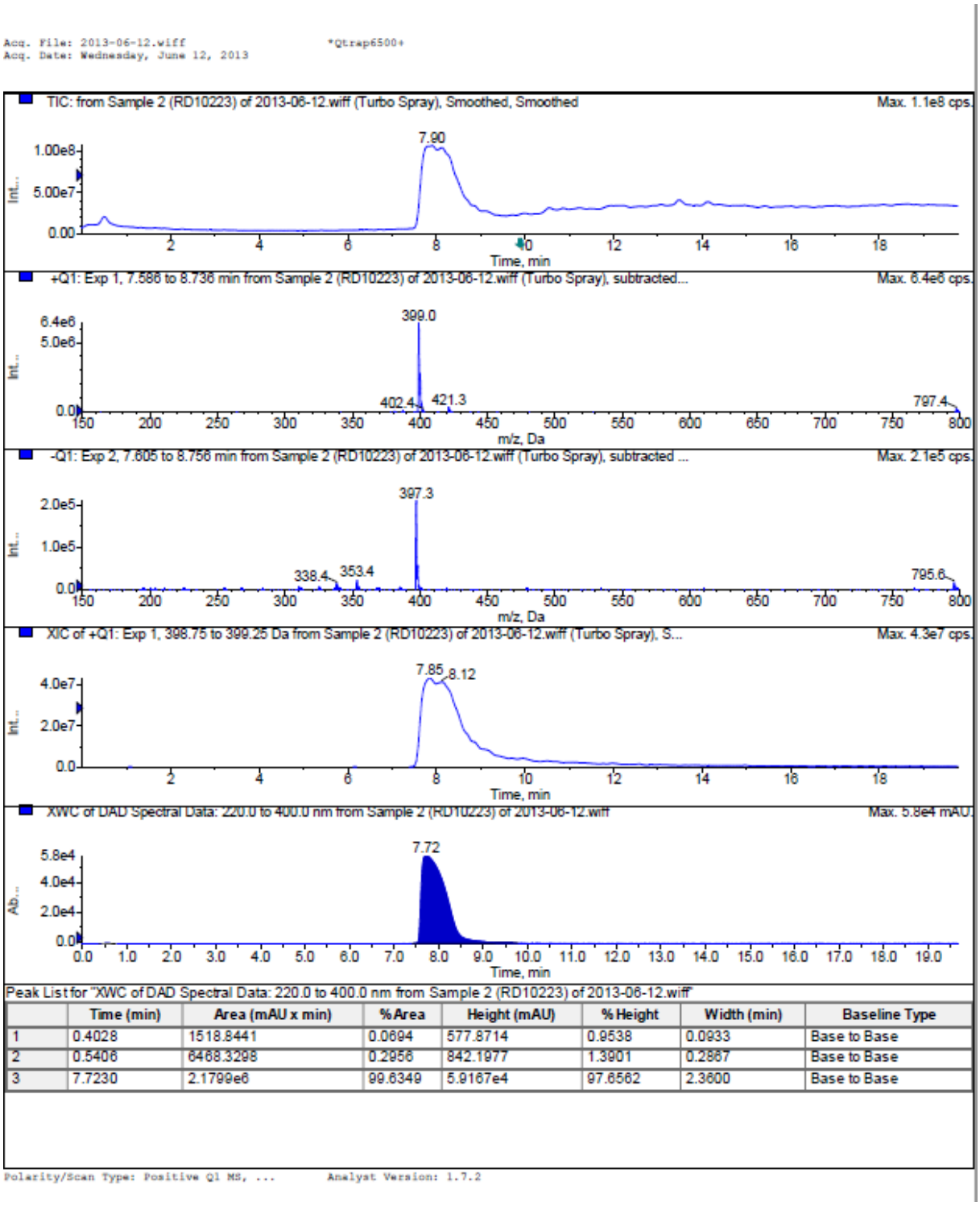

	Time (min)	Area (mAU x min)	% Area	Height (mAU)	% Height	Width (min)	Baseline Type
1	0.4028	1518.8441	0.0694	577.8714	0.9538	0.0933	Base to Base
2	0.5406	6468.3298	0.2956	842.1977	1.3901	0.2867	Base to Base
3	7.7230	2.1799e6	99.6349	5.9167e4	97.6562	2.3600	Base to Base

Figure S34. LC/MS data set of compound **67**

^{1}H- and ^{13}C-NMR spectra of 2-(5-([1,1'-biphenyl]-3-yl)furan-2-carboxamido)-5-methoxybenzoic acid (20)

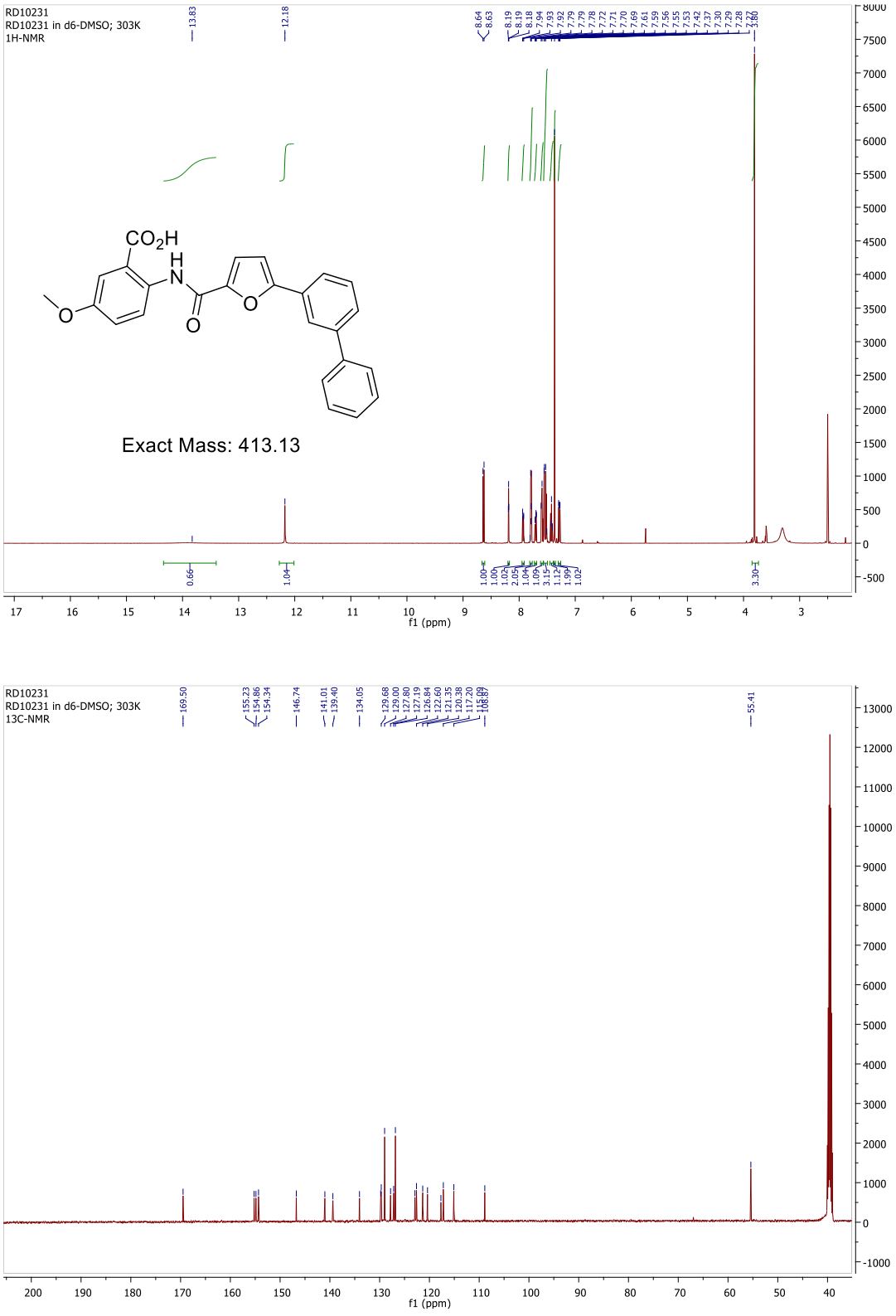

Figure S35. ^{1}H- and ^{13}C-NMR spectra of compound **20**

LC/MS data set of 2-(5-([1,1'-biphenyl]-3-yl)furan-2-carboxamido)-5-methoxybenzoic acid (20)

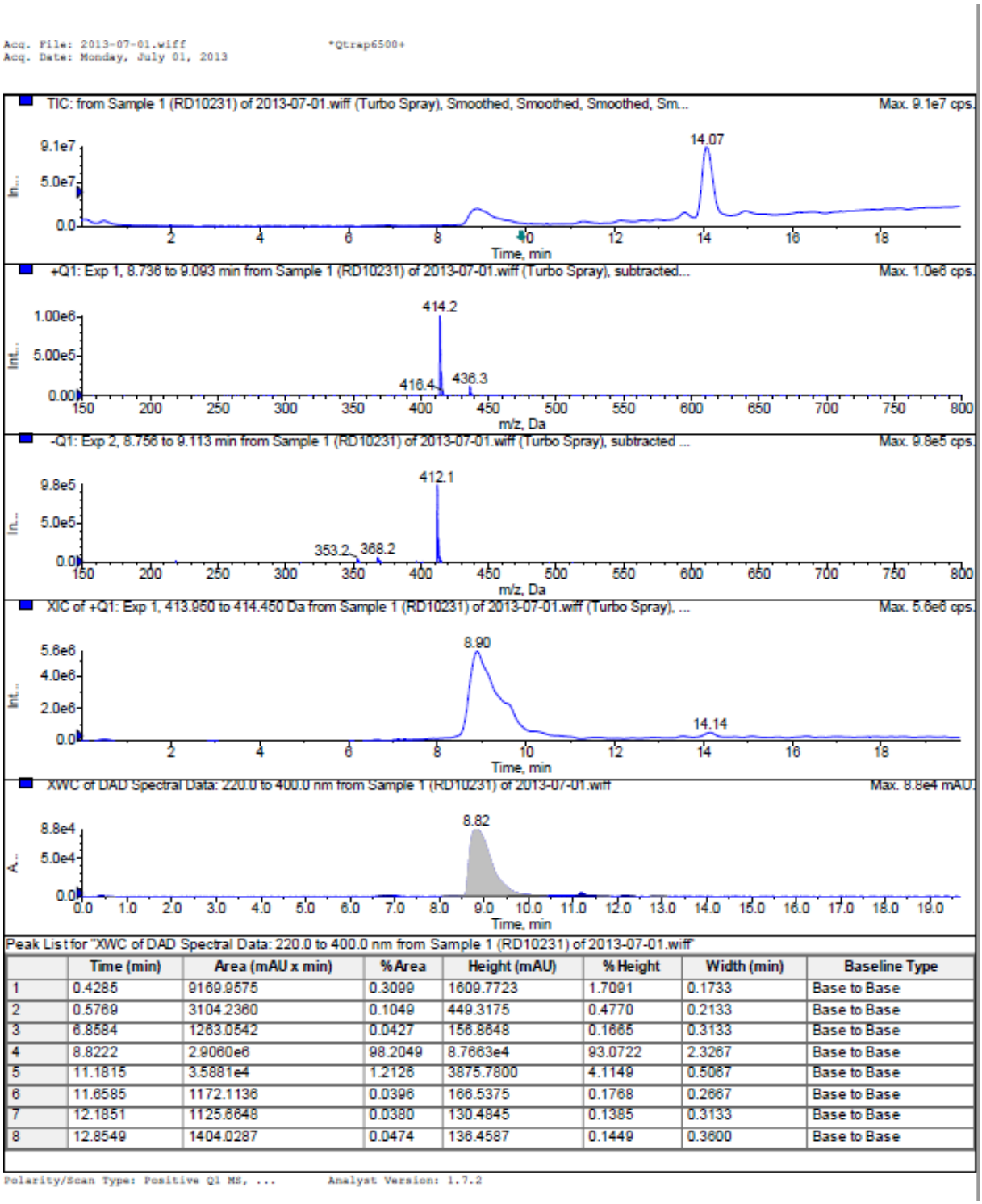

Peak List for "XWC of DAD Spectral Data: 220.0 to 400.0 nm from Sample 1 (RD10231) of 2013-07-01.wiff"

	Time (min)	Area (mAU x min)	%Area	Height (mAU)	%Height	Width (min)	Baseline Type
1	0.4285	9169.9575	0.3099	1609.7723	1.7091	0.1733	Base to Base
2	0.5769	3104.2360	0.1049	449.3175	0.4770	0.2133	Base to Base
3	6.8584	1263.0542	0.0427	156.8648	0.1665	0.3133	Base to Base
4	8.8222	2.9060e6	98.2049	8.7663e4	93.0722	2.3267	Base to Base
5	11.1815	3.5881e4	1.2126	3875.7800	4.1149	0.5067	Base to Base
6	11.6585	1172.1136	0.0396	166.5375	0.1768	0.2667	Base to Base
7	12.1851	1125.6648	0.0380	130.4845	0.1385	0.3133	Base to Base
8	12.8549	1404.0287	0.0474	136.4587	0.1449	0.3600	Base to Base

Polarity/Scan Type: Positive Q1 MS, ... Analyst Version: 1.7.2

Figure S36. LC/MS data set of compound **20**

^{1}H- and ^{13}C-NMR spectra of 2-(5-(3'-methoxy-[1,1'-biphenyl]-2-yl)furan-2-carboxamido)benzoic acid (14)

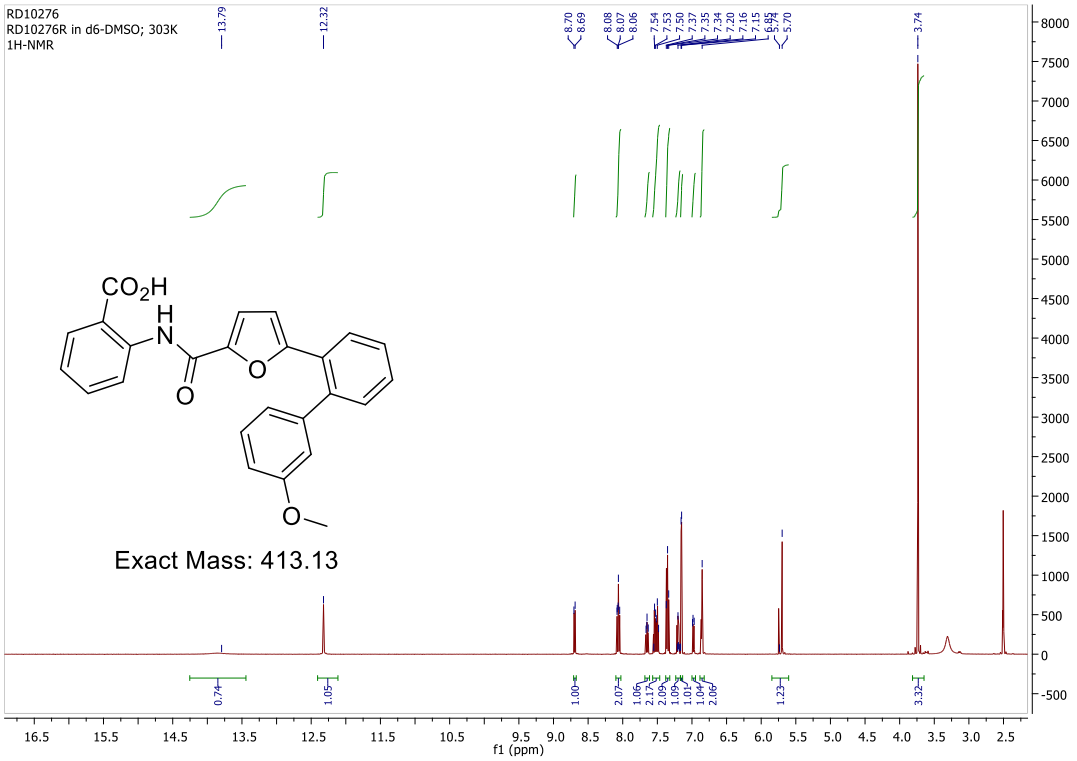

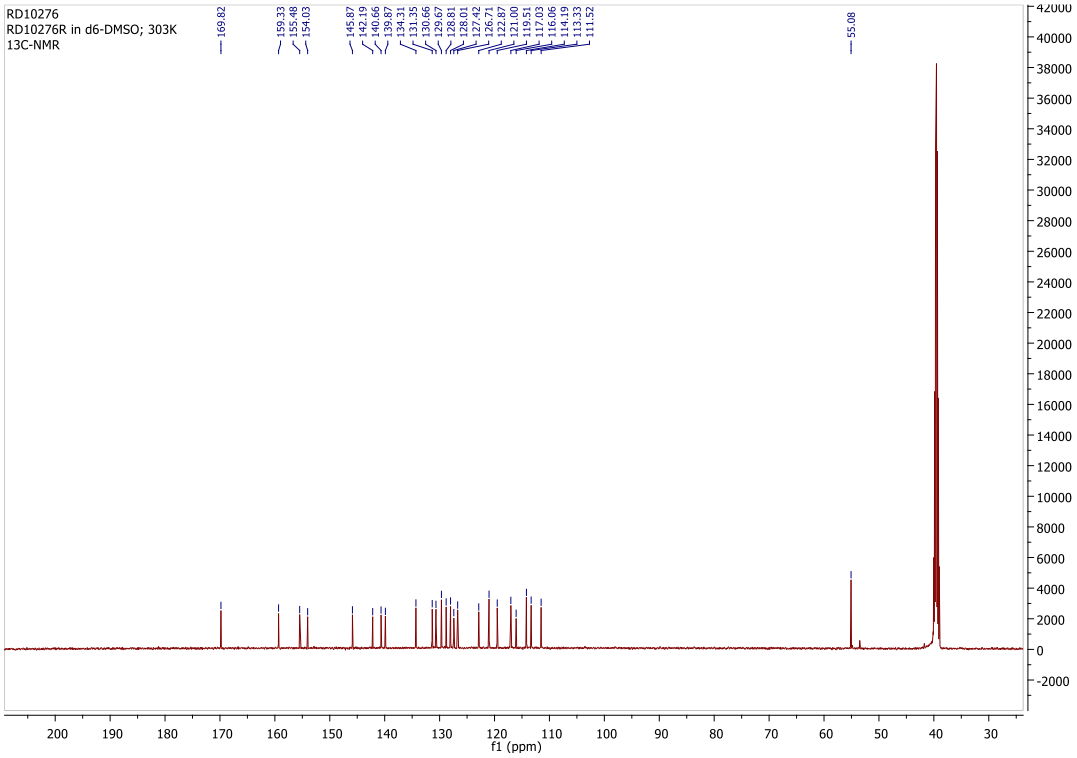

Figure S37. ^{1}H- and ^{13}C-NMR spectra of compound **14**

LC/MS data set of 2-(5-(3'-methoxy-[1,1'-biphenyl]-2-yl)furan-2-carboxamido)benzoic acid (14)

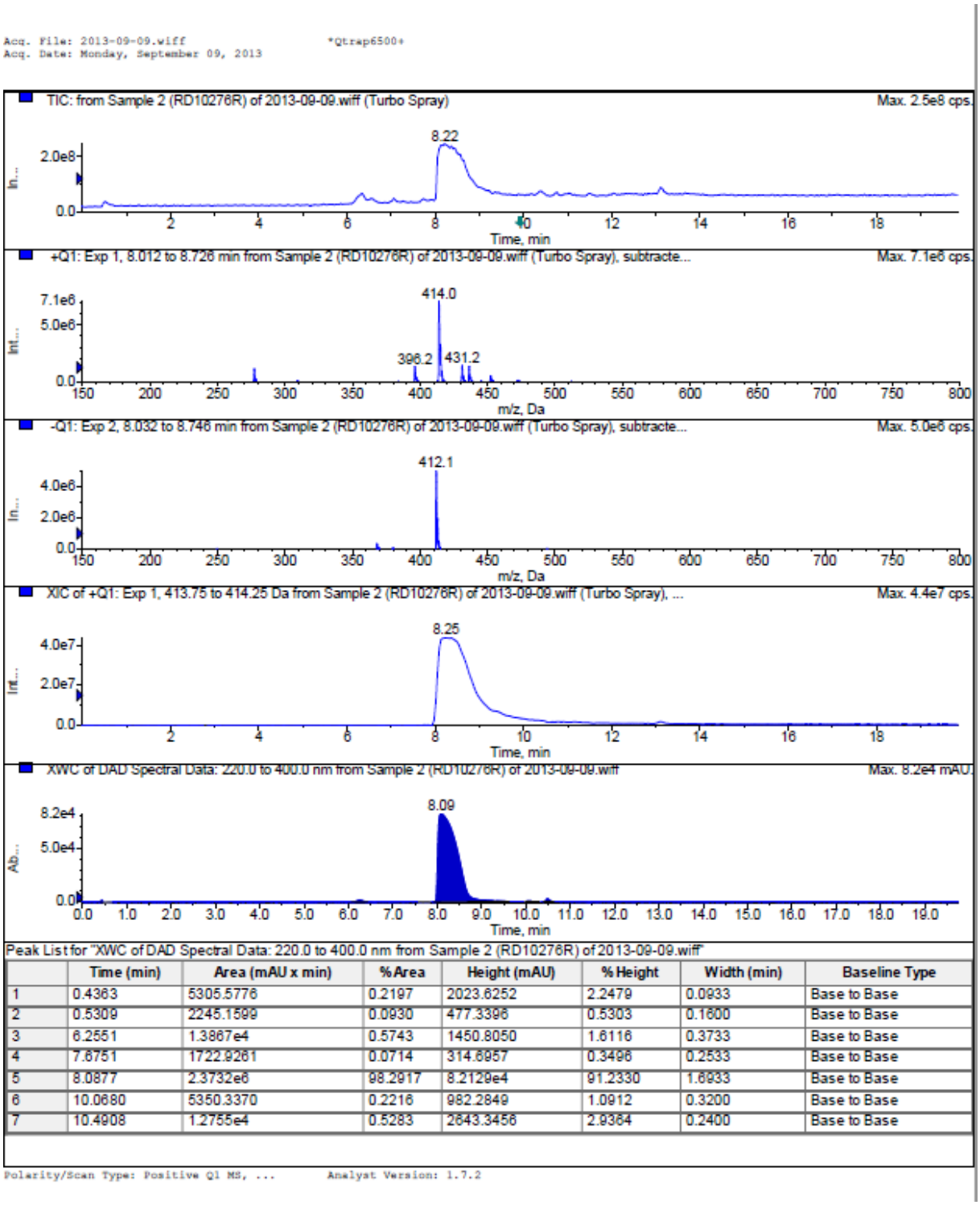

Peak List for "XWC of DAD Spectral Data: 220.0 to 400.0 nm from Sample 2 (RD10276R) of 2013-09-09.wiff"

	Time (min)	Area (mAU x min)	% Area	Height (mAU)	% Height	Width (min)	Baseline Type
1	0.4363	5305.5776	0.2197	2023.6252	2.2479	0.0933	Base to Base
2	0.5309	2245.1599	0.0930	477.3396	0.5303	0.1600	Base to Base
3	6.2551	1.3867e4	0.5743	1450.8050	1.6116	0.3733	Base to Base
4	7.6751	1722.9261	0.0714	314.6957	0.3496	0.2533	Base to Base
5	8.0877	2.3732e6	98.2917	8.2129e4	91.2330	1.6933	Base to Base
6	10.0680	5350.3370	0.2216	982.2849	1.0912	0.3200	Base to Base
7	10.4908	1.2755e4	0.5283	2643.3456	2.9364	0.2400	Base to Base

Polarity/Scan Type: Positive Q1 MS, ... Analyst Version: 1.7.2

Figure S38. LC/MS data set of compound **14**

^{1}H- and ^{13}C-NMR spectra of 5-fluoro-2-(5-(2-isopropylphenyl)furan-2-carboxamido)benzoic acid (48)

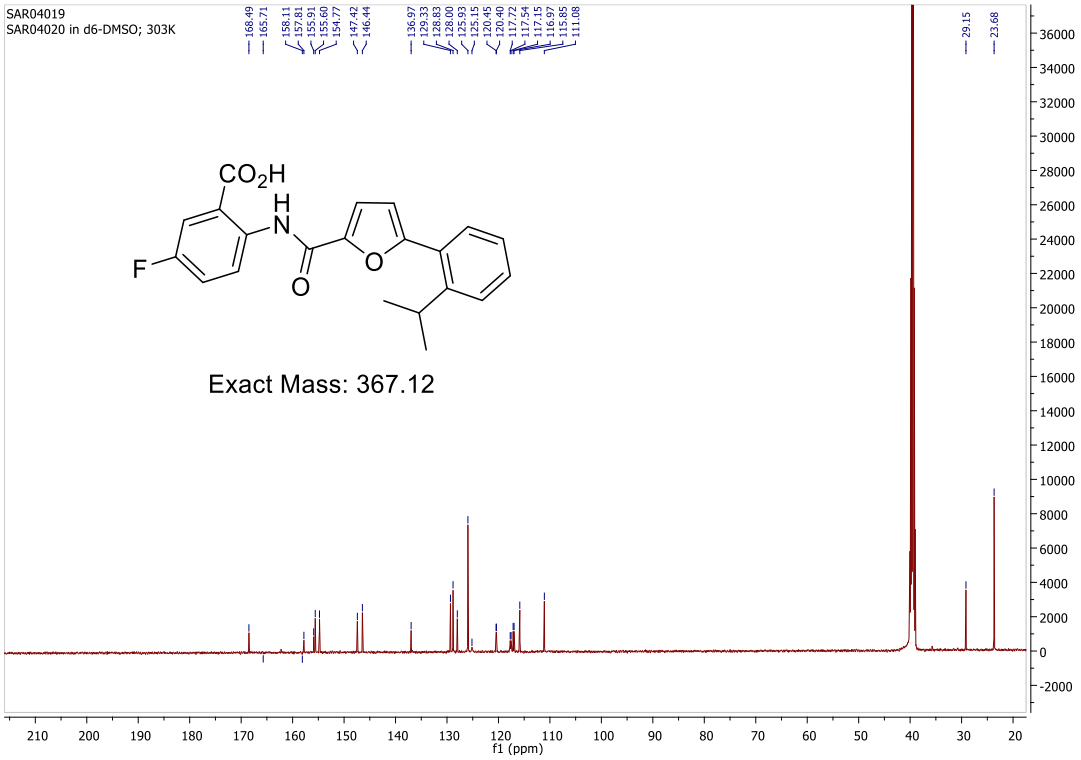

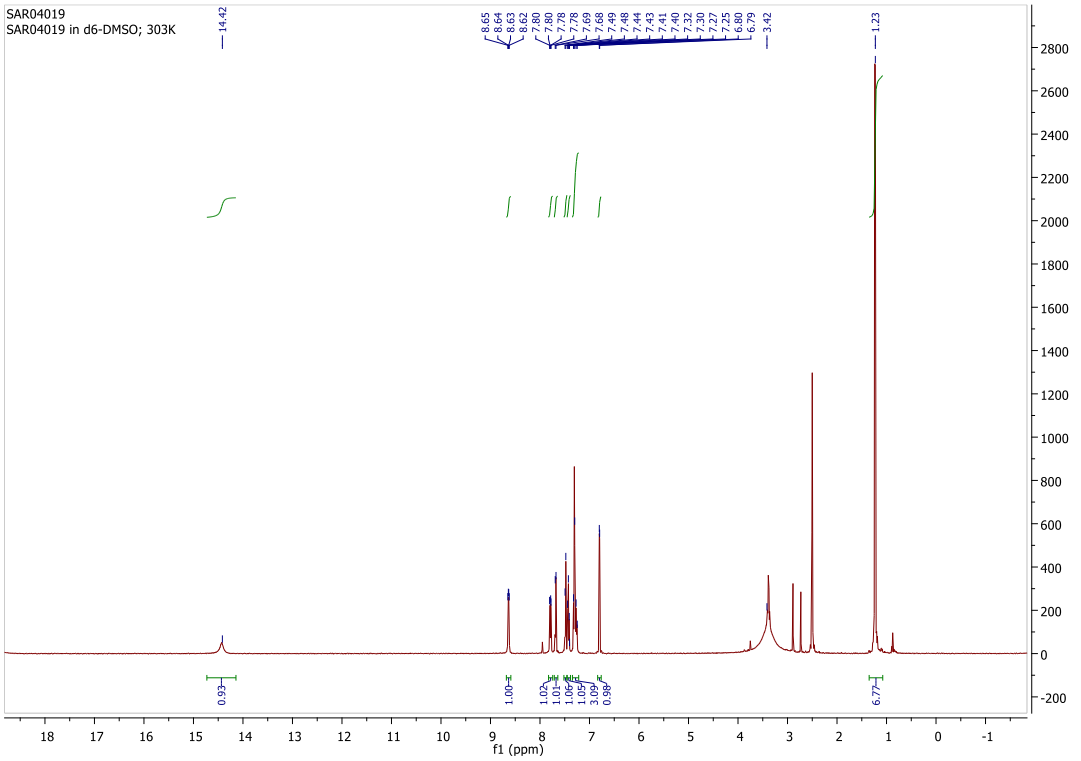

Figure S39. ^{1}H- and ^{13}C-NMR spectra of compound **48**

LC/MS data set of 5-fluoro-2-(5-(2-isopropylphenyl)furan-2-carboxamido)benzoic acid (48)

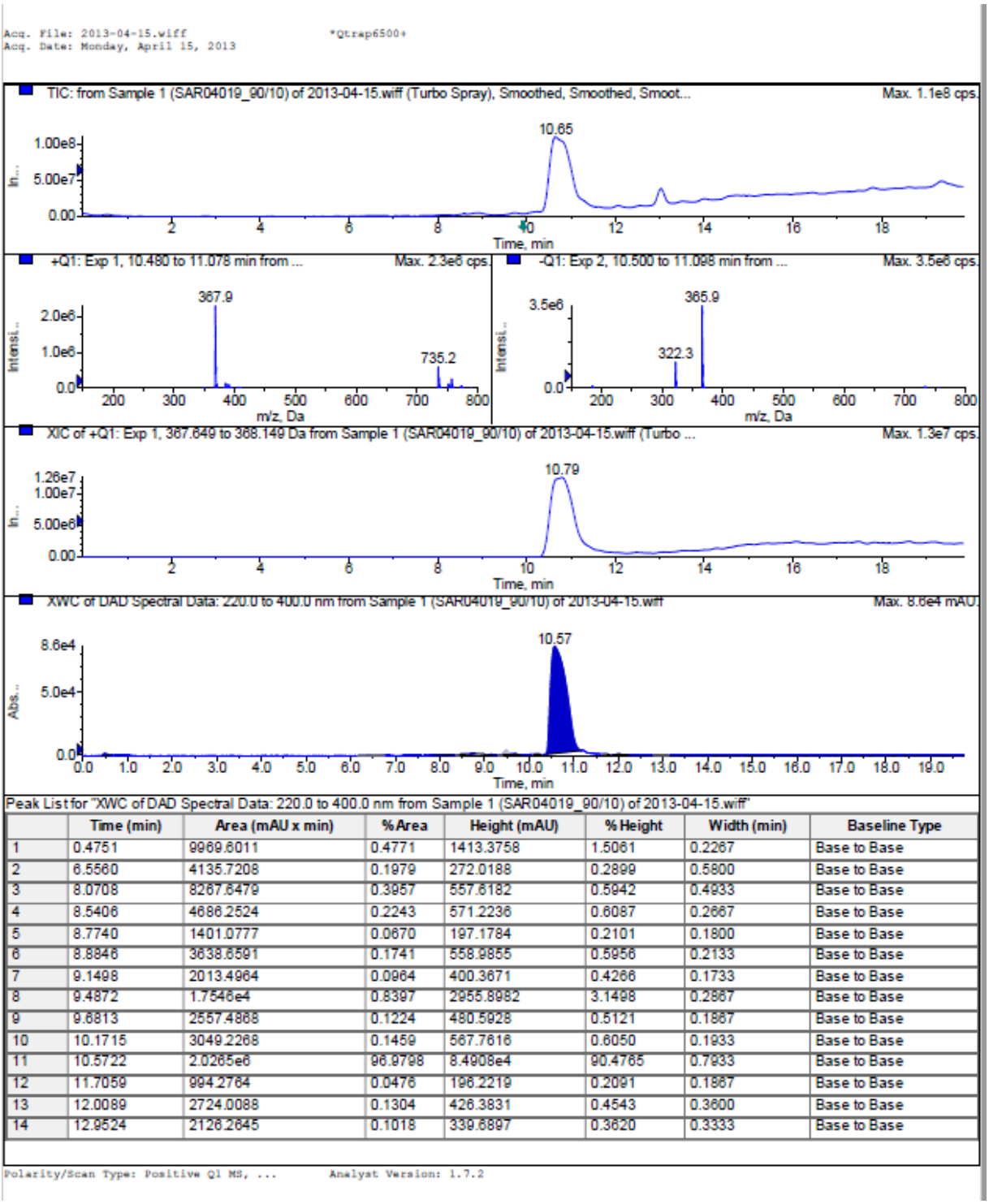

	Time (min)	Area (mAU x min)	%Area	Height (mAU)	%Height	Width (min)	Baseline Type
1	0.4751	9969.6011	0.4771	1413.3758	1.5061	0.2267	Base to Base
2	6.5560	4135.7208	0.1979	272.0188	0.2899	0.5800	Base to Base
3	8.0708	8267.6479	0.3957	557.6182	0.5942	0.4933	Base to Base
4	8.5406	4686.2524	0.2243	571.2236	0.6087	0.2667	Base to Base
5	8.7740	1401.0777	0.0670	197.1784	0.2101	0.1800	Base to Base
6	8.8846	3638.6591	0.1741	558.9855	0.5956	0.2133	Base to Base
7	9.1498	2013.4964	0.0964	400.3671	0.4266	0.1733	Base to Base
8	9.4872	1.7546e4	0.8397	2955.8982	3.1498	0.2867	Base to Base
9	9.6813	2557.4868	0.1224	480.5928	0.5121	0.1867	Base to Base
10	10.1715	3049.2268	0.1459	567.7616	0.6050	0.1933	Base to Base
11	10.5722	2.0265e6	96.9798	8.4908e4	90.4765	0.7933	Base to Base
12	11.7059	994.2764	0.0476	196.2219	0.2091	0.1867	Base to Base
13	12.0089	2724.0088	0.1304	426.3831	0.4543	0.3600	Base to Base
14	12.9524	2126.2645	0.1018	339.6897	0.3620	0.3333	Base to Base

Figure S40. LC/MS data set of compound **48**

^{1}H- and ^{13}C-NMR spectra of 5-cyclopropyl-2-(5-(naphthalen-1-yl)furan-2-carboxamido)benzoic acid (37)

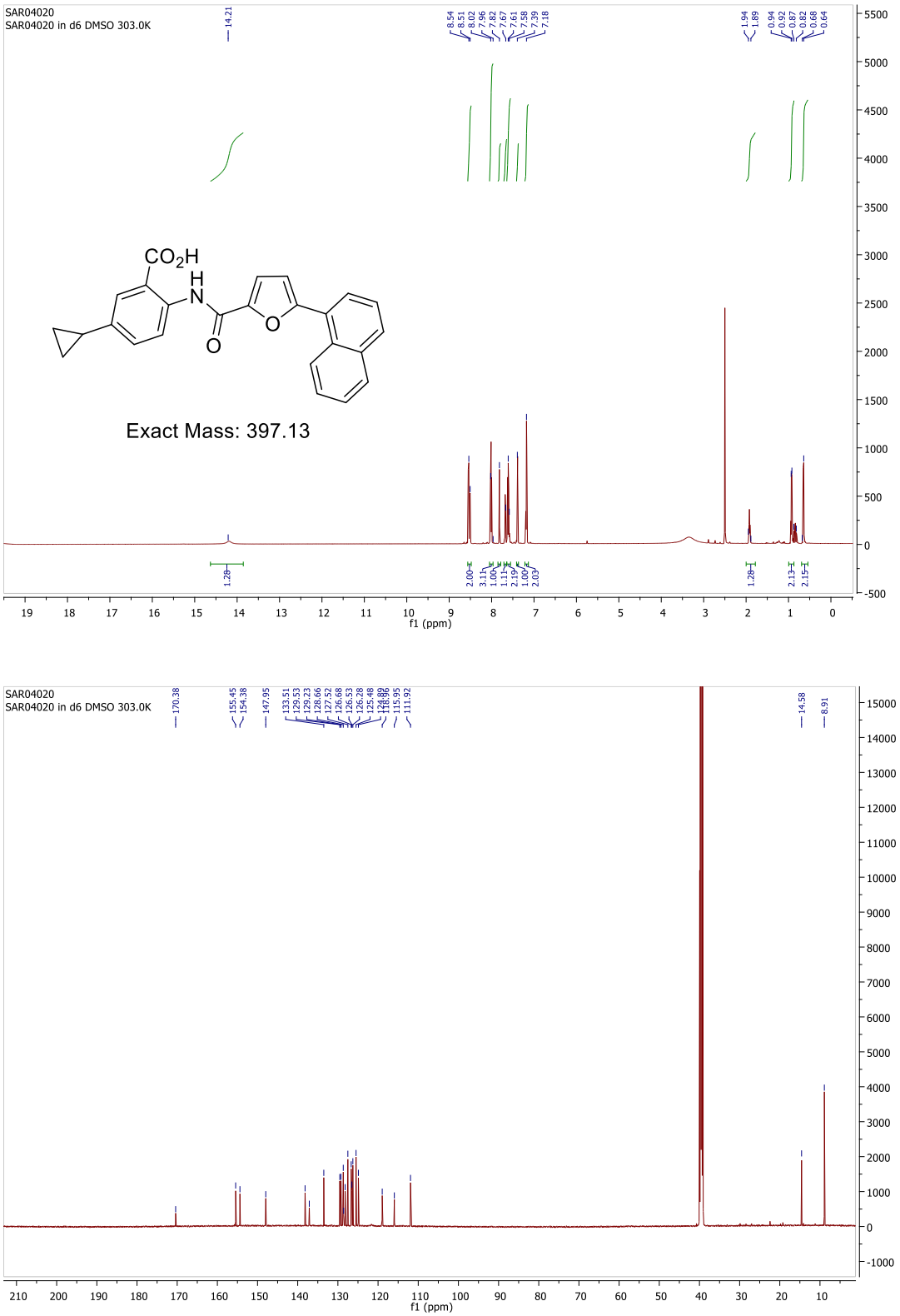

Figure S41. ^{1}H- and ^{13}C-NMR spectra of compound **37**

LC/MS data set of 5-cyclopropyl-2-(5-(naphthalen-1-yl)furan-2-carboxamido)benzoic acid (37)

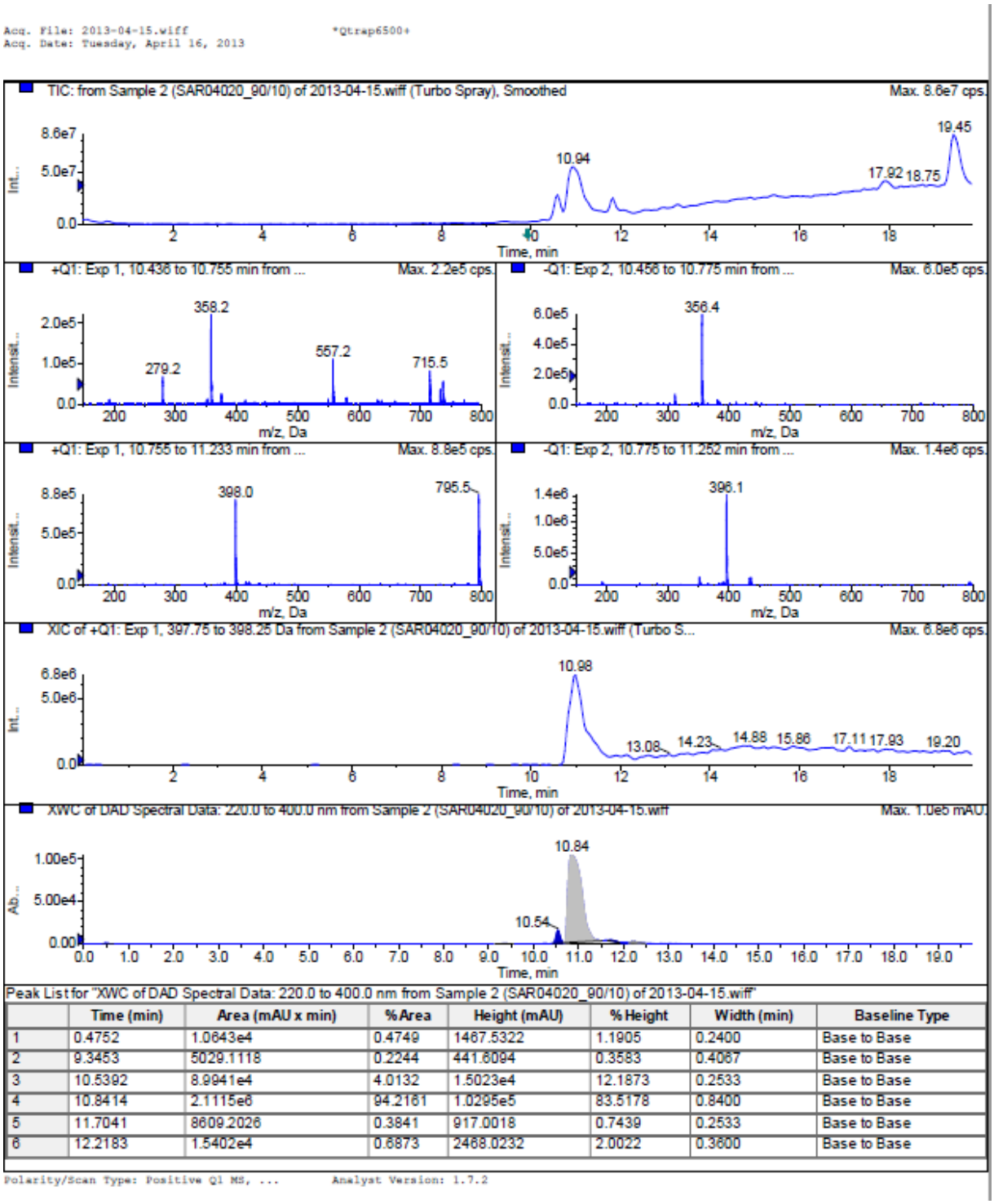

	Time (min)	Area (mAU x min)	% Area	Height (mAU)	% Height	Width (min)	Baseline Type
1	0.4752	1.0643e4	0.4749	1467.5322	1.1905	0.2400	Base to Base
2	9.3453	5029.1118	0.2244	441.6094	0.3583	0.4067	Base to Base
3	10.5392	8.9941e4	4.0132	1.5023e4	12.1873	0.2533	Base to Base
4	10.8414	2.1115e6	94.2161	1.0295e5	83.5178	0.8400	Base to Base
5	11.7041	8609.2026	0.3841	917.0018	0.7439	0.2533	Base to Base
6	12.2183	1.5402e4	0.6873	2468.0232	2.0022	0.3600	Base to Base

Figure S42. LC/MS data set of compound **37**

^{1}H- and ^{13}C-NMR spectra of 4,5-dimethoxy-2-(6-(naphthalen-1-yl)picolinamido)benzoic acid (65)

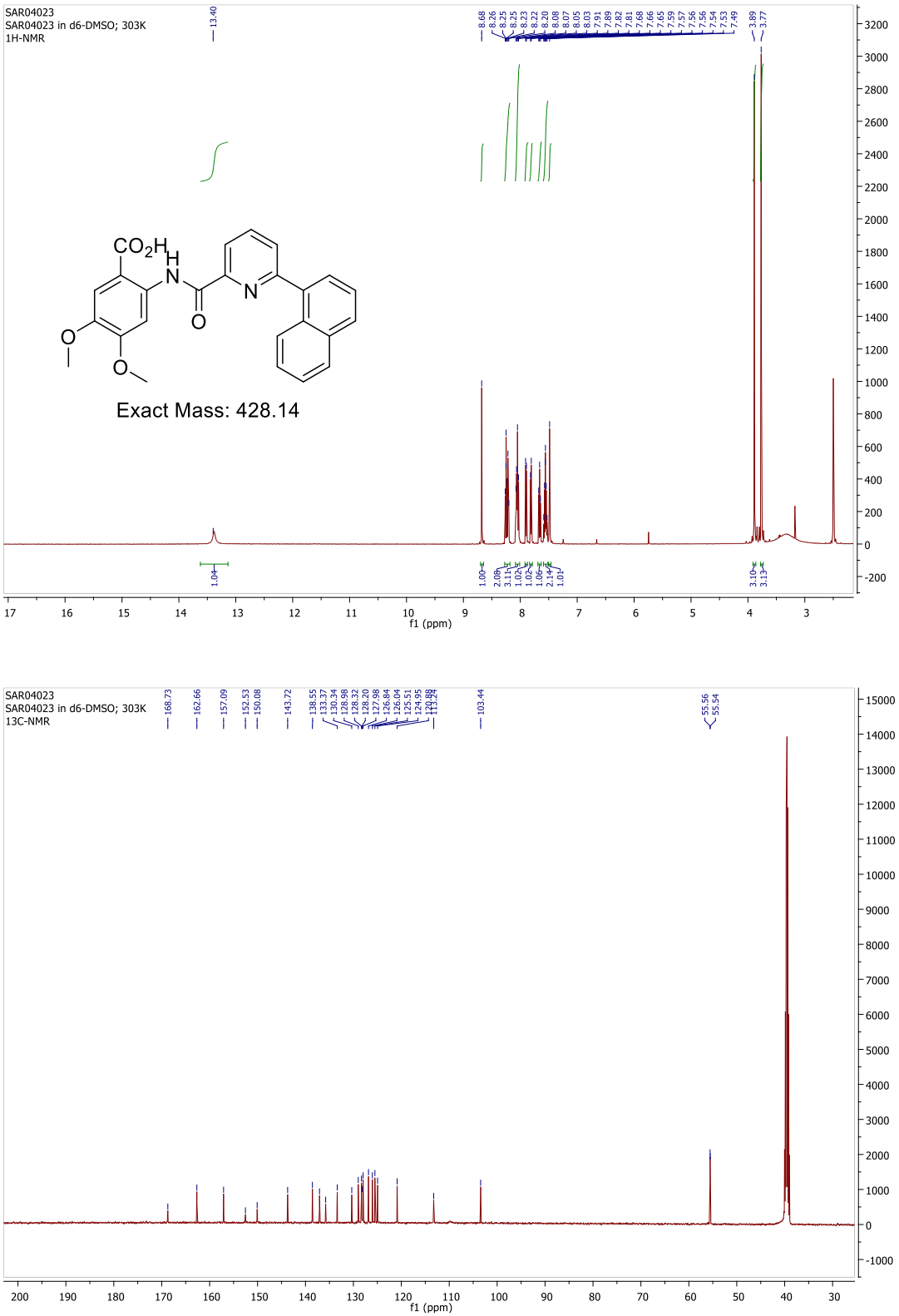

Figure S43. ^{1}H- and ^{13}C-NMR spectra of compound **65**

LC/MS data set of 4,5-dimethoxy-2-(6-(naphthalen-1-yl)picolinamido)benzoic acid (65)

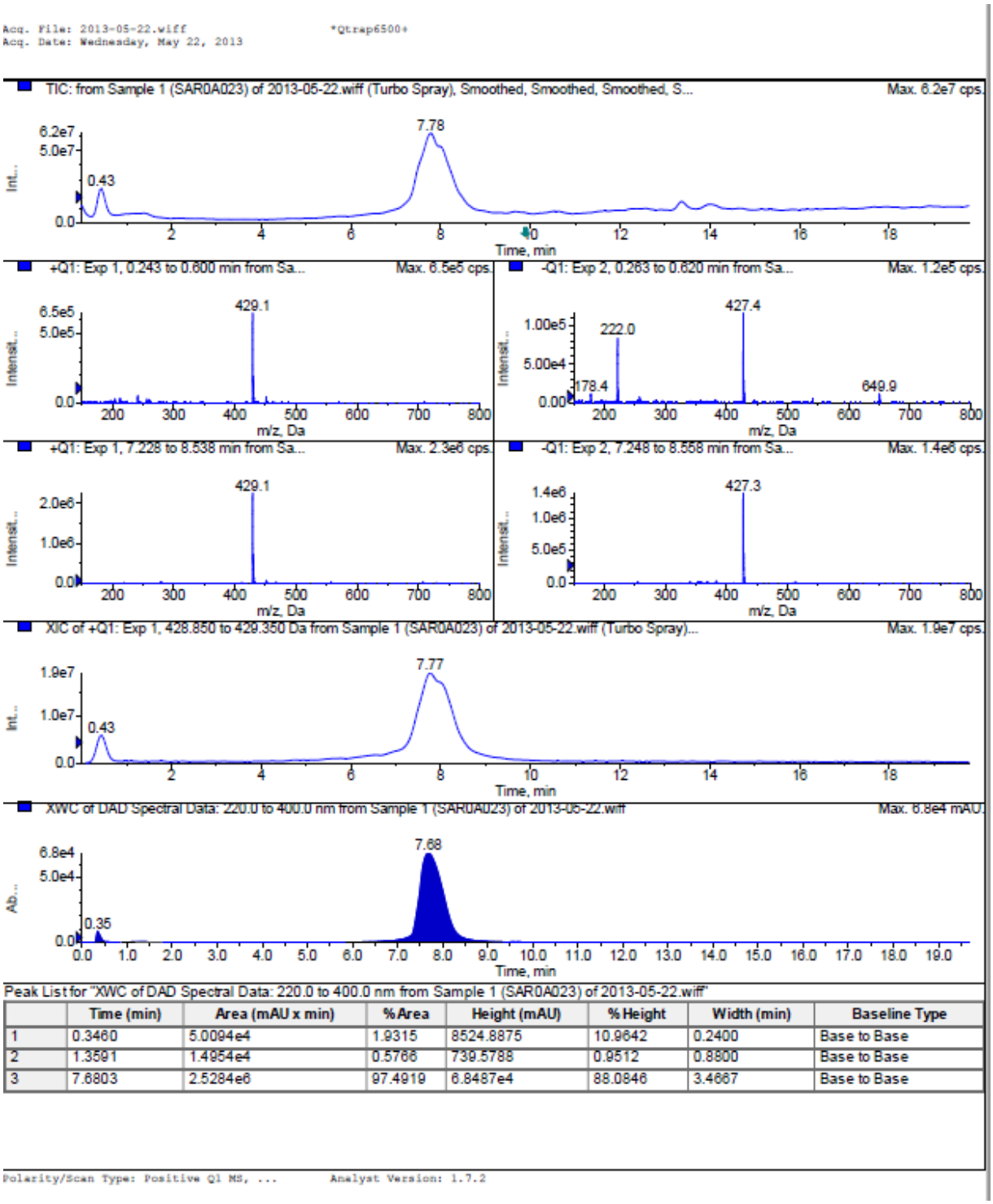

	Time (min)	Area (mAU x min)	%Area	Height (mAU)	%Height	Width (min)	Baseline Type
1	0.3460	5.0094e4	1.9315	8524.8875	10.9642	0.2400	Base to Base
2	1.3591	1.4954e4	0.5766	739.5788	0.9512	0.8800	Base to Base
3	7.6803	2.5284e6	97.4919	6.8487e4	88.0846	3.4667	Base to Base

Figure S44. LC/MS data set of compound **65**

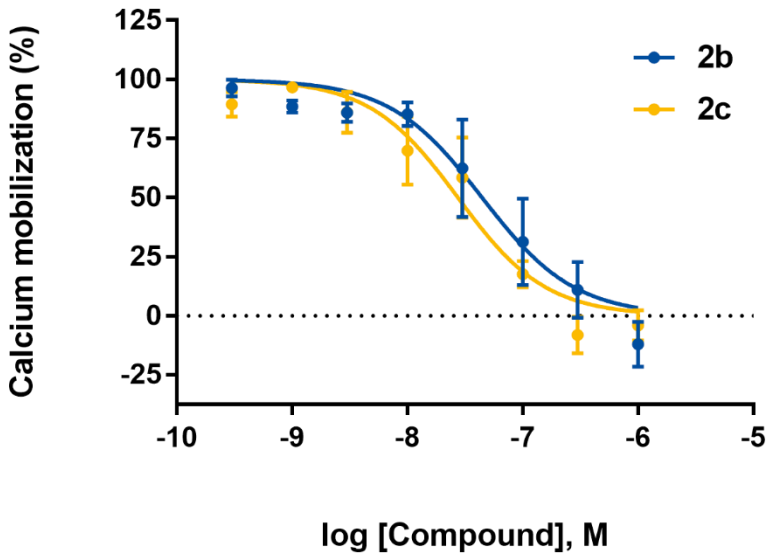

Figure S45. Concentration-inhibition curves of known antagonists determined in Ca^{2+} mobilization assays performed using 1321N1-hGPR17 cells. An EC_{80} concentration of agonist **1** was used for receptor activation. Data points represent means ± SEM from three to five independent experiments performed in duplicate.

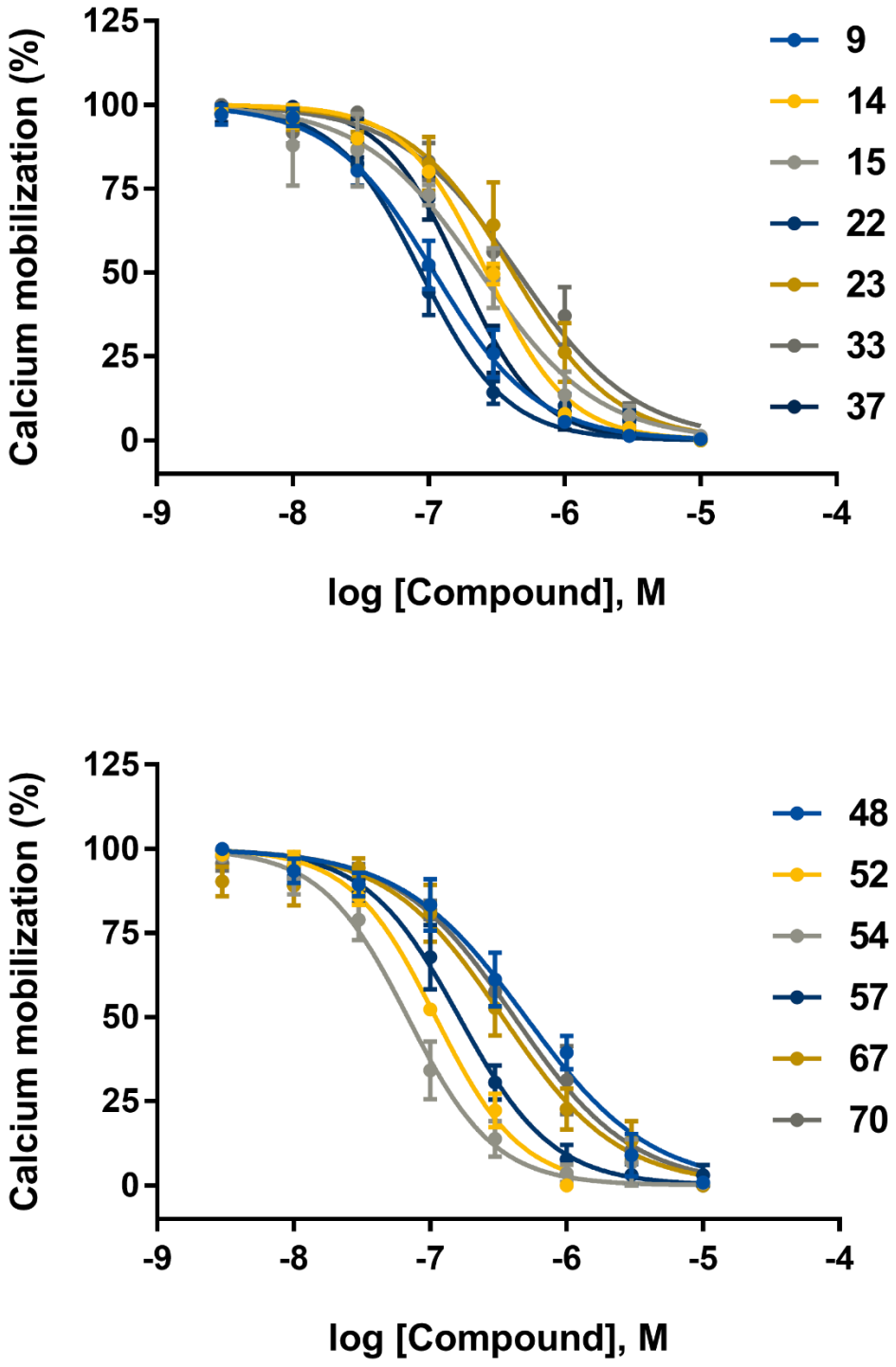

Figure S46. Concentration-inhibition curves of selected anthranilic acid derivatives determined in Ca^{2+} mobilization assays performed with 1321N1-hGPR17 cells. An EC_{80} concentration of agonist **1** was used for receptor activation. Data points repesent means ± SEM of three to five independent experiments performed in duplicate. For pIC_{50} values see Table 6 in the main text.

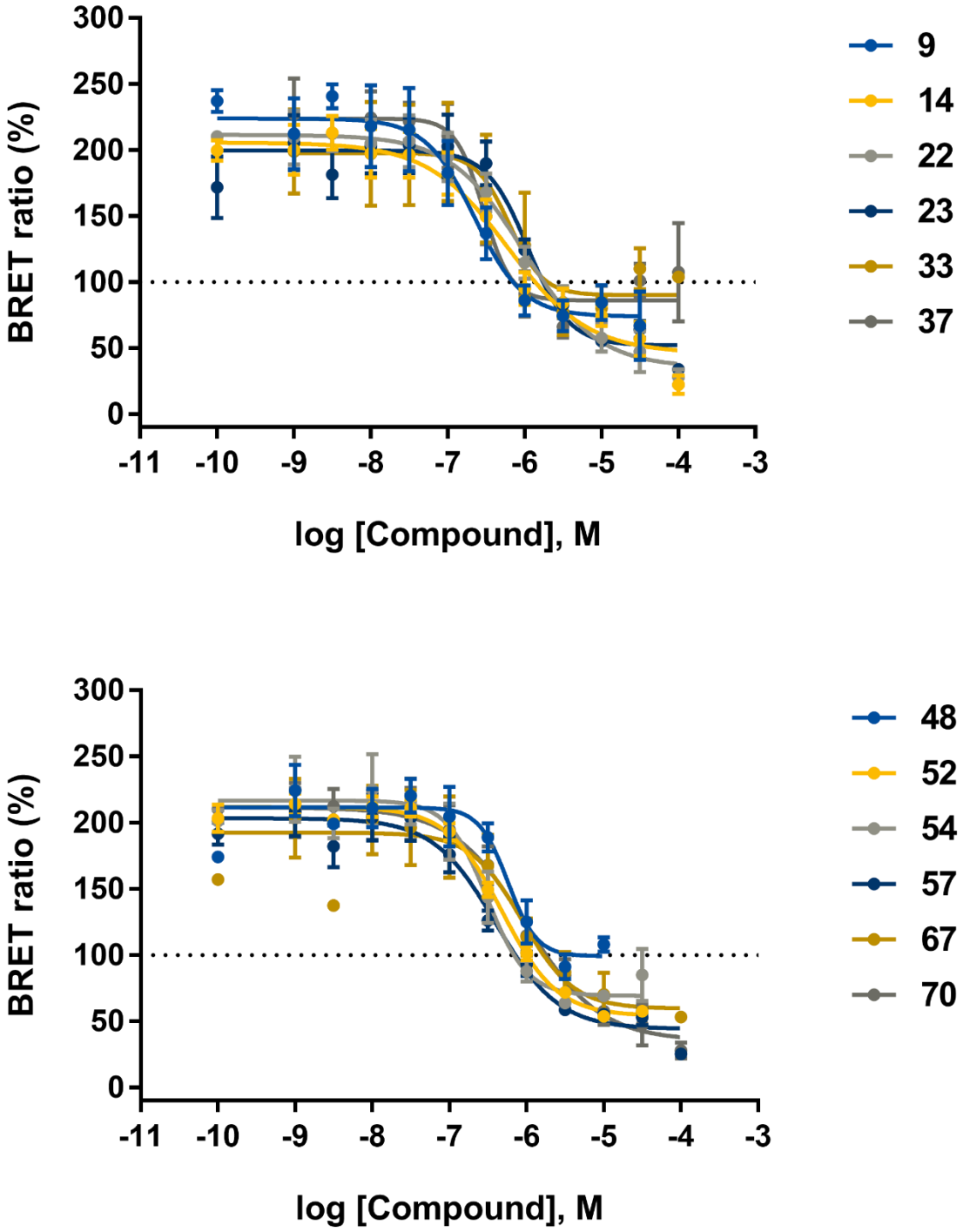

Figure S47. Concentration-inhibition curves of selected anthranilic acid derivatives determined in G protein effector-membrane translocation assays (GEMTA) performed with HEK293-hGPR17 cells. The receptor was activated by an EC_{80} concentration of agonist **1**. Basal activation = 100 %. Data points represent means ± SEM from four independent experiments performed in duplicate. For pIC_{50} values see Table 6 in the main text.

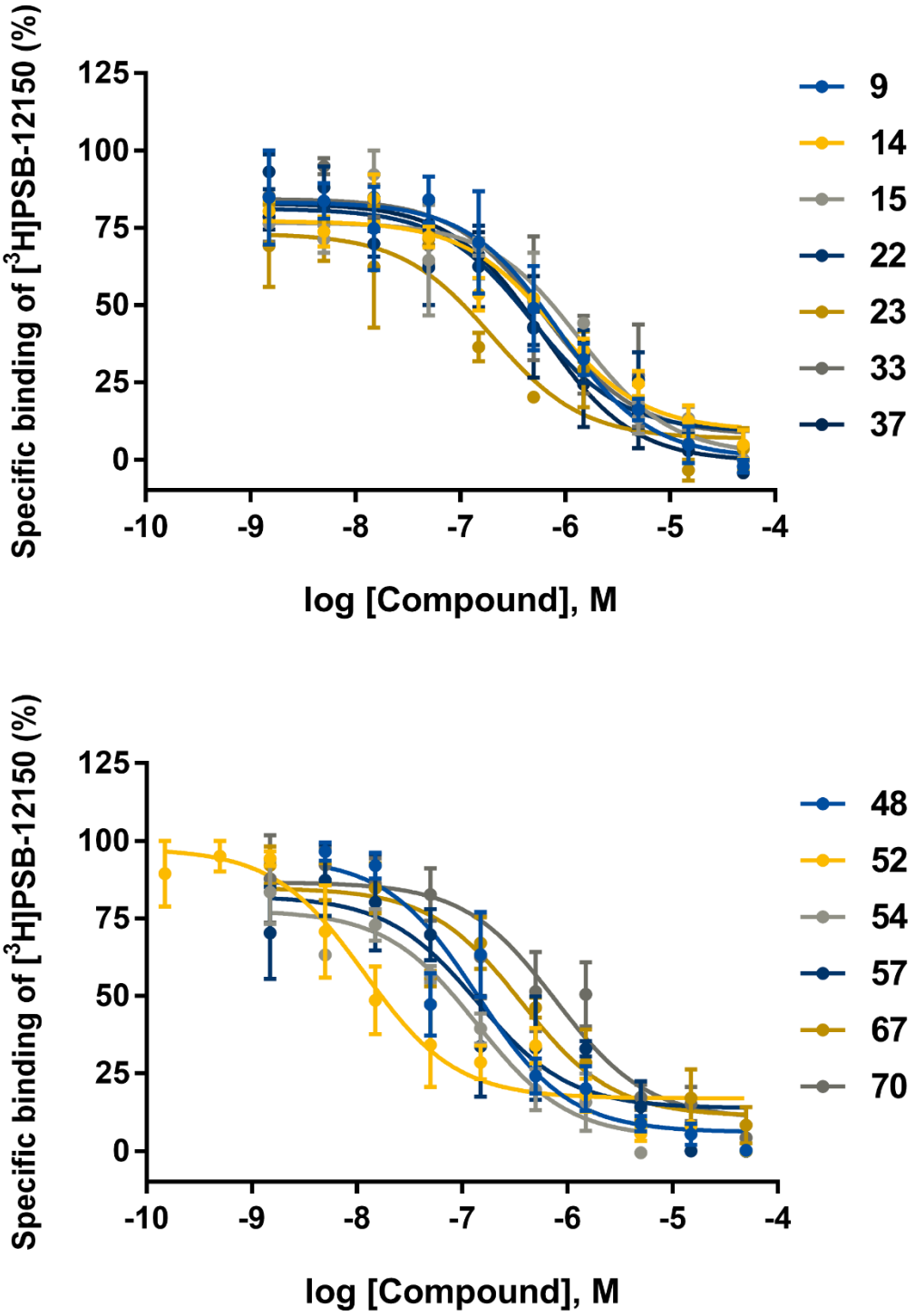

Figure S48. Binding competition curves of selected anthranilic acid derivatives versus [^{3}H]PSB-12150 at human GPR17 in membrane preparations of CHO-FITR-hGPR17 cells. Data points represent means ± SEM from three independent experiments performed in duplicate. For pK_i values see Table 6 in the main text.

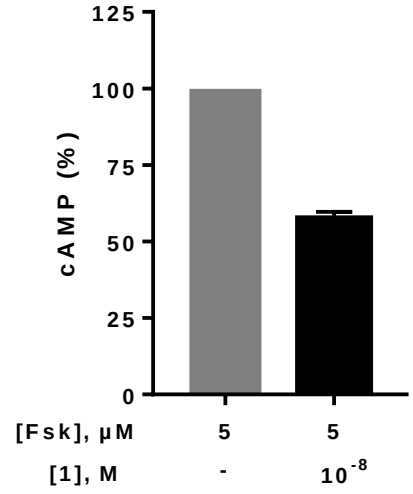

Figure S49. Inhibition of forskolin-stimulated cAMP production by agonist **1** (10 nM, EC_{90}) determined in CHO-FITR-hGPR17 cells.

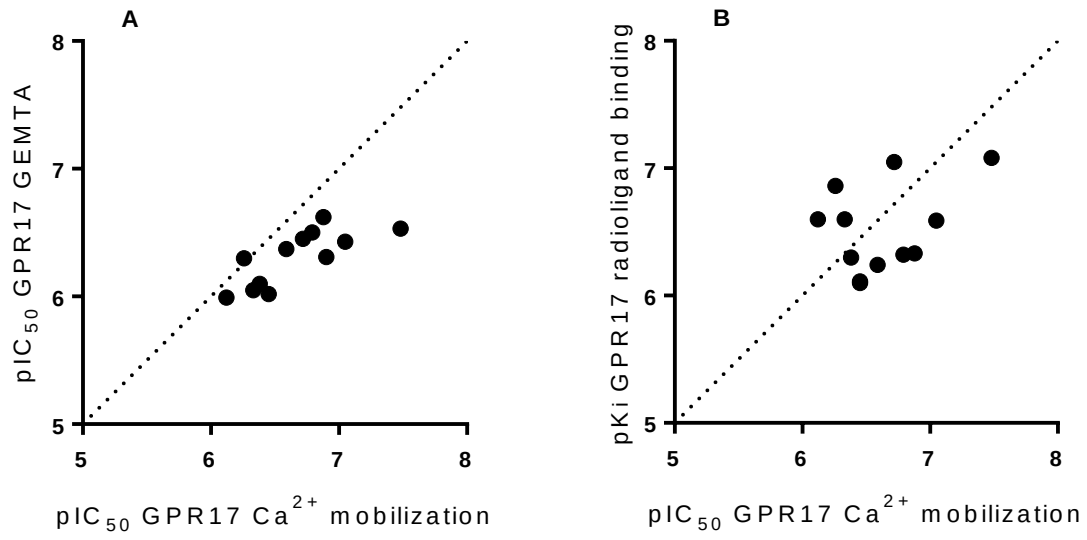

Figure S50. (**A**) Correlation of data obtained for selected anthranilic acid derivatives as GPR17 antagonists, determined in calcium mobilization assays and GEMTA assays at human GPR17. (**B**) Correlation of data obtained for selected anthranilic acid derivatives as GPR17 antagonists, determined in calcium mobilization assays and in radioligand binding assays at human GPR17. Data point for **52** was excluded as an outlier.

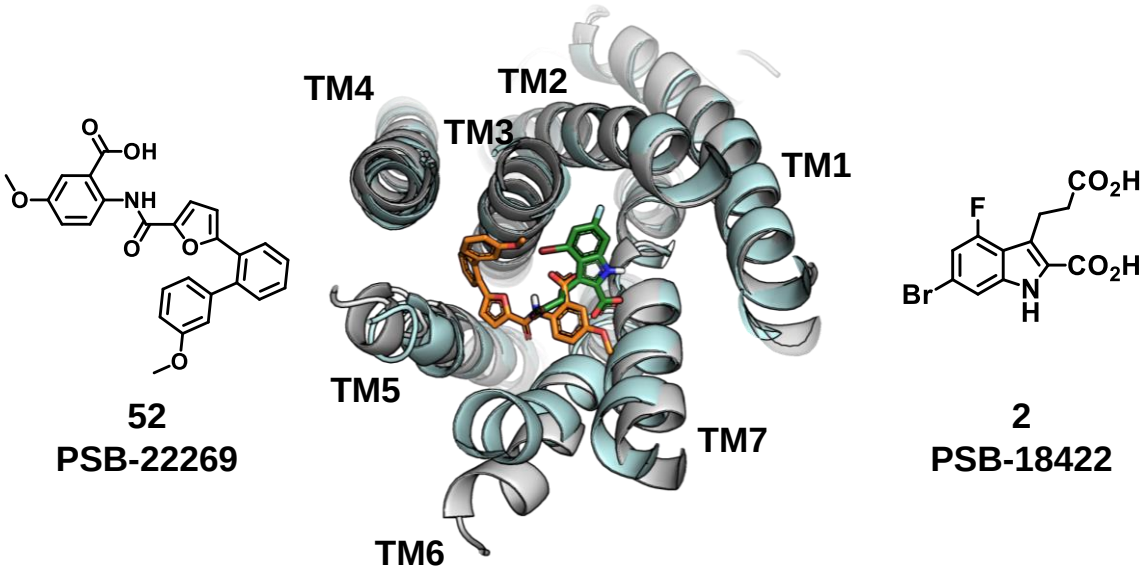

Figure S51. Overlay of the active-state structure of the human GPR17 (pale green, derived from the agonist-bound human $P2Y_{12}R$ crystal structure, PDB 4PXZ) and the inactive-state GPR17 structure (gray, derived from the antagonist-bound human $P2Y_{12}R$ crystal structure, PDB 4NTJ), depicted in a cartoon representation showing the predicted binding pose of agonist **2** (PSB-18422, dark green) and antagonist **52** (orange), depicted as stick models.

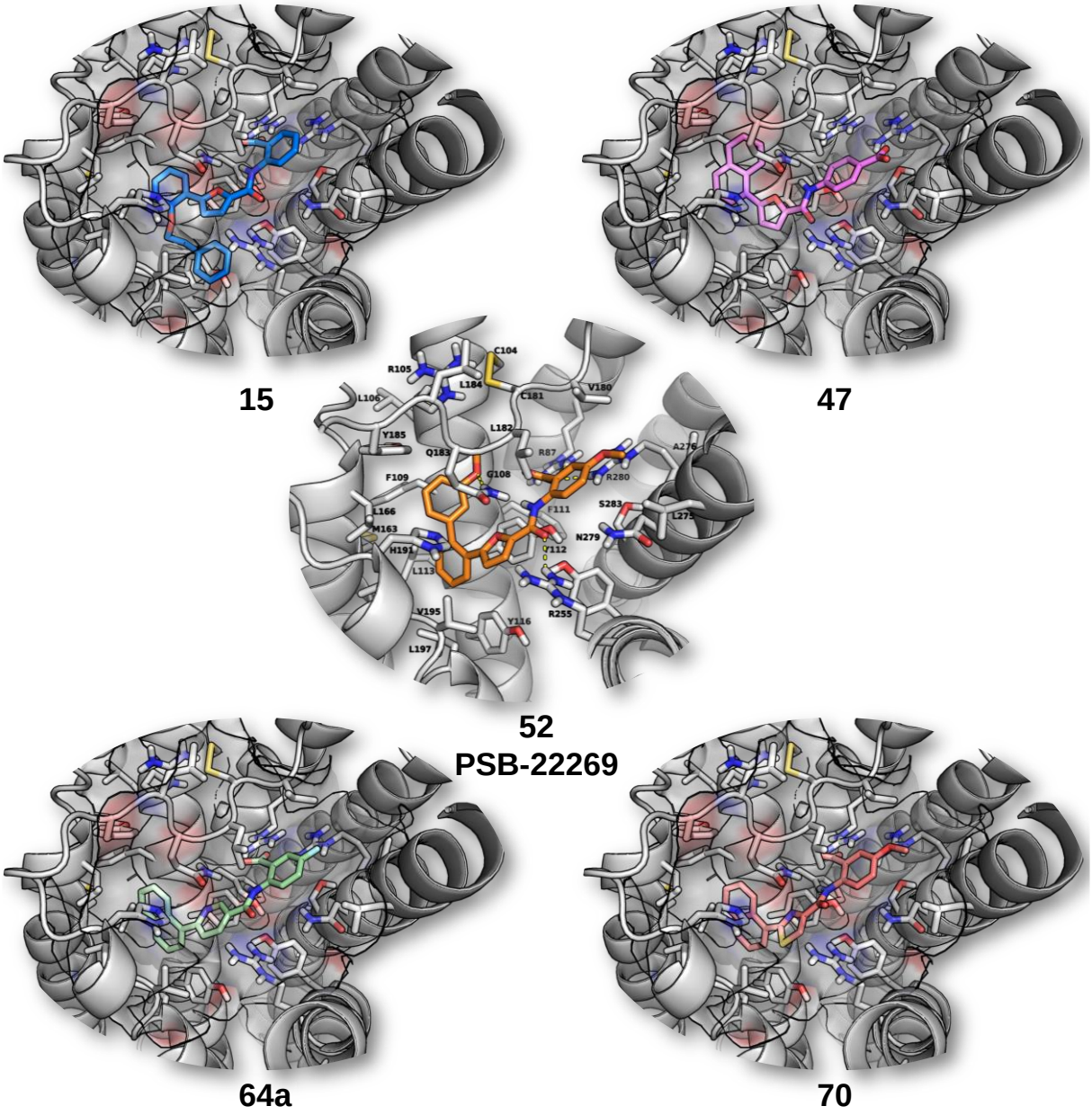

Figure S52. The predicted binding pose of **52** (colored orange) is compared with the binding poses of **15** (colored blue), **47** (colored magenta), **64a** (colored light green), and **70** (colored light red), represented as stick models docked into the inactive state of the human GPR17 receptor model (based on the human $P2Y_{12}R$ crystal structure, PDB 4NTJ) shown in cartoon (colored gray) with the important amino acids in the binding pocket (colored gray).